Innovative Materials for Water Purification

Maryam Hmoudah

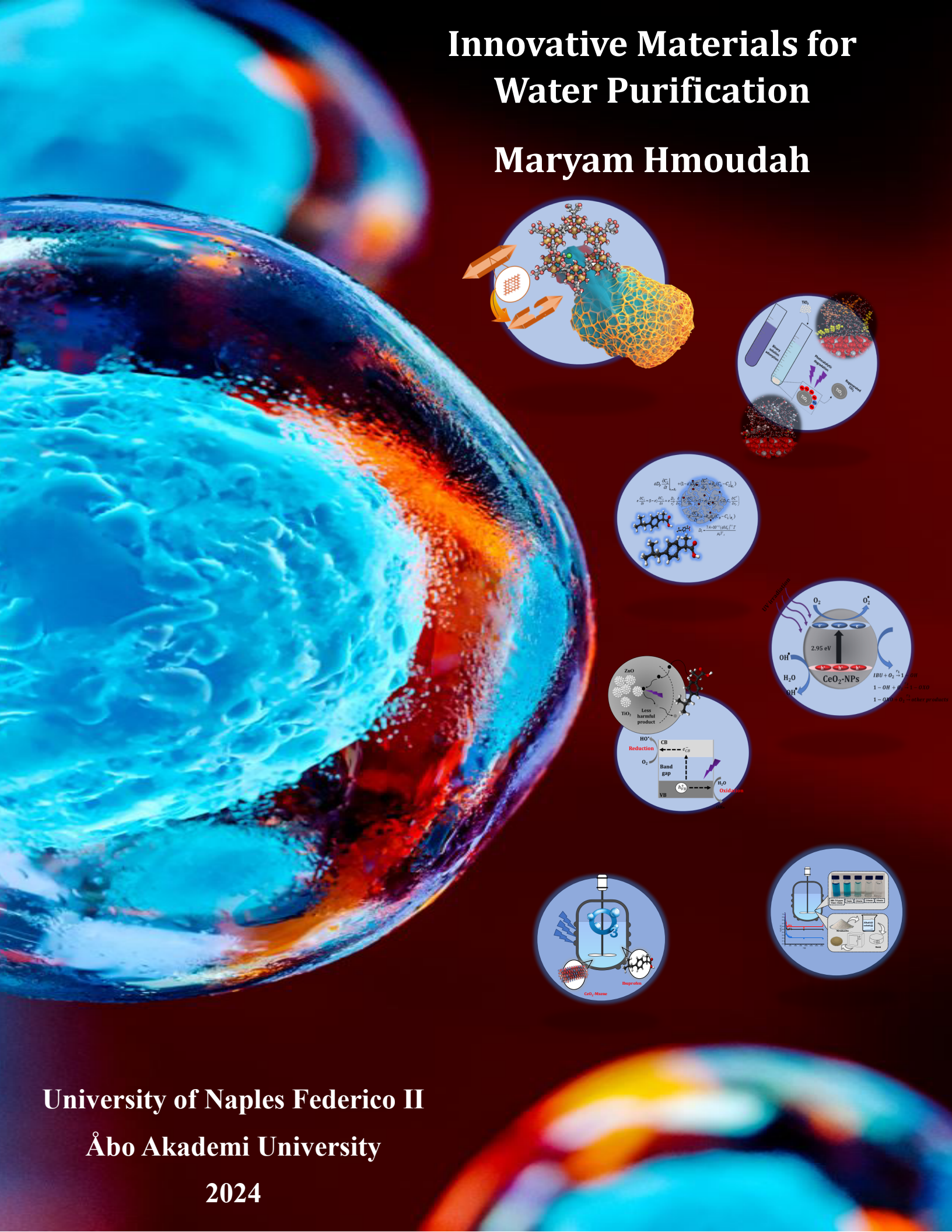

University of Naples Federico II

Åbo Akademi University

2024

Maryam Hmoudah

Born in 1986 in Nablus, Palestine

MSc., Chemical Engineering 2016

Department of Chemical and Petroleum Engineering, Calgary, Canada

Innovative Materials for Water Purification

Maryam Hmoudah

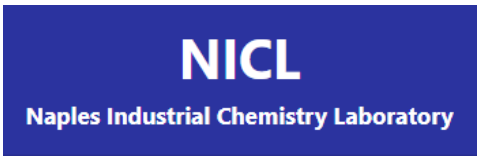

Naples Industrial Chemistry Laboratory/ University of Naples Federico II

Laboratory of Industrial Chemistry and Reaction Engineering/Åbo Akademi University

2024

Agreement on Joint Doctoral Supervision and Training

Accordo sulla supervisione e la formazione congiunta del dottorato

A CONVENTION FOR THESIS CO-TUTELAGE

CONVENZIONE DI CO-TUTELA DI TESI

between

UNIVERSITA' DEGLI STUDI DI NAPOLI FEDERICO II (UNINA), ITALY

And

ÅBO AKADEMI UNIVERSITY (ÅAU), FINLAND

Thesis supervisors and examiners		
Martino Di Serio	Professor, University of Naples Federico II, Naples, Italy	Supervisor
Vincenzo Russo	Professor, University of Naples Federico II, Naples, Italy	Supervisor
Tapio Salmi	Professor, Åbo Akademi University, Turku/ Åbo, Finland	Supervisor
Moisés Canle López	Professor, University of A Coruña, A Coruña, Spain	Examiner

ISBN: (Printed version)

ISBN: (Electronic version)

ISSN: (Acta technologiae chemicae Aboensia 2024 A/1)

Painosalama OY Turku/Åbo 2024

To my beloved home country, the Holy Land;
"Palestine"

Preface

With a grateful heart and a sense of accomplishment, I take this moment to acknowledge the completion of my PhD journey. First and foremost, all praises to Allah SWT for the great blessings I have in my life and for the opportunities and challenges that have allowed me to grow and evolve.

To my advisors, the superstars of chemical reaction engineering, Prof. Martino Di Serio and Prof. Vincenzo Russo at University of Naples Federico II (UniNa) in Italy, and Prof. Tapio Salmi at Åbo Akademi University (ÅAU), Finland. The most humble, professional, and knowledgeable scientists, who have guided me with wisdom and patience. Thank you for shaping my thoughts, for guiding me, and for the opportunities you opened towards the completion of this journey. I will be always grateful for opening your labs and hearts for me to join the beautiful NICL and TKR families. I would like also to thank Prof. Riccardo Tesser, Prof. Dmitry Murzin, Dr. Kari Eränen, and Dr. Pasi Tolvanen for all the discussions and advice you shared with me.

I would like to thank my tutor at UniNa Prof. Flavia Nastri for the great feedback that helped me to shape the current layout of my thesis. I really am super thankful to Prof. Valeria Costantino and Prof. Angela Lombardi at UniNa, for being very supportive and open to help in all aspects.

No words can express how grateful I am to my soulmate, role model scientist, and altruistic hero "Amjad", I could not make it without your marvelous support and encouragement. You are my friend and the love of my life. You sacrificed lots of things for me, I hope that I will always meet your trust.

My beloved parents and moral compass, Bilal and Alia, and my brothers in the holy land "Palestine", you always believed in me and supported me through the ups and downs, thank you for being my rock and my home. Your love and encouragement have been my driving force.

My parents-in-law, Yaser and Samar, you made this journey possible because you always treated me as your daughter and covered us with your unconditional love. Thank you from the bottom of my heart. Baba Yaser, you did not live enough to see me completing my PhD degree. May your soul rest in peace.

My gorgeous kids and stars, Osayd, Samar, and Milana. It was the toughest thing that happened to me to stay away from you. Your talks and smiles helped me to surmount all challenges. I hope you will always be proud of your dad and mom.

To my Italian friends Tommaso, Francesco, Carmelina, Rosa, Rosita, Michele, Rosanna, Carmela, Marica, Michela, Eleonora, Benedetta, Carmen, Roberto, Massimo, Luca, Federica, and Emiliano who have made this journey a little easier and a lot more fun, thank you for every greeting Ciao, Boungiorno, Buongiornissimo, or good morning. All the selfies we had reflect the very positive vibes you always shared with me. Big thanks to my friends Mouad Hachhach and Nemanja Vučetić for the unlimited support and kindness you showed during my stay in Turku.

Last but not least, I am very grateful to my teacher and life mentor Prof. Amer El-Hamouz at An-Najah National University (ANNU). You will always be a source of inspiration on the personal and professional levels. I am also very thankful for the support I received from my home institution ANNU and all my teachers and colleagues. Big thanks also extend to my sweet loving friends Weam and Saja for being very supportive and caring during this journey.

No words can describe how thankful I am to every Palestinian woman who always demonstrates immense strength, resilience, perseverance, and determination in the face of numerous challenges and hardships we live in the beloved Palestine. The tremendous sacrifices made by our Palestinian women are exceptional and inspiring. Together, we will pave the way for a brighter future in our pursuit of freedom insh'Allah. And yes, we teach life.

Maryam
January 2024

Abstract

The insecure future of freshwater resources is undoubtedly a serious challenge for all living beings. Human activities generate harmful compounds or pollutants that should be treated before they are released into the aquatic ecosystems. The chaotic discharge of organic and inorganic compounds is considered a long-standing and aggravated global problem. Particularly, emerging contaminants, such as pharmaceutically active compounds (PhACs), personal care products, surfactants, various industrial additives, and endocrine-disrupting chemicals have proven to harm human health and ecological systems. Most of the current physical, chemical, and biological technologies used in wastewater treatment are prohibitively expensive they and face many operational challenges. Therefore, the development of economic, viable, and scalable techniques can profoundly secure access to safe and good drinking water quality.

The advancement in the last two decades of wastewater purification methods including adsorption on non-conventional solids, advanced oxidation, and photodegradation is gaining massive attention. These technologies have many advantages, once compared to other treatment techniques, such as simplicity, cost feasibility, and the ease of operation including applying moderate operating conditions.

The main aim of this doctoral thesis is to investigate the efficiency of novel in-house prepared materials to remove emerging contaminants from wastewaters such as ibuprofen, bromocresol green, alizarin red s, and methylene blue, and to compare them with classical commercial materials through adsorption and photodegradation. Both batch and semibatch operating modes were studied considering different operational parameters to investigate the kinetics. This work also includes experimental data validation through simulations for batch and semibatch systems. Advanced reactor modelling was carried out, describing the collected data in both scales with a rigorous approach, considering both physical and chemical phenomena appearing in the reaction network, i.e. discriminating between the mass transfer and reaction limiting steps.

Referat

Den osäkra framtiden för sötvattenresurserna är utan tvekan en allvarlig utmaning för levande organismer. Människans aktiviteter genererar skadliga kemiska föreningar och föroreningar som borde destrueras innan de släpps ut i ekosystemet. Det kaotiska utsläppet av organiska och oorganiska föreningar är ett långvarit och förvärrat globalt problem. Speciellt nya föroreningar, såsom farmaceutiskt aktiva föreningar (PhAC), produkter för personligt vård, ytaktiva ämnen, diverse industriella komponenter och hormonstörande kemikalier har visat sig vara skadliga för människans hälsa och ekosystemet i helhet. De flesta av nuvarande kemiska, fysikaliska och biologiska teknologierna som används för att rena avloppsvatten är orimligt dyra och de är förknippade med många praktiska problem. Därför ska utvecklingen av ekonomiskt lönsamma och skalbara förfaranden garantera tillgången till säker och god dricksvattenkvalitet.

Framsteg har tagits under de senaste två decennierna i metoder för rening av avloppsvatten, bl.a. adsorption av föroreningar på icke-konventionella fasta ämnen, avancerade oxidationsprocesser och fotokatalytisk nedbrytning har fått stor uppmärksamhet. Dessa teknologier har många fördelar jämfört med konventionella metoder, såsom enkelhet, rimliga kostnader och relativt enkla driftsbetingelser.

Det huvudsakliga syftet med detta doktorsarbete var att undersöka effektiviteten av nya material som vi har preparerat i laboratorieskala för borttagning av föoreningar från avloppsvatten, bl.a. ibuprofen, grön bromkresol, alizarin och metylenblått samt att jämföra dem med klassiska kommersiella material för adsorption och fotokatalytisk nedbrytning. Både satsvisa och halvkontinuerlierliga reaktionsförfaranden studerades genom att variera experimentella parametrar för att kartlägga reaktionskinetiken. Experimentella resultat validerades med hjälp av simulering av satsvisa och halvkontinuerliga reaktorsystem. Avancerad reaktormodellering tillämpades för att beskriva experimentella data på ett rigoröst sätt, genom att beakta kemiska och fysikaliska fenomen som förekom i reaktionssystemen. På detta sätt kunde massöverföringseffekter och kinetiska effekter kartläggas i detalj.

Sommario

Il futuro insicuro delle risorse di acqua dolce rappresenta senza dubbio una sfida seria per gli esseri viventi. Le attività umane generano composti nocivi o inquinanti che dovrebbero essere trattati prima di essere rilasciati nell'ecosistema. Lo scarico non regolamentato di composti organici e inorganici è considerato un problema globale di lunga data e aggravato. In particolare, i contaminanti emergenti, come i composti farmaceuticamente attivi (PhAC), i prodotti per la cura personale, i tensioattivi, vari additivi industriali e le sostanze chimiche che alterano il sistema endocrino hanno dimostrato di danneggiare la salute umana e i sistemi ecologici. La maggior parte delle attuali tecnologie fisiche, chimiche e biologiche utilizzate nel trattamento delle acque reflue sono proibitivamente costose e devono affrontare molte sfide operative. Pertanto, lo sviluppo di tecniche economiche, fattibili e scalabili può garantire profondamente l'accesso ad acqua potabile sicura e di buona qualità.

Il progresso negli ultimi due decenni dei metodi di purificazione delle acque reflue, compreso l'adsorbimento su solidi non convenzionali, l'ossidazione avanzata e la fotodegradazione, sta guadagnando enorme attenzione. Queste tecnologie presentano molti vantaggi, rispetto ad altre tecniche di trattamento, come semplicità, fattibilità dei costi e facilità di funzionamento, inclusa l'applicazione di condizioni operative moderate.

Lo scopo principale di questa tesi di dottorato è studiare l'efficienza di nuovi materiali preparati internamente per rimuovere contaminanti emergenti dalle acque reflue come ibuprofene, verde bromocresolo, rosso alizarina e blu di metilene, e confrontarli con i classici materiali commerciali attraverso un maggiore adsorbimento. e fotodegradazione. Entrambe le modalità batch e semibatch sono state studiate considerando diversi parametri operativi per studiare la cinetica della reazione chimica. Questo lavoro include anche la validazione dei dati sperimentali attraverso simulazioni per sistemi batch e semibatch. È stata effettuata una modellazione avanzata di reattori chimici, descrivendo i dati raccolti in entrambe le scale con un approccio rigoroso, considerando sia i fenomeni fisici che chimici che si verificano nella rete di reazione, ovvero distinguendo il trasferimento di massa e le fasi limitanti della reazione.

List of publications

I. V. Russo, ***M. Hmoudah***, F. Broccoli, M. R. Iesce, O. S. Jung, and M. Di Serio, Applications of Metal Organic Frameworks in Wastewater Treatment: A Review on Adsorption and Photodegradation, Front. Chem. Eng, 2 (2020): 581487. doi.org/10.3389/fceng.2020.581487

II. ***M. Hmoudah***, A. El-Qanni, R. Tesser, R. Esposito, A. Petrone, O. Jung, T. Salmi, V. Russo, and M. Di Serio Assessment of the Robustness of MIL-88A in an Aqueous Solution: Experimental and DFT Investigations, Materials Science and Engineering: B 288 (2023): 116179. doi.org/10.1016/j.mseb.2022.116179

III. ***M. Hmoudah***, A. El-Qanni, S. Abuhatab, N. N. Marei, A. El-Hamouz, B. J. Abu Tarboush, I. H Alsurakji, H. M. Baniowda, V. Russo, M. Di Serio, Competitive adsorption of Alizarin Red S and Bromocresol Green from aqueous solutions using brookite TiO_2 nanoparticles: experimental and molecular dynamics simulation, Environmental Science and Pollution Research 29(51), (2022): 77992-78008. doi.org/10.1007/s11356-022-21368-7

IV. ***M. Hmoudah***, M. E. Fortunato, R. Paparo, M. Trifuoggi, A. El-Qanni, R. Tesser, D. Murzin, T. Salmi, V. Russo, M. Di Serio, Ibuprofen adsorption on activated carbon: thermodynamic and kinetic investigation via adsorption dynamic intraparticle model (ADIM), Langmuir, 2023. doi.org/10.1021/acs.langmuir.2c03350

V. N. Gallucci, ***M. Hmoudah***, E. Martinez, A. El-Qanni, M. Di Serio, L. Paduano, G. Vitiello, V. Russo, Sustainable photodegradation of ibuprofen using CeO_2 nanostructured materials, Journal of Environmental Chemical Engineering 10.3 (2022): 107866. doi.org/10.1016/j.jece.2022.107866

VI. ***M. Hmoudah***, C. Chianese, A. El-Qanni, V. Russo, M. Di Serio, T. Salmi, Photodegradation of ibuprofen using ZnO and TiO_2 nanoparticles: Comprehensive kinetics modeling, mechanisms, and thermodynamics study, Environmental Pollution. *(submitted)*

VII. ***M. Hmoudah***, R. Paparo, M. De Luca, M. E. Fortunato, R. Tesser, M. Di Serio, C. Ferone, G. Roviello, O. Tarallo, V. Russo, Adsorption of methylene blue on metakaolin-based geopolymers: a kinetic and thermodynamic investigation, Langmuir. *(submitted)*

Related publications

VIII. M. Melchiorre, D. Lentini, M. Cucciolito, F. Taddeo, ***M. Hmoudah***, M. Di Serio, F. Ruffo, V. Russo, and R. Esposito. Sustainable ketalization of glycerol with ethyl levulinate catalyzed by the iron(III)-based Metal-Organic Framework MIL-88A, Molecules 27, no. 21 (2022): 7229. doi.org/10.3390/molecules27217229

IX. M. Toscanesi, V. Russo, A. Medici, A. Giarra, ***M. Hmoudah***, M. Di Serio, M. Trifuoggi, Heterogeneous Photodegradation for the Abatement of Recalcitrant COD in Synthetic Tanning Wastewater, Journal of ChemEngineering 6, no. 2 (2022): 25. doi.org/10.3390/chemengineering6020025

X. A. El-Qanni, M. Alsayed, I. H. Alsurakji, M. Najjar, D. Odeh, S. Najjar, ***M. Hmoudah***, M. Zubair, V. Russo, and M. Di Serio. A technoeconomic assessment of biological sludge dewatering using a thermal rotary dryer: a case study of design applicability, economics, and managerial feasibility, Biomass Conversion and Biorefinery (2022): 1-15. doi.org/10.1007/s13399-022-03480-3

List of related contributions

1. ***M. Hmoudah***, C. Chianese, V. Russo, M. Di Serio, T. Salmi, Investigating Photocatalytic Performance and Kinetics of Commercial TiO_2-P25 and ZnO Nanoparticles for Ibuprofen Photodegradation. 15th European congress on catalysis, Prague, Czech Republic, August 27th – September 1st, 2023. (Poster presentation)
2. ***M. Hmoudah***, P. Tolvanen, V. Russo, M. Di Serio, T. Salmi, Revolutionizing Wastewater Treatment: The Potential of Mxenes in Removing Emerging Contaminants, Finnish Young Scientist Forum for Catalysis, March 31st, 2023 (Poster presentation)
3. ***M. Hmoudah***, V. Russo, M. Di Serio, T. Salmi, The role of Women in STEM, Schlumberger Foundation Faculty for the Future Fellows & Alumnae Regional Forum, Cambridge, United Kingdom, October 23rd-26th, 2022. (Poster presentation)
4. ***M. Hmoudah***, V. Russo, M. Di Serio, T. Salmi, Innovative Materials for Water Purification, October 21st, 2022, Aurum day (Poster presentation)
5. ***M. Hmoudah***, A. El-Qanni, R. Tesser, R. Esposito, A. Petrone, F. Taddeo, O.S. Jung, T. Salmi, V. Russo, M. Di Serio, Assessment of the Robustness of MIL-88A in an Aqueous Solution: experimental and DFT investigations, XXII National Congress on Catalysis 2022, Riccione, Italy, 4-7 September, 2022. (Poster presentation)
6. O. Tammaro, M. Chianese, ***M. Hmoudah***, R. Tesser, L. Fabris, M. Camellone, B. Masenelli, V. Russo, M. Di Serio, S. Esposito, Reverse Micelles Synthesis of Mesoporous Fe-doped CeO_2 as UV/Visible Photocatalyst for Ibuprofen Degradation, 1° Congress Nazionale della Divisione di Chimica per le Tecnologie della Società Chimica Italiana, Naples, Italy, 21-25 August, 2022. (Oral presentation)
7. ***M. Hmoudah***, M. E. Fortunato, R. Paparo, M. Trifuoggi, R. Tesser, M. Di Serio, V. Russo, Adsorption of Ibuprofen on Activated Carbon: Experimental Data Validation using Adsorption Dynamic Intraparticle Model (ADIM)., 26th International Congress of Chemical and Process Engineering (CHISA), Prague, Czech Republic, 21-25 August, 2022. (Poster presentation)

8. ***M. Hmoudah***, M. Di Serio, V. Russo, Promising Applications of Metal Organic Frameworks (MOFs) in Wastewater Treatment through Adsorption and Photodegradation., 7th CUCS, Naples, Italy, April 21st-23rd, 2021. (Oral presentation)
9. ***M. Hmoudah***, N. Gallucci, E. Martinez, A. El-Qanni, M. Di Serio, L. Paduano, G. Vitiello, V. Russo, Sustainable Photodegradation of Ibuprofen using CeO_2 Nanostructured Materials, Merk Young Chemists Symposium, Rimini, Italy, November 22nd-24th, 2021. (Oral presentation)
10. ***M. Hmoudah***, V. Russo and M. Di Serio, Assessment of the Robustness of Iron-Based Metal organic Frameworks (MIL-88A) in an Aqueous Environment, XXVII Congresso Nazionale della Società Chimica Italiana September 14th-23rd, 2021, Virtual Conference. (Oral presentation)
11. ***M. Hmoudah***, V. Russo and M. Di Serio, Adsorption and Photocatalytic Degradation of Congo Red Dye from Aqueous Solution using MIL-88 A: Kinetics and Modeling, IUPAC-CCCE 2021 Virtual Conference, Canada, August 13th-20th, 2021. (Oral presentation)

Awards

1st place of best poster contest, sponsored by the Wiley-VCH magazine "Chemical Engineering and Technology" at the International Congress of Chemical and Process Engineering (CHISA 2022), Prague, Czech Republic, August 21st to 25th, 2022, Adsorption of Ibuprofen on actived carbon: experimental data validation using adsorption dynamic intraparticle model (ADIM).

2nd place, Ice Breaker Contest, Schlumberger Foundation Faculty for the Future Fellows and Alumnae Regional Forum, Cambridge, United Kingdom October 23rd to 26th, 2022.

Featured work

Selected front cover art for Langmuir Journal that is associated with the published article "Ibuprofen Adsorption on Activated Carbon: Thermodynamic and Kinetic Investigation via the Adsorption Dynamic Intraparticle Model (ADIM)".

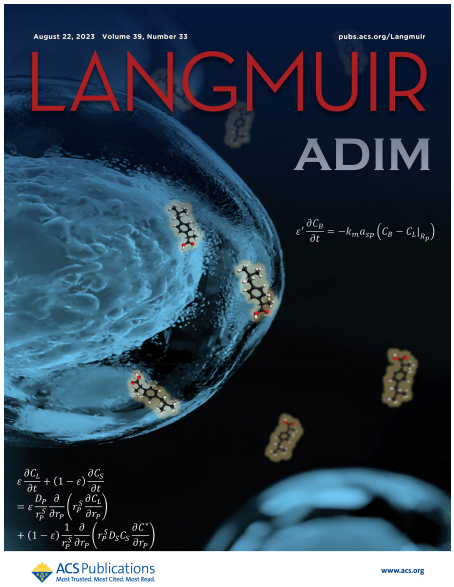

Table of contents

Chapter 1 — Introduction

"Life is not easy for any of us. But what of that? We must have perseverance and above all confidence in ourselves. We must believe that we are gifted for something, and that this thing must be attained."

Marie Skłodowska Curie

1.1. Emerging contaminants in wastewater

A wide range of compounds that are not frequently controlled or observed throughout wastewater treatment operations are referred to as "emerging contaminants (ECs)", micropollutants (MPs), emerging pollutants (EPs), contaminants of emerging concern (CEC), or trace organic compounds (TrOCs) [1]. Pharmaceuticals, personal care items, insecticides, dyes, and industrial chemicals are some examples of these pollutants [2, 3]. Concerns about their occurrence in wastewater stem from their potential impacts on human health and ecosystems [4]. More than 700 emerging pollutants categorized into 20 classes were detected in the European aquatic environment in 2015 [5]. Figure 1.1 highlights the potential impacts of ECs on human health.

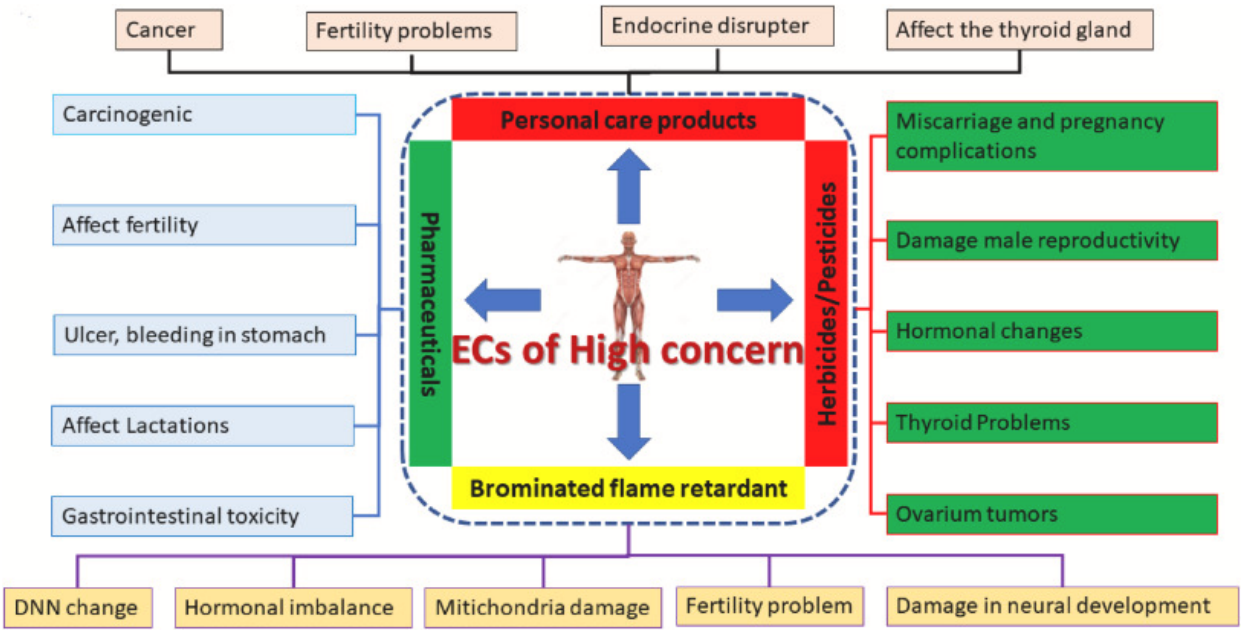

Figure 1.1 Serious consequences for human's exposure to ECs [1].

Some of the ways that ECs enter the aquatic environment are shown in Figure 1.2; they include municipal, industrial wastewater treatment plants (WWTPs), hospitals, sewer overflows as well as leaks, landfill leachate, and surface runoff from agricultural or urban areas [2, 6]. The existence of ECs in wastewater pauses incalculable risks to abiotic and biotic components [6, 7]. Many of these substances are made to be resistant to deterioration, which makes it challenging to remove them using standard wastewater treatment techniques [7]. Due to their persistence, they might eventually accumulate in water bodies, which could have long-term consequences on the environment. While the concentrations of these substances in treated wastewater are often low, in the range of parts per trillion (ppt or ng/L) to parts per billion (ppb or µg/L), the long-term exposure, particularly through the consumption of contaminated water or through food chain can cause many risks [1, 8]. These risks include: i) hormone disruption and reproductive disorders [9] ii) disrupting the aquatic ecosystems, leading to reduced biodiversity [10] iii) contributing to antibiotic resistance, making infections more challenging to treat [8, 11]. The persistence of these contaminants in the environment further exacerbates their risks. Addressing these issues requires monitoring programs, improved treatment

technologies, responsible disposal practices, and effective regulations to minimize their release and protect human health and ecosystems [7, 12]. However, many of these substances are not yet included or poorly regulated in the European directives on wastewater treatment (Directive 2000/60/EC, Directive 2008/56/EC, and Directive 2013/39/EU) [1, 6, 13, 14]. Thus, they are randomly disposed into water bodies without monitoring.

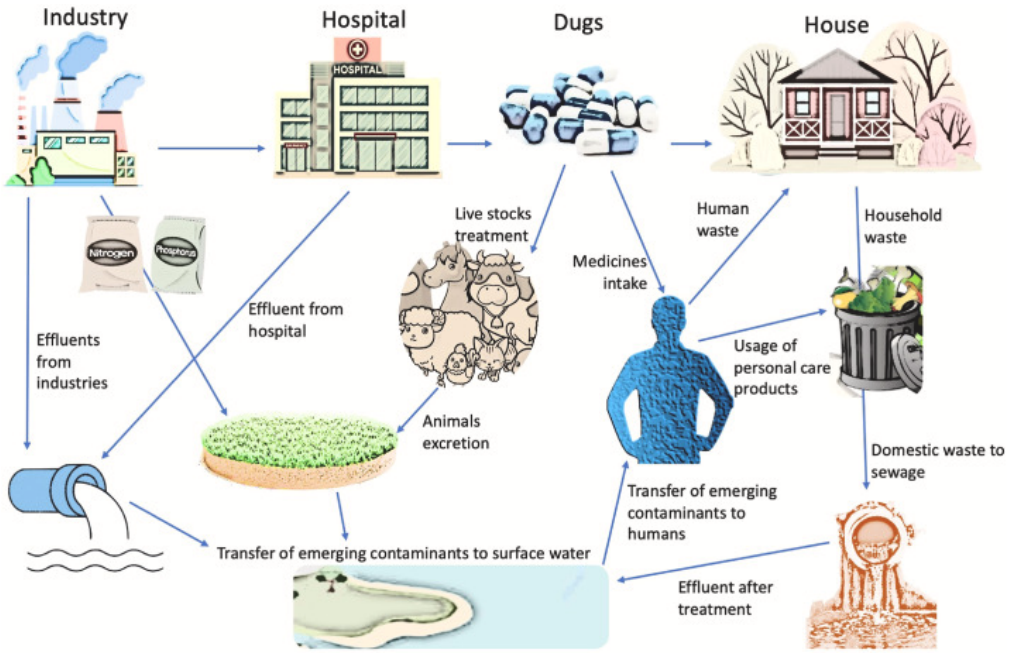

Figure 1.2 Sources and pathways of the occurrence of ECs [15].

Most of the current physical, chemical, and biological technologies used in wastewater treatment are prohibitively expensive and face many operational challenges [16]. Therefore, the development of economic, viable, and scalable techniques can profoundly secure access to safe and good drinking water quality. The advancement in the last two decades of emerging removal methods including adsorption on conventional and non-conventional solids, and advanced oxidation processes have garnered much attention. Efforts are underway to develop advanced and economically viable treatment technologies that can effectively remove emerging contaminants and to establish regulations and monitoring programs to safeguard the water quality and human health [14]. For instance, a literature assessment is shown in Figure 1.3 to provide a global overview of the state of the art over the years 2003 to 2023 as per Scopus search engine, with keywords used: removal of emerging contaminants in wastewater treatment. The figure shows that a significant increase in the number of publications is noticed in the last five years. Clearly, around 70% of the majority of the literature is through journal articles followed by around 20% as review articles. This manifests that finding new materials, solutions, and technologies for the aggravated problem is receiving considerable attention worldwide.

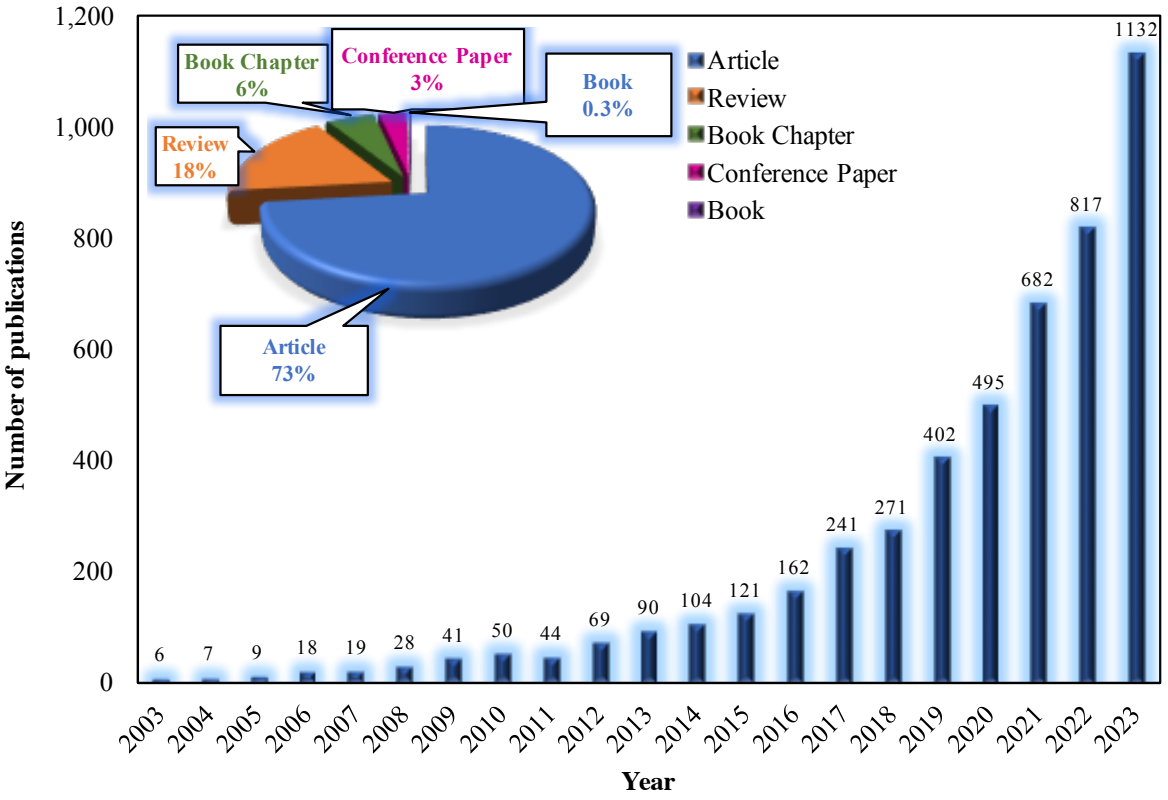

Figure 1.3 Number of publications on EC between 2003 and 2023 according to Scopus database.

1.2. Ibuprofen

Ibuprofen (IBU) [2-(4-isobutyl phenyl) propionic acid] is one of the most extensively used non-steroidal anti-inflammatory drugs (NSAID) in the world [17]. It is a colorless, crystalline solid with a distinctive odor. The characteristics of IBU are represented in Table 1.1 and the chemical structure of IBU is shown in Figure 1.4.

Table 1.1 Structure and physico-chemical properties of IBU.

Property	**IBU**
CAS ID	15687-27-1
Chemical formula	$C_{13}H_{18}O_2$
Molecular weight $(g.mol^{-1})$	206.28
Solubility in distilled water (at 25 °C) $(mg.mL^{-1})$	21
Melting point (°C)	75-79
pKa (at 25 °C)	4.91
λmax (nm)	222

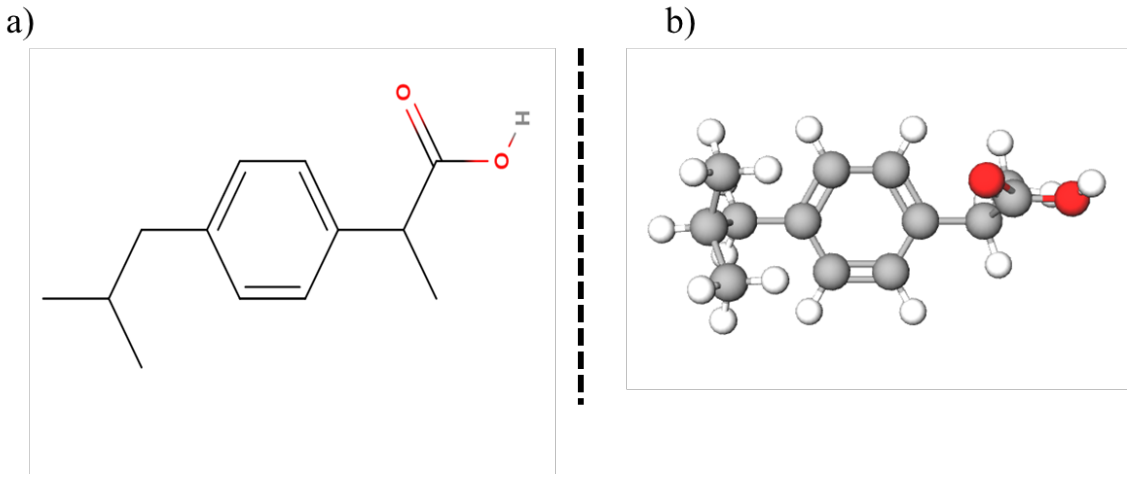

Figure 1.4 Chemical structure of IBU a) 2-D molecular structure b) 3-D ball and stick molecular structure.

The occurrence of ibuprofen in water has become a growing concern due to its widespread use and incomplete removal during wastewater treatment processes [18]. The detection of IBU in surface water, groundwater, and even drinking water sources is increasing rapidly due to the booming industrialization and global population [19]. The presence of IBU is primarily attributed to the incomplete removal of IBU during sewage treatment, as conventional treatment methods are not specifically designed to target pharmaceutical compounds. Additionally, improper disposal of unused medications and the excretion of IBU by humans contribute to its entry into the aquatic environment. Studies have reported that the concentrations of IBU in water bodies can vary widely, ranging from trace levels such as 159 nanograms per liter in the Baltic Sea in 2017 [20, 21] to 5.3 micrograms per liter in the Vistula river in 2019 [22]. The occurrence of IBU in water raises concerns about its potential impact on aquatic organisms and the potential for human exposure through drinking water sources. The study of Moro et al. [23], revealed that structural and morphological alterations in microorganisms were detected with IBU of (1 mg/L). In this vein, drastic efforts are being made to develop more effective treatment technologies to remove pharmaceuticals like IBU from wastewater and to promote responsible disposal practices to minimize their release into the environment [17, 18].

1.3. Bromocresol green

Bromocresol green (BCG) dye is a synthetic anionic dye of the triphenylmethane family. It is commonly used in various laboratory applications and as an indicator in analytical chemistry and as a tracking dye for DNA agarose gel electrophoresis [24]. In addition, it is also used in mammalian albumin measurement and the textile industry [25]. The characteristics of BCG are described in Table 1.2 and the chemical structure is shown in Figure 1.5.

Table 1.2 Structure and physico-chemical properties of BCG.

Property	**BCG**
CAS ID	76-60-8
Chemical formula	$C_{21}H_{13}Br_4NaO_5S$
Molecular weight ($g.mol^{-1}$)	698.01
Solubility in distilled water (at 25 °C) ($mg.mL^{-1}$)	40
Melting point (°C)	230
pKa (at 25 °C)	4.7
λmax (nm)	616

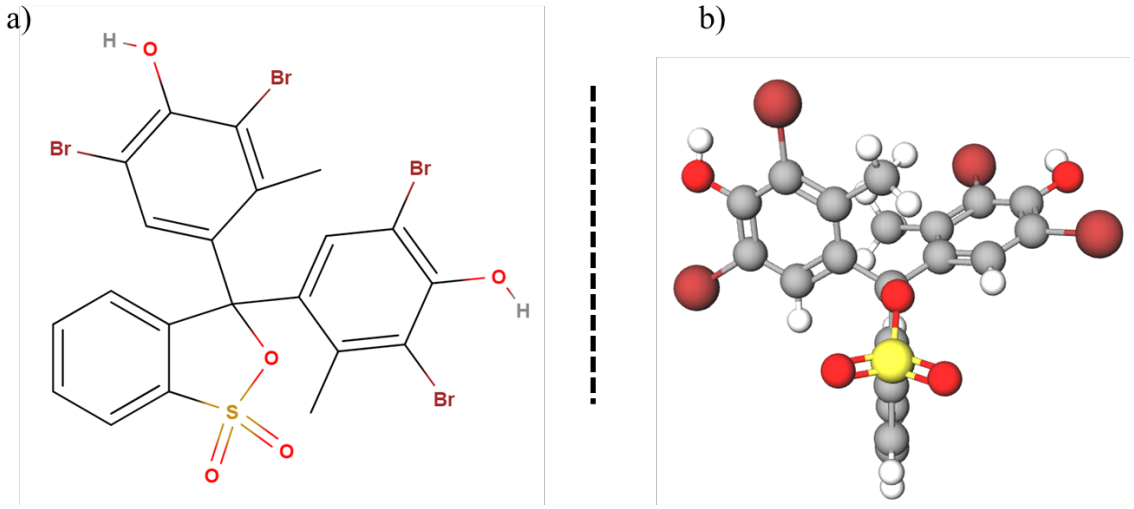

Figure 1.5 Chemical structure of BCG a) 2-D molecular structure b) 3-D ball and stick molecular structure.

While BCG itself is not considered a highly toxic substance, its occurrence in water has raised concerns due to its complex aromatic molecular structure [24, 26]. It can block sunlight from penetrating water and reduce the photosynthetic activities of autotrophic organisms [27]. BCG can enter aquatic systems through industrial discharges, laboratory waste, and improper disposal practices [28]. Once released into water, BCG can persist for a certain period depending on environmental conditions. Its persistence is attributed to its resistance to degradation and slow breakdown. Consequently, BCG can accumulate in water bodies, leading to potential risks to the aquatic species and food chain and inducing environmental issues. Studies have shown that BCG can have toxic effects on aquatic life, including fish and invertebrates, by interfering with their metabolic processes, growth, and reproduction. Thus, the presence of BCG in water emphasizes the need for selective and efficient wastewater treatment processes to minimize its release into the environment.

1.4. Alizarin red S

Alizarin Red S (ARS) is an anthraquinone anionic dye commonly used in various industries, including textile, paper, and leather manufacturing. It has a complex structure of aromatic rings that gives it high physicochemical, thermal, and optical stability [29]. The physicochemical properties of ARS are represented in Table 1.3 and the chemical structure is displayed in Figure 1.6.

Table 1.3 Structure and physico-chemical properties of ARS.

Property	ARS
CAS ID	130-22-3
Chemical formula	$C_{14}H_7NaO_7S$
Molecular weight ($g.mol^{-1}$)	342.64
Solubility in distilled water (at 25 °C) ($mg.mL^{-1}$)	1
Melting point (°C)	>250
pKa (at 25 °C)	4.5, 11
λmax (nm)	286

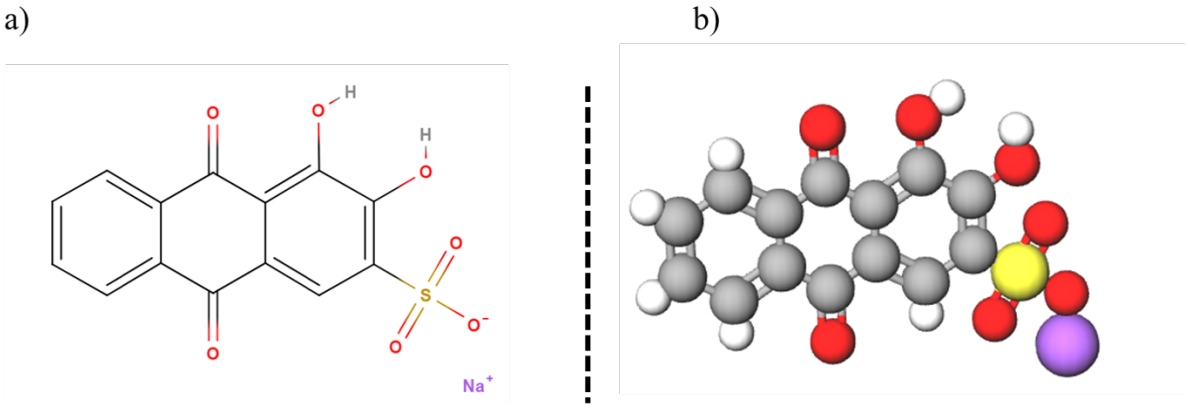

Figure 1.6 Chemical structure of ARS a) 2-D molecular structure b) 3-D ball and stick molecular structure.

ARS can enter aquatic systems through industrial wastewater discharges, improper disposal practices, and the release of treated effluents containing residual dye [27]. Once introduced into water, ARS can persist for a certain period, depending on environmental conditions [29]. Its persistence is attributed to its chemical stability and resistance to degradation. Therefore, it is considered one of the most recalcitrant and durable dyes, which cannot be completely degraded by conventional chemical, physical, and biological processes [30]. Consequently, ARS can accumulate in water bodies, potentially impacting aquatic ecosystems [31]. Studies have shown that ARS can be toxic to aquatic organisms, including fish and invertebrates, by interfering with their respiratory systems and causing physiological stress [32].

1.5. Methylene blue

Methylene blue (MB) is a cationic thiazine dye that is widely utilized in medicine and dyeing industries such as cotton, wood, and silk [33, 34]. The applications of MB expanded in the last decade to be used as a drug to treat diseases such as malaria, methemoglobinemia, and psychosis [34]. Moreover, it is used as a photosensitizer in photodynamic therapy [35]. However, MB is considered poisonous, carcinogenic, and non-biodegradable when it is typically discharged into untreated natural water sources [36]. It endangers the health of people and other living organisms as it has a complex aromatic heterocyclic and planar structure [36]. Table 1.4 lists the physiochemical properties of MB while the chemical structure is depicted in Figure 1.7.

Table 1.4 Structure and physico-chemical properties of MB.

Property	**MB**
CAS ID	61-73-4
Chemical formula	$C_{16}H_{18}ClN_3S$
Molecular weight ($g.mol^{-1}$)	319.9
Solubility in distilled water (at 25 °C) ($mg.mL^{-1}$)	43.6
Melting point (°C)	100-110
pKa (at 25 °C)	3.8
λmax (nm)	665

a) b)

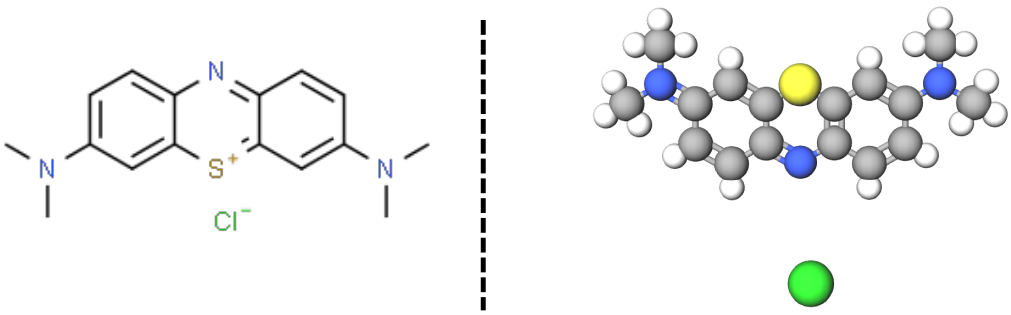

Figure 1.7 Chemical structure of MB a) 2-D molecular structure b) 3-D ball and stick molecular structure.

MB was first time synthesized by Heinrich Caro in 1800 to be used as a redox indicator [34]. The possible adverse impacts of the continuous discharge and accumulation of MB into the environment include respiratory, abdominal, and mental disorders [34]. Furthermore, the reduction of sunlight transmittance will affect the photosynthetic activity of many living organisms [36]. Thus, MB is widely employed in literature as a model molecule contaminant because of its high water-solubility, forming stable solutions at room temperature [33, 37]. Many studies have reported the removal of MB via adsorption, photodegradation, and bioremediation as promising technologies [33, 38]. However, the operating parameters should be monitored and controlled to consider these technologies in industrial scale.

1.6. Adsorption

Adsorption is a natural surface phenomenon that is widely employed in the industry for both compound separation and wastewater treatment [39]. Figure 1.7 demonstrates the typical mechanism of adsorption where the dissolved or suspended molecules (adsorbates) deposit or accumulate on the surface of solid materials (adsorbents). Different adsorption systems can be considered depending on the types of phases in contact, namely, liquid–gas, liquid–liquid, solid–liquid, and solid–gas [39]. Adsorption is considered a viable technology in wastewater treatment and purification due to its effectiveness in removing a wide range of pollutants, low energy demand, and versatile operational designs [40]. Nevertheless, many parameters should be considered further to assess the technical feasibility of the adsorption process, such as the type of adsorbent, the nature of pollutants to be removed, process configuration, and the stability and sustainability of the adsorbent [41].

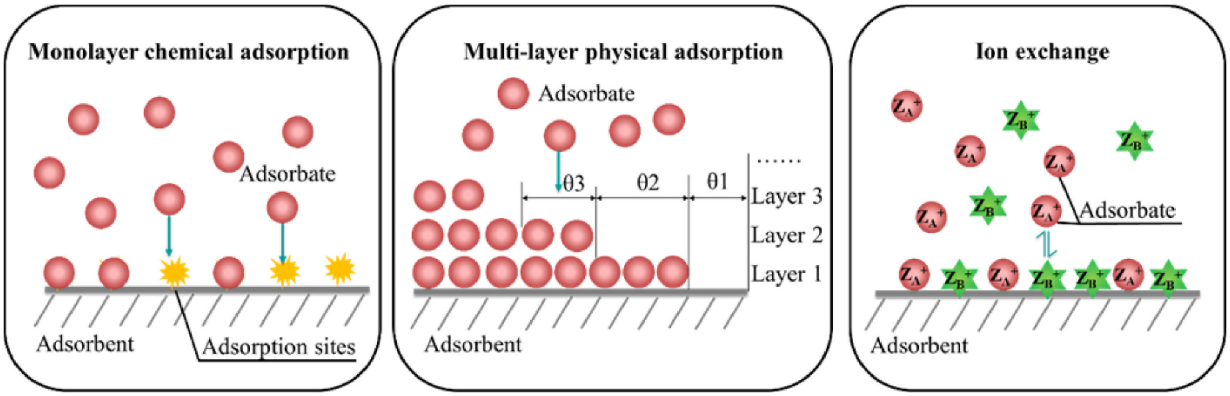

Figure 1.7 Schematization of adsorption mechanisms [42].

The type and the surface properties of the adsorbent are of paramount importance in this process. An efficient adsorbent offers a high surface area, good abrasion resistance, and a variety of functional groups to interact with the pollutants present in the wastewater [43]. The surface area of the adsorbent provides more sites for pollutant molecules to adhere on the surface. These interactions can be physical, such as Van der Waals forces or electrostatic interactions, or chemical such as ion exchange or complex formation [42-44].

Many types of adsorbents are available for a large number of different applications. The most commonly employed adsorbents include silica, polymers, activated alumina, activated carbon, zeolites, and clay. Activated carbon is the widely used adsorbent as it provides a high adsorption capacity and versatility for various organic compounds [45]. However, advances in nanotechnology have resulted in the development of novel adsorbent materials with enhanced adsorption capacities and selectivities, offering new perspectives for efficient wastewater treatment [43].

Adsorption can be conducted using different types of reactors, including batch, fixed bed column, and continuous stirred tank reactors. In batch adsorption, the adsorbent is mixed with wastewater in a container, allowing the pollutants to be adsorbed over a certain period. It involves passing wastewater through a column packed with the adsorbent for continuous

pollutant removal. A continuous stirred tank reactor utilizes a tank with an impeller to mix the adsorbent and wastewater, ensuring constant contact and efficient adsorption. These processes can be combined with other treatment methods to achieve comprehensive and effective purification of wastewater.

1.7. Photodegradation

Photocatalysis is known as a photon-assisted reaction in the presence of a semiconductor catalyst [46]. It has been studied extensively in the fields of science and technology for various applications, such as degradation of toxic pollutants, organic synthesis, water splitting, metal reduction, and removal of harmful gases [47-50]. Moreover, it holds great promise for the removal of organic pollutants from wastewater. Complete mineralization of a pollutant can be achieved without secondary contamination under mild conditions by using low-cost nanostructured semiconductors. The concept of photocatalysis in wastewater treatment involves the absorption of photons by the pollutants, leading to the generation of reactive species such as hydroxyl radicals ($OH^{\bullet}$) or singlet oxygen (O_2^-), that have strong oxidizing power and could degrade and convert many organic pollutants into harmless products [51, 52].

Heterogeneous photocatalysts are typically semiconductors (SC) either sulfides (e.g. ZnS, CdS) or oxides (e.g. TiO_2, ZrO_2, CeO_2, ZnO): these materials are characterized by a specific value of energy gap between the conduction and valence band. A photocatalytic reaction involves the following steps: the catalyst absorbs a photon with energy, *hv*, that is equal or higher than the band-gap, thus triggering a photoexcitation process (i), an electron (e^-) is promoted from the valence band of the catalyst to its conduction band, leaving an electron hole in the valence band (h^+) (ii), electron transfer takes place from solid surface to adsorbed acceptor (A) molecules and from adsorbed donor (D) molecules to the solid [52, 53] (iii). The steps are summarized below.

Photoexcitation: $SC \xrightarrow{h\nu} e^- + h^+$ (1.1)

Reduction of acceptor: $(A)_{ads} + e^- \rightarrow A^-$ (1.2)

Oxidation of donor: $(D)_{ads} + h^+ \rightarrow D^+$ (1.3)

Each ion resulting from this mechanism reacts, forming the primary intermediates, and then final oxidation products. Figure 1.8 illustrates a basic scheme for the SC photocatalysis.

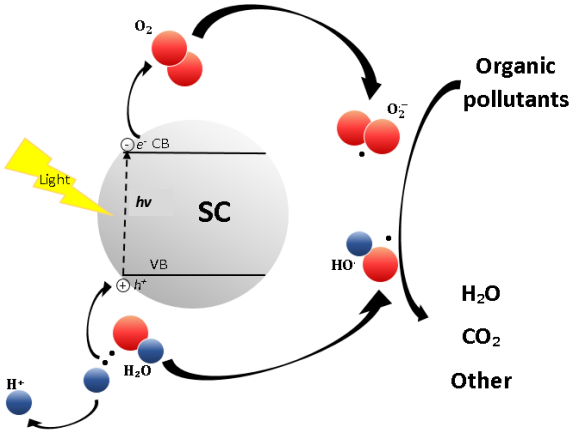

Figure 1.8 Schematization of a photoexcitation process.

Photoelectric energy dispersion occurs due to the electron-hole recombination,

$$e^- + h^+ \rightarrow N + E \tag{1.4}$$

where E is the energy released in the form of heat or light ($hv' \leq hv$), and N is the neutral center resulting in a reduction of the photoexcitation process efficiency [53].

Photodegradation offers several advantages, including its ability to target a wide range of organic pollutants, its effectiveness in mineralizing contaminants, and its environmentally friendly nature as it does not require the addition of chemicals. The efficiency of photodegradation in wastewater treatment depends on several factors, including the wavelength and intensity of the light source, the presence of sensitizers or catalysts, the characteristics of the aqueous medium, and the characteristics of the organic pollutant [54-56]. Ultraviolet (UV) light in the range of 200-400 nm is commonly used in photodegradation processes, as it is capable to activate many organic compounds [57]. The presence of other substances in the wastewater, such as dissolved organic matter or inorganic ions, might also influence the efficiency of photodegradation by competing for light absorption or interfering with the degradation reactions.

When treating wastewater, photodegradation can be used in a variety of reactor configurations. Batch reactors, continuous flow reactors, and immobilized systems are the most frequently utilized setups [58]. Photodegradation takes place in batch reactors because the wastewater is exposed to the light source for a set amount of time. The continuous flow of wastewater through a reaction chamber, where it is exposed to light, ensures a steady degradation process in continuous flow reactors. Immobilized catalysts and photocatalysts are used in immobilized systems, enabling effective light absorption and extended contact times between the catalyst surface and the contaminants.

Although photodegradation has the potential for wastewater treatment, the complexity and variety of organic contaminants found in wastewater frequently restrict its use. Some substances, such as those with minor light absorption or those in low concentrations, do not degrade as well as others. A further difficulty with operating large-scale photodegradation

systems is the energy requirements. Therefore, to achieve thorough and effective wastewater treatment, photodegradation is frequently combined with other treatment technologies, such as adsorption and biological processes. Combination of methods can improve the elimination of contaminants and guarantee the overall efficacy of the treatment processes.

1.8. Ozonation

Ozonation is one of the most extensively applied method for treating water contaminants [59]. Ozone (O_3) is a very strong oxidant when compared with other oxidants such as potassium permanganate ($KMnO_4$), chlorine dioxide (ClO_2), hydrogen peroxide (H_2O_2) and oxygen (O_2). Ozone is used to break down a wide range of organic and inorganic contaminants present in wastewater [60]. In general, direct and indirect reactions are the principal ways that ozone interacts with organic materials in an aqueous environment as illustrated in Figure 1.9 [61]. Ozone molecules react directly with organic materials in a process called the direct reaction [62]. The indirect reaction occurs when powerful oxidizing free radicals (mostly $^{\bullet}OH$) are produced by the initial breakdown of ozone in water, after which these free radicals react with organic molecules [62]. Although ozonation can be considered as an effective method for removing ECs, it has the drawback of potentially forming toxic by-products when reacting with some organic and inorganic compounds (such as $NH4^{+}$ and saturated aliphatic acid) [63]. As a result, destruction processes can be slow or incomplete [64]. On the other hand, ozone is an unstable oxidant that needs to be generated in-situ using a high-voltage alternating field with a low storage stability characteristics [61].

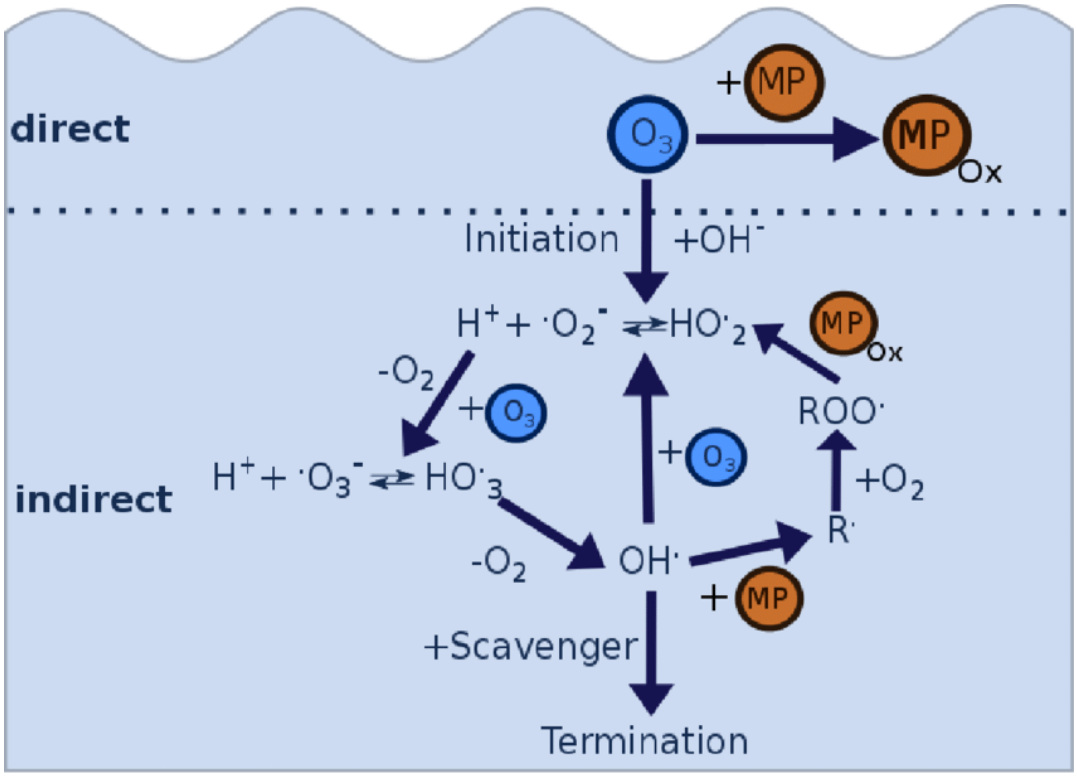

Figure 1.9 Schematization of ozonation via direct and indirect mechanisms, R presents the reaction product and MP presents the micropollutant [61].

Therefore, catalytic ozonation can be considered as a highly effective and innovative approach in wastewater treatment, combining the power of ozone with catalytic materials to enhance the pollutant degradation at ambient temperatures and pressures [60]. The incorporation of heterogeneous catalysts, typically metal-based materials, accelerates the reaction kinetics and promotes the generation of highly reactive species, such as hydroxyl radicals. These radicals play a crucial role in the degradation of recalcitrant pollutants, ensuring a more comprehensive and efficient wastewater treatment process [65].

1.9. Aim of the research

The main aim of this work was to study the efficiency of novel in-house prepared materials in removing emerging contaminants from wastewater which are ibuprofen, bromocresol green, and alizarin red S, through adsorption and photodegradation techniques in both batch and semibatch reactors. The performance of classical commercial materials, such as activated carbon and metal oxides was studied too. **Chapter 1** provides a general overview of the issue of emerging contaminants as a current evolving problem in wastewater. This is followed by the introduction of the concepts of adsorption and photodegradation. **Chapter 2** represents an exhaustive and critical review of the applications of metal organic frameworks (MOFs) in wastewater treatment through adsorption and photodegradation (**Publication I**). Subsequently, MIL-88A was selected to be investigated as an adsorbent. However, the preliminary tests showed that this material has some stability shortcomings. Therefore, the stability of MIL-88A in an aqueous solution was studied experimentally and computationally by DFT calculations under different experimental conditions (**Publication II**). In **Chapter 3**, Brookite TiO_2 Nanoparticles are employed for competitive adsorption of Bromocresol green and Alizarin red S anionic dyes investigation through experimental and molecular dynamics simulation (**Publication III**). **Chapter 4** focuses on the removal IBU by adsorption on activated carbon offering thermodynamic and kinetic investigation via the adsorption dynamic intraparticle model (ADIM) (**Publication IV**). In **Chapter 5,** the sustainable photodegradation of IBU using CeO_2 nanostructured materials is presented considering reaction kinetics, modelling, and thermodynamics (**Publication V**). The photodegradation of IBU using ZnO and TiO_2 nanoparticles is discussed in **Chapter 5**, where comprehensive kinetics modelling, mechanisms, and thermodynamics are thoroughly addressed (**Publication VI**). **Chapter 6** presents geopolymers to be studied as adsorbents, giving in-depth kinetic and thermodynamic understanding for the removal of MB (**Publication VII**). **Chapter 7** gives insight on the promising application of CeO_2-Mxene composite for the destruction of IBU in a hybrid catalytic ozonation-photodegradation system. **Chapter 8** summarizes the main results obtained in this work along with some futuristic perspectives and recommendations.

1.10. List of abbreviations

EC	emerging contaminant
MP	micropollutant
EP	emerging pollutant
CEC	contaminants of emerging concern
TrOC	trace organic compound
WWTP	wastewater treatment plant
ppt	parts per trillion
ppb	parts per billion
IBU	ibuprofen
NSAID	non-steroidal anti-inflammatory drug
BCG	bromocresol green
ARS	alizarin Red S
MB	methylene blue
SC	semiconductors
UV	ultraviolet
MOF	metal organic framework
ADIM	adsorption dynamic intraparticle model
DFT	density function theory
R	reaction product
MP	micropollutant

1.11. References

[1] R. Kumar, M. Qureshi, D.K. Vishwakarma, N. Al-Ansari, A. Kuriqi, A. Elbeltagi, A. Saraswat, A review on emerging water contaminants and the application of sustainable removal technologies, Case Studies in Chemical and Environmental Engineering 6 (2022) 100219. https://doi.org/https://doi.org/10.1016/j.cscee.2022.100219.
[2] H. Sarma, Chapter 1 - Understanding emerging contaminants in soil and water: current perspectives on integrated remediation approaches, in: H. Sarma, D.C. Dominguez, W.-Y. Lee (Eds.), Emerging Contaminants in the Environment, Elsevier2022, pp. 1-38. https://doi.org/https://doi.org/10.1016/B978-0-323-85160-2.00002-0.
[3] B.M. Sharma, J. Bečanová, M. Scheringer, A. Sharma, G.K. Bharat, P.G. Whitehead, J. Klánová, L. Nizzetto, Health and ecological risk assessment of emerging contaminants (pharmaceuticals, personal care products, and artificial sweeteners) in surface and groundwater (drinking water) in the Ganges River Basin, India, Science of The Total Environment 646 (2019) 1459-1467. https://doi.org/https://doi.org/10.1016/j.scitotenv.2018.07.235.
[4] O.M. Rodriguez-Narvaez, J.M. Peralta-Hernandez, A. Goonetilleke, E.R. Bandala, Treatment technologies for emerging contaminants in water: A review, Chemical Engineering Journal 323 (2017) 361-380. https://doi.org/https://doi.org/10.1016/j.cej.2017.04.106.
[5] V. Geissen, H. Mol, E. Klumpp, G. Umlauf, M. Nadal, M. van der Ploeg, S.E.A.T.M. van de Zee, C.J. Ritsema, Emerging pollutants in the environment: A challenge for water resource management, International Soil and Water Conservation Research 3(1) (2015) 57-65. https://doi.org/https://doi.org/10.1016/j.iswcr.2015.03.002.
[6] D. Stipaničev, Z. Dragun, S. Repec, K. Rebok, M. Jordanova, Broad spectrum screening of 463 organic contaminants in rivers in Macedonia, Ecotoxicology and Environmental Safety 135 (2017) 48-59. https://doi.org/https://doi.org/10.1016/j.ecoenv.2016.09.004.
[7] K.E. Murray, S.M. Thomas, A.A. Bodour, Prioritizing research for trace pollutants and emerging contaminants in the freshwater environment, Environmental Pollution 158(12) (2010) 3462-3471. https://doi.org/https://doi.org/10.1016/j.envpol.2010.08.009.
[8] S. Khan, M. Naushad, M. Govarthanan, J. Iqbal, S.M. Alfadul, Emerging contaminants of high concern for the environment: Current trends and future research, Environmental Research 207 (2022) 112609. https://doi.org/https://doi.org/10.1016/j.envres.2021.112609.
[9] W. Shi, H. Tan, Mechanisms of Action of Emerging Contaminants: Pharmaceuticals and Personal Care Products (PPCP), in: L.-H. Guo, M. Mortimer (Eds.), Advances in Toxicology and Risk Assessment of Nanomaterials and Emerging Contaminants, Springer Singapore, Singapore, 2022, pp. 255-276. https://doi.org/10.1007/978-981-16-9116-4_11.
[10] A.J. Reid, A.K. Carlson, I.F. Creed, E.J. Eliason, P.A. Gell, P.T.J. Johnson, K.A. Kidd, T.J. MacCormack, J.D. Olden, S.J. Ormerod, J.P. Smol, W.W. Taylor, K. Tockner, J.C. Vermaire, D. Dudgeon, S.J. Cooke, Emerging threats and persistent conservation challenges for freshwater biodiversity, Biological Reviews 94(3) (2019) 849-873. https://doi.org/https://doi.org/10.1111/brv.12480.
[11] H.K. Patel, R.K. Kalaria, P.H. Jokhakar, C.R. Patel, B.Y. Patel, Chapter 17 - Removal of emerging contaminants in water treatment by an application of nanofiltration and reverse osmosis, in: M. Shah, S. Rodriguez-Couto, J. Biswas (Eds.), Development in Wastewater Treatment Research and Processes, Elsevier2022, pp. 385-400. https://doi.org/https://doi.org/10.1016/B978-0-323-85583-9.00005-3.
[12] I. Haddaoui, J. Mateo-Sagasta, A review on occurrence of emerging pollutants in waters of the MENA region, Environmental Science and Pollution Research 28(48) (2021) 68090-68110. https://doi.org/10.1007/s11356-021-16558-8.

[13] N. Morin-Crini, E. Lichtfouse, M. Fourmentin, A.R.L. Ribeiro, C. Noutsopoulos, F. Mapelli, É. Fenyvesi, M.G.A. Vieira, L.A. Picos-Corrales, J.C. Moreno-Piraján, L. Giraldo, T. Sohajda, M.M. Huq, J. Soltan, G. Torri, M. Magureanu, C. Bradu, G. Crini, Removal of emerging contaminants from wastewater using advanced treatments. A review, Environmental Chemistry Letters 20(2) (2022) 1333-1375. https://doi.org/10.1007/s10311-021-01379-5.
[14] C.J. Houtman, Emerging contaminants in surface waters and their relevance for the production of drinking water in Europe, Journal of Integrative Environmental Sciences 7(4) (2010) 271-295. https://doi.org/10.1080/1943815X.2010.511648.
[15] M. Coccia, E. Bontempi, New trajectories of technologies for the removal of pollutants and emerging contaminants in the environment, Environmental Research 229 (2023) 115938. https://doi.org/https://doi.org/10.1016/j.envres.2023.115938.
[16] S.F. Ahmed, M. Mofijur, S. Nuzhat, A.T. Chowdhury, N. Rafa, M.A. Uddin, A. Inayat, T.M.I. Mahlia, H.C. Ong, W.Y. Chia, P.L. Show, Recent developments in physical, biological, chemical, and hybrid treatment techniques for removing emerging contaminants from wastewater, Journal of Hazardous Materials 416 (2021) 125912. https://doi.org/https://doi.org/10.1016/j.jhazmat.2021.125912.
[17] E. Brillas, A critical review on ibuprofen removal from synthetic waters, natural waters, and real wastewaters by advanced oxidation processes, Chemosphere 286 (2022) 131849. https://doi.org/https://doi.org/10.1016/j.chemosphere.2021.131849.
[18] S.N. Oba, J.O. Ighalo, C.O. Aniagor, C.A. Igwegbe, Removal of ibuprofen from aqueous media by adsorption: A comprehensive review, Science of The Total Environment 780 (2021) 146608. https://doi.org/https://doi.org/10.1016/j.scitotenv.2021.146608.
[19] S. Chopra, D. Kumar, Ibuprofen as an emerging organic contaminant in environment, distribution and remediation, Heliyon 6(6) (2020) e04087. https://doi.org/https://doi.org/10.1016/j.heliyon.2020.e04087.
[20] T. Austin, F. Bregoli, D. Höhne, A.J. Hendriks, A.M.J. Ragas, Ibuprofen exposure in Europe; ePiE as an alternative to costly environmental monitoring, Environmental Research 209 (2022) 112777. https://doi.org/https://doi.org/10.1016/j.envres.2022.112777.
[21] N. Vieno, P. Hallgren, P. Wallberg, M. Pyhälä, S. Zandaryaa, B.M.E.P. Commission, Pharmaceuticals in the aquatic environment of the Baltic Sea region: a status report, Unesco Publishing2017.
[22] S. Mishra, P. Kumar, I. Mehrotra, M. Kumar, Prevalence of organic micropollutants in the Yamuna River, Delhi, India: seasonal variations and governing factors, Science of The Total Environment 858 (2023) 159684. https://doi.org/https://doi.org/10.1016/j.scitotenv.2022.159684.
[23] I. Moro, V. Matozzo, A. Piovan, E. Moschin, F.D. Vecchia, Morpho-physiological effects of ibuprofen on Scenedesmus rubescens, Environmental Toxicology and Pharmacology 38(2) (2014) 379-387. https://doi.org/https://doi.org/10.1016/j.etap.2014.06.005.
[24] D. Liu, J. Yuan, J. Li, G. Zhang, Preparation of Chitosan Poly(methacrylate) Composites for Adsorption of Bromocresol Green, ACS Omega 4(7) (2019) 12680-12686. https://doi.org/10.1021/acsomega.9b01576.
[25] M. Islam, M. Hossain, S. Mahbub, M.A. Hoque, D. Kumar, S.M. Wabaidur, M.A. Habila, M.M. Al-Anazy, M. Kabir, Influences of alcohol and diol on the aggregation behaviour, modes of interaction and the thermodynamic properties of the mixture of bromocresol green dye and sodium dodecyl sulphate at numerous temperatures, Molecular Physics 119(12) (2021) e1925364. https://doi.org/10.1080/00268976.2021.1925364.
[26] M. Abniki, A. Moghimi, Synthesis of chitosan functionalized magnetic carbon nanotubes for dispersive solid-phase extraction of bromocresol green, Micro & Nano Letters 16(9) (2021) 455-462. https://doi.org/https://doi.org/10.1049/mna2.12067.

[27] H. Biglari, S. RodríguezíCouto, Y.O. Khaniabadi, H. Nourmoradi, M. Khoshgoftar, A. Amrane, M. Vosoughi, S. Esmaeili, R. Heydari, M.J. Mohammadi, R. Rashidi, Cationic Surfactant-modified Clay as an Adsorbent for the Removal of Synthetic Dyes from Aqueous Solutions, 16(5) (2018). https://doi.org/doi:10.1515/ijcre-2017-0064.
[28] C.E. Onu, B.N. Ekwueme, P.E. Ohale, C.P. Onu, C.O. Asadu, C.C. Obi, K.T. Dibia, O.O. Onu, Decolourization of bromocresol green dye solution by acid functionalized rice husk: Artificial intelligence modeling, GA optimization, and adsorption studies, Journal of Hazardous Materials Advances 9 (2023) 100224. https://doi.org/https://doi.org/10.1016/j.hazadv.2022.100224.
[29] F. Fu, Z. Gao, L. Gao, D. Li, Effective Adsorption of Anionic Dye, Alizarin Red S, from Aqueous Solutions on Activated Clay Modified by Iron Oxide, Industrial & Engineering Chemistry Research 50(16) (2011) 9712-9717. https://doi.org/10.1021/ie200524b.
[30] P. Zucca, C. Vinci, F. Sollai, A. Rescigno, E. Sanjust, Degradation of Alizarin Red S under mild experimental conditions by immobilized 5,10,15,20-tetrakis(4-sulfonatophenyl)porphine–Mn(III) as a biomimetic peroxidase-like catalyst, Journal of Molecular Catalysis A: Chemical 288(1) (2008) 97-102. https://doi.org/https://doi.org/10.1016/j.molcata.2008.04.001.
[31] A.B. Albadarin, C. Mangwandi, Mechanisms of Alizarin Red S and Methylene blue biosorption onto olive stone by-product: Isotherm study in single and binary systems, Journal of Environmental Management 164 (2015) 86-93. https://doi.org/https://doi.org/10.1016/j.jenvman.2015.08.040.
[32] Ž. Jurgelėnė, D. Montvydienė, S. Stakėnas, J. Poviliūnas, S. Račkauskas, R. Taraškevičius, V. Skrodenytė-Arbačiauskienė, N. Kazlauskienė, Impact evaluation of marking Salmo trutta with Alizarin Red S produced by different manufacturers, Aquatic Toxicology 242 (2022) 106051. https://doi.org/https://doi.org/10.1016/j.aquatox.2021.106051.
[33] I. Khan, K. Saeed, I. Zekker, B. Zhang, A.H. Hendi, A. Ahmad, S. Ahmad, N. Zada, H. Ahmad, L.A. Shah, T. Shah, I. Khan, Review on Methylene Blue: Its Properties, Uses, Toxicity and Photodegradation, Water, 2022.
[34] J. Pomicpic, G.C. Dancel, P.J. Cabalar, J. Madrid, Methylene blue removal by poly(acrylic acid)-grafted pineapple leaf fiber/polyester nonwoven fabric adsorbent and its comparison with removal by gamma or electron beam irradiation, Radiation Physics and Chemistry 172 (2020) 108737. https://doi.org/https://doi.org/10.1016/j.radphyschem.2020.108737.
[35] J.d.S. Martins, J.C. Junqueira, R.L. Faria, N.F. Santiago, R.D. Rossoni, C.E.D. Colombo, A.O.C. Jorge, Antimicrobial photodynamic therapy in rat experimental candidiasis: evaluation of pathogenicity factors of Candida albicans, Oral Surgery, Oral Medicine, Oral Pathology, Oral Radiology, and Endodontology 111(1) (2011) 71-77. https://doi.org/https://doi.org/10.1016/j.tripleo.2010.08.012.
[36] P.O. Oladoye, T.O. Ajiboye, E.O. Omotola, O.J. Oyewola, Methylene blue dye: Toxicity and potential elimination technology from wastewater, Results in Engineering 16 (2022) 100678. https://doi.org/https://doi.org/10.1016/j.rineng.2022.100678.
[37] F. Mashkoor, A. Nasar, Magsorbents: Potential candidates in wastewater treatment technology – A review on the removal of methylene blue dye, Journal of Magnetism and Magnetic Materials 500 (2020) 166408. https://doi.org/https://doi.org/10.1016/j.jmmm.2020.166408.
[38] M.A. Dutt, M.A. Hanif, F. Nadeem, H.N. Bhatti, A review of advances in engineered composite materials popular for wastewater treatment, Journal of Environmental Chemical Engineering 8(5) (2020) 104073. https://doi.org/https://doi.org/10.1016/j.jece.2020.104073.
[39] A. Dąbrowski, Adsorption — from theory to practice, Advances in Colloid and Interface Science 93(1) (2001) 135-224. https://doi.org/https://doi.org/10.1016/S0001-8686(00)00082-8.

[40] G.L. Dotto, G. McKay, Current scenario and challenges in adsorption for water treatment, Journal of Environmental Chemical Engineering 8(4) (2020) 103988. https://doi.org/https://doi.org/10.1016/j.jece.2020.103988.
[41] R. Rashid, I. Shafiq, P. Akhter, M.J. Iqbal, M. Hussain, A state-of-the-art review on wastewater treatment techniques: the effectiveness of adsorption method, Environmental Science and Pollution Research 28(8) (2021) 9050-9066. https://doi.org/10.1007/s11356-021-12395-x.
[42] J. Wang, X. Guo, Adsorption isotherm models: Classification, physical meaning, application and solving method, Chemosphere 258 (2020) 127279. https://doi.org/ https://doi.org/ 10.1016/j.chemosphere.2020.127279.
[43] P. Kumari, M. Alam, W.A. Siddiqi, Usage of nanoparticles as adsorbents for waste water treatment: An emerging trend, Sustainable Materials and Technologies 22 (2019) e00128. https://doi.org/https://doi.org/10.1016/j.susmat.2019.e00128.
[44] S.D. Faust, O.M. Aly, Adsorption processes for water treatment, Elsevier2013.
[45] S. Wong, N. Ngadi, I.M. Inuwa, O. Hassan, Recent advances in applications of activated carbon from biowaste for wastewater treatment: A short review, Journal of Cleaner Production 175 (2018) 361-375. https://doi.org/https://doi.org/10.1016/j.jclepro.2017.12.059.
[46] R.C. Pawar, C.S. Lee, Chapter 3 - Heterogeneous Photocatalysts Based on Organic/Inorganic Semiconductor, in: R.C. Pawar, C.S. Lee (Eds.), Heterogeneous Nanocomposite-Photocatalysis for Water Purification, William Andrew Publishing, Boston, 2015, pp. 43-96. https://doi.org/https://doi.org/10.1016/B978-0-323-39310-2.00003-5.
[47] R. Ameta, M.S. Solanki, S. Benjamin, S.C. Ameta, Chapter 6 - Photocatalysis, in: S.C. Ameta, R. Ameta (Eds.), Advanced Oxidation Processes for Waste Water Treatment, Academic Press2018, pp. 135-175. https://doi.org/https://doi.org/10.1016/B978-0-12-810499-6.00006-1.
[48] N. Manfredi, C.L. Boldrini, A. Abbotto, Organic Sensitizers for Photoanode Water Splitting in Dye-Sensitized Photoelectrochemical Cells, ChemElectroChem 5(17) (2018) 2395-2402. https://doi.org/https://doi.org/10.1002/celc.201800592.
[49] C.-C. Wang, X.-D. Du, J. Li, X.-X. Guo, P. Wang, J. Zhang, Photocatalytic Cr(VI) reduction in metal-organic frameworks: A mini-review, Applied Catalysis B: Environmental 193 (2016) 198-216. https://doi.org/https://doi.org/10.1016/j.apcatb.2016.04.030.
[50] A. Mills, R.H. Davies, D. Worsley, Water purification by semiconductor photocatalysis, Chemical Society Reviews 22(6) (1993) 417-425. https://doi.org/10.1039/CS9932200417.
[51] R. Pawar, C.S. Lee, Heterogeneous nanocomposite-photocatalysis for water purification, William Andrew2015.
[52] V. Russo, M. Hmoudah, F. Broccoli, M.R. Iesce, O.-S. Jung, M. Di Serio, Applications of Metal Organic Frameworks in Wastewater Treatment: A Review on Adsorption and Photodegradation, Frontiers in Chemical Engineering 2 (2020). https://doi.org/10.3389/ fceng.2020.581487.
[53] J.-M. Herrmann, Heterogeneous photocatalysis: fundamentals and applications to the removal of various types of aqueous pollutants, Catalysis Today 53(1) (1999) 115-129. https://doi.org/https://doi.org/10.1016/S0920-5861(99)00107-8.
[54] R. Gusain, N. Kumar, S.S. Ray, Factors Influencing the Photocatalytic Activity of Photocatalysts in Wastewater Treatment, Photocatalysts in Advanced Oxidation Processes for Wastewater Treatment2020, pp. 229-270. https://doi.org/https://doi.org/10.1002/ 9781119631422.ch8.
[55] N. Yahya, F. Aziz, N.A. Jamaludin, M. A. Mutalib, A.F. Ismail, W.N. W. Salleh, J. Jaafar, N. Yusof, N. A. Ludin, A review of integrated photocatalyst adsorbents for wastewater treatment, Journal of Environmental Chemical Engineering 6(6) (2018) 7411-7425. https://doi.org/https://doi.org/10.1016/j.jece.2018.06.051.

[56] N. Gallucci, M. Hmoudah, E. Martinez, A. El-Qanni, M. Di Serio, L. Paduano, G. Vitiello, V. Russo, Photodegradation of ibuprofen using CeO2 nanostructured materials: Reaction kinetics, modeling, and thermodynamics, Journal of Environmental Chemical Engineering 10(3) (2022) 107866. https://doi.org/https://doi.org/10.1016/j.jece.2022.107866.
[57] F. Jentzsch, O. Olsson, J. Westphal, M. Reich, C. Leder, K. Kümmerer, Photodegradation of the UV filter ethylhexyl methoxycinnamate under ultraviolet light: Identification and in silico assessment of photo-transformation products in the context of grey water reuse, Science of The Total Environment 572 (2016) 1092-1100. https://doi.org/https://doi.org/10.1016/j.scitotenv.2016.08.017.
[58] R. Binjhade, R. Mondal, S. Mondal, Continuous photocatalytic reactor: Critical review on the design and performance, Journal of Environmental Chemical Engineering 10(3) (2022) 107746. https://doi.org/https://doi.org/10.1016/j.jece.2022.107746.
[59] X. Li, L. Fu, F. Chen, S. Zhao, J. Zhu, C. Yin, Application of Heterogeneous Catalytic Ozonation in Wastewater Treatment: An Overview, Catalysts, 2023.
[60] J. Wang, H. Chen, Catalytic ozonation for water and wastewater treatment: Recent advances and perspective, Science of The Total Environment 704 (2020) 135249. https://doi.org/https://doi.org/10.1016/j.scitotenv.2019.135249.
[61] M. Voigt, A. Wirtz, K. Hoffmann-Jacobsen, M. Jaeger, Prior art for the development of a fourth purification stage in wastewater treatment plant for the elimination of anthropogenic micropollutants-a short-review, AIMS Environmental Science 7(1) (2020) 69-98.
[62] S.N. Malik, P.C. Ghosh, A.N. Vaidya, S.N. Mudliar, Hybrid ozonation process for industrial wastewater treatment: Principles and applications: A review, Journal of Water Process Engineering 35 (2020) 101193. https://doi.org/https://doi.org/10.1016/j.jwpe.2020.101193.
[63] R. Julia Liliana, F. Iliana, A. Claudia Marissa, V. Miguel Angel, P. Tatiana, C. Isaac, Catalytic Ozonation as a Promising Technology for Application in Water Treatment: Advantages and Constraints, in: D. Ján, K. Marian (Eds.), Ozone in Nature and Practice, IntechOpen, Rijeka, 2018, p. Ch. 2. https://doi.org/10.5772/intechopen.76228.
[64] S. Tripathi, T. Hussain, Chapter 7 - Water and Wastewater Treatment through Ozone-based technologies, in: M. Shah, S. Rodriguez-Couto, J. Biswas (Eds.), Development in Wastewater Treatment Research and Processes, Elsevier2022, pp. 139-172. https://doi.org/https://doi.org/10.1016/B978-0-323-85583-9.00015-6.
[65] W. Chen, H. He, J. Liang, X. Wei, X. Li, J. Wang, L. Li, A comprehensive review on metal based active sites and their interaction with O3 during heterogeneous catalytic ozonation process: Types, regulation and authentication, Journal of Hazardous Materials 443 (2023) 130302. https://doi.org/https://doi.org/10.1016/j.jhazmat.2022.130302.

Chapter 2 — Metal Organic Frameworks: Applications in Wastewater Treatment through Adsorption, Photodegradation Processes, and Stability Investigations

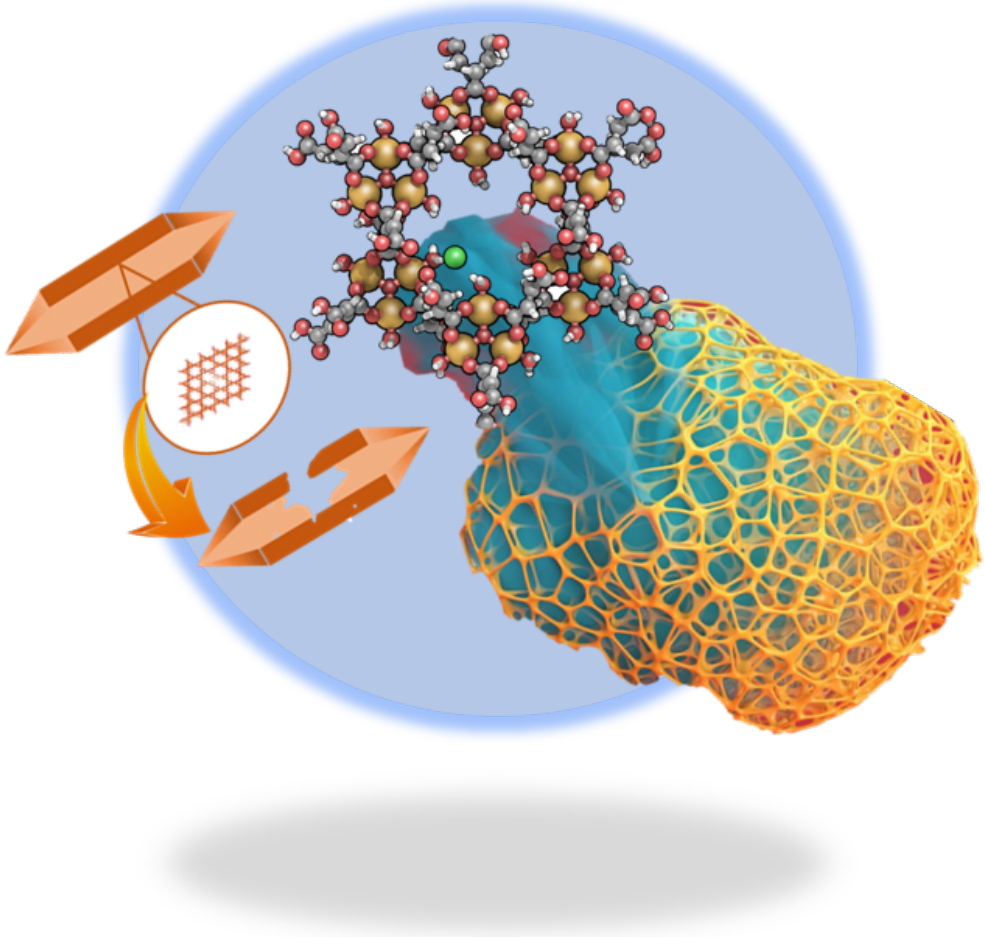

V. Russo, ***M. Hmoudah***, F. Broccoli, M. R. Iesce, O. S. Jung, and M. Di Serio, Applications of Metal Organic Frameworks in Wastewater Treatment: A Review on Adsorption and Photodegradation, Front. Chem. Eng, 2 (2020): 581487. doi.org/10.3389/fceng.2020.581487

M. Hmoudah, A. El-Qanni, R. Tesser, R. Esposito, A. Petrone, O. Jung, T. Salmi, V. Russo, and M. Di Serio Assessment of the Robustness of MIL-88A in an Aqueous Solution: Experimental and DFT Investigations, Materials Science and Engineering: B 288 (2023): 116179. doi.org/10.1016/j.mseb.2022.116179

2.1. Introduction

Metal organic frameworks (MOFs), a novel family of porous materials, composed of metal ions or clusters connected by organic ligands, have attracted great interest during the past two decades [1]. These substances have been researched for a variety of revolutionary uses in wastewater treatment, gas purification, energy conversion and light harvesting, separation processes, medication delivery, and catalysis [2]. Metal centers and organic linkers are combined to produce endless crystalline networks in the structure of MOFs (Figure 2.1a). Figure 2.1b gives examples on the different MOFs with their corresponding metallic clusters and organic linkers [3], while the most common structures of MOFs are shown in Figure 2.1c [4]. These substances have crystalline structures with a high porosity and modular nature [5]. MOFs are very flexible in terms of pore size, pore shape, and other properties offering a vast library of materials with tunable properties and functionalities [2, 4]. The precise control of their structure and composition allows the design of MOFs with tailored properties, which enables the incorporation of different metal ions and ligands, offering a vast library of materials with tunable properties and functionalities [2].

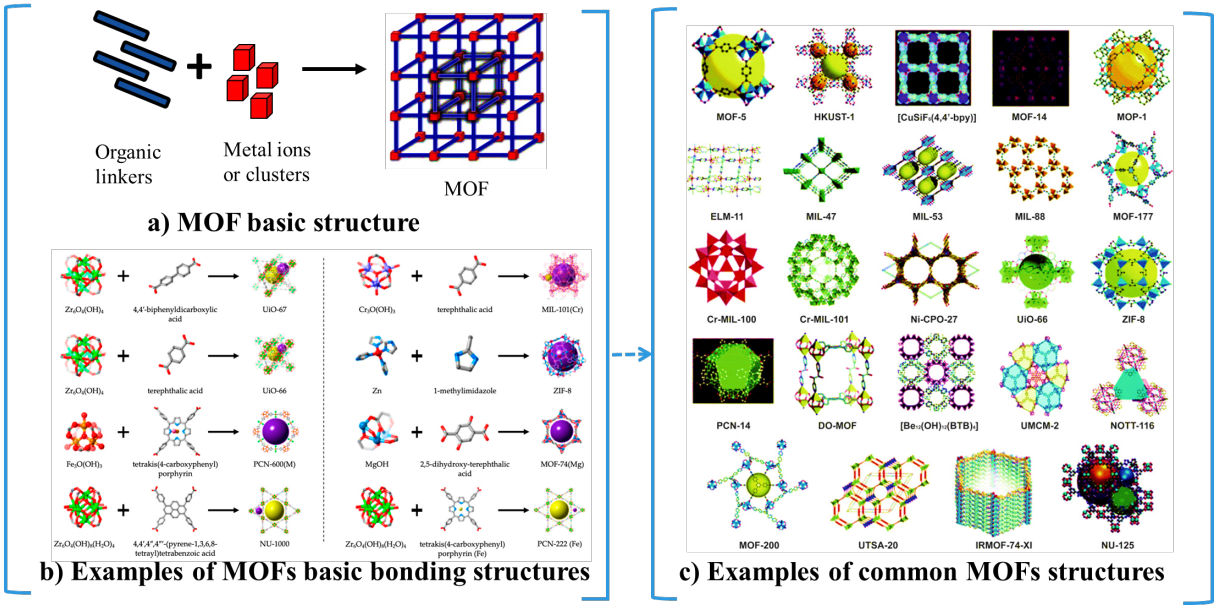

Figure 2.1 a) Basic MOF structure b) Examples of different MOFs structures with their corresponding metallic clusters and organic linkers [3] c) Examples of common MOFs structures [4].

The various potential uses of MOFs in the treatment of wastewater have been presented in several articles. Particularly, in adsorption, catalytic degradation, and membrane-based separation techniques, MOFs have shown a significant promise for removing contaminants from wastewater in a cost-efficient and long-lasting way. However, the actual industrial uses of MOFs have not been sufficiently studied and evaluated [6]. The innate fragility of these forms, however, limits the practical performance of MOF, since they might collapse in aqueous settings [7]. New MOF forms are currently being created to address their fragility drawback,

such as MOF-based aerogels and hydrogels, MOF-derived carbons (MDCs), hydrophobic MOFs, and magnetic framework composites (MFCs) to remove oily pollutants from water [8]. Recently, growing interest has been shown in the framework materials (MILs) prepared at Institute Lavoisier as efficient environmental adsorbents in wastewater treatment. Trivalent cations such as iron(III), aluminum(III), gallium(III), indium(III), vanadium(III), and chromium(III) are frequently found in carboxylate forms in modern MILs. Hence, this chapter sheds the light on the stability performance of MIL-88A with iron(III) as the central metal and fumaric acid as the organic ligand, as a case study of the MOF stability in aqueous solutions. Various characterization techniques were used to give a deeper insight into the robustness MIL-88A in aqueous solutions.

2.2. MOFs in wastewater treatment

MOFs have become good candidates for adsorption and catalytic applications in water treatment processes due to their high surface area, wide pore volume, and various functionalities [9]. Heavy metals, organic pollutants, and dyes are just a few of the pollutants that MOFs can be selectively adsorbed from wastewaters [10-13]. Their specially designed porosity enables strong adsorption capacity and effective water purification. Additionally, the surface chemistry of MOFs can be changed to improve the selectivity towards particular contaminants, making them useful materials for tackling a variety of water pollution problems [14, 15]. MOFs are suitable in water treatment applications because they can be engineered to have increased stability and recyclability. The recovered heavy metals from the MOFs can be used to recycle resources contributing to sustainable wastewater management. Figure 2.2 shows possible selective adsorption mechanisms of organic pollutants on MOFs.

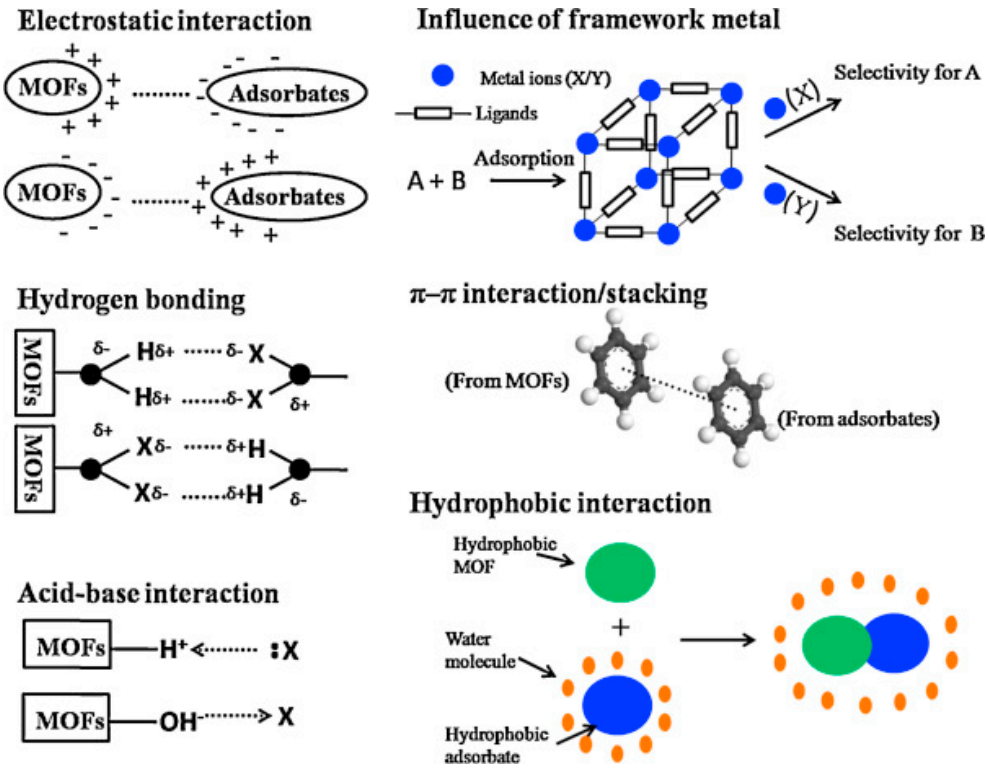

Figure 2.2 Plausible adsorption mechanisms of organic molecules on MOFs [16].

Another application for MOFs in wastewater treatment is the catalytic destruction of organic contaminants. MOFs can act as catalysts or catalyst supports for a variety of advanced oxidation processes, including photocatalysis and electrocatalysis [17]. Their distinct structure enables the immobilization of catalytic metal species, increasing the stability and activity of the catalyst. MOFs can help to produce of reactive species such as hydroxyl radicals as illustrated in Figure 2.3. Hydroxyl radicals are very good at breaking down organic pollutants [18]. Hence, the treatment of recalcitrant organic contaminants in wastewaters can be effectively accomplished by utilizing the catalytic properties of MOFs, resulting in cleaner water resources.

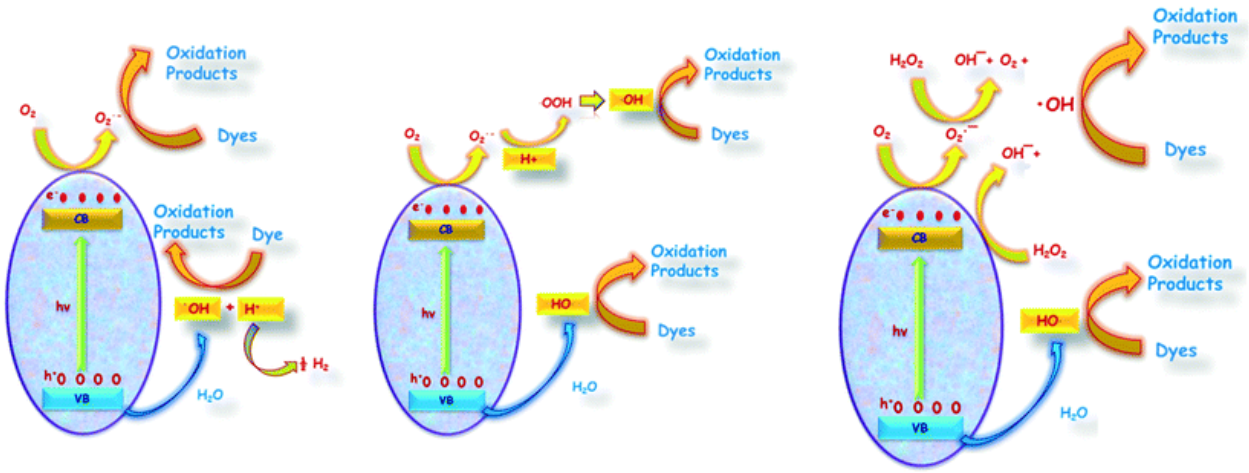

Figure 2.3 The generation of reactive oxidant species and dye oxidation via different AOPs under irradiation in the presence of MOF-based photocatalyst in aqueous solution [19].

MOFs can be used for membrane-based separation procedures in wastewater treatment in addition to adsorption and catalysis. The potential for the selective removal of particular contaminants, such as heavy metals, organic compounds, and emerging pollutants, has been explored by MOF-based membranes. Target contaminants can be effectively separated from water thanks to the customized pore size and functional groups of MOF membranes, which allow for a precise control of molecular transport [20]. The addition of MOF membranes to wastewater treatment systems has the advantage of cost and energy effective pollutant removal compared to nano-based materials [14, 20]. This will contribute in advancing the development of environmentally friendly water purification technologies. Impressively, Prince et al [21] explored an innovative surface chemistry for a self-cleaning MOF-based membrane with prevented bio-fouling by incorporating antibacterial silver nanoparticles as illustrated in Figure 2.4 [20, 21].

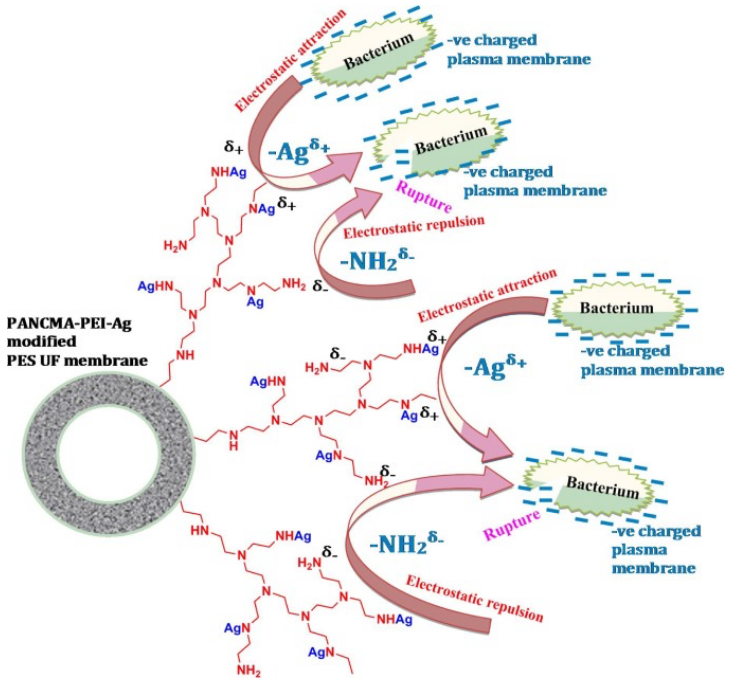

Figure 2.4 The self-cleaning property of MOF-based membrane [20].

2.3. MOFs stability in water: Assessment of the robustness of MIL-88A in an aqueous solution through experimental and DFT investigations

The stability of MOFs in a water-rich environment is an issue of huge interest, especially for adsorption and water purification applications. Chemical, thermal, and hydrolytic stability of MOFs in aqueous conditions are the key factors to evaluate their structural robustness. Chemical stability deals with bond breaking and structural collapse. More specifically, the more stable MOF is produced, the stronger the ion-covalent bond is between the organic linker and the metal structure. Moreover, the chemical and hydrolytic resilience of MOFs is significantly influenced by the pH of the solution. A metal-linker bond may be broken as a result of hydrolysis or linker displacement in acidic, neutral, or basic environments. The thermal stability of MOFs is undoubtedly of high importance for commercial applications in future, particularly in separation, energy, and catalytic processes. The hydrolytic stability is assessed by the susceptibility of metal-ligand bonds to hydrolysis. Many factors can play a significant role in stabilizing the structure MOFs, such as the choice of metal ions, ligands, and synthesis conditions. Researchers have made great strides in improving the hydrolytic stability of MOFs by developing techniques including the creation of hydrolytically stable ligands or metal nodes, post-synthetic alterations, and protective encapsulation.

2.3.1. MIL-88A synthesis and characterization

A previously described technique was used to synthesize MIL 88A with a few minor adjustments [22]. In a nutshell, 1 mmol of ferric chloride and 1 mmol of fumaric acid were mixed in 5 mL of deionized water water over the course of 4 hours while being stirred magnetically at 300 rpm in a round bottom flask. The flask was left to passively cool to room temperature after the heater have been switched off. To get rid of all the extra unreacted fumaric

acid and metal, the produced solid was decanted, collected, and washed three times with ethanol and deionized water in a 1:1 ratio and after that, it was washed once with acetone. Each time, the precipitate was obtained by centrifuging the solution for 10 minutes at 3500 rpm. The precipitate was allowed to dry for 10 h at 60 °C in a vacuum oven. Figure 2.5 shows the hydrothermal synthesis scheme of MIL-88A.

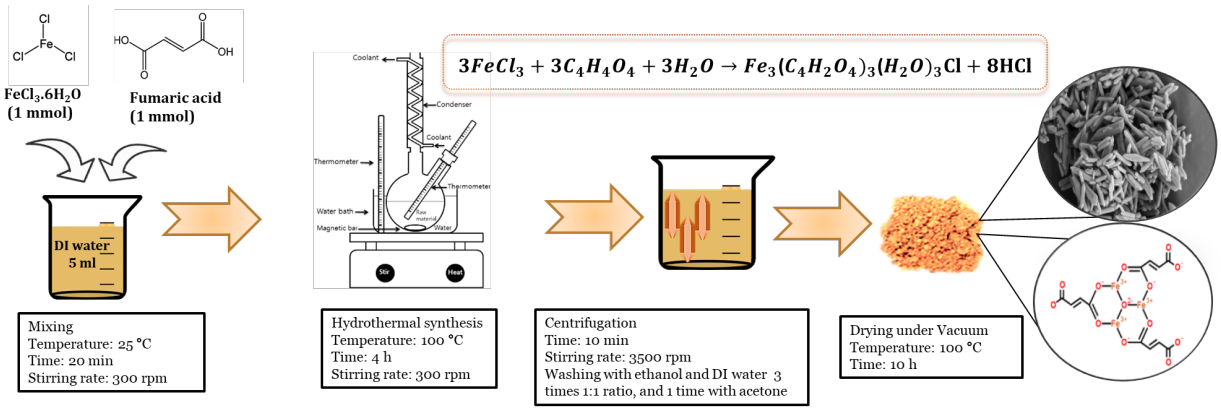

Figure 2.5 MIL-88A hydrothermal synthesis.

Figure 2.6a displays the XRD pattern of MIL-88A. Strong peaks at two angles 10.5° and 11.9° confirm the crystallinity of the prepared MIL-88A. Using the Scherrer equation at the aforementioned peaks, the average crystallographic domain size of MIL-88A was determined to be 17.4 nm. The UV-VIS spectra of MIL-88A in an aqueous solution is depicted in Figure 2.6b. The ligand-to-metal charge transfer (LMCT) optical transition is represented by the absorption peak at 250 nm, and the existence of iron complexes in the solution is indicated by the wavelength range from 290 to 380 nm. Figure 2.6c shows the SEM image of MIL-88A and a uniform rod-like structure at the nanometer scale was observed, with diameters between 100 and 800 nm which are consistent with the information reported previously. As can be seen in Figure 2.6d, the band at 672 cm^{-1} can be attributed to the vibration mode of the Fe-O bond, the FTIR spectrum at 1396 cm^{-1} and 1603 cm^{-1} can be attributed to the symmetric and asymmetric vibrations of the carboxyl group. According to the TGA analysis (Figure 2.6e), fumaric acid substantial mass loss of fumaric acid became visible at roughly 170 °C with a heating rate of 10 °C/min, and total dissociation was reached at 600 °C. Figure 2.6f, shows the DRS spectrum of the solid-state orange MIL-88A sample. By extrapolating linearization of the plot of $(F(R) h\nu)^{1/2}$ against the photon energy, the absorption peaks at 400 nm, where the optical band-gap was calculated and the result was found to be 2.78 eV, in accordance with information published in literature.

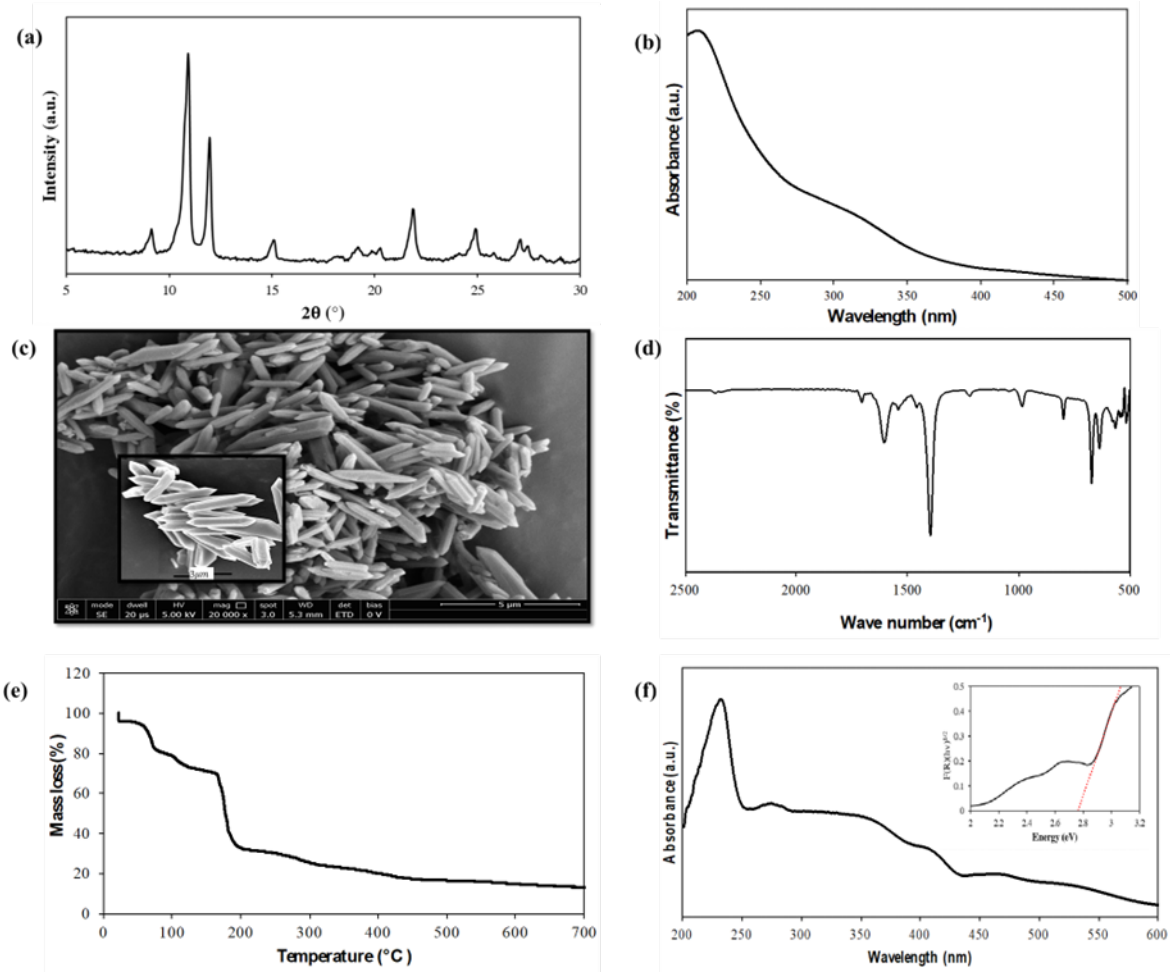

Figure 2.6 Synthesized MIL-88 A characterization a) XRD pattern b) UV-VIS spectrum in aqueous solution c) SEM image d) FTIR spectrum e)TGA analysis f) UV-VIS/DRS analysis with an estimation of the optical band-gap using the modified Kubelka-Munk function.

2.3.2 Chemical, thermal, and hydrolytic stability of MIL-88A

The impact of pH on the robustness of MIL-88A was examined under acidic, basic, and neutral conditions. The UV-VIS spectra of the solution upon interaction with MIL-88A are shown in Figure 2.7a at different pH values. Figures 2.7b and c display the SEM images for MIL-88A in both basic and acidic solutions. Figure 2.7d also shows the XRD patterns of MIL-88A in various media. The significant signal at wavelengths between 250 and 300 nm (Figure 2.7a) makes it abundantly clear that MIL-88A dissociates more readily in a basic medium than in acidic and neutral ones. This may be explained by hydrolysis, in which the cleavage of the iron-fumarate link causes MIL-88A to degrade in the presence of basic media. The SEM image of MIL-88A in basic media (Figure 2.7b) reveals that the crystals have been significantly fragmented. On the other hand, the crystals in the acidic medium (Figure 2.7c) resembled the original MIL-88A quite closely. These findings are consistent with the MIL-88A XRD patterns in various media (Figure 2.7d), which demonstrated how significantly the crystallinity in basic solution is impacted. Further details can be found in **Publication II**.

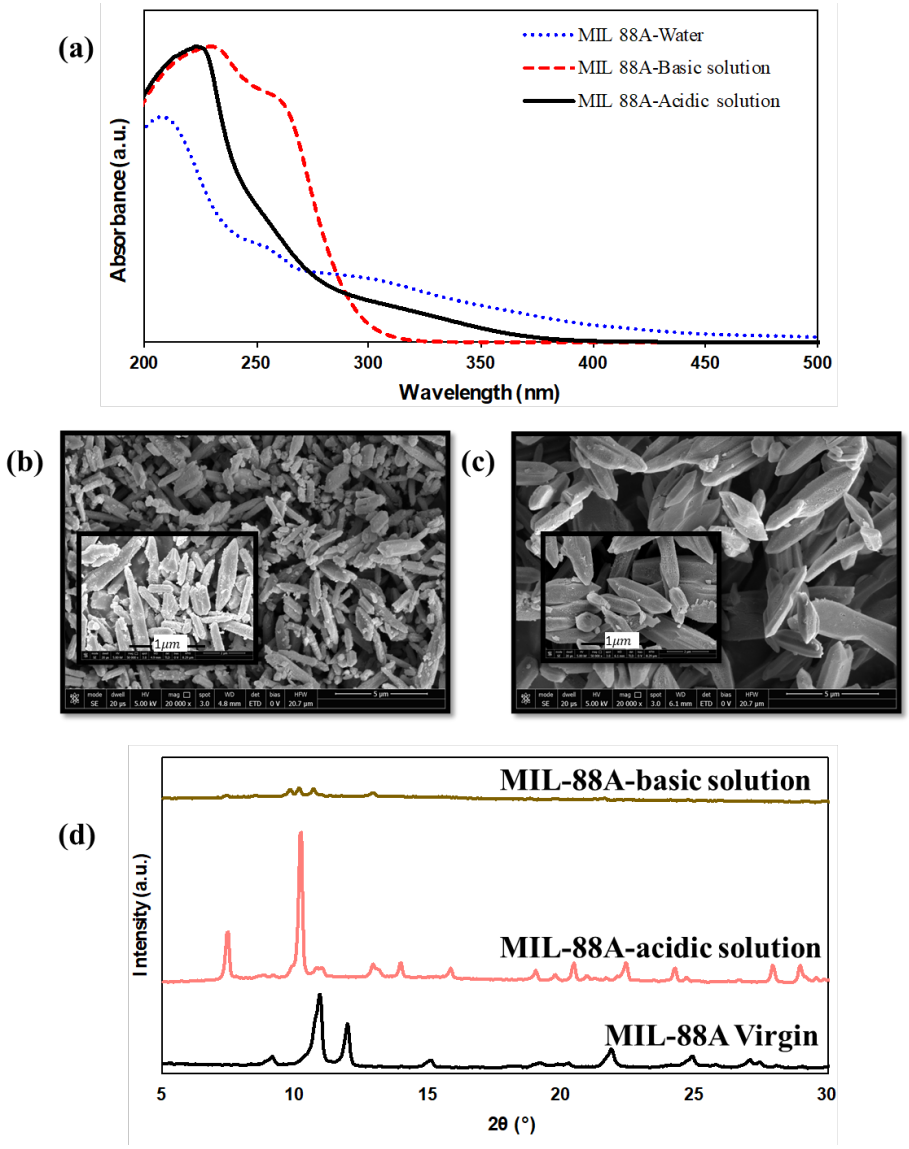

Figure 2.7 MIL-88A in basic and acidic media a) UV-VIS spectra of solutions b) SEM image of MIL-88A in contact with basic solution c) SEM image of MIL-88A in contact with acidic solution d) XRD patterns of MIL-88A in both acidic and basic solutions.

The thermal stability of MIL-88A, the UV-VIS spectra of contact solution, XRD pattern, and SEM images for the collected powder at different temperatures are presented in Figures 2.8a-c. It is evident that increasing the temperature of the aqueous solution has a direct impact on the MIL-88A stability. The UV-VIS spectra at 100 °C revealed a broad hub between 230 and 350 nm that indicated a large release of Fe (III) complexes into the solution. The thermally treated MIL-88A XRD patterns and SEM pictures (Figures 2.8b and c) demonstrated that the structure entirely degraded at 100 °C.

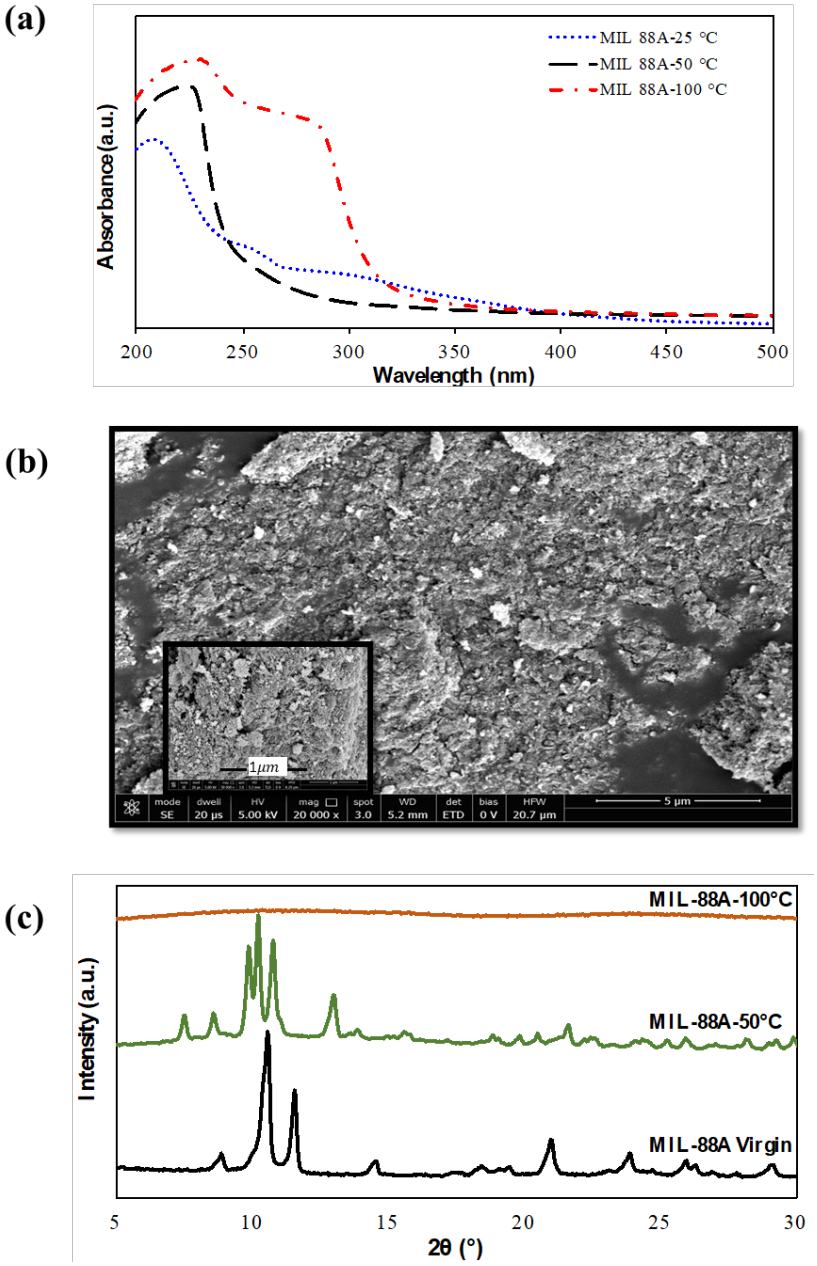

Figure 2.8 MIL 88A thermal stability a) UV-VIS spectra of contact solutions at different temperatures b) SEM and c) XRD patterns of MIL88A after hydrothermal treatment at 50°C and 100°C.

The hydrolytic stability of MIL-88A to a certain amount of water for four cycles presented in Figure 2.9 referred to as R1–R4 (short-term stability). The dry powder that has not yet been in contact with water is referred to as MIL-88A virgin. By carefully weighing the virgin MIL-88A before and after it was exposed to water, the disintegration during the four cycles of MIL-88A exposure was investigated and total mass loss was determined to 20%. MIL-88A was meticulously separated using centrifugation after each cycle, and it was dried overnight under vacuum at 60 °C. The broadening of the XRD peaks and the disappearance of some peaks in Figure 2.9a demonstrate that a collapse occurred, causing a partial loss of crystallinity. The

corresponding UV-VIS spectra of each cycle are displayed in Figure 2.9b. The absorbance intensities at wavelengths 208 nm and 298 nm vary, which confirms that the dissociation of iron ions changes in every cycle. The SEM image of MIL-88A after R4, showed a very large swelling effect, where the edges of the rod-like structure almost disappeared in most of the rods (Figure 2.9c). Further analysis can be found in **Publication II**.

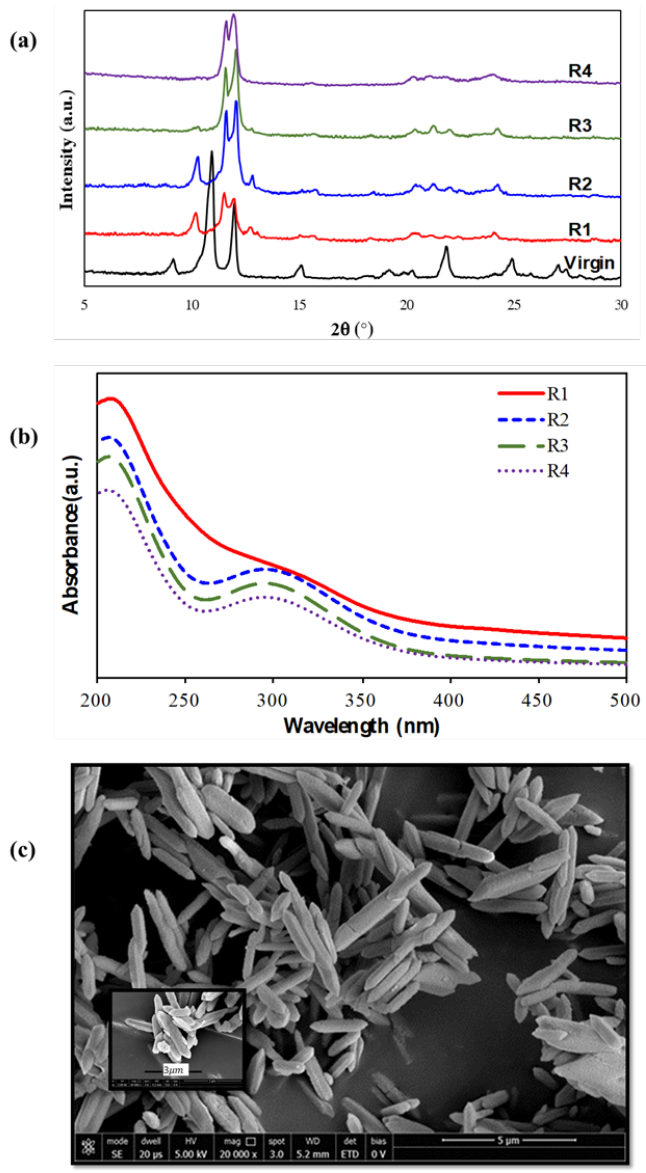

Figure 2.9 MIL-88A hydrolytic stability a) XRD spectra b) UV-VIS spectra c) SEM image for the solid after R4 cycle.

2.3.3. Nanocluster modelling and electronic structure

The MIL-88A nanocrystal was modeled preserving a C_3 rotational symmetry and it is reported in Figure 18. This nanocluster included six units containing three Fe^{3+} ions to preserve the symmetry. Each Fe^{3+} presents an almost octahedral coordination, where each iron-containing unit presents six carboxylate bidentate ligands, where two are kept as bridging ligands between two different units. Each unit has a cavity, where the oxygen atoms are almost equally shared

among the three iron atoms. The cluster presents thus an internal cavity of ~ 1.1 nm diameter enabling it to accommodate at least two chlorine ions, 0.7 nm apart from each other. The electronic structure of the nanocluster results in a stable antiferromagnetic coupled high-spin sextet ground state for the iron(III) centera, where also the spin density (right panel of Figure 2.10) preserves the C_3 symmetry. This result is in agreement with similar iron-containing catalytically active MOF systems [51].

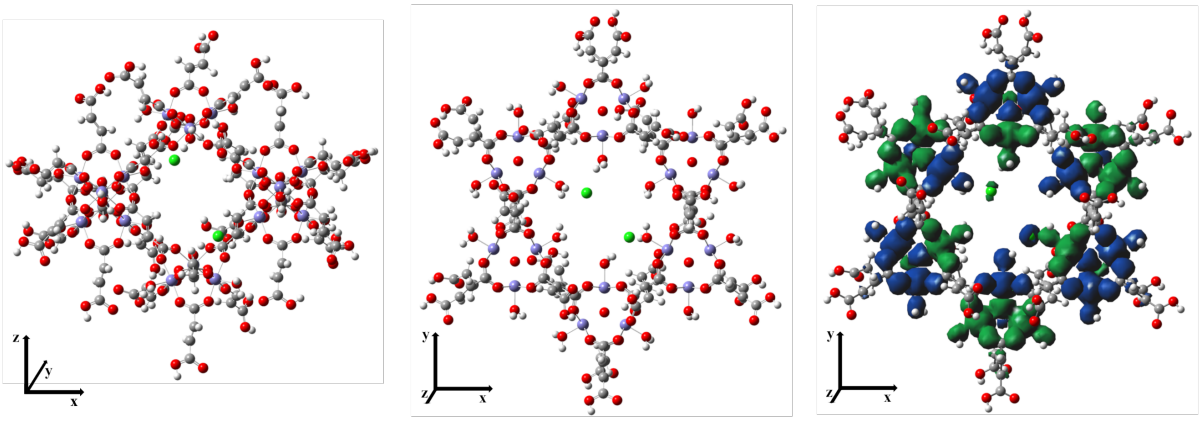

Figure 2.10 MIL-88A ball and stick nanocluster representation. Lateral (left) and front (middle) views. DFT calculated spin density (right, the difference between α and β densities, green and blue as positive and negative, respectively) iso-surface (isovalue= $4 \cdot 10^{-4}$).

Notably, the spin density spreads further from the iron centra and involving almost all atoms in the first coordination shell of the iron ions, resulting in an alternating spin density also in the water molecules inside the main cavity. Although the results are conceptual, it is interesting to point out the delocalization of spin density, since the water sites might be directly involved in the catalytic activity of the system.

2.4. Conclusions

Many MOFs which currently being used in numerous applications and could be deemed revolutionary, are unstable in water. Significant improvements have been made in the MOF design and synthesis in recent years. Innovative methods have been devised by researchers to regulate the crystal size, shape, and functionality of MOFs. These include coordination modulation methods, template-directed syntheses, and post-synthetic alterations. Additionally, computational techniques such as molecular modelling have been useful in understanding and forecasting the characteristics and behavior of MOFs, facilitating the logical development of novel and stable materials with an improved performance. Therefore, to advance towards future industrial applications, the MOF stability research is of utmost significance. The stability of MOFs in water is influenced by a number of parameters, including metal-ligand bonding, ligand design, and synthesis conditions. By using different characterization techniques including XRD, SEM, UV-Vis, the robustness of MIL-88A in aqueous solutions was studied under various conditions to evaluate its the chemical, thermal, and hydrolytic stability. The basic medium, where iron complexes were released in the solution, has a substantial impact on the

structure of MIL-88A. The crystal structure was noticeably altered as the water temperature increased to 100 °C, which indicated that this kind of MOFs are thermodynamically unstable. The kinetic stability of MIL-88A was revealed by hydrolytic stability tests with a loss in weight of 20% after the exposure to water four times. In conclusion, to fully utilize MOFs in wastewater treatment, a number of issues must be resolved. The major obstacle is the scalability of MOFs. Large-scale, reliable MOF synthesis still represents a considerable barrier. Furthermore, there is a need to enhance the long-term stability of MOFs under challenging wastewater conditions, such as the change in pH, high salinity, and complex organic matrices. Long-term performance and practical application of MOFs might be constrained by their vulnerability to structural deterioration and metal ion leaching. On the other hand, MOFs can be more expensive to produce and use than traditional treatment options. Therefore, cost-effective synthesis methods should be explored and hybrid systems that mix MOFs with other materials should be investigated. This could improve their performance and cost effectiveness. To overcome these challenges and enable the successful deployment of MOFs in large-scale wastewater treatment applications, interdisciplinary efforts and collaborations between researchers, industry, and policymakers are essential.

2.5. List of abbreviations

MOF	metal organic framework
MDC	MOF-derived carbon
MFC	magnetic framework composite
MIL	Framework materials from institute Lavoisier
DI	deionized
LMCT	ligand-to-metal charge transfer
XRD	X-ray diffraction
UV-VIS	ultraviolet-visible spectrophotometry
SEM	scanning electron microscopy
FTIR	Fourier transform infrared
TGA	thermogravimetric analysis
UV-VIS/DRS	ultraviolet–visible diffuse reflectance spectroscopy

2.6. References

[1] V. Russo, M. Hmoudah, F. Broccoli, M.R. Iesce, O.-S. Jung, M. Di Serio, Applications of Metal Organic Frameworks in Wastewater Treatment: A Review on Adsorption and Photodegradation, Frontiers in Chemical Engineering 2 (2020). https://doi.org/10.3389/fceng.2020.581487.
[2] R. Pallach, J. Keupp, K. Terlinden, L. Frentzel-Beyme, M. Kloß, A. Machalica, J. Kotschy, S.K. Vasa, P.A. Chater, C. Sternemann, M.T. Wharmby, R. Linser, R. Schmid, S. Henke, Frustrated flexibility in metal-organic frameworks, Nature Communications 12(1) (2021) 4097. https://doi.org/10.1038/s41467-021-24188-4.
[3] A.J. Howarth, A.W. Peters, N.A. Vermeulen, T.C. Wang, J.T. Hupp, O.K. Farha, Best Practices for the Synthesis, Activation, and Characterization of Metal–Organic Frameworks, Chemistry of Materials 29(1) (2017) 26-39. https://doi.org/10.1021/acs.chemmater.6b02626.
[4] S. Qiu, M. Xue, G. Zhu, Metal–organic framework membranes: from synthesis to separation application, Chemical Society Reviews 43(16) (2014) 6116-6140. https://doi.org/10.1039/C4CS00159A.
[5] P. Cheng, C. Wang, Y.V. Kaneti, M. Eguchi, J. Lin, Y. Yamauchi, J. Na, Practical MOF Nanoarchitectonics: New Strategies for Enhancing the Processability of MOFs for Practical Applications, Langmuir 36(16) (2020) 4231-4249. https://doi.org/10.1021/acs.langmuir.0c00236.
[6] H.U. Escobar-Hernandez, L.M. Pérez, P. Hu, F.A. Soto, M.I. Papadaki, H.-C. Zhou, Q. Wang, Thermal Stability of Metal–Organic Frameworks (MOFs): Concept, Determination, and Model Prediction Using Computational Chemistry and Machine Learning, Industrial & Engineering Chemistry Research 61(17) (2022) 5853-5862. https://doi.org/10.1021/acs.iecr.2c00561.
[7] N.C. Burtch, H. Jasuja, K.S. Walton, Water Stability and Adsorption in Metal–Organic Frameworks, Chemical Reviews 114(20) (2014) 10575-10612. https://doi.org/10.1021/cr5002589.
[8] N. Hanikel, M.S. Prévot, O.M. Yaghi, MOF water harvesters, Nature Nanotechnology 15(5) (2020) 348-355. https://doi.org/10.1038/s41565-020-0673-x.
[9] S. Zhang, J. Wang, Y. Zhang, J. Ma, L. Huang, S. Yu, L. Chen, G. Song, M. Qiu, X. Wang, Applications of water-stable metal-organic frameworks in the removal of water pollutants: A review, Environmental Pollution 291 (2021) 118076. https://doi.org/https://doi.org/10.1016/j.envpol.2021.118076.
[10] G. Lin, B. Zeng, J. Li, Z. Wang, S. Wang, T. Hu, L. Zhang, A systematic review of metal organic frameworks materials for heavy metal removal: Synthesis, applications and mechanism, Chemical Engineering Journal 460 (2023) 141710. https://doi.org/https://doi.org/10.1016/j.cej.2023.141710.
[11] W.-G. Jin, W. Chen, P.-H. Xu, X.-W. Lin, X.-C. Huang, G.-H. Chen, F. Lu, X.-M. Chen, An Exceptionally Water Stable Metal–Organic Framework with Amide-Functionalized Cages: Selective CO2/CH4 Uptake and Removal of Antibiotics and Dyes from Water, Chemistry – A European Journal 23(53) (2017) 13058-13066. https://doi.org/https://doi.org/10.1002/chem.201701884.
[12] V.K.-M. Au, Recent Advances in the Use of Metal-Organic Frameworks for Dye Adsorption, Frontiers in Chemistry 8 (2020). https://doi.org/10.3389/fchem.2020.00708.
[13] G. Sriram, A. Bendre, E. Mariappan, T. Altalhi, M. Kigga, Y.C. Ching, H.-Y. Jung, B. Bhaduri, M. Kurkuri, Recent trends in the application of metal-organic frameworks (MOFs) for the removal of toxic dyes and their removal mechanism-a review, Sustainable Materials and Technologies 31 (2022) e00378. https://doi.org/https://doi.org/10.1016/j.susmat.2021.e00378.

[14] R.S. Forgan, The surface chemistry of metal–organic frameworks and their applications, Dalton Transactions 48(25) (2019) 9037-9042. https://doi.org/10.1039/C9DT01710K.
[15] R.M. Rego, G. Kuriya, M.D. Kurkuri, M. Kigga, MOF based engineered materials in water remediation: Recent trends, Journal of Hazardous Materials 403 (2021) 123605. https://doi.org/https://doi.org/10.1016/j.jhazmat.2020.123605.
[16] Z. Hasan, S.H. Jhung, Removal of hazardous organics from water using metal-organic frameworks (MOFs): Plausible mechanisms for selective adsorptions, Journal of Hazardous Materials 283 (2015) 329-339. https://doi.org/https://doi.org/10.1016/j.jhazmat.2014.09.046.
[17] X. Li, D. Wu, T. Hua, X. Lan, S. Han, J. Cheng, K.-S. Du, Y. Hu, Y. Chen, Micro/macrostructure and multicomponent design of catalysts by MOF-derived strategy: Opportunities for the application of nanomaterials-based advanced oxidation processes in wastewater treatment, Science of The Total Environment 804 (2022) 150096. https://doi.org/https://doi.org/10.1016/j.scitotenv.2021.150096.
[18] V.K. Sharma, M. Feng, Water depollution using metal-organic frameworks-catalyzed advanced oxidation processes: A review, Journal of Hazardous Materials 372 (2019) 3-16. https://doi.org/https://doi.org/10.1016/j.jhazmat.2017.09.043.
[19] A. Singh, A.K. Singh, J. Liu, A. Kumar, Syntheses, design strategies, and photocatalytic charge dynamics of metal–organic frameworks (MOFs): a catalyzed photo-degradation approach towards organic dyes, Catalysis Science & Technology 11(12) (2021) 3946-3989. https://doi.org/10.1039/D0CY02275F.
[20] P. Kumar, V. Bansal, K.-H. Kim, E.E. Kwon, Metal-organic frameworks (MOFs) as futuristic options for wastewater treatment, Journal of Industrial and Engineering Chemistry 62 (2018) 130-145. https://doi.org/https://doi.org/10.1016/j.jiec.2017.12.051.
[21] J.A. Prince, S. Bhuvana, V. Anbharasi, N. Ayyanar, K.V.K. Boodhoo, G. Singh, Self-cleaning Metal Organic Framework (MOF) based ultra filtration membranes - A solution to bio-fouling in membrane separation processes, Scientific Reports 4(1) (2014) 6555. https://doi.org/10.1038/srep06555.
[22] T. Chalati, P. Horcajada, R. Gref, P. Couvreur, C. Serre, Optimisation of the synthesis of MOF nanoparticles made of flexible porous iron fumarate MIL-88A, Journal of Materials Chemistry 21(7) (2011) 2220-2227. https://doi.org/10.1039/C0JM03563G.

Chapter 3 —TiO_2 Brookite Nanoparticles: Adsorption of Bromocresol Green and Alizarin Red S

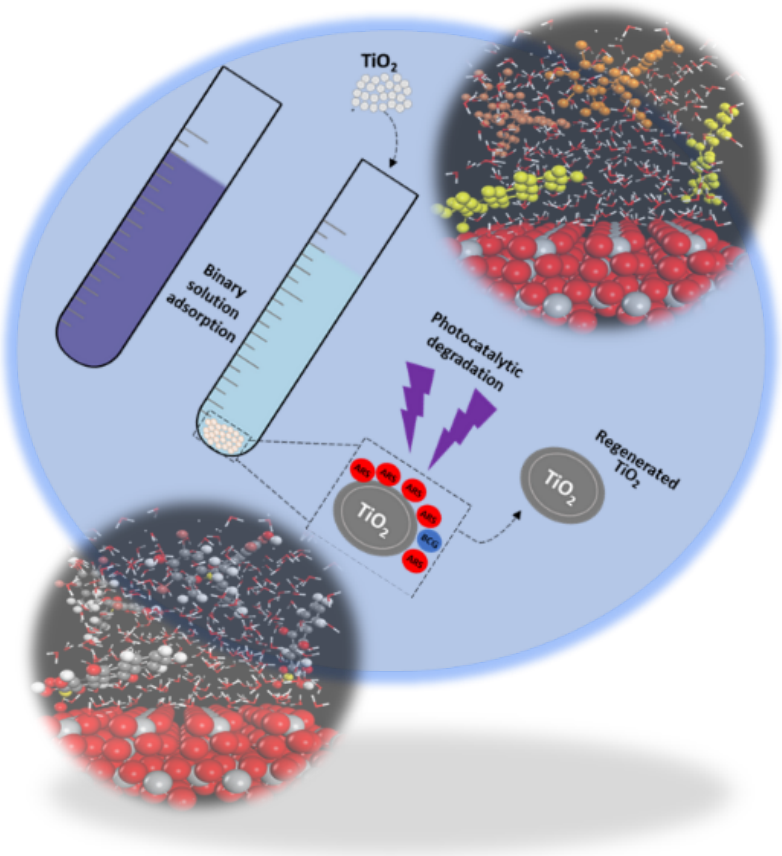

M. Hmoudah, A. El-Qanni, S. Abuhatab, N. N. Marei, A. El-Hamouz, B. J. Abu Tarboush, I. H Alsurakji, H. M. Baniowda, V. Russo, M. Di Serio, Competitive adsorption of Alizarin Red S and Bromocresol Green from aqueous solutions using brookite TiO_2 nanoparticles: experimental and molecular dynamics simulation, Environmental Science and Pollution Research 29(51), (2022): 77992-78008. doi.org/10.1007/s11356-022-21368-7

3.1. Introduction

TiO_2 nanoparticles have gained significant attention in wastewater treatment [1, 2]. When exposed to ultraviolet (UV) light, TiO_2 nanoparticles generate highly reactive hydroxyl radicals, which have strong oxidizing capabilities [3]. These radicals can effectively degrade various organic pollutants present in wastewaters, including emerging contaminants [3]. The high surface area and unique crystal structure of TiO_2 nanoparticles enhance their photocatalytic activity, making them a promising candidate for advanced wastewater treatment applications [4].

TiO_2 nanoparticles can be used in a variety of ways for wastewater treatment applications, including suspended nanoparticles, immobilized films, and coatings on different support materials [3, 4]. They are useful for effective pollutant removal through adsorption and photodegradation due to their high surface area-to-volume ratio and high stability. Furthermore, the size and shape of TiO_2 nanoparticles are easily adjusted to enhance their activity. Enhancing the activity and stability of the TiO_2 nanoparticles, examining their potential in combination with other treatment technologies, and addressing any potential environmental and health issues related to their use, are the main goals of many studies [4]. TiO_2 nanoparticles used in wastewater treatment show enormous promise, efficiency, and long-lasting water purification methods, assisting in the preservation of water resources.

In this chapter, TiO_2 brookite nanoparticles are used to competitively adsorb two anionic dyes namely; Alizarin Red S (ARS) and Bromocresol Green (BCG). Moreover, the adsorption mechanisms, kinetics, isotherms, thermodynamics, and molecular dynamics simulation are included in this work. Finally, the photoregeneration of the TiO_2 brookite nanoparticles under UV light irradiation, is also explored.

3.2. TiO_2 Brookite

A large number of documented works on the utilization of rutile and anatase forms of TiO_2 are reported in literature. However, the brookite phase is the least studied one [5-7], because it is challenging to create a highly pure composition of this phase. Nevertheless, Tomita et al. [8] investigated the hydrothermal method of producing nanocrystalline brookite. Additionally, Kozawa et al. [9] succeeded in developing a hydrothermal method for converting Mg_2TiO_4 into TiO_2 brookite. Recently, Machida et al. [10] were able to look at the synthetic conditions needed to make high-purity brookite. Additionally, it has been demonstrated that brookite TiO_2 nanoparticles have a high photocatalytic performance which can surpass that of the anatase phase [11]. This behavior is directly related to the defect levels through the thermodynamic equilibria of the point defects and electronic structures of pristine and defective brookite, by producing Ti_i^{4+} which produces ideal shallow defect levels in brookite whereas Ti^{4+} causes deep level formations [11].

3.3. Experimental procedure of adsorption and photodegradation tests

Batch experiments were conducted for both single and binary studies at 25°C to assess the adsorption of ARS and BCG as the organic model molecules on the TiO_2 nanoparticles. When needed, the pH was adjusted by introducing NaOH and HCl of 0.1M initial concentrations. As a result, the pH of the mixture was maintained at around 7. In each single adsorption experiment, a set of vials containing 5 ml solutions of ARS or BCG at various starting concentrations were mixed with 25 mg of nanopowder. The experimental adsorption and photodegradation systems for single and binary experiments are shown in Figure 3.1. The optical spectra scan captured during UV-Vis analysis for the wavelength in the range of 200 to 800 nm and the corresponding absorbance results of the solutions were recorded. The absorbance measurements were reported for a binary system of ARS and BCG at their maximal absorbance wavelengths, which are 286 nm for ARS and 616 nm for BCG, respectively. All further the details about the experimental procedures can be found in **Publication III**.

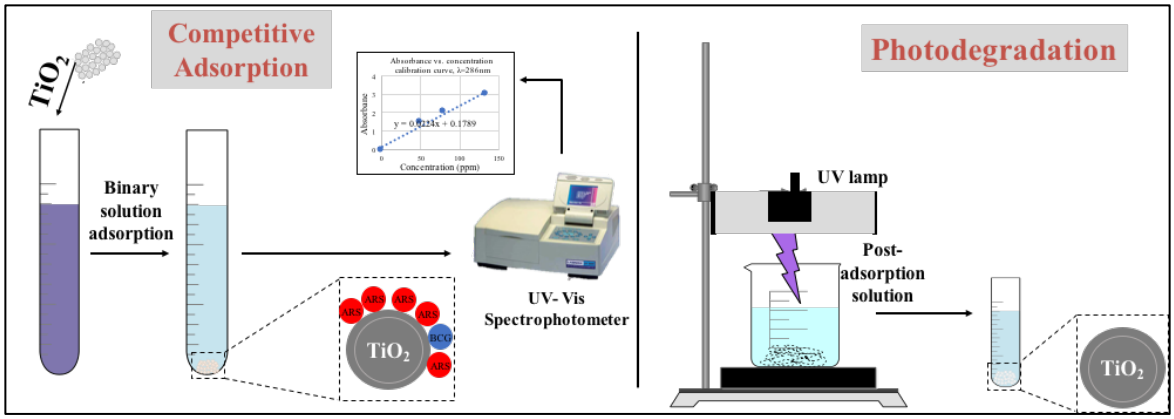

Figure 3.1 A schematic representation of the experimental adsorption and photoregeneration procedures.

3.3.1. Adsorption isotherms of single and binary systems

In the design of adsorption equipment, adsorption isotherm models offer mechanistic information about the adsorption process and the maximum adsorption capacity, to assess the performance of any adsorbent [12]. In this work, single adsorption isotherm data were fitted and analysed using the Sips model which combines Langmuir and Freundlich models deduced for predicting the adsorption in heterogeneous systems as shown below [13, 14];

$$Q_e = \frac{Q_m\,(k_s C_e)^{n_s}}{1 + (k_s C_e)^{n_s}} \tag{3.1}$$

where Q_e is the adsorption capacity at equilibrium $(mg.g^{-1})$, $Q_m\,is\,the$ maximum adsorbed amount $(mg.g^{-1}), k_s$ is the Sips adsorption equilibrium constant $(L.mg^{-1})$, C_e is the equilibrium concentration $(mg.L^{-1}), n_s$ is the Sips constant (dimensionless).

After recording the UV-Vis absorbance values, the following equations were used to perform the adsorption uptake analysis of the binary solutions [15, 16];

$$C_A = \frac{k_{B_2}A_1 - k_{B_1}A_2}{k_{A_1}k_{B_2} - k_{A_2}k_{B_1}} \quad (3.2)$$

$$C_B = \frac{k_{A_2}A_2 - k_{A_1}A_1}{k_{A_1}k_{B_2} - k_{A_2}k_{B_1}} \quad (3.3)$$

where C_A and C_B $(mg.L^{-1})$ are the concentrations of the organic contaminants in the binary solution, $k_{A_1}$and k_{A_2} are the slopes of the calibration curves of ARS and BCG at the maximum wavelengths (λ_{max}), $k_{B_1}$and k_{B_2} are the slopes of the calibration curves of ARS and BCG, respectively. In addition, A_1 and A_2 (dimensionless) are the absorbances of ARS and BCG in the binary solution at λ_{max} of each model molecule.

The experimental data for the binary solutions of competitive adsorption were analyzed using the Extended-Sips isotherm model [17, 18],

$$Q_e = \frac{Q_m\,(k_{si}C_{ei})^{n_{si}}}{1 + (k_{si}C_{ei})^{n_{si}} + (k_{sj}C_{ej})^{n_{sj}}} \quad (3.4)$$

where Q_e is the adsorption capacity at equilibrium $(mg.g^{-1})$, k_s is the Sips adsorption equilibrium constant $(L.mg^{-1})$, n_s is the Sips constant (dimensionless), Q_m is the maximum adsorbed amount $(mg.g^{-1})$, indices i and j represent the sorbate species.

The non-linear Chi-square (χ^2) analysis was employed to assess the goodness of the data fitting results. The χ^2 values were obtained using the following equation [19],

$$\chi^2 = \sum \frac{(Q_e - Q_{e(model)})^2}{Q_{e(model)}} \quad (3.5)$$

where Q_e and $Q_{e(model)}$ are the equilibrium uptake obtained experimentally and estimated by model fitting $(mg.g^{-1})$, respectively. The estimation of the isotherm parameters and the χ^2 analysis were performed using the Excel 2019 software. The low values of χ^2 indicate the agreement of the model and the experimental data.

The percentage of adsorption was calculated using the formula in the equation below:

$$\%A = \frac{C_o - C_e}{C_o} \times 100\% \quad (3.6)$$

where % A is the percentage of adsorption of the dyes, C_o is the initial concentration of the sample before irradiation under UV light $(mg.L^{-1})$; C_e is the concentration of the sample after irradiation under UV light $(mg.L^{-1})$.

Figure 3.2 illustrates the excellent agreement between the experimental data and the Sips model for the single case of ARS and BCG molecules at 25 °C and pH 7.0, whichwas confirmed by the low values of χ^2 for the Sips model which were 0.019 and 0.13 for the ARS and BCG models, respectively.

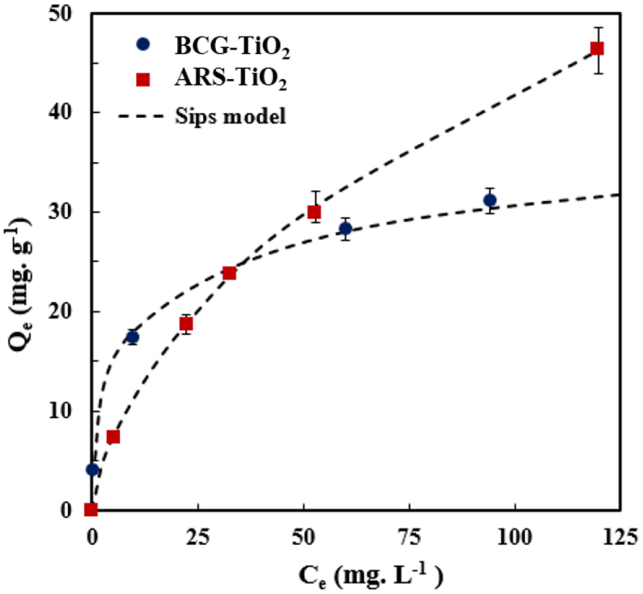

Figure 3.2 Macroscopic single solution-phase adsorption isotherms of BCG and ARS on TiO_2 nanoparticles. Experimental conditions: nanopowder dose, 5 $g.L^{-1}$; contact time, 120 *min*; temperature, 25 ℃; and pH, 7.0. The symbols are experimental data, and the solid dashed lines are the Sips model.

Table 3.1 provides a summary of the Sips model fitting parameters for the single adsorption isotherm. Understanding the nature of interaction between the dyes and the surface of TiO_2 nanoparticles depends primarily on the heterogeneity factor (n_s) values in the Sips model. The acquired data in this study show that the dimensionless (n_s) parameter depends more on adsorbate rather than adsorbent, and qualitatively defines the heterogeneity of the adsorbate-adsorbent interaction. The heterogeneous adsorption process is confirmed by the reported n_s data for both cases being less than 1 (n_s =0.68 and 0.42 for ARS and BCG, respectively).

Table 3.1 Parameters estimated for single adsorption isotherms of the Sips model.

ARS			**BCG**		
Q_m	k_s	n_s	Q_m	k_s	n_s
147.57	0.017	0.68	53.30	0.19	0.42

Figure 3.3 shows the Extended-Sips model of ARS and BCG molecules on TiO_2 nanoparticles at pH of around 7 and 25 ºC. The χ^2 values for the applied Extended-Sips model were 6.7×10^{-3} and 4.5×10^{-5} for ARS and BCG in the binary solution, respectively. As indicated in Table 3.2, it is important to note that the n_s values for the ARS in both single and binary systems remain 0.68, indicating that the ARS-TiO_2 adsorption isotherm was comparable to that in the single system. This supports the selectivity TiO_2 nanoparticles toward the selective adsorption of ARS molecules in the presence of BCG molecules, as the energy of the binding sites remained

constant, supporting the selective adsorption of ARS molecules. On the other hand, the presence of ARS molecules, the adsorption behavior of BCG-TiO_2 moves towards the Langmuir regime. It might be assumed that BCG molecules in the binary solution are chemisorbed in a monolayer on the surface of TiO_2 nanoparticles because the n_s value increased from 0.42 to 0.92 in the presence of ARS molecules. Further interpretations can be found in **Publication III**.

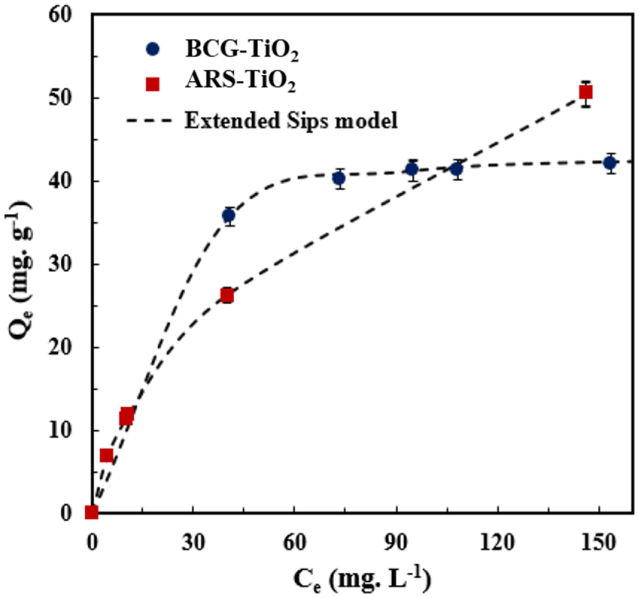

Figure 3.3 Macroscopic binary solution-phase adsorption isotherm of BCG and ARS on TiO_2 nanoparticles. Experimental conditions: TiO_2 dose, 5 $g.L^{-1}$; contact time, 120 *min*; temperature, 25 ℃; and pH, 7.0. The symbols represent the experimental data, and the solid lines represent the Extended Sips model.

Table 3.2 Parameters of competitive adsorption isotherm.

ARS			BCG		
Q_m	k_s	n_s	Q_m	k_s	n_s
140.01	0.0029	0.68	45.45	0.1	0.92

3.3.2. Adsorption kinetics

To find the time needed to reach equilibrium for the adsorption of ARS and BCG ions on TiO_2 nanoparticles, the adsorption uptake was determined at different time intervals from 2 to 180 *min*. The kinetic study was carried out at a constant adsorbent dose (25 mg). The initial concentration of the adsorbates was fixed at 50 $mg.L^{-1}$, the pH was controlled at around 7.0 at 25 ℃. The following external mass transfer model was used to fit the experimental kinetic data [20],

$$\frac{dC}{dt} = -k_m a(C - C_s) \quad (3.7)$$

where k_m is the external mass transfer coefficient in the liquid phase ($m.min^{-1}$); a is the specific surface area per the volume of the adsorbent ($m^2.m^{-3}$); C is the concentration of the model molecule ($mg.L^{-1}$) at any time; and C_s is the concentration of the molecules at the interface with the adsorbent ($mg.L^{-1}$). The value of C_s can be determined from reforming the Sips model parameters in section 3.1, as shown below,

$$C_s = \left[\frac{Q}{{k_s}^{n_s}(Q_m - Q)}\right]^{{n_s}^{-1}} \tag{3.8}$$

Parameter Q was obtained from the following mass balance equation,

$$Q = \frac{V\,(C_o - C)}{m} \tag{3.9}$$

where V is the volume of the solution (mL) and m is the mass of the nanoparticles (mg). The following first-order differential equation was obtained by substituting equations (3.8) and (3.9) into equation (3.7),

$$\frac{dC}{dt} = -k_m a\left[C - \left[\frac{V\,(C_o - C)}{{k_s}^{n_s}\left(m\,Q_m - V\,(C_o - C)\right)}\right]^{n_s^{-1}}\right] \tag{3.10}$$

The initial condition of this ordinary differential equation is $C = C_o$ at time zero. The Sips constants can be obtained from the adsorption isotherm of the binary system. Polymath 6.10 software was used to estimate the $k_m a$ (min^{-1}) values by fitting the experimental data to equation (3.10).

Figures 3.4 and 3.5 show the results of the single adsorption of ARS and BCG on TiO_2 nanoparticles at predefined time intervals. The experimental findings were validated using the external mass transfer model. Particularly, within the first 7 min, the concentration of ARS dramatically dropped before becoming constant, which confirms how quickly ARS was eliminated. On the contrary, as demonstrated in Figure 3.5, the concentration of BCG gradually decreased over time to reach the equilibrium with more than 180 minutes. In this way, the adsorption of ARS on TiO_2 is dominant. This could be attributed to the very low molecular weight of ARS and the ease with which relatively small molecules can move easily in comparison with BCG molecules, thus, reducing the external mass transfer limitation. The observed pattern can also be described well by size effects, which are explained in terms of the steric effect (steric barrier). While big bulky molecules will have fewer chemical interactions due to size effects, steric hindrance, which results from steric effects, entails lowering chemical interactions as a result of steric bulk. It is significant to note that once the adsorption isotherm was examined, a comparable pattern was observed, where similar analysis was used. Thus, the slow and gradual decrease in BCG kinetics can be attributed to the slow external diffusion of BCG on TiO_2 nanoparticles, which has been confirmed by the relatively low $k_m a$ value being 0.59 min^{-1}.

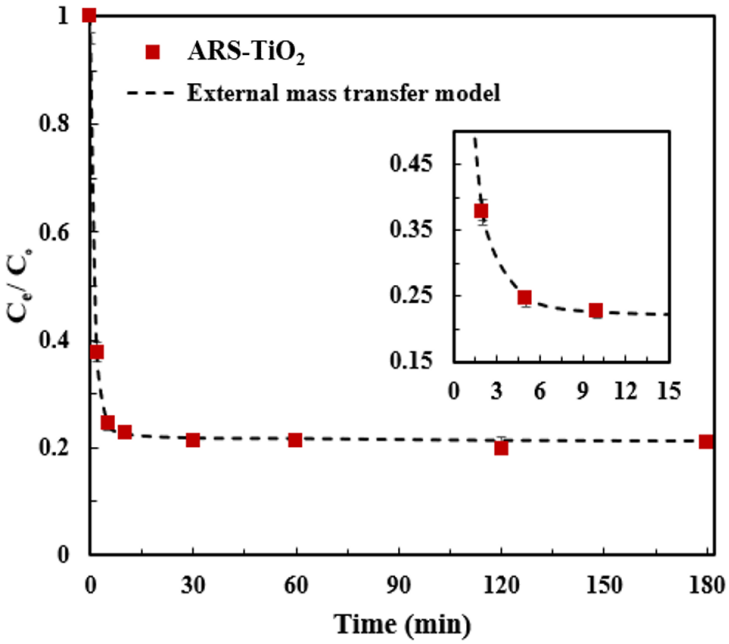

Figure 3.4 Adsorption kinetics of ARS on TiO_2 nanoparticles. Experimental conditions: TiO_2 dose, 5 $g.L^{-1}$; contact time, 60 *min*; temperature, 25°C; and pH, 7.0. The symbols are experimental data, and the solid dashed lines are the external mass transfer model.

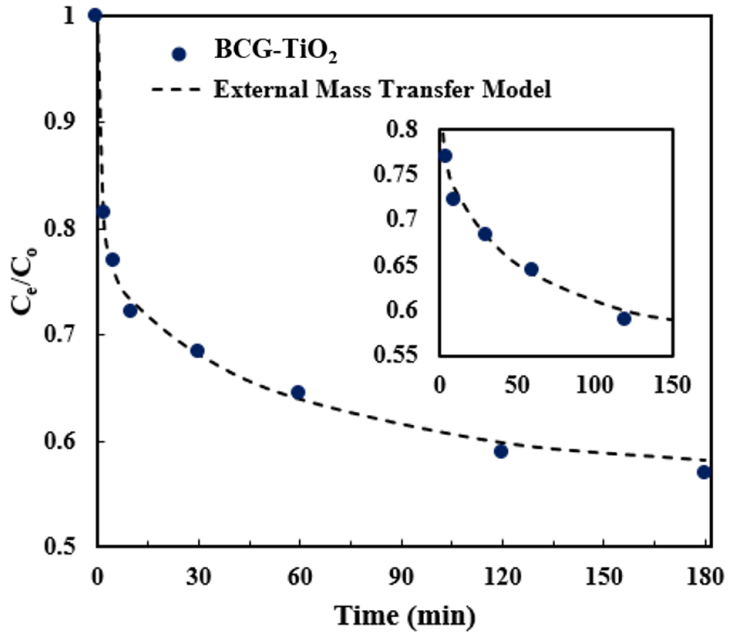

Figure 3.5 Adsorption kinetics of BCG on TiO_2 nanoparticles. Experimental conditions: TiO_2 dose, 5 $g.L^{-1}$; contact time, 60 *min*; temperature, 25°C; and pH, 7.0. The symbols are experimental data, and the solid dashed lines are the external mass transfer model.

3.3.3. Adsorption thermodynamics for single and binary systems

The investigation of the adsorption thermodynamics of ARS and BCG on the TiO_2 nanoparticles was conducted in batch experiments at three different temperatures, 25, 35, and 45 ℃, under identical experimental conditions of adsorption isotherm experiments and using Sips model for fitting the adsorption experimental data. The values of the thermodynamic parameters, i.e; Gibbs free energy (ΔG^o), enthalpy (ΔH^o), and entropy (ΔS^o) were determined using the following equations,

$$\Delta G^{\circ}_{ads} = -R\,T\,ln(K) \tag{3.11}$$

where $K = \mathrm{k_s}\,Cs^{ns}$

$$ln(K) = \frac{\Delta S^{\circ}_{ads}}{R} - \frac{\Delta H^{\circ}_{ads}}{R\,T} \tag{3.12}$$

The trends of adsorption isotherms and the values of the thermodynamics parameters are reported in Figure 3.6 and Table 3.3 for the adsorption of ARS-TiO_2 in the binary solution. The negative value of ΔG°_{ads} indicates spontaneous adsorption. The of ΔG°_{ads} values decreased as the temperature increased, indicating that the adsorption is spontaneous and inversely related to temperature. The positive value of ΔS°_{ads} suggests that the system appears to exhibit random behaviour. The calculated ΔH°_{ads} positive value which is less than 40.0 $kJ.mol^{-1}$ implies that the interaction between the surface ARS and the TiO_2 nanoparticles in this binary solution is physisorption [56]. As a result, a rise in temperature causes higher physical adsorption of ARS at the equilibrium of ARS molecules.

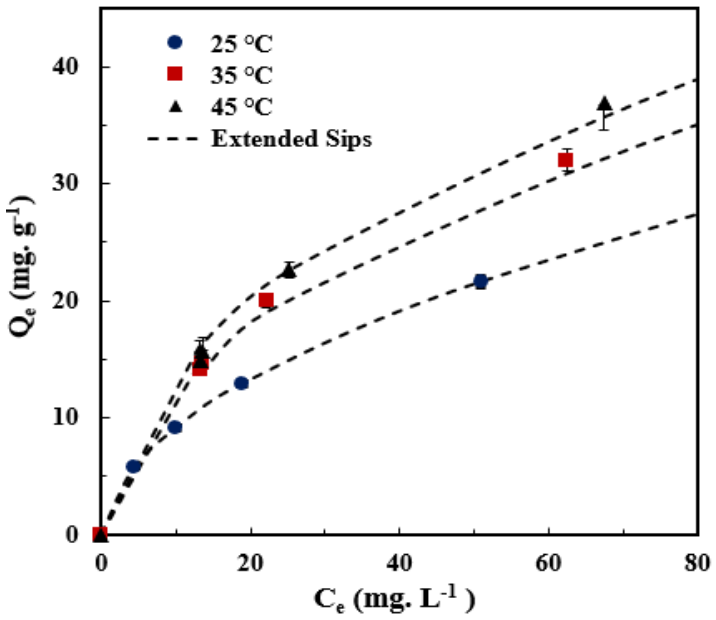

Figure 3.6 Adsorption isotherms of ARS on TiO_2 in the binary solution of BCG and ARS at different temperatures.

Table 3.3. Estimated parameters of ARS adsorption on TiO_2 at different temperatures in binary systems of BCG and ARS.

Temperature (°C)	Q_m	k_s	n_s	ΔG°_{ads} $(kJ.mol^{-1})$	ΔH°_{ads} $(kJ.mol^{-1})$	ΔS°_{ads} $(J.mol^{-1}.K^{-1})$
25	143.18	0.00107	0.594	-6.81	27.62	116.13
35	148.43	0.00186	0.596	-8.53	--	--
45	154.12	0.00207	0.597	-9.11	--	--

The adsorption isotherms of BCG on TiO_2 in binary solution of BCG and ARS at different temperatures are displayed in Figure 3.7. Table 3.4 lists the thermodynamic parameters of BCG adsorption on TiO_2 nanoparticles. The ΔG°_{ads}value was negative, indicating spontaneous adsorption. The temperature-dependent value of ΔG°_{ads} indicates that the spontaneous nature of adsorption is inversely correlated with the adsorption temperature. Furthermore, the system appears to behave randomly based on the positive value of ΔS°_{ads}. The fact that the ΔH°_{ads} value was positive (41.82 kJ. mol-1) suggested that BCG had chemisorbed on the surface of the TiO_2 nanoparticles [56]. Therefore, to provide a thorough examination of this sorption behavior, mathematical modelling was investigated.

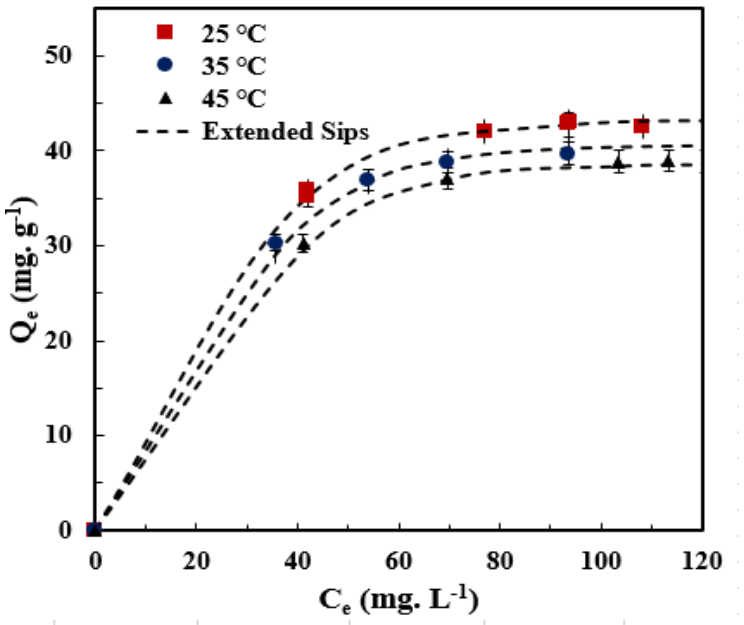

Figure 3.7 Adsorption isotherms of BCG on TiO_2 in a binary solution of BCG and ARS at different temperatures.

Table 3.4 Estimated parameters of BCG adsorption on TiO_2 at different temperatures in binary systems of BSG and ARS.

Temperature (°C)	Q_m	k_s	n_s	ΔG°_{ads} $(kJ.mol^{-1})$	ΔH°_{ads} $(kJ.mol^{-1})$	ΔS°_{ads} $(J.mol^{-1}.K^{-1})$
25	45.45	0.099	0.913	-33.73	41.82	252.73
35	43.93	0.1	0.925	-35.51	--	--
45	43.69	0.11	0.96	-38.82	--	--

3.3.4. Computational modelling of TiO_2 nanoparticles

The adsorption mechanism and the interaction between the adsorbate molecules and the surfaces of the TiO_2 nanoparticles was analyzed with computational modelling which was performed using Accelrys Material Studio Software [21] for ARS and BCG molecules in the single and binary cases, taking into account the presence of water molecules. The structure geometry was optimized by Forcite. The condensed-phase optimized molecular potentials for atomistic simulation studies were obtained through (COMPASS) forcefield calculations. The TiO_2 brookite (100) surface was created and optimized using the same optimization procedure. Additional information about the TiO_2 optimized structure can be found in **Publication III**.

3.3.5. Adsorption simulation of BCG and ARS on TiO_2 (100)

ARS molecules tend to to be in a tilted position on the surface of TiO_2 nanoparticles. The results of the adsorption studies confirmed that the ARS molecules showed higher adsorption affinity than the BCG adsorption on the surface. This is due to the ARS adsorption lower energy in comparison with the BCG molecules. A closer interaction with the Ti atoms in the TiO_2 structure was created due to the S-O and S=O bonds and Na^+. The ARS molecules bound to TiO_2 by the interaction of electron pairs on the hydroxyl oxygens in Alizarin with the d orbitals of the Ti atoms. ARS chemical binding with TiO_2 can exist through a Ti-O bond, through two Ti-O bonds directed at a single or two separate Ti atoms [66]. For a binary system, BCG molecules showed a higher adsorption energy and a lower affinity towards the TiO_2 surface. This could be due to the atomic distribution and shape of the BCG molecules resulted in increasing the adsorption energy and a higher adsorption distance between the surface and the BCG molecule, as shown in Figure 3.8. Additional simulation results are elaborated in **Publication III**.

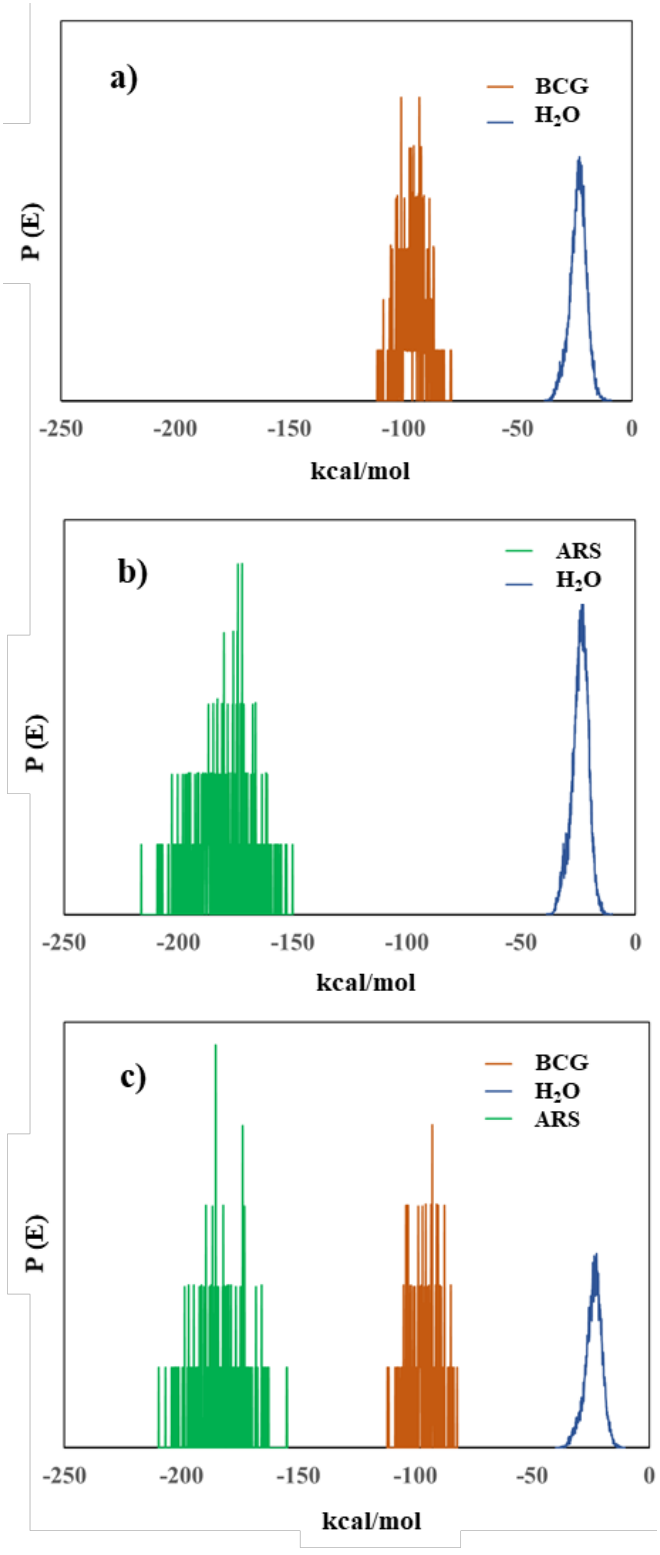

Figure 3.8 The adsorption energies distribution of the adsorbed molecules ARS and BCG in single and binary systems: a) BCG and H_2O adsorption energy in the 4 BCG single component adsorption system, b) ARS and H_2O adsorption energy in the 4 ARS single component adsorption system, and c) BCG, ARS, and H_2O adsorption energy in the 4 BCG binary components adsorption system.

3.4. Photoregenaration of TiO_2 nanoparticles

To develop catalysts that are affordable, scalable, and environmentally friendly. The regeneration research is of utmost importance. TiO_2 nanoparticles were regenerated using a UV light lamp (6 W, λ = 365 nm) inside a 50 mL glass beaker with continuous magnetic stirring after the dyes were adsorbed on the TiO_2 surface. All the experimental conditions are reported in detail in **Publication III**. Figure 3.9 shows the effectiveness of TiO_2 nanoparticles after two cycles of photo regeneration. The efficiency of TiO_2 decreased by 10.9% after the adsorption of ARS, while the adsorption efficiency of the BCG declined significantly by almost 29.4%. This might be alluded to the larger molecular weight of BCG molecule. Similarly, a study by Lachheb et al. explained that the variation and effectiveness of photodegradation rates of five different dyes might be relevant to their molecular weights [68].

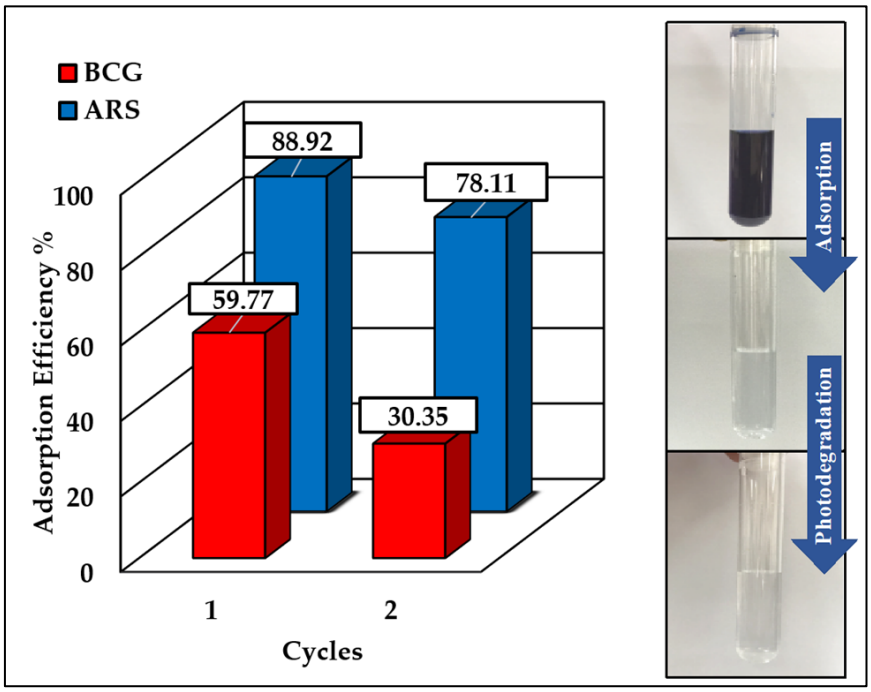

Figure 3.9 First and second cycle binary adsorption efficiencies of ARS and BCG on TiO_2 nanoparticles.

3.5. Conclusions

In this study, the batch adsorption and the subsequent photodegradation activity of TiO_2 brookite nanoparticles was screened for the elimination of the anionic dyes, ARS and BCG in single and binary solutions. In the single adsorption experiment, an excellent agreement between the experimental results and the Sips model for the ARS and BCG molecules was obtained, with a higher adsorption affinity toward BCG and a higher adsorption uptake capacity of ARS. In the binary adsorption systems, TiO_2 brookite nanoparticles were successful in adsorbing both model molecules, verifying the selective adsorption of the ARS molecules and demonstrating the quality of the Extended-Sips model fitting results. The kinetic findings revealed that the majority of the adsorption of ARS on TiO_2 nanoparticles is external, with ARS reaching equilibrium more quickly than BCG. The findings of the thermodynamic study

demonstrated that the adsorption process was spontaneous, with behaviors for the ARS and BCG dyes both the physisorption and chemosorption effects, respectively. Lower adsorption energies for ARS molecules were observed in the range of 150 – 250 $kcal.mol^{-1}$, in both the single and binary systems. This explains the higher entropy value for the ARS adsorption, as revealed by the thermodynamic analysis. Two regeneration cycles of the TiO_2 nanoparticles were conducted under UV irradiation. The adsorption efficiency of the TiO_2 nanoparticles decreased about 11% for the adsorption of ARS per each cycle, whereas it dropped significantly to 29% for the adsorption of BCG per each cycle.

3.6. List of abbreviations

UV	ultraviolet
ARS	Alizarin red s
BCG	Bromocresol green

3.7. References

[1] M.S. Waghmode, A.B. Gunjal, J.A. Mulla, N.N. Patil, N.N. Nawani, Studies on the titanium dioxide nanoparticles: biosynthesis, applications and remediation, SN Applied Sciences 1(4) (2019) 310. https://doi.org/10.1007/s42452-019-0337-3.
[2] M.A. Irshad, R. Nawaz, M.Z.u. Rehman, M. Adrees, M. Rizwan, S. Ali, S. Ahmad, S. Tasleem, Synthesis, characterization and advanced sustainable applications of titanium dioxide nanoparticles: A review, Ecotoxicology and Environmental Safety 212 (2021) 111978. https://doi.org/https://doi.org/10.1016/j.ecoenv.2021.111978.
[3] D. Kanakaraju, B.D. Glass, M. Oelgemöller, Titanium dioxide photocatalysis for pharmaceutical wastewater treatment, Environmental Chemistry Letters 12(1) (2014) 27-47. https://doi.org/10.1007/s10311-013-0428-0.
[4] F. Han, V.S.R. Kambala, M. Srinivasan, D. Rajarathnam, R. Naidu, Tailored titanium dioxide photocatalysts for the degradation of organic dyes in wastewater treatment: A review, Applied Catalysis A: General 359(1) (2009) 25-40. https://doi.org/https://doi.org/10.1016/j.apcata.2009.02.043.
[5] A.D.P.M.B.L. Palmisano, Brookite, the Least Known TiO_2 Photocatalyst, Catalysts 3(1) (2013) 36-73.
[6] M.R. Al-Mamun, S. Kader, M.S. Islam, M.Z.H. Khan, Photocatalytic activity improvement and application of UV-TiO2 photocatalysis in textile wastewater treatment: A review, Journal of Environmental Chemical Engineering 7(5) (2019) 103248. https://doi.org/https://doi.org/10.1016/j.jece.2019.103248.
[7] M. Choi, J. Lim, M. Baek, W. Choi, W. Kim, K. Yong, Investigating the Unrevealed Photocatalytic Activity and Stability of Nanostructured Brookite TiO_2 Film as an Environmental Photocatalyst, ACS Applied Materials & Interfaces 9(19) (2017) 16252-16260. https://doi.org/10.1021/acsami.7b03481.
[8] K. Tomita, V. Petrykin, M. Kobayashi, M. Shiro, M. Yoshimura, M. Kakihana, A Water-Soluble Titanium Complex for the Selective Synthesis of Nanocrystalline Brookite, Rutile, and

Anatase by a Hydrothermal Method, Angewandte Chemie International Edition 45(15) (2006) 2378-2381. https://doi.org/10.1002/anie.200503565.
[9] T. Kozawa, H. Hattori, S. Ogo, Y. Ide, Y. Suzuki, Hydrothermal conversion of Mg_2TiO_4 into brookite-type TiO_2 under mild conditions, Journal of Materials Science 48(22) (2013) 7969-7973. https://doi.org/10.1007/s10853-013-7607-z.
[10] M. Machida, M. Kobayashi, Y. Suzuki, H. Abe, Facile synthesis of > 99% phase-pure brookite TiO_2 by hydrothermal conversion from Mg_2TiO_4, Ceramics International 44(14) (2018) 17562-17565. https://doi.org/https://doi.org/10.1016/j.ceramint.2018.06.170.
[11] S. Khan, M. Je, D. Kim, S. Lee, S.-H. Cho, T. Song, H. Choi, Mapping Point Defects of Brookite TiO_2 for Photocatalytic Activity Beyond Anatase and P25, The Journal of Physical Chemistry C 124(19) (2020) 10376-10384. https://doi.org/10.1021/acs.jpcc.0c02091.
[12] J. Wang, X. Guo, Adsorption isotherm models: Classification, physical meaning, application and solving method, Chemosphere 258 (2020) 127279. https://doi.org/https://doi.org/10.1016/j.chemosphere.2020.127279.
[13] K.Y. Foo, B.H. Hameed, Insights into the modeling of adsorption isotherm systems, Chemical Engineering Journal 156(1) (2010) 2-10. https://doi.org/https://doi.org/10.1016/j.cej.2009.09.013.
[14] J. Febrianto, A.N. Kosasih, J. Sunarso, Y.-H. Ju, N. Indraswati, S. Ismadji, Equilibrium and kinetic studies in adsorption of heavy metals using biosorbent: A summary of recent studies, Journal of Hazardous Materials 162(2) (2009) 616-645. https://doi.org/https://doi.org/10.1016/j.jhazmat.2008.06.042.
[15] G. McKay, B. Al-Duri, Prediction of bisolute adsorption isotherms using single-component data for dye adsorption onto carbon, Chemical Engineering Science 43(5) (1988) 1133-1142. https://doi.org/https://doi.org/10.1016/0009-2509(88)85073-5.
[16] D.T. Sawyer, W.R. Heineman, J.M. Beebe, Chemistry experiments for instrumental methods, 3rd ed., John Wiley & Sons1984.
[17] J. Zolgharnein, M. Bagtash, T. Shariatmanesh, Simultaneous removal of binary mixture of Brilliant Green and Crystal Violet using derivative spectrophotometric determination, multivariate optimization and adsorption characterization of dyes on surfactant modified nano-γ-alumina, Spectrochimica Acta Part A: Molecular and Biomolecular Spectroscopy 137 (2015) 1016-1028. https://doi.org/https://doi.org/10.1016/j.saa.2014.08.115.
[18] D. Kumar, A. Singh, J.P. Gaur, Mono-component versus binary isotherm models for Cu(II) and Pb(II) sorption from binary metal solution by the green alga Pithophora oedogonia, Bioresource Technology 99(17) (2008) 8280-8287. https://doi.org/https://doi.org/10.1016/j.biortech.2008.03.008.
[19] D.C. Montgomery, G.C. Runger, Applied statistics and probability for engineers, John Wiley & Sons, New York, 2006.
[20] E. Worch, Adsorption Technology in Water Treatment: Fundamentals, Processes, and Modeling, De Gruyter2012. https://doi.org/doi:10.1515/9783110240238.
[21] A. Crake, K.C. Christoforidis, A. Kafizas, S. Zafeiratos, C. Petit, CO2 capture and photocatalytic reduction using bifunctional TiO_2/MOF nanocomposites under UV–vis irradiation, Applied Catalysis B: Environmental 210 (2017) 131-140. https://doi.org/https://doi.org/10.1016/j.apcatb.2017.03.039.
[22] N.N. Marei, N.N. Nassar, G. Vitale, The effect of the nanosize on surface properties of NiO nanoparticles for the adsorption of Quinolin-65, Physical Chemistry Chemical Physics 18(9) (2016) 6839-6849. https://doi.org/10.1039/C6CP00001K.
[23] BIOVIA Materials Studio Modeling and Simulation Software, Dassault Systemes, 2017

Chapter 4 — Activated Carbon: Adsorption of Ibuprofen

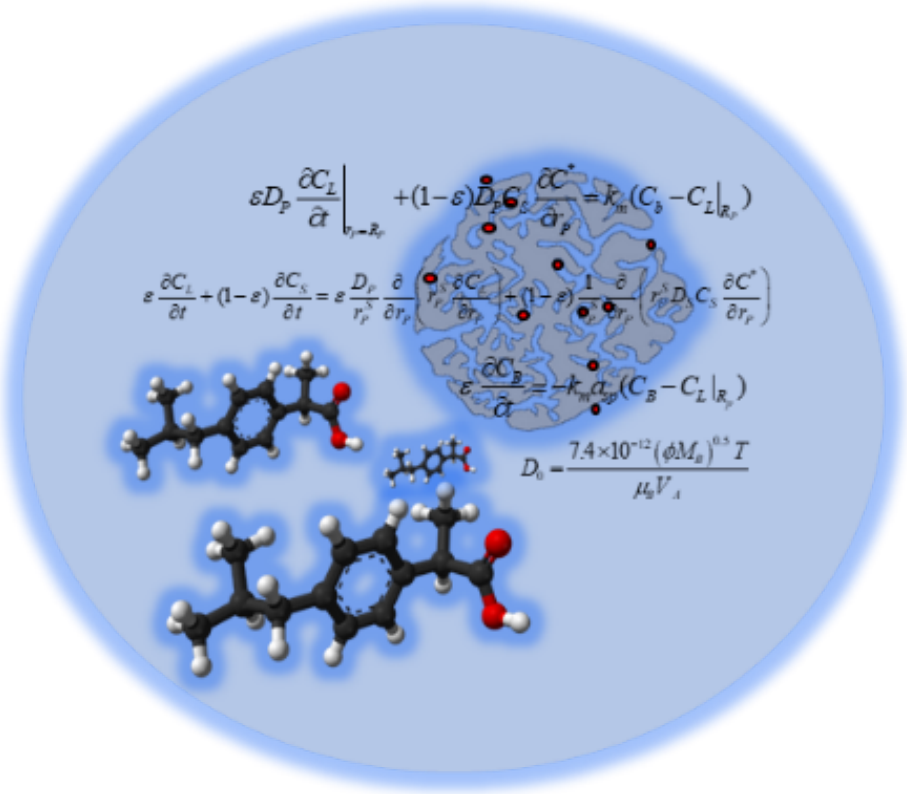

M. Hmoudah, M. E. Fortunato, R. Paparo, M. Trifuoggi, A. El-Qanni, R. Tesser, D. Murzin, T. Salmi, V. Russo, M. Di Serio, Ibuprofen adsorption on activated carbon: thermodynamic and kinetic investigation via adsorption dynamic intraparticle model (ADIM), Langmuir, 2023. doi.org/10.1021/acs.langmuir.2c03350

4.1. Introduction

Ibuprofen (IBU) is a popular nonsteroidal anti-inflammatory medicine (NSAID) that people frequently take to relieve pain and reduce inflammation [1]. As an unpleasant result, it is frequently found in wastewater streams, because of human excrement [2]. In light of rising pharmaceutical usage and wastewater contamination, it is essential to give the removal of IBU from wastewater the first priority to preserve both environmental sustainability and human well-being [3]. IBU and other pharmaceutical substances enter water bodies if not properly handled, having serious negative ecological effects [3, 4]. These compounds have the potential to linger in the environment, endangering humans' health, aquatic life, and upsetting the balance of natural ecosystems due to the continued accumulation in water bodies [5]. The removal of IBU from wastewaters will minimize human exposure to these compounds and will lessen any related hazards. New technology is needed with establishing efficient wastewater treatment procedures to eliminate IBU [5].

Adsorption is considered as one of the best strategies for removal of IBU from wastewaters [6]. Adsorbent materials with high surface areas and pore structures such as activated carbon and zeolites can attract the IBU molecules and retain them [7]. The large surface areas give the adsorbent and IBU a plenty of opportunities to interact, increasing the removal capacity [8]. Adsorption can be used as a stand-alone treatment process or it can be integrated with other processes, such as filtration or biological processes [9]. It is considered a practical and an adaptable technology that can be customized to meet the unique infrastructure of the wastewater treatment [10].

To characterize the adsorption process in terms of design, control, and optimization, it is crucial to create reliable experimental and computational models. It is imperative to explain the kinetic data of adsorption using trustworthy models based on the description of the relevant transport phenomena, including fluid-solid, intraparticle, and surface diffusion effects. Therefore, our research team created an adsorption dynamic intraparticle model (ADIM) for fluid-solid adsorption kinetics [11], which has been successfully tested by other authors [12-14]. The importance of this model resides in its ability to concurrently describe the thermodynamics and kinetics of fluid-solid adsorption data. Additionally, it is considered to be general and simple to modify for particular cases [15].

In this chapter, an in-depth kinetic and thermodynamic investigation was conducted using commercial activated carbon materials, namely DARCO 20-40. The experimental data were interpreted by the ADIM model to retrieve physicochemical parameters which are needed for a future design of continuously operating adsorption columns [16].

4.2 Activated carbon

Activated carbon is a solid carbonaceous material with an amorphous structure [17]. It is a highly versatile adsorbent for its physicochemical properties [8, 18]. It has a high degree of porosity and a well-developed surface area containing various oxygenated functional groups such as carboxylic acids, phenols, carbonyls, and lactones [19]. Activated carbon has three

kinds of pores: microspores, mesopores, and macropores, with microspores and mesopores playing a crucial role in increasing surface area and facilitating gas adsorption [19]. Additionally, the presence of functional groups increases the adsorption capabilities of activated carbon [20]. These unique characteristics make it a very versatile material that can be used as an adsorbent for water and gases, as well as a catalyst and co-catalyst for pollutant removal and chemical recovery [21].

Activated carbon is traditionally derived from expensive and finite resources such as coal, lignite, peat, and petroleum residue, but there is a growing demand for less expensive and sustainable alternatives [22]. Biochar, obtained through thermal treatment of biomass, has emerged as a promising resource for activated carbon. It serves as the primary precursor for activated carbon and can be produced via thermochemical conversion processes such as pyrolysis, hydrothermal carbonization, torrefaction, microwave heating, and gasification [23].

Various activation methods can be employed to produce activated carbon from biochar and biomass, including physical, chemical, physiochemical, and microwave-assisted activation [18]. Physical activation involves the exposure of heat and gases such as steam, CO_2, or N_2, while chemical activation utilizes agents such as acids, bases, metal oxides, or alkaline metals. Physio-chemical activation combines heat and chemical treatment, and microwave-assisted activation employs microwave irradiation. The activation process depends on factors such as particle size, retention time, impregnation ratio, procedure configuration, activation time, precursor properties, and chemical substances used [24]. Many researchers are exploring the loading of nanoparticles on the activated carbon surfaces to enhance the performance in the removal of emerging pollutants from wastewaters [25-27].

In this work, commercial granular activated carbon was used, DARCO 20-40 mesh (specific surface area of 629 m^2/g, average pore diameter of 3.7 nm, total pore volume of 0.748 cm^3/g). The pore volume distribution of the used sorbent is reported in Table 4.1.

Table 4.1. DARCO 20-40 mesh pores volume distribution [28].

V_{tot} [cm^3/g]	V_{micro} [cm^3/g]	V_{meso} [cm^3/g]	V_{macro} [cm^3/g]
0.748	0.264	0.190	0.294

4.3. Adsorption modelling

In our previous research, we have introduced and validated the ADIM model, which was employed for both batch and continuous adsorption systems. This model aimed to interpret the collected data on adsorption kinetics, taking into account various diffusion processes and adsorption equilibria. The ADIM model is based on a plausible mechanism comprising four consecutive steps: i) diffusion of the solute from the bulk liquid phase (with a constant solute concentration, C_B,, at a given time, t) to the solid surface; ii) intraparticle diffusion; iii) establishment of an equilibrium between the solute concentrations in the liquid and solid

phases; iv) diffusion of the adsorbate species to the particle surface. Several assumptions were adopted: 1. the system is isothermal; 2. the particles have a single mode of particle size distribution; 3. adsorption equilibria prevail within the pore with an average porosity and tortuosity; 4. the adaptability of the particle mass balance based on the shape factor.

The dynamic intraparticle model (ADIM) was proposed and applied to both the batch and continuous adsorption modes according to our previous research [11, 16, 29], and it was used to interpret the collected data on adsorption kinetics by considering all the possible diffusion processes and adsorption equilibria. This model hypothesis is based on four successive steps: i) diffusion of the solute from the bulk liquid phase (the solute concentration in the bulk liquid phase, C_B, is assumed constant at a generic time t) to the solid surface; ii) intraparticle diffusion; iii) equilibrium of the solute concentration between the liquid and solid phase; iv) diffusion of the adsorbate species to the particle surface. The following assumptions were adopted:

1. isothermal system;
2. monomodal particle size;
3. adsorption equilibrium in the pores with an average porosity and tortuosity of the particle;
4. particle mass balance is adaptable based on the shape factor.

Based on these fundamental assumptions, it is possible to derive the mass balance equations for the bulk liquid phase (Eq. 4.1) and for the solid phase for a batch system (Eq. 4.2) [11] by considering both the film diffusion and the intraparticle diffusion effects. The component accumulation is equal to the mass transfer inside the film (Eq. 4.1), and the overall accumulation for both liquid and solid phases is the sum of the pore and the surface intraparticle diffusion (Eq. 4.2).

$$\varepsilon' \frac{\partial C_B}{\partial t} = -k_m a_{sp}(C_B - C_L|_{R_p}) \tag{4.1}$$

where C_B is the liquid bulk concentration, t the simulation time, k_m the liquid-solid mass transfer coefficient, a_{sp} the sorbent specific surface area per volume of particle, C_L the concentration in the liquid pores, and ε' the fluid bulk-to-solid phase volumetric ratio,

$$\varepsilon \frac{\partial C_L}{\partial t} + (1-\varepsilon)\frac{\partial C_S}{\partial t} = \varepsilon \frac{D_P}{r_P^S}\frac{\partial}{\partial r_P}\left(r_P^S \frac{\partial C_L}{\partial r_P}\right) + (1-\varepsilon)\frac{1}{r_P^S}\frac{\partial}{\partial r_P}\left(r_P^S D_S C_S \frac{\partial C^*}{\partial r_P}\right) \tag{4.2}$$

where ε is the sorbent porosity, C_S is the concentration on the solid surface, r_p the sorbent radius, D_P the effective diffusion coefficient, D_S the surface diffusion coefficient, S is the shape factor, and C^* is defined by,

$$C^* = \ln\left(\frac{C_S}{K_F}\right)^n \tag{4.3}$$

where K_F and n are the Freundlich isotherm parameters.

The boundary conditions of the partial differential equations are derived below, Eqs. (4.4-4.5) represent the symmetry condition at the center of the particle (r_p=0) for both liquid and adsorbed phases, whereas Eq. (4.6) expresses the steady-state hypothesis at the solid surface (r_p=R_p).

$$\left.\frac{\partial C_L}{\partial r_P}\right|_{r_P=0} = 0 \tag{4.4}$$

$$\left.\frac{\partial C_S}{\partial r_P}\right|_{r_P=0} = 0 \tag{4.5}$$

$$\varepsilon D_P \left.\frac{\partial C_L}{\partial t}\right|_{r_P=R_P} + (1-\varepsilon) D_P C_S \frac{\partial C^*}{\partial r_P} = k_m (C_b - C_L|_{R_P}) \tag{4.6}$$

Furthermore, the Freundlich isotherm (Eq. 4.7) was considered to express the solute concentration in the solid at equilibrium.

$$C_S = K_F C_L^{1/n} \tag{4.7}$$

where K_F is the Freundlich constant related to the adsorption capacity, and $1/n$ is the adsorption intensity factor.

The physical and chemical parameters include the pore diffusivity (D_P) presented according to the mean transport pore model in Eq. 4.8, which is obtained from the molecular diffusivity, adjusted with the porosity ε and tortuosity τ of the solid material. The corresponding molecular diffusivity (D_0) was estimated from the Wilke-Chang equation (Eq. 4.9).

$$D_P = \frac{\varepsilon}{\tau} D_0 \tag{4.8}$$

$$D_0 = \frac{7.4\times10^{-12} \left(\phi M_B\right)^{0.5} T}{\mu_B V_A} \tag{4.9}$$

where ϕ is the association factor (set to 2.6 for associating molecules such as water), M_B is the molecular weight of the solvent, T is the temperature, μ_B is the viscosity of the solvent, and V_A is the molar volume of the solute calculated at standard boiling point estimated from the Le Bas correlation, V_A= 268 cm^3/mol.

Additional theoretical information about the ADIM and the mathematical demonstration of the mass balance equations can be found in the references [11, 16]. The simultaneous numerical solution of these equations was performed using the gPROMS ModelBuilder v.4.0. The model input parameters are listed in Table 4.2. The surface diffusivity D_S and the mass transfer coefficient k_m were estimated by submitting the experimental data to non-linear regression analysis by using the MXLKHD mathematical solver. More details about the modelling activity can be found in **Publication IV**.

Table 4.2. Input parameters for ADIM.

Symbol	Value	Unit
R_P	0.35×10^{-3}	m
s	2	-
a_{sp}	8.57×10^{3}	m^2 m^{-3}
ε	0.38	-
τ	4.46	-
ρ_{solid}	1950	kg m^{-3}

4.4. Batch adsorption of IBU on activated carbon

4.4.1. Adsorption isotherms

The adsorption equilibrium experiments were performed at three different temperatures: 303 K, 313 K, and 323 K. Vials containing 10 mL solutions with an initial concentration of 10 mg L^{-1} were utilized, and various quantities of activated carbon were added, thereby altering the adsorbent-to-IBU ratio. The vials were subjected to continuous stirring at a constant temperature for a duration of three days to ensure the attainment of thermodynamic equilibrium. Three separate sets of solutions were prepared to investigate the impact of temperature on adsorption performance. The aim of the experiments was to examine the relationship between temperature and the adsorption capacity of activated carbon, as well as to establish the corresponding adsorption isotherms. The outcomes of these experiments are presented in Figure 4.1, illustrating the observed adsorption isotherms trends that follow the Freundlich model and the corresponding adsorption capacity at different temperatures. As observed, the adsorption of IBU on activated carbon exhibits an increase with rising temperature. This model characterizes the adsorption on a heterogeneous surface, where various adsorption energies are associated with different sites, allowing for interactions between the adsorbed molecules [30]. The estimated parameters, along with their 95% confidence intervals, are presented in Table 4.3 for the three different temperatures. The values of the empirical constant *n* was within the range 1-10, indicating a strong interaction between IBU and the activated carbon [31]. Furthermore, parameter *n* increases with temperature, suggesting a stronger interaction between the sorbent and adsorbate at higher temperatures, which indicates an endothermic adsorption mechanism. A possible explanation could be the conformational changes of IBU with temperature, leading to a more strongly adsorbed conformer. However, it is important to note that the influence of mass transfer might be a potential factor, too. These explanations are speculative and require further dedicated experimentation and quantum chemical computations to verify their validity.

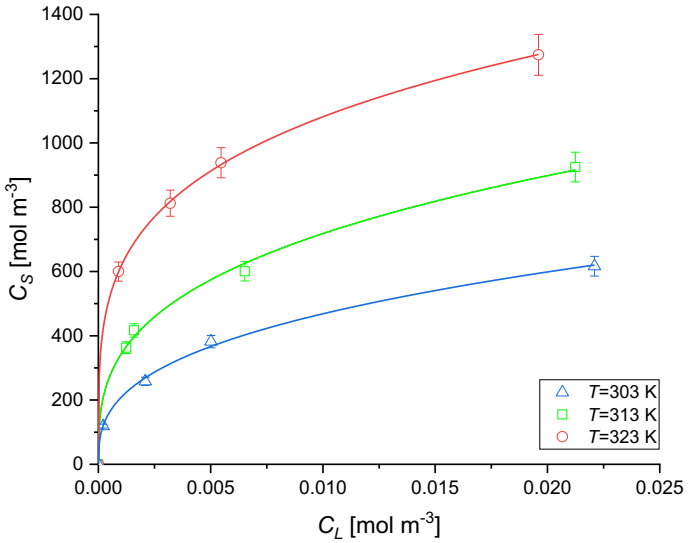

Figure 4.1 Adsorption isotherms at different temperatures. The symbols represent the experimental data and the lines for the calculated profiles.

Table 4.3 Parameters estimated for the adsorption isotherms (Eq 4.3).

T [K]	K_F [(mol m^{-3})$^{1-1/n}$]	n [-]
303	2400±100	2.8±0.1
313	3000±200	3.1±0.1
323	3300±40	4.1±0.1

4.4.2. Adsorption kinetics

The kinetic study was conducted using a jacketed batch vessel. For all the experiments, a fixed quantity of sorbent was added to 150 mL of an IBU solution at a concentration of 10 mg L^{-1} and neutral pH. The ratio between the adsorbate and the adsorbent was determined through preliminary investigations to ensure measurable experimental kinetic data. The temperature of the solution was regulated using an external thermostat, while the stirring rate was controlled by a mechanical stirring system. Liquid samples of approximately 0.5 cm^3 were periodically withdrawn to monitor the changes in the IBU concentration over time. To prevent sorbent loss during sampling, a sintered stainless steel filter was installed in the sampling line. The samples were stored in sealed vials, and the residual IBU concentration in the aqueous solutions was measured using a spectrophotometer (Jasco V-550 UV/VIS). A typical spectrum and a calibration curve were obtained for the IBU concentrations with absorbance values at λ=222nm and a concentration range of 0-0.05 mol m^{-3}. To explore the adsorption kinetics and the potential mass transfer effects, multiple experiments were conducted at different operating conditions.

Due to the significant percentage of micropores present in DARCO 20-40 as given in Table 4.1, the adsorption kinetics is undoubtedly constrained by intraparticle diffusion. In order to confirm the aforementioned assumption, Bangham's equation (Eq. 4.10) was first applied to check if intraparticle diffusion is the rate-determining step in the adsorption process.

$$\log\log\left(\frac{C_{B,0}}{C_{B,0}-q_t\rho_{bulk}}\right)=\log\left(\frac{k_b\rho_{bulk}}{2.303V}\right)+\alpha\log(t) \tag{4.10}$$

The adsorbed quantity is calculated as q_t=($C_{B,0}$-C_B)/ρ_{bulk}. The plot of loglog[$C_{B,0}$/($C_{B,0}-q_t\rho_{bulk}$)] vs log$t$ is reported in Figure 4.2 as an example for the experiments performed at different temperatures.

The indication of intraparticle diffusion limitations is evident from the good fit of the Bangham model. Consequently, higher temperatures lead to decreased R^2 values, suggesting that intraparticle diffusion limitation becomes less significant at elevated temperatures. This conclusion is valid as diffusion adsorption becomes more prominent at higher temperatures. Due to these observations, it is evident that a comprehensive model accounting for intraparticle diffusion is necessary. Thus, the ADIM model was used to give a deeper insight into liquid-solid, pore and surface diffusion effects.

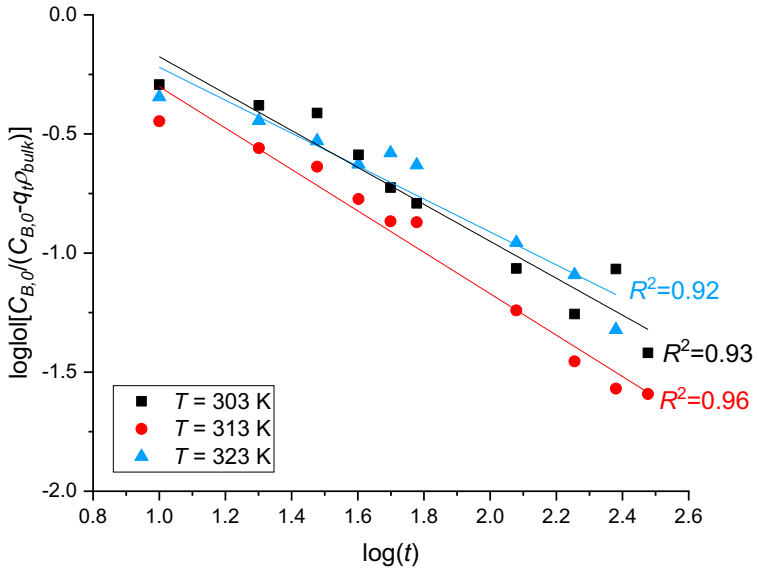

Figure 4.2 Bangham model for the adsorption of IBU on activated carbon at different temperatures. Experimental conditions are: ρ_{bulk}=0.39 kg/m^3, $C_{B,0}$=0.05 mol/m^3 and v=500 rpm.

Different parameters which affect the adsorption kinetics were investigated. Figures 4.3 and 4.4 display the effect of the initial concentration of IBU and the bulk densities of the adsorbent. The initial slope of the concentration profiles increases when increasing the concentration of IBU (Figure 4.3). Additionally, the adsorption kinetics demonstrate a significant dependence on the quantity of adsorbent employed in the experiment (Figure 4.4). Further results for the effect of the stirring rate on the adsorption kinetics can be found in **Publication IV**.

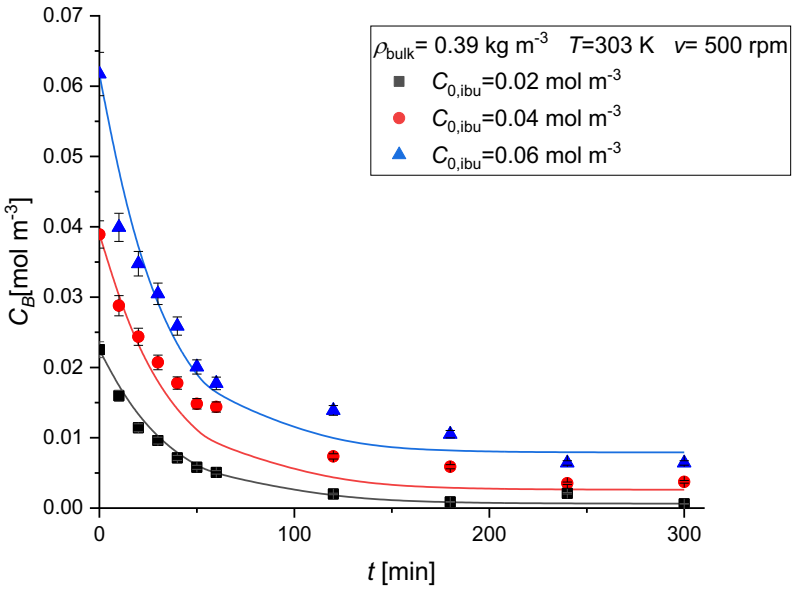

Figure 4.3 The effect of the initial concentration of IBU on the adsorption kinetics, experimental conditions: ρ_{bulk} = 0.39 kg/m^3, T=303K, and v=500rpm. Symbols represent the experimental data, lines the calculated profiles.

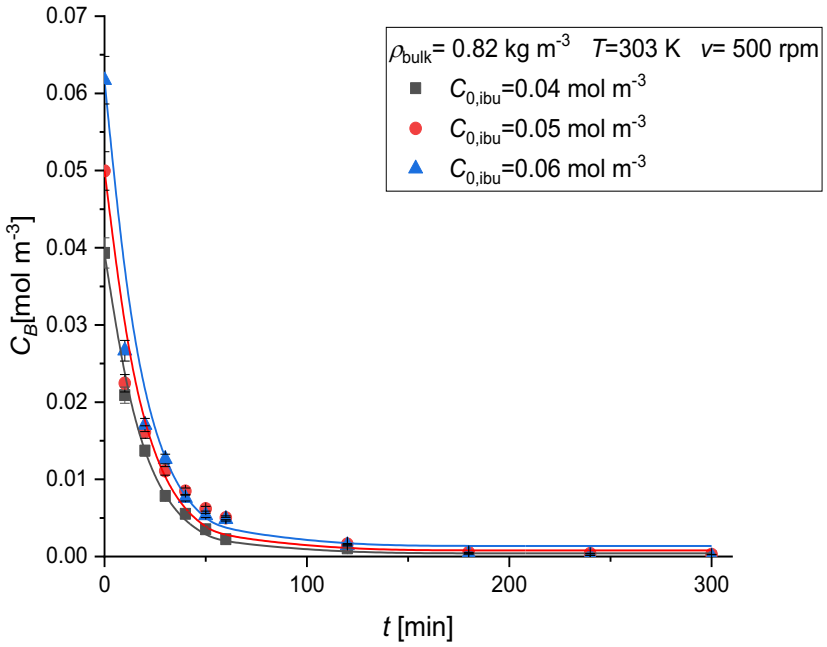

Figure 4.4 The effect of the initial concentration of IBU on the adsorption kinetics, experimental conditions: ρ_{bulk}=0.82 kg/m^3, T=303 K, and v=500 rpm. Symbols represent the experimental data, lines the calculated profiles.

Figure 4.5A depicts the relationship between the surface diffusivity and temperature. It can be seen that it follows an Arrhenius-like trend as demonstrated by Russo et al. [29]. As a result, the mathematical expression given in Eq. 4.11 can be used.

$$D_S = D_{S,0} \exp\left(-\frac{E_s}{RT}\right) \tag{4.11}$$

An estimate of the surface activation energy E_S=60±7 kJ/mol was made from the non-linear regression analysis. Similarly, a linear trend is obtained (Figure 4.5B) by plotting the natural logarithm of k_m as a function of $1/T$, assuming an Arrhenius-like dependence. The activation energy E_A=16±1 kJ/mol, needed by the molecules to diffuse from the bulk liquid phase to the solid phase can be calculated from the slope of the fitting curve.

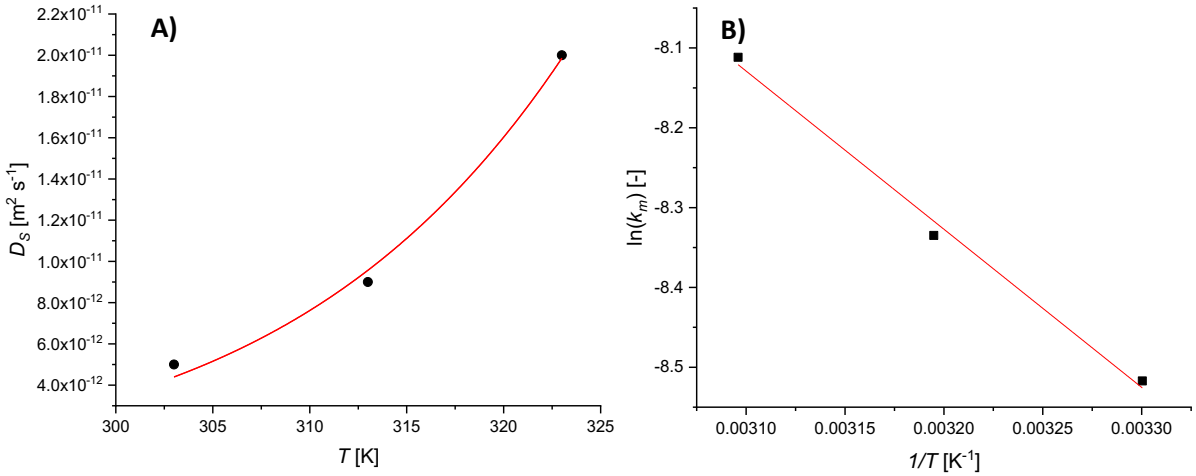

Figure 4.5 A. Surface diffusion coefficient as a function of temperature. B. Fluid-solid external mass transfer coefficient as a function of temperature.

4.5. Conclusions

This study aimed to investigate the adsorption of IBU, an emerging contaminant, on activated carbon. The optimal conditions for removing IBU were optimized through extensive batch experiments to examine the impact of key operational factors on the adsorption process. The findings revealed a strong bond between IBU and activated carbon, with the Freundlich model effectively describing the adsorption equilibrium and the heterogeneity of surface sites with varying adsorption energies. The ADIM model was utilized to understand the diffusion mechanism of IBU by determining the k_m and D_S parameter values that are important for designing an adsorption column. It is important to note that the results obtained in this study pertain to a model system, specifically IBU in water, which was used to test the ADIM model for the IBU adsorption. The behavior in a real matrix could be more complex, as the presence of other organic and inorganic compounds might interfere, which would decrease the adsorption efficiency of the selected sorbent. Since the composition of wastewater varies depending on its source, replicating a real matrix in laboratory scale is challenging, necessitating the testing of different sorbents and various of adsorption parameters.

4.6. List of abbreviations

IBU	ibuprofen
NSAID	nonsteroidal anti-inflammatory medicine
ADIM	adsorption dynamic intraparticle model

4.7. References

[1] S. Chopra, D. Kumar, Ibuprofen as an emerging organic contaminant in environment, distribution and remediation, Heliyon 6(6) (2020) e04087. https://doi.org/https://doi.org/10.1016/j.heliyon.2020.e04087.
[2] C.F. Couto, L.C. Lange, M.C.S. Amaral, Occurrence, fate and removal of pharmaceutically active compounds (PhACs) in water and wastewater treatment plants—A review, Journal of Water Process Engineering 32 (2019) 100927. https://doi.org/https://doi.org/10.1016/j.jwpe.2019.100927.
[3] V. Contardo-Jara, C. Lorenz, S. Pflugmacher, G. Nützmann, W. Kloas, C. Wiegand, Exposure to human pharmaceuticals Carbamazepine, Ibuprofen and Bezafibrate causes molecular effects in Dreissena polymorpha, Aquatic Toxicology 105(3) (2011) 428-437. https://doi.org/https://doi.org/10.1016/j.aquatox.2011.07.017.
[4] J. Martín, D. Camacho-Muñoz, J.L. Santos, I. Aparicio, E. Alonso, Occurrence of pharmaceutical compounds in wastewater and sludge from wastewater treatment plants: Removal and ecotoxicological impact of wastewater discharges and sludge disposal, Journal of Hazardous Materials 239-240 (2012) 40-47. https://doi.org/https://doi.org/10.1016/j.jhazmat.2012.04.068.
[5] A. Durán, J.M. Monteagudo, I. San Martín, Operation costs of the solar photo-catalytic degradation of pharmaceuticals in water: A mini-review, Chemosphere 211 (2018) 482-488. https://doi.org/https://doi.org/10.1016/j.chemosphere.2018.07.170.
[6] C. Tien, Introduction to adsorption: Basics, analysis, and applications, Elsevier2018.
[7] C.P. Bergmann, F.M. Machado, Carbon nanomaterials as adsorbents for environmental and biological applications, Springer2015.
[8] A.I. Osman, A. Ayati, M. Farghali, P. Krivoshapkin, B. Tanhaei, H. Karimi-Maleh, E. Krivoshapkina, P. Taheri, C. Tracey, A. Al-Fatesh, I. Ihara, D.W. Rooney, M. Sillanpaä, Advanced adsorbents for ibuprofen removal from aquatic environments: a review, Environmental Chemistry Letters (2023). https://doi.org/10.1007/s10311-023-01647-6.
[9] S. Kim, S.-N. Nam, A. Jang, M. Jang, C.M. Park, A. Son, N. Her, J. Heo, Y. Yoon, Review of adsorption–membrane hybrid systems for water and wastewater treatment, Chemosphere 286 (2022) 131916. https://doi.org/https://doi.org/10.1016/j.chemosphere.2021.131916.
[10] V. Bernal, L. Giraldo, J.C. Moreno-Piraján, Insight into adsorbate–adsorbent interactions between aromatic pharmaceutical compounds and activated carbon: equilibrium isotherms and thermodynamic analysis, Adsorption 26(2) (2020) 153-163. https://doi.org/10.1007/s10450-019-00057-x.
[11] V. Russo, R. Tesser, M. Trifuoggi, M. Giugni, M. Di Serio, A dynamic intraparticle model for fluid–solid adsorption kinetics, Computers & Chemical Engineering 74 (2015) 66-74. https://doi.org/https://doi.org/10.1016/j.compchemeng.2015.01.001.
[12] V.J. Inglezakis, M.M. Fyrillas, J. Park, Variable diffusivity homogeneous surface diffusion model and analysis of merits and fallacies of simplified adsorption kinetics equations, Journal of Hazardous Materials 367 (2019) 224-245. https://doi.org/https://doi.org/10.1016/j.jhazmat.2018.12.023.
[13] P. Suresh Kumar, L. Korving, K.J. Keesman, M.C.M. van Loosdrecht, G.-J. Witkamp, Effect of pore size distribution and particle size of porous metal oxides on phosphate adsorption capacity and kinetics, Chemical Engineering Journal 358 (2019) 160-169. https://doi.org/https://doi.org/10.1016/j.cej.2018.09.202.
[14] E. Baltrėnaitė-Gedienė, T. Leonavičienė, P. Baltrėnas, Comparison of Cu(II), Mn(II) and Zn(II) adsorption on biochar using diagnostic and simulation models, Chemosphere 245 (2020) 125562. https://doi.org/https://doi.org/10.1016/j.chemosphere.2019.125562.

[15] A. Mashayekh-Salehi, G. Moussavi, Removal of acetaminophen from the contaminated water using adsorption onto carbon activated with NH_4Cl, Desalination and Water Treatment 57(27) (2016) 12861-12873. https://doi.org/10.1080/19443994.2015.1051588.
[16] V. Russo, D. Masiello, M. Trifuoggi, M. Di Serio, R. Tesser, Design of an adsorption column for methylene blue abatement over silica: From batch to continuous modeling, Chemical Engineering Journal 302 (2016) 287-295. https://doi.org/https://doi.org/10.1016/j.cej.2016.05.020.
[17] F. Çeçen, Ö. Aktas, Activated carbon for water and wastewater treatment: integration of adsorption and biological treatment, John Wiley & Sons2011.
[18] S. Wong, N. Ngadi, I.M. Inuwa, O. Hassan, Recent advances in applications of activated carbon from biowaste for wastewater treatment: A short review, Journal of Cleaner Production 175 (2018) 361-375. https://doi.org/https://doi.org/10.1016/j.jclepro.2017.12.059.
[19] A. Bhatnagar, W. Hogland, M. Marques, M. Sillanpää, An overview of the modification methods of activated carbon for its water treatment applications, Chemical Engineering Journal 219 (2013) 499-511. https://doi.org/https://doi.org/10.1016/j.cej.2012.12.038.
[20] İ. Demiral, C. Samdan, H. Demiral, Enrichment of the surface functional groups of activated carbon by modification method, Surfaces and Interfaces 22 (2021) 100873. https://doi.org/https://doi.org/10.1016/j.surfin.2020.100873.
[21] M. Lewoyehu, Comprehensive review on synthesis and application of activated carbon from agricultural residues for the remediation of venomous pollutants in wastewater, Journal of Analytical and Applied Pyrolysis 159 (2021) 105279. https://doi.org/https://doi.org/10.1016/j.jaap.2021.105279.
[22] J. Jjagwe, P.W. Olupot, E. Menya, H.M. Kalibbala, Synthesis and Application of Granular Activated Carbon from Biomass Waste Materials for Water Treatment: A Review, Journal of Bioresources and Bioproducts 6(4) (2021) 292-322. https://doi.org/https://doi.org/10.1016/j.jobab.2021.03.003.
[23] W. Xiang, X. Zhang, J. Chen, W. Zou, F. He, X. Hu, D.C.W. Tsang, Y.S. Ok, B. Gao, Biochar technology in wastewater treatment: A critical review, Chemosphere 252 (2020) 126539. https://doi.org/https://doi.org/10.1016/j.chemosphere.2020.126539.
[24] N. Muttil, S. Jagadeesan, A. Chanda, M. Duke, S.K. Singh, Production, Types, and Applications of Activated Carbon Derived from Waste Tyres: An Overview, Applied Sciences, 2023.
[25] S. Moosavi, C.W. Lai, S. Gan, G. Zamiri, O. Akbarzadeh Pivehzhani, M.R. Johan, Application of Efficient Magnetic Particles and Activated Carbon for Dye Removal from Wastewater, ACS Omega 5(33) (2020) 20684-20697. https://doi.org/10.1021/acsomega.0c01905.
[26] M.S. Reza, C.S. Yun, S. Afroze, N. Radenahmad, M.S.A. Bakar, R. Saidur, J. Taweekun, A.K. Azad, Preparation of activated carbon from biomass and its' applications in water and gas purification, a review, Arab Journal of Basic and Applied Sciences 27(1) (2020) 208-238. https://doi.org/10.1080/25765299.2020.1766799.
[27] L.S. Rocha, D. Pereira, É. Sousa, M. Otero, V.I. Esteves, V. Calisto, Recent advances on the development and application of magnetic activated carbon and char for the removal of pharmaceutical compounds from waters: A review, Science of The Total Environment 718 (2020) 137272. https://doi.org/https://doi.org/10.1016/j.scitotenv.2020.137272.
[28] C.K. Ahn, Y.M. Kim, S.H. Woo, J.M. Park, Selective adsorption of phenanthrene dissolved in surfactant solution using activated carbon, Chemosphere 69(11) (2007) 1681-1688. https://doi.org/https://doi.org/10.1016/j.chemosphere.2007.06.018.
[29] V. Russo, R. Tesser, D. Masiello, M. Trifuoggi, M. Di Serio, Further verification of adsorption dynamic intraparticle model (ADIM) for fluid–solid adsorption kinetics in batch

reactors, Chemical Engineering Journal 283 (2016) 1197-1202. https://doi.org/https://doi.org/10.1016/j.cej.2015.08.066.
[30] A.S. Mestre, J. Pires, J.M.F. Nogueira, J.B. Parra, A.P. Carvalho, C.O. Ania, Waste-derived activated carbons for removal of ibuprofen from solution: Role of surface chemistry and pore structure, Bioresource Technology 100(5) (2009) 1720-1726. https://doi.org/https://doi.org/10.1016/j.biortech.2008.09.039.
[31] L. Anah, N. Astrini, Isotherm adsorption studies of Ni(II) ion removal from aqueous solutions by modified carboxymethyl cellulose hydrogel, IOP Conference Series: Earth and Environmental Science 160(1) (2018) 012017. https://doi.org/10.1088/17551315/160/1/012017.

Chapter 5 — CeO_2, ZnO, and TiO_2 Nanoparticles: Photodegradation of Ibuprofen

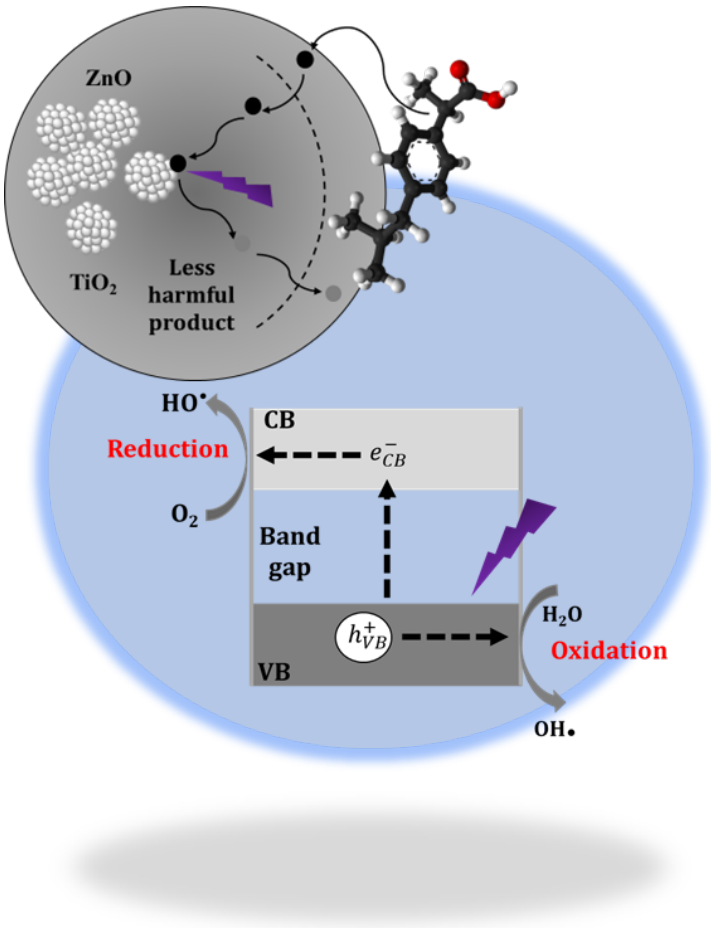

N. Gallucci, ***M. Hmoudah***, E. Martinez, A. El-Qanni, M. Di Serio, L. Paduano, G. Vitiello, V. Russo, Sustainable photodegradation of ibuprofen using CeO_2 nanostructured materials, Journal of Environmental Chemical Engineering 10.3 (2022): 107866. doi.org/10.1016/j.jece.2022.107866

M. Hmoudah, C. Chianese, A. El-Qanni, V. Russo, M. Di Serio, T. Salmi, Photodegradation of ibuprofen using ZnO and TiO_2 nanoparticles: Comprehensive kinetics modeling, mechanisms, and thermodynamics study, Environmental Pollution. *(submitted)*

5.1. Introduction

Emerging contaminants (ECs) are chemicals and materials, whether naturally occurring or created by humans, which are persistent or toxic in the environment and has recently been found to influence the metabolism of human body [1]. Most of these materials have not yet been subjected to environmental restrictions, despite being a major threat to both the environment and human health [2]. These pollutants might include substances that have been just recently found in the environment or substances that might have been there for some time but only recently caused concern. They have been discovered in a variety of aquatic habitats, including estuaries, freshwater lakes, rivers, and oceans [3]. These compounds are usually detected in water at trace quantities between ng - µg per liter [4]. Therefore, it is difficult to detect and analyze them, posing a challenge to wastewater treatment systems. Ibuprofen (IBU) is a discarded drug from aquaculture and pharmaceutical industries [5]. It contaminates water and soil through the excretion of the non-metabolized and metabolized forms in the urine of humans and animals upon medical treatment or through chaotic disposal of expired or non-consumed drug in domestic landfills [6]. As previously discussed in Chapter 1, IBU and its intermediate compounds formed during the chlorination process in treatment plants are considered persistent, ecotoxic, and dangerous to human bodies and the ecosystem [6].

Advanced Oxidation Processes (AOPs) have been recently investigated extensively for the degradation of ECs [7, 8]. In these processes, photon energy is directly used to break down the contaminants. The majority of the processes have been investigated by using catalysts that, when exposed to light, can produce radical species [9]. While in the case of photochemical degradation processes, a combination of light irradiation and oxidants such as O_3, H_2O_2, and Cl_2 [7]. Semiconductor particles employed as photocatalysts, which have recently made strides in the creation of novel semiconductor materials, is also referred to as heterogeneous photocatalysis [10]. In order to degrade ECs, numerous heterogeneous photocatalysts have been studied, and new substances appeared to be acceptable photocatalysts. Therefore, it is essential to carry out a comprehensive analysis of chemical reaction kinetics when considering the implementation of larger AOP systems. Furthermore, conducting experiments to examine the reaction rate, rate constant, and activation energy, which remain consistent regardless of scale, can yield valuable information on the advancement and expected duration of the reaction.

Herein, the scope of this chapter is to describe the modelling of photodegradation kinetics, photodegradation mechanisms, and thermodynamics of in-house prepared cerium oxide (CeO_2) and commercial titanium dioxide (TiO_2) and zinc oxide (ZnO) nanoparticles (NPs) towards IBU. Different parameters were considered in the kinetic study. First, the effectiveness of these NPs in terms of temperature, catalyst bulk density, and the initial concentration of the IBU solution. Second, kinetic modelling was investigated considering descriptive models of the reaction. Consequently, the parameter estimation was carried out and the corresponding activation energies were determined. Finally, thermodynamics parameters ($\Delta G°$, $\Delta H°$, and $\Delta S°$) were assessed.

5.2. CeO_2 nanoparticles

CeO_2 NPs have recently attracted attention because of their ability to photodegrade organic pollutants in water [11-15]. They emerged as promising candidates in photodegradation applications in wastewater treatment. They have outstanding biocompatibility, high stability, and excellent photocatalytic activity and reusability [16-18]. Additionally, CeO_2 NPs can be easily synthesized using cost-effective methods, making them a practical and viable option for large-scale wastewater treatment processes [19].

CeO_2 NPs are able to efficiently destruct a variety of organic contaminants found in wastewaters because of their capacity to produce reactive oxygen species (ROS) in the presence of light [20]. They absorb photons and generate electron-hole pairs when exposed to ultraviolet or visible light [21]. When these charge carriers come into contact with water molecules and pollutants that have been adsorbed, ROS, for example, hydroxyl radicals ($^{\bullet}OH$) are created. Through the oxidation processes, these highly reactive species are essential for the breakdown of complex organic contaminants into less dangerous, simpler molecules.

CeO_2 is an n-type semiconductor with a band-gap at 3.1 eV [22, 23], hence UV light is needed to activate the process. It is important to increase the number of defects in the CeO_2 NPs to shift the band gap from 3.1 eV to lower values and enhance their efficiency. Particle size, textural characteristics, and surface structure are all intimately connected to the photocatalytic activity of CeO_2 [24]. The ratio of Ce^{3+} to Ce^{4+}, which varies based on the size of the NPs and affects the photocatalytic activity, is thus a crucial parameter [25, 26]. Without changing the structure of the fluorite lattice, the transition of Ce^{3+} to Ce^{4+} results in considerable oxygen mobility in the CeO_2 lattice and, as a result, a large catalytic potential [27, 28]. Another important factor in determining the photocatalytic activity is the number of oxygen vacancies in the CeO_2 lattice; as the oxygen vacancies vary, so do the characteristics of the NPs[12, 14, 27, 29]. Further details about the synthesis and characterization of CeO_2 NPs can be found in **Publication V**.

5.3. ZnO and TiO_2 nanoparticles

ZnO and TiO_2 NPs are widely utilized for various applications due to their high catalytic activity, non-toxicity, low cost, excellent electron mobility, and chemical stability [30, 31]. They have demonstrated encouraging outcomes in the elimination of a variety of pollutants, such as dyes [30, 32-34], pharmaceuticals [31, 35], and insecticides [36, 37]. Therefore, they are considered as good candidates for advanced oxidation processes in wastewater treatment.

ZnO and TiO_2 NPs are synthesized by different procedures including physical and chemical vapor deposition, the sol-gel method, precipitation techniques, hydrothermal methodologies, and others [30]. Among these established methods, the sol-gel technique stands out as the most convenient and advantageous for TiO_2 and ZnO synthesis, due to its simplicity, controlled morphology, and cost-effectiveness [38, 39]. In this study commercial ZnO and TiO_2 NPs supplied by Sigma-Aldrich (Milan, Italy) and Evonik Industries (Essen, Germany) respectively were utilized. The Physio-chemical characteristics can be found in **Publication VI**.

ZnO and TiO_2 possess equal band gap energies around 3.2 eV [38]. One would expect that their photocatalytic capacities would be comparable, but when ZnO is exposed to UV light, photocorrosion commonly takes place leading to metal leaching. This process is thought to be one of the main causes of the decline in the photocatalytic activity of ZnO in aqueous solutions [40]. On the other hand, some research has shown that ZnO outperforms TiO_2 in the photocatalytic degradation of certain dyes. It exhibits a better absorption efficiency across a large fraction of the solar spectrum along with anti-fouling and antibacterial properties [41].

Investigating the performance and effectiveness of these NPsin water purification is of paramount importance to understand the mechanisms of degradation of pollutants. However, for large-scale utilization of these NPs for wastewater treatment, agglomeration and potential toxicity are crucial factors to be considered [42]. Doping, co-doping and immobilization of metal oxide NPs on support materials such as activated carbon and membranes can be used to increase the stability and reusability of ZnO and TiO_2 NPs [42-44]. With these strategies, the NPs are retained and controlled more effectively during the water purification process.

5.4. Photodegradation experiments

Photodegradation experiments were conducted in a 1.5 L jacketed glass vessel with a three-neck head. The vessel was connected to an ultra-thermostat to maintain a constant temperature. Air was introduced into the reactor system through a digital flow meter regulator connected to a sintered filter, serving as a gas sparger to ensure efficient gas-liquid interaction for air transfer into the liquid phase, and maintaining a pressure of 1 bar. A 4W UV lamp (Toshiba FL4BLB) with a wavelength of 365 nm was positioned inside the reactor.

In a typical photodegradation experiment, an IBU solution with the desired concentration was prepared and loaded into the reactor vessel, where it was stirred magnetically. The reactor was sealed with a lid and connected to the thermostat, to set at a specific reaction temperature. To minimize dispersion of rays, the reactor was shielded before turning on the UV lamp. Samples were periodically withdrawn to monitor the reaction kinetics for a maximum duration of 5 hours. Each sample was subsequently centrifuged, and the resulting liquid was analyzed using UV-VIS spectroscopy (UV-Vis Jasco V-550) and a calibration curve was obtained at a wavelength of 222 nm, corresponding to the maximum absorption of IBU, enabling quantitative analysis within a concentration range of 0-0.05 mol/m^3.

5.5. Modelling and parameter estimation

The parameter estimation activity was performed using *nlparci* algorithm. The objective function was calculated as follows [34],

$$F_{obj} = \frac{1}{N_{data}} \sqrt{\sum_{i=1}^{N_{data}} \left(\frac{c_{i,EXP} - c_{i,CALC}}{c_{i,EXP}} \right)^2} \tag{5.1}$$

5.6. Results and discussion

5.6.1. CeO_2 NPs synthesis and characterization

CeO_2 NPs were prepared using the solvothermal synthesis approach based on a previous work [45]. Initially, 30 mL of an aqueous solution (0.5 M) of of $Ce(NO_3)_3 \cdot 6H_2O$ salt was prepared and magnetically stirred for 10 minutes until the salt was completely dissolved. Next, 117 µL of hydrogen peroxide was added to the Ce(III) salt solution, which was stirred for 5 minutes to promote the oxidation of Ce^{3+} to Ce^{4+}. To initiate the precipitation reaction, about 6 mL of a diluted ammonia solution (7 M) was added to the mixture adjusting the pH to 8.8. The reaction was allowed to proceed under continuous stirring at 80 °C. Then, a yellow precipitate consisting of $Ce(OH)_4$ was formed and washed three times with bidistilled Milli-Q water with centrifugation at 9000 rpm for 10 minutes. The pH was adjusted to pH 10 by using the ammonia solution and 30 mL of washed precipitate were treated at 120 °C for 24 hours in a minireactor. Finally, CeO_2-NPs were further washed repeatedly with bidistilled Milli-Q water by centrifugation at 9000 rpm for 10 minutes.

XRD and XPS measurements were used to characterize the synthesized CeO_2 NPs. Figure 5.1 shows the XRD pattern of CeO_2 NPs displaying the typical peaks associated with a face-centered cubic (FCC) structure (JCPDS no81-0792) [24, 46, 47]. The peaks were observed at specific diffraction angles (2θ) of 29°, 33°, 47°, 56°, and 59° corresponding to the Miller indices (hkl) representing the crystalline planes (111), (200), (220), (311), and (222), respectively. This demonstrates the formation of CeO_2 NPs with fluorite-type crystalline structure. According to Scherrer's formula, the estimated average crystallite size was approximately18 ± 1 nm.

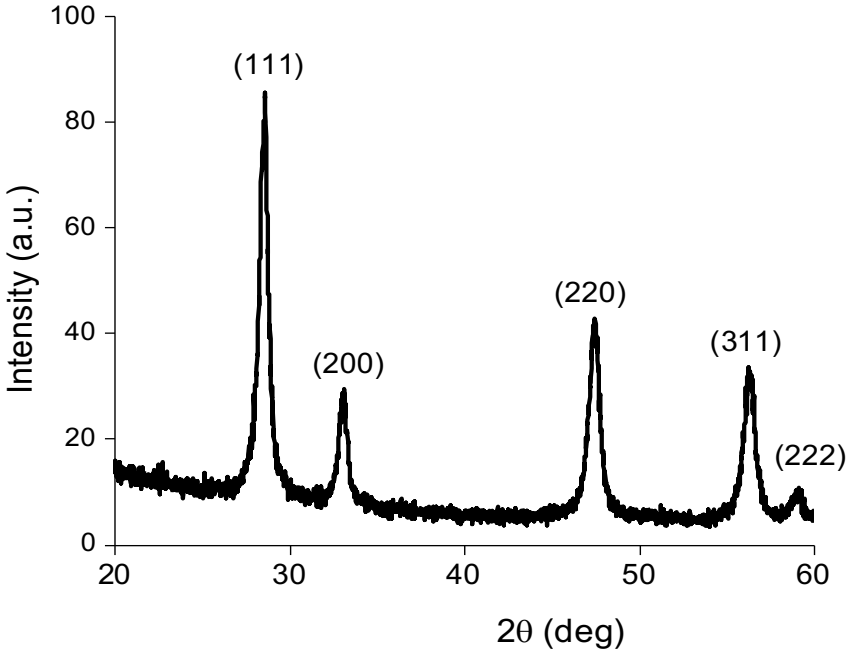

Figure 5.1 XRD pattern of CeO_2 NPs.

The chemical composition of the surface of the CeO_2 NPs was explored using XPS analysis. The survey spectrum is plotted in Figure 5.2A presenting the main characteristic peaks of CeO_2

(Ce 3*d*, Ce 4*d* and O 1*s*) together with indications of some carbon contamination (C 1*s*). The inset provides a deeper look on oxygen O1*s* core level that highlights two contributions: O-Ce bonds from the CeO_2 NPs and O-C bonds from hydrocarbon surface contamination. The spectrum of the Ce3*d* core can be seen in Figure 5.2B, exhibiting notable satellite features (cf^1L) to the major peaks (cf^0). Five peaks were used to account to evaluate the Ce $3d_{5/2}$ - Ce $3d_{3/2}$ doublet, where each peak corresponds to a particular Ce oxidation state (Ce^{3+} and Ce^{4+}). The Ce^{3+}/Ce^{4+} ratio was estimated to be equal to 0.4 based on areas under the peaks of these different compounds.

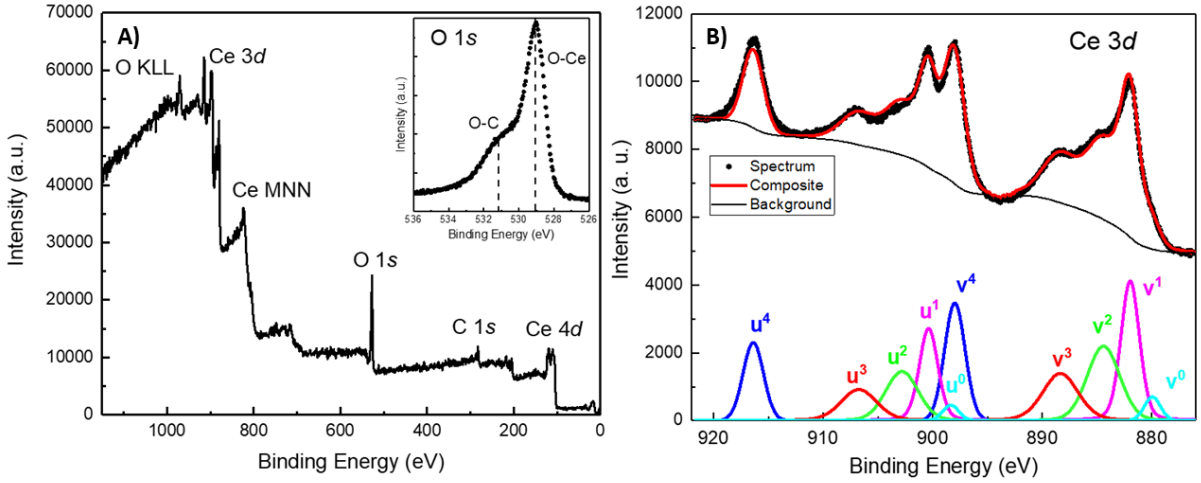

Figure 5.2 A) XPS survey scan and O 1*s* spectrum **B**) Ce 3*d* XPS spectrum of the CeO_2 NPs.

TEM was used to examine the morphological and textural characteristics of CeO_2-NPs (Figure 5.3A). A typical TEM picture demonstrates the emergence of tiny, amorphous NPs of about 15 nm in size. It also implies that these NPs have a significant propensity to self-aggregate, resulting in clusters that are similar in size to those found using DLS analysis (Figure 5.3B). The primary population is centered at about 530 ± 70 nm, as shown by the hydrodynamic radius distribution, which supports a quick and large self-aggregation of CeO_2 NPs when they are in an aqueous suspension. Nitrogen adsorption at 77K was used to determine the surface area (S_{BET}) of CeO_2-NPs and the measured surface area was equal to 76 ± 5 m^2/g. According to the BJH model, the desorption branch of the isotherm was used to estimate the pore size distribution. The total volume of the pores was 0.22 cm^3/g, while the pore distribution (defined as derivative of the pore volume to the radius) reveals the presence of a single population of pores with a diameter of 1.35 ± 0.15 nm.

Besides, by recording the DRS spectrum, the optical properties of CeO_2-NPs at solid-state were examined and displayed in Figure 5.3C. The measured intensity was expressed as the value of the Kubelka-Munk function F(R) (Figure 5.3D), indicating an absorption at $\lambda < 300$ nm. The optical band gap of CeO_2 NPs was 3.1 eV. The transition from the valence band (V_B) to the conduction band (C_B) was calculated by linearization of the graph of $(F(R)h\nu)^{1/2}$ against photon energy (Figure 5.3D) in agreement with the literature [48].

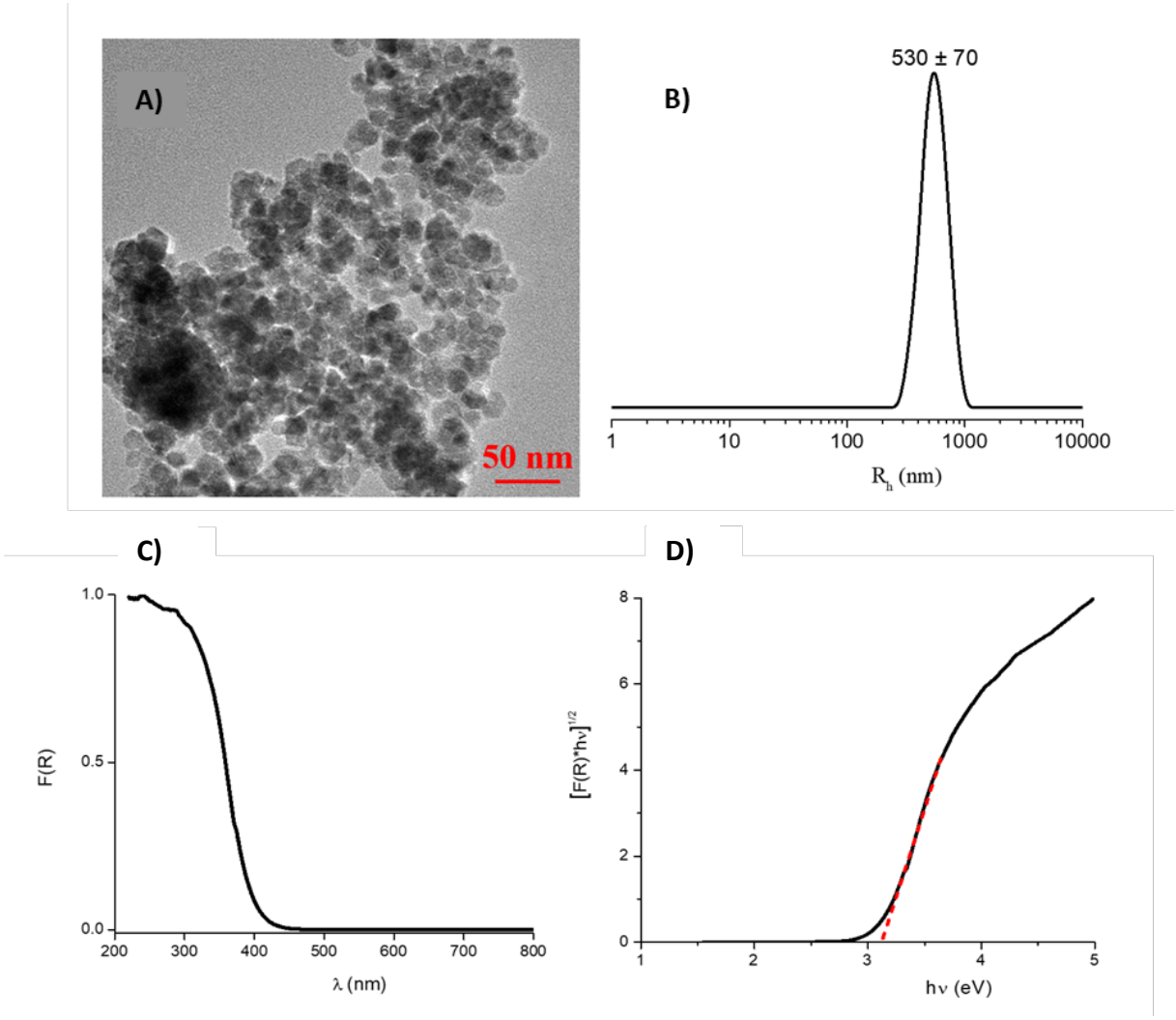

Figure 5.3 A) TEM image, **B**) hydrodynamic radius distribution of CeO_2 NP in the aqueous medium, **C**) UV-DRS spectrum of powdered CeO_2-NPs, and **D**) estimation of the optical band gap using the modified Kubelka-Munk function.

5.6.2. Photodegradation of IBU using CeO_2 NPs kinetics and thermodynamics

The photodegradation of IBU using different bulk densities of catalysts was studied to investigate how the catalyst loading affected the reaction rate. The photodegradation of IBU significantly increased by an increasing catalyst concentration as shown in Figure 5.4A. Consequently, the concentration of the by-product 1-OXO IBU increased at a higher rate of formation as shown Figures 5.4B and 5.4C.

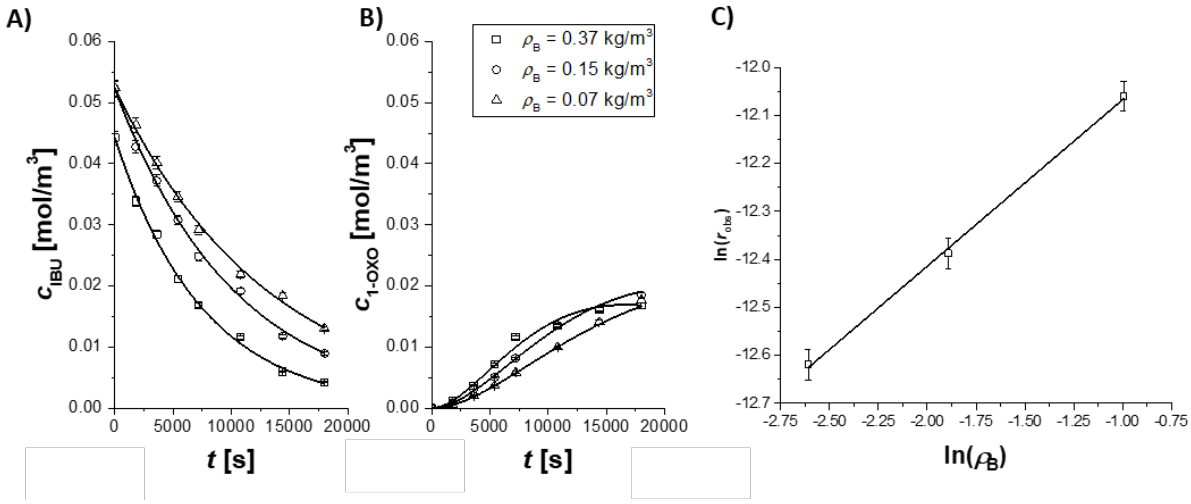

Figure 5.4 Experimental results of the kinetic tests conducted at different catalyst loading. Adopted reaction conditions: $c_{IBU,0} = 5 \cdot 10^{-2}$ mol/m^3, $T = 303$ K, $Q_{air} = 1.0 \cdot 10^{-6}$ m^3/s and $v = 750$ rpm. Trends of the concentration profiles *vs* the reaction time for **A**) IBU and **B**) 1-OXO IBU. Lines are the calculated profiles. The subplots refer to the same legend. The panel **C**) represents catalyst bulk density linearization test.

To confirm the reaction order, three independent experiments were carried out by varying the initial concentration of IBU (Figure 5.5). The findings indicate a first-order reaction kinetics as confirmed by the logarithmic plot in Figure 5.5C. The 1-OXO form of IBU displayed the same pattern, indicating a higher rate of formation when the concentration of the solution is increased.

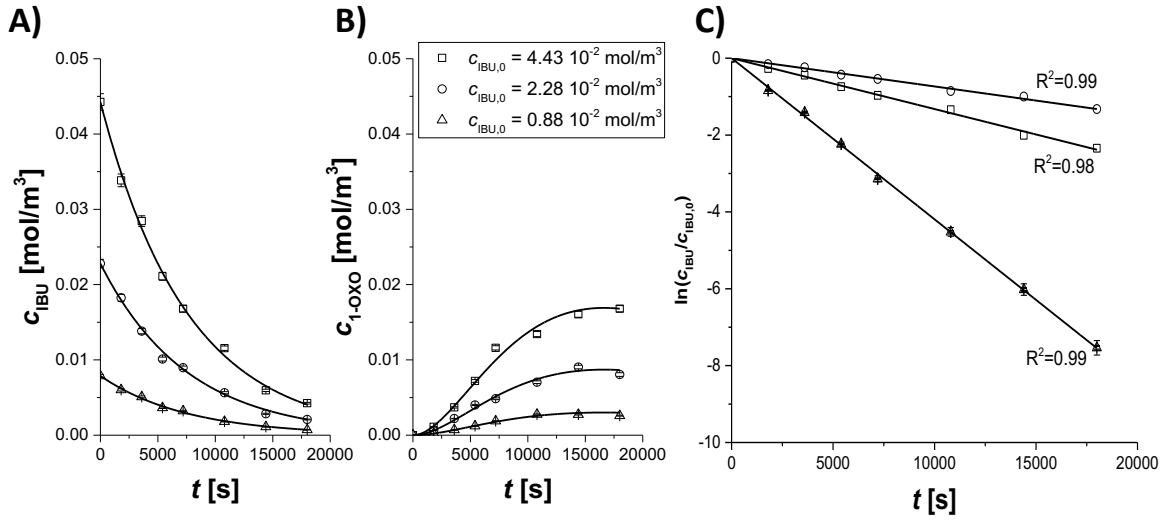

Figure 5.5 Experimental results of the kinetic tests conducted at different initial concentrations of IBU. Adopted reaction conditions: $T = 303$ K, $\rho_B = 0.37$ kg/m^3, $Q_{air} = 1.0 \cdot 10^{-6}$ m^3/s and $v =$ 750 rpm. Trends of the concentration profiles *vs* the reaction time for **A**) IBU and **B**) 1-OXO IBU. Lines are the calculated profiles. The subplots refer to the same legend. Panel **C**) represents first-order linearization test.

Further details on the reaction mechanisms, kinetics model and the calculation approach are discussed in **Publications V** and **VI**.

The temperature effect on the photodegradation of IBU using CeO_2-NPs was investigated. The obtained rate constants and the corresponding values of the thermodynamic parameters $\Delta G°$, $\Delta H°$, and $\Delta S°$ are listed in Table 5.1. It can be seen that increasing the reaction temperature, increases the rate constants and the corresponding photodegradation efficiency. To estimate the thermodynamic parameters, Eq. 5.2 – 5.4 were employed.

$$\Delta H° = E_a + RT \quad (5.2)$$
$$\ln(k/T) = \ln(K_B/h) + (\Delta S°/R) - (\Delta H°/RT) \quad (5.3)$$
$$\Delta G° = \Delta H° - T\Delta S° \quad (5.4)$$

where $\Delta G°$ is the Gibbs free energy, $\Delta H°$ the change in enthalpy, $\Delta S°$ is the change in entropy, R is the general gas constant (8.314 J/mol.K), K_B is Boltzmann constant (1.38×10^{-23} $m^2.kg/s^2.K$), h is Plank constant (6.63×10^{-34} $m^2.kg/s$), k is the kinetics rate constant $(m^3/mol)s^{-1}$.

Table 5.1 Kinetic and thermodynamic parameters for the photodegradation of IBU using CeO_2-NPs at $E_{a1} = 55.8kJ/mol$.

T (K)	**K** $(m^3/mol)s^{-1}$	$\boldsymbol{ln(k/T)}$	$\boldsymbol{\Delta H°/RT}$	$\boldsymbol{\Delta H°}$ $(kJ.mol^{-1})$	$\boldsymbol{\Delta S°}$ $(kJ.mol^{-1}K^{-1})$	$\boldsymbol{\Delta G°}$ $(kJ.mol^{-1})$
293	2.7×10^{-5}	-16.18	23.91	58.2	-0.14	100.0
303	5.9×10^{-5}	-15.45	23.15	58.3		101.5
313	1.2×10^{-4}	-14.78	22.44	58.4		103.0
323	2.3×10^{-4}	-14.15	21.78	58.5		104.5

The relatively high positive values of $\Delta G°$ and $\Delta H°$ designate the endothermic non-spontaneous reaction forming a highly hydrated transition state complex with weak bonds for a rapid degradation of the activated complex [49-51]. Moreover, the negative value of $\Delta S°$, which is close to zero, suggests that the system exhibits a random behavior that supports a higher degree of degradation of IBU into simple products [50].

5.6.3. Photodegradation of IBU using ZnO and TiO_2 NPs kinetics and thermodynamics

The effect of the catalyst bulk density was assessed by changing the catalyst load while the other experimental parameters were fixed. Figure 5.6 presents the trends detected using different catalyst loads of TiO_2 (Figure 5.6A) and ZnO (Figure 5.6B) NPs in the range of 0.05 and 0.5 kg/m^3. Generally, the concentration of IBU decreases upon increasing the catalyst load.

The IBU concentration almost approached zero in case of TiO_2 NPs at ρ_B value of 0.5 kg/m^3. The possible explanation is that the increase in the number of active surface sites available for the photocatalytic reaction, enhances the generation of hydroxyl radicals due to the increase of the concentration of charge carriers [52]. This in agreement with the findings of Jallouli and coworkers [53] where the IBU removal reached 100% showing no screen effect at catalyst load up to 4 kg/m^3. On the other hand, increasing the catalyst load of ZnO NPs in the range of ρ_B 0.2 to 0.5 kg/m^3 showed no significant effect on the performance, as the three curves are almost overlapped. Conversely, increasing the load beyond 0.37 kg/m^3, reduced the degradation efficiency of ZnO NPs. This observation can be explained by the screen effect that the catalyst exerts on the penetration of UV light, thus retarding the chemical reaction [52, 53]. In other words, when the catalyst concentration increases, the reaction rate increases and then the screen effect prevails. Moreover, a possible loss in the surface area of the NPs can be caused by the agglomeration at high loadings, and thus prevents the absorption of photons by the catalyst [52].

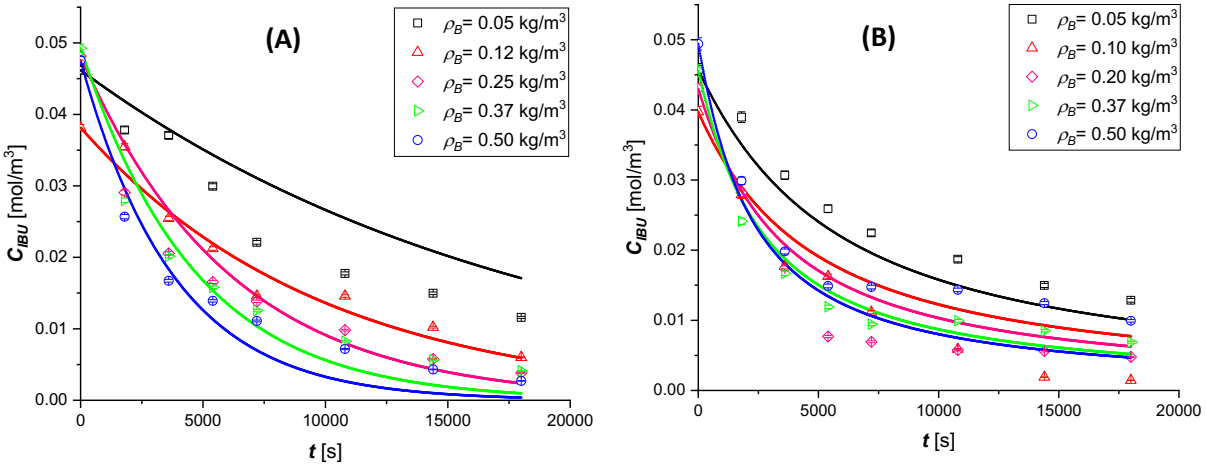

Figure 5.6 Results of the kinetic experiments conducted at different catalyst loadings. Adopted reaction conditions: $C_{IBU,0} = 4 \cdot 10^{-2}$ mol/m^3, $T = 303$ K, $Q_{air} = 0.94 \cdot 10^{-6}$ m^3/s and $v = 750$ rpm. Trends of the concentration profiles *vs* the reaction time for **A**) TiO_2 and **B**) ZnO.

The initial concentration effect of IBU was studied to verify the reaction order as demonstrated in Figure 5.7. Evidently, the higher the concentration of IBU in the solution, the lower photodegradation efficiency. This observation goes in line with the findings of Choina and coworkers [54] where photodegradation of IBU on ZnO was higher at low concentrations (<5 ppm) in comparison with concentrated solutions. Plausibly, fewer radicals were shared for each IBU molecule and so the lower percentage of degradation is obtained, as attributed by Bennemla et al. [52]. Nevertheless, the detected IBU concentrations in wastewater bodies are usually less that 1µg/L [53], which is sufficiently low. However, further studies are needed to evaluate the efficiency of these systems with lower pollutant concentrations.

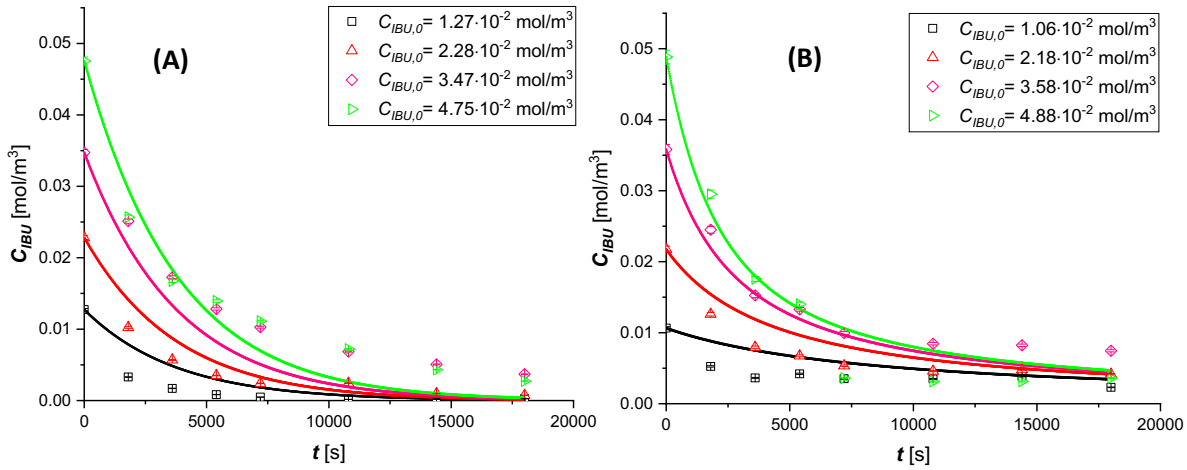

Figure 5.7 Results of the kinetic experiments conducted at different initial concentrations of IBU. Adopted reaction conditions: ρ_B = 0.5 kg/m^3, T = 303 K, Q_{air} = 0.94·10^{-6} m^3/s and v = 750 rpm. Trends of the concentration profiles *vs* the reaction time for **A**) TiO_2 and **B**) ZnO.

The estimated values of $\Delta G°$, $\Delta H°$ and $\Delta S°$ for TiO_2 NPs (Table 5.2) show that the reaction is non-spontaneous, endothermic with a minor random behavior. Moreover, the increasing $\Delta G°$ values for TiO_2 NPs, as the temperature increases reduces the spontaneity of the reaction producing, highly hydrated transition state complex, which needs enough energy to be produced [49-51]. The obtained small and negative $\Delta S°$ value suggests that weak bonds are present in the activated complex leading to a rapid degradation of IBU into simple products [50].

Table 5.2 Kinetic and thermodynamic parameters for the photodegradation of IBU using TiO_2 NPs at $E_{a1} = 26.9 kJ/mol$.

T (K)	k $(m^3/mol)s^{-1}$	$ln(k/T)$	$\Delta H°/RT$	$\Delta H°$ $(kJ.mol^{-1})$	$\Delta S°$ $(kJ.mol^{-1}K^{-1})$	$\Delta G°$ $(kJ.mol^{-1})$
288	6.3×10^{-4}	-13.0	12.3	29.3	-0.21	90.9
293	7.6×10^{-4}	-12.9	12.1	29.4		92.0
303	1.1×10^{-3}	-12.5	11.7	29.5		94.2
313	1.5×10^{-3}	-12.2	11.4	29.5		96.4
323	2.1×10^{-3}	-11.9	11.0	29.6		98.6

For ZnO NPs, the rate constants and the corresponding values of the thermodynamic parameters, $\Delta G°, \Delta H°$, and $\Delta S°$ for ZnO NPs show that increasing the reaction temperature, notably increases the rate constants (Table 5.3). Yet, the appreciably high positive activation enthalpy proves that the endothermic reaction nature is possibly due to electrostatic attraction

between the ZnO NPs and IBU, leading to a uniform adsorption of IBU molecules on ZnO particles to accomplish an efficient photodegradation.

Table 5.3 Kinetic and thermodynamic parameters for the photodegradation of IBU using ZnO NPs at $E_{a1} = 102.8 kJ/mol$.

T (K)	k $(m^3/mol)s^{-1}$	$ln(k/T)$	$\Delta H°/RT$	$\Delta H°$ $(kJ.mol^{-1})$	$\Delta S°$ $(kJ.mol^{-1}K^{-1})$	$\Delta G°$ $(kJ.mol^{-1})$
288	0.6	-6.2	43.9	105.2	0.11	74.5
293	1.2	-5.5	43.2	105.3		74.0
303	4.7	-4.2	41.8	105.3		73.0
313	10.7	-2.9	40.5	105.4		72.0
323	50.8	-1.7	39.2	105.5		71.0

5.7. Conclusions

This chapter summarized the photodegradation kinetics of IBU, using three semiconductor catalysts, namely CeO_2, TiO_2 and ZnO NPs. The experiments were carried out in a laboratory-scale batch reactor by varying the operating conditions such as temperature, catalyst loading, and initial concentration of IBU. The analysis of the various samples was carried out by UV-Vis spectrophotometry. The air flow rate and stirring rate were useful experimental parameters to exclude limitations by fluid-fluid and solid-fluid mass transfer, while further evaluations were done to neglect the intraparticle diffusion effect. Subsequently, after evaluating the reaction order and defining a kinetic law for each material, a kinetic model was proposed, both to describe the trend of the experimental data and to estimate adjustable parameters such as frequency factors, activation energies, pre-exponential factors of adsorption constants and enthalpy variations. Finally, to further characterize the system, thermodynamic analysis was carried out. In general, CeO_2, TiO_2 and ZnO materials demonstrated a good photodegradation capacity of IBU, showing different behaviors under varying operating conditions. The reaction system was found to be suitable for the IBU photodegradation reaction and it may be tested in the future to investigate different reaction conditions as well as be used for any studies on other emerging pollutants. In this perspective, this study will be the door for possible future applications of these NPs in continuous processes that could be coupled with a post-biological unit to convert IBU to less harmful products.

5.8. List of abbreviations

EC	emerging contaminant
AOP	advanced oxidationprocess
IBU	ibuprofen
NPs	nanoparticles
ROS	reactive oxygen species

5.9. References

[1] H. Sarma, Chapter 1 - Understanding emerging contaminants in soil and water: current perspectives on integrated remediation approaches, in: H. Sarma, D.C. Dominguez, W.-Y. Lee (Eds.), Emerging Contaminants in the Environment, Elsevier 2022, pp. 1-38. https://doi.org/https://doi.org/10.1016/B978-0-323-85160-2.00002-0.
[2] A. Egea-Corbacho, S. Gutiérrez Ruiz, J.M. Quiroga Alonso, Removal of emerging contaminants from wastewater using nanofiltration for its subsequent reuse: Full–scale pilot plant, Journal of Cleaner Production 214 (2019) 514-523. https://doi.org/https://doi.org/10.1016/j.jclepro.2018.12.297.
[3] J.A.P. Duarte, A.K.N. Ribeiro, P. de Carvalho, J.C. Bortolini, I.C. Ostroski, Emerging contaminants in the aquatic environment: phytoplankton structure in the presence of sulfamethoxazole and diclofenac, Environmental Science and Pollution Research 30(16) (2023) 46604-46617. https://doi.org/10.1007/s11356-023-25589-2.
[4] K. Samal, S. Mahapatra, M. Hibzur Ali, Pharmaceutical wastewater as Emerging Contaminants (EC): Treatment technologies, impact on environment and human health, Energy Nexus 6 (2022) 100076. https://doi.org/https://doi.org/10.1016/j.nexus.2022.100076.
[5] E. Brillas, A critical review on ibuprofen removal from synthetic waters, natural waters, and real wastewaters by advanced oxidation processes, Chemosphere 286 (2022) 131849. https://doi.org/https://doi.org/10.1016/j.chemosphere.2021.131849.
[6] J. Jan-Roblero, J.A. Cruz-Maya, Ibuprofen: Toxicology and Biodegradation of an Emerging Contaminant, Molecules, 2023.
[7] N. Taoufik, W. Boumya, M. Achak, M. Sillanpää, N. Barka, Comparative overview of advanced oxidation processes and biological approaches for the removal pharmaceuticals, Journal of Environmental Management 288 (2021) 112404. https://doi.org/https://doi.org/10.1016/j.jenvman.2021.112404.
[8] T. Jiang, B. Wang, B. Gao, N. Cheng, Q. Feng, M. Chen, S. Wang, Degradation of organic pollutants from water by biochar-assisted advanced oxidation processes: Mechanisms and applications, Journal of Hazardous Materials 442 (2023) 130075. https://doi.org/https://doi.org/10.1016/j.jhazmat.2022.130075.
[9] Y. Deng, R. Zhao, Advanced Oxidation Processes (AOPs) in Wastewater Treatment, Current Pollution Reports 1(3) (2015) 167-176. https://doi.org/10.1007/s40726-015-0015-z.
[10] A. Pattnaik, J.N. Sahu, A.K. Poonia, P. Ghosh, Current perspective of nano-engineered metal oxide based photocatalysts in advanced oxidation processes for degradation of organic pollutants in wastewater, Chemical Engineering Research and Design 190 (2023) 667-686. https://doi.org/https://doi.org/10.1016/j.cherd.2023.01.014.

[11] M. Vatanparast, L. Saedi, Sonochemical-assisted synthesis and characterization of CeO_2 nanoparticles and its photocatalytic properties, Journal of Materials Science: Materials in Electronics 29(9) (2018) 7107-7113. https://doi.org/10.1007/s10854-018-8698-8.
[12] S. Yuán, B. Xu, Q. Zhang, S. Liu, J. Xie, M. Zhang, T. Ohno, Development of the Visible-Light Response of CeO_{2-x} with a high Ce^{3+} Content and Its Photocatalytic Properties, ChemCatChem 10(6) (2018) 1267-1271. https://doi.org/https://doi.org/10.1002/cctc.201701767.
[13] L. Gnanasekaran, R. Hemamalini, R. Saravanan, K. Ravichandran, F. Gracia, S. Agarwal, V.K. Gupta, Synthesis and characterization of metal oxides (CeO_2, CuO, NiO, Mn_3O_4, SnO_2 and ZnO) nanoparticles as photo catalysts for degradation of textile dyes, Journal of Photochemistry and Photobiology B: Biology 173 (2017) 43-49. https://doi.org/https://doi.org/10.1016/j.jphotobiol.2017.05.027.
[14] M. Aslam, M.T. Qamar, M.T. Soomro, I.M.I. Ismail, N. Salah, T. Almeelbi, M.A. Gondal, A. Hameed, The effect of sunlight induced surface defects on the photocatalytic activity of nanosized CeO_2 for the degradation of phenol and its derivatives, Applied Catalysis B: Environmental 180 (2016) 391-402. https://doi.org/https://doi.org/10.1016/j.apcatb.2015.06.050.
[15] P. Borker, A.V. Salker, Solar assisted photocatalytic degradation of Naphthol Blue Black dye using $Ce_{1-x}MnxO_2$, Materials Chemistry and Physics 103(2) (2007) 366-370. https://doi.org/https://doi.org/10.1016/j.matchemphys.2007.02.034.
[16] F. Naaz, U. Farooq, T. Ahmad, Ceria as an Efficient Nanocatalyst for Organic Transformations, Nanocatalysts, IntechOpen2019. https://doi.org/10.5772/intechopen.82688.
[17] J.A. Rodriguez, D.C. Grinter, Z. Liu, R.M. Palomino, S.D. Senanayake, Ceria-based model catalysts: fundamental studies on the importance of the metal–ceria interface in CO oxidation, the water–gas shift, CO_2 hydrogenation, and methane and alcohol reforming, Chemical Society Reviews 46(7) (2017) 1824-1841. https://doi.org/10.1039/C6CS00863A.
[18] C. Maria Magdalane, K. Kaviyarasu, A. Raja, M.V. Arularasu, G.T. Mola, A.B. Isaev, N.A. Al-Dhabi, M.V. Arasu, B. Jeyaraj, J. Kennedy, M. Maaza, Photocatalytic decomposition effect of erbium doped cerium oxide nanostructures driven by visible light irradiation: Investigation of cytotoxicity, antibacterial growth inhibition using catalyst, Journal of Photochemistry and Photobiology B: Biology 185 (2018) 275-282. https://doi.org/https://doi.org/10.1016/j.jphotobiol.2018.06.011.
[19] D. Majumder, I. Chakraborty, K. Mandal, S. Roy, Facet-Dependent Photodegradation of Methylene Blue Using Pristine CeO_2 Nanostructures, ACS Omega 4(2) (2019) 4243-4251. https://doi.org/10.1021/acsomega.8b03298.
[20] A.A. Fauzi, A.A. Jalil, N.S. Hassan, F.F.A. Aziz, M.S. Azami, I. Hussain, R. Saravanan, D.V.N. Vo, A critical review on relationship of CeO_2-based photocatalyst towards mechanistic degradation of organic pollutant, Chemosphere 286 (2022) 131651. https://doi.org/https://doi.org/10.1016/j.chemosphere.2021.131651.
[21] C. Sun, H. Li, L. Chen, Nanostructured ceria-based materials: synthesis, properties, and applications, Energy & Environmental Science 5(9) (2012) 8475-8505. https://doi.org/10.1039/C2EE22310D.
[22] Y.-C. Zhang, Z. Li, L. Zhang, L. Pan, X. Zhang, L. Wang, A. Fazal e, J.-J. Zou, Role of oxygen vacancies in photocatalytic water oxidation on ceria oxide: Experiment and DFT studies, Applied Catalysis B: Environmental 224 (2018) 101-108. https://doi.org/https://doi.org/10.1016/j.apcatb.2017.10.049.
[23] M. Ahamed, M.J. Akhtar, M.A.M. Khan, Z.M. Alaizeri, H.A. Alhadlaq, Evaluation of the Cytotoxicity and Oxidative Stress Response of CeO_2-RGO Nanocomposites in Human Lung Epithelial A549 Cells, Nanomaterials 9(12) (2019) 1709.

[24] G. Jayakumar, A. Albert Irudayaraj, A. Dhayal Raj, Particle Size Effect on the Properties of Cerium Oxide (CeO_2) Nanoparticles Synthesized by Hydrothermal Method, Mechanics, Materials Science & Engineering Journal 9(1) (2017). https://doi.org/10.2412/mmse.3.4.481.
[25] S.S. Naghavi, A.A. Emery, H.A. Hansen, F. Zhou, V. Ozolins, C. Wolverton, Giant onsite electronic entropy enhances the performance of ceria for water splitting, Nature Communications 8(1) (2017) 285. https://doi.org/10.1038/s41467-017-00381-2.
[26] N. Gallucci, M. Hmoudah, E. Martinez, A. El-Qanni, M. Di Serio, L. Paduano, G. Vitiello, V. Russo, Photodegradation of ibuprofen using CeO2 nanostructured materials: Reaction kinetics, modeling, and thermodynamics, Journal of Environmental Chemical Engineering 10(3) (2022) 107866. https://doi.org/https://doi.org/10.1016/j.jece.2022.107866.
[27] M.M. Khan, S.A. Ansari, D. Pradhan, D.H. Han, J. Lee, M.H. Cho, Defect-Induced Band Gap Narrowed CeO_2 Nanostructures for Visible Light Activities, Industrial & Engineering Chemistry Research 53(23) (2014) 9754-9763. https://doi.org/10.1021/ie500986n.
[28] B. Choudhury, A. Choudhury, Ce^{3+} and oxygen vacancy mediated tuning of structural and optical properties of CeO_2 nanoparticles, Materials Chemistry and Physics 131(3) (2012) 666-671. https://doi.org/https://doi.org/10.1016/j.matchemphys.2011.10.032.
[29] C. Yang, X. Yu, P.N. Pleßow, S. Heißler, P.G. Weidler, A. Nefedov, F. Studt, Y. Wang, C. Wöll, Rendering Photoreactivity to Ceria: The Role of Defects, Angewandte Chemie International Edition 56(45) (2017) 14301-14305. https://doi.org/https://doi.org/10.1002/anie.201707965.
[30] A. Gnanaprakasam, V.M. Sivakumar, P.L. Sivayogavalli, M. Thirumarimurugan, Characterization of TiO_2 and ZnO nanoparticles and their applications in photocatalytic degradation of azodyes, Ecotoxicology and Environmental Safety 121 (2015) 121-125. https://doi.org/https://doi.org/10.1016/j.ecoenv.2015.04.043.
[31] S. Zeinali Heris, M. Etemadi, S.B. Mousavi, M. Mohammadpourfard, B. Ramavandi, Preparation and characterizations of TiO_2/ZnO nanohybrid and its application in photocatalytic degradation of tetracycline in wastewater, Journal of Photochemistry and Photobiology A: Chemistry 443 (2023) 114893. https://doi.org/https://doi.org/10.1016/j.jphotochem.2023.114893.
[32] L. Gnanasekaran, A.K. Priya, A.A. Ghfar, K. Sekar, M. Santhamoorthy, M. Arthi, M. Soto-Moscoso, The influence of heterostructured TiO_2/ZnO nanomaterials for the removal of azo dye pollutant, Chemosphere 308 (2022) 136161. https://doi.org/https://doi.org/10.1016/j.chemosphere.2022.136161.
[33] I.A. Khattab, M.Y. Ghaly, L. Österlund, M.E.M. Ali, J.Y. Farah, F.M. Zaher, M.I. Badawy, Photocatalytic degradation of azo dye Reactive Red 15 over synthesized titanium and zinc oxides photocatalysts: a comparative study, Desalination and Water Treatment 48(1-3) (2012) 120-129. https://doi.org/10.1080/19443994.2012.698803.
[34] S.O. Fatin, H.N. Lim, W.T. Tan, N.M. Huang, Comparison of Photocatalytic Activity and Cyclic Voltammetry of Zinc Oxide and Titanium Dioxide Nanoparticles toward Degradation of Methylene Blue, International Journal of Electrochemical Science 7(10) (2012) 9074-9084. https://doi.org/https://doi.org/10.1016/S1452-3981(23)16181-5.
[35] A.H. Zyoud, A. Zubi, S. Hejjawi, S.H. Zyoud, M.H. Helal, S.H. Zyoud, N. Qamhieh, A. Hajamohideen, H.S. Hilal, Removal of acetaminophen from water by simulated solar light photodegradation with ZnO and TiO_2 nanoparticles: Catalytic efficiency assessment for future prospects, Journal of Environmental Chemical Engineering 8(4) (2020) 104038. https://doi.org/https://doi.org/10.1016/j.jece.2020.104038.
[36] I. Garrido, M. Pastor-Belda, N. Campillo, P. Viñas, M.J. Yañez, N. Vela, S. Navarro, J. Fenoll, Photooxidation of insecticide residues by ZnO and TiO_2 coated magnetic nanoparticles

under natural sunlight, Journal of Photochemistry and Photobiology A: Chemistry 372 (2019) 245-253. https://doi.org/https://doi.org/10.1016/j.jphotochem.2018.12.027.
[37] K. Yari, A. Seidmohammadi, M. Khazaei, A. Bhatnagar, M. Leili, A comparative study for the removal of imidacloprid insecticide from water by chemical-less UVC, UVC/TiO_2 and UVC/ZnO processes, Journal of Environmental Health Science and Engineering 17(1) (2019) 337-351. https://doi.org/10.1007/s40201-019-00352-3.
[38] C.B. Ong, L.Y. Ng, A.W. Mohammad, A review of ZnO nanoparticles as solar photocatalysts: Synthesis, mechanisms and applications, Renewable and Sustainable Energy Reviews 81 (2018) 536-551. https://doi.org/https://doi.org/10.1016/j.rser.2017.08.020.
[39] M. Hussain, R. Ceccarelli, D.L. Marchisio, D. Fino, N. Russo, F. Geobaldo, Synthesis, characterization, and photocatalytic application of novel TiO_2 nanoparticles, Chemical Engineering Journal 157(1) (2010) 45-51. https://doi.org/https://doi.org/10.1016/j.cej.2009.10.043.
[40] C.M. Taylor, A. Ramirez-Canon, J. Wenk, D. Mattia, Enhancing the photo-corrosion resistance of ZnO nanowire photocatalysts, Journal of Hazardous Materials 378 (2019) 120799. https://doi.org/https://doi.org/10.1016/j.jhazmat.2019.120799.
[41] T. Saad Algarni, N.A.Y. Abduh, A. Al Kahtani, A. Aouissi, Photocatalytic degradation of some dyes under solar light irradiation using ZnO nanoparticles synthesized from Rosmarinus officinalis extract, Green Chemistry Letters and Reviews 15(2) (2022) 460-473. https://doi.org/10.1080/17518253.2022.2089059.
[42] S. Mustapha, M.M. Ndamitso, A.S. Abdulkareem, J.O. Tijani, D.T. Shuaib, A.O. Ajala, A.K. Mohammed, Application of TiO_2 and ZnO nanoparticles immobilized on clay in wastewater treatment: a review, Applied Water Science 10(1) (2020) 49. https://doi.org/10.1007/s13201-019-1138-y.
[43] S.M. Sosa, R. Huertas, V.J. Pereira, Combination of Zinc Oxide Photocatalysis with Membrane Filtration for Surface Water Disinfection, Membranes, 2023.
[44] C. Belver, C. Han, J.J. Rodriguez, D.D. Dionysiou, Innovative W-doped titanium dioxide anchored on clay for photocatalytic removal of atrazine, Catalysis Today 280 (2017) 21-28. https://doi.org/https://doi.org/10.1016/j.cattod.2016.04.029.
[45] A.I.Y. Tok, F.Y.C. Boey, Z. Dong, X.L. Sun, Hydrothermal synthesis of CeO_2 nano-particles, Journal of Materials Processing Technology 190(1) (2007) 217-222. https://doi.org/https://doi.org/10.1016/j.jmatprotec.2007.02.042.
[46] D. Girija, H.S.B. Naik, C. Sudhamani, B.V. Kumar, Cerium Oxide Nanoparticles—A Green, Reusable, and Highly Efficient Heterogeneous Catalyst for the Synthesis of Polyhydroquinolines under Solvent-Free Conditions, Archives of Applied Science Research 3(3) (2011) 373-382.
[47] M. Okuda, Y. Suzumoto, I. Yamashita, Bioinspired Synthesis of Homogenous Cerium Oxide Nanoparticles and Two- or Three-Dimensional Nanoparticle Arrays Using Protein Supramolecules, Crystal Growth & Design 11(6) (2011) 2540-2545. https://doi.org/10.1021/cg200299y.
[48] E. Kusmierek, A CeO_2 Semiconductor as a Photocatalytic and Photoelectrocatalytic Material for the Remediation of Pollutants in Industrial Wastewater: A Review, Catalysts 10(12) (2020). https://doi.org/10.3390/catal10121435.
[49] M. Rezaei, A. Nezamzadeh-Ejhieha, The ZnO-NiO nano-composite: A brief characterization, kinetic and thermodynamic study and study the Arrhenius model on the sulfasalazine photodegradation, International Journal of Hydrogen Energy 45(46) (2020) 24749-24764. https://doi.org/https://doi.org/10.1016/j.ijhydene.2020.06.258.

[50] K. Byrappa, A.K. Subramani, S. Ananda, K.M.L. Rai, R. Dinesh, M. Yoshimura, Photocatalytic degradation of rhodamine B dye using hydrothermally synthesized ZnO, Bulletin of Materials Science 29(5) (2006) 433-438. https://doi.org/10.1007/BF02914073.
[51] A.S.M. Kuba, A.M.J.A.L. Shamari, Kinetics and thermodynamics study for photodegradation of Brown HT dye by MnO and NiO as catalysis, Materials Today: Proceedings 49 (2022) 2741-2746. https://doi.org/https://doi.org/10.1016/j.matpr.2021.09.256.
[52] M. Bennemla, S. Bouafia-Chergui, A. Amrane, M. Chabani, The photocatalytic degradation kinetics of the anti-inflammatory drug ibuprofen in aqueous solution under UV/TiO_2 system and neural networks modeling, International Journal of Chemical Reactor Engineering (2022). https://doi.org/doi:10.1515/ijcre-2021-0170.
[53] N. Jallouli, L.M. Pastrana-Martínez, A.R. Ribeiro, N.F.F. Moreira, J.L. Faria, O. Hentati, A.M.T. Silva, M. Ksibi, Heterogeneous photocatalytic degradation of ibuprofen in ultrapure water, municipal and pharmaceutical industry wastewaters using a TiO_2/UV-LED system, Chemical Engineering Journal 334 (2018) 976-984. https://doi.org/https://doi.org/10.1016/j.cej.2017.10.045.
[54] J. Choina, A. Bagabas, C. Fischer, G.U. Flechsig, H. Kosslick, A. Alshammari, A. Schulz, The influence of the textural properties of ZnO nanoparticles on adsorption and photocatalytic remediation of water from pharmaceuticals, Catalysis Today 241 (2015) 47-54. https://doi.org/https://doi.org/10.1016/j.cattod.2014.05.014.

Chapter 6 — Adsorption of Methylene Blue on Metakaolin-based Geopolymers: A Kinetic and Thermodynamic Investigation

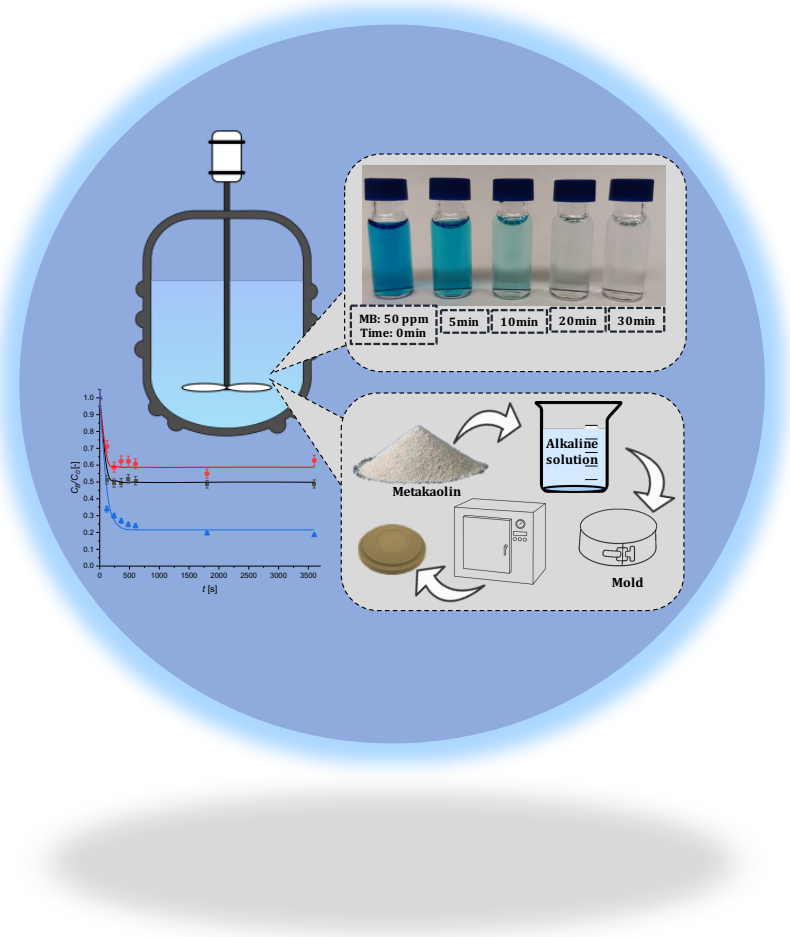

M. Hmoudah, R. Paparo, M. De Luca, M. E. Fortunato, R. Tesser, M. Di Serio, C. Ferone, G. Roviello, O. Tarallo, V. Russo, Adsorption of methylene blue on metakaolin-based geopolymers: a kinetic and thermodynamic investigation, Langmuir. *(submitted)*

6.1. Introduction

As the world population rises, so does the need for industrial products, which fuels the growth of numerous industrial sectors [1, 2]. This quick increase in the production leads to a significant volume of effluent, which may contain harmful chemicals and dyes. [3, 4]. These compounds, if not treated, can have negative impacts on the public health and the ecosystem [5]. Consequently, wastewater treatment is of paramount importance because harmful contaminants and pollutants will be removed from wastewaters before being discharged into the environment [6, 7]. It is essential for maintaining sustainable production methods and lowering the environmental impact of industry. A typical example of a sector with a significant water use is textile industry. [8]. Textile wastewaters are highly contaminated with hazardous organic compounds such as colors and poisonous metals e.g. chromium, antimony, and cobalt. Their unconstrained discharge results in serious contamination [8, 9]. More than 700 thousand tons per year of dyes are produced annually [10] and the 2% of them are disposed directly in aqueous effluents generating huge volumes of colored wastewater [11].

Dyes are classified according to chemical constitution, application class, and end use [12] and many of them are toxic and even carcinogenic [13]. Furthermore, they can reduce the transmission of light altering the biological metabolism of the hydrosphere and they cause microtoxicity to marine life due to their tendency to sequester metals [14-17]. Thus, treatment of wastewaters containing dyes is challenging and it is still in the spotlight of the scientific community since these compounds are recalcitrant organic molecules that show a high resistance to aerobic digestion and high stability to light, heat, and oxidizing agents [11, 18-20]. Several methods of dye wastewater treatment have been screened and reviewed in the last 30 years including photocatalytic degradation [4, 21], sonochemical degradation, electrochemical degradation, integrated chemical-biological degradation, precipitation processes, coagulation, flocculation, and use of cation exchange membrane [10, 22-24]. To date, by considering the advantages and disadvantages of these removal techniques, adsorption represents an interesting and promising technology that can be applied on industrial scale due to its affordability, simplicity of design, ease of operation and insensitivity to toxic substances [25] and it does not result in the formation of harmful substances [26].

Methylene blue (MB) is used extensively in industries such as cotton, wood, and silk dyeing. Although it is not typically considered acutely toxic, the widespread release of MB can lead to the development of diseases and other adverse health effects in exposed populations [27, 28]. At the actual state of art, several papers deal with the adsorption of MB with different kinds of adsorbents. Commercial activated carbon represents the most popular choice for the removal of MB [29]. However, the focus of the scientific community has moved to find less expensive alternatives. Therefore, unconventional adsorbents have been tested, such as fly ash, pine leaves, mango seeds, and clays [30] showing in some cases good removal capacities. Table 1 lists the recent studies of MB removal over the last two years, using different unconventional adsorbents, and various parameters have been studied in order to explore economic, environmentally benign, and efficient adsorbents.

This work focuses on having an in-depth kinetic and thermodynamic understanding of the adsorption of metakoilin-based geopolymers for the removal MB, and compare it to the

performance of a commercial activated carbon. The collected data obtained from the kinetic study were analyzed using the dynamic intraparticle model (ADIM) for fluid–solid adsorption developed and investigated by our research group. The retrieved physico-chemical parameters are necessary for the development of a continuously operating adsorption column. This work will be useful in the future design of adsorption columns that can continuously remove organic contaminants from wastewater.

6.2. Metakaolin-based geopolymers

Hence, geopolymers (alkali-activated aluminum silicates) were tested in this work for the removal of MB. They are synthetic materials, typically amorphous, aluminum silicate based [31]. They have a structure similar to tectosilicates consisting of a three-dimensional network of SiO_4- tetrahedral units covalently linked together [32]. Often the silicon atoms, the center of the tetrahedral units, are replaced by aluminum atoms as in clays [31, 33]. They are obtained via condensation polymerization, the so-called geopolymerization or geosynthesis, through mixing an aluminum-silicate powder such as metakaolin, fly ash, blast furnace slag, or synthetic raw materials (alumina and silica) with a strongly alkaline activating solution [31, 34]. The binders are silicates and/or alkali metal hydroxides. During geopolymerization, a gel is formed which acts as a glue for the unreacted particles and any fillers added as reinforcement. The process takes place at low temperatures, between 25 and 120 °C, with minimal shrinkage and rapid consolidation, from 5 to 10 hours, similar to quick-setting cements [35, 36]. The most significant advantage of using geopolymers lies mainly in their environmental and economic sustainability [33]. Other advantages are the short preparation time, the controllable process, the low cost due to the low synthesis temperature and the absence of mechanical processing to obtain the final product, and the possibility of producing the material in situ [37].
Metakaolins are a class of materials used to prepare geopolymers [33, 37]. One of the key advantages of metakaolin is its high pozzolanic reactivity, which allows it to react quickly with alkali activators and form a strong, hardened materials [38]. Metakaolin also has a high silica content, which contributes to the strength and durability of the final product [33, 39]. Furthermore, the use of metakaolin in geopolymers synthesis can reduce the amount of waste materials generated from industrial processes, as it can be derived from the waste products of kaolin mining [40].

6.3. Synthesis and characterization of geopolymers

The preparation of the four types of metakaolin-based geopolymers was carried out as dense specimens. The amounts of the different components are listed in Table 6.1, while Table 6.2 shows the molar ratios of Si/Al, Si/Na, and Al/Na.

Table 6.1: Summary of the masses of the various components used to produce metakaolin-based geopolymers.

Geopolymers	Metakaolin METAMAX [g]	Metakaolin MEFISTO [g]	Activating solution [g]	NaOH [g]	Water [g]	Total mass [g]
Type A	43.682	0.000	44.784	4.644	6.890	100.000
Type B	37.457	0.000	55.340	7.203	0.000	100.000
Type C	0.000	47.104	47.993	4.903	0.000	100.000
Type D	0.000	37.216	55.183	7.601	0.000	100.000

Table 6.2: Chemical composition of the metakaolin-based geopolymers and Si/Al/Na molar ratios.

Campione	Na_2O [mol]	SiO_2 [mol]	H_2O [mol]	Al_2O_3 [mol]	Si/Al [mol/mol]	Na/Al [mol/mol]	Si/Na [mol/mol]
Type A	1.00	4.93	16.75	1.63	1.51	0.61	2.47
Type B	1.00	3.52	12.06	1.01	1.74	0.99	1.76
Type C	1.00	5.09	13.80	1.56	1.64	0.64	2.55
Type D	1.00	3.46	11.78	0.91	1.89	1.10	1.73

In a typical synthesis, an activating alkaline solution was prepared by dissolving solid sodium hydroxide in a sodium silicate solution. This highly exothermic reaction was carried out in a water and ice bath by gradual addition of sodium hydroxide to the sodium silicate solution, and stirred until completely dissolved. The resulting solution was left to cool for 24 hours at room temperature. The composition of the solution obtained can be expressed as Na_2O: 1.34 SiO_2:10.48 H_2O. Metakaolin was added to the activating solution in variable quantities and mixed mechanically at 500 rpm. The mixtures were then poured into molds. The obtained samples were sealed at 95% relative humidity and stored at room temperature (23 ± 2°C) for 24 h. After which, they were placed in an oven at 60°C for the next 24h. The samples were left sealed at room temperature for further five days and finally opened and left for 21 days at room temperature. The images of the produced geopolymers are shown in Figure 6.1.

Type A **Type B** **Type C** **Type D**

Figure 6.1: Images of the produced geopolymers.

Different tools were employed to characterize the synthesized metakaolin-based geopolymers. All the specifications of each tool can be found in **Publication VII**. Figure 6.2 displays the WAXD patterns of the four types of metakaolin-based geopolymers synthesized. It can be observed that the samples are mostly amorphous with some diffraction peaks due to the presence of unreacted kaolinite, quartz and anatase that were already present in the starting metakaolins and to some trona (sodium hydrogen carbonate hydrate) formed during reaction.

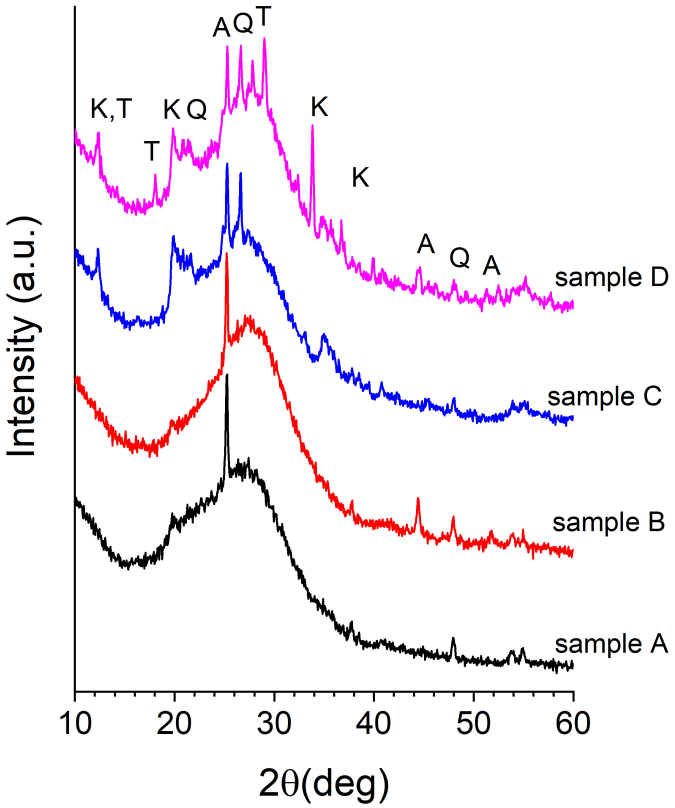

Figure 6.2 WAXD patterns of the geopolymers A, B, C, and D. Main diffraction peaks of the crystalline phases have been indicated: A – anatase (01-070-7348); K – kaolinite (01-080-0886); Q- quartz (01-083-0539), T- trona (00-001-1077).

SEM images shown in Figure 6.3 describe the morphology of the samples. In all cases (Figure 6.3A-D), the morphology is typical of a geopolymeric material. In particular, a rather homogeneous and continuous structure is observed, with some small fractures most likely due to the mechanical stress to which the sample was subjected to obtain a fresh fracture surface to be observed by SEM. The lamellar crystals of unreacted kaolinite (detectable also in the X-ray pattern reported in Figure 6.2) are still evident and can be identified thanks to their distinctive morphology. Finally, the high-magnification images (Figure 6.3A'-D') point out the typical fine morphology of geopolymeric samples, i.e. characterized by the presence of a sort of nanometric spheres deriving from the gel phase that the geopolymer undergoes during the polycondensation process.

The results of the surface area, pore size, and pore volume for the tested adsorbents are listed in Table 6.3. Information about commercial activated carbon used as the reference material are

reported, too. As apparent, the geopolymer based adsorbent is characterized by a surface area that is at least one order of magnitude lower than the commercial activated carbon. As far as the pore dimensions, in case of commercial activated carbon we found an average pore volume of around 0.75 cm^3/g while in case of the geopolymer samples, the average volume ranged from 0.2 to 0.4 cm^3/g, thus being around ¼ to ½ in respect to that of activated carbon.

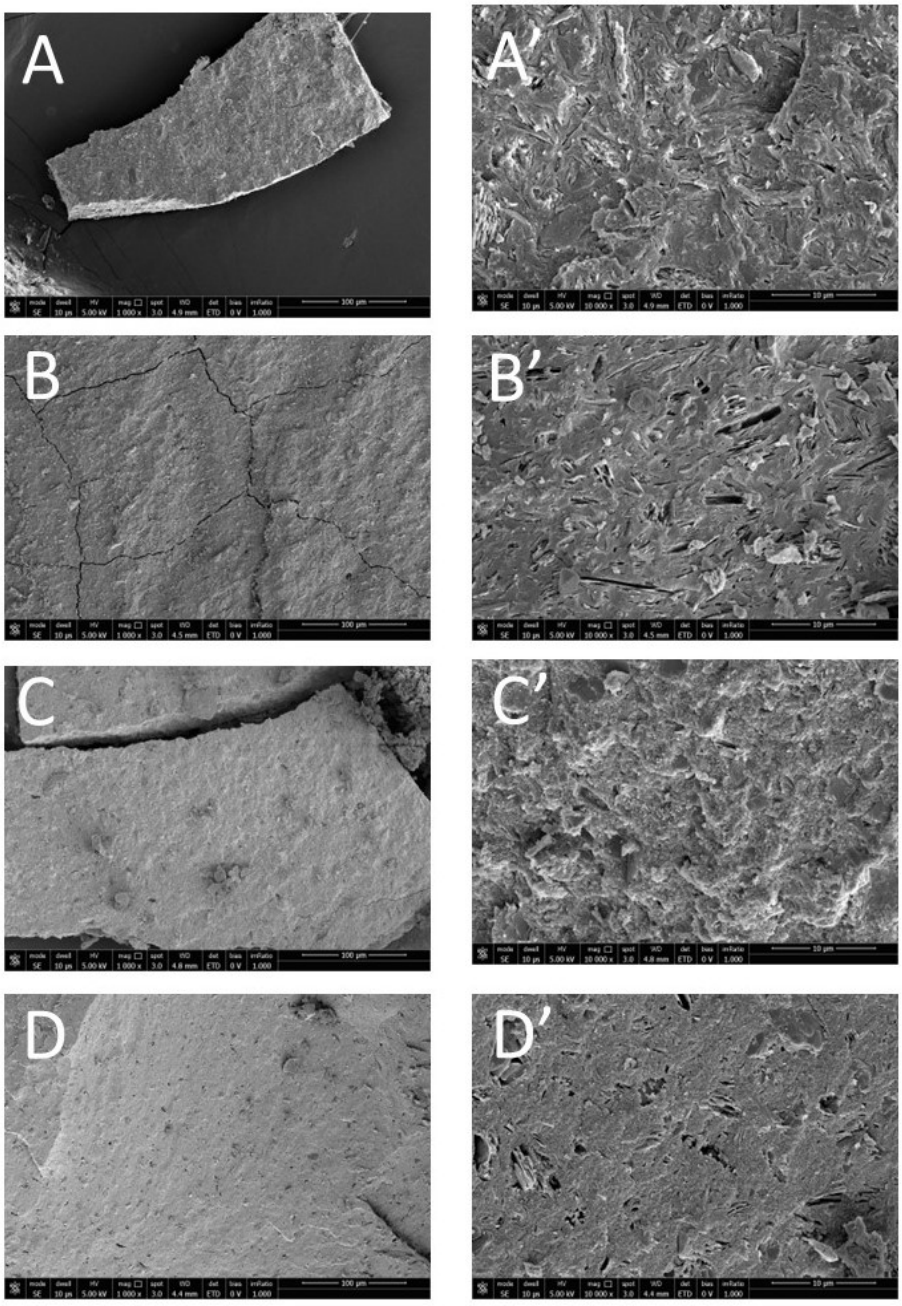

Figure 6.3 SEM images of fresh fracture surfaces of geopolymers A, B, C, and D at different magnifications: A, B, C, D 1000x; A', B', C', D' 10000x.

Table 6.3 Textural properties of the adsorbents.

Geopolymer	Surface area [$m^2\ g^{-1}$]	Average pore volume [$cm^3\ g^{-1}$]	Si/Al [mol mol^{-1}]
Type A	51	0.371	1.51
Type B	44	0.186	1.74
Type C	43	0.256	1.64
Type D	34	0.237	1.89
Activated carbon	650	0.748	-

6.4. Batch adsorption of MB on geopolymers

6.4.1. Adsorption isotherms

The adsorption capacity towards MB was measured for the four prepared geopolymers and commercial activated carbon. The corresponding adsorption performance was evaluated under identical experimental conditions (T= 30°C, C_0=8.02×10^{-2} mol m^{-3}; ρ_{bulk}= 0.50 kg m^{-3}, v=450 rpm, pH= 7). Type A geopolymer showed a significantly higher adsorption uptake than that of activated carbon for the same surface area. Therefore, Type A geopolymer was selected for detailed thermodynamic and kinetic investigations (The screening test details are explained in **Publication VII**).

The adsorption capacity of the Type A geopolymer was determined and the adsorption isotherm experiments were conducted at three different temperatures i.e., 30, 40 and 50 °C. The experimental adsorption data were fitted using both Langmuir and Freundlich adsorption isotherms, to describe the trend of C_S vs C_B and to understand the equilibrium phenomena behind the adsorption process. The results shown in Figure 6.4, clearly indicate that the experimental data were best fitted by the Langmuir isotherm. Moreover, the plateau values of the concentration, collected from the kinetic experiments, match the Langmuir fitting line. According to the Langmuir model (Eq. 6.1), the adsorption of the adsorbate is limited to a monolayer assuming a homogeneous adsorption process with no interaction between the adsorbed molecules. The estimated model parameters are shown in Table 6.4 along with the 95% confidence intervals.

$$C_S(t,r_p) = C_s^* b \frac{C_L(t,r_p)}{1+bC_L(t,r_p)} \tag{6.1}$$

where b is Langmuir adsorption parameter ($m^3 \cdot mol^{-1}$), C_S is the solute concentration in the solid ($mol \cdot m^{-3}$), C_S^* is the saturation solute solid concentration ($mol \cdot m^{-3}$), and C_L is the solute concentration in the liquid of the pore ($mol \cdot m^{-3}$).

Table 6.4 Estimated adsorption parameters of Langmuir model.

T [°C]	Cs^* [mol m^{-3}]	b [m^3 mol^{-1}]
30	120±10	1900±500
40	130±10	1800±400
50	134±3	1200±100

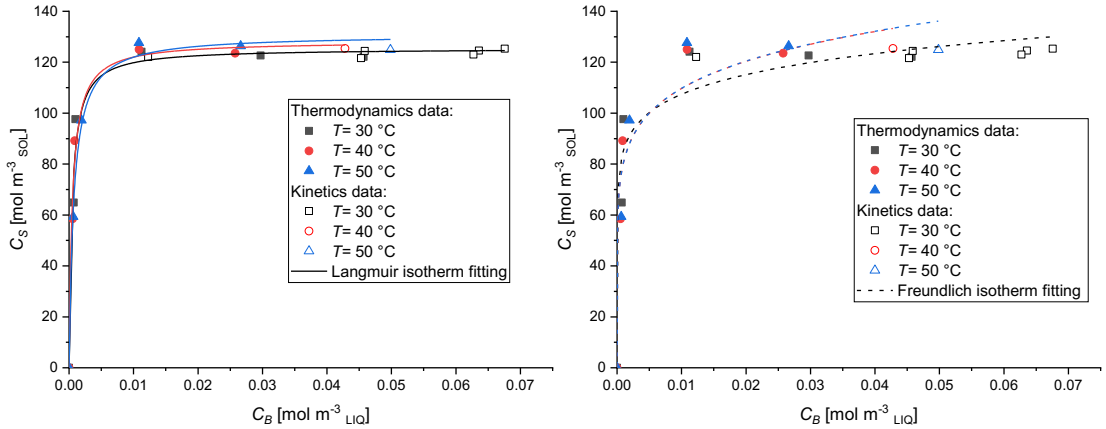

Figure 6.4 (a) Langmuir and (b) Freundlich isotherm plots for the adsorption of MB dye on Type A geopolymer at different temperatures.

Table 6.5 summarizes the calculated values of the key thermodynamic parameters which are $\Delta G°$, $\Delta H°$, and $\Delta S°$ at different temperatures, i.e., 303, 313, and 323 K of the adsorption of MB on Type A geopolymer. The thermodynamic parameters were estimated according to Eqs 6.2 – 6.3.

$$\ln b = \frac{\Delta S^\circ}{R} - \frac{\Delta H^\circ}{RT} \tag{6.2}$$

$$\Delta G^\circ = -RT \ln K_C \tag{6.3}$$

where b is the Langmuir adsorption parameter (m^3 mol^{-1}), $\Delta G°$ (kJ mol^{-1}) is the activation Gibbs free energy, $\Delta H°$ (kJ mol^{-1}) is the change in enthalpy, $\Delta S°$ (kJ mol^{-1} K^{-1}) is the change in entropy, R is the general gas constant (8.314 J mol^{-1} K^{-1}), and T is the absolute temperature (K).

The obtained thermodynamic parameters are listed in Table 5. The negative values of $\Delta G°$ indicate that the adsorption process is spontaneous and that the MB molecules have a high affinity and uptake on geopolymer Type A. On the other hand, the negative value of $\Delta H°$ indicated that the adsorption process was relatively exothermic, this might be due to the destruction of binding sites between MB dye and the geopolymer. In this study, $\Delta H°$ is lower than 40 kJ/mol confirming that the adsorption is mainly physical in nature. The positive value of $\Delta S°$ supports the randomness of the adsorbent surface after adsorption which is beneficial for spontaneous adsorption process.

Table 6.5 Kinetic and thermodynamic parameters for the adsorption of MB using Type A geopolymer.

T [K]	ΔH° [kJ/mol]	ΔS° [kJ/(mol K)]	ΔG° [kJ/mol]	R^2
303			-19.02	
313	-18.54	0.25	-19.50	0.99
323			-19.04	

6.4.2. Adsorption kinetics

The evaluation of adsorption kinetics is important as it provides insights into the adsorption mechanism. In this section, the obtained results are reported in terms of the bulk liquid concentration of MB normalized by the initial concentration in the solution (C_B/C_0) as a function of the time (t). The adsorption kinetics of MB on Type A geopolymer was studied at different experimental conditions by varying the stirring rate, the initial concentration of the dye, the adsorbent bulk density, and the temperature. It is worth noting that the development of a mathematical model is necessary for the interpretation of the kinetic data, collected from the batch experiments, considering all the possible phenomena proceeding on the molecular scale. Specifically, the ADIM was used to describe the adsorption kinetics of MB on the type A geopolymer. The details of the modelling activities and the input parameters can be found in **Publication VII**.

Figure 6.5 shows the concentration profiles at different stirring rates (v). The curves are overlapped and a common uptake value of 50 % is obtained at different stirring rates, clearly indicating the absence of external mass transfer limitations. This conclusion justified us to fix the fluid-solid mass transfer coefficient k_m to a large value during the simulations.
The effect of the initial concentration of MB is shown in Figure 6.6. It can be noticed that the higher the initial concentration of MB, the lower the adsorption efficiency. This result can be considered to be in line with the assumption of a monolayer adsorption mechanism according to the Langmuir model.

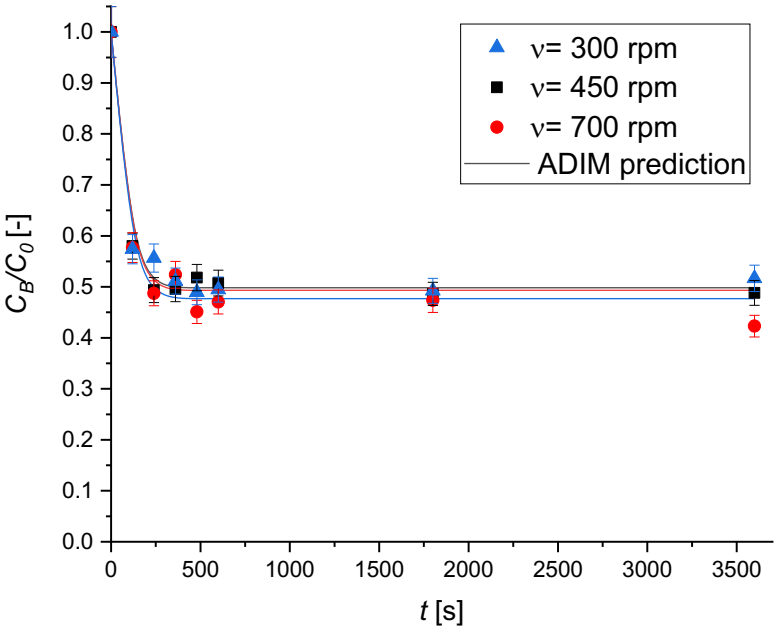

Figure 6.5 The effect of the stirring rate on the MB adsorption kinetics over Type A geopolymer. Experimental conditions are: T=30°C; C_0=8.02×10^{-2} mol m^{-3}; ρ_{bulk}= 0.50 kg m^{-3}.

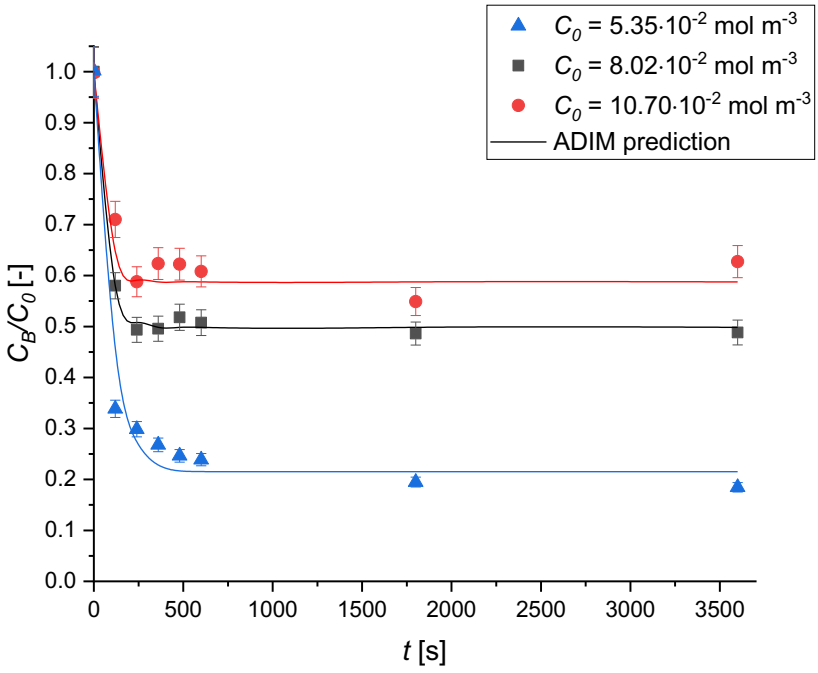

Figure 6.6 The effect of the initial concentration on the MB adsorption kinetics over Type A geopolymer. Experimental conditions are: T=30°C; v= 450 rpm; ρ_{bulk}= 0.50 kg m^{-3}.

The effect of the adsorbent bulk density on the adsorption kinetics was studied by varying the amount of the geopolymer added to the MB solution as illustrated in Figure 6.7.

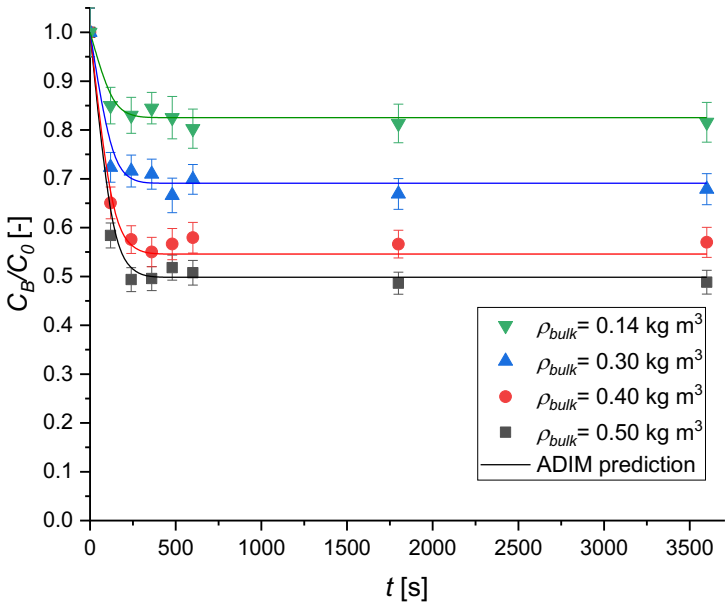

Figure 6.7 The effect of the adsorbent bulk density on the MB adsorption kinetics over Type A geopolymer. Experimental conditions are: T=30°C; v= 450 rpm; C_0= 8.02×10^{-2} mol m^{-3}.

It is evident that using a higher loading of the solid material enhances the adsorption kinetics. In fact, the slope of the curves is steeper, thus the adsorption is faster, by increasing the adsorbent bulk density. The uptake of the dye on the solid increases from 15 to 50 % by changing ρ_{bulk} from 0.14 to 0.50 kg m^{-3}.

In the end, kinetic experiments at different temperatures were carried out to study the effect of temperature. The obtained results are presented in Figure 6.8 and they agree with those observed in the adsorption isotherm study. It can be seen that the temperature does not have a significant effect on the removal efficiency of MB and no appreciable improvement on the adsorption kinetics and solute uptake was observed.

The experimental data were analyzed by nonlinear regression, and it was possible to estimate the values of the tortuosity of the particles τ and that of the surface diffusivity (D_S). The latter one is a temperature-dependent parameter, so it was necessary to determine its value at different temperatures. The results of the parameter estimation are listed in Table 6.6.

The dependence of surface diffusivity on the temperature can be expressed by an Arrhenius-like equation (Eq. 6.4). The estimated values of D_S are plotted against the temperature in Figure 6.9.

$$D_S = D_{S,0} \exp\left(-\frac{E_s}{RT}\right) \tag{6.4}$$

where D_s is the surface diffusivity, (m^2·s^{-1}), E_s is the activation energy (kJ.mol^{-1}), R is the universal gas constant (kJ mol^{-1}K^{-1}), and T is the temperature in K.

From the fitting of the values of D_S vs T, a surface activation energy E_S of 35±5 kJ/mol is obtained.

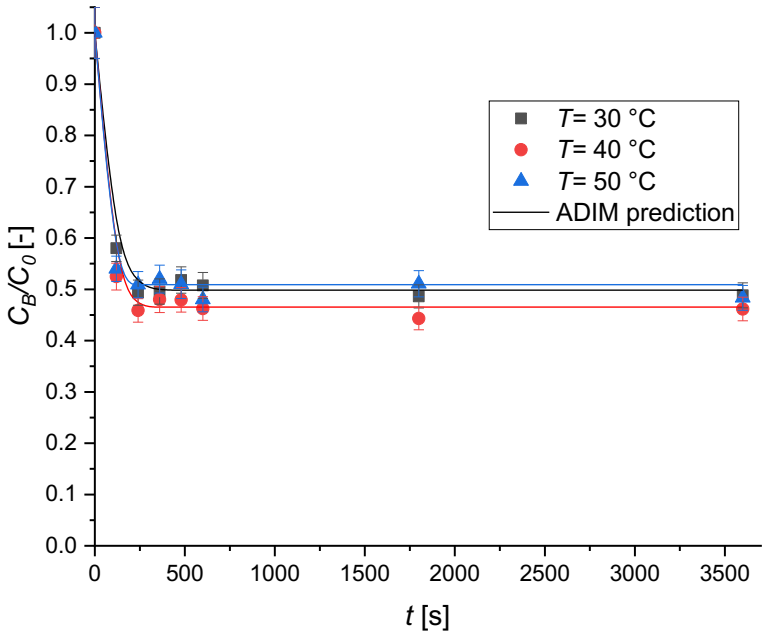

Figure 6.8 The effect of the temperature on the MB adsorption kinetics over Type A geopolymer. Experimental conditions were set as: v= 450 rpm; C_0= 8.02×10^{-2} mol m^{-3}, ρ_{bulk}= 0.50 kg m^{-3}.

Table 6.6 Estimated parameters with statistical analysis.

PARAMETER	***T*=30° C**	***T*=40° C**	***T*=50° C**
Ds×10^{13} [m^2 s^{-1}]	1.1±0.1	1.6±0.4	2.6±0.2
τ [-]		5±1	

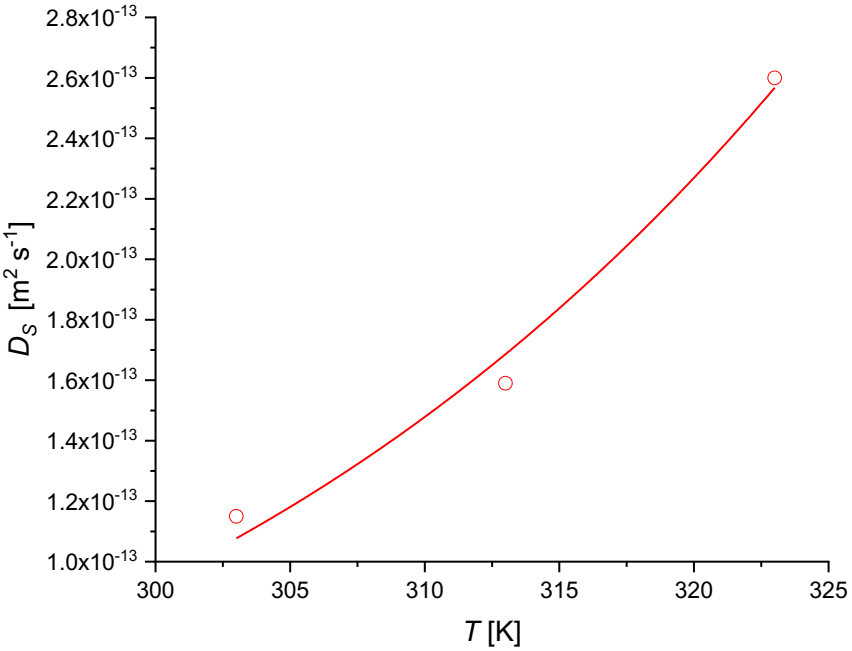

Figure 6.9 Surface diffusion coefficient as a function of temperature.

It must be emphasized that a good fitting is obtained in each case, thus the ADIM was able to describe the behavior of the system under the investigated conditions and to provide extended information on the adsorption kinetics. This was further confirmed by the parity plot displayed in Figure 6.10, which shows a reasonably good agreement between the calculated and the experimental data within a confidence interval of ± 10%. In addition, the overall correlation factor R^2 is equal to 0.99.

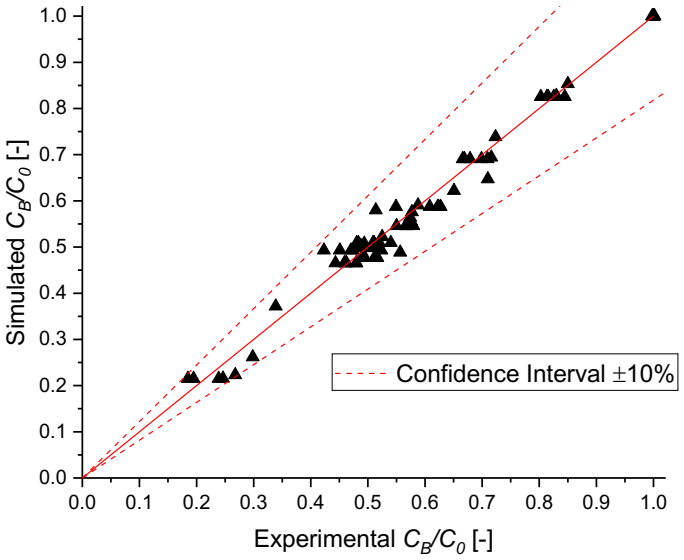

Figure 6.10 Parity plot of MB normalized concentration.

6.5. Conclusions

In this work, metakaolin-based geopolymers were synthesized and applied for the removal of MB as a cationic model dye. Four different kinds of geopolymers were synthesized with different molar ratios of Si/Al. Multiple analytical tools were applied in the characterization of the synthesized geopolymers, confirming the formation of geopolymer particles with amorphous structure and morphology. Screening tests for the four types of geopolymers alluded that the geopolymer of type A has the highest adsorption capacity with the highest uptake and affinity towards MB. Moreover, the adsorption capacity of the type A geopolymer towards MB was significantly higher than that of activated carbon for the same surface area, owing to the electrostatic interactions between the cationic dye and the geopolymer, and the unique structural properties of these geopolymers. Subsequently, an extensive kinetic and equilibrium study was carried out in batch experiments to explore the effect of the main operation conditions such as temperature, solid bulk density, initial concentration of MB, and agitation speed on the adsorption kinetics of MB on Type A geopolymer. The Langmuir adsorption model showed the best agreement to the adsorption equilibrium, indicating the strong bond between MB and Type A geopolymer and indicating that the adsorption process can be described as monolayer adsorption with uniform surface sites and adsorption energies. The ADIM model provided insights into the diffusion mechanism of MB through the determination of km and DS values, parameters needed to design an adsorption column working in flow. Additionally, the

thermodynamic analysis indicated that the adsorption of MB on type A geopolymer was exothermic and spontaneous. Lastly, it is concluded from the results of this study that these geopolymers have a good potential as adsorbent materials for the use in wastewater treatment applications.

6.6. List of abbreviations

MB	methylene blue
ADIM	adsorption dynamic intraparticle model

6.7. References

[1] A. Tebeje, Z. Worku, T.T.I. Nkambule, J. Fito, Adsorption of chemical oxygen demand from textile industrial wastewater through locally prepared bentonite adsorbent, International Journal of Environmental Science and Technology 19(3) (2022) 1893-1906. https://doi.org/10.1007/s13762-021-03230-4.
[2] V. Russo, M. Hmoudah, F. Broccoli, M.R. Iesce, O.-S. Jung, M. Di Serio, Applications of Metal Organic Frameworks in Wastewater Treatment: A Review on Adsorption and Photodegradation, Frontiers in Chemical Engineering 2 (2020). https://doi.org/10.3389/fceng.2020.581487.
[3] S. Manikandan, R. Subbaiya, M. Saravanan, M. Ponraj, M. Selvam, A. Pugazhendhi, A critical review of advanced nanotechnology and hybrid membrane based water recycling, reuse, and wastewater treatment processes, Chemosphere 289 (2022) 132867. https://doi.org/https://doi.org/10.1016/j.chemosphere.2021.132867.
[4] N. Gallucci, M. Hmoudah, E. Martinez, A. El-Qanni, M. Di Serio, L. Paduano, G. Vitiello, V. Russo, Photodegradation of ibuprofen using CeO_2 nanostructured materials: Reaction kinetics, modeling, and thermodynamics, Journal of Environmental Chemical Engineering 10(3) (2022) 107866. https://doi.org/https://doi.org/10.1016/j.jece.2022.107866.
[5] S. Garg, Z.Z. Chowdhury, A.N.M. Faisal, N.P. Rumjit, P. Thomas, Impact of Industrial Wastewater on Environment and Human Health, in: S. Roy, A. Garg, S. Garg, T.A. Tran (Eds.), Advanced Industrial Wastewater Treatment and Reclamation of Water: Comparative Study of Water Pollution Index during Pre-industrial, Industrial Period and Prospect of Wastewater Treatment for Water Resource Conservation, Springer International Publishing, Cham, 2022, pp. 197-209. https://doi.org/10.1007/978-3-030-83811-9_10.
[6] J.O. Eniola, R. Kumar, M.A. Barakat, J. Rashid, A review on conventional and advanced hybrid technologies for pharmaceutical wastewater treatment, Journal of Cleaner Production 356 (2022) 131826. https://doi.org/https://doi.org/10.1016/j.jclepro.2022.131826.
[7] B.S. Rathi, P.S. Kumar, Application of adsorption process for effective removal of emerging contaminants from water and wastewater, Environmental Pollution 280 (2021) 116995. https://doi.org/https://doi.org/10.1016/j.envpol.2021.116995.
[8] R.P. Singh, P.K. Singh, R. Gupta, R.L. Singh, Treatment and Recycling of Wastewater from Textile Industry, in: R.L. Singh, R.P. Singh (Eds.), Advances in Biological Treatment of Industrial Waste Water and their Recycling for a Sustainable Future, Springer Singapore, Singapore, 2019, pp. 225-266. https://doi.org/10.1007/978-981-13-1468-1_8.
[9] K. Yang, Y. Liu, Y. Li, Z. Cao, C. Zhou, Z. Wang, X. Zhou, S.A. Baig, X. Xu, Applications and characteristics of Fe-Mn binary oxides for Sb(V) removal in textile wastewater: Selective

adsorption and the fixed-bed column study, Chemosphere 232 (2019) 254-263. https://doi.org/https://doi.org/10.1016/j.chemosphere.2019.05.194.
[10] G. Crini, Non-conventional low-cost adsorbents for dye removal: A review, Bioresource Technology 97(9) (2006) 1061-1085. https://doi.org/https://doi.org/10.1016/j.biortech.2005.05.001.
[11] C.I. Pearce, J.R. Lloyd, J.T. Guthrie, The removal of colour from textile wastewater using whole bacterial cells: a review, Dyes and Pigments 58(3) (2003) 179-196. https://doi.org/https://doi.org/10.1016/S0143-7208(03)00064-0.
[12] Y.M. Slokar, A. Majcen Le Marechal, Methods of decoloration of textile wastewaters, Dyes and Pigments 37(4) (1998) 335-356. https://doi.org/https://doi.org/10.1016/S0143-7208(97)00075-2.
[13] W. Delée, C. O'Neill, F.R. Hawkes, H.M. Pinheiro, Anaerobic treatment of textile effluents: A review, Journal of Chemical Technology & Biotechnology 73(4) (1998) 323-335. https://doi.org/https://doi.org/10.1002/(SICI)1097-4660(199812)73:4<323::AID-JCTB976>3.0.CO;2-S.
[14] S.M. Ghoreishi, R. Haghighi, Chemical catalytic reaction and biological oxidation for treatment of non-biodegradable textile effluent, Chemical Engineering Journal 95(1) (2003) 163-169. https://doi.org/https://doi.org/10.1016/S1385-8947(03)00100-1.
[15] M.F.R. Pereira, S.F. Soares, J.J.M. Órfão, J.L. Figueiredo, Adsorption of dyes on activated carbons: influence of surface chemical groups, Carbon 41(4) (2003) 811-821. https://doi.org/https://doi.org/10.1016/S0008-6223(02)00406-2.
[16] P.C. Vandevivere, R. Bianchi, W. Verstraete, Review: Treatment and reuse of wastewater from the textile wet-processing industry: Review of emerging technologies, Journal of Chemical Technology & Biotechnology 72(4) (1998) 289-302. https://doi.org/https://doi.org/10.1002/(SICI)1097-4660(199808)72:4<289::AID-JCTB905>3.0.CO;2-#.
[17] T. Robinson, G. McMullan, R. Marchant, P. Nigam, Remediation of dyes in textile effluent: a critical review on current treatment technologies with a proposed alternative, Bioresource Technology 77(3) (2001) 247-255. https://doi.org/https://doi.org/10.1016/S0960-8524(00)00080-8.
[18] G. McMullan, C. Meehan, A. Conneely, N. Kirby, T. Robinson, P. Nigam, I. Banat, R. Marchant, W. Smyth, Microbial decolourisation and degradation of textile dyes, Applied Microbiology and Biotechnology 56(1) (2001) 81-87. https://doi.org/10.1007/s002530000587.
[19] S. Ibrahim, W.Z. Shuy, H.-M. Ang, S. Wang, Preparation of bioadsorbents for effective adsorption of a reactive dye in aqueous solution, Asia-Pacific Journal of Chemical Engineering 5(4) (2010) 563-569. https://doi.org/https://doi.org/10.1002/apj.446.
[20] M. Hmoudah, A. El-Qanni, S. Abuhatab, N.N. Marei, A. El-Hamouz, B.J.A. Tarboush, I.H. Alsurakji, H.M. Baniowda, V. Russo, M. Di Serio, Competitive adsorption of Alizarin Red S and Bromocresol Green from aqueous solutions using brookite TiO2 nanoparticles: experimental and molecular dynamics simulation, Environmental Science and Pollution Research 29(51) (2022) 77992-78008. https://doi.org/10.1007/s11356-022-21368-7.
[21] M. Toscanesi, V. Russo, A. Medici, A. Giarra, M. Hmoudah, M. Di Serio, M. Trifuoggi, Heterogeneous Photodegradation for the Abatement of Recalcitrant COD in Synthetic Tanning Wastewater, ChemEngineering, 2022.
[22] K.A. Adegoke, O.S. Bello, Dye sequestration using agricultural wastes as adsorbents, Water Resources and Industry 12 (2015) 8-24. https://doi.org/https://doi.org/10.1016/j.wri.2015.09.002.
[23] J. Qiu, P. Fan, Y. Feng, F. Liu, C. Ling, A. Li, Comparison of the adsorption behaviors for methylene blue on two renewable gels with different physical state, Environmental Pollution 254 (2019) 113117. https://doi.org/https://doi.org/10.1016/j.envpol.2019.113117.

[24] L.Y. Jun, R.R. Karri, N.M. Mubarak, L.S. Yon, C.H. Bing, M. Khalid, P. Jagadish, E.C. Abdullah, Modelling of methylene blue adsorption using peroxidase immobilized functionalized Buckypaper/polyvinyl alcohol membrane via ant colony optimization, Environmental Pollution 259 (2020) 113940. https://doi.org/https://doi.org/10.1016/j.envpol.2020.113940.
[25] V.K. Garg, M. Amita, R. Kumar, R. Gupta, Basic dye (methylene blue) removal from simulated wastewater by adsorption using Indian Rosewood sawdust: a timber industry waste, Dyes and Pigments 63(3) (2004) 243-250. https://doi.org/https://doi.org/10.1016/j.dyepig.2004.03.005.
[26] B. Li, J. Guo, K. Lv, J. Fan, Adsorption of methylene blue and Cd(II) onto maleylated modified hydrochar from water, Environmental Pollution 254 (2019) 113014. https://doi.org/https://doi.org/10.1016/j.envpol.2019.113014.
[27] S. Abuhatab, A. El-Qanni, N.N. Marei, M. Hmoudah, A. El-Hamouz, Sustainable competitive adsorption of methylene blue and acid red 88 from synthetic wastewater using NiO and/or MgO silicate based nanosorbcats: experimental and computational modeling studies, RSC Advances 9(61) (2019) 35483-35498. https://doi.org/10.1039/C9RA07001J.
[28] A. El-Qanni, N.N. Nassar, G. Vitale, A. Hassan, Maghemite nanosorbcats for methylene blue adsorption and subsequent catalytic thermo-oxidative decomposition: Computational modeling and thermodynamics studies, Journal of Colloid and Interface Science 461 (2016) 396-408. https://doi.org/https://doi.org/10.1016/j.jcis.2015.09.041.
[29] M. Rafatullah, O. Sulaiman, R. Hashim, A. Ahmad, Adsorption of methylene blue on low-cost adsorbents: A review, Journal of Hazardous Materials 177(1) (2010) 70-80. https://doi.org/https://doi.org/10.1016/j.jhazmat.2009.12.047.
[30] M.T. Yagub, T.K. Sen, S. Afroze, H.M. Ang, Dye and its removal from aqueous solution by adsorption: A review, Advances in Colloid and Interface Science 209 (2014) 172-184. https://doi.org/https://doi.org/10.1016/j.cis.2014.04.002.
[31] C. Ferone, G. Roviello, F. Colangelo, R. Cioffi, O. Tarallo, Novel hybrid organic-geopolymer materials, Applied Clay Science 73 (2013) 42-50. https://doi.org/https://doi.org/10.1016/j.clay.2012.11.001.
[32] G. Roviello, L. Ricciotti, O. Tarallo, C. Ferone, F. Colangelo, V. Roviello, R. Cioffi, Innovative Fly Ash Geopolymer-Epoxy Composites: Preparation, Microstructure and Mechanical Properties, Materials, 2016.
[33] G. Roviello, C. Menna, O. Tarallo, L. Ricciotti, C. Ferone, F. Colangelo, D. Asprone, R. di Maggio, E. Cappelletto, A. Prota, R. Cioffi, Preparation, structure and properties of hybrid materials based on geopolymers and polysiloxanes, Materials & Design 87 (2015) 82-94. https://doi.org/https://doi.org/10.1016/j.matdes.2015.08.006.
[34] G. Roviello, E. Chianese, C. Ferone, L. Ricciotti, V. Roviello, R. Cioffi, O. Tarallo, Hybrid Geopolymeric Foams for the Removal of Metallic Ions from Aqueous Waste Solutions, Materials, 2019.
[35] G. Roviello, C. Menna, O. Tarallo, L. Ricciotti, F. Messina, C. Ferone, D. Asprone, R. Cioffi, Lightweight geopolymer-based hybrid materials, Composites Part B: Engineering 128 (2017) 225-237. https://doi.org/https://doi.org/10.1016/j.compositesb.2017.07.020.
[36] F. Messina, C. Ferone, F. Colangelo, R. Cioffi, Low temperature alkaline activation of weathered fly ash: Influence of mineral admixtures on early age performance, Construction and Building Materials 86 (2015) 169-177. https://doi.org/https://doi.org/10.1016/j.conbuildmat.2015.02.069.
[37] J. Zhao, L. Tong, B. Li, T. Chen, C. Wang, G. Yang, Y. Zheng, Eco-friendly geopolymer materials: A review of performance improvement, potential application and sustainability

assessment, Journal of Cleaner Production 307 (2021) 127085. https://doi.org/https://doi.org/10.1016/j.jclepro.2021.127085.
[38] A.L. Yadav, V. Sairam, K. Srinivasan, L. Muruganandam, Synthesis and characterization of geopolymer from metakaolin and sugarcane bagasse ash, Construction and Building Materials 258 (2020) 119231. https://doi.org/https://doi.org/10.1016/j.conbuildmat.2020.119231.
[39] P. Duxson, S.W. Mallicoat, G.C. Lukey, W.M. Kriven, J.S.J. van Deventer, The effect of alkali and Si/Al ratio on the development of mechanical properties of metakaolin-based geopolymers, Colloids and Surfaces A: Physicochemical and Engineering Aspects 292(1) (2007) 8-20. https://doi.org/https://doi.org/10.1016/j.colsurfa.2006.05.044.
[40] I. Perná, M. Šupová, T. Hanzlíček, A. Špaldoňová, The synthesis and characterization of geopolymers based on metakaolin and high LOI straw ash, Construction and Building Materials 228 (2019) 116765. https://doi.org/https://doi.org/10.1016/j.conbuildmat.2019.116765.

Chapter 7 — The Potential of CeO_2-Mxene Catalyst for the Destruction of Ibuprofen

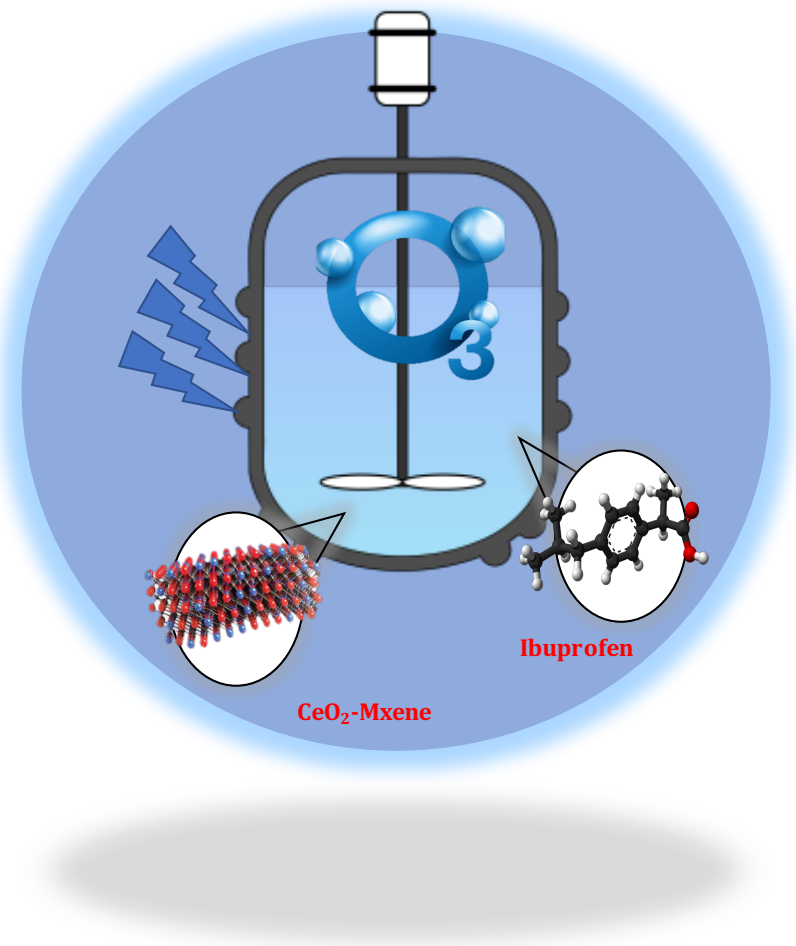

7.1. Introduction

Since the world population is increasing annually with an unsustainable rate, the rapid depletion of clean water sources on the planet is continuously increasing [1]. Therefore, the need of wastewater treatment is surely relevant as ever. Nowadays, more than 700 emerging contaminants (ECs) that are either synthetically or naturally produced are chaotically disposed in water bodies, resulting in the creation of recalcitrant wastewater containing hazardous contaminants. [2, 3]. These ECs include personal-care products, organic wastewater compounds, and pharmaceutically active compounds that can be harmful to both ecological and human health.

Ibuprofen, 2-(4-isobutylphenyl) propionic acid (IBU) is a well-known nonsteroidal anti-inflammatory drug that is widely detected in wastewaters, as reported in many investigations [4-6]. Thus, finding sustainable methods to treat contaminated water is one of the global priorities. Most of the existing advanced wastewater treatment options include physical separation of contaminants and biological oxidation, that are expensive technologies facing many operational challenges [7, 8]. Hence, integrating technologies such as ozonation and photodegradation alongside using non-conventional solids can be one of the sustainable and promising approaches for water purification [9].

Advanced oxidation processes (AOPs) are considered very promising for the abatement of a wide range of organic pollutants in wastewater [6]. AOPs include five main categories involving single and combined processes namely; photocatalysis (PC), ozonation (O_3), fenton, wet air oxidation (WAO), hydrogen peroxide (H_2O_2), and sonication. Coupled processes include PC/H_2O_2, PC/chlorine, O_3/H_2O_2, PC/O_3, etc [10]. The production of strongly oxidizing radicals is the fundamental principle behind AOPs [11]. Hybrid ozonation in wastewater treatment is considered a successful solution for the degradation, mineralization, and detoxification of different contaminants in wastewater effluents [11]. It also overcomes the drawbacks of the sole ozonation technology that includes the selective nature of ozone, limited mass transfer, slow reaction rates, and the expensive ozone generation due to high energy consumption [11, 12].

This chapter sheds the light on the potential of CeO_2-Mxene as a promising catalytic candidate in ozonation-photocatalytic hybrid system for the destruction of IBU.

7.2. Mxenes

Mxene, is a new class of 2D nanomaterials derived from a family of transition metal carbides, nitrides, and carbonitrides, has recently piqued interest in various fields [13]. Figure 7.1 shows Mxene precursors and their synthesis that consists of three types of mono-M MAX phases which include M_2AX, M_3AX_2, M_4AX_3 and the selective etching process of the Agroup layers and the possible elements in the Mxene phases [13]. Mxenes have gained tremendous interest since Drexel University academics discovered them in 2011 [14].

Mxenes represent a new and innovative solution for the elimination of emerging contaminants from wastewaters, offering a more effective and sustainable approach compared to traditional

methods [15, 16]. They have been widely employed in the fields of electronics, catalysis, environmental remediation, and energy storage because of these exceptional features [15, 17]. Their phenomenal characteristics involve very active sites and high specific surface areas, high metallic conductivity, environmentally friendly nature, high chemical stability, tunable surface chemistry, and superior sorption/reduction capacity [17].

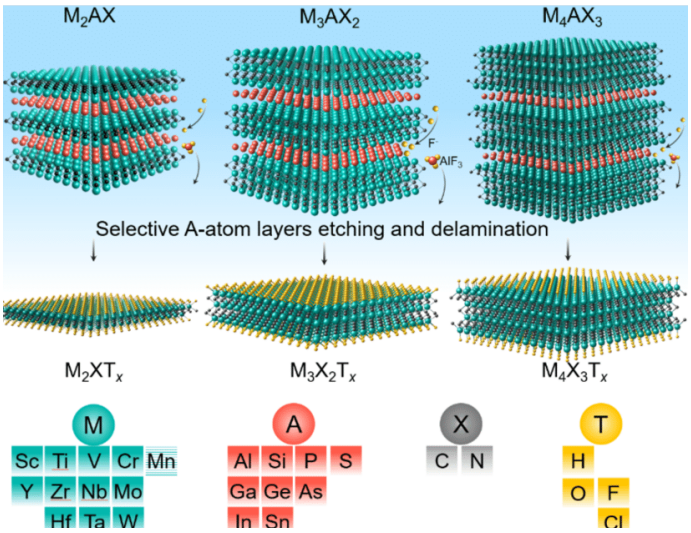

Figure 7.1 Mxene precursors and their synthesis [13].

The use of Mxenes in wastewater treatment has the potential to be applied to treat the effluenets of various industries and sectors such as pharmaceuticals and personal care products, textile industries, as well as heavy metals and other toxic pollutants removal [16]. Nonetheless, Mxenes frequently undergo degradation in an aqueous environment when molecular oxygen is present because of their low stability and hydrophilicity [16,18]. Thus, the versatility and the effectiveness of Mxenes by incorporating them in other material structures, make them promising compounds to treat the occurrence of emerging contaminants in wastewaters [18].

7.3. Synthesis and characterization of CeO_2-5%Mxene

CeO_2-Mxene composites were synthesized following the procedure of previous study [19] with some modifications as the HF solvent was replaced by a LiF/HCl solution [20] as illustrated in Figure 7.2. In brief, 1 g of the MAX phase powder (Ti_3AlC_2) was exfoliated using 0.67 g of LiF that was added to 10 ml of 9M HCl solution and. Five washing and decantation steps were conducted to maximize the purity of the collected Mxene. The collected powder was functionalized with CeO_2, following a hydrothermal route with a molar ratio CeO_2/5%Mxene [19]. Lastly, the collected powder was dried at room temperature overnight to be further characterized.

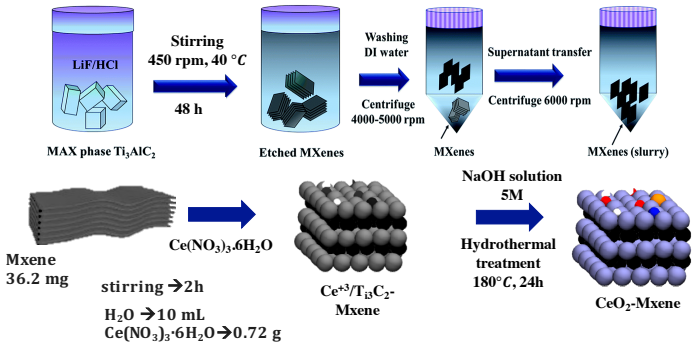

Figure 7.2 Synthesis of CeO_2-5%Mxene.

The characterization techniques included XRD analysis, which was performed using Malvern Panalytical Aeris benchtop X-ray diffractometer. Figure 7.3 confirms the formation of the CeO_2-Mxene composite, however, the Mxene peak at an angle of around 7.8º, is not visible due to the low molar ratio of Mxene in the structure which was 5%.

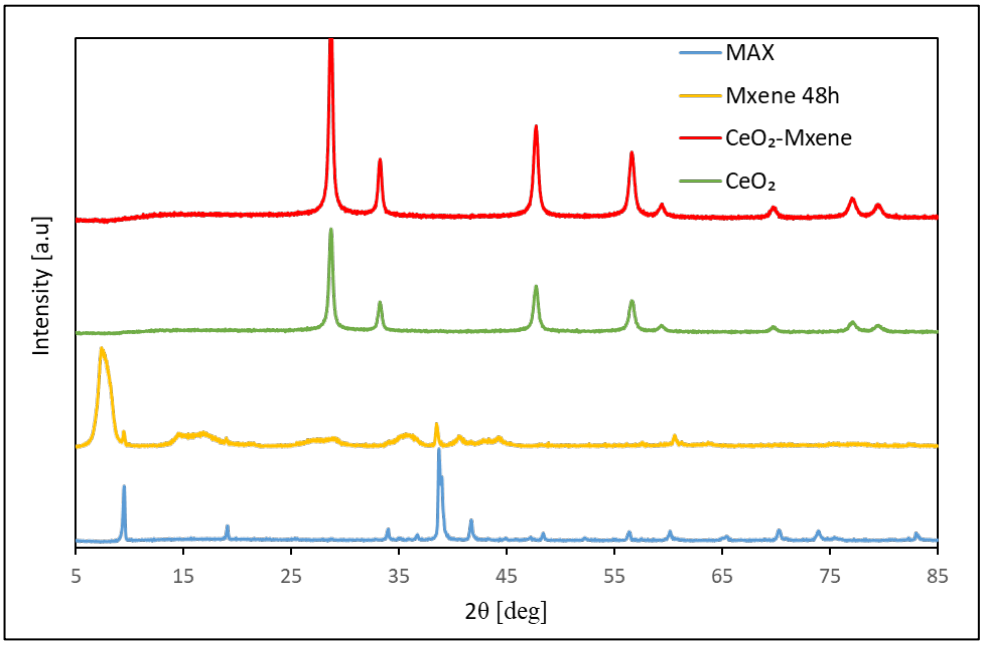

Figure 7.3 XRD spectra of Max, CeO_2, Mxene and CeO_2-Mxene composite.

The SEM images (SEM Zeiss Leo Gemini 1530) shown in Figure 7.4 confirm the sheet-like structure of Mxene and the CeO_2-Mxene composite. Moreover, the EDS analysis confirmed the presence of titanium in the surface scan performed for the CeO_2-Mxene composite (Figure 7.5). Nitrogen physisorption (Micromeritics 3 Flex 3500) was used to determine the Brunauer–Emmett–Teller (BET) surface areas of the synthesized compounds and the corresponding N_2 adsorption-desorption hysteresis isotherms as illustrated in Figure 7.6. It was found that the BET surface areas for the pure CeO_2, Mxene, CeO_2-Mxene composite were 49.6, 2.4, 14.2 m^2/g, respectively, showing reduction in CeO_2 surface area.

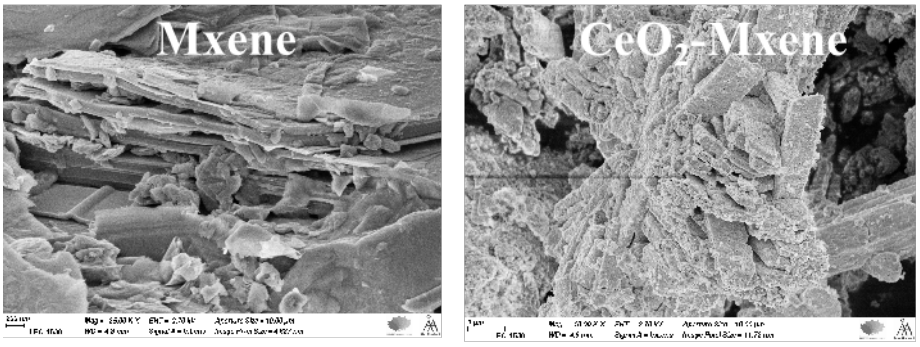

Figure 7.4 SEM images of Mxene and CeO_2-Mxene composite.

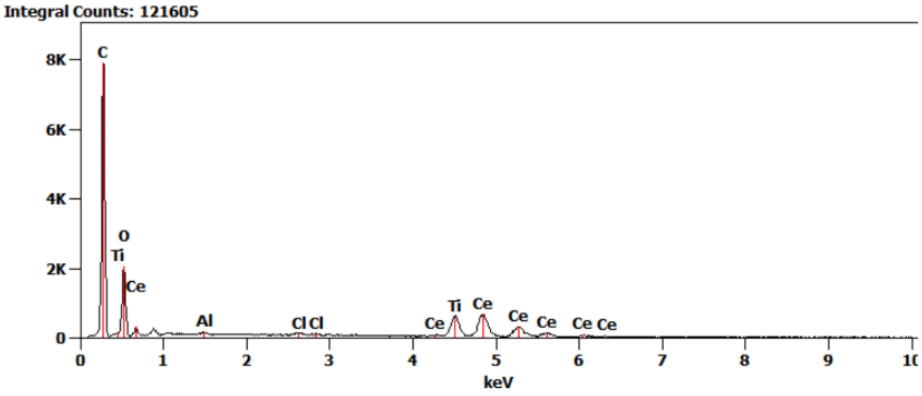

Figure 7.5 EDS scanning image of CeO_2-Mxene composite.

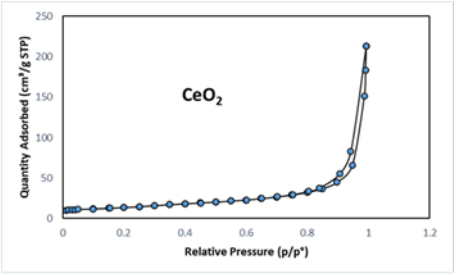

Component	BET surface area [m^2/g]
CeO_2	49.59 ± 0.34
Mxene	2.41 ± 0.01
CeO_2-Mxene	14.23 ± 0.28

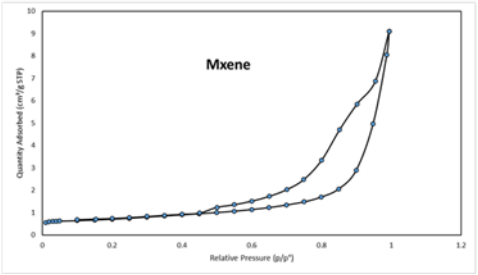

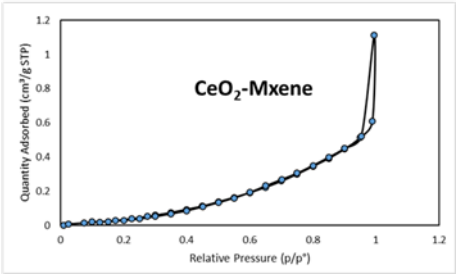

Figure 7.6 BET surface areas and adsorption-desorption isotherms.

Figures 7.8 and 7.9 show the UV-DRS spectra (Shimadzu UV-2501PC spectrophotometer) for the compounds and the absorption edge which is centered at around 410 nm for both CeO_2 and CeO_2-Mxene. The corresponding bandgap energies estimated using the Tauc model [21] were 2.53 and 2.34, respectively.

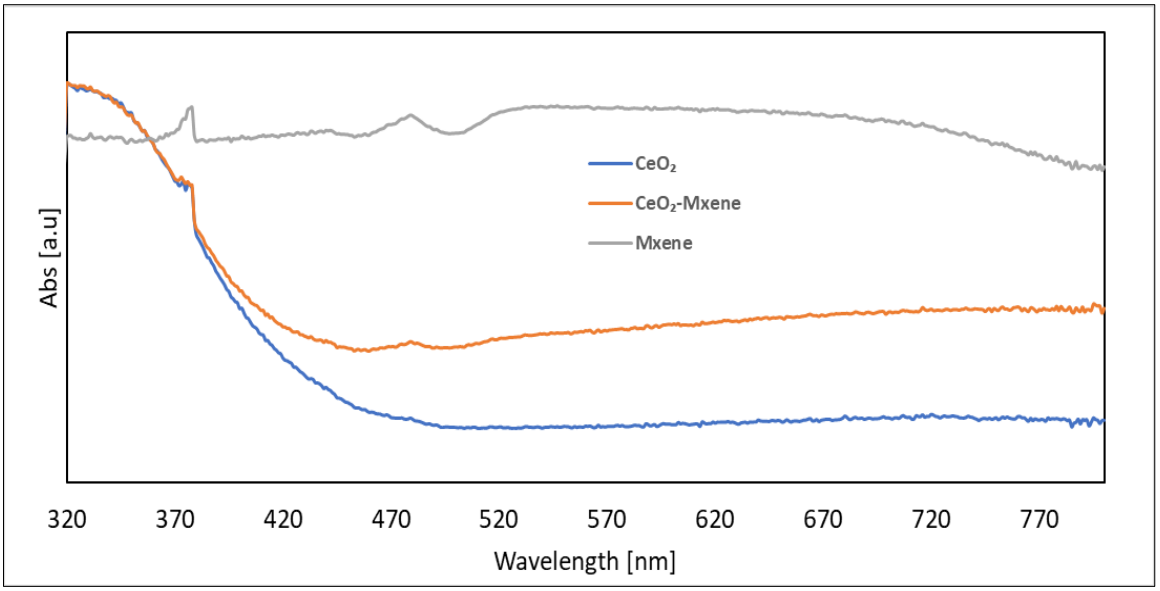

Figure 7.8 UV spectra of the CeO_2, Mxene, and CeO_2-Mxene.

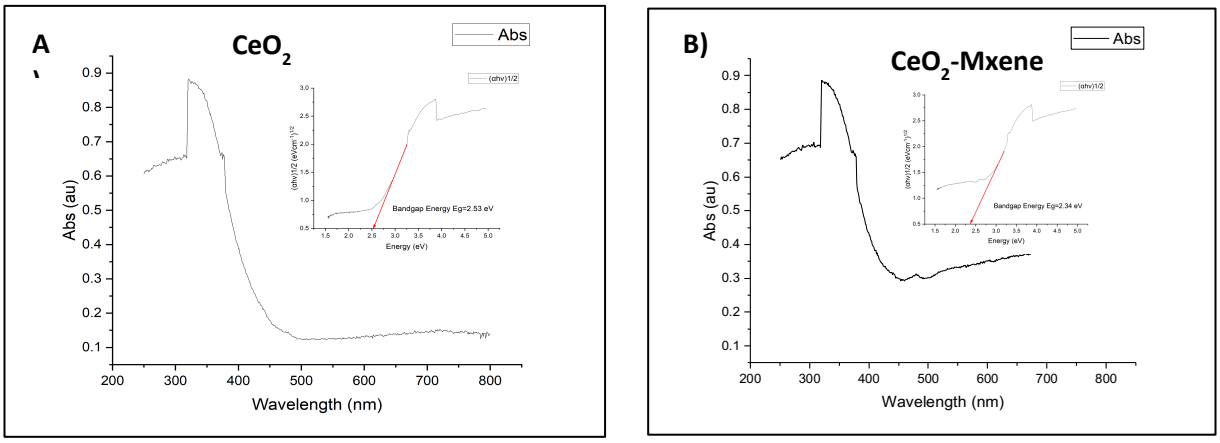

Figure 7.9 UV-DRS of the tested compounds. A) CeO_2 B) CeO_2-Mxene composite.

7.4. Semibatch destruction of IBU in a catalytic ozonation-photodegradation system

The catalytic ozonation-photodegradation experiments were conducted in a gas-liquid reactor system operating in semibatch mode. In this system, a double jacket glass reactor with a capacity of 1100 ml was connected to an ozone generator (Absolute Ozone, Nano model, Canada). UV-lamps of 125W and 6W were tested to check the performance of the system. However, the final screening experiments were performed with an UV-lamp of 6W for safety reasons. The reactor system is displayed in Figure 7.10.

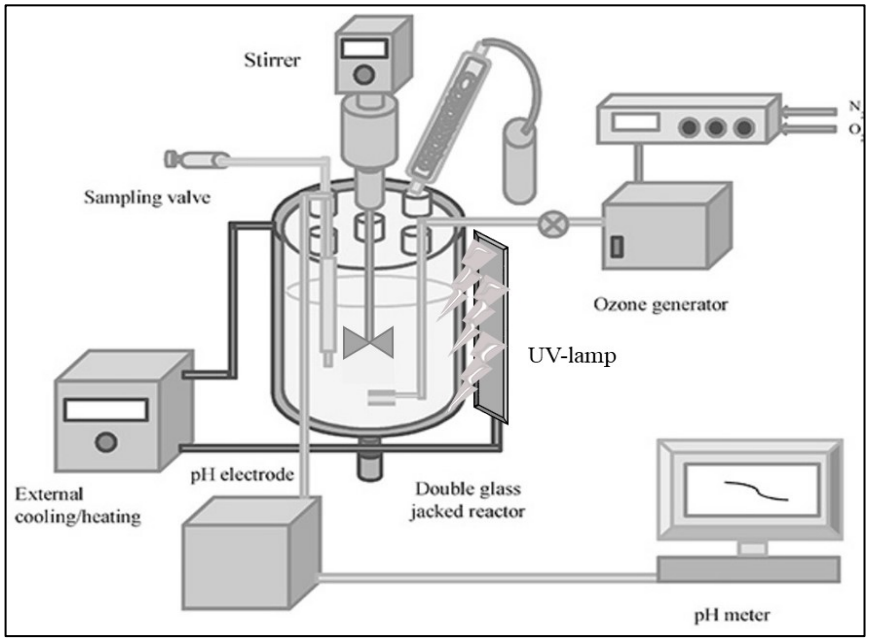

Figure 7.10 Schematic presentation of the hybrid ozonation-photodegradation set-up.

In the standard execution of the experiment, the IBU solution was prepared with the desired concentration and then loaded into the reactor vessel and stirred at the set value. The reactor was closed with the lid and connected to the thermostat, set at a pre-specified reaction temperature. pH-stat device (Metrohm Tiamo) was used to control the pH of the solution by adding a 1M sodium hydroxide solution. The ozone flow rate was adjusted with oxygen gas flow rate entering the ozone generator of 450 mL/min, which produces approximately a 60 mg/L concentration of ozone. At this point, the catalyst was loaded into the reactor. The reactor was shielded before the UV lamp to reduce the ray dispersion, thus avoiding any risk to the operator. A first sample was collected to measure the concentration of IBU (time = 0 sample). The reaction was started by switching on the lamp and the ozone generator was turned on 10 min before the lamp to allow the solution to be saturated with Ozone. Samples were periodically withdrawn to follow the reaction kinetics until a maximum time of 3 h. Each sample was centrifuged at 3000 rpm for 5 min and filtered using 0.20 µm filters. The resulting liquid sample was analyzed by Agilent 1100 HPLC system to detect the concentration of IBU and to construct the calibration curve (Eq 7.1 and Figure 7.11) which is valid in a concentration range between 0-0.1 mol/m^3. 50% w/w acetonitrile, 50% w/w water mobile phase were used in C18 column, the UV-Vis photo array detector was set at 222 nm, and the sample injection volume was 5 µL, with the retention time 20 min at 40 °C, and the flow rate 1.5 ml/min.

$$c_{IBU} = (0.0006X + 0.001)Abs, R^2 = 0.99 \quad (7.1)$$

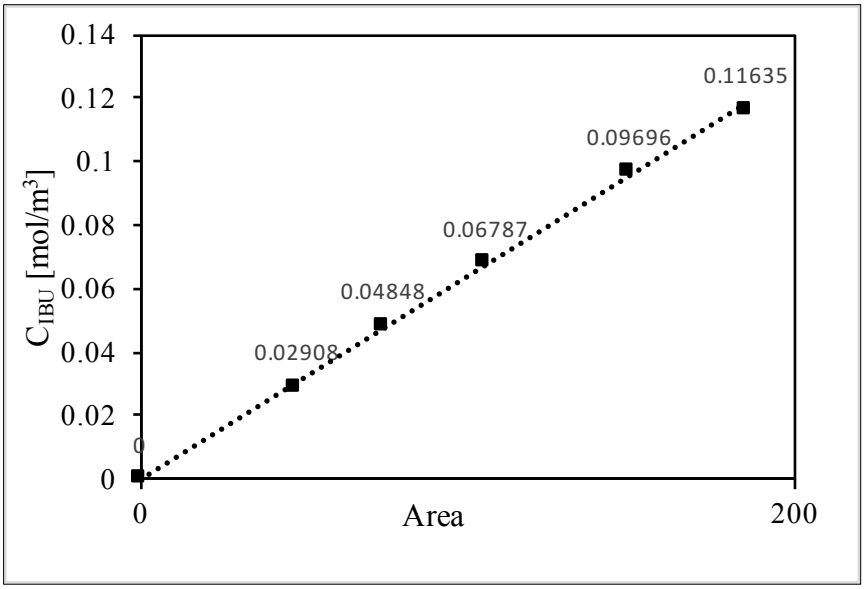

Figure 7.11 HPLC calibration curve for IBU.

Several experiments were conducted to verify the effectiveness of the hybrid ozonation-photodegradation setup. The main preliminary results of the destruction of IBU using the hybrid system are presented in Figure 7.12.

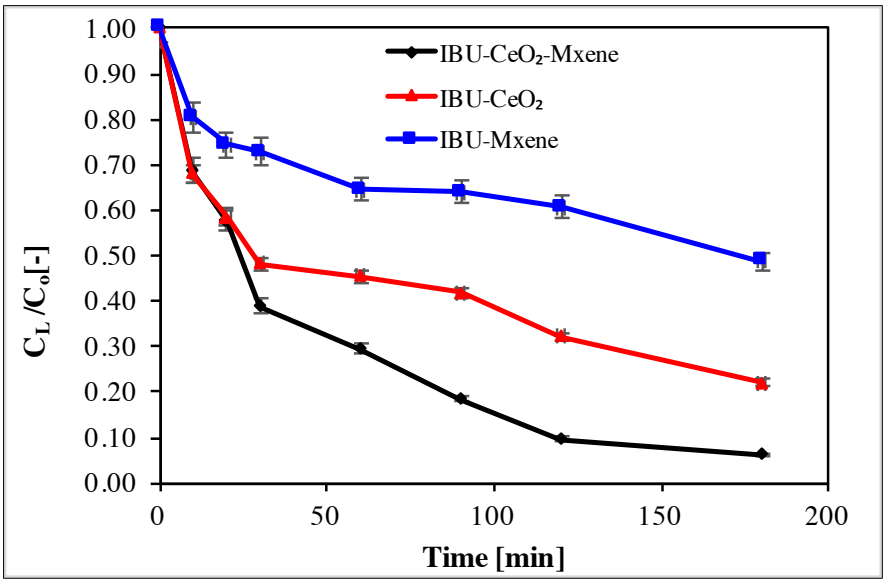

Figure 7.12 Destruction of IBU using the catalytic ozonation-photodegradation hybrid system.

It is evident that CeO_2-Mxene showed accelerated kinetics of IBU destruction in comparison with CeO_2 and Mxene compounds. This could be attributed to the formation of the Schottky junction when 5% Mxene incorporated in the CeO_2 structure as has been investigated by Shen et al, [19]. The inherent electric field might have been induced promoting the transfer of the electrons from CeO_2 to Mxene and repelling the holes from Mxene, resulting in the spatial separation of the electron-hole pairs [19]. However, further experiments are still needed to confirm this effect and explore the mineralization mechanism of the reaction using LC-MS

technique. Furthermore, the recyclability of CeO_2-Mxene composite, should be thoroughly investigated. Lastly, the CeO_2-Mxene composite should be tested in the system under visible light, because the Mxene conductivity can enhance the performance of CeO_2 under visible light.

7.5. Conclusions

In summary, the CeO_2-Mxene composite was fabricated via hydrothermal method and characterized to be tested in the catalytic ozonation-photocatalytic hybrid system for the destruction of IBU. The improved catalytic performance was attributed to the Schottky junction in the CeO_2-Mxene structure, which promoted the movement of the photoinduced electrons and hindered holes from approaching Mxene, resulting in the spatial separation of the electron-hole pairs. Further studies should focus on the by-products of the reaction and the corresponding mechanism using this hybrid system. The recyclability of CeO_2-Mxene should be investigated to confirm the stability of the catalyst for wastewater treatment. Additionally, the performance of the CeO_2-Mxene composite should be explored under visible light.

7.6. List of abbreviations

EC	emerging contaminant
IBU	ibuprofen
AOP	advanced oxidation processe
PC	photocatalysis
WAO	wet air oxidation
BET	Brunauer–Emmett–Teller

7.7. References

[1] A. Boretti, L. Rosa, Reassessing the projections of the World Water Development Report, npj Clean Water 2(1) (2019) 15. https://doi.org/10.1038/s41545-019-0039-9.
[2] L.B. Barber, 1.13 - Emerging Contaminants, in: S. Ahuja (Ed.), Comprehensive Water Quality and Purification, Elsevier, Waltham, 2014, pp. 245-266. https://doi.org/ https://doi.org/10.1016/B978-0-12-382182-9.00015-3.
[3] V. Geissen, H. Mol, E. Klumpp, G. Umlauf, M. Nadal, M. van der Ploeg, S.E.A.T.M. van de Zee, C.J. Ritsema, Emerging pollutants in the environment: A challenge for water resource management, International Soil and Water Conservation Research 3(1) (2015) 57-65. https://doi.org/https://doi.org/10.1016/j.iswcr.2015.03.002.
[4] S. Chopra, D. Kumar, Ibuprofen as an emerging organic contaminant in environment, distribution and remediation, Heliyon 6(6) (2020) e04087. https://doi.org/https://doi.org/ 10.1016/j.heliyon.2020.e04087.

[5] P. Iovino, S. Chianese, S. Canzano, M. Prisciandaro, D. Musmarra, Ibuprofen photodegradation in aqueous solutions, Environmental Science and Pollution Research 23(22) (2016) 22993-23004. https://doi.org/10.1007/s11356-016-7339-0.
[6] E. Brillas, A critical review on ibuprofen removal from synthetic waters, natural waters, and real wastewaters by advanced oxidation processes, Chemosphere 286 (2022) 131849. https://doi.org/https://doi.org/10.1016/j.chemosphere.2021.131849.
[7] A. Nqombolo, A. Mpupa, R.M. Moutloali, P.N. Nomngongo, Wastewater treatment using membrane technology, Wastewater and water quality 29 (2018).
[8] R. Raj, A. Tripathi, S. Das, M.M. Ghangrekar, Removal of caffeine from wastewater using electrochemical advanced oxidation process: A mini review, Case Studies in Chemical and Environmental Engineering 4 (2021) 100129. https://doi.org/https://doi.org/10.1016/j.cscee.2021.100129.
[9] I. Ortiz, M.J. Rivero, M. Margallo, Chapter 6 - Advanced oxidative and catalytic processes, in: C.M. Galanakis, E. Agrafioti (Eds.), Sustainable Water and Wastewater Processing, Elsevier2019, pp. 161-201. https://doi.org/https://doi.org/10.1016/B978-0-12-816170-8.00006-5.
[10] T. Manasfi, Chapter Four - Ozonation in drinking water treatment: an overview of general and practical aspects, mechanisms, kinetics, and byproduct formation, in: T. Manasfi, J.-L. Boudenne (Eds.), Comprehensive Analytical Chemistry, Elsevier2021, pp. 85-116. https://doi.org/https://doi.org/10.1016/bs.coac.2021.02.003.
[11] S.N. Malik, P.C. Ghosh, A.N. Vaidya, S.N. Mudliar, Hybrid ozonation process for industrial wastewater treatment: Principles and applications: A review, Journal of Water Process Engineering 35 (2020) 101193. https://doi.org/https://doi.org/10.1016/j.jwpe.2020.101193.
[12] J. Wang, H. Chen, Catalytic ozonation for water and wastewater treatment: Recent advances and perspective, Science of The Total Environment 704 (2020) 135249. https://doi.org/https://doi.org/10.1016/j.scitotenv.2019.135249.
[13] B. Anasori, W. Hong, S.K. Nemani, B.C. Wyatt, Double transition-metal MXenes: Atomistic design of two-dimensional carbides and nitrides, MRS Bulletin 45(10) (2020) 850-861. https://doi.org/10.1557/mrs.2020.251.
[14] M. Naguib, M. Kurtoglu, V. Presser, J. Lu, J. Niu, M. Heon, L. Hultman, Y. Gogotsi, M.W. Barsoum, Two-Dimensional Nanocrystals Produced by Exfoliation of Ti_3AlC_2, Advanced Materials 23(37) (2011) 4248-4253. https://doi.org/https://doi.org/10.1002/adma.201102306.
[15] L. Damptey, B.N. Jaato, C.S. Ribeiro, S. Varagnolo, N.P. Power, V. Selvaraj, D. Dodoo-Arhin, R.V. Kumar, S.P. Sreenilayam, D. Brabazon, V. Kumar Thakur, S. Krishnamurthy, Surface Functionalized MXenes for Wastewater Treatment—A Comprehensive Review, Global Challenges 6(6) (2022) 2100120. https://doi.org/https://doi.org/10.1002/gch2.202100120.
[16] M. Tawalbeh, S. Mohammed, A. Al-Othman, M. Yusuf, M. Mofijur, H. Kamyab, MXenes and MXene-based materials for removal of pharmaceutical compounds from wastewater: Critical review, Environmental Research 228 (2023) 115919. https://doi.org/https://doi.org/10.1016/j.envres.2023.115919.

[17] I. Ihsanullah, M. Bilal, M. Sajid, A.W. Mohammad, M.A. Atieh, N. Ghaffour, Emerging MXenes: Revolutionizing oily wastewater treatment - a comprehensive and critical review, Separation and Purification Technology 329 (2024) 125181. https://doi.org/https://doi.org/10.1016/j.seppur.2023.125181.
[18] T. Rasheed, F. Kausar, K. Rizwan, M. Adeel, F. Sher, N. Alwadai, F.H. Alshammari, Two dimensional MXenes as emerging paradigm for adsorptive removal of toxic metallic pollutants from wastewater, Chemosphere 287 (2022) 132319. https://doi.org/https://doi.org/10.1016/j.chemosphere.2021.132319.
[19] J. Shen, J. Shen, W. Zhang, X. Yu, H. Tang, M. Zhang, Zulfiqar, Q. Liu, Built-in electric field induced CeO_2/Ti_3C_2-MXene Schottky-junction for coupled photocatalytic tetracycline degradation and CO_2 reduction, Ceramics International 45(18, Part A) (2019) 24146-24153. https://doi.org/https://doi.org/10.1016/j.ceramint.2019.08.123.
[20] T. Zhang, L. Pan, H. Tang, F. Du, Y. Guo, T. Qiu, J. Yang, Synthesis of two-dimensional $Ti_3C_2T_x$ MXene using HCl+LiF etchant: Enhanced exfoliation and delamination, Journal of Alloys and Compounds 695 (2017) 818-826. https://doi.org/https://doi.org/10.1016/j.jallcom.2016.10.127.
[21] P. Makuła, M. Pacia, W. Macyk, How To Correctly Determine the Band Gap Energy of Modified Semiconductor Photocatalysts Based on UV–Vis Spectra, The Journal of Physical Chemistry Letters 9(23) (2018) 6814-6817. https://doi.org/10.1021/acs.jpclett.8b02892.

Chapter 8 — Conclusions and Future Remarks

"You cannot hope to build a better world without improving the individuals. To that end, each of us must work for his own improvement and, at the same time, share a general responsibility for all humanity, our particular duty being to aid those to whom we think we can be most useful."

Marie Skłodowska Curie

8.1 Conclusions

Water plays a pivotal role in promoting the sustainability and advancing the socio-economic progress, energy generation, food cultivation, maintaining thriving ecosystems, and ensuring human survival. Moreover, it functions as a crucial element in adapting to climate change, acting as the vital connection between the human society and the natural environment. Consequently, it is incontrovertibly evident that there is an urgent global imperative to formulate immediate strategies and initiatives aimed at preserving our water resources. Hence, the principal objective of this research was to assess the effectiveness of newly developed materials, created in-house, for the removal of emerging contaminants specifically, ibuprofen, bromocresol green, alizarin red S, and methylene blue from wastewaters. Adsorption and photodegradation technologies in both batch and semibatch reactors were investigated. Additionally, the study included an evaluation of the performance of conventional commercial materials i.e. activated carbon and metal oxides. It can be deduced that adsorption and photodegradation represent highly promising technologies for wastewater treatment. Nevertheless, further research should be performed to delve into and enhance the performance of several new innovative materials used for this purpose. For example, the structure of certain categories of MOFs can be stabilized in aqueous solutions, thereby optimizing their performance in water purification applications. The models applied to understand the diffusion mechanism of the contaminant were elucidating. Nonetheless, designing and testing adsorption columns are essential steps, necessitating experimentation in the presence of diverse organic and inorganic compounds to replicate real-world scenarios. It is anticipated that the current results and models applied using the different semiconductors for photodegradation experiments in this work, will open doors for possible future applications of these nanoparticles in continuous processes for wastewater treatment.

8.2 Future remarks

The following points present some guidelines for future work;

- Investigate the impact of additional substances that might interfere with both adsorption processes and photodegradation reactions.
- Enhance the stability of MOFs in aqueous solutions through ligand and metal anode selection, post synthetic alterations, and protective encapsulation.
- Validate the models by comparing their effectiveness in describing the removal of other emerging contaminates from wastewaters.
- Explore the potential of new materials such as Mxene-based compounds for the removal of ibuprofen from wastewater and compare the performance with studied compounds.
- Assess the environmental safety of the investigated materials in terms of their biological toxicity when used for removing emerging contaminants, ensuring that they are environmentally benign.
- Conduct feasibility and techno-economic assessments for the various studied materials to evaluate their cost-effectiveness when employed in large-scale wastewater treatment facilities.

Publications

Publication I

frontiers in Chemical Engineering

MINI REVIEW
published: 23 October 2020
doi: 10.3389/fceng.2020.581487

Applications of Metal Organic Frameworks in Wastewater Treatment: A Review on Adsorption and Photodegradation

Vincenzo Russo[1], *Maryam Hmoudah*[1,2], *Francesco Broccoli*[1], *Maria Rosaria Iesce*[1], *Ok-Sang Jung*[3] *and Martino Di Serio*[1]*

[1] Department of Chemical Sciences, University of Naples Federico II, Naples, Italy, [2] Chemical Engineering Department, An-Najah National University, Nablus, Palestine, [3] Department of Chemistry, Pusan National University, Busan, South Korea

The growing accumulation of emerging contaminants in the environment can cause direct and indirect water pollution that puts human lives at risk. The fact that these contaminants are not or cannot be eliminated from the municipal water utilities, poses a significant concern. Researchers are currently pulling massive attention to improve existing technologies, develop new strategies, and provide environmentally durable solutions to mitigate water contamination problems. Adsorption and photodegradation are two of the most sustainable technologies that are used in water purification. These technologies have many advantages because of the economic, simple, and easily operated designs needed to treat wastewater. Within these applications, metal organic frameworks (MOFs) are playing a significant role as novel class of porous materials characterized by a crystalline structure. MOFs are considered good candidates to be employed in wastewater treatment technologies because of the tunability of their features. The scope of this review article is to provide a comprehensive description of the recent studies published in the literature about the adsorptive and photocatalytic use of MOFs for the removal of organic emerging contaminants from wastewater. Furthermore, this study briefly highlights the synthesis technologies of MOFs. Finally, future perspective and challenges associated with MOF large-scale production are discussed.

Keywords: metal organic frameworks, MOFs, emerging contaminants, adsorption, photodegradation, wastewater treament

OPEN ACCESS

Edited by:
Ali Reza Oveisi,
Zabol University, Iran

Reviewed by:
Sarah Farrukh,
National University of Sciences and Technology (NUST), Pakistan
Amarajothi Dhakshinamoorthy,
Madurai Kamaraj University, India

***Correspondence:**
Martino Di Serio
diserio@unina.it

Specialty section:
This article was submitted to Catalytic Engineering, a section of the journal Frontiers in Chemical Engineering

Received: *08 July 2020*
Accepted: *24 September 2020*
Published: *23 October 2020*

Citation:
Russo V, Hmoudah M, Broccoli F, Iesce MR, Jung O-S and Di Serio M (2020) Applications of Metal Organic Frameworks in Wastewater Treatment: A Review on Adsorption and Photodegradation. Front. Chem. Eng. 2:581487. doi: 10.3389/fceng.2020.581487

INTRODUCTION

In the last few decades, much attention has been devoted to emerging contaminants (ECs), a new class of water pollutants, including natural and synthetic chemicals and their transformation products, e.g., personal care products, pharmaceutical compounds, and endocrine-disrupting products. The presence of these ECs in wastewater is considered an environmental issue due to the consequent verified toxicity for water ecosystems and health (Rodriguez-Narvaez et al., 2017). On the other hand, these products are not commonly monitored in the environment (Tran et al., 2018). Other emerging contaminants in the environment are nanomaterials, perfluorinated compounds, pesticides, industrial chemicals, surfactants, flame retardants, disinfection byproducts (DBPs), artificial sweeteners (Richardson and Kimura, 2017), etc. These contaminants come from

many different sources, such as industrial, municipal, and hospital wastewater treatment plants (WWTP), sewer leakage, landfill leachate, etc. (Rasheed et al., 2019). Typical wastewater treatment processes do not adequately remove ECs (Ryu et al., 2014; Tran et al., 2018). Although their concentration in the environment is low, ranging from ng/L to μg/L, these compounds are pseudo-persistent due to their continuous discharge (Fairbairn et al., 2018). This creates the risk of chronic exposure for living organisms, especially due to pharmaceuticals. The adverse effects of the interaction of ECs with living organisms include alteration of animal endocrine systems, reduced fertility and fecundity, and masculinization of females and feminization of males (Ruhí et al., 2016). Moreover, continuous discharge of antimicrobial agents and antibiotics can lead to the development of antibiotic-resistant bacteria, thus, reducing the effectiveness of these compounds against pathogens (Rodriguez-Narvaez et al., 2017). Richardson and Ternes investigated in their biennial review the recent developments and the current issues about ECs (Richardson and Ternes, 2018). They highlighted the presence, analysis, and the fate of different ECs in the environment. In addition, they presented the acceptable levels of ECs in water that are regulated by the World Health Organization (WHO) for water quality (Dhakshinamoorthy et al., 2019).

Water treatment technologies can be divided into biological treatment, phase changing, and advanced oxidation processes (Cheremisinoff, 2007). The most common technologies for biological treatment of waste waters involve the use of activated sludge in aerobic or anaerobic conditions; phase-changing processes are based on the sorption of the contaminant from the aqueous phase to the surface of a porous solid material (adsorbent); advanced oxidation processes (AOPs) are based on *in situ* formation of non-selective, highly oxidizing radicals to degrade the contaminant molecules. Investigation and development of water treatment technologies, which are effective for the abatement of this class of contaminants, are imperative to ensure the use of safe water and reduce environmental damage (Crini and Lichtfouse, 2019). Research is very active in the development and performance improvement of new nanomaterials, which could be employed as nanosorbcats (El-Qanni, 2017).

In the last two decades, attention has been drawn to an innovative class of porous materials, known as metal organic frameworks (MOFs). These compounds have been first synthesized by Yaghi et al. (1995) and investigated for numerous applications in wastewater treatment (Hasan et al., 2012; Seo et al., 2016; Wu et al., 2016; Akpinar and Yazaydin, 2017; Martinez-Costa et al., 2018; Daliran et al., 2020; Hu et al., 2020), gas purification (Trickett et al., 2017), light capture and energy conversion (Kreno et al., 2012), separation processes (Yaghi et al., 2019), drug delivery (Rojas et al., 2019), and catalysis (Dhakshinamoorthy et al., 2019; Yang and Gates, 2019; Wang Z. et al., 2020). The structure of MOFs consists of metal centers and organic linkers to form infinite crystalline networks (Butova et al., 2016; Yang and Gates, 2019). These organic and inorganic hybrid structures can be categorized into metal carboxylate frameworks, metal azolate frameworks, and MOFs, including hydrophobic functionalities. These compounds are characterized by a crystalline structure with a great flexibility in pore size, pore shape, functionality, thermal stability, and high surface area (Eddaoudi et al., 2000; Farha et al., 2012; Han et al., 2016). Such features grant their versatility in sustainable removal of various contaminants (Hasan and Jhung, 2015).

Several reviews summarized the different applications of MOFs in wastewater purification (Furukawa et al., 2013; Dhakshinamoorthy et al., 2018; Kumar et al., 2018; Mon et al., 2018; Bedia et al., 2019; Rego et al., 2020; Wang Q. et al., 2020). However, MOF real industrial applications were not thoroughly investigated and assessed (Kumar et al., 2018). These structures pose some drawbacks that can be critical in the industrial utilization in water treatment, i.e., the intrinsic instability could limit the practical performance of MOF as they may collapse in aqueous environments (Rego et al., 2020).

The main focus of this study is to review the most recent technologies in employing MOFs for the adsorptive and photocatalytic removal of emerging contaminants in wastewater streams. This is achieved by identifying the actual gaps and the state-of-the-art trends in the scientific literature in this promising research field.

ABATEMENT TECHNIQUES

Many different processes are reported recently for the abatement of ECs as shown in **Figure 1**. These effective technologies are (1) advanced oxidation processes, (2) phase-changing processes including adsorption in different solid matrices and membrane processes, and (3) biological treatment.

The main features of the mentioned technologies are listed below, as an example for ibuprofen removal.

- Biological Filtration: water containing low levels of ibuprofen were treated with a biologically active granular activated carbon (GAC) filter unit, managing to reduce the concentration to below the limits of quantification (< 1 ng/L) (Vieno et al., 2007).
- Membrane separation: this kind of process has been proven to be effective in eliminating ibuprofen from water sources. Removal rates ranged between 92 and 99% using nanofilter (NF) and reverse osmosis (RO) membranes with different hydrodynamic ratios and starting ibuprofen concentrations (Xu et al., 2005).
- Ozonation: one bench-scale study conducted on various sources of wastewater found that the ibuprofen removal rate ranged from 40 to 77%, varying as a function of organic carbon concentration and pH (Nakada et al., 2007). Two other bench-scale studies gave very different results, one reported an average of 80% removal for four spiked surface waters (ozone concentration range: 2.5–4 mg/L) (Huber et al., 2003), and another one reported 12% removal in distilled water spiked with ibuprofen (ozone concentration: 1 mg/L) (Westerhoff et al., 2005). Results from another study about contaminated surface water treatment using a pilot-scale system showed an ibuprofen removal efficiency $> 89\%$ (Vieno et al., 2007).

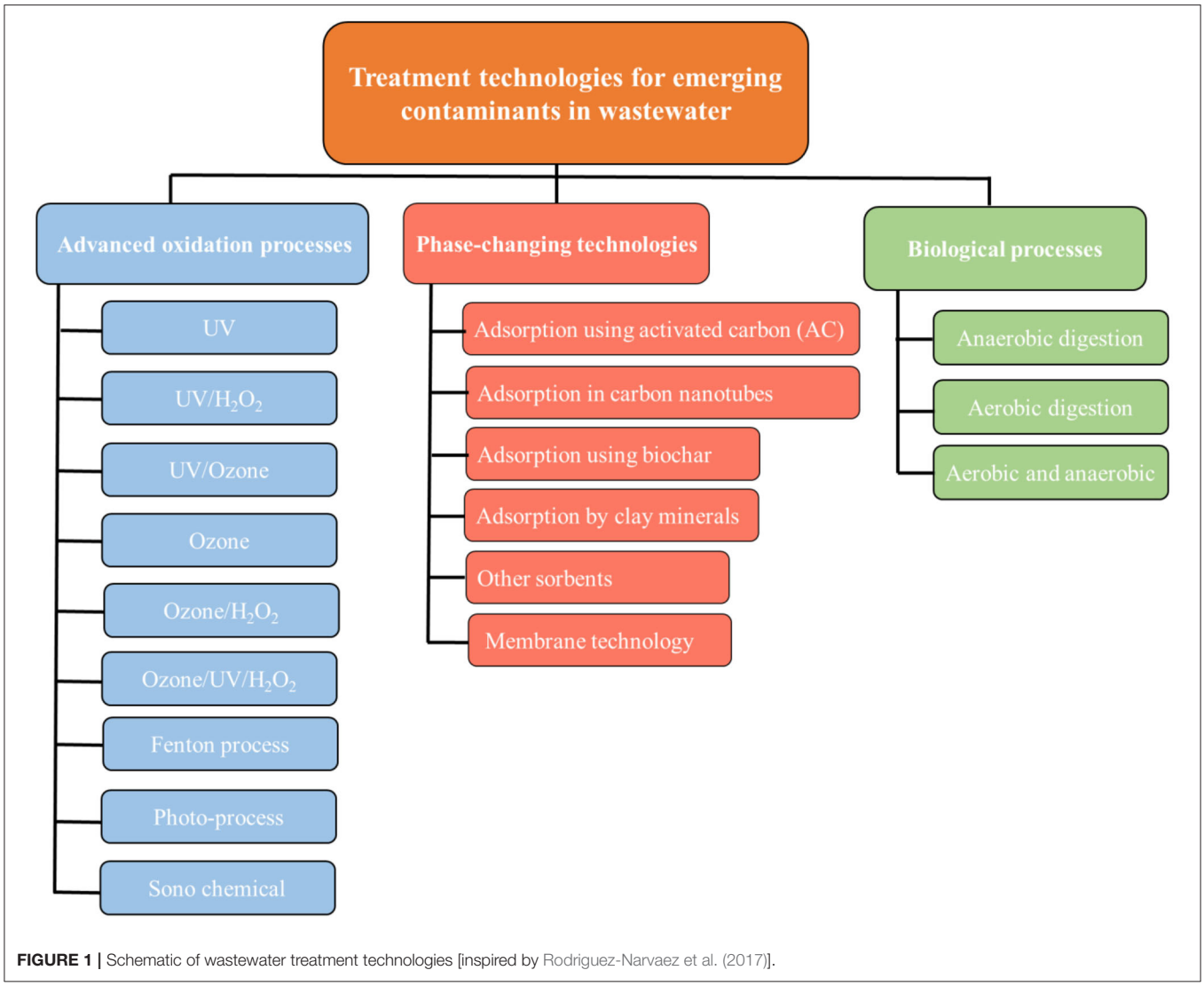

FIGURE 1 | Schematic of wastewater treatment technologies [inspired by Rodriguez-Narvaez et al. (2017)].

- Adsorption: removal of ibuprofen with powdered activated carbon (PAC) was reported to increase with PAC concentration. In one bench-scale study it was found that the ibuprofen removal rates ranged between 2 and 80% with varying PAC concentrations in the 1–20-mg/L range (Westerhoff et al., 2005).
- Ultraviolet (UV) radiation with an intensity designed to simulate solar irradiation was reported to cause a range of 62–67% ibuprofen photodegradation in various source waters spiked with high contaminant concentrations (10–40 mg/L) (Mohamed et al., 2018).

ADSORPTION

Adsorption is a natural phenomenon where one or more components of a fluid mixture are transferred on the surface of a solid material by physical or chemical interaction, bringing to a concentration variation compared to the adjacent phases (Russo et al., 2016, 2017). Adsorption processes are commonly employed in industrial environment for both compound separation and wastewater treatment. This technology is characterized by many attractive features, including cost effectiveness, ease of design and operation, and resistance to toxic substances. The key point of the cost analysis for adsorption technique is the cost of the employed adsorbent (Russo et al., 2016). Since the extent of adsorption greatly depends on the surface area of the adsorbent, small particles characterized by high porosity are required for industrial applications. **Figure 2** demonstrates the typical mechanism of adsorption where the sorbate molecules covers the solid to form a film on the surface of the adsorbent (Lowell et al., 2004).

Good mechanical properties such as abrasion resistance are also needed for the adsorbent to be effectively used for a great number of times (Tareq et al., 2019). There are many types of adsorbents for great number of different applications. The most commonly employed adsorbents include silica, polymers, activated alumina, activated carbon, zeolites, and clay, etc.

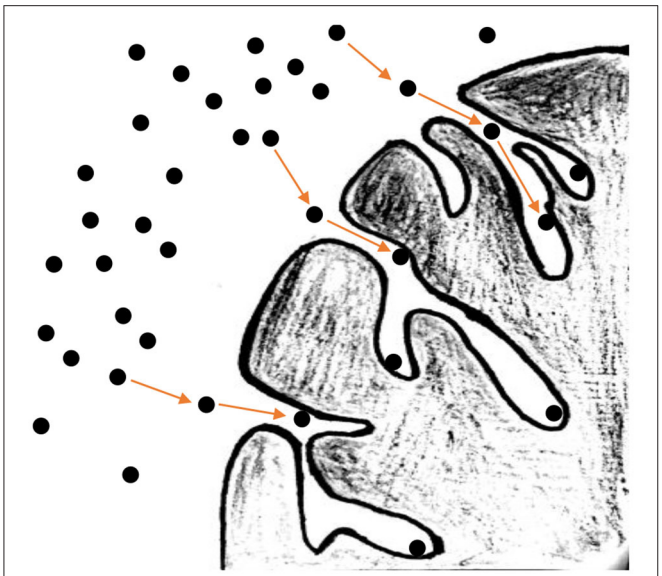

FIGURE 2 | Adsorption process schematization.

PHOTOCATALYTIC DECOMPOSIION

Advanced oxidation processes (AOPs) are a special class of wastewater treatment technologies aiming at the conversion of the pollutants to water, CO_2, and inorganic substances (by mineralization). When not feasible, their conversion to smaller and harmless products is preferred. Their potential to degrade stable and bio-refractory compounds under ambient conditions makes them prominent in the field of water purification research (Gogate and Pandit, 2004). The denomination AOP comprises a large variety of different technologies, all of which involve the generation of hydroxyl radicals (OH), which rapidly attack most organic species. The powerful, non-selective oxidative action makes AOPs suitable for the degradation of complex mixtures containing many different species (Ameta and Ameta, 2018).

Within AOPs, heterogeneous photodegradation is an interesting option for wastewater treatment compared to homogeneous processes, since the catalyst can be separated from the reaction media, and hence reused, leading to a reduction in costs and environmental issues (Poyatos et al., 2010). AOPs can be conducted either in gas or liquid phase, the latter both in aqueous and organic solutions. The process consists of five elementary steps:

1. Migration of the reactant from the liquid bulk phase to the photocatalyst surface;
2. Adsorption;
3. Surface reaction;
4. Desorption of the products;
5. Transfer of the products to the liquid bulk phase.

The catalyst is activated by photonic irradiation instead of thermal means, as it occurs with conventional heterogeneous catalysis. Heterogeneous photocatalysts are typically semiconductors (SCs) either sulfides (e.g., ZnS and CdS) or oxides (e.g., TiO_2, ZrO_2, CeO_2, and ZnO). These materials are characterized by a specific value of energy gap between conduction and valence band. A photocatalytic reaction is initiated when the catalyst absorbs a photon whose energy, $h\nu$, is greater than the band-gap, thus triggering a photoexcitation process. In this process, an electron (e^-) is promoted from the valence band of the catalyst to its conduction band, leaving an electron hole in the valence band (h^+). At this point, electron transfer takes place from solid surface to the adsorbed acceptor (A) molecules and from the adsorbed donor (D) molecules to the solid:

$$\text{Photoexcitation}: SC \xrightarrow{h\nu} e^{-\circ} + {}^{\circ}h^{+}$$
$$\text{Reduction of acceptor}: (A)_{ads}{}^{\circ} + {}^{\circ}e^{-} \rightarrow A^{-}$$
$$\text{Oxidation of donor}: (D)_{ads}{}^{\circ} + {}^{\circ}h^{+} \rightarrow D^{+}$$

Each ion resulting from this mechanism reacts, forming first intermediates, then final oxidation products. **Figure 3** is a sketch of the AOP process.

Photoelectric energy dispersion occurs due to the electron–hole recombination:

$$e^{-} + h^{+} \rightarrow N + E$$

where E is the energy released in the form of heat or light ($h\nu'^{\circ} \leq^{\circ} h\nu$), and N is the neutral center resulting in a reduction of the photoexcitation process efficiency (Herrmann, 2000).

The efficiency of the photodegradation reactions generally depends upon the following operational parameters:

- Irradiation intensity

The photocatalytic reaction rate depends mainly on the quantity of photons absorbed by the photocatalyst (Curcó et al., 2002). Consequently, by increasing the light intensity, a corresponding increase in the rate of the reaction is observed.

- Structure and concentration of the substrate

These parameters influence the tendency of the substrate to adhere to the catalyst surface with higher adhesion results in a greater effectiveness of the oxidation process (Tariq et al., 2007). However, if the substrate concentration is too high, the catalyst surface becomes saturated, thus leading to a reduction of photonic efficiency and deactivation (Araña et al., 2004).

- Nature and morphology of the photocatalyst

These parameters influence the quantity of photons absorbed by the catalyst. Photocatalysts characterized by small particle size lead to higher conversion in photodecomposition of organic compounds than those with large particles (Maira et al., 2001).

- Photocatalyst concentration

The rate of heterogeneous photocatalytic reactions increases with catalyst concentration until a maximum. Further addition of catalyst causes an unwanted light scattering, hence, a decrease in the penetration of the light into the reacting solution, thus resulting in a reduction in the reaction rate

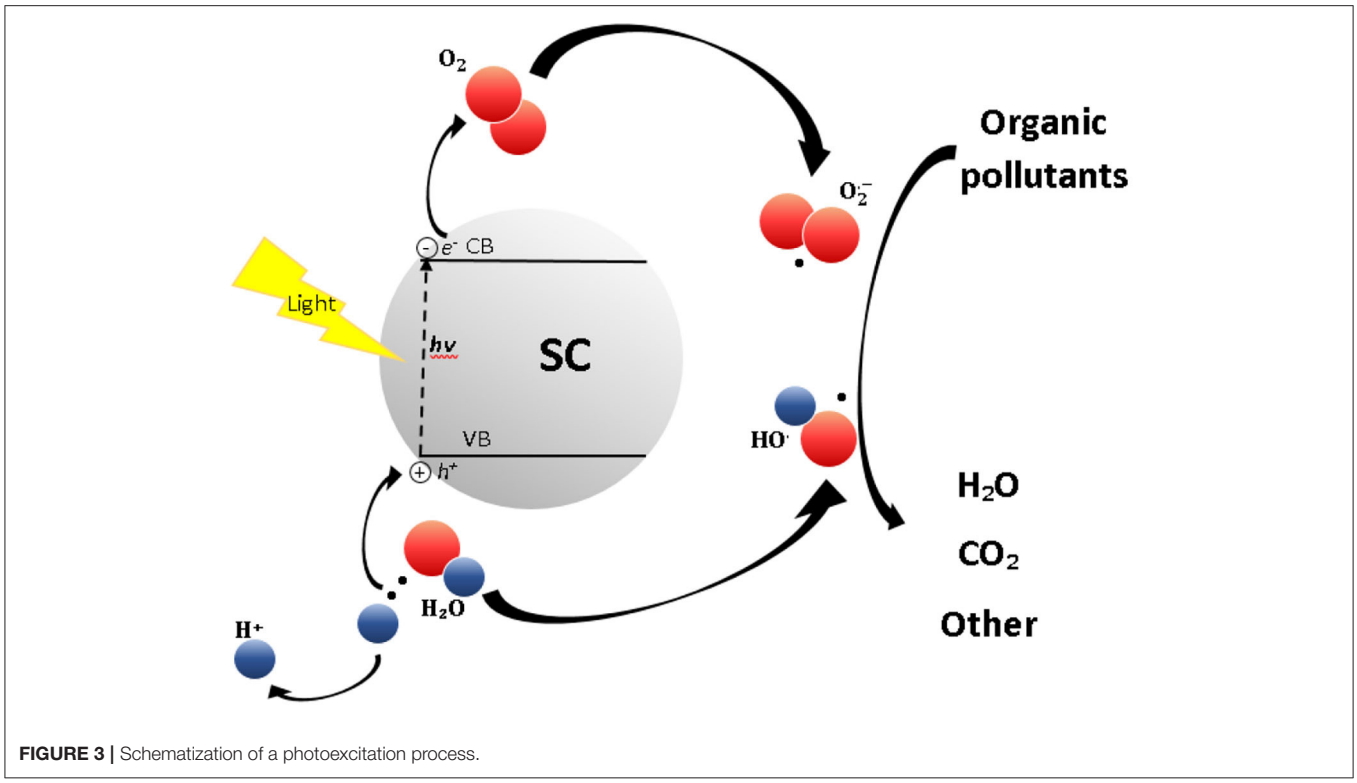

FIGURE 3 | Schematization of a photoexcitation process.

(Chun et al., 2000). This makes it necessary to determine the optimum catalyst concentration, to maximize the catalyst light absorption.

- Solution pH

The pH of the solution imposes properties of the surface, its charge, and, hence, the kind of aggregates that can be formed on the catalyst surface. This fact clearly influences substrate adhesion and ultimately reaction rate (Haque and Muneer, 2007).

- Temperature of the reaction

Photocatalytic systems do not require heating and work at room temperature, as the catalysts are activated by light. Heating enhances the reaction kinetics, occurring at generally a temperature range of $20°C \leq T \leq 80°C$. Above 80°C, the adsorption of the reactants becomes disfavored, being an exothermic process, becoming the rate-limiting step of the reaction network (Alnaizy and Akgerman, 2000). At lower temperatures ($-40°C \leq T \leq 0°C$), the activity decreases, since the rate-limiting step is the desorption of the final products (Herrmann, 2000).

For industrial applications, heterogeneous photocatalysts should be characterized by a series of characteristics, such as activity, long-term stability at high reaction conditions, poisoning resistance, attrition resistance, mechanical stability, and chemical stability. The pretreatment of the catalyst, such as calcination, sulfurization, or reduction, can influence the final activity, and/or stability of the catalyst.

METAL ORGANIC FRAMEWORKS

Metal organic frameworks (MOFs) are coordination polymers consisting of inorganic–organic hybrid frameworks showing high porosity. Their structures are composed of metal centers as connectors and organic ligands as linkers (Eddaoudi et al., 2000; Cheng et al., 2020). **Figure 4A** represents the MOF basic structure with organic linkers and the metal ions, and **Figure 4B** gives examples on the different MOFs with their corresponding metallic clusters and organic linkers (Howarth et al., 2017). The most common structures of MOFs (Qiu et al., 2014) are shown in **Figure 4C**.

MOFs are characterized by large pore surface area, with micro- and mesopores, and very high designability of pore shape, pore size, and surface functionality (Butova et al., 2016; Li G. et al., 2020). These properties are very promising for addressing various different challenges, which include treatment of emerging contaminants through adsorption and catalysis (Farrusseng, 2011). Currently, MOF synthesis is a very relevant topic. In 2019, the Cambridge Structural Database (CSD) reports 75,600 different structures (Moghadam et al., 2017), with the MOF types doubling every 3.9 years (Tranchemontagne et al., 2008). A search in the Scopus database for articles on MOFs gives the increased recent interest on this topic as shown in **Figure 5**.

There are many different methods for the synthesis of MOFs. The most common and facile route is the solvothermal method, where a mixture of metal salt is heated, and organic linkers are dissolved in a solvent, above the boiling point of the solvent itself (Yang and Bai, 2019). This method requires several

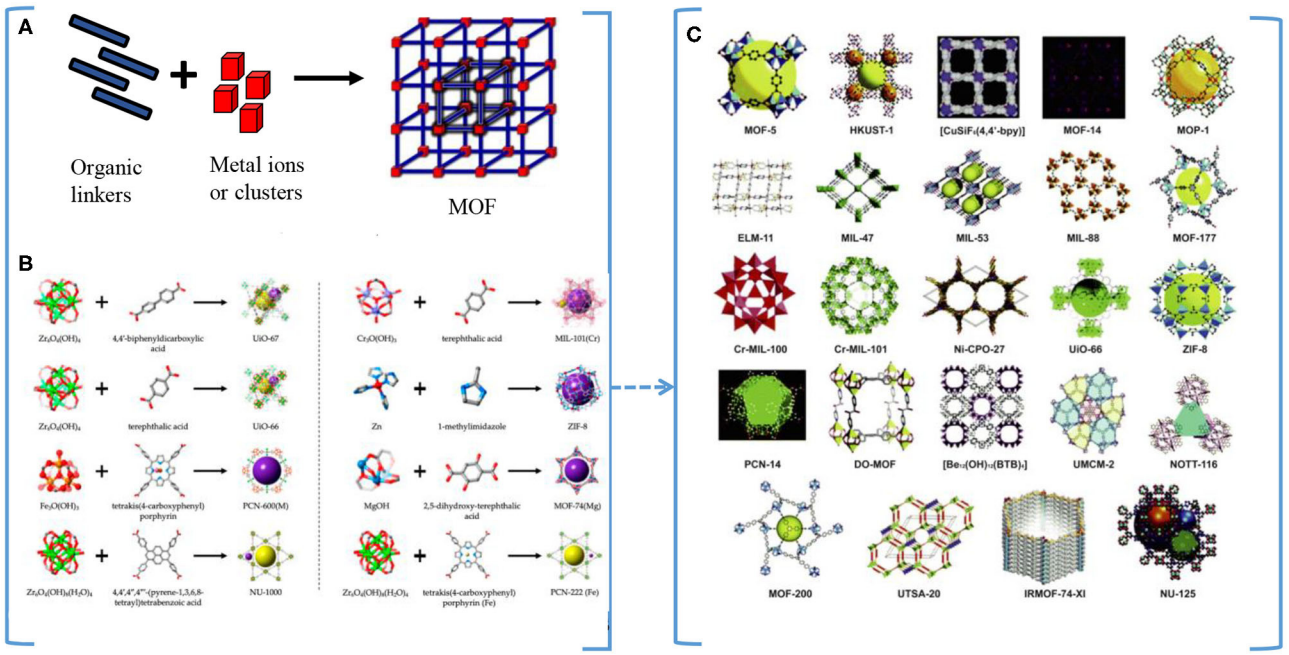

FIGURE 4 | (A) Metallic organic framework (MOF) basic structure. **(B)** Examples of different MOFs structures with their corresponding metallic clusters and organic linkers (Howarth et al., 2017), with permission from the American Chemical Society. **(C)** Examples of common MOFs structures (Qiu et al., 2014), with permission from the Royal Society of Chemistry.

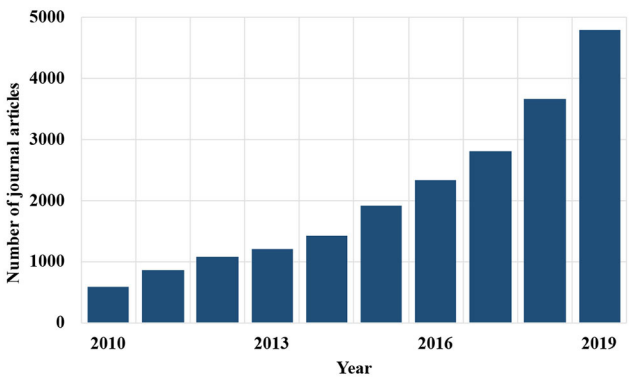

FIGURE 5 | Chronological literature researches on MOFs, keywords, metal organic frameworks, and MOFs (retrieved from Scopus).

hours to weeks to lead to the production of crystals that can undergo to single crystal X-ray diffraction analysis and is not applicable when using starting materials that are unstable at high temperatures (Stock and Biswas, 2012). For some MOFs, crystallization requires a short time, thus they are obtained at room temperature by the direct precipitation method, which consists in just mixing the starting materials. Other methods include microwave-assisted, electrochemical, mechanochemical, and sonochemical synthesis; these approaches differ in how energy is introduced in the synthetic system and result in different reaction time, yields, particle size, and morphology.

Application of MOFs is a multidirection research field. Several applications include H_2/CH_4 storage (Yang et al., 2012; Akhbari and Morsali, 2013), CO_2 capture (Ding et al., 2016), gas separations (Zhao et al., 2013), and catalysis (Doonan and Sumby, 2017). Very promising results have been obtained by studying the applications of MOFs in adsorption and photocatalytic degradation processes for the abatement of inorganic and organic contaminants. The review pays attention just on these two applications to organic ECs.

MOFS AS ADSORBENTS

MOFs are good materials for a future application in the field of EC removal from wastewater through adsorption due to the high porosity and the specific adsorbate/adsorbent interactions (Dias and Petit, 2015). ZIF-8 belongs to the zeolitic imidazolate frameworks (ZIFs), a promising class of MOFs for water-phase adsorption application with good chemical and thermal stability and similar pore topologies to zeolites. ZIF-8 was used by Khan et al. (2015) for phthalic acid adsorption in water. The authors compared the adsorption capacity of ZIF8 with activated carbon (AC), UiO-66, and NH_2-UiO-66, for 24 h at room temperature. Their results for the sorption capacity q_t (mg/g) are reported in **Table 1**.

The highest sorption capacity was found in ZIF-8, and this was explained by a good interaction between the positively charged surface of ZIF-8 and the phthalic acid anions. ZIF-8 proved stable after washing with methanol.

TABLE 1 | Phthalic acid adsorption tests.

Adsorbent	q_t (mg/g)
ZIF-8	≈530
AC	≈220
NH_2-UiO-66	≈175
UiO-66	≈140

TABLE 2 | Dye removal using Materials Institut Lavoisiers (MILs).

Adsorbent	Dye removal (%)		
	Basic blue 41	Methylene blue	Basic red 46
MIL-125(Ti)	41	39	45
NH_2-MIL-125(Ti)	93	97	99
MIL-X1	45	43	50
MIL-X2	80	89	75
MIL-X3	86	91	79

Oveisi et al. (2018) synthesized five MOFs named Materials Institut Lavoisiers (MILs) using tetraisopropyl orthotitanate as a metal source and 1,4-benzenedicarboxylate (BDC) and 2-amino-1,4-benzenedicarboxylate (NH_2-BDC) as organic linkers. The five nanomaterials were MIL-125(Ti), NH_2-MIL-125(Ti), MIL-X1 (BDC/NH_2-BDC molar ratio: 75/25), MIL-X2 (BDC/NH_2-BDC molar ratio: 50/50), and MIL-X3 (BDC/NH_2-BDC molar ratio: 25/75). Adsorption of three dyes was tested: basic red 46, basic blue 41, and methylene blue. **Table 2** shows the results.

The better performances of the amino-functionalized material were attributed to the fact that it has the highest electron density and zeta potential among the tested materials. The authors also studied the adsorbent loading effect, the concentration of each dye, the pH of the solution, and the contact time on the adsorption process. The following results were obtained: (i) the adsorption efficiency increased with the sorbent loading, since a higher amount of active sites was available, while it decreased with increasing concentration of the dyes due to the saturation of the active sites and/or dye aggregation; (ii) the equilibrium time for the process was 30 min; (iii) no effect was observed as a consequence of pH variation. This was explained by assuming that the dye adsorption was mainly based on π-π interactions between adsorbate and adsorbent, which are not influenced by pH variation.

Andrew Lin and Hsieh (2015) used HKUST-1, a copper-based MOF, for the adsorption of p-nitrophenol (PNP) in water, finding an adsorption capacity of ≈ 400 mg/g. This high value was attributed to the affinity of the metal site of HKUST-1with the NO_2 group of PNP as well as π-π interactions between adsorbate and adsorbent. At 20°C, adsorption reached equilibrium after 60 min, while at 60°C, the adsorption capacity was higher, and the equilibrium time decreased to 30 min.

A common drawback of MOFs is a poor processability and low thermal and chemical stability (Li and Huo, 2015). To overcome these drawbacks, a combination of MOFs with other functional materials has been proposed (Han et al., 2016), in order to realize composites characterized by good performances, improved morphology, and better stability and mechanical properties.

TABLE 3 | Aniline adsorption tests.

Adsorbent	q_t (mg/g)
7%SiO_2@MIL-68	531.9
SiO_2	≈50
MIL-68	402.0
SiO_2/MIL-68 mixture	≈400

Han et al. (2016) prepared a hybrid material by combining MIL-68, an aluminum-based MOF, with SiO_2. They found that the incorporation of SiO_2 in MIL-68 results in smaller particle size of MIL-68(Al). The sorption capacity of the 7%SiO_2@MIL-68(Al) composites for aqueous solution of aniline was investigated and compared with that of the individual SiO_2 and MIL-68 and a physical mixture of both. The results are listed in **Table 3**.

The 7%SiO_2@MIL-68 composite showed a high adsorption capacity and fast adsorption dynamics (the equilibrium was reached in 40 s). These results were attributed to the pore size decrease due to incorporation of SiO_2 and the likely hydrogen bond interaction between $-NH_2$ of aniline and the bridging μ_2-O in the adsorbent, as well as the π-π interaction between the adsorbent and the benzene rings. Moreover, incorporation of SiO_2 in the MIL-68 framework reduces its particle size and increases the surface area of the material. The 7%SiO_2@MIL-68 also showed good reusability. After the fourth reuse, with a regeneration procedure consisting in washing the adsorbent with ethanol then drying it under vacuum at 373 K, the adsorption capacity underwent only a slight reduction.

Jabbari et al. (2016) synthesized hybrid nanocomposites based on Cu-BTC (BTC: benzene tricarboxylate) MOF, carbon nanotubes (CNTs), graphene oxide (GO), and Fe_3O_4 magnetic nanoparticles (MNPs) and tested the adsorption capacity of these materials over methylene blue (MB) in 50 and 100 ppm aqueous solutions of the pollutant. Their results are reported in **Table 4**, where CuG12, CuG11, CuG21, and CuG51 indicate composites with MOF:GO ratios of 1:2, 1:1, 2:1, and 5:1, respectively; FCuG refers to the Fe_3O_4/Cu-BTC@GO nanocomposite; CuC12, CuC11, CuC21, and CuC51 indicate composites with MOF/CNT ratio 1:2, 1:1, 2:1, and 5:1, respectively; FCuC indicates a hybrid nanocomposite of Fe_3O_4/Cu-BTC@CNT.

Results show that the nanocomposites performed better than the parent materials, due to the synergistic effect of the composite constituents, nano-size of the Cu-BTC MOF, well separation of the MOF, inhibition of distortion and bundling in GO and CNT, and increasing in pore volume. Unsaturated bonds and the carboxylate group negative charge favors the π-π and electrostatic interactions between the adsorbent and adsorbate. The best adsorption performances were shown by CuC21; the measured dye adsorption of the non-magnetic CuC hybrid nanocomposites is slightly higher than the one obtained with

TABLE 4 | Methylene blue (MB) adsorption capacities, Q_e in mg/g, of various hybrid nanocomposites.

Adsorbent	Q_e (mg/g)	
	C_{MB}: 50 ppm	C_{MB}: 100 ppm
Fe_3O_4 MNPs	62	80
Graphene oxide (GO)	71	94
F-CNT	110	125
Cu-BTC MOF	46	67
CuG12	48	128
CuG11	88	96
CuG21	32	152
CuG51	28	40
FCuG	79	136
CuC12	90	108
CuC11	78	160
CuC21	130	172
CuC51	136	132
FCuC	112	152

TABLE 5 | Bisphenol A (BPA) adsorption capacities of various hybrid nanocomposites.

Adsorbent	q_e (mg/g)
GO	99.7
F-CNT	82.9
Cu-BDC	60.2
Cu1GrO1	161.8
Cu1GrO3	182.2
Cu3GrO1	148.9
Cu1CNT1	146.7
Cu1CNT3	164.1
Cu3CNT1	129.7

the magnetic hybrid nanocomposite of FCuC. This could be explained by the filling of the pores formed between the MOF and the substrate by magnetic nanoparticles and/or disruption of the connection between the parent materials after loading of MNPs.

Recently, Ahsan et al. (2019) prepared a similar set of MOF-GO and MOF-CNT nanocomposites, this time using Cu-BDC (BDC: benzene dicarboxylate) for adsorption of bisphenol A (BPA) in 100 ppm aqueous solutions. **Table 5** reports their results.

The data show that the newly formed CuMOF-based hybrid nanocomposites have higher adsorption capacities for the BPA removal. This is attributed to the synergy coming into play when the parent materials are combined. Moreover, the functionalized graphene layer (i) suppresses aggregation, benefits dispersion, and increases the formation of small pores, (ii) reduces inter-MOF voids and preserves MOF formation and growth, and (iii) prevents the distortions and buckling/bundling of the GrO and CNTs. Another effect, which could favor BPA adsorption is the formation of new pores at the interface of Cu-BDC with MOF/CNT and Cu-BDC with MOF/GrO, due to the binding of the Cu-BDC MOF to the graphene layers in CNTs and GrO.

The wide literature has highlighted a number of different selective adsorption mechanisms in the abatement of organic compounds by MOFs:

- **Electrostatic**: this type of interaction has been the most frequently observed. The surface charge of the MOF depends on the pH of the solution; the charged MOF undergoes electrostatic interaction with an oppositely charged contaminant.
- **Hydrogen bonding**: MOFs can be functionalized with NH_2, –OH, –COOH, and $–SO_3H$ groups, to enable adsorptive removal applications via hydrogen bonding (Hasan et al., 2013). The different groups induce different strengths of the hydrogen bonding.
- **Acid–base**: Ahmed and Jhung (2017) reported the effects of the functionalization of the MOF MIL-101-Cr with either acidic or basic groups on naproxen adsorption. Results showed that the basic functionalized MOF was a better adsorbent than the acidic functionalized and the neutral MIL-101. This is due to the interaction between the modified MOFs' with $–NH_2$ groups with the sorbates –COOH groups.
- **π-π interactions/stacking**: Qin et al. (2015) reported that the amount of bisphenol A adsorbed over MIL-101-Cr was 1.84 times higher than on activated carbon, suggesting the existence of π-π interactions between the adsorbent and benzene rings.
- **Pore/size-selective adsorption**: one of the most interesting features of MOFs is the related pore size tunability, which enables selective adsorption of appropriately sized sorbates. As shown by Huang et al. (2012), it is possible to favor mesopore formation during MOF synthesis in order to enhance methylene blue (MB) adsorption.
- **Hydrophobic interactions**: higher hydrophobicity in MOFs favors their adsorption of non-polar, water-insoluble molecules, as reported by Sann et al. (2018) who observed high adsorption of oil over the highly hydrophobic MOF ZIF-8 (zinc-methylimidazolate framework-8).

Table 6 reports up-to-date studies and the corresponding adsorption capacity of different types of MOFs in ECs remediation.

METAL ORGANIC FRAMEWORKS AS PHOTOCATALYSTS

Photodegradation is theoretically a better method than adsorption for wastewater treatment, mainly because it causes a complete elimination of the pollutant instead of its simple phase transfer, so no further treatment is required. The presence of organic linkers in MOFs allows them to have a relatively wide absorption spectrum permitting the generation of a charge-separated state, which decays in the microseconds, thus permitting photocatalytic applications (Hariganesh et al., 2020; Wang C. et al., 2020).

Alvaro et al. (2007) investigated the behavior of MOF-5, containing clusters of ZnO, as a semiconductor. They found that

TABLE 6 | Comparison of the adsorption capacity of different types of metal organic frameworks (MOFs) for emerging contaminant (EC) remediation.

Functionalized MOF	Surface area (m^2/g)	EC remediated	Adsorption capacity (mg/g)	References
MIL-53(Fe)	52.12	Tetracycline antibiotics	247.70	Yu et al., 2019
NH_2-MIL-53(Fe)	65.64		271.90	
NO_2-MIL-53(Fe)	30.01		272.60	
Br-MIL-53(Fe)	39.75		309.60	
Al-MOF-Fe_3O_4@P4 V P	123.67	Naproxen	31.67	Li Y. et al., 2020
SCNU-Z_2	960.00	Methylene blue	455.60	Deng et al., 2019
		Crystal violet	847.40	
		Rhodamine B	751.80	
$Ti_3C_2T_x$MXene and Al-MOF	9.00 and 630.00	Methylene blue	∼140	Jun et al., 2020
		Acid blue 80	∼200	
Ni-BDC MOF	–	Methylene blue	73.48	Ahsan et al., 2020
Ni-BDC MOF@GO			222.80	
Ni-MOF@CNT			181.96	
ZIF-8-chitosan composite beads	15.30	Tetracycline	495.04	Zhao et al., 2020
ZIF-8@CS/PVA-ENF(2)	–	Malachite green	1,000.00	Mahmoodi et al., 2020
Zr-MOF(bpy)	2,141.88	Rhodamine B	918.90	Cui et al., 2019
BMDC-12 h	1,449.00	Atenolol	552.00	Bhadra and Jhung, 2018
		Clofibric acid	540.00	

TABLE 7 | Photodegradation of phenol with various catalysts.

Catalyst	Molephenol degraded/g catalyst	Mole phenol degraded/catalyst metal atom
MOF-5	0.0045	1.30
P25	0.0125	0.92
ZnO	0.0120	0.90

TABLE 8 | Methylene Blue (MB) photodegradation using TiO_2@Cu_3BTC_2 and TiO_2.

Catalyst	MB C/C_0			
	t: 2 min	t: 6 min	t: 10 min	t: 30 min
TiO_2@Cu_3BTC_2	0.3	0.15	0.10	0.09
TiO_2	0.9	0.8	0.7	0.2

this material is stable to light exposure, has an absorption onset at 450 nm and a 3.4 eV band gap. Irradiation with $\lambda < 450$ nm gives rise to an electron–hole couple lasting for microseconds, thus permitting application in photocatalytic processes. The activity of MOF-5 was tested in the photodegradation reaction of phenol and compared with Degussa P25 (TiO_2 nanoparticles) and another semiconductor, ZnO. The degradation of MOF-5 generates ZnO, and this could be responsible for the photocatalytic activity.

As shown in **Table 7**, MOF-5 has a high photocatalytic activity, which is not caused by ZnO clusters eventually formed during the test, due to the higher phenol conversion per metal atom when compared to ZnO.

Effect on photocatalytic activity of MOF modification, especially by inclusion of inorganic semiconductors, was also studied by Binh et al. (2015). The authors prepared a Cu_3BTC_2 (BTC = benzene-1,3,5-tricarboxylate) MOF with a specific surface area of 1,350 m^2/g, which was then modified by including TiO_2 in its framework and converted to TiO_2@Cu_3BTC_2. The catalytic activity of the novel material was tested in the photodegradation of methylene blue (MB) and compared to that with the commercial TiO_2 photocatalyst Degussa P25. The photocatalytic experiments were performed using 50 ml of aqueous methylene blue solution (2×10^{-5} M) in which the photocatalyst was dispersed (3 mg/ml). The resulting mixture was irradiated under UV-Vis lamps, at different irradiation times, from 2 to 30 min. **Table 8** shows the experimental data.

The data show that TiO_2@Cu_3BTC_2 is a promising photodegradation catalyst since it performs faster than Degussa P25 in the photocatalytic degradation of Methylene Blue. This has been attributed to spectral sensitization of the colored Cu-MOF for TiO_2 in the visible region, to the large contact area of the catalyst, to high porosity, and to Cu_3BTC_2 acting as template for the formation of fine nano TiO_2 with an increase in surface area.

In an effort to increase the photocatalytic activity of MOFs toward solar light, Gómez-Avilés et al. (2019) synthesized mixed Ti-Zr MOFs by substituting partially Ti by Zr atoms in the framework of NH_2-MIL-125(Ti) MOF and tested them in acetaminophen (ACE) photodegradation experiments under solar-simulated radiation. The synthesized materials had different Ti:Zr molar percentages and were named TiZr15, TiZr30, TiZr60, and TiZr80, the number standing for the Zr molar percentage. Before the photocatalytic runs, adsorption and solar irradiation tests were performed, showing that adsorption ranged between 0.6 and 2% and that the ACE concentration was

TABLE 9 | Acetaminophen (ACE) photodegradation using different catalysts.

Catalyst	ACE C/C_0								
	t: 15 min	t: 30 min	t: 45 min	t: 60 min	t: 90 min	t: 120 min	t: 180 min	t: 240 min	t: 360 min
NH_2-MIL-125(Ti)	0.93	0.86	0.73	0.57	0.26	0.09	0	0	0
TiZr15	0.82	0.66	0.41	0.23	0.03	0	0	0	0
TiZr30	0.9	0.72	0.6	0.45	0.23	0.02	0	0	0
TiZr60	0.97	0.93	0.9	0.88	0.82	0.76	0.7	0.64	0.53
TiZr80	0.97	0.93	0.9	0.88	0.82	0.76	0.69	0.61	0.51

unchanged after 6 h of solar irradiation in the absence of catalyst. The photocatalytic tests were performed at 20°C with 150 ml of solution containing 5 mg/L of ACE at time zero, in which a catalyst amount of 250 mg/L was added, at an initial pH of 6.9, with an intensity of irradiation equal to 600 W/m^2. **Table 9** shows the results.

The non-crystalline samples with the highest Zr percentage (TiZr60 and TiZr80) yielded lower acetaminophen conversion. TiZr15 and TiZr30, characterized by the lower Zr amounts, caused complete ACE photodegradation in < 3 h of irradiation. The high performance of TiZr15, which allowed complete ACE conversion within 90 min was explained by the high porosity and lower band gap value resulting from the partial substitution of Ti^{4+} by Zr^{4+} in the structure of the MOF. The incorporation of Zr ions, which are able to act as charge trappers, increases the charge carrier lifetimes and reduces the recombination processes, resulting in an increase in photoactivity.

The incorporation of the $-NH_2$ group to the organic linker also affects the photoactivity of these materials. It causes the formation of a red shifted band at the valance bond (VB) of the MOF, reducing the band gap value to 2.7 eV, thus enabling photoexcitation as a result of irradiation with photons with $\lambda = 460$ nm and lower. Moreover, the amine group increases the charge transfer between metal and organic linker and inhibits electron–hole recombination. It is also notable that no aromatic intermediates were detected using HPLC (probably due to low initial ACE concentration and/or fast conversion to other organics). TiZr15, the most active photocatalyst, was active after three successive runs.

Another recent work focused on the synthesis of MOF-based photocatalysts activated by visible light. He et al. (2019) prepared a magnetic (M-) MIL-101(Fe)/TiO_2 composite for the photodegradation of tetracycline under solar light irradiation. The catalytic efficiency of M-MIL-101(Fe)/TiO_2(magnetic) and MIL-101(Fe)/TiO_2 (non-magnetic) for tetracycline (TC) degradation was investigated under visible light: after 3 h of TC conversion, 91.24 and 84.85%, respectively. This difference was attributed to the lower recombination rate observed for the magnetic material. Process optimization tests showed that using 1 g/L of catalyst in a 20-mg/L of aqueous solution of TC at initial pH of 7 at 25°C under direct solar irradiation, 92.76% TC conversion was obtained in 10 min. The material was magnetically separated from the solution and reused, showing similar performances after five catalytic cycles. It is important to point out that this high degradation rate was obtained under solar irradiation, while artificial visible light irradiation yielded poorer results, suggesting that UV photons in solar light have an important role in the photoexcitation process.

CONCLUSIONS, CHALLENGES, AND FUTURE PERSPECTIVE

Up to now, various applications of MOFs are under investigation, as they exhibit high versatility, low production costs, and high efficiency. Particularly, MOFs show promising incorporation in wastewater treatment technologies on an industrial scale. The tunability of their structural and electronic features gives the possibility to prepare materials, which can be both good adsorbents and efficient photodegradation catalysts. However, the development and the sophistication of new synthetic MOFs face challenges that stem from the chemistry of these materials and their future applications. In addition, the prospect of wide-scale implementation of MOFs in wastewater treatment is promising but needs further investigation, mainly considering scaling up application to study their performances in real conditions. In this review, we have summarized the fundamentals of adsorption and photodegradation as common applications in MOFs for EC remediation in wastewater. Moreover, focus has been given to cutting edge researches pertaining to these applications. MOF pore size can be appropriately tuned to accommodate a specific pollutant. MOFs can also be functionalized to enhance electrostatic, acid–base, π-π interactions, or hydrogen bonding. They can be combined with metals, inorganic semiconductors, or organic linkers to enhance their photoexcitation rate and reduce electron–hole recombination in order to obtain composites with high photocatalytic efficiencies. In summary, MOFs are one of the hottest topics of research today. Their phenomenal and promising features in EC remediation make MOFs very tempting materials for researchers to further explore and investigate in different potential directions.

AUTHOR CONTRIBUTIONS

VR and FB wrote the original draft of the manuscript with support from MI and MD. The main conceptual ideas were drawn from the interactions between VR and MD, while the

funds were obtained by the synergistic effect of the cooperation between O-SJ and MD. The development of the artworks, the data elaboration, and the formal analysis were conducted by VR, MH, and FB. The final draft was corrected by MH, MI, and MD. All authors contributed to the article and approved the submitted version.

FUNDING

The 12th executive program for scientific and technological cooperation between the Italian Republic and the Republic of Korea for the years 2019–2021 is acknowledged for the financial support.

REFERENCES

Ahmed, I., and Jhung, S. H. (2017). Applications of metal-organic frameworks in adsorption/separation processes via hydrogen bonding interactions. *Chem. Eng. J.* 310, 197–215. doi: 10.1016/j.cej.2016.10.115

Ahsan, M. A., Jabbari, V., Imam, M. A., Castro, E., Kim, H., Curry, M. L., et al. (2020). Nanoscale nickel metal organic framework decorated over graphene oxide and carbon nanotubes for water remediation. *Sci. Total Environ.* 698:134214. doi: 10.1016/j.scitotenv.2019.134214

Ahsan, M. A., Jabbari, V., Islam, M. T., Turley, R. S., Dominguez, N., Kim, H., et al. (2019). Sustainable synthesis and remarkable adsorption capacity of MOF/graphene oxide and MOF/CNT based hybrid nanocomposites for the removal of Bisphenol A from water. *Sci. Total Environ.* 673, 306–317. doi: 10.1016/j.scitotenv.2019.03.219

Akhbari, K., and Morsali, A. (2013). Modulating methane storage in anionic nano-porous MOF materials via post-synthetic cation exchange process. *Dalton Trans.* 42, 4786–4789. doi: 10.1039/c3dt32846e

Akpinar, I., and Yazaydin, A. O. (2017). Rapid and efficient removal of carbamazepine from water by UiO-67. *Ind. Eng. Chem. Res.* 56, 15122–15130. doi: 10.1021/acs.iecr.7b03208

Alnaizy, R., and Akgerman, A. (2000). Advanced oxidation of phenolic compounds. *Adv. Environ. Res.* 4, 233–244. doi: 10.1016/S1093-0191(00)00024-1

Alvaro, M., Carbonell, E., Ferrer, B., Llabrés i Xamena, F. X., and Garcia, H. (2007). Semiconductor behavior of a Metal-Organic Framework (MOF). *Chemistry* 13, 5106–5112. doi: 10.1002/chem.200601003

Ameta, S. C., and Ameta, R. (2018). *Advanced Oxidation Processes for Waste Water Treatment*. Cambridge: Academic Press.

Andrew Lin, K. Y., and Hsieh, Y. T. (2015). Copper-based metal organic framework (MOF), HKUST-1, as an efficient adsorbent to remove p-nitrophenol from water. *J. Taiwan Inst. Chem. Eng.* 50, 223–228. doi: 10.1016/j.jtice.2014.12.008

Araña, J., Martinez Nieto, J. L., Herrera Melián, J. A., Doña Rodriguez, J. M., González Diaz, O., Pérez Peña, J., et al. (2004). Photocatalytic degradation of formaldehyde containing wastewater from veterinarian laboratories. *Chemosphere* 55, 893–904. doi: 10.1016/j.chemosphere.2003.11.060

Bedia, J., Muelas-Ramos, V., Peñas-Garzón, M., Gómez-Avilés, A., Rodríguez, J. J., and Belver, C. (2019). A review on the synthesis and characterization of metal organic frameworks for photocatalytic water purification. *Catalysts*. 9:52. doi: 10.3390/catal9010052

Bhadra, B. N., and Jhung, S. H. (2018). Adsorptive removal of wide range of pharmaceuticals and personal care products from water using bio-MOF-1 derived porous carbon. *Micropor. Mesopor. Mater.* 270, 102–108. doi: 10.1016/j.micromeso.2018.05.005

Binh, N. T., Thu, P. T., Le, N. T. H., Tien, D. M., Khuyen, H. T., Giang, L. T. K., et al. (2015). Study on preparation and properties of a novel photo-catalytic material based on copper-centred metal-organic frameworks (Cu-MOF) and titanium *dioxide. Int. J. Nanotech.* 12, 447–455. doi: 10.1504/IJNT.2015.067902

Butova, V. V., Soldatov, M. A., Guda, A. A., Lomachenko, K. A., and Lamberti, C. (2016). Metal-organic frameworks: structure, properties, methods of synthesis and characterization. *Russian Chem. Rev.* 85, 280 −307. doi: 10.1070/RCR4554

Cheng, P., Wang, C., Kaneti, Y. V., Eguchi, M., Lin, J., Yamauchi, Y., et al. (2020). Practical MOF nanoarchitectonics: new strategies for enhancing the processability of MOFs for practical applications. *Langmuir* 36, 4231–4249. doi: 10.1021/acs.langmuir.0c00236

Cheremisinoff, N. P. (2007). *Handbook of Water and Wastewater Treatment Technologies*. Waltham: Butterworth-Heinemann.

Chun, H., Yizhong, W., and Hongxiao, T. (2000). Destruction of phenol aqueous solution by photocatalysis or direct photolysis. *Chemosphere* 41, 1205–1209. doi: 10.1016/S0045-6535(99)00539-1

Crini, G., and Lichtfouse, E. (2019). Advantages and disadvantages of techniques used for wastewater treatment. *Environ. Chem. Lett.* 17, 145–155. doi: 10.1007/s10311-018-0785-9

Cui, W., Kang, X., Zhang, X., and Cui, X. (2019). Gel-like ZnO/Zr-MOF(bpy) nanocomposite for highly efficient adsorption of Rhodamine B dye from aqueous solution. *J. Phys. Chem. Solids* 134, 165–175. doi: 10.1016/j.jpcs.2019.06.004

Curcó, D., Giménez, J., Addardak, A., Cervera-March, S., and Esplugas, S. (2002). Effects of radiation absorption and catalyst concentration on the photocatalytic degradation of pollutants. *Cataly. Today* 76, 177–188. doi: 10.1016/S0920-5861(02)00217-1

Daliran, S., Ghazagh-Miri, M., Oveisi, A. R., Khajeh, M., Navalón, S., Âlvaro, M., et al. (2020). A pyridyltriazol functionalized zirconium metal–organic framework for selective and highly efficient adsorption of palladium. *ACS Appl. Mater. Interfaces* 12, 25221–25232. doi: 10.1021/acsami.0c06672

Deng, S. Q., Miao, Y. L., Tan, Y. L., Fang, H. N., Li, Y. T., Mo, X. J., et al. (2019). An Anionic nanotubular metal–organic framework for high-capacity dye adsorption and dye degradation in darkness. *Inorg. Chem.* 58, 13979–13987. doi: 10.1021/acs.inorgchem.9b01959

Dhakshinamoorthy, A., Asiri, A. M., and Garcia, H. (2019). 2D metal–organic frameworks as multifunctional materials in heterogeneous catalysis and electro/photocatalysis. *Adv. Mater.* 31:1900617. doi: 10.1002/adma.201900617

Dhakshinamoorthy, A., Li, Z., and Garcia, H. (2018). Catalysis and photocatalysis by metal organic frameworks. *Chem. Soc. Rev.* 47, 8134–8172. doi: 10.1039/C8CS00256H

Dias, E. M., and Petit, C. (2015). Towards the use of metal–organic frameworks for water reuse: a review of the recent advances in the field of organic pollutants removal and degradation and the next steps in the field. *J. Mater. Chem. A* 3, 22484–22506. doi: 10.1039/C5TA05440K

Ding, N., Li, H., Feng, X., Wang, Q., Wang, S., Ma, L., et al. (2016). Partitioning MOF-5 into confined and hydrophobic compartments for carbon capture under humid conditions. *J. Am. Chem. Soc.* 138, 10100–10103. doi: 10.1021/jacs.6b06051

Doonan, C. J., and Sumby, C. J. (2017). Metal–organic framework catalysis. *CrystEngComm*. 19, 4044–4048. doi: 10.1039/C7CE90106B

Eddaoudi, M., Li, H., and Yaghi, O. M. (2000). Highly porous and stable metal–organic frameworks: structure design and sorption properties. *J. Am. Chem. Soc.* 122, 1391–1397. doi: 10.1021/ja9933386

El-Qanni, A. (2017). Development of sustainable nanosorbcats based technology for hydrocarbons and organic pollutants recovery from industrial wastewater. Doctoral thesis. doi: 10.11575/PRISM/28735

Fairbairn, D. J., Elliott, S. M., Kiesling, R. L., Schoenfuss, H. L., Ferrey, M. L., and Westerhoff, B. M. (2018). Contaminants of emerging concern in urban stormwater: spatiotemporal patterns and removal by iron-enhanced sand filters (IESFs). *Water Res.* 145, 332–345. doi: 10.1016/j.watres.2018.08.020

Farha, O. K., Eryazici, I., Jeong, N. C., Hauser, B. G., Wilmer, C. E., Sarjeant, A. A., et al. (2012). Metal–organic framework materials with ultrahigh surface areas: is the sky the limit? *J. Am. Chem. Soc.* 134, 15016–15021. doi: 10.1021/ja3055639

Farrusseng, D. (2011). *Metal-Organic Frameworks Applications From Catalysis to Gas Storage*. Weinheim: Wiley-VCH. doi: 10.1002/9783527635856

Furukawa, H., Cordova, K. E., O'Keeffe, M., and Yaghi, O. M. (2013). The chemistry and applications of metal-organic frameworks. *Science* 341:1230444. doi: 10.1126/science.1230444

Gogate, P. R., and Pandit, A. B. (2004). A review of imperative technologies for wastewater treatment I: oxidation technologies at ambient conditions. *Adv. Environ. Res.* 8, 501–551. doi: 10.1016/S1093-0191(03)00032-7

Gómez-Avilés, A., Peñas-Garzón, M., Bedia, J., Dionysiou, D. D., Rodríguez, J. J., and Belver, C. (2019). Mixed Ti-Zr metal-organic-frameworks for the photodegradation of acetaminophen under solar irradiation. *Appl. Cataly. B* 253, 253–262. doi: 10.1016/j.apcatb.2019.04.040

Han, T., Li, C., Guo, X., Huang, H., Liu, D., and Zhong, C. (2016). *In-situ* synthesis of SiO2@MOF composites for high-efficiency removal of aniline from aqueous solution. *Appl. Surf. Sci.* 390, 506–512. doi: 10.1016/j.apsusc.2016.08.111

Haque, M. M., and Muneer, M. (2007). Photodegradation of norfloxacin in aqueous suspensions of titanium dioxide. *J. Hazard. Mater.*. 145, 51–57. doi: 10.1016/j.jhazmat.2006.10.086

Hariganesh, S., Vadivel, S., Maruthamani, D., Kumaravel, M., Paul, B., Balasubramanian, N., et al. (2020). Facile large scale synthesis of CuCr2O4/CuO nanocomposite using MOF route for photocatalytic degradation of methylene blue and tetracycline under visible light. *Appl. Organomet. Chem.* 34:e5365. doi: 10.1002/aoc.5365

Hasan, Z., Choi, E. J., and Jhung, S. H. (2013). Adsorption of naproxen and clofibric acid over a metal–organic framework MIL-101 functionalized with acidic and basic groups. *Chem. Eng. J.* 219, 537–544. doi: 10.1016/j.cej.2013.01.002

Hasan, Z., Jeon, J., and Jhung, S. H. (2012). Adsorptive removal of naproxen and clofibric acid from water using metal-organic frameworks. *J. Hazard. Mater.* 209–210, 151–157. doi: 10.1016/j.jhazmat.2012.01.005

Hasan, Z., and Jhung, S. H. (2015). Removal of hazardous organics from water using metal-organic frameworks (MOFs): plausible mechanisms for selective adsorptions. *J. Hazard. Mater.* 283, 329–339. doi: 10.1016/j.jhazmat.2014.09.046

He, L., Dong, Y., Zheng, Y., Jia, Q., Shan, S., and Zhang, Y. (2019). A novel magnetic MIL-101(Fe)/TiO2 composite for photo degradation of tetracycline under solar light. *J. Hazard. Mater.* 361, 85–94. doi: 10.1016/j.jhazmat.2018.08.079

Herrmann, J. M. (2000). Heterogeneous photocatalysis: fundamentals and applications to the removal of various types of aqueous pollutants. *Cataly. Today* 53, 115–129. doi: 10.1016/S0920-5861(99)00107-8

Howarth, A. J., Peters, A. W., Vermeulen, N. A., Wang, T. C., Hupp, J. T., and Farha, O. K. (2017). Best practices for the synthesis, activation, and characterization of metal–organic frameworks. *Chem. Mater.* 29, 26–39. doi: 10.1021/acs.chemmater.6b02626

Hu, C., Hu, X., Li, R., and Xing, Y. (2020). MOF derived ZnO/C nanocomposite with enhanced adsorption capacity and photocatalytic performance under sunlight. *J. Hazard. Mater.* 385:121599. doi: 10.1016/j.jhazmat.2019.121599

Huang, X. X., Qiu, L. G., Zhang, W., Yuan, Y. P., Jiang, X., Xie, A. J., et al. (2012). Hierarchically mesostructured MIL-101 metal–organic frameworks: supramolecular template-directed synthesis and accelerated adsorption kinetics for dye removal. *CrystEngComm* 14, 1613–1617. doi: 10.1039/C1CE06138K

Huber, M. M., Canonica, S., Park, G. Y., and von Gunten, U. (2003). Oxidation of pharmaceuticals during ozonation and advanced oxidation processes. *Environ. Sci. Technol.* 37, 1016–1024. doi: 10.1021/es025896h

Jabbari, V., Veleta, J. M., Zarei-Chaleshtori, M., Gardea-Torresdey, J., and Villagrán, D. (2016). Green synthesis of magnetic MOF@GO and MOF@CNT hybrid nanocomposites with high adsorption capacity towards organic pollutants. *Chem. Eng. J.* 304, 774–783. doi: 10.1016/j.cej.2016.06.034

Jun, B. M., Heo, J., Taheri-Qazvini, N., Park, C. M., and Yoon, Y. (2020). Adsorption of selected dyes on Ti3C2Tx MXene and Al-based metal-organic framework. *Ceramics Int.* 46, 2960–2968. doi: 10.1016/j.ceramint.2019.09.293

Khan, N. A., Jung, B. K., Hasan, Z., and Jhung, S. H. (2015). Adsorption and removal of phthalic acid and diethyl phthalate from water with zeolitic imidazolate and metal–organic frameworks. *J. Hazard. Mater.* 282, 194–200. doi: 10.1016/j.jhazmat.2014.03.047

Kreno, L. E., Leong, K., Farha, O. K., Allendorf, M., Van Duyne, R. P., and Hupp, J. T. (2012). Metal–organic framework materials as chemical sensors. *Chem. Rev.* 112, 1105–1125. doi: 10.1021/cr200324t

Kumar, P., Bansal, V., Kim, K. H., and Kwon, E. E. (2018). Metal-organic frameworks (MOFs) as futuristic options for wastewater treatment. *J. Ind. Eng. Chem.* 62, 130–145. doi: 10.1016/j.jiec.2017.12.051

Li, G., Xia, L., Dong, J., Chen, Y., and Li, Y. (2020). "10 - Metal-organic frameworks," in *Solid-Phase Extraction*, ed C. F. Poole (Oxford: Elsevier), 285–309. doi: 10.1016/B978-0-12-816906-3.00010-8

Li, S., and Huo, F. (2015). Metal–organic framework composites: from fundamentals to applications. *Nanoscale* 7, 7482–7501. doi: 10.1039/C5NR00518C

Li, Y., Wang, Y., He, L., Meng, L., Lu, H., and Li, X. (2020). Preparation of poly(4-vinylpyridine)-functionalized magnetic Al-MOF for the removal of naproxen from aqueous solution. *J. Hazard. Mater.* 383:121144. doi: 10.1016/j.jhazmat.2019.121144

Lowell, S., Shields, J. E., Thomas, M. A., and Thommes, M. (2004). "Adsorption mechanism," in *Characterization of Porous Solids and Powders: Surface Area, Pore Size and Density,* eds S. Lowell, J. E. Shields, M. A. Thomas, and M. Thommes (Dordrecht: Springer Netherlands), 15–57. doi: 10.1007/978-1-4020-2303-3_4

Mahmoodi, N. M., Oveisi, M., Taghizadeh, A., and Taghizadeh, M. (2020). Synthesis of pearl necklace-like ZIF-8@chitosan/PVA nanofiber with synergistic effect for recycling aqueous dye removal. *Carbohydr. Polym.* 227:115364. doi: 10.1016/j.carbpol.2019.115364

Maira, A. J., Yeung, K. L., Soria, J., Coronado, J. M., Belver, C., Lee, C. Y., et al. (2001). Gas-phase photo-oxidation of toluene using nanometer-size TiO2 catalysts. *Appl. Cataly. B Environ.* 29, 327–336. doi: 10.1016/S0926-3373(00)00211-3

Martinez-Costa, J. I., Leyva-Ramos, R., and Padilla-Ortega, E. (2018). Sorption of diclofenac from aqueous solution on an organobentonite and adsorption of cadmium on organobentonite saturated with diclofenac. *Clays Clay Miner.* 66, 515–528. doi: 10.1346/CCMN.2018.064119

Moghadam, P. Z., Li, A., Wiggin, S. B., Tao, A., Maloney, A. G. P., Wood, P. A., et al. (2017). Development of a Cambridge structural database subset: a collection of metal–organic frameworks for past, present, and future. *Chem. Mater.* 29, 2618–2625. doi: 10.1021/acs.chemmater.7b00441

Mohamed, A., Salama, A., Nasser, W. S., and Uheida, A. (2018). Photodegradation of ibuprofen, cetirizine, and naproxen by PAN-MWCNT/TiO2–NH2 nanofiber membrane under UV light irradiation. *Environ. Sci. Eur.* 30:47. doi: 10.1186/s12302-018-0177-6

Mon, M., Bruno, R., Ferrando-Soria, J., Armentano, D., and Pardo, E. (2018). Metal–organic framework technologies for water remediation: towards a sustainable ecosystem. *J. Mater. Chem. A* 6, 4912–4947. doi: 10.1039/C8TA00264A

Nakada, N., Shinohara, H., Murata, A., Kiri, K., Managaki, S., Sato, N., et al. (2007). Removal of selected pharmaceuticals and personal care products (PPCPs) and endocrine-disrupting chemicals (EDCs) during sand filtration and ozonation at a municipal sewage treatment plant. *Water Res.* 41, 4373–4382. doi: 10.1016/j.watres.2007.06.038

Oveisi, M., Asli, M. A., and Mahmoodi, N. M. (2018). MIL-Ti metal-organic frameworks (MOFs) nanomaterials as superior adsorbents: Synthesis and ultrasound-aided dye adsorption from multicomponent wastewater systems. *J. Hazard. Mater.* 347, 123–140. doi: 10.1016/j.jhazmat.2017.12.057

Poyatos, J. M., MuÒio, M. M., Almecija, M. C., Torres, J. C., Hontoria, E., and Osorio, F. (2010). Advanced oxidation processes for wastewater treatment: state of the art. *Water Air Soil Pollut.* 205, 187–204. doi: 10.1007/s11270-009-0065-1

Qin, F. X., Jia, S. Y., Liu, Y., Li, H. Y., and Wu, S. H. (2015). Adsorptive removal of bisphenol A from aqueous solution using metal-organic frameworks. *Desalination Water Treat.* 54, 93–102. doi: 10.1080/19443994.2014.883331

Qiu, S., Xue, M., and Zhu, G. (2014). Metal–organic framework membranes: from synthesis to separation application. *Chem. Soc. Rev.* 43, 6116–6140. doi: 10.1039/C4CS00159A

Rasheed, T., Bilal, M., Nabeel, F., Adeel, M., and Iqbal, H. M. N. (2019). Environmentally-related contaminants of high concern: potential sources and analytical modalities for detection, quantification, and treatment. *Environ. Int.* 122, 52–66. doi: 10.1016/j.envint.2018.11.038

Rego, R. M., Kuriya, G., Kurkuri, M. D., and Kigga, M. (2020). MOF based engineered materials in water remediation: recent trends. *J. Hazard. Mater.* 403:123605. doi: 10.1016/j.jhazmat.2020.123605

Richardson, S. D., and Kimura, S. Y. (2017). Emerging environmental contaminants: challenges facing our next generation and potential engineering solutions. *Environ. Tech. Innov.* 8, 40–56. doi: 10.1016/j.eti.2017.04.002

Richardson, S. D., and Ternes, T. A. (2018). Water analysis: emerging contaminants and current issues. *Anal. Chem*. 90, 398–428. doi: 10.1021/acs.analchem.7b04577

Rodriguez-Narvaez, O. M., Peralta-Hernandez, J. M., Goonetilleke, A., and Bandala, E. R. (2017). Treatment technologies for emerging contaminants in water: a review. *Chem. Eng. J*. 323, 361–380. doi: 10.1016/j.cej.2017.04.106

Rojas, S., Arenas-Vivo, A., and Horcajada, P. (2019). Metal-organic frameworks: A novel platform for combined advanced therapies. *Coord. Chem. Rev*. 388, 202–226. doi: 10.1016/j.ccr.2019.02.032

Ruhí, A., Acuña, V., Barceló, D., Huerta, B., Mor, J. R., Rodríguez-Mozaz, S., et al. (2016). Bioaccumulation and trophic magnification of pharmaceuticals and endocrine disruptors in a Mediterranean river food web. *Sci. Total Environ*. 540, 250–259. doi: 10.1016/j.scitotenv.2015.06.009

Russo, V., Masiello, D., Trifuoggi, M., Di Serio, M., and Tesser, R. (2016). Design of an adsorption column for methylene blue abatement over silica: from batch to continuous modeling. *Chem. Eng. J*. 302, 287–295. doi: 10.1016/j.cej.2016.05.020

Russo, V., Trifuoggi, M., Di Serio, M., and Tesser, R. (2017). Fluid-solid adsorption in batch and continuous processing: a review and insights into modeling. *Chem. Eng. Technol*. 40, 799–820. doi: 10.1002/ceat.201600582

Ryu, J., Oh, J., Snyder, S. A., and Yoon, Y. (2014). Determination of micropollutants in combined sewer overflows and their removal in a wastewater treatment plant (Seoul, South Korea). *Environ. Monit. Assess*. 186, 3239–3251. doi: 10.1007/s10661-013-3613-5

Sann, E. E., Pan, Y., Gao, Z., Zhan, S., and Xia, F. (2018). Highly hydrophobic ZIF-8 particles and application for oil-water separation. *Sep. Purif. Technol*. 206, 186–191. doi: 10.1016/j.seppur.2018.04.027

Seo, P. W., Khan, N. A., Hasan, Z., and Jhung, S. H. (2016). Adsorptive removal of artificial sweeteners from water using metal–organic frameworks functionalized with urea or melamine. *ACS Appl. Mater. Interfaces* 8, 29799–29807. doi: 10.1021/acsami.6b11115

Stock, N., and Biswas, S. (2012). Synthesis of metal-organic frameworks (mofs): routes to various mof topologies, morphologies, and composites. *Chem. Rev*. 112, 933–969. doi: 10.1021/cr200304e

Tareq, R., Akter, N., and Azam, M. S. (2019). "Chapter 10 - biochars and biochar composites: low-cost adsorbents for environmental remediation," in *Biochar from Biomass and Waste*, eds Y. S. Ok, D. C. W. Tsang, N. Bolan, and J. M. Novak (Oxford: Elsevier), 169–209. doi: 10.1016/B978-0-12-811729-3.00010-8

Tariq, M. A., Faisal, M., Muneer, M., and Bahnemann, D. (2007). Photochemical reactions of a few selected pesticide derivatives and other priority organic pollutants in aqueous suspensions of titanium dioxide. *J. Mol. Cataly. A* 265, 231–236. doi: 10.1016/j.molcata.2006.10.013

Tran, N. H., Reinhard, M., and Gin, K. Y. H. (2018). Occurrence and fate of emerging contaminants in municipal wastewater treatment plants from different geographical regions-a review. *Water Res*. 133, 182–207. doi: 10.1016/j.watres.2017.12.029

Tranchemontagne, D. J., Hunt, J. R., and Yaghi, O. M. (2008). Room temperature synthesis of metal-organic frameworks: MOF-5, MOF-74, MOF-177, MOF-199, and IRMOF-0. *Tetrahedron* 64, 8553–8557. doi: 10.1016/j.tet.2008.06.036

Trickett, C. A., Helal, A., Al-Maythalony, B. A., Yamani, Z. H., Cordova, K. E., and Yaghi, O. M. (2017). The chemistry of metal–organic frameworks for CO2 capture, regeneration and conversion. *Nat. Rev. Mater*. 2:17045. doi: 10.1038/natrevmats.2017.45

Vieno, N. M., Härkki, H., Tuhkanen, T., and Kronberg, L. (2007). Occurrence of pharmaceuticals in river water and their elimination in a pilot-scale drinking water treatment plant. *Environ. Sci. Technol*. 41, 5077–5084. doi: 10.1021/es062720x

Wang, C. C., Wang, X., and Liu, W. (2020). The synthesis strategies and photocatalytic performances of TiO2/MOFs composites: a state-of-the-art review. *Chem. Eng. J*. 391:123601. doi: 10.1016/j.cej.2019.123601

Wang, Q., Gao, Q., Al-Enizi, A. M., Nafady, A., and Ma, S. (2020). Recent advances in MOF-based photocatalysis: environmental remediation under visible light. *Inorg. Chem. Front*. 7, 300–339. doi: 10.1039/C9QI01120J

Wang, Z., Huang, J., Mao, J., Guo, Q., Chen, Z., and Lai, Y. (2020). Metal–organic frameworks and their derivatives with graphene composites: preparation and applications in electrocatalysis and photocatalysis. *J. Mater. Chem. A* 8, 2934–2961. doi: 10.1039/C9TA12776C

Westerhoff, P., Yoon, Y., Snyder, S., and Wert, E. (2005). Fate of endocrine-disruptor, pharmaceutical, and personal care product chemicals during simulated drinking water treatment processes. *Environ. Sci. Technol*. 39, 6649–6663. doi: 10.1021/es0484799

Wu, Z., Yuan, X., Zhong, H., Wang, H., Zeng, G., Chen, X., et al. (2016). Enhanced adsorptive removal of p-nitrophenol from water by aluminum metal–organic framework/reduced graphene oxide composite. *Sci. Rep*. 6:25638. doi: 10.1038/srep25638

Xu, P., Drewes, J. E., Bellona, C., Amy, G., Kim, T. U., Adam, M., et al. (2005). Rejection of emerging organic micropollutants in nanofiltration-reverse osmosis membrane applications. *Water Environ. Res*. 77, 40–48. doi: 10.2175/106143005X41609

Yaghi, O. M., Kalmutzki, M. J., and Diercks, C. S. (2019). Liquid- and Gas-Phase Separation in MOFs. *Introd. Reticular Chem*. 365–393. doi: 10.1002/9783527821099.ch16

Yaghi, O. M., Li, G., and Li, H. (1995). Selective binding and removal of guests in a microporous metal–organic framework. *Nature* 378, 703–706. doi: 10.1038/378703a0

Yang, D., and Gates, B. C. (2019). Catalysis by metal organic frameworks: perspective and suggestions for future research. *ACS Catal*. 9, 1779–1798. doi: 10.1021/acscatal.8b04515

Yang, M., and Bai, Q. (2019). Flower-like hierarchical Ni-Zn MOF microspheres: Efficient adsorbents for dye removal. *Colloids Surf. A* 582:123795. doi: 10.1016/j.colsurfa.2019.123795

Yang, S. J., Kim, T., Im, J. H., Kim, Y. S., Lee, K., Jung, H., et al. (2012). MOF-derived hierarchically porous carbon with exceptional porosity and hydrogen storage capacity. *Chem Mater*. 24, 464–470. doi: 10.1021/cm202554j

Yu, J., Xiong, W., Li, X., Yang, Z., Cao, J., Jia, M., et al. (2019). Functionalized MIL-53(Fe) as efficient adsorbents for removal of tetracycline antibiotics from aqueous solution. *Micropor. Mesopor. Mater*. 290:109642. doi: 10.1016/j.micromeso.2019.109642

Zhao, R., Ma, T., Zhao, S., Rong, H., Tian, Y., and Zhu, G. (2020). Uniform and stable immobilization of metal-organic frameworks into chitosan matrix for enhanced tetracycline removal from water. *Chem. Eng. J*. 382:122893. doi: 10.1016/j.cej.2019.122893

Zhao, Z., Ma, X., Kasik, A., Lin, Y. S., and Li, Z. (2013). Gas separation properties of metal organic framework (MOF-5) membranes. *Ind. Eng. Chem. Res*. 52, 1102–1108. doi: 10.1021/ie202777q

Conflict of Interest: The authors declare that the research was conducted in the absence of any commercial or financial relationships that could be construed as a potential conflict of interest.

Publication II

Materials Science and Engineering B 288 (2023) 116179

Contents lists available at ScienceDirect

Materials Science & Engineering B

journal homepage: www.elsevier.com/locate/mseb

Assessment of the robustness of MIL-88A in an aqueous solution: Experimental and DFT investigations

Maryam Hmoudah [a,b], Amjad El-Qanni [b], Riccardo Tesser [a], Roberto Esposito [a], Alessio Petrone [a,c], Ok-Sang Jung [d], Tapio Salmi [e], Vincenzo Russo [a,e,*], Martino Di Serio [a,*]

[a] University of Naples Federico II, Department of Chemical Sciences, IT-80126 Naples, Italy
[b] An-Najah National University, Department of Chemical Engineering, Nablus, Palestine
[c] Scuola Superiore Meridionale, Largo San Marcellino 10, I-80138, Napoli, Italy
[d] Pusan National University, Department of Chemistry, Busan, South Korea
[e] Åbo Akademi University, PCC, Laboratory of Industrial Chemistry and Reaction Engineering (TKR), FI-20500 Turku/ Åbo, Finland

ARTICLE INFO

Keywords:
MOFs
MIL-88A
Stability
DFT
Aqueous solution

ABSTRACT

The stability of metal organic frameworks (MOFs) in a water-rich environment is a topic of significant importance, especially for adsorption and water purification applications. MIL-88A containing iron ions and fumaric acid ligands, was synthesized through a water-based viable strategy. The robustness of MIL-88A in aqueous solutions was studied experimentally, through evaluating the chemical, thermal, and hydrolytic stability of this compound by varying the conditions and properties of aqueous solutions. Different characterization techniques were employed to explore the features of the synthesized MIL-88A such as XRD, SEM, FTIR, TGA, UV–vis DRS, zeta potential, and MP-AES measurements. The electronic structure was studied on a model nanocrystal with density functional theory (DFT) calculations. The MIL-88A structure was drastically affected in basic medium as confirmed by the characterization techniques used. MIL-88A became completely amorphous upon exposure to boiling water. The hydrolytic stability results showed that MIL-88A loses gradually its structural integrity in each water cycle.

1. Introduction

Metal organic frameworks (MOFs) are a class of compounds containing of metal ions and organic molecules that are linked together forming porous crystalline solid networks [1]. Nowadays, these materials have aroused massive attention among the scientific community due to the considerable promising applications in various fields such as gas adsorption and separation, CO_2 capturing, hydrogen and methane storage, water sorption, and biomedical applications [2–4]. Moreover, MOF hybrid structures development accelerates producing gigantic surface areas, different functionalities, and improved physical and chemical properties [1]. Nevertheless, these compounds have shown a high sensitivity when exposed to an aqueous environment which renders their exploration as effective heterogeneous catalysts [5]. However, stability concerns might hinder promising industrial applications of MOFs when compared with zeolites, activated carbon, and silica gels [6]. In the comprehensive review of Burtch et al [7] on water stability and adsorption in MOFs, they emphasized that further stability tests are required for any MOF candidates, especially for adsorption applications in aqueous solutions. Thus, further studies should be conducted in terms of structural design, and optimized synthesis strategies of these materials to enhance their stability, cost, environmental impact, and sustainability towards potential industrialization [8]. In general, the structural robustness of MOFs in aqueous conditions is assessed based on the chemical, thermal, and hydrolytic stability [7,9]. Therefore, investigating these conditions plays an important role in understanding the behaviors of MOFs. Consequently, the performance of MOFs in diverse applications can be improved. Chemical stability is among the most serious concerns, because it deals with the bond breakage and the subsequent structural crumbling. More specifically, the stronger the ion-covalent bond between the organic linker and the metal structure is, the more stable MOF is obtained. The pH of the solution has a significant influence on the chemical and hydrolytic robustness of MOFs. Acidic, neutral, and basic media can cause hydrolysis or linker displacement resulting in a possible break in a metal-linker bond [1,8]. On the other hand, the thermal stability of MOFs has a tremendous impact on their

* Corresponding authors at: University of Naples Federico II, Department of Chemical Sciences, IT-80126 Naples, Italy (V. Russo).
E-mail addresses: v.russo@unina.it (V. Russo), diserio@unina.it (M. Di Serio).

https://doi.org/10.1016/j.mseb.2022.116179
Received 28 June 2022; Received in revised form 10 November 2022; Accepted 22 November 2022
Available online 30 November 2022

Table 1
MIL-88A synthesis conditions and recyclability for various applications.

Application	Solvent	Synthesis conditions	Recyclability test	Techniques recyclability test	Remarks	Ref
Degradation of naproxen in water through persulfate activation.	Water	85 °C, 24 h	Four cycles	XRD, SEM	• The solid recovered after the first cycle was 80 % and 53 and 47 % after the second and third cycles. This was attributed to the difficulty in collecting lower amounts of MIL-88A. Broadening in the XRD peaks was observed. Some of MIL-88A homogeneity was lost with a change in the size of the rods.	[31]
Adsorption of tetracycline hydrochloride from aqueous solution.	Water	85 °C, 2 h	Three cycles	XRD, SEM	• Recyclability characterization was performed for MIL-88A.	[16]
Degradation of rhodamine B and bisphenol A under visible light.	Water	Room temperature, 24 h	Five cycles	XRD, SEM, XPS, TGA, EDS	• The weight loss difference in the TGA of the recycled MIL-88A was attributed to the changes in the guest molecules. Broadening in the XRD peaks was observed.	[14]
Enhanced Fenton-like performance for phenol removal.	Water/ DMF	65 °C, 4 h	Three cycles	XRD, SEM, XPS	• A slight decline of 3 % after at least three times recycling. SEM picture and XPS survey were almost the same, Fe ions in the solution after the reaction was not detected.	[38]
Microbial reduction of metal–organic for synergistic chromium removal.	Water	65 °C, 12 h	Stability in the presence of *S. oneidensis*	XRD	• XRD post-reduction patterns showed that MIL-88A eventually decomposed under biotic conditions after 48 h	[39]
Steering charge flow for enhanced visible-light photocatalytic degradation of ibuprofen.	DMF	100 °C, 12 h	Four cycles	XRD, ICP-OES	• Recyclability was tested only for Ag/AgCl on MIL-88A with (Fe: Ag = 2:1). The amount of leached metal ions showed that the leached amount of Fe (0.34 mg L^{-1}, 0.25 wt% of total Fe) and Ag (0.27 mg L^{-1}, 0.4 wt% of total Ag).	[18]
Decolorization of methylene blue dye.	Water	65 °C, 12 h	Four cycles	XRD, XPS, inductively coupled plasma atomic emission spectrometer	• A slight difference in the XRD peaks' sharpness was observed. The XPS data did not change after 4 cycle usages. A trace amount of Fe ions was detected after 4 cycle usages.	[40]
Removal of inorganic and organic arsenic pollutants from water with MIL-88A(Fe) decorated on cotton fibers.	Water	Room temperature, 24 h	One cycle only for MIL-88A decorated on cotton fibers	XPS, FTIR, XRD for MIL-88A powder. SEM only for MIL-88A decorated on cotton fibers	● It was hard to separate MIL-88A from the treated water for reuse. The powder mass declined to be suspended in the water solution.	[32]
ZnO doped MIL-88A for degradation of methylene blue dyes.	Water	Room temperature, 4 h	Five cycles	XRD	• XRD revealed that the catalyst had no obvious transformation with broadening in the peaks. The degradation rate of the MB with ZnO doped MIL-88A decreased due to the mass loss of the catalyst and possible iron leaching during the reaction.	[41]
Arsenic removal from water.	Water	70 °C, 12 h	NA	NA	• Low uptakes at high pH values were attributed to the possible agglomeration of MIL-88A particles.	[17]
MIL-88A for photocatalytic ozonation 4-nitrophenol (4-NP) degradation and mineralization	Water	65 °C, 12 h	Four cycles	ICP-OES, XRD, FTIR, SEM	• About 0.85 mg/L of iron is detected in the solution after 30 mins reaction. No apparent differences found in the XRD patterns, FTIR spectra, and SEM images before and after using the catalyst.	[21]

future industrial applications, especially in separation, energy relevant contexts, as well as catalytic process applications.

Environmental and cheap materials with magnetic and/or photo-degradation properties for wastewater treatment applications attracted huge attention [4,10–12]. These materials are easy to recover and regenerate. MIL-88A is an iron-based MOF that is environmentally friendly since iron is an abundant and naturally occurring element [13–15]. Besides, it is considered tempting for many adsorptive [16,17] and advanced oxidation applications [18–23], as it shows adaptability to a wide range of organic compounds, emerging contaminants, and gases and due to the low synthesis cost [24,25], and fumaric acid is high biocompatible. Additionally, the phenomena of breathing, swelling, linker rotation, and subnetwork displacement, that it exhibits, are introduced in the scientific community. Mellot-Draznieks et al., [26] described in their powder diffraction and computational study that this category of materials has an unusual flexibility feature. Nevertheless, these phenomena can directly affect the hydrolytic stability and the corresponding kinetic and thermodynamic water stability [7,25]. In recent years, several studies have explored the potential applications for MIL-88A in various fields such as wastewater treatment, corrosion inhibition, drug delivery, CO_2 capturing, and Li-S batteries [6,24,27–30]. Table 1 lists the synthesis conditions and recyclability of MIL-88A for adsorption applications. On one hand, water-based MIL-88A is favored, because DMF based MIL-88A is problematic and harmful to the environment. On the other hand, the reusability of MIL-88A is an important factor of investigation. For instance, El Asmar and co-workers [31] studied the degradation of the pharmaceutical compound naproxen, using MIL-88A, the recovered amount of MIL-88A after the first, second, and third cycles of recyclability were 80 %, 53 %, and 47 %, respectively. The authors elucidated that collecting MOFs at low amounts was hard. In another study [17] devoted to arsenic removal from water, the authors attributed the very low uptake at high pH values due to the

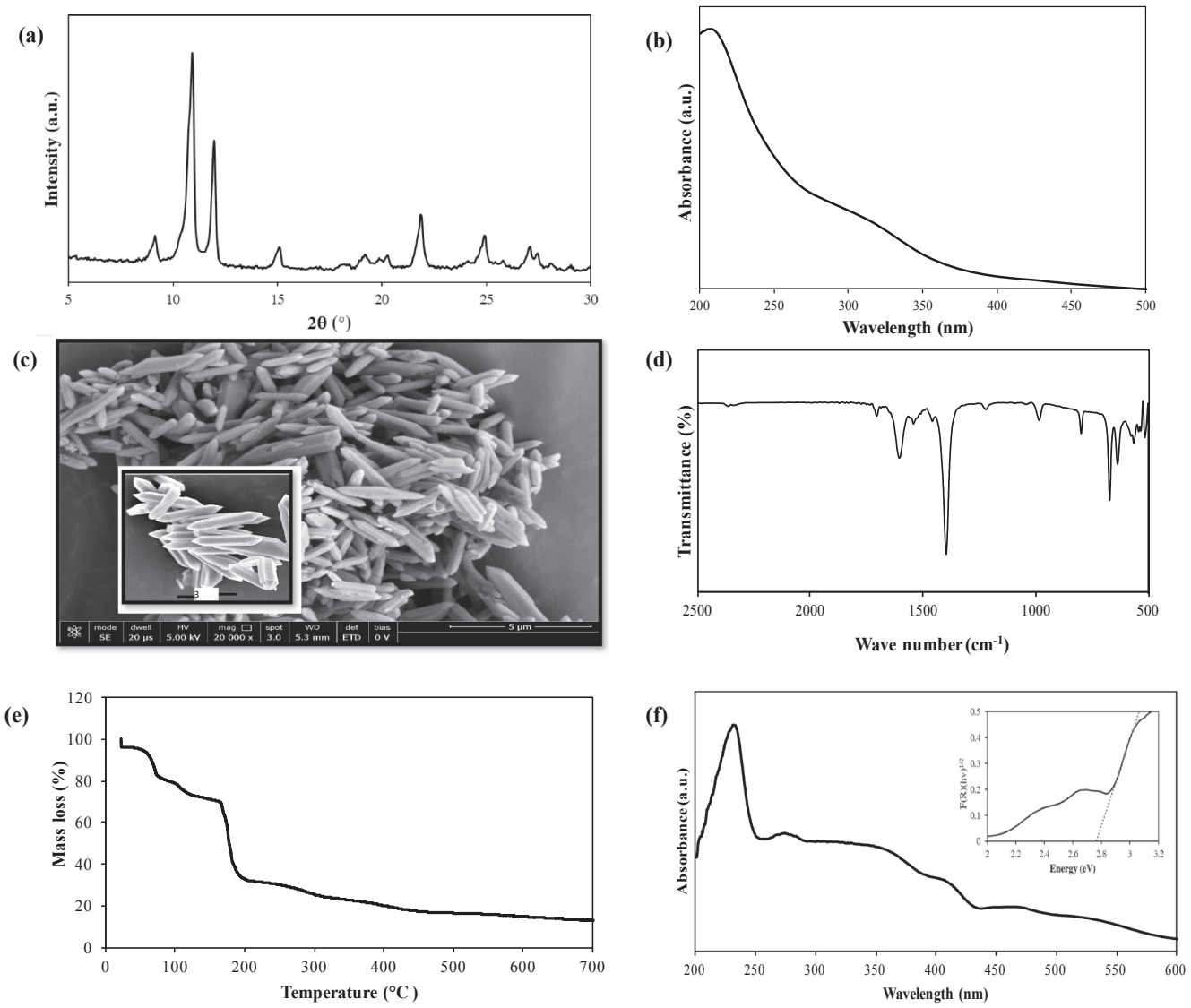

Fig. 1. Synthesized MIL-88 A characterization (a) XRD pattern (b) UV–vis spectrum in aqueous solution (c) SEM image (d) FTIR spectrum (e)TGA analysis (f) UV–vis/DRS analysis with an estimation of the optical band-gap using the modified Kubelka-Munk function.

possible agglomeration of MIL-88A. Furthermore, Pang and co-workers [32] in their study on using MIL-88A for organic and inorganic arsenic removal, highlighted that it was difficult to recover MIL-88A from the aqueous solution to be reused. Likewise, Fu and co-workers [14] investigated the synthesis of controlled size of MIL-88A via room-temperature stirring method. They concluded that smaller size shows better performance of MIL-88A and the mass loss in the reusability test could be due to the changes of the guest molecules in MIL-88A. On another hand, many studies nowadays are presenting MIL-88A as a hybrid, supported, and functionalized compound for various applications without raising the point that this category of MOFs has some stability shortcomings when used solely [18,33–35]. Furthermore, the electronic structure of MIL88-A is also investigated on a model nanocrystal *via* density functional theory (DFT) calculations. This approach has proven promising for the electronic structure and vibrational properties of inorganic and organic quantum dots used in technological applications [36,37].

Hence, this study sheds the light on the stability performance of MIL-88A in an aqueous solution, experimentally by linking what is computationally studied in this work and literature with the different experimental conditions adopted. To the best of our knowledge, experimental investigation on the stability of MIL-88A, using various characterization techniques, is explicitly addressed for the first time. This will give a deeper insight into the unusual flexibility and the mechanism of the transitions of MIL-88A.

2. Materials and methods

2.1. Materials

Iron chloride ($FeCl_3{\cdot}6H_2O$) was provided by Carlo Erba Reagents, ≥ 99.0 %, Milano, fumaric acid ($C_4H_4O_4$) was purchased from Merck, ≥ 99.0 %, Germany. Absolute ethanol (CH_3CH_2OH) was purchased from Carlo Erba Reagents, ≥ 99.5 %, Milano. For pH control, NaOH pellets and HCl 0.1 M were supplied from Merck, ≥ 99.0 %, Germany. All chemicals were commercially available and used as received without further purification. Distilled-ion exchanged (DI) water was used to exhibit<18 MOhm-cm. Calibration solution of $FeCl_3{\cdot}6H_2O$ in HCl purchased from Carlo Erba Reagents, Milan was used for digestion in MP-AES measurements.

2.2. Synthesis of MIL-88A

MIL 88A was synthesized applying a previously reported procedure

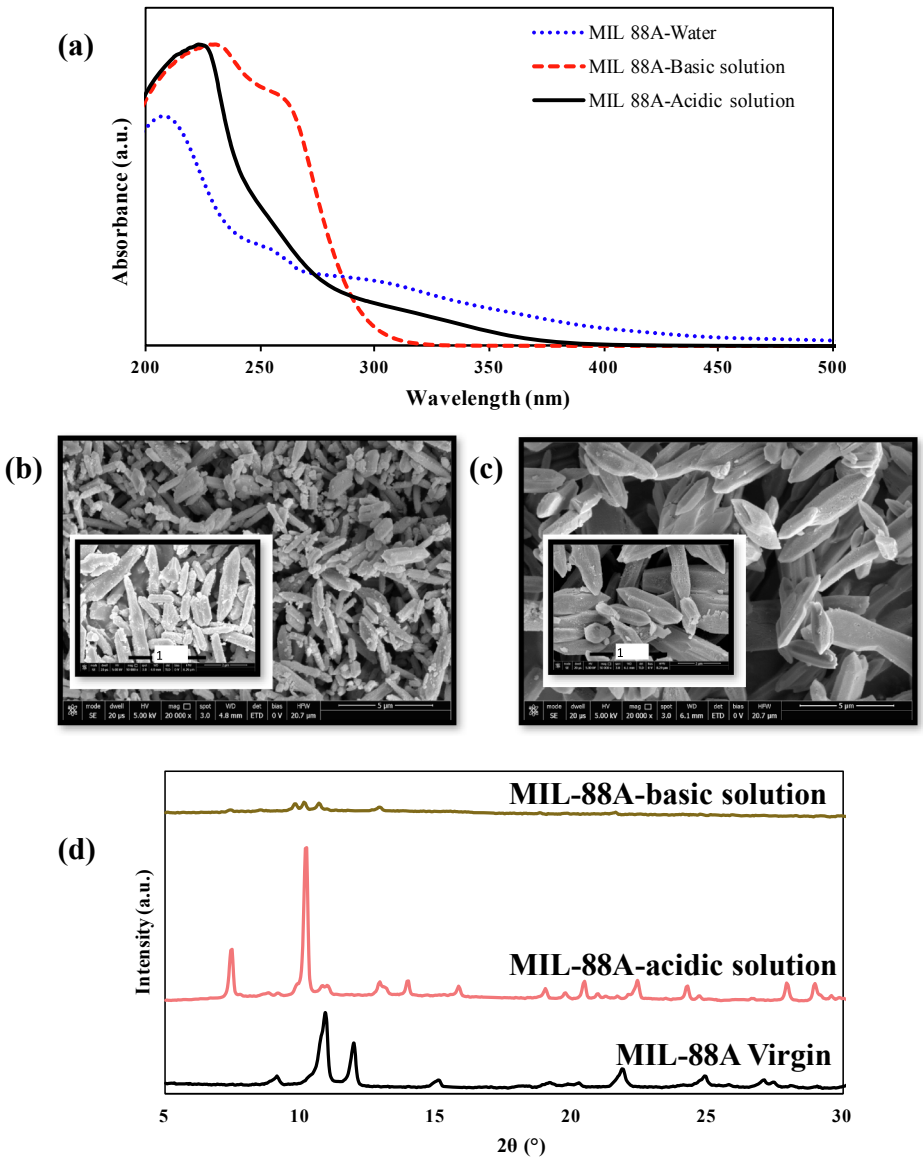

Fig. 2. MIL-88A in basic and acidic media (a) UV–vis spectra of solutions (b) SEM image of MIL-88A in contact with basic solution (c) SEM image of MIL-88A in contact with acidic solution (d) XRD patterns of MIL-88A in both acidic and basic solutions.

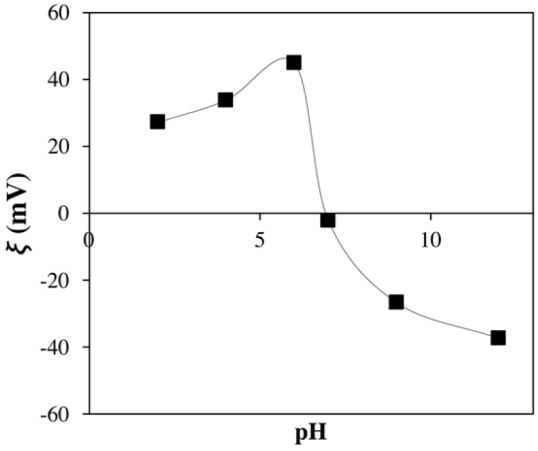

Fig. 3. Zeta potential analysis of MIL-88A.

with minor modifications [42]. In brief, 1 mmol of ferric chloride was mixed with 1 mmol of fumaric acid in 5 ml of DI water using magnetic stirring at 300 rpm, in a round bottom flask at 100 °C for 4 h. The heater then was turned off and the flask was allowed to passively cool down to room temperature. The formed solid was decanted, collected, and washed with a 1:1 ratio of ethanol and DI water three times, and the solid then was washed once with acetone to remove all the extra unreacted fumaric acid and metal. Each time, the precipitate was collected by centrifugation at 3500 rpm for 10 min. The precipitate was dried for 10 h at 60 °C in a vacuum oven (Medline scientific, Jeio Tech OV-11).

2.3. Characterization of MIL-88A

X-ray diffraction (XRD) was used to investigate the crystallinity and the crystalline domain sizes of the dried powder of MIL-88A. X-ray PANalytical Diffractometer (Malvern, Worcestershire, United Kingdom) diffraction system was used equipped with a nickel filter Cu Kα radiation operating at 40 kV and 40 mA with a θ–2θ goniometer. MIL-88A powder was placed on a zero-background holder and the scan range was 5–60°

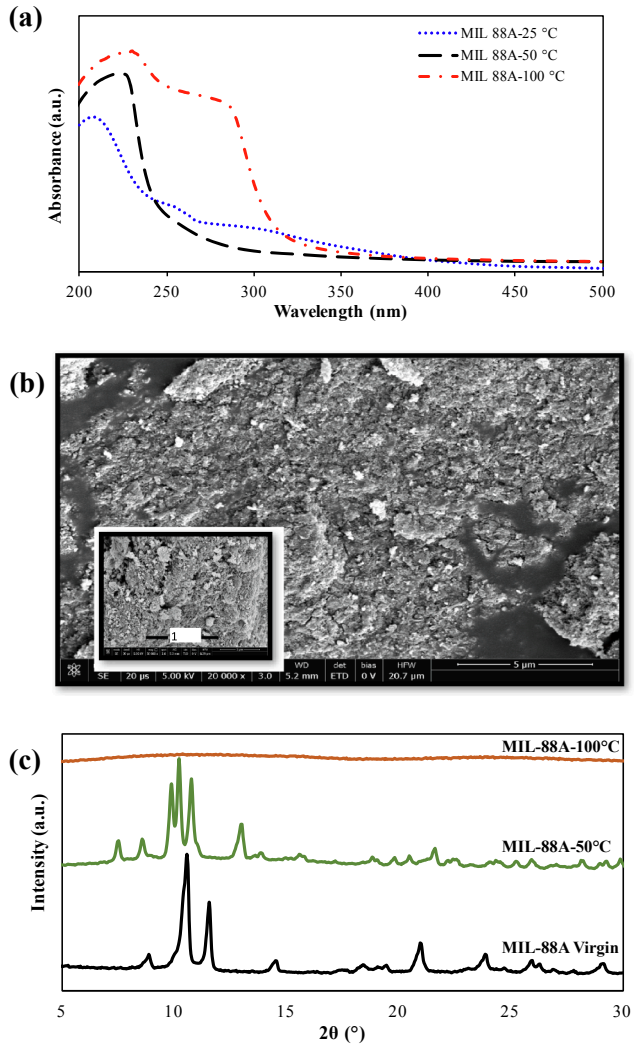

Fig. 4. MIL 88A thermal stability (a) UV–vis spectra of contact solutions at different temperatures (b) SEM and (c) XRD patterns of MIL88A after hydrothermal treatment at 50 °C and 100 °C.

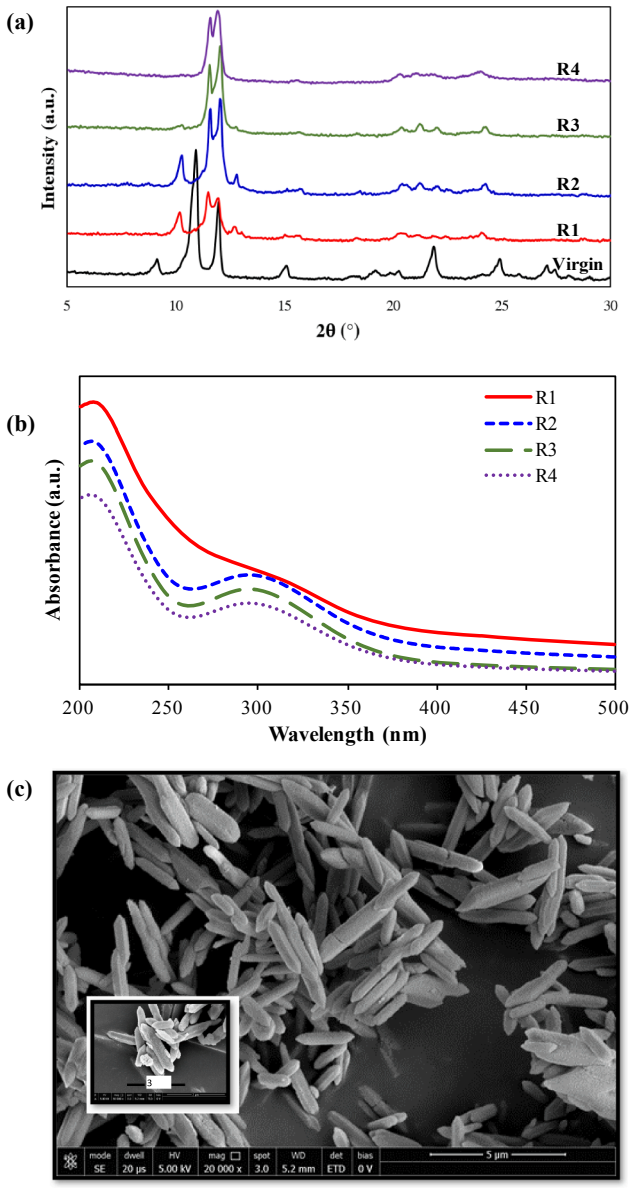

Fig. 5. MIL-88A hydrolytic stability (a) XRD spectra (b) UV–vis spectra (c) SEM image for the solid after R4 cycle.

2θ degrees using a 0.05° step and a counting time of 187 s per step. The crystalline domain size of the prepared MIL 88A was determined using the Debye–Scherrer equation by fitting the experimental profile to a pseudo-Voigt profile function, and then, calculating the full width at half maximum (FWHM) of the peak. Jasco Ultra-violet and visible (V-550 UV/VIS Spectrophotometer) was used to detect the presence of organic and inorganic compounds in the aqueous medium. Morphological properties of MIL-88A were investigated using Scanning Electron Microscopy (SEM) technique. SEM images were observed by FEI Nova NanoSEM 450 at an accelerating voltage of 5 kV with Everhart Thornley Detector (ETD) and Lens Detector (TLD) at high magnification. Infrared analysis was carried out using Thermo Nicolet Avatar 360 FTIR system. Spectrum was recorded as an average of 16 scans (range: 4000–480 cm^{-1}, resolution: 4 cm^{-1}). Thermogravimetric analysis (TGA) was performed in the presence of airflow of 100 cm^3/min and a heating rate of 10 °C/min using TG/DTG analyzer (STGA-1000, SANAF, Istanbul, Turkey). The TGA sample mass was (~20 mg). Jasco V-550 UV/VIS DRS Spectrophotometer was used to check the bandgap energy of MIL-88A. Barium sulfate was exploited as a reflectance standard. The measured intensity was expressed as the value of the Kubelka–Munk function F(R), while the band-gap value was evaluated by linearization of the plot of $(F(R)h\nu)^{1/2}$ against $h\nu$. The zeta potential values at different pH ranges were determined using Malvern Zetasizer (Malvern instruments, 300-HS, UK). MP-AES (4210 Agilent Technologies) was used to detect iron leaching in the solid. Calibration solutions were prepared volumetrically by dilution of multi-element calibration solution of $FeCl_3{\cdot}6H_2O$ in HCl.

2.4. Stability tests

Chemical stability tests were performed on the dried powder sample of MIL-88A at 60 °C under vacuum for 12 h. 0.1 g of the powder was dispersed in a glass vial and brought in contact with 50 ml of DI water of pH 6 ± 0.1 under magnet stirring for 24 h. The same procedure was repeated for the other two vials with controlled pH of 2 and 12. Each sample was then centrifuged at 3000 rpm for 30 min. The supernatant was then analyzed using UV–vis and the precipitate was characterized using XRD and SEM techniques. Similarly, for the thermal stability test, 0.1 g of the dried powder of MIL 88A was dispersed in DI water in three vials with pH 6 ± 0.1 at three different temperatures: 25 °C, 50 °C, and 100 °C. Hydrolytic stability tests were conducted by soaking 0.1g of dried powder of MIL-88A in a vial of 50 ml of DI water and pH 6 ± 0.1 with a contact time of 30 min, then each solution was centrifuged at

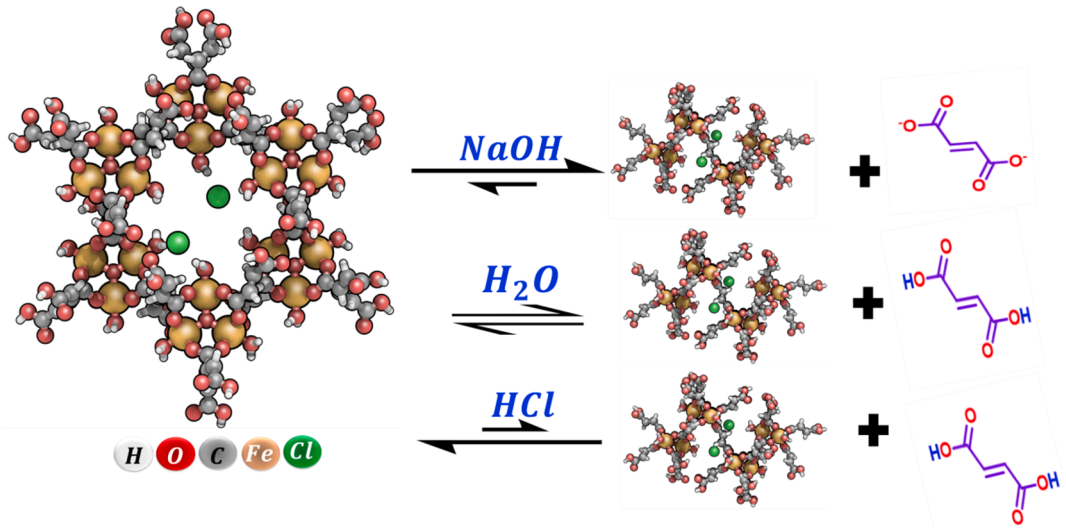

Scheme 1. Suggested dissociation of MIL-88A in different media.

Table 2
MP-AES measurements for iron content.

Wavelength	248 [nm]	260 [nm]	372 [nm]	Avg Fe content [g/m^3]
Virgin MIL-88A	14	10	15	13
4 cycles stability of MIL-88A	7	5	8	7

3000 rpm for 30 min. The supernatant was carefully decanted after centrifugation for the UV–vis measurement, and the solid was collected and dried at 60 °C under vacuum to be exposed again to fresh DI water with the same volume. This was repeated four times and the final solid was weighed to determine the mass loss. For the soaking time tests, 0.1g of dried powder of MIL-88A was added to another three vials of 50 ml of DI water and pH 6 ± 0.1 and sealed for 24 h and 14 days. The same protocol of UV–vis, XRD, and SEM analyses was repeated for all samples.

2.5. Computational details

All calculations were performed employing Density Functional Theory (DFT) using the most recent version of Gaussian electronic structure package G16.C01 [43]. A nearly C3h symmetric nanocrystal is built starting from the crystallographic unit cells (MIL-88A) [44]. Nanocluster was modeled preserving a pseudo C_3 rotational symmetry and included 6 units containing 3 Fe(III) ions each to preserve the symmetry. Each unit contains three neighboring metal centers (along a single helical chain) and their first coordination sphere. The coordination is saturated with three neutral water ligands, where each unit exposes a water molecule in the main cavity (six in total), according also previous studies, where free water molecules are located within the narrow bipyramidal cages delimited by five trimers interacting with counteranions [26,44]. Hydrogen atoms were added, and partially protonated fumarate dandling ligands, $(O_2CCH = CHCO_2H)^-$ were used for saturating the surface, preserving the overall pseudo-symmetry. The cluster also included two Cl^- counterions, obtaining a final resulting stoichiometry of $C_{120}H_{120}Cl_2Fe_{18}O_{144}^{4+}$. The electronic structure was obtained solving Kohn-Sham equation using the hybrid M06 density functional [45] with the Los Alamos double-ζ pseudocode potential and the associated valence double-ζ basis (LANL2DZ) [46,47] for the Fe and Cl, and 6-31G(d) for all other elements. The level of theory, and more in general Minnesota M06 hybrid functionals, has shown an excellent agreement with experiments, along with accurately describing the electronic structure of antiferromagnetic coupled iron-containing clusters and MOF systems [48–51]. A Broken symmetry solution was obtained by imposing a starting C_3 symmetry spin density guess. The resulting converged wavefunction preserved antiferromagnetic coupled high spin Fe^{3+} (d5) ions. The stability of the resulting optimized wavefunction was tested [52]. Only hydrogen and Cl positions were optimized. The nanocrystal was considered optimized when both the forces [maximum and root-mean-square (rms) of the force 0.0017 hartree/bohr] and displacement [rms displacement 0.01bohr] values were below the threshold criteria.

3. Results and discussion

3.1 MIL 88A characterization

The XRD pattern of MIL-88A is presented in Fig. 1a. Strong peaks appear at 2θ positions 9.1°, 10.5° and 11.9° confirming the crystallinity of the prepared MIL-88A. The average crystalline domain size of MIL-88A was calculated using the Scherrer equation at the aforementioned peaks to be 17.4 nm. Fig. 1b shows the UV–vis spectrum of MIL-88A in an aqueous solution. The absorption peak at $\lambda < 250$ nm corresponds to the ligand-to-metal charge transfer (LMCT) optical transition [24,40], while the range between 290 and 380 nm represents the presence of iron complexes in the solution [53]. The SEM image in Fig. 1c, illustrates the uniform rod-like shape of MIL-88A in the nanometer-scale, with sizes between 100 and 800 nm matching what is reported in the literature [17,40]. FTIR spectrum presented in Fig. 1d with the bands at 1396 cm^{-1} and 1603 cm^{-1} can be attributed to the symmetric and asymmetric vibration of the carboxyl group, while the band at 672 cm^{-1} can be assigned to the vibration mode of the Fe-O bond [14]. TGA analysis was used and fumaric acid significant mass loss started at around 170° C with a heating rate 10° C/min (Fig. 1e), where complete dissociation was achieved at 600° C. It is worth noting that the complete dissociation of pure fumaric acid, as reported in the literature, is around 300° C [24,54]. This confirms that fumaric acid is trapped in MIL-88A structure. Finally, Fig. 1f demonstrates the DRS spectrum of MIL-88A solid-state orange sample with the corresponding inset for the measured intensity that was expressed as the value of the Kubelka-Munk function F(R). The results indicate that MIL-88A has a wide light- absorption range (200–600 nm), which could be beneficial for photocatalytic applications. The absorption peaks of $\lambda < 400$ nm, where the optical band-gap for the transition from the valence band to the conduction band appears, was calculated by extrapolating linearization of the plot of $(F(R)h\nu)^{1/2}$ against photon energy and resulted to be equal to 2.78 eV, complying with information published in literature [18,40].

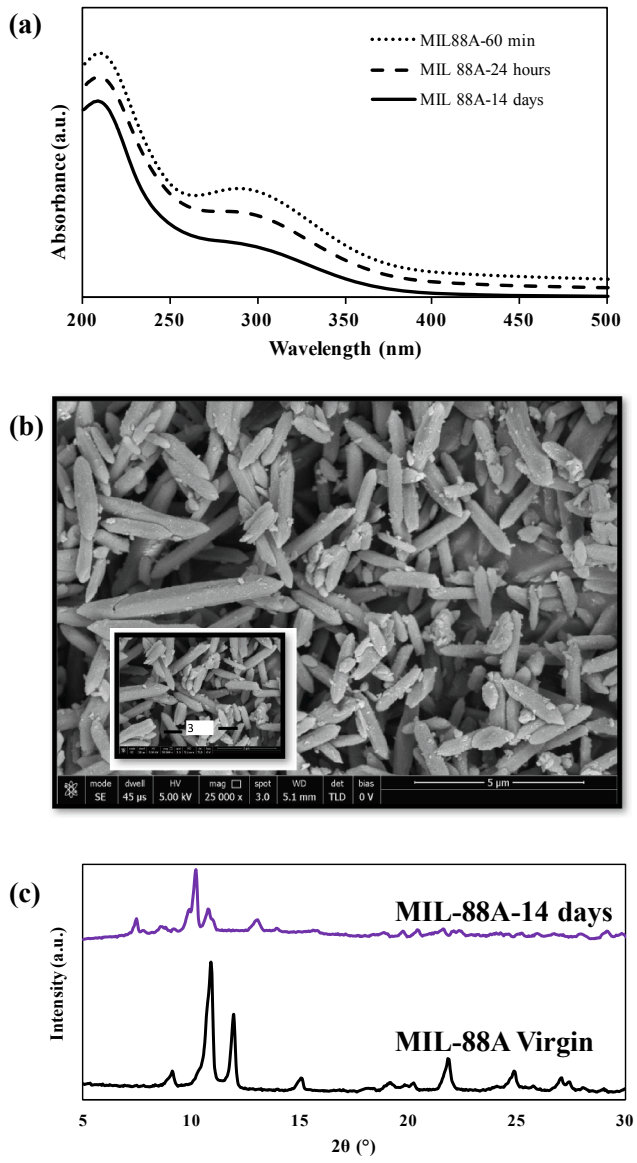

Fig. 6. MIL-88A hydrolytic stability (a) UV–vis spectra (b) SEM image of 14 days soaking time (c) XRD patterns of both virgin and 14 days of soaking in water.

3.2. Chemical stability

The pH effect on the robustness of MIL-88A was investigated under acidic, basic, and neutral conditions. Fig. 2a shows the UV–vis spectra of the solution after contact with MIL-88A in each condition. The corresponding SEM images are presented in Fig. 2b and c for both MIL-88A in basic and acidic solutions. Also, the XRD patterns of MIL-88A in different media are displayed in Fig. 2d. Clearly, the strong signal at wavelength 250 – 300 nm (Fig. 2a) indicates that dissociation of MIL-88A in the basic medium is higher compared to both acidic and neutral solutions. This could be attributed to hydrolysis, where the degradation of MIL-88A in the presence of basic medium is initiated by the cleavage of the iron-fumarate bond. Subsequently, a hydroxylated secondary building unit is formed, and the fumarate is released [1]. The SEM image of MIL-88A in basic medium (Fig. 2b) indicates the significant fragmentation of the crystals. Conversely, the crystals in the acidic medium (Fig. 2c) were very similar to the virgin MIL-88A. These observations are in line with the XRD patterns of MIL-88A in different media (Fig. 2d), which confirmed that the crystallinity in basic solution is tremendously affected. Conversely, the peaks in the acidic medium were shifted and showed a higher sharpness.

The obtained values for zeta potential analysis given in Fig. 3 show a wide range between + 27 mV and −37 mV for the pH range 2–12, indicating that MIL-88A crystals have good physical stability of nano-suspensions due to electrostatic repulsion of individual particles [55]. The high negative values in the basic range confirm that the particle surface charge is highly negative due to the iron hydrolysis, whereas in the neutral region around the point of zero charge, the values are between − 5 mV and + 5 mV indicating that MIL-88-A crystals are prone to settling and continuous stirring is recommended to maintain suspension [31,32].

3.3. Thermal stability

For the thermal stability of MIL-88A, the UV–vis spectra of contact solution, XRD pattern, and SEM images for the collected powder at different temperatures are presented in Fig. 4a-c. It is evident that raising the aqueous solution temperature directly affects the stability of MIL-88A. At 100° C, the UV–vis spectra showed a wide hub between 230 and 350 nm designating the significant release in of Fe (III) complexes in the solution. Both XRD patterns and SEM images of the thermally treated MIL-88A samples (Fig. 4b and c) confirmed that the structure became completely amorphous at 100° C.

3.4. Hydrolytic stability

The hydrolytic stability was assessed by exposing MIL-88A to a specific water amount for four cycles described as R1-R4 (short-term stability). MIL-88A virgin denotes the dried powder before being exposed to an aqueous solution. The partial dissolution over the four cycles of MIL-88A, lead to a total mass loss of 20 %, which was verified by carefully weighing the virgin MIL-88A before and after it was exposed to water. After each cycle, MIL-88A was separated carefully using centrifugation and then dried *via* a vacuum oven at 60 °C overnight. The broadening in the XRD peaks and the disappearance of some peaks as shown in Fig. 5a confirm that partial collapse in the pores occurred due to partial loss in crystallinity and the formation of an amorphous side phase. This behavior is similar to the Zn-based MOF (DMOF-TM) which decomposes upon soaking in water and loses its structural integrity, yet after the first cycle of water exposure [56]. Moreover, the corresponding UV–vis spectra of each cycle are presented in Fig. 5b. The absorbance intensities at λ values 208 nm and 298 nm vary, which confirms that the dissociation of iron ions changes in every cycle. The suggested dissociation of MIL-88A in basic, neutral, and acidic media is demonstrated in Scheme 1. Generally speaking, the Fe^{+3} ions are categorized as intermediate acids [1]. Therefore, based on the hard-soft acid-base (HSAB) theory, in the presence of water only, fumarate ligands are displaced by a combination of hydroxyls and water coordinating species, leaving the charge of the particle almost unchanged. This will lead to neutral fumaric acid being expelled from the structure. Notice that the coordinating water can undergo deprotonation and let the particles become neutral at pH of 7 as affirmed by zeta potential measurements in Fig. 3. On the contrary, in the basic medium, the fumarate ligands are displaced by hydroxyls inevitably because of the high affinity between Fe^{+3} ions and OH^{-} [57]. Thus, the negative charge of the particles will increase. This also leads to the expulsion of negatively charged fumarate ions. Conclusively, the excellent stability of MIL-88A in the acidic solution can be assigned to the low pKa of fumaric acid that endows MIL-88A structure under this condition [57,58]. These findings go also in line with the observation of Wang and coworkers study [20], who noticed that fumaric acid inhibited the performance of MIL-88A in their reaction, however, they considered that the excess fumaric acid used in the preparation of MIL-88A is the reason behind the lower catalytic degradation performance once the solid dose increased.

Fig. 5c corresponds to the SEM image of MIL-88A after R4, showing a

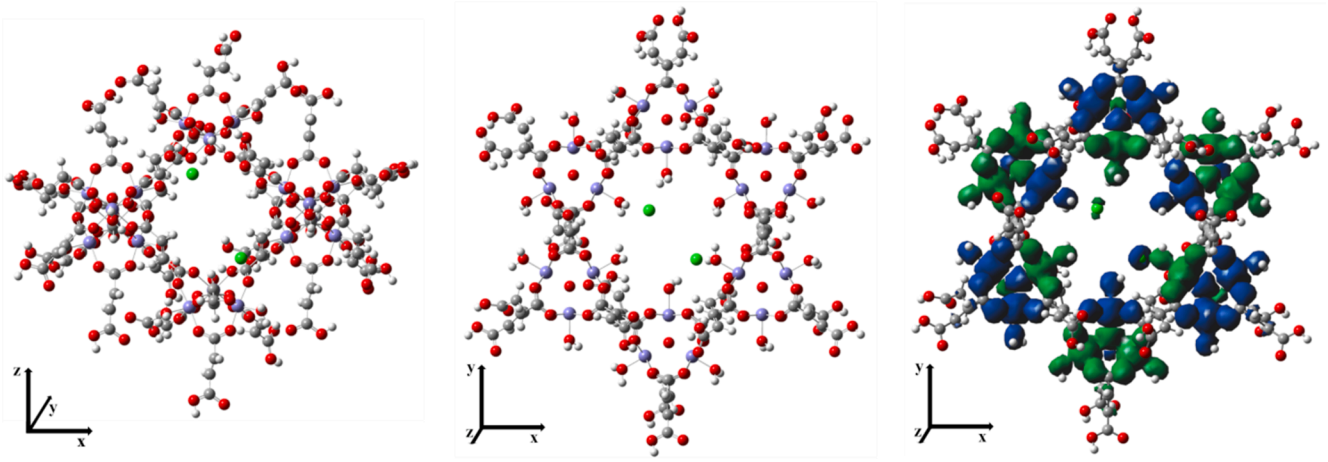

Fig. 7. MIL-88A ball and stick nanocluster representation. Lateral (left) and front (middle) views. DFT calculated spin density (right, the difference between α and β densities, green and blue as positive and negative, respectively) isosurface (isovalue = $4{\cdot}10^{-4}$). (For interpretation of the references to colour in this figure legend, the reader is referred to the web version of this article.)

very large swelling effect where the edges of the rod-like structure almost disappeared in most of the rods. This observation is in accordance with the findings of Mellot-Draznieks and co-workers [26], where the swelling phenomenon was the highest in the presence of water compared to other solvents such as methanol, ethanol, and butanol. Besides, the authors mentioned that distortion and tilting in the simulated crystal structure were noticed in the presence of water, justifying the water effect on the crystallinity robustness of these compounds.

In addition, the MP-AEs measurements reported in Table 2 for the collected solid revealed that the average iron content of virgin MIL-88A dramatically decreased, from 13 mg/m^3 to 7 mg/m^3 in R4, emphasizing that iron was leached into the aqueous solution.

The UV–vis results (Fig. 6a) for the soaking time effect (long-term stability) confirmed the presence of iron complexes, as discussed previously. Also, the SEM image for MIL-88A after 14 days of soaking (Fig. 6b) showed fragmentations in the crystals which were, however, not as significant as those observed in the basic medium. These losses in the crystallinity indicate the low thermodynamic stability of MIL88A [7] as also confirmed by the XRD spectra Fig. 6c, which showed broadening in the peaks with a lesser intensity, after 14 days of soaking in water.

3.5. *Nanocluster modeling and electronic structure*

MIL-88A nanocrystal was modeled preserving a C_3 rotational symmetry and it is reported in Fig. 7. This nanocluster included six units containing three Fe^{3+} ions to preserve the symmetry. Each Fe^{3+} presents an almost octahedral coordination, where each iron-containing unit presents six carboxylate bidentate ligands, where two are kept as bridging ligands between two different units. Each unit has a cavity, where the oxygen atoms are almost equally shared among the three iron atoms. The cluster presents thus an internal cavity of ~ 11 Å diameter enabling it to accommodate at least two chlorine ions, 7 Å apart from each other. The electronic structure of the nanocluster results in a stable antiferromagnetic coupled high-spin sextet ground state for the iron(III) centra, where also the spin density (right panel of Fig. 7) preserves the C_3 symmetry. This result is in agreement with similar iron-containing catalytic active MOF systems [51].

Notably, the spin density spreads further from the iron centra and involves almost all atoms in the first coordination shell of the iron ions, resulting in an alternating spin density also in the water molecules inside the main cavity. Although these are conceptual results, it is interesting to point out the spin density delocalization, since water sites might be directly involved in the catalytic activity of the system.

4. Conclusions

Nowadays, many MOFs that can be considered of revolutionizing applications, are unstable in water. Therefore, the stability studies of MOFs can be of paramount importance to take the stride towards future industrialization. Hence, the robustness of MIL-88A in aqueous solution was investigated experimentally, in terms of chemical, thermal, and hydrolytic stability under various conditions and by employing the characterization techniques such as XRD, SEM, zeta potential, and MP-AES. Based on the aforementioned results obtained of the chemical stability, it can be concluded that the basic medium, has a significant effect on the rigidity of MIL-88A, where iron complexes were released in the solution. On the other hand, thermal stability results assured that this category of MOFs is thermodynamically unstable since the crystal structure was remarkably affected when water temperature increases up to 100° C. The hydrolytic stability tests provided insights into the kinetic stability of MIL-88A. The notable 20 % loss in weight after the exposure to water four times indicates these compounds are not very competitive to zeolite-based materials, for example. Also, the conducted XRD investigation revealed that the crystallinity of the structure is affected in each water exposure cycle. The MP-AEs iron content results of virgin MIL-88A and that exposed to water for four cycles, confirmed that iron was seriously leached from the structure. The nanocrystal cluster model was employed to unveil important electronic and structural properties of MIL-88A, to understand the possible dissociation mechanism. Based on parameters studied, it can be concluded that the structure of MIL-88A can be strongly affected by the presence of water and in the future we plan to also understand the mechanism and the energetic effect of such attack. Therefore, further investigations should be conducted to improve the stability of MIL-88A and to expand its potential industrial green applications. Also, spectroscopic studies should be performed to include the effect of different surrounding atoms because they can affect vibrational and electronic spectra.

Declaration of Competing Interest

The authors declare that they have no known competing financial interests or personal relationships that could have appeared to influence the work reported in this paper.

Data availability

No data was used for the research described in the article.

Acknowledgments

The authors wish to thank Rocco Di Girolamo from the University of Naples Federico II, for his.

help in running the XRD and SEM tests, and Nafith Dwaikat from An-Najah National University for running the TGA and FTIR tests. The fellowship provided by Faculty for the Future Program—Schlumberger Foundation to Maryam Hmoudah is deeply acknowledged and appreciated.

Funding

12th executive program for scientific and technological cooperation between the Italian Republic and the Republic of Korea for the years 2019-2021 is acknowledged for financial support. Italian Ministry of Education, University and Research (MIUR), is also gratefully acknowledged for financial support (AP: Project AIM1829571-1 CUP E61G19000090002). Financial support by Academy of Finland is acknowledged (Grant 319002).

Author Contributions

Maryam Hmoudah wrote the original draft of the manuscript. The main conceptual ideas, supervision, planning, and coordination of research activities were monitored by Vincenzo Russo and Martino Di Serio. The experimental work was conducted by Maryam Hmoudah. Data elaboration, and the formal analysis were conducted by Maryam Hmoudah, Amjad El-Qanni, Riccardo Tesser, and Ok-Sang Jung. Alessio Petrone conceived the cluster model, performing and analyzing the electronic structure calculations. Roberto Esposito contributed to the synthesis of the MIL-88A. The mechanism interpretation was provided by Maryam Hmoudah, Tapio Salmi, and Vincenzo Russo. The final draft was revised by all the authors. Funding was obtained by Martino Di Serio and Tapio Salmi.

References

[1] O.M. Yaghi, M.J. Kalmutzki, C. Diercks, Introduction to reticular chemistry, Mol. Front. J. 4 (2019).
[2] S. Chuhadiya, D. Himanshu, S.L. Suthar, M.S.D. Patel, Metal organic frameworks as hybrid porous materials for energy storage and conversion devices: A review, Coord. Chem. Rev. 446 (2021), 214115, https://doi.org/10.1016/j.ccr.2021.214115.
[3] S. Li, S. Shan, S. Chen, H. Li, Z. Li, Y. Liang, J. Fei, L. Xie, J. Li, Photocatalytic degradation of hazardous organic pollutants in water by Fe-MOFs and their composites: A review, J. Environ. Chem. Eng. 9 (5) (2021), 105967, https://doi.org/10.1016/j.jece.2021.105967.
[4] V. Russo, M. Hmoudah, F. Broccoli, M.R. Iesce, O.-S. Jung, M. Di Serio, Applications of Metal Organic Frameworks in Wastewater Treatment: A Review on Adsorption and Photodegradation, Frontiers, Chem. Eng. 2 (15) (2020), https://doi.org/10.3389/fceng.2020.581487.
[5] M. Ding, X. Cai, H.-L. Jiang, Improving MOF stability: approaches and applications, Chem. Sci. 10 (44) (2019) 10209–10230, https://doi.org/10.1039/C9SC03916C.
[6] A.J. Howarth, Y. Liu, P. Li, Z. Li, T.C. Wang, J.T. Hupp, O.K. Farha, Chemical, thermal and mechanical stabilities of metal–organic frameworks, Nat. Rev. Mater. 1 (3) (2016) 15018, https://doi.org/10.1038/natrevmats.2015.18.
[7] N.C. Burtch, H. Jasuja, K.S. Walton, Water Stability and Adsorption in Metal-Organic Frameworks, Chem. Rev. 114 (20) (2014) 10575–10612, https://doi.org/10.1021/cr5002589.
[8] B.S. Gelfand, G.K.H. Shimizu, Parameterizing and grading hydrolytic stability in metal–organic frameworks, Dalton Trans. 45 (9) (2016) 3668–3678, https://doi.org/10.1039/C5DT04049C.
[9] B. Liu, K. Vikrant, K.-H. Kim, V. Kumar, S.K. Kailasa, Critical role of water stability in metal–organic frameworks and advanced modification strategies for the extension of their applicability, Environ. Sci. Nano 7 (5) (2020) 1319–1347, https://doi.org/10.1039/C9EN01321K.
[10] M. Hmoudah, A. El-Qanni, S. Abuhatab, N.N. Marei, A. El-Hamouz, B.J. A. Tarboush, I.H. Alsurakji, H.M. Baniowda, V. Russo, M. Di Serio, Competitive adsorption of Alizarin Red S and Bromocresol Green from aqueous solutions using brookite TiO2 nanoparticles: experimental and molecular dynamics simulation, Environ. Sci. Pollut. Res. 29 (51) (2022) 77992–78008, https://doi.org/10.1007/s11356-022-21368-7.
[11] N. Gallucci, M. Hmoudah, E. Martinez, A. El-Qanni, M. Di Serio, L. Paduano, G. Vitiello, V. Russo, Photodegradation of ibuprofen using CeO2 nanostructured materials: Reaction kinetics, modeling, and thermodynamics, J. Environ. Chem. Eng. 10 (3) (2022), 107866, https://doi.org/10.1016/j.jece.2022.107866.
[12] A. El-Qanni, N.N. Nassar, G. Vitale, A. Hassan, Maghemite nanosorbcats for methylene blue adsorption and subsequent catalytic thermo-oxidative decomposition: Computational modeling and thermodynamics studies, J. Colloid Interface Sci. 461 (2016) 396–408, https://doi.org/10.1016/j.jcis.2015.09.041.
[13] Y. Li, Y. Fang, Z. Cao, N. Li, D. Chen, Q. Xu, J. Lu, Construction of g-C3N4/PDI@MOF heterojunctions for the highly efficient visible light-driven degradation of pharmaceutical and phenolic micropollutants, Appl Catal B 250 (2019) 150–162, https://doi.org/10.1016/j.apcatb.2019.03.024.
[14] H. Fu, X.-X. Song, L. Wu, C. Zhao, P. Wang, C.-C. Wang, Room-temperature preparation of MIL-88A as a heterogeneous photo-Fenton catalyst for degradation of rhodamine B and bisphenol a under visible light, Mater. Res. Bull. 125 (2020), 110806, https://doi.org/10.1016/j.materresbull.2020.110806.
[15] M. Melchiorre, D. Lentini, M.E. Cucciolito, F. Taddeo, M. Hmoudah, M. Di Serio, F. Ruffo, V. Russo, R. Esposito, Sustainable Ketalization of Glycerol with Ethyl Levulinate Catalyzed by the Iron(III)-Based Metal-Organic Framework MIL-88A, Molecules 27 (21) (2022) 7229.
[16] Z. Zhang, Y. Chen, Z. Wang, C. Hu, D. Ma, W. Chen, T. Ao, Effective and structure-controlled adsorption of tetracycline hydrochloride from aqueous solution by using Fe-based metal-organic frameworks, Appl. Surf. Sci. 542 (2021), 148662, https://doi.org/10.1016/j.apsusc.2020.148662.
[17] H. Wu, M.-D. Ma, W.-Z. Gai, H. Yang, J.-G. Zhou, Z. Cheng, P. Xu, Z.-Y. Deng, Arsenic removal from water by metal-organic framework MIL-88A microrods, Environ. Sci. Pollut. Res. 25 (27) (2018) 27196–27202, https://doi.org/10.1007/s11356-018-2751-2.
[18] W. Huang, C. Jing, X. Zhang, M. Tang, L. Tang, M. Wu, N. Liu, Integration of plasmonic effect into spindle-shaped MIL-88A(Fe): Steering charge flow for enhanced visible-light photocatalytic degradation of ibuprofen, Chem. Eng. J. 349 (2018) 603–612, https://doi.org/10.1016/j.cej.2018.05.121.
[19] J.-S. Wang, X.-H. Yi, X. Xu, H. Ji, A.M. Alanazi, C.-C. Wang, C. Zhao, Y.V. Kaneti, P. Wang, W. Liu, Y. Yamauchi, Eliminating tetracycline antibiotics matrix via photoactivated sulfate radical-based advanced oxidation process over the immobilized MIL-88A: Batch and continuous experiments, Chem. Eng. J. 431 (2022), 133213, https://doi.org/10.1016/j.cej.2021.133213.
[20] J. Wang, J. Wan, Y. Ma, Y. Wang, M. Pu, Z. Guan, Metal–organic frameworks MIL-88A with suitable synthesis conditions and optimal dosage for effective catalytic degradation of Orange G through persulfate activation, RSC Adv. 6 (113) (2016) 112502–112511, https://doi.org/10.1039/C6RA24429G.
[21] D. Yu, L. Li, M. Wu, J.C. Crittenden, Enhanced photocatalytic ozonation of organic pollutants using an iron-based metal-organic framework, Appl Catal B 251 (2019) 66–75, https://doi.org/10.1016/j.apcatb.2019.03.050.
[22] X.-H. Yi, H. Ji, C.-C. Wang, Y. Li, Y.-H. Li, C. Zhao, A. Wang, H. Fu, P. Wang, X. Zhao, W. Liu, Photocatalysis-activated SR-AOP over PDINH/MIL-88A(Fe) composites for boosted chloroquine phosphate degradation: Performance, mechanism, pathway and DFT calculations, Appl Catal B 293 (2021), 120229, https://doi.org/10.1016/j.apcatb.2021.120229.
[23] X.-W. Zhang, F. Wang, C.-C. Wang, P. Wang, H. Fu, C. Zhao, Photocatalysis activation of peroxodisulfate over the supported Fe3O4 catalyst derived from MIL-88A(Fe) for efficient tetracycline hydrochloride degradation, Chem. Eng. J. 426 (2021), 131927, https://doi.org/10.1016/j.cej.2021.131927.
[24] N. Alipanah, H. Yari, M. Mahdavian, B. Ramezanzadeh, G. Bahlakeh, MIL-88A (Fe) filler with duplicate corrosion inhibitive/barrier effect for epoxy coatings: Electrochemical, molecular simulation, and cathodic delamination studies, J. Ind. Eng. Chem. 97 (2021) 200–215, https://doi.org/10.1016/j.jiec.2021.01.035.
[25] A. Schneemann, V. Bon, I. Schwedler, I. Senkovska, S. Kaskel, R.A. Fischer, Flexible metal–organic frameworks, Chem. Soc. Rev. 43 (16) (2014) 6062–6096, https://doi.org/10.1039/C4CS00101J.
[26] C. Mellot-Draznieks, C. Serre, S. Surblé, N. Audebrand, G. Férey, Very Large Swelling in Hybrid Frameworks: A Combined Computational and Powder Diffraction Study, J. Am. Chem. Soc. 127 (46) (2005) 16273–16278, https://doi.org/10.1021/ja054900x.
[27] A. Benítez, J. Amaro-Gahete, D. Esquivel, F.J. Romero-Salguero, J. Morales, Á. Caballero, MIL-88A Metal-Organic Framework as a Stable Sulfur-Host Cathode for Long-Cycle Li-S Batteries, Nanomaterials 10 (3) (2020), https://doi.org/10.3390/nano10030424.
[28] D. Yu, L. Wang, T. Yang, G. Yang, D. Wang, H. Ni, M. Wu, Tuning Lewis acidity of iron-based metal-organic frameworks for enhanced catalytic ozonation, Chem. Eng. J. 404 (2021), 127075, https://doi.org/10.1016/j.cej.2020.127075.
[29] X. Liao, F. Wang, Y. Wang, Y. Cai, H. Liu, X. Wang, Y. Zhu, L. Chen, Y. Yao, Q. Hao, Constructing Fe-based bi-MOFs for photo-catalytic ozonation of organic pollutants in Fischer-Tropsch waste water, Appl. Surf. Sci. 509 (2020), 145378, https://doi.org/10.1016/j.apsusc.2020.145378.
[30] X. Wu, H. Zhao, J. Xu, Z. Zhang, W. Sheng, S. Dai, T. Xu, S. Zhang, X. Wang, Y. Wang, X. Li, Facile synthesis of MOFs derived Fe7S8/C composites for high capacity and long-life rechargeable lithium/sodium batteries, Appl. Surf. Sci. 492 (2019) 504–512, https://doi.org/10.1016/j.apsusc.2019.06.217.
[31] R. El Asmar, A. Baalbaki, Z. Abou Khalil, S. Naim, A. Bejjani, A. Ghauch, Iron-based metal organic framework MIL-88-A for the degradation of naproxen in water through persulfate activation, Chemical Engineering Journal 405 (2021), 126701, https://doi.org/10.1016/j.cej.2020.126701.
[32] D. Pang, C.-C. Wang, P. Wang, W. Liu, H. Fu, C. Zhao, Superior removal of inorganic and organic arsenic pollutants from water with MIL-88A(Fe) decorated on cotton fibers, Chemosphere 254 (2020), 126829, https://doi.org/10.1016/j.chemosphere.2020.126829.

[33] L. Wang, Y. Zhang, X. Li, Y. Xie, J. He, J. Yu, Y. Song, The MIL-88A-Derived Fe3O4-Carbon Hierarchical Nanocomposites for Electrochemical Sensing, Sci. Rep. 5 (1) (2015) 14341, https://doi.org/10.1038/srep14341.
[34] R. Yuan, J. Qiu, C. Yue, C. Shen, D. Li, C. Zhu, F. Liu, A. Li, Self-assembled hierarchical and bifunctional MIL-88A(Fe)@ZnIn2S4 heterostructure as a reusable sunlight-driven photocatalyst for highly efficient water purification, Chem. Eng. J. 401 (2020), 126020, https://doi.org/10.1016/j.cej.2020.126020.
[35] B. Xue, L. Du, J. Jin, H. Meng, J. Mi, In situ growth of MIL-88A into polyacrylate and its application in highly efficient photocatalytic degradation of organic pollutants in water, Appl. Surf. Sci. 564 (2021), 150404, https://doi.org/10.1016/j.apsusc.2021.150404.
[36] R.A. Beck, A. Petrone, J.M. Kasper, M.J. Crane, P.J. Pauzauskie, X. Li, Effect of Surface Passivation on Nanodiamond Crystallinity, J. Phys. Chem. C 122 (15) (2018) 8573–8580, https://doi.org/10.1021/acs.jpcc.8b00354.
[37] E.Q. Chong, D.B. Lingerfelt, A. Petrone, X. Li, Classical or Quantum? A Computational Study of Small Ion Diffusion in II–VI Semiconductor Quantum Dots, J. Phys. Chem. C 120 (34) (2016) 19434–19441, https://doi.org/10.1021/acs.jpcc.6b05883.
[38] X. Liao, F. Wang, F. Wang, Y. Cai, Y. Yao, B.-T. Teng, Q. Hao, L. Shuxiang, Synthesis of (100) surface oriented MIL-88A-Fe with rod-like structure and its enhanced fenton-like performance for phenol removal, Appl Catal B 259 (2019), 118064, https://doi.org/10.1016/j.apcatb.2019.118064.
[39] S.K. Springthorpe, C.M. Dundas, B.K. Keitz, Microbial reduction of metal-organic frameworks enables synergistic chromium removal, Nat. Commun. 10 (1) (2019) 5212, https://doi.org/10.1038/s41467-019-13219-w.
[40] W.-T. Xu, L. Ma, F. Ke, F.-M. Peng, G.-S. Xu, Y.-H. Shen, J.-F. Zhu, L.-G. Qiu, Y.-P. Yuan, Metal–organic frameworks MIL-88A hexagonal microrods as a new photocatalyst for efficient decolorization of methylene blue dye, Dalton Trans. 43 (9) (2014) 3792–3798, https://doi.org/10.1039/C3DT52574K.
[41] G. Ren, K. Zhao, L. Zhao, A Fenton-like method using ZnO doped MIL-88A for degradation of methylene blue dyes, RSC Adv. 10 (66) (2020) 39973–39980, https://doi.org/10.1039/D0RA08076D.
[42] T. Chalati, P. Horcajada, R. Gref, P. Couvreur, C. Serre, Optimisation of the synthesis of MOF nanoparticles made of flexible porous iron fumarate MIL-88A, J. Mater. Chem. 21 (7) (2011) 2220–2227, https://doi.org/10.1039/C0JM03563G.
[43] M.J. Frisch, G.W. Trucks, H.B. Schlegel, G.E. Scuseria, M.A. Robb, J.R. Cheeseman, G. Scalmani, V. Barone, G.A. Petersson, H. Nakatsuji, X. Li, M. Caricato, A.V. Marenich, J. Bloino, B.G. Janesko, R. Gomperts, B. Mennucci, H.P. Hratchian, J.V. Ortiz, A.F. Izmaylov, J.L. Sonnenberg, Williams, F. Ding, F. Lipparini, F. Egidi, J. Goings, B. Peng, A. Petrone, T. Henderson, D. Ranasinghe, V.G. Zakrzewski, J. Gao, N. Rega, G. Zheng, W. Liang, M. Hada, M. Ehara, K. Toyota, R. Fukuda, J. Hasegawa, M. Ishida, T. Nakajima, Y. Honda, O. Kitao, H. Nakai, T. Vreven, K. Throssell, J.A. Montgomery Jr., J.E. Peralta, F. Ogliaro, M.J. Bearpark, J.J. Heyd, E.N. Brothers, K.N. Kudin, V.N. Staroverov, T.A. Keith, R. Kobayashi, J. Normand, K. Raghavachari, A.P. Rendell, J.C. Burant, S.S. Iyengar, J. Tomasi, M. Cossi, J.M. Millam, M. Klene, C. Adamo, R. Cammi, J.W. Ochterski, R.L. Martin, K. Morokuma, O. Farkas, J.B. Foresman, D.J. Fox, Gaussian 16 Rev. C.01, Wallingford, CT, 2016.
[44] C. Serre, C. Mellot-Draznieks, S. Surblé, N. Audebrand, Y. Filinchuk, G. Férey, Role of Solvent-Host Interactions That Lead to Very Large Swelling of Hybrid Frameworks, Science 315 (5820) (2007) 1828–1831, https://doi.org/10.1126/science.1137975.
[45] Y. Zhao, D.G. Truhlar, The M06 suite of density functionals for main group thermochemistry, thermochemical kinetics, noncovalent interactions, excited states, and transition elements: two new functionals and systematic testing of four M06-class functionals and 12 other functionals, Theor. Chem. Acc. 120 (1) (2008) 215–241, https://doi.org/10.1007/s00214-007-0310-x.
[46] P.J. Hay, W.R. Wadt, Ab initio effective core potentials for molecular calculations, Potentials for K to Au including the outermost core orbitals, The Journal of Chemical Physics 82 (1) (1985) 299–310, https://doi.org/10.1063/1.448975.
[47] W.R. Wadt, P.J. Hay, Ab initio effective core potentials for molecular calculations, Potentials for main group elements Na to Bi, The Journal of Chemical Physics 82 (1) (1985) 284–298, https://doi.org/10.1063/1.448800.
[48] M.A. Ortuño, V. Bernales, L. Gagliardi, C.J. Cramer, Computational Study of First-Row Transition Metals Supported on MOF NU-1000 for Catalytic Acceptorless Alcohol Dehydrogenation, J. Phys. Chem. C 120 (43) (2016) 24697–24705, https://doi.org/10.1021/acs.jpcc.6b06381.
[49] N. Planas, J.E. Mondloch, S. Tussupbayev, J. Borycz, L. Gagliardi, J.T. Hupp, O. K. Farha, C.J. Cramer, Defining the Proton Topology of the Zr6-Based Metal-Organic Framework NU-1000, The Journal of Physical Chemistry Letters 5 (21) (2014) 3716–3723, https://doi.org/10.1021/jz501899j.
[50] R. Esposito, U. Raucci, M.E. Cucciolito, R. Di Guida, C. Scamardella, N. Rega, F. Ruffo, Iron(III) Complexes for Highly Efficient and Sustainable Ketalization of Glycerol: A Combined Experimental and Theoretical Study, ACS Omega 4 (1) (2019) 688–698, https://doi.org/10.1021/acsomega.8b02546.
[51] D.J. Xiao, E.D. Bloch, J.A. Mason, W.L. Queen, M.R. Hudson, N. Planas, J. Borycz, A.L. Dzubak, P. Verma, K. Lee, F. Bonino, V. Crocellà, J. Yano, S. Bordiga, D. G. Truhlar, L. Gagliardi, C.M. Brown, J.R. Long, Oxidation of ethane to ethanol by N2O in a metal–organic framework with coordinatively unsaturated iron(II) sites, Nat. Chem. 6 (7) (2014) 590–595, https://doi.org/10.1038/nchem.1956.
[52] R. Bauernschmitt, R. Ahlrichs, Stability analysis for solutions of the closed shell Kohn-Sham equation, J. Chem. Phys. 104 (22) (1996) 9047–9052, https://doi.org/10.1063/1.471637.
[53] H. Gallard, J. De Laat, B. Legube, Spectrophotometric study of the formation of iron(III)-hydroperoxy complexes in homogeneous aqueous solutions, Water Res. 33 (13) (1999) 2929–2936, https://doi.org/10.1016/S0043-1354(99)00007-X.
[54] E.Y. Ionashiro, F.J. Caires, A.B. Siqueira, L.S. Lima, C.T. Carvalho, Thermal behaviour of fumaric acid, sodium fumarate and its compounds with light trivalent lanthanides in air atmosphere, J. Therm. Anal. Calorim. 108 (3) (2012) 1183–1188, https://doi.org/10.1007/s10973-011-1660-0.
[55] A.A. Barba, S. Bochicchio, A. Dalmoro, D. Caccavo, S. Cascone, G. Lamberti, Chapter 10 - Polymeric and lipid-based systems for controlled drug release: an engineering point of view, in: A.M. Grumezescu (Ed.), Nanomaterials for Drug Delivery and Therapy, William Andrew Publishing, 2019, pp. 267–304.
[56] H. Jasuja, N.C. Burtch, Y.-G. Huang, Y. Cai, K.S. Walton, Kinetic Water Stability of an Isostructural Family of Zinc-Based Pillared Metal-Organic Frameworks, Langmuir 29 (2) (2013) 633–642, https://doi.org/10.1021/la304204k.
[57] S. Yuan, L. Feng, K. Wang, J. Pang, M. Bosch, C. Lollar, Y. Sun, J. Qin, X. Yang, P. Zhang, Q. Wang, L. Zou, Y. Zhang, L. Zhang, Y. Fang, J. Li, H.-C. Zhou, Stable Metal-Organic Frameworks: Design, Synthesis, and Applications, Adv. Mater. 30 (37) (2018) 1704303, https://doi.org/10.1002/adma.201704303.
[58] H. Furukawa, F. Gándara, Y.-B. Zhang, J. Jiang, W.L. Queen, M.R. Hudson, O. M. Yaghi, Water Adsorption in Porous Metal-Organic Frameworks and Related Materials, J. Am. Chem. Soc. 136 (11) (2014) 4369–4381, https://doi.org/10.1021/ja500330a.

Publication III

Environmental Science and Pollution Research (2022) 29:77992–78008
https://doi.org/10.1007/s11356-022-21368-7

RESEARCH ARTICLE

Competitive adsorption of Alizarin Red S and Bromocresol Green from aqueous solutions using brookite TiO_2 nanoparticles: experimental and molecular dynamics simulation

Maryam Hmoudah[1,2] · Amjad El-Qanni[1] · Saqr Abuhatab[3] · Nedal N. Marei[3] · Amer El-Hamouz[1] · Belal J. Abu Tarboush[4] · Ihab H. Alsurakji[5] · Hanaa M. Baniowda[1] · Vincenzo Russo[2] · Martino Di Serio[2]

Received: 19 March 2022 / Accepted: 5 June 2022 / Published online: 11 June 2022

Abstract

In this work, the effective adsorption and the subsequent photodegradation activity, of TiO_2 brookite nanoparticles, for the removal of anionic dyes, namely, Alizarin Red S (ARS) and Bromocresol Green (BCG) were studied. Batch adsorption experiments were conducted to investigate the effect of both dyes' concentration, contact time, and temperature. Photodegradation experiments for the adsorbed dyes were achieved using ultraviolet light illumination (6 W, $\lambda = 365$ nm). The single adsorption isotherms were fitted to the Sips model. The binary adsorption isotherms were fitted using the Extended-Sips model. The results of adsorption isotherms showed that the estimated maximum adsorption uptakes in the binary system were around 140 mg g^{-1} and 45.5 mg g^{-1} for ARS and BCG, respectively. In terms of adsorption kinetics, the uptake toward ARS was faster than BCG molecules in which the equilibrium was obtained in 7 min for ARS, while it took 180 min for BCG. Moreover, the thermodynamics results showed that the adsorption process was spontaneous for both anionic dyes. All these macroscopic competitive adsorption results indicate high selectivity toward ARS molecules in the presence of BCG molecules. Additionally, the TiO_2 nanoparticles were successfully regenerated using UV irradiation. Moreover, molecular dynamics computational modeling was performed to understand the molecules' optimum coordination, TiO_2 geometry, adsorption selectivity, and binary solution adsorption energies. The simulation energies distribution exhibits lower adsorption energies for ARS in the range from − 628 to − 1046 kJmol^{-1} for both single and binary systems. In addition to that, the water adsorption energy was found to be between − 42 and − 209 kJmol^{-1}.

Keywords TiO_2 nanoparticles · Brookite · Anionic dyes · Competitive adsorption · Photodegradation · Experimental · Molecular dynamics simulation

Introduction

The world faces a serious water challenge that affects living beings. The substantial need for water for many human activities is dramatically growing due to the global population growth, inefficient water consumption, and industrial use. The current produced industrial waste and its classical management methods such as dumping, industrial runoff, leaks and spills, mining, and many other processes generated devastating impacts on human lives and the ecosystem (Ashraf and Hanfiah 2017; Goel 2006). Dyes, especially synthetic ones sourced from textiles and tanneries, pigment and leather making, cosmetics, etc., are one of the problematic contaminants that are produced and released in wastewater without being efficiently remediated (Abuhatab et al. 2019; Asgari et al. 2020; Badawi et al. 2021; Badran and Talie

Responsible Editor: Tito Roberto Cadaval Jr

✉ Amjad El-Qanni
a.elqanni@najah.edu

[1] Department of Chemical Engineering, An-Najah National University, P.O. Box 7, Nablus, West Bank, Palestine

[2] Department of Chemical Sciences, University of Naples Federico II, Naples, Italy

[3] Department of Chemical and Petroleum Engineering, University of Calgary, Calgary, AB, Canada

[4] Department of Petroleum and Chemical Engineering, College of Engineering, Sultan Qaboos University, Muscat, Oman

[5] Department of Mechanical Engineering, An-Najah National University, P.O. Box 7, Nablus, West Bank, Palestine

2021; Bhardwaj and Ballabh 2022; El-Qanni et al. 2017; Foroutan et al. 2020a, 2021a; Mounteer et al. 2019; Sawalha et al. 2020). The wastewater streams generated from the textile industry include complex chemicals that can cause serious health and environmental problems (Ding et al. 2011; Kurade et al. 2012; Sharma et al. 2016). The annual global production of dyestuff is more than 70 million tonnes, while synthetic dyes discharged to aquatic systems are more than 100 thousand tonnes (Feng et al. 2017; Shabbir et al. 2017). Recent advances and applications of nanotechnology through physiochemical approaches in wastewater treatment are currently gaining a lot of attention to mitigate water contamination problems and provide environmentally sound solutions (Adeleye et al. 2016; Alakhras et al. 2020; Aryee et al. 2021; Baresel et al. 2019; Dastgerdi et al. 2019; El-Qanni 2017; Foroutan et al. 2020b; Gehrke et al. 2015; Gutierrez et al. 2017; Ibrahim et al. 2019; Muniandy et al. 2016; Singh et al. 2019; Wang et al. 2021a, b).

Most existing wastewater treatment options, such as distillation, membrane filtration, and electrochemical treatment, are prohibitively expensive and face many operational challenges. Furthermore, some of the wastewater pollutants do not require extreme treatment approaches. Hence, adsorption and photodegradation using nanomaterials and functionalized nanonetworks are considered one of the states of sustainable technologies that are used in water purification (Adeleye et al. 2016; Ahmad et al. 2015; Azha et al. 2021; Behera et al. 2021; Dong et al. 2015; Gehrke et al. 2015; Hasan et al. 2021; Hou and Hao 2021; Ihsanullah 2022; Kiani Ghaleh sardi et al. 2021; Mohamed et al. 2022; Qian et al. 2021; Russo et al. 2020; Yadav et al. 2021; Zhang et al. 2022). These technologies have many advantages, once compared to other treatment techniques, such as simplicity, cost feasibility, and ease of operation including applying moderate operating conditions. Different magnetic-based and/or metal oxide-based nanocomposites were developed and applied recently in the field of dye removal, mainly the cationic ones (Badran and Khalaf 2020; Elkhider et al. 2020; Foroutan et al. 2022; Foroutan et al. 2021b, c; Alsurakji et al. 2021; Khan et al. 2020a; Lin et al. 2019). Owing to their unique characteristics, TiO_2 nanoparticles were intensively studied in several related fields, especially in the rutile and anatase forms (Escribá et al. 2021; Palmisano 2013). Many research works introduced nanoparticles that are envisaged to treat wastewater contaminated with different types of dyes. Nonetheless, the exceptional and captivating photocatalytic properties of TiO_2 nanoparticles, virgin, supported, and functionalized forms, aid in considering these high-value materials to affordably and effectively treat wastewater (Peñas-Garzón et al. 2021). Despite the large volume of reported works on the use of rutile and anatase forms of TiO_2 in wastewater treatment, the brookite phase is the least studied in the literature (Al-Mamun et al. 2019; Choi et al. 2017; Palmisano 2013). This is due to the difficulties in producing a highly pure composition in this phase purely. Nevertheless, Tomita et al. (2006) studied the synthesis of nanocrystalline brookite by the hydrothermal method. In addition, Kozawa et al. (2013) succeeded in developing TiO_2 brookite by hydrothermal conversion of Mg_2TiO_4. In the last few years, Machida et al. (2018) managed to investigate synthetic conditions to produce high-purity brookite. Furthermore, brookite TiO_2 nanoparticles have proven to have excellent photocatalytic performance that can exceed that of the anatase phase (Khan et al. 2020b). This behavior is directly dependent on the defect levels through the thermodynamic equilibria of point defects and electronic structures of pristine and defective brookite, by forming Ti_i^{4+} that induces ideal shallow defect levels in brookite, while Ti_O^{4+} results in deep level formations (Khan et al. 2020b).

For several years, great effort has been devoted to the study of dye adsorption; therefore, a literature overview on experimental and theoretical studies, mainly using molecular dynamics simulation, of anionic dyes throughout the years 2012–2022 has been conducted. Figure S1 (Supplementary Material) shows the number of articles published in this domain using some keywords on Scopus. Clearly, when the search was narrowed down from "adsorption of anionic dyes" which showed around 3650 published articles to "combined experimental and theoretical adsorption of anionic dyes," the number was only 2 publications. This indeed indicates the importance of addressing such kinds of studies that help both scientific and industrial communities.

However, the concepts of selective and competitive adsorption of organic and inorganic pollutants are important for optimizing the types of adsorbents and nanomaterials that can be used in wastewater treatment processes. Different parameters such as type of process, recyclability, cost, the fate of spent nanomaterials, etc., play a vital role in environmental management. Therefore, researchers, scientists, environmentalists, and chemical engineers alongside decision-makers are striving genuinely to find immediate and efficient water purification solutions. In this sense, the combination between adsorption and photodegradation via nanoparticle technology can be integrated with the existing treatment technologies. Yet, still, there is a need for comprehensive insights into the interaction of different pollutants onto the surfaces of any used/tested nanoparticles.

Hence, Table S1 lists some recent publications that address the competitive adsorption of dyes and/or some inorganic pollutants using either natural or synthetic adsorbents that fall into many applicable themes. It is crystal clear that most studies report experimental adsorption conditions and lack the mechanistic insights behind hypothesized adsorption mechanisms.

Herein, in this work, TiO_2 brookite nanoparticles are used to competitively adsorb and subsequently photodegrade two

anionic dyes, namely, Alizarin Red S (ARS) and Bromocresol Green (BCG) under UV light irradiation. Moreover, the adsorption mechanisms, kinetics, isotherms, thermodynamics, and molecular dynamics simulation are also included in this study. Finally, the regeneration of the TiO_2 brookite nanoparticles under UV light irradiation is also explored.

Materials and methods

Materials

Two model anionic dyes were used in this study, namely, Alizarin Red S (ARS) and Bromocresol Green (BCG). Both were supplied from Honeywell, Jordan and used as received without further purification. The characteristics of the dyes are represented in Table 1. The concentrations of the dye solutions ranged from 20 to 400 gL^{-1}. The solutions were prepared using deionized water. Commercial TiO_2 brookite nanopowder (product number: 791326, CAS number: 12188–41-9, formula weight 79.87 $gmol^{-1}$, and 99.99% trace metal basis, nanosized less than 100 nm) has been purchased from Merck (Haifa) via local sub-vendor BioTech Medical Supplies (Ramallah, Palestine).

Nanoparticle characterization

The commercial TiO_2 nanoparticles were characterized using Rigaku Ultima III X-ray diffraction (Rigaku Americas Corp., The Woodlands, TX) with Cu Kα radiation operating at 40 kV and 44 mA with a θ-2θ goniometer used to confirm the TiO_2 brookite phase. The surface areas of the TiO_2 brookite nanoparticles were measured using the Brunauer–Emmett–Teller (BET). This was accomplished by performing nitrogen physisorption at 77 K using a surface area and porosity analyzer (TriStar II 3020, Micromeritics Corporate, Norcross, GA). The test sample was firstly pretreated at 150 °C under N_2 flow overnight before analysis to remove any existed moisture. Scanning electron microscopy (SEM) was performed to investigate the surface morphology and the level of aggregation of the TiO_2 brookite nanoparticles. A field emission Quanta 250 electron microscope manufactured by FEI was used, with an accelerating voltage of 20 kV and a spot size of 3.0. to view the morphology of the sample. A very small quantity of the powdered sample was placed over a carbon tape sample holder, and it was tapped to release excess and loose particles.

Table 1 Structures and physicochemical properties of the examined anionic dyes ARS and BCG

Property	BCG	ARS
Chemical formula	$C_{21}H_{13}Br_4NaO_5S$	$C_{14}H_7NaO_7S$
Molecular weight $(gmol^{-1})$	720	342.64
Soluble in distilled water $(mgmL^{-1})$	1	1
Melting point (°C)	230	> 250
pKa (at 25 °C)	4.7	4.5, 11
λ_{max} (nm)	616	286

Adsorption and photodegradation using TiO_2 nanoparticles

"Adsorption tests of ARS and BCG organic model molecules onto the TiO_2 nanoparticles were performed in batch experiments for both single and binary studies at 25 °C, and the pH was adjusted by adding NaOH and HCl of 0.1 M initial concentrations, as needed. Therefore, the pH of the solution was kept neutral (7.0 ± 0.1). In all experiments, 25 mg of nanopowder was added to a set of vials containing 5 ml solutions at different initial concentrations of ARS or BCG. Figure 1 represents the experimental adsorption and photodegradation procedure for single and binary studies. The absorbance data of the solution samples were obtained from the optical spectra recorded on UV–Vis analysis using a model with wavelengths ranging from 200 to 800 nm, respectively. In a binary system with components ARS and BCG, the measurement would be carried out at their maximum absorbance wavelength $\lambda = 286$ nm for ARS and $\lambda = 616$ nm for BCG.

The binary solution was prepared by fixing the concentration of the ARS solution at 50 mgL^{-1} and varying the BCG concentrations from 50to250 mgL^{-1}. The same procedure was repeated at a fixed concentration of BCG to be 50 mgL^{-1} and by varying the concentration of ARS from 50to320 mgL^{-1}. The adsorption study of the two sets was tested at high and low concentrations. The vials were sealed firmly to avoid any loss of water. The vials were kept under vigorous mixing at a shaker in dark for 2 h (Grant OLS200 Orbital Shaking Water Bath, Grant Instruments, Cambridge, UK) with a mixing speed of 200 rpm to ensure that the equilibrium was attained. Then, the aqueous phase was separated from the solid phase using a centrifuge at 3000 rpm for 10 min. The supernatant was decanted and tested using UV–Vis spectrophotometer (Genesys 10S, Thermo Scientific Instruments Canada Inc., Mississauga, ON). Some experiments were performed in triplicate to quantify the amount adsorbed and to verify the adsorption capacity on the surface of the TiO_2 nanoparticles. To define the adsorption mechanism of ARS and BCG on TiO_2 nanoparticles in single cases, isotherm data were fitted and analyzed using the Sips model shown below (Febrianto et al. 2009, Foo and Hameed 2010):

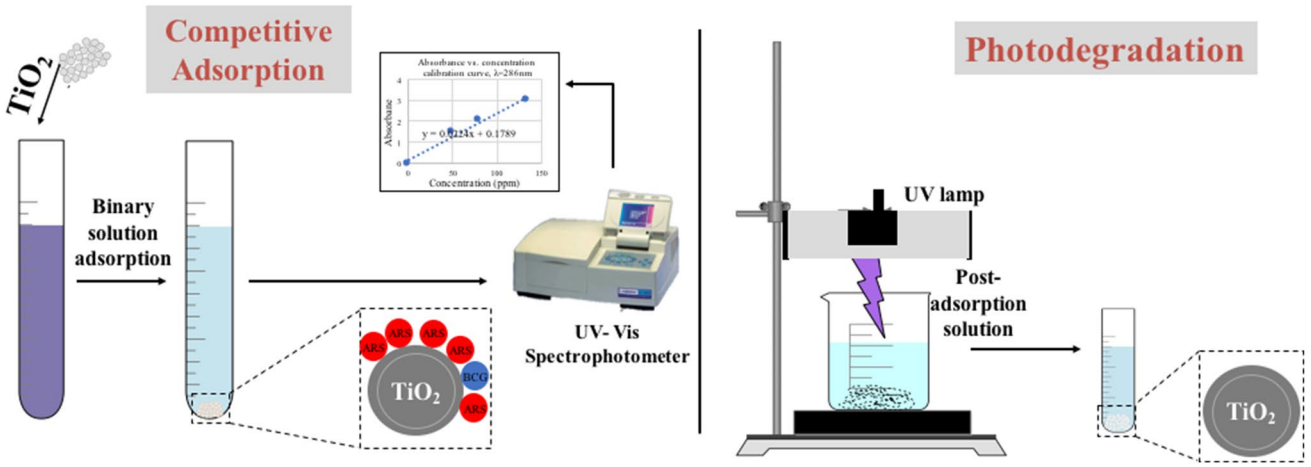

Fig. 1 A schematic representation of the experimental adsorption and photodegradation procedure for single and binary studies

$$Q_e = \frac{Q_m \left(k_s C_e\right)^{n_s}}{1 + \left(k_s C_e\right)^{n_s}} \tag{1}$$

where Q_e is the adsorption capacity at equilibrium ($\mathrm{mgg^{-1}}$), $Q_m isthe$ maximum adsorbed amount $\left(\mathrm{mgg^{-1}}\right)$, k_s is the Sips adsorption equilibrium constant ($\mathrm{Lmg^{-1}}$), C_e is the equilibrium concentration $\left(\mathrm{mgL^{-1}}\right)$, n_s is the Sips constant (dimensionless).

The adsorption uptake analysis of the binary solution was performed by measuring the UV–Vis absorbance and then by applying the following equations (McKay and Al-Duri 1988; Sawyer et al. 1984):

$$C_A = \frac{k_{B2}A_1 - k_{B1}A_2}{k_{A1}k_{B2} - k_{A2}k_{B1}} \tag{2}$$

$$C_B = \frac{k_{A2}A_2 - k_{A1}A_1}{k_{A1}k_{B2} - k_{A2}k_{B1}} \tag{3}$$

where C_A and C_B ($\mathrm{mgL^{-1}}$) are the concentrations of organics in the binary solution, k_{A1} and k_{A2} are the slopes of the calibration curves of ARS and BCG at the maximum wavelengths (λ_{max}), k_{B1} and k_{B2} are the slopes of the calibration curves of ARS and BCG, respectively. In addition, A_1 and A_2 (dimensionless) are the absorbance of ARS and BCG in the binary solution at λ_{max} of each model molecule.

The experimental data for the binary solutions of competitive adsorption were analyzed using the Extended-Sips isotherm model (Kumar et al. 2008; Zolgharnein et al. 2015):

$$Q_e = \frac{Q_m (k_{si} C_{ei})^{n_{si}}}{1 + (k_{si} C_{ei})^{n_{si}} + (k_{sj} C_{ej})^{n_{sj}}} \tag{4}$$

where Q_e is the adsorption capacity at equilibrium ($\mathrm{mgg^{-1}}$), k_s is the Sips adsorption equilibrium constant ($\mathrm{Lmg^{-1}}$), n_s is the Sips constant (dimensionless), Q_m is the maximum adsorbed amount $\left(\mathrm{mgg^{-1}}\right)$, i and j represent the sorbate species.

The non-linear Chi-square (χ^2) analysis was employed to assess the goodness of the fitting results. All isotherm model parameters and the χ^2 analysis were performed using Excel 2019 software. The low values of χ^2 indicate the agreement between the model and the experimental data. The χ^2 values were obtained using the following equation (Montgomery and Runger 2006):

$$\chi^2 = \sum \frac{\left(Q_e - Q_{e(model)}\right)^2}{Q_{e(model)}} \tag{5}$$

where Q_e and $Q_{e(model)}$ are the equilibrium uptake obtained experimentally and by model fitting ($\mathrm{mgg^{-1}}$), respectively.

The photocatalytic reaction of TiO_2 took place using a UV light lamp (power = 6 W, light intensity = 830 μW $\mathrm{cm^{-1}}$, and with $\lambda = 365$ nm) inside a 50-mL glass beaker with continuous stirring over a magnetic stirrer. The dyes were adsorbed on the TiO_2 surface for 2 h before being irradiated with the UV light lamp for the next 12 h. Binary solutions which contain initial concentrations of 100 $\mathrm{mgL^{-1}}$ ARS with 50 $\mathrm{mgL^{-1}}$ BCG and 100 $\mathrm{mgL^{-1}}$ BCG with 50 $\mathrm{mgL^{-1}}$ ARS were chosen to be tested for the regeneration study. The photocatalytic activity of TiO_2 was evaluated by measuring the time dependence of the concentration loss based on the adsorbed and the degraded dye compounds. The percentage of adsorption–photodegradation process was calculated using the formula in the equation below:

$$\%A - P = \frac{C_o - C_e}{C_o} \times 100\% \tag{6}$$

where $\%A-P$ is the percentage of adsorption and photodegradation of the dyes, C_o is the initial concentration of the sample before irradiation under UV light $\left(\mathrm{mgL}^{-1}\right)$, C_e is the concentration of the sample after irradiation under UV light (mgL^{-1}).

Adsorption kinetics

To find the time needed to reach equilibrium for the adsorption of ARS and BCG ions onto TiO_2 nanoparticles, the adsorption uptake was determined at different time intervals of 2 to 180 min. The kinetics study was carried out at a constant adsorbent dose: 25 mg. The initial concentration of the adsorbates was fixed at 50 mgL^{-1}; the pH was controlled at around 7.0 at 25 °C. The following external mass transfer model was used to fit the kinetics experimental data (Worch 2012):

$$\frac{dC}{dt}=-k_m a\left(C-C_s\right) \tag{7}$$

where k_m is the external mass transfer coefficient in the liquid phase (mmin^{-1}); a is the specific surface area per the volume of the adsorbent $(\mathrm{m}^2\mathrm{m}^{-3})$; C is the concentration of the model molecules (mgL^{-1}) at any time; and C_s is the concentration of the molecules at the interface with the adsorbent (mgL^{-1}). The value of C_s can be determined from reforming the Sips model parameters in the results "Binary adsorption isotherms" sections, as shown below:

$$C_s=\left[\frac{Q}{k_s{}^{n_s}\left(Q_m-Q\right)}\right]^{n_s{}^{-1}} \tag{8}$$

Q was obtained from the following mass balance equation:

$$Q=\frac{V\left(C_o-C\right)}{m} \tag{9}$$

where V is the volume of the solution (mL) and m is the mass of the nanoparticles (mg). The following first-order differential equation was obtained by substituting Eqs. (8) and (9) into Eq. (7):

$$\frac{dC}{dt}=-k_m a\left[C-\left[\frac{V\left(C_o-C\right)}{k_s{}^{n_s}\left(mQ_m-V\left(C_o-C\right)\right)}\right]^{n_s^{-1}}\right] \tag{10}$$

The initial condition to solve this ordinary differential equation is $C=C_o$ at time zero. The Sips constants can be obtained from the adsorption isotherm study for the binary system in the results. Polymath 6.10 software was used to estimate the $k_m a$ (min^{-1}) values by fitting the experimental data to Eq. (10).

Thermodynamics study

The adsorption of ARS and BCG ions onto the TiO_2 nanoparticles was performed at three different temperatures 25, 35, and 45 ℃ in a batch mode. The effect of changing the temperature on the adsorption performance and the isotherm model parameters was investigated. The values of the thermodynamic parameters that describe the adsorption behavior, such as Gibbs free energy (ΔG^o), enthalpy (ΔH^o), and entropy (ΔS^o), were determined. The experimental design and operating conditions were identical to those in the adsorption isotherm study.

Fourier-transform infrared spectroscopy (FT-IR)

A Nicolet iS5 FT-IR spectrometer instrument (Thermo Scientific Instruments) with iD3 ATR accessory plates and DTGS KBr detector was used to study the mid-infrared region before and after adsorption to infer and investigate the interaction of ARS and BCG with TiO_2 nanoparticles. The spectra were recorded from 400 to 4000 cm^{-1} with resolutions of 8 cm^{-1} and 16 scans for each spectrum.

Computational modeling

To understand the adsorption mechanism and the interaction between molecules and the surfaces of adsorbents, computational modeling was performed on Accelrys Material Studio Software (Crake et al. 2017) for ARS and BCG model molecules in the single and binary cases in the presence of water molecules. Forcite was used to optimize the structure geometry, and the condensed-phase optimized molecular potentials for atomistic simulation studies (COMPASS) forcefield calculations were selected and put on fine precision. The TiO_2 brookite (100) surface was created and optimized using the same optimization procedure. The TiO_2 optimized structure is shown in Fig. 2. The electrostatic forces and van der Waals forces were set to atom-based calculations (Marei et al. 2016).

Results and discussion

Characterization studies

The characterization results, XRD, textural properties, and SEM images of the commercial TiO_2 nanoparticles are shown in Fig. 3. The X-ray diffraction pattern (Fig. 3a) of the TiO_2 nanoparticles confirms the material is crystalline TiO_2 with a brookite phase, as reported by the manufacturer. The structure was identified by comparison of the XRD signals with those reported in the pdf

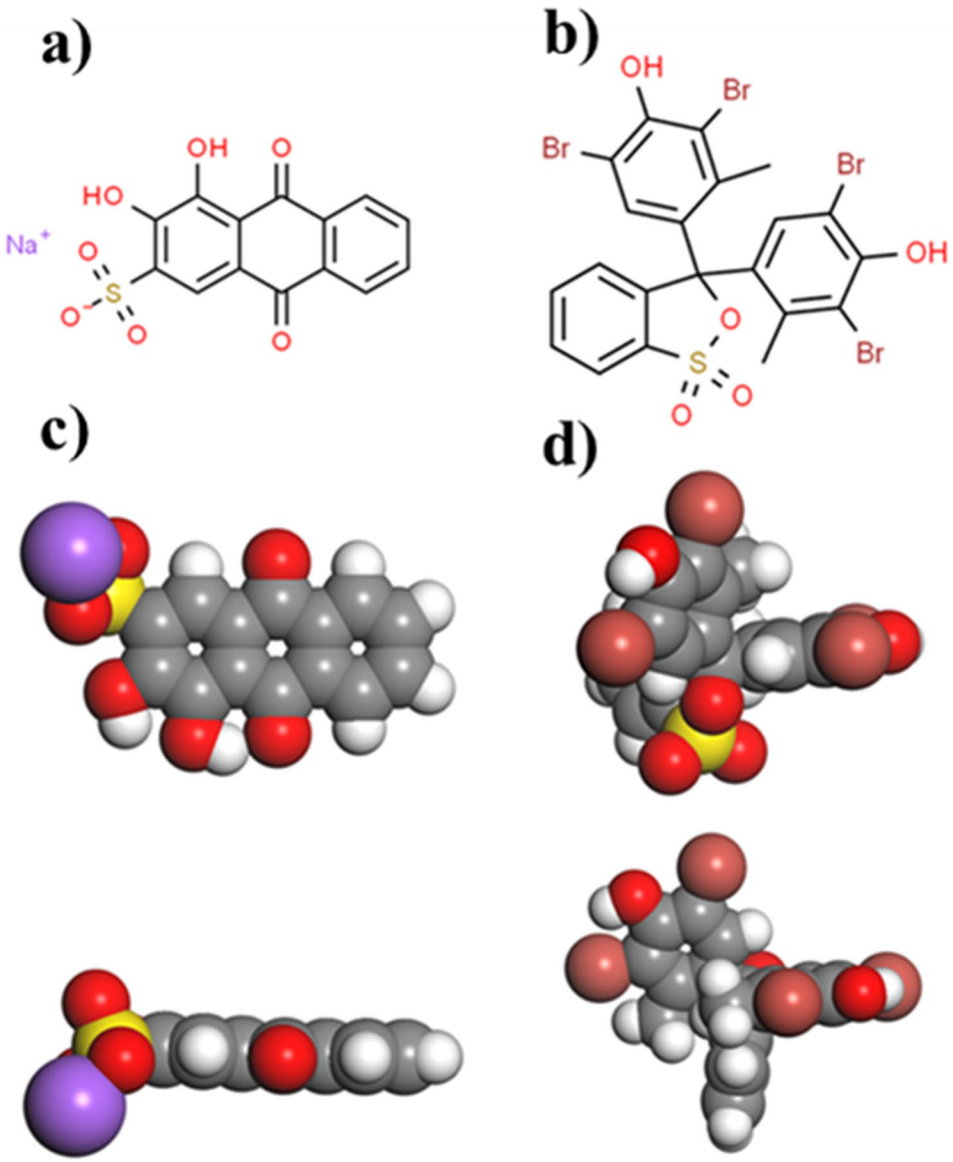

Fig. 2 Chemical structure of (**a**) ARS and (**b**) BCG; CPK representation of the optimized (**c**) ARS molecule (top and side views, respectively) and (**d**) BCG (top and side views, respectively). Grey atoms represent carbon, red atoms represent oxygen, white atoms represent hydrogen, yellow atoms represent sulfur, purple atoms represent sodium, and light red atoms represent bromide. The geometry optimization in forcite was set to fine and the forcefield to COMPASS

card 01–076-4113 of the 2005 ICDD (International Centre for Diffraction Data) database included in the program JADE V.7.5.1 (Materials Data XRD Pattern Processing Identification and Quantification). As seen, the existence of brookite in the XRD patterns is evidenced by the presence of the (121) peak at $2\theta = 30.2°$. Figure 3b shows the N_2 physisorption isotherm of the TiO_2 nanoparticles. The surface areas of the TiO_2 brookite nanoparticles and the pore width were measured using the BET method and found to be 32.2 m^2g^{-1} and 9.3 nm, respectively. International Union for Pure and Applied Chemistry (IUPAC) has classified the physisorption isotherms into six categories (Types I to VI) and the possible hysteresis loops in these isotherms into five categories (Types H1 to H5) (Sing 1985; Thommes et al. 2015). Although it is well known in the literature that most metal-oxide-based nanoparticles are non-porous materials (Type II isotherm) (El-Qanni et al. 2017), there is a mesoporosity with a hysteresis loop (Type IV isotherm) which is usually attributed to the synthesis method of the nanoparticles. Lastly, the SEM images (Fig. 3c) show the morphology of the TiO_2 nanoparticles which looks like a cubic shape in an orderly manner.

Single adsorption isotherms

Isotherm studies indicate the way that the solution transmits from the solution phase to the adsorbent phase at

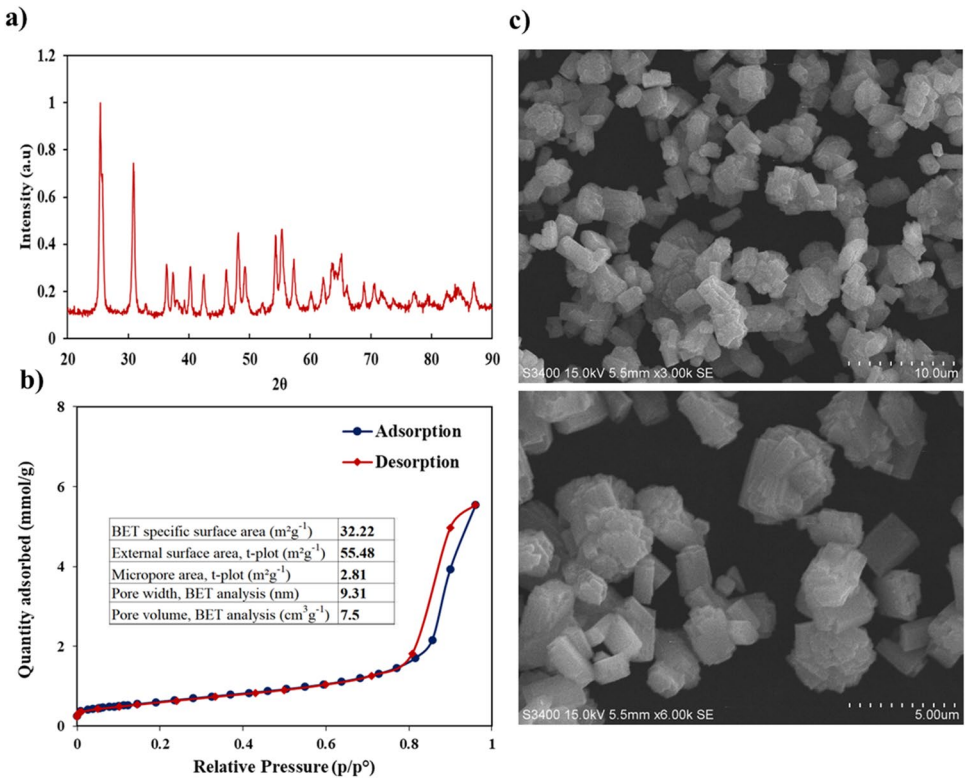

Fig. 3 Characterization results of the TiO_2 brookite nanoparticles. (**a**) X-ray diffraction powder pattern, (**b**) N_2 physisorption isotherm, and (**c**) SEM images

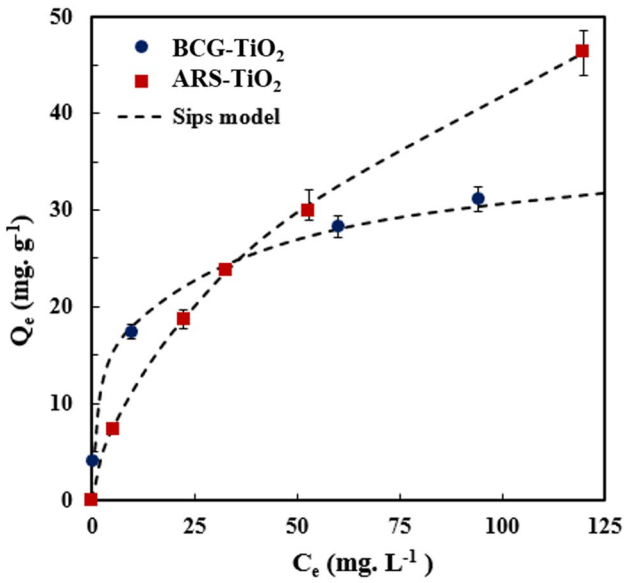

Fig. 4 Macroscopic single solution-phase adsorption isotherm of BCG and ARS onto TiO_2 nanoparticles. Experimental conditions: nanopowder dose, 5 gL^{-1}; contact time, 120 min; temperature, 25 °C; and pH, 7.0. The symbols are experimental data, and the solid dashed lines are the Sips model

equilibrium (Arfi et al. 2017). As seen in Fig. 4, excellent agreement between the experimental data and the Sips model for ARS and BCG molecules was obtained

Table 2 Estimated single adsorption isotherm of the Sips model fitting parameters

ARS			BCG		
Q_m	k_s	n_s	Q_m	k_s	n_s
147.57	0.017	0.68	53.30	0.19	0.42

in such a case at a temperature of 25 °C and pH of 7.0. This was confirmed by the low values of χ^2 for the Sips model: 0.019 and 0.13 for ARS and BCG, respectively. The error bars of each experimental measurement represent the standard error. The TiO_2 nanoparticles succeeded in adsorbing both model molecules, and significant changes in the initial concentrations were observed. An obvious color change was observed after the adsorption of ARS and BG which confirms the occurrence of adsorption visually. As shown in Fig. 4, at relatively low dye concentrations, the adsorption capacity of BCG onto TiO_2 nanoparticles increased significantly compared to ARS, suggesting that the adsorption affinity of BCG was higher once compared to ARS molecule. Despite the high adsorption affinity of BCG onto TiO_2 nanoparticles, the TiO_2 nanoparticles exhibited higher uptake capacities toward ARS. The uptake of ARS and BCG was found to be 147.6 and 53.3 mgg^{-1}, respectively, indicating different adsorption behaviors of the two model molecules.

The higher uptake of ARS could be attributed to its low molecular weight compared to BCG. The summary of the single adsorption isotherm of the Sips model fitting parameters is listed in Table 2. The n_s values in the Sips model play an important role in understanding the type of interaction between dyes and the surface of TiO_2 nanoparticles. The dimensionless n_s parameter qualitatively characterizes the heterogeneity of the adsorbate-adsorbent interaction and depends on adsorbate rather than on adsorbent as can be seen by the obtained data in this study. The reported n_s data for both cases is less than 1 ($n_s = 0.68$ and 0.42 for ARS and BCG, respectively) confirming the heterogeneous adsorption process as suggested by the values of the heterogeneity factor (n_s). Thus, the isotherm that best describes the adsorption mechanism of ARS and BCG onto the TiO_2 nanoparticles is the Sips isotherm."

Binary adsorption isotherms

Figure 5 shows the Extended-Sips model of ARS and BCG molecules onto TiO_2 nanoparticles at pH of around 7 and 25 °C. The χ^2 values for the applied Extended-Sips model were 6.7×10^{-3} and 4.5×10^{-5} for ARS and BCG in the binary solution, respectively. The TiO_2 nanoparticles succeeded in adsorbing both model molecules in the binary adsorption systems. The results and the fitting parameters are shown in Table 3. Interestingly, the adsorption capacity did not change notably by the presence of the other model molecules. It is worth noting here that the ARS-TiO_2 adsorption isotherm was similar to that in the single system where the heterogeneity factor (n_s) values remain 0.68 for both ARS single and binary systems. This suggests the selectivity of TiO_2 nanoparticles toward adsorption of the ARS molecules in the presence of BCG molecules, that the energy of the binding sites did not face any change confirming the selective adsorption of ARS molecules. The adsorption behavior of BCG-TiO_2 goes to Langmuir by the presence of ARS molecules. The n_s value increased from 0.42 to 0.92 in the presence of ARS molecules; therefore, it can be assumed that BCG molecules in the binary solution are chemisorbed in a monolayer onto the surface of TiO_2 nanoparticles. Furthermore, the initial concentration of ARS was almost diminished after adsorption, while BCG concentration did not highly change in all cases. This was observed as the red color caused by ARS molecules almost disappeared, while the blue color caused

Table 3 Competitive adsorption isotherm fitting parameters

ARS			BCG		
Q_m	k_s	n_s	Q_m	k_s	n_s
140.01	0.0029	0.68	45.45	0.1	0.92

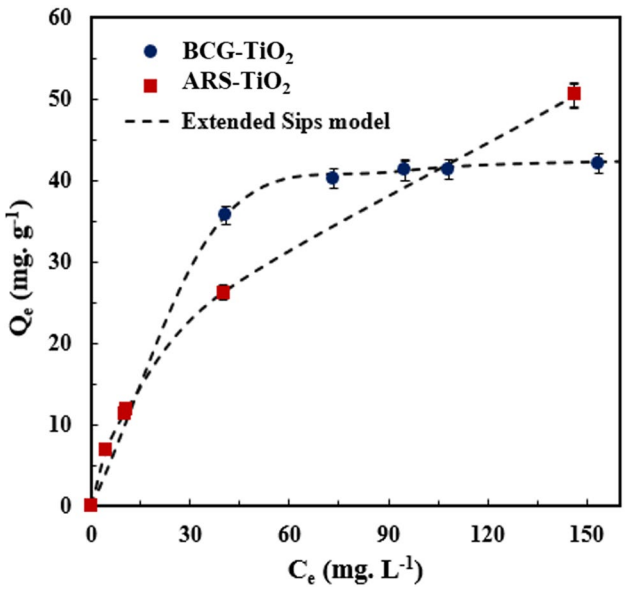

Fig. 5 Macroscopic binary solution-phase adsorption isotherm of BCG and ARS onto TiO_2 nanoparticles. Experimental conditions: TiO_2 dose, 5 gL^{-1}; contact time, 120 min; temperature, 25 °C; and pH, 7.0. The symbols represent the experimental data, and the solid lines represent the Extended-Sips model

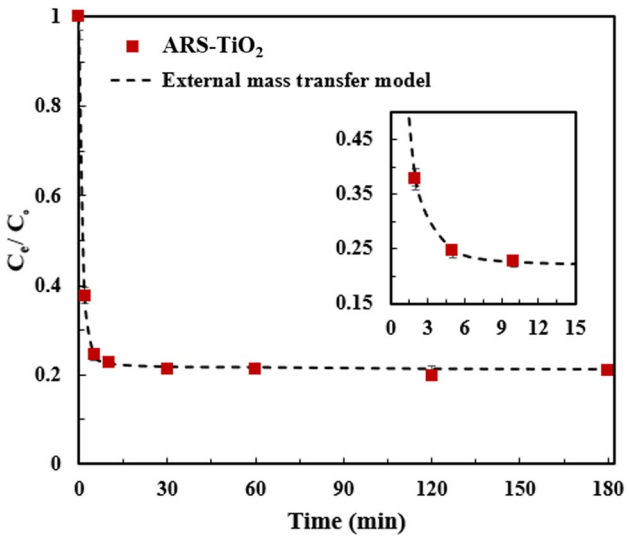

Fig. 6 Adsorption kinetics of ARS onto TiO_2 nanoparticles. Experimental conditions: TiO_2 dose, 5 gL^{-1}; contact time, 60 min; temperature, 25 °C; and pH, 7.0. The symbols are experimental data, and the solid dashed lines are the external mass transfer model

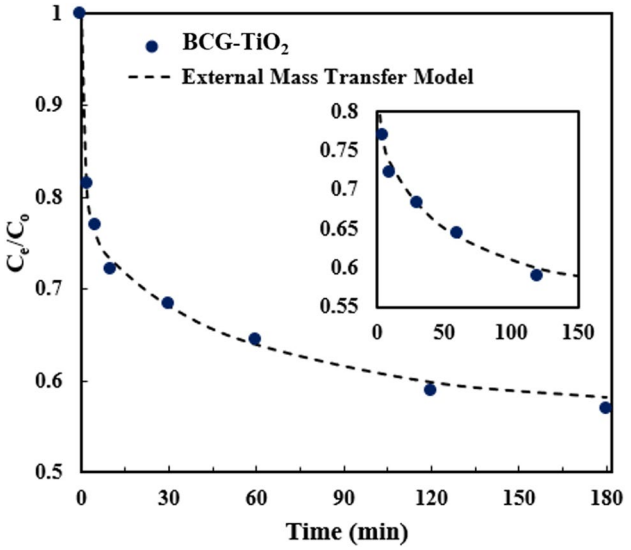

Fig. 7 Adsorption kinetics of BCG onto TiO_2 nanoparticles. Experimental conditions: TiO_2 dose, 5 gL^{-1}; contact time, 60 min; temperature, 25 °C; and pH, 7.0. The symbols are experimental data, and the solid dashed lines are the external mass transfer model

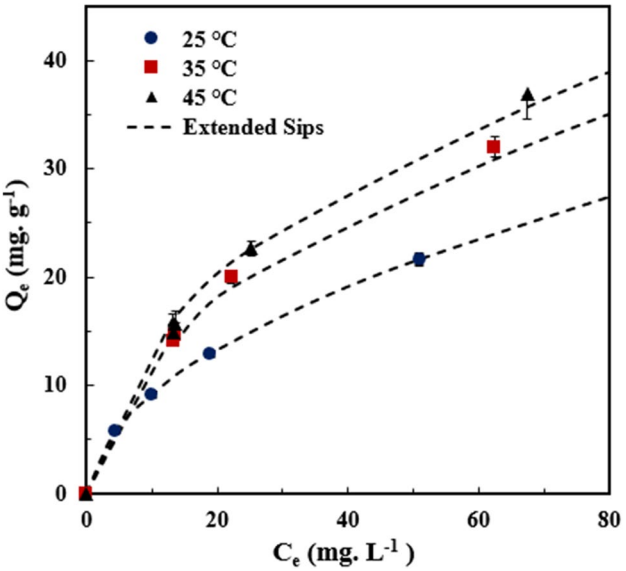

Fig. 8 Adsorption isotherms for ARS onto TiO_2 in binary solution at different temperatures

by BCG remained in the solution. This supports the idea that the ARS molecules were selectively and preferably adsorbed and separated from BCG in the binary solution adsorption. Further explanations will be discussed and presented in the computational modeling part.

Adsorption kinetics

The results of the single adsorption of ARS and BCG onto TiO_2 nanoparticles at predetermined time intervals are presented in Figs. 6 and 7. The phenomenological external mass transfer model was used to validate the experimental data. This model assumes that the film diffusion is the slowest step; thus, the equilibrium is obtained on the surface of the nanoparticles (Hines and Maddox 1985; Ruthven 1984; Wang and Guo 2020). The latter concentration gradient in liquid films is the driving force of external diffusion (Wang and Guo 2020). Herein, the concentration of ARS decreased significantly within the first 7 min, and then it remained constant. This reflects the quick removal of ARS. On the contrary, the concentration of BCG decreased slowly over time as shown in Fig. 9. It took more than 180 min to reach equilibrium. In this sense, the adsorption of ARS onto TiO_2 nanoparticles is dominantly external. Achieving equilibrium in a short time, for ARS compared to BCG, can be due to the low molecular weight of ARS which reduces external mass transfer limitations due to the ease of movement of relatively small molecules compared to a large one. Moreover, the heterogeneity of ARS molecules is less compared to BCG as can be seen in Fig. 5, and these differences in structure will affect the adsorption mechanisms. In addition to that, size effects, which can be explained in light of the steric effect (steric hindrance), can provide a good explanation for the observed trends. Steric hindrance, which comes because of steric effects, involves reducing chemical interactions as a result of steric bulk, whereas large bulky molecules will experience lower chemical interactions due to size effects. It is important to mention that a similar trend was observed once the adsorption isotherm was discussed, where the same analysis can be applied. In conclusion, the slow and gradual decrease in BCG kinetics can be attributed to the slow external diffusion of BCG atoms on the surface of TiO_2 nanoparticles confirmed by the relatively low $k_m a$ value which was 0.59 min^{-1}.

Adsorption thermodynamics

Thermodynamics of ARS adsorption onto TiO_2 nanoparticles in binary solution

Figure 8 shows the adsorption isotherms for ARS onto TiO_2 in binary solution at different temperatures. Worth

Table 4 Fitting parameters of ARS adsorption onto TiO_2 at different temperatures in binary systems

Temperature (°C)	Q_m	k_s	n_s	ΔG°_{ads} $(kJmol^{-1})$	ΔH°_{ads} $(kJmol^{-1})$	ΔS°_{ads} $(Jmol^{-1}K^{-1})$
25	143.18	0.00107	0.594	−6.81	27.62	116.13
35	148.43	0.00186	0.596	−8.53	–	–
45	154.12	0.00207	0.597	−9.11	–	–

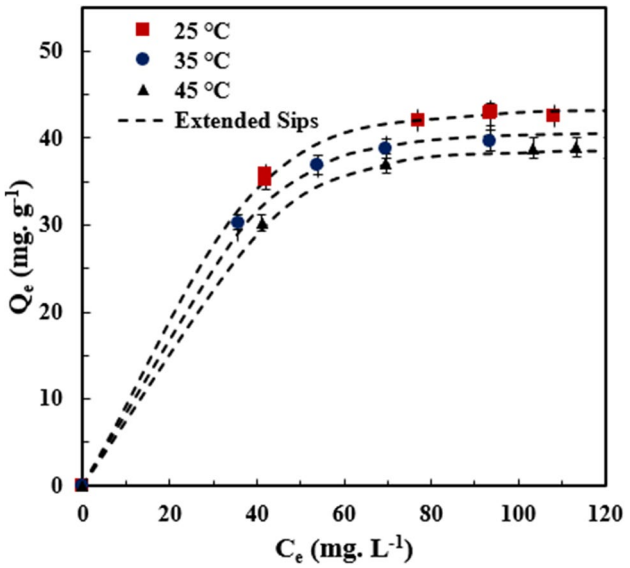

Fig. 9 Adsorption isotherms for BCG onto TiO_2 in binary solution at different temperatures

mentioning, the Sips isotherm was used to determine the thermodynamic parameters, namely the changes in adsorption Gibbs free energy $\left(\Delta G^{\circ}_{ads}\right)$, enthalpy $\left(\Delta H^{\circ}_{ads}\right)$, and entropy $\left(\Delta S^{\circ}_{ads}\right)$ using these equations:

$$\Delta G^{\circ}_{ads} = -RTln(K) \tag{11}$$

where $K = k_s\, Cs^{ns}$

$$ln(K) = \frac{\Delta S^{\circ}_{ads}}{R} - \frac{\Delta H^{\circ}_{ads}}{RT}. \tag{12}$$

For the study of thermodynamics for ARS-TiO_2 in binary solution adsorption, ΔG°_{ads} value was negative indicating spontaneous adsorption. The value of ΔG°_{ads} decreased with temperature, which means that the spontaneous nature of the adsorption is proportional to the temperature as shown in Table 4. Moreover, the positive value of ΔS°_{ads} suggests that the system exhibits a random behavior. Furthermore, the estimated ΔH°_{ads} value was positive 27.62 $kJmol^{-1}$, and since this value is less than 40.0 $kJmol^{-1}$, this suggests that the interaction between the surface ARS and TiO_2 nanoparticles in this binary solution is physisorption (Worch 2012). Therefore, an increase in the temperature leads to higher adsorption of ARS at equilibrium and makes it physical by nature.

Thermodynamics of BCG adsorption onto TiO_2 nanoparticles in binary solution

Figure 9 represents adsorption isotherms for BCG onto TiO_2 in binary solution at different temperatures. For this thermodynamics study, ΔG°_{ads} value was negative indicating spontaneous adsorption as illustrated in Table 5. The value of ΔG°_{ads} decreased with the temperature, which means that the spontaneous nature of adsorption is proportional to temperature. Moreover, the positive value of ΔS°_{ads} suggests that the system exhibits a random behavior. However, ΔH°_{ads} value was positive (41.82 $kJmol^{-1}$) possibly indicating the chemisorption of BCG onto the surface of TiO_2 nanoparticles (Worch 2012). Therefore, molecular dynamics simulation is needed here to give deep insight into this adsorption behavior.

FT-IR analysis

The infrared spectra of TiO_2 nanoparticles before and after the adsorption of organic model molecules in binary solution are shown in Fig. 10. As shown, the

Table 5 Fitting parameters of BCG adsorption onto TiO_2 at different temperatures in binary systems

Temperature (°C)	Q_m	k_s	n_s	ΔG°_{ads} $(kJmol^{-1})$	ΔH°_{ads} $(kJmol^{-1})$	ΔS°_{ads} $(Jmol^{-1}K^{-1})$
25	45.45	0.099	0.913	−33.73	41.82	252.73
35	43.93	0.1	0.925	−35.51	–	–
45	43.69	0.11	0.96	−38.82	–	–

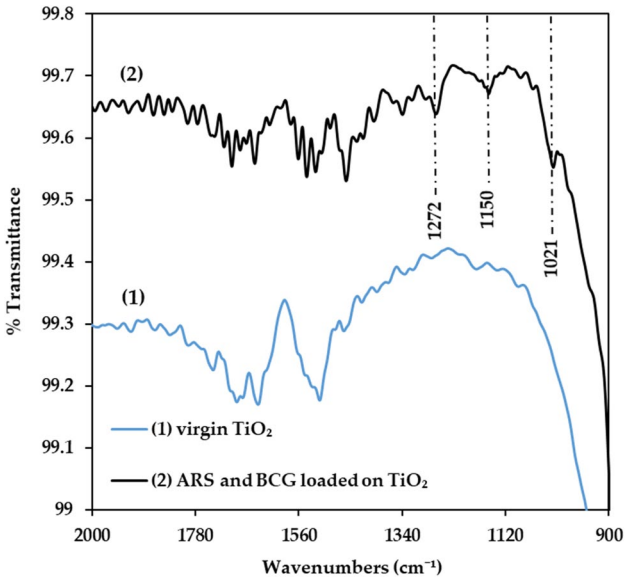

Fig. 10 FT-IR spectra for (1) virgin TiO_2 nanoparticles; and (2) TiO_2 nanoparticles loaded with ARS and BCG

framework region was from around 900 and 2000 cm^{-1} of which modifications to the original TiO_2 signals were noticed. Noticeable modifications on the IR signal at 1021 cm^{-1} could be assigned to S—O and S—C stretching vibrations from ARS adsorption (Albadarin and Mangwandi 2015; Yang et al. 2018). Another clear IR band at around 1150 cm^{-1} corresponds to S = O of the —SO_3^- group for BCG was reported (Murmu et al. 2018). The IR band at 1272 cm^{-1} could be assigned to C—O modes in ARS adsorption (Moriguchi et al. 2003). Nonetheless, the adsorption has shifted the signals from 900 to 2000 cm^{-1} with new different intensities. Additionally, upon binary adsorption, signals around 1640–1520 cm^{-1} assigned to aromatic C = C stretching vibration (El-Qanni et al. 2016) attributed to both anionic dyes ARS and BCG are noticed. Furthermore, some broad IR bands centered at around 1560–1340 cm^{-1} could be assigned to –OH bending vibration modes (El-Qanni et al. 2017). A similar signal case was previously reported for TiO_2-mediated photodegradation of ARS on silver nanoparticles (de Souza and Corio 2013). With this information, the adsorption of ARS and BCG in binary solution onto TiO_2 nanoparticles was successfully confirmed.

Adsorption simulation of BCG and ARS onto TiO_2 (100)

The adsorption calculations have occurred with the presence of 400 water molecules per run. First, each molecule of BCG and ARS was simulated individually. Second, four molecules of each component were applied to the adsorption run. Then, two molecules of each component were tested together in the same simulation, to mimic the binary solution adsorption. The vacuum slap was set to 27 Å, and the supercell range was set to be 2 nm × 2 nm which included 224 O and 128 Ti atoms, as shown in Fig. 11.

In most cases, adsorbed ARS molecules tend to lie tilted on the surface of TiO_2. The affinity of ARS molecules was proven to be higher from BCG adsorption on the surface. This is due to the ARS adsorption's low energy in comparison with the BCG molecules. The S–O and S = O bonds and Na^+ helped in creating closer interaction with the Ti atoms on TiO_2 surface. Furthermore, ARS molecules were shown to bind to TiO_2 by the interaction of electron pairs on the hydroxyl oxygens in alizarin with the d orbitals of Ti atoms. ARS chemical binding with TiO_2 can be through one Ti–O bond and

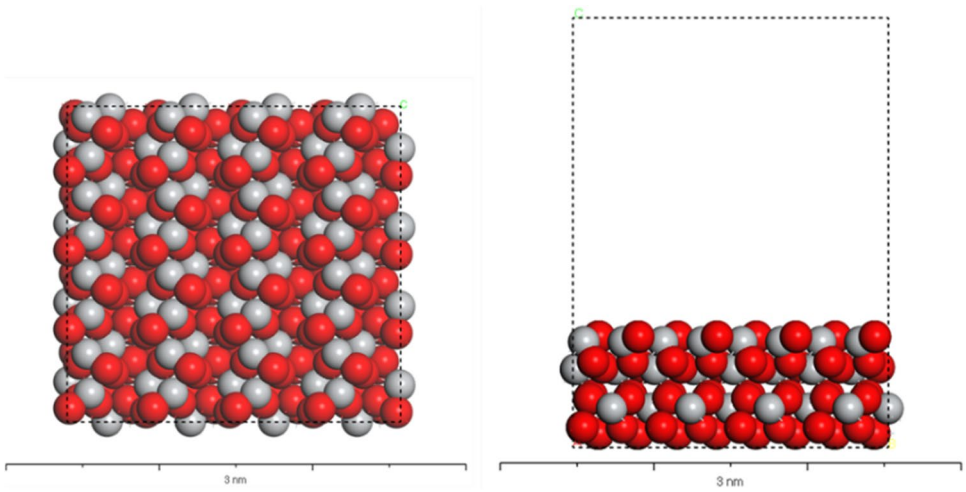

Fig. 11 TiO_2 (100) surface top and side view. Red atoms represent oxygen, and grey atoms represent titanium

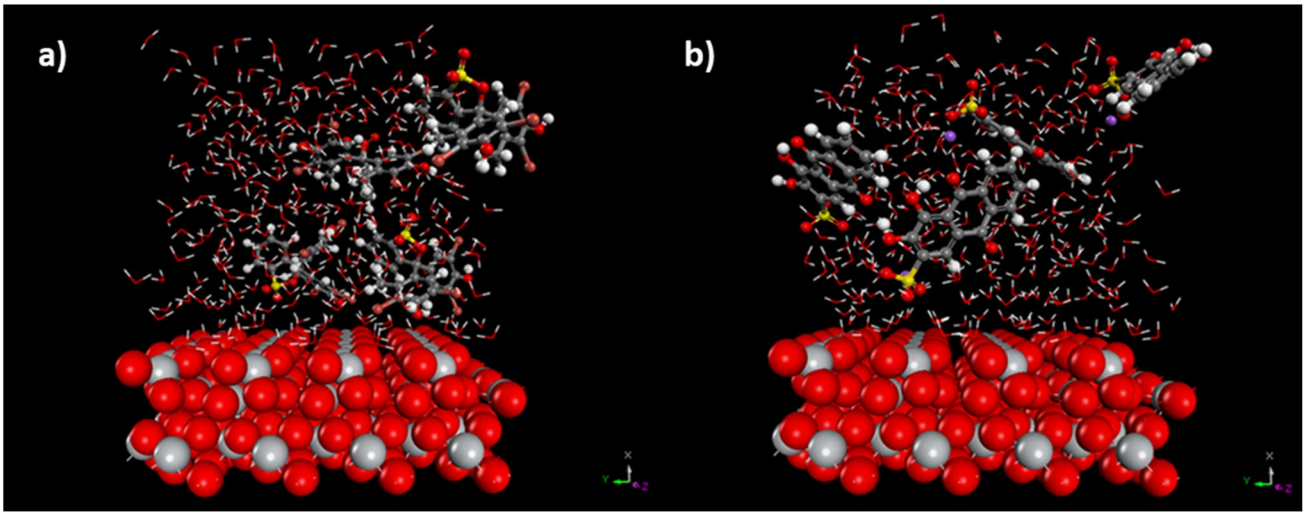

Fig.12 **a**) Adsorption system of 4 BCG molecules onto TiO_2 (100) surface and **b**) adsorption of 4 ARS molecules onto TiO_2 (100) surface. Both cases were simulated in the presence of 400 water molecules. Gray atoms represent carbon, red atoms represent oxygen, white atoms represent hydrogen, yellow atoms represent sulfur, purple atoms represent sodium, light gray atoms represent titanium, and light red atoms represent bromide

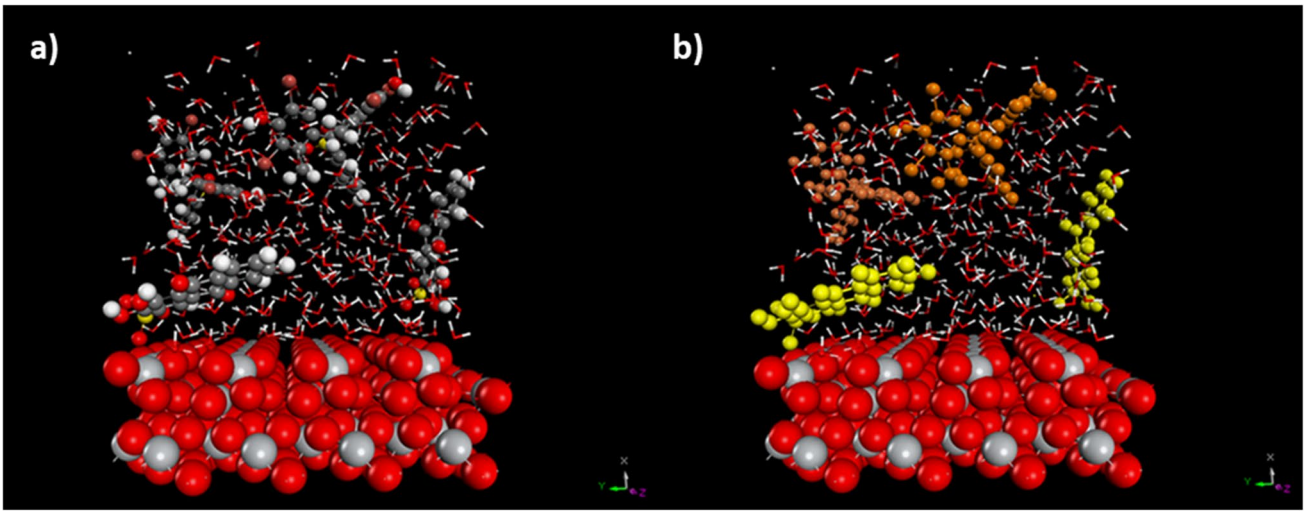

Fig. 13 **a**) Binary adsorption system of 2 BCG and 2 ARS molecules onto TiO_2 (100) surface in the presence of 400 water molecules. Gray atoms represent carbon, red atoms represent oxygen, white atoms represent hydrogen, yellow atoms represent sulfur, purple atoms represent sodium, gray atoms represent titanium, and light red atoms represent bromide. **b**) Same as **a**, but each molecule type was colored differently to clarify the visual representation. ARS was colored yellow and orange for BCG

through two Ti–O bonds directed at a single or two separate Ti atoms (Duncan et al. 2005). In both cases, binary and individual systems, BCG molecules showed higher adsorption energy and lower affinity toward the TiO_2 surface. The atomic distribution and shape of the BCG molecules resulted in increasing the adsorption energy and higher adsorption distance between the surface and the BCG molecule, as shown in Figs. 12 and 13. This confirms the findings obtained via experimental adsorption isotherms, shown in "Binary adsorption isotherms" section. In addition, the simulation energy distributions are demonstrated in Fig. 14. The negative values of the interaction energy for both dyes indicate that the adsorption processes were spontaneous supporting the findings

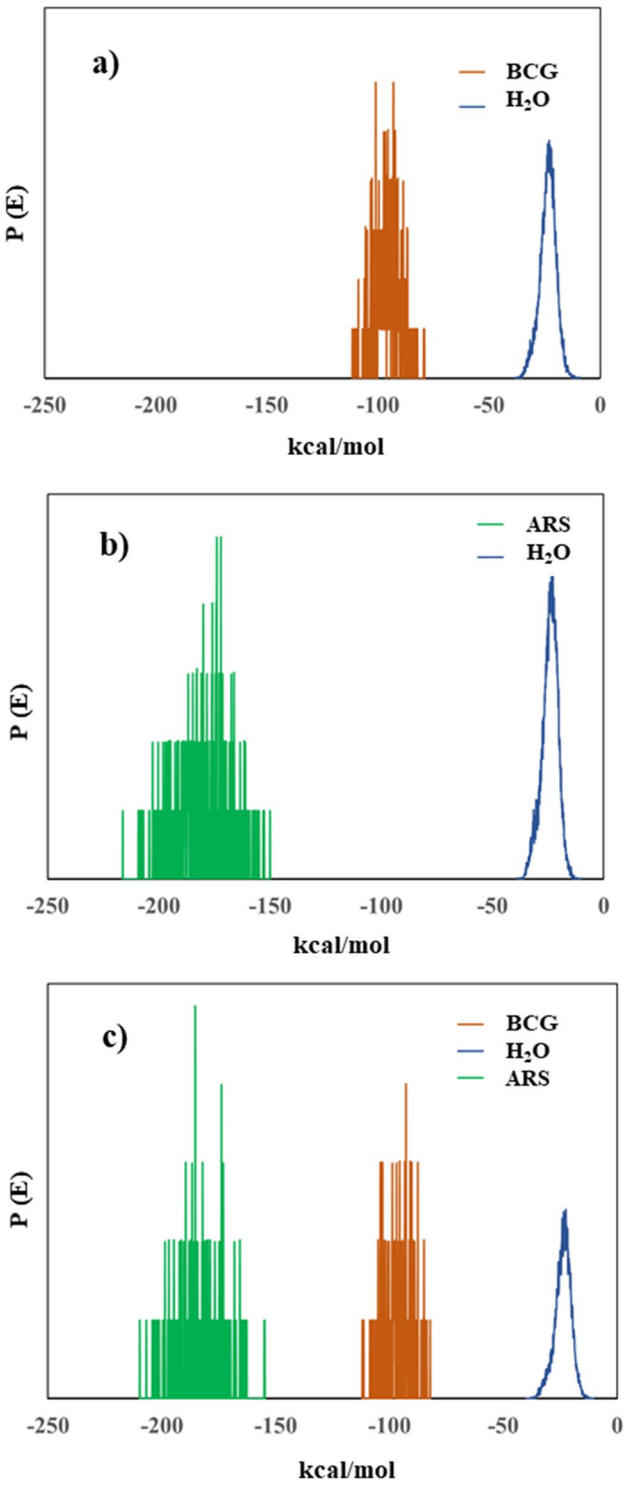

Fig. 14 The adsorption energy distribution of the adsorbed molecules ARS and BCG in single and binary systems. **a**) BCG and H_2O adsorption energy in the 4 BCG single component adsorption system, **b**) ARS and H_2O adsorption energy in the 4 ARS single component adsorption system, and **c**) BCG, ARS, and H_2O adsorption energy in the 4 BCG binary component adsorption system

of thermodynamics: Sections "Thermodynamics of ARS adsorption onto TiO2 nanoparticles in binary solution" and "Thermodynamics of BCG adsorption onto TiO2 nanoparticles in binary solution". Similar energy interaction trends for anionic dyes, eriochrome black T and Direct Red-23, adsorbed onto chitosan and sepioliteclay adsorbents, respectively, were observed in recent publications (Khnifira et al. 2021; Largo et al. 2020). Moreover, Fig. 14 shows lower adsorption energies for ARS of – 150 to – 250 kcalmol^{-1} (– 628 to – 1046 kJmol^{-1}) in both scenarios, single and binary systems. This explains the higher adsorption affinity and removal in the experimental part: adsorption isotherms. The water adsorption energy seems to be stable between – 10 and – 50 kcalmol^{-1} (– 42 to – 209 kJmol^{-1}) which is lower than BCG and ARS. The lower adsorption energy of the water may explain the higher entropy value in the thermodynamics study, as a result of the water desorption and the replacement of BCG and ARS molecules.

Photodegradation of TiO_2 nanoparticles

Regeneration study is considered of paramount importance to achieve environmentally benign, scalable, and cheap catalysts. Therefore, the TiO_2 nanoparticles loaded with the dyes were regenerated by photodegradation for the study of second cycle adsorption. The efficiencies of ARS and BCG through the first and second adsorption cycles were calculated. Results show that the efficiency of TiO_2 decreased by 10.9% after the adsorption of ARS, while the adsorption efficiency of BCG dropped significantly by almost 29.4%, as shown in Fig. 15. The higher reduction in efficiency of BCG (698.01 gmol^{-1}) compared to ARS (360.28 gmol^{-1}) could be associated with its larger molecular weight (Chiu et al. 2019). Similarly, a study by Lachheb et al. explained the variation in the photodegradation rates of five different dyes according to their molar weight (Lachheb et al. 2002). The higher regeneration efficiency of ARS supports the conclusion of TiO_2 selectivity toward adsorbing ARS molecules.

Conclusions

In this study, batch adsorption and subsequent photodegradation activity of TiO_2 brookite nanoparticles, for the removal of single and binary solutions of anionic dyes, ARS and BCG, were successfully achieved. Excellent agreement was obtained between the experimental data and the Sips model for ARS and BCG molecules in the

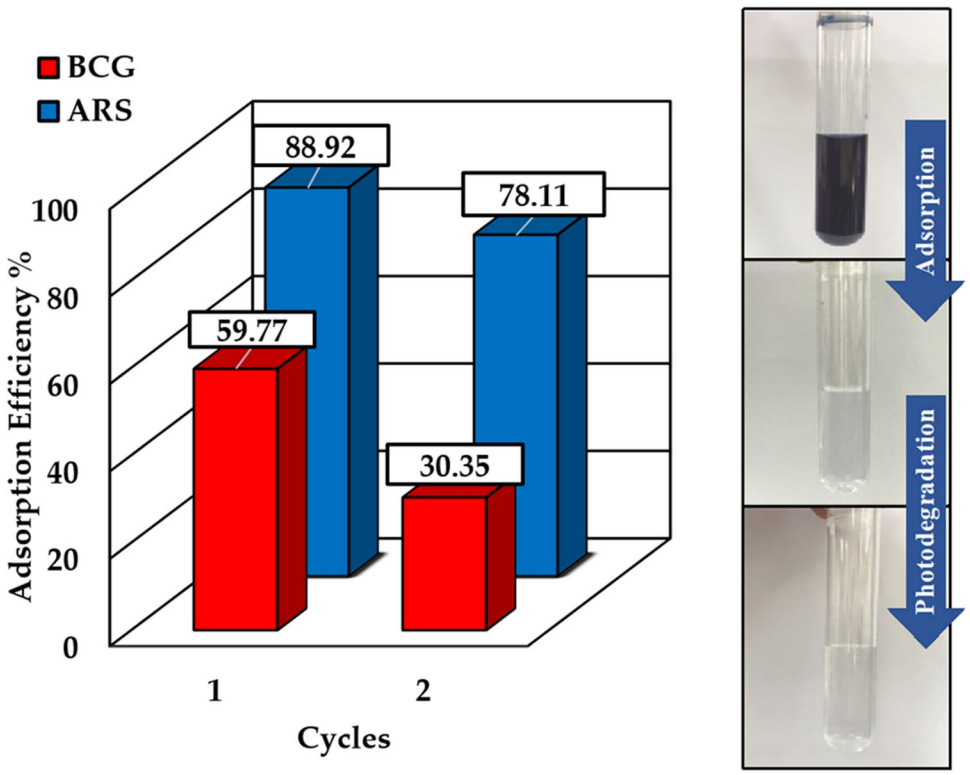

Fig. 15 First and second cycle binary adsorption efficiency of ARS and BCG onto TiO_2 nanoparticles

single adsorption case, with higher adsorption affinity toward BCG and higher adsorption uptake capacity of ARS. TiO_2 brookite nanoparticles succeeded in adsorbing both model molecules in the binary adsorption systems confirming the selective adsorption of ARS molecules and showing the goodness of the fitting results of the Extended-Sips model as verified by χ^2 analysis. The kinetics results revealed that the adsorption of ARS onto TiO_2 nanoparticles is predominantly external, achieving equilibrium in a short time for ARS when compared to BCG. The results of the thermodynamics study showed that the adsorption process was spontaneous with physisorption and chemosorption behaviors for both ARS and BCG dyes, respectively. The simulation energy distribution investigated through molecular dynamics simulation exhibited higher adsorption energies for ARS in the range from − 628 to − 1046 $kJmol^{-1}$ for both single and binary systems explaining the higher entropy value in the thermodynamics study. Finally, two regeneration cycles of TiO_2 nanoparticles using UV irradiation showed that the decrease of TiO_2 nanoparticles efficiency was around 11% for the adsorption of ARS, while the adsorption efficiency in the case of BCG dropped significantly to be 29%. The mechanistic insights for such a system can be investigated in futuristic works through complete photodegradation kinetics modeling.

Supplementary Information The online version contains supplementary material available at https://doi.org/10.1007/s11356-022-21368-7.

Acknowledgements The authors would like to thank Prof. Ismail Warrad for providing the SEM images. The fellowship provided by Faculty for the Future Program—Schlumberger Foundation to Maryam Hmoudah is deeply acknowledged and appreciated.

Author contribution MH wrote the original draft of the manuscript. The main conceptual ideas and coordination of research activities were monitored by AEQ. The experimental work was conducted by SA and HMB. Data elaboration and the formal analysis were conducted by AEQ, IHA, and BJAT. NNM conceived the cluster model, performing and analyzing the molecular dynamics computational modeling. AEH contributed to experimental methodology and the results validation. VR and MDS performed data curation and manuscript editing. The final draft was revised by all authors.

Data availability Data generated and analyzed during this study are included in this manuscript.

Declarations

Ethics approval and consent to participate Not applicable.

Consent for publication Not applicable.

Conflict of interest The authors declare no competing interests.

References

Abuhatab S, El-Qanni A, Marei NN, Hmoudah M, El-Hamouz A (2019) Sustainable competitive adsorption of methylene blue and acid red 88 from synthetic wastewater using NiO and/or MgO silicate based nanosorbcats: experimental and computational modeling studies. RSC Adv 9:35483–35498

Adeleye AS, Conway JR, Garner K, Huang Y, Su Y, Keller AA (2016) Engineered nanomaterials for water treatment and remediation: costs, benefits, and applicability. Chem Eng J 286:640–662

Ahmad A, Mohd-Setapar SH, Chuong CS, Khatoon A, Wani WA, Kumar R, Rafatullah M (2015) Recent advances in new generation dye removal technologies: novel search for approaches to reprocess wastewater. RSC Adv 5:30801–30818

Al-Mamun MR, Kader S, Islam MS, Khan MZH (2019) Photocatalytic activity improvement and application of UV-TiO2 photocatalysis in textile wastewater treatment: a review. J Environ Chem Eng 7:103248

Alakhras F, Alhajri E, Haounati R, Ouachtak H, Addi AA, Saleh TA (2020) A comparative study of photocatalytic degradation of Rhodamine B using natural-based zeolite composites. Surf Interfaces 20:100611

Albadarin AB, Mangwandi C (2015) Mechanisms of Alizarin Red S and Methylene blue biosorption onto olive stone by-product: isotherm study in single and binary systems. J Environ Manag 164:86–93

Arfi RB, Karoui S, Mougin K, Ghorbal A (2017) Adsorptive removal of cationic and anionic dyes from aqueous solution by utilizing almond shell as bioadsorbent. Euro-Mediterr J Environ Integr 2:20

Aryee AA, Dovi E, Guo Q, Liu M, Han R, Li Z, Qu L (2021) Selective removal of anionic dyes in single and binary system using Zirconium and iminodiacetic acid modified magnetic peanut husk. Environ Sci Pollut Res 28:37322–37337

Asgari G, Shabanloo A, Salari M, Eslami F (2020) Sonophotocatalytic treatment of AB113 dye and real textile wastewater using ZnO/persulfate: modeling by response surface methodology and artificial neural network. Environ Res 184:109367

Ashraf MA, Hanfiah MM (2017) Recent advances in assessment on clear water, soil and air. Environ Sci Pollut Res 24:22753–22754

Azha SF, Shamsudin MS, Bonilla-Petriciolet A, Ismail S (2021) Kinetics, process design and implementation of zwitterionic adsorbent coating for dipolar dyes removal in wastewater treatment industry. Environ Technol Innov 23:101763

Badawi AK, AbdElkodous M, Ali GAM (2021) Recent advances in dye and metal ion removal using efficient adsorbents and novel nano-based materials: an overview. RSC Adv 11:36528–36553

Badran I, Khalaf R (2020) Adsorptive removal of alizarin dye from wastewater using maghemite nanoadsorbents. Sep Sci Technol 55:2433–2448

Badran I, Talie Z (2021) Kinetics of alizarin dye hydrolysis in alkaline medium for wastewater treatment. Iran J Chem Chem Eng 40:1490–1501

Baresel C, Schaller V, Jonasson C, Johansson C, Bordes R, Chauhan V, Sugunan A, Sommertune J, Welling S (2019) Functionalized magnetic particles for water treatment. Heliyon 5:e02325

Behera M, Nayak J, Banerjee S, Chakrabortty S, Tripathy SK (2021) A review on the treatment of textile industry waste effluents towards the development of efficient mitigation strategy: an integrated system design approach. J Environ Chem Eng 9:105277

Bhardwaj V, Ballabh A (2022) A series of multifunctional pivalamide based Low Molecular Mass Gelators (LMOGs) with potential applications in oil-spill remediation and toxic dye removal. Colloids Surf A 632:127813

Chiu Y-H, Chang T-FM, Chen C-Y, Sone M, Hsu Y-J (2019) Mechanistic insights into photodegradation of organic dyes using heterostructure photocatalysts. Catalysts 9:430

Choi M, Lim J, Baek M, Choi W, Kim W, Yong K (2017) Investigating the unrevealed photocatalytic activity and stability of nanostructured brookite TiO2 film as an environmental photocatalyst. ACS Appl Mater Interfaces 9:16252–16260

Crake A, Christoforidis KC, Kafizas A, Zafeiratos S, Petit C (2017) CO2 capture and photocatalytic reduction using bifunctional TiO2/MOF nanocomposites under UV–vis irradiation. Appl Catal B 210:131–140

Dastgerdi ZH, Meshkat SS, Esrafili MD (2019) Enhanced adsorptive removal of Indigo carmine dye performance by functionalized carbon nanotubes based adsorbents from aqueous solution: equilibrium, kinetic, and DFT study. J Nanostruct Chem 9:323–334

de Souza ML, Corio P (2013) Effect of silver nanoparticles on TiO2-mediated photodegradation of Alizarin Red S. Appl Catal B 136:325–333

Ding F, Liu W, Diao J-X, Sun Y (2011) Characterization of Alizarin Red S binding sites and structural changes on human serum albumin: a biophysical study. J Hazard Mater 186:352–359

Dong S, Feng J, Fan M, Pi Y, Hu L, Han X, Liu M, Sun J, Sun J (2015) Recent developments in heterogeneous photocatalytic water treatment using visible light-responsive photocatalysts: a review. RSC Adv 5:14610–14630

Duncan WR, Stier WM, Prezhdo OV (2005) Ab initio nonadiabatic molecular dynamics of the ultrafast electron injection across the Alizarin−TiO_2 interface. J Am Chem Soc 127:7941–7951

El-Qanni A (2017) Development of sustainable nanosorbcats based technology for hydrocarbons and organic pollutants recovery from industrial wastewater, PhD Thesis, University of Calgary, Calgary, Canada

El-Qanni A, Nassar NN, Vitale G, Hassan A (2016) Maghemite nanosorbcats for methylene blue adsorption and subsequent catalytic thermo-oxidative decomposition: computational modeling and thermodynamics studies. J Colloid Interfaces Sci 461:396–408

El-Qanni A, Nassar NN, Vitale G (2017) Experimental and computational modeling studies on silica-embedded NiO/MgO nanoparticles for adsorptive removal of organic pollutants from wastewater. RSC Adv 7:14021–14038

Elkhider KHA, Ihsanullah I, Zubair M, Manzar MS, Mu'azu ND, Alharthi MA (2020) Synthesis, characterization and dye adsorption performance of strontium ferrite decorated bentonite-CoNiAl magnetic composite. Arab J Sci Eng 45:7397–7408

Escribá A, Thome Da Silva BAT, Lourenço SA, Cava CE (2021) Incorporation of nanomaterials on the electrospun membrane process with potential use in water treatment. Colloids Surf A 624:126775

Febrianto J, Kosasih AN, Sunarso J, Ju Y-H, Indraswati N, Ismadji S (2009) Equilibrium and kinetic studies in adsorption of heavy metals using biosorbent: a summary of recent studies. J Hazard Mater 162:616–645

Feng Y, Xue L, Duan J, Dionysiou DD, Chen Y, Yang L, Guo Z (2017) Purification of dye-stuff contained wastewater by a hybrid adsorption-periphyton reactor (HAPR): performance and mechanisms. Sci Rep 7:9635

Foo KY, Hameed BH (2010) Insights into the modeling of adsorption isotherm systems. Chem Eng J 156:2–10

Foroutan R, Mohammadi R, MousaKhanloo F, Sahebi S, Ramavandi B, Kumar PS, Vardhan KH (2020a) Performance of montmorillonite/graphene oxide/CoFe2O4 as a magnetic and recyclable nanocomposite for cleaning methyl violet dye-laden wastewater. Adv Powder Technol 31:3993–4004

Foroutan R, Peighambardoust SJ, Aghdasinia H, Mohammadi R, Ramavandi B (2020b) Modification of bio-hydroxyapatite

generated from waste poultry bone with MgO for purifying methyl violet-laden liquids. Environ Sci Pollut Res 27:44218–44229
Foroutan R, Peighambardoust SJ, Esvandi Z, Khatooni H, Ramavandi B (2021a) Evaluation of two cationic dyes removal from aqueous environments using CNT/MgO/CuFe2O4 magnetic composite powder: a comparative study. J Environ Chem Eng 9:104752
Foroutan R, Peighambardoust SJ, Hemmati S, Khatooni H, Ramavandi B (2021b) Preparation of clinoptilolite/starch/CoFe2O4 magnetic nanocomposite powder and its elimination properties for cationic dyes from water and wastewater. Int J Biol Macromol 189:432–442
Foroutan R, Peighambardoust SJ, Peighambardoust SH, Pateiro M, Lorenzo JM (2021c) Adsorption of crystal violet dye using activated carbon of lemon wood and activated carbon/Fe3O4 magnetic nanocomposite from aqueous solutions: a kinetic, equilibrium and thermodynamic study. Molecules 26:2241
Foroutan R, Mohammadi R, Ahmadi A, Bikhabar G, Babaei F, Ramavandi B (2022) Impact of ZnO and Fe3O4 magnetic nanoscale on the methyl violet 2B removal efficiency of the activated carbon oak wood. Chemosphere 286:131632
Gehrke I, Geiser A, Somborn-Schulz A (2015) Innovations in nanotechnology for water treatment. Nanotechnol Sci Appl 8:1–17
Goel PK (2006) Water pollution: causes, effects and control. New Age International, New Delhi
Gutierrez AM, Dziubla TD, Hilt JZ (2017) Recent advances on iron oxide magnetic nanoparticles as sorbents of organic pollutants in water and wastewater treatment. Rev Environ Health 32:111–117
Hasan N, Dalayoan DJC, Lee J, Lee J, Kim J, Bae J-S, Liu C (2021) Ag0/Au0 nanocluster loaded Bi2O4 photocatalyst for methyl orange dye photodegradation. RSC Adv 11:26607–26619
Hines AL, Maddox RN (1985) Mass transfer: fundamentals and applications, 434. Prentice-Hall Englewood Cliffs, NJ
Hou C, Hao J (2021) A three-dimensional nano-network WO3/F-TiO2-{001} heterojunction constructed with OH-TiOF2 as the precursor and its efficient degradation of methylene blue. RSC Adv 11:26063–26072
Ibrahim SM, Badawy AA, Essawy HA (2019) Improvement of dyes removal from aqueous solution by nanosized cobalt ferrite treated with humic acid during coprecipitation. J Nanostruct Chem 9:281–298
Ihab H Alsurakji, Amjad El-Qanni, Emad Salahat, Abdelkareem Arman MA, Abuzaina W (2021) Effective wastewater treatment using advanced oxidation process combined with magnetic nanoparticle setup. In: Al-Qodah Z (Hrsg.), Proceedings of the 9th Jordan International Chemical Engineering Conference. JICHEC, pp 14
Ihsanullah I (2022) Applications of MOFs as adsorbents in water purification: progress, challenges and outlook. Curr Opin Environ Sci Health 26:100335
Khan FSA, Mubarak NM, Tan YH, Karri RR, Khalid M, Walvekar R, Abdullah EC, Mazari SA, Nizamuddin S (2020a) Magnetic nanoparticles incorporation into different substrates for dyes and heavy metals removal—a review. Environ Sci Pollut Res 27:43526–43541
Khan S, Je M, Kim D, Lee S, Cho S-H, Song T, Choi H (2020b) Mapping point defects of brookite TiO2 for photocatalytic activity beyond anatase and P25. J Phys Chem C 124:10376–10384
Khnifira M, Boumya W, Abdennouri M, Sadiq Mh, Achak M, Serdaroğlu G, Kaya S, Şimşek S, Barka N (2021) A combined molecular dynamic simulation, DFT calculations, and experimental study of the eriochrome black T dye adsorption onto chitosan in aqueous solutions. Int J Biol Macromol 166:707–721
Kiani Ghalehsardi F, Behpour M, Ramezani Z, Masoum S (2021) Simultaneous removal of Basic Blue41 and Basic Red46 dyes in binary aqueous systems via activated carbon from palm bio-waste: optimization by central composite design, equilibrium, kinetic, and thermodynamic studies. Environ Technol Innov 24:102039
Kozawa T, Hattori H, Ogo S, Ide Y, Suzuki Y (2013) Hydrothermal conversion of Mg2TiO4 into brookite-type TiO2 under mild conditions. J Mater Sci 48:7969–7973
Kumar D, Singh A, Gaur JP (2008) Mono-component versus binary isotherm models for Cu(II) and Pb(II) sorption from binary metal solution by the green alga Pithophora oedogonia. Biores Technol 99:8280–8287
Kurade MB, Waghmode TR, Kagalkar AN, Govindwar SP (2012) Decolorization of textile industry effluent containing disperse dye Scarlet RR by a newly developed bacterial-yeast consortium BL-GG. Chem Eng J 184:33–41
Lachheb H, Puzenat E, Houas A, Ksibi M, Elaloui E, Guillard C, Herrmann J-M (2002) Photocatalytic degradation of various types of dyes (Alizarin S, Crocein Orange G, Methyl Red, Congo Red, Methylene Blue) in water by UV-irradiated titania. Appl Catal B 39:75–90
Largo F, Haounati R, Akhouairi S, Ouachtak H, El Haouti R, El Guerdaoui A, Hafid N, Santos DMF, Akbal F, Kuleyin A, Jada A, Addi AA (2020) Adsorptive removal of both cationic and anionic dyes by using sepiolite clay mineral as adsorbent: experimental and molecular dynamic simulation studies. J Mol Liq 318:114247
Lin Y, Ma J, Liu W, Li Z, He K (2019) Efficient removal of dyes from dyeing wastewater by powder activated charcoal/titanate nanotube nanocomposites: adsorption and photoregeneration. Environ Sci Pollut Res 26:10263–10273
Machida M, Kobayashi M, Suzuki Y, Abe H (2018) Facile synthesis of > 99% phase-pure brookite TiO2 by hydrothermal conversion from Mg2TiO4. Ceram Int 44:17562–17565
Marei NN, Nassar NN, Vitale G (2016) The effect of the nanosize on surface properties of NiO nanoparticles for the adsorption of Quinolin-65. Phys Chem Chem Phys 18:6839–6849
McKay G, Al-Duri B (1988) Prediction of bisolute adsorption isotherms using single-component data for dye adsorption onto carbon. Chem Eng Sci 43:1133–1142
Mohamed SK, Elhgrasi AM, Ali OI (2022) Facile synthesis of mesoporous nano Ni/NiO and its synergistic role as super adsorbent and photocatalyst under sunlight irradiation. Environ Sci Pollut Res
Montgomery DC, Runger GC (2006) Applied statistics and probability for engineers. Wiley, New York
Moriguchi T, Yano K, Nakagawa S, Kaji F (2003) Elucidation of adsorption mechanism of bone-staining agent alizarin red S on hydroxyapatite by FT-IR microspectroscopy. J Colloid Interface Sci 260:19–25
Mounteer AH, Arcanjo GS, Coimbra ECL, da Silva LMM (2019) ADMI color and toxicity reductions in raw textile mill effluent and dye mixtures by TiO2/UV is limited by presence of vat dyes. Environ Sci Pollut Res 26:4260–4265
Muniandy L, Adam F, Mohamed AR, Ng E-P, Rahman NRA (2016) Carbon modified anatase TiO2 for the rapid photo degradation of methylene blue: a comparative study. Surf Interfaces 5:19–29
Murmu B, Behera S, Das S, Mohapatra R, Bindhani B, Parhi P (2018) Extensive investigation on the study for the adsorption of Bromocresol Green (BCG) dye using activated Phragmites karka
Palmisano ADPMBL (2013) Brookite, the least known TiO2 photocatalyst. Catalysts 3:36–73
Peñas-Garzón M, Abdelraheem WHM, Belver C, Rodriguez JJ, Bedia J, Dionysiou DD (2021) TiO2-carbon microspheres as photocatalysts for effective remediation of pharmaceuticals under simulated solar light. Sep Purif Technol 275:119169
Qian C, Yin J, Zhao J, Li X, Wang S, Bai Z, Jiao T (2021) Facile preparation and highly efficient photodegradation performances of self-assembled Artemia eggshell-ZnO nanocomposites for wastewater treatment. Colloids Surf A 610:125752

Russo V, Hmoudah M, Broccoli F, Iesce MR, Jung O-S, Di Serio M (2020) Applications of metal organic frameworks in wastewater treatment: a review on adsorption and photodegradation. Front Chem Eng 2

Ruthven DM (1984) Principles of adsorption and adsorption processes. Wiley

Sawalha H, Al-Jabari M, Elhamouz A, Abusafa A, Rene ER (2020) Chapter 25—Tannery wastewater treatment and resource recovery options. In: Bhaskar T, Pandey A, Rene ER, Tsang DCW (eds) Waste biorefinery. Elsevier, pp 679–705

Sawyer DT, Heineman WR, Beebe JM (1984) Chemistry experiments for instrumental methods. Wiley

Shabbir S, Faheem M, Ali N, Kerr PG, Wu Y (2017) Evaluating role of immobilized periphyton in bioremediation of azo dye amaranth. Bioresour Technol 225:395–401

Sharma P, Borah DJ, Das P, Das MR (2016) Cationic and anionic dye removal from aqueous solution using montmorillonite clay: evaluation of adsorption parameters and mechanism. Desalin Water Treat 57:8372–8388

Sing KSW (1985) Reporting physisorption data for gas/solid systems with special reference to the determination of surface area and porosity (Recommendations 1984). Pure Appl Chem 57:603–619

Singh S, Kumar V, Romero R, Sharma K, Singh J (2019) Applications of nanoparticles in wastewater treatment. In: Prasad R, Kumar V, Kumar M, Choudhary D (eds) Nanobiotechnology in bioformulations. Springer International Publishing, Cham, pp 395–418

Thommes M, Kaneko K, Neimark AV, Olivier JP, Rodriguez-Reinoso F, Rouquerol J, Sing KSW (2015) Physisorption of gases, with special reference to the evaluation of surface area and pore size distribution (IUPAC Technical Report). Pure Appl Chem 87:1051–1069

Tomita K, Petrykin V, Kobayashi M, Shiro M, Yoshimura M, Kakihana M (2006) A water-soluble titanium complex for the selective synthesis of nanocrystalline brookite, rutile, and anatase by a hydrothermal method. Angew Chem Int Ed 45:2378–2381

Wang J, Guo X (2020) Adsorption kinetic models: physical meanings, applications, and solving methods. J Hazard Mater 390:122156

Wang Z, Lü S, Yang F, Kabir SMF, Mahmud S, Liu H (2021a) Hyaluronate macromolecules reduced-stabilized colloidal palladium nanocatalyst for azo contaminated wastewater treatment. Colloids Surf A 628:127345

Wang Z, Wu Z, Zhi X, Tu T, Nie J, Du X, Luo Y (2021b) TiO2/CTS/ATP adsorbent modification and its application in adsorption-ultrafiltration process for dye wastewater purification. Environ Sci Pollut Res 28:59963–59973

Worch E (2012) Adsorption technology in water treatment: fundamentals, processes, and modeling. De Gruyter

Yadav A, Bagotia N, Yadav S, Sharma AK, Kumar S (2021) Adsorptive studies on the removal of dyes from single and binary systems using Saccharum munja plant-based novel functionalized CNT composites. Environ Technol Innov 24:102015

Yang J-Y, Jiang X-Y, Jiao F-P, Yu J-G (2018) The oxygen-rich pentaerythritol modified multi-walled carbon nanotube as an efficient adsorbent for aqueous removal of alizarin yellow R and alizarin red S. Appl Surf Sci 436:198–206

Zhang Y, Qi H, Zhang L, Wang Y, Zhong L, Zheng Y, Wen X, Zhang X, Xue J (2022) A RGO aerogel/TiO2/MoS2 composite photocatalyst for the removal of organic dyes by the cooperative action of adsorption and photocatalysis. Environ Sci Pollut Res 29:8980–8995

Zolgharnein J, Bagtash M, Shariatmanesh T (2015) Simultaneous removal of binary mixture of Brilliant Green and Crystal Violet using derivative spectrophotometric determination, multivariate optimization and adsorption characterization of dyes on surfactant modified nano-γ-alumina. Spectrochim Acta A Mol Biomol Spectrosc 137:1016–1028

Publication IV

LANGMUIR

pubs.acs.org/Langmuir Article

Ibuprofen Adsorption on Activated Carbon: Thermodynamic and Kinetic Investigation via the Adsorption Dynamic Intraparticle Model (ADIM)

Maryam Hmoudah, Michele Emanuele Fortunato, Rosanna Paparo, Marco Trifuoggi, Amjad El-Qanni, Riccardo Tesser, Dmitry Yu. Murzin, Tapio Salmi, Vincenzo Russo,* and Martino Di Serio

Cite This: https://doi.org/10.1021/acs.langmuir.2c03350 Read Online

ACCESS | Metrics & More | Article Recommendations | Supporting Information

ABSTRACT: The adsorption efficiency of commercial activated carbon toward ibuprofen (IBU) was investigated and described using the adsorption dynamic intraparticle model (ADIM). Although the adsorption capacity of activated carbon has been widely studied, the kinetic models used in the literature are simplified, treating adsorption kinetics with pseudo-kinetic approaches. In this paper, a realistic model is proposed, quantitatively describing the influence of the main operation parameters on the adsorption kinetics and thermodynamics. The thermodynamic data were interpreted successfully with the Freundlich isotherm, deriving an endothermic adsorption mechanism. The system was found to be dominated by the intraparticle diffusion regime, and the collected data allowed the determination of the surface activation energy (E_S = 60 ± 7 kJ/mol) and the fluid−solid apparent activation energy (E_A = 6 ± 1 kJ/mol). The obtained parameters will be used to design adsorption columns, allowing the scale-up of the process.

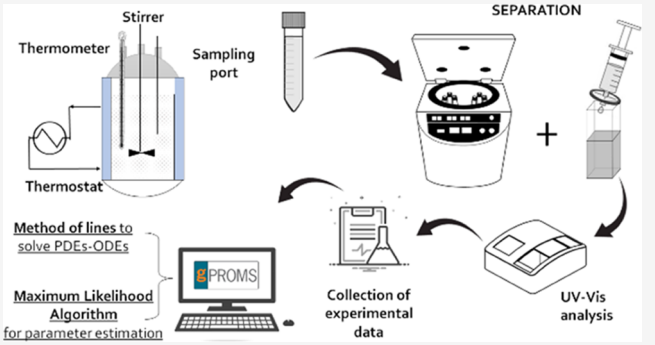

INTRODUCTION

Water is a vital resource for all living beings on Earth. Over the past 20 years, the demand of water increased due to industrialization and global population growth that is expected to reach 9.7 billion in 2064.[1] Nowadays, the presence of pharmaceutical compounds in wastewaters is steadily increasing. Ibuprofen (IBU) ($C_{13}H_{18}O_2$) is one of the most common pharmaceutical products classified under nonsteroidal anti-inflammatory drugs (NSAIDs)[2−4] found in wastewaters.[2,5,6] The conventional water treatment technologies are not designed to treat pharmaceutical compounds,[7] and thus there is a real risk of IBU accumulation in the environment leading to serious risks to human beings and the ecological system.[6,8] Therefore, the development of low-cost and scalable technologies is a real need to ensure high water quality. Adsorption is a separation process where one or more component of a fluid mixture (liquid or gaseous) is transferred on a solid surface.[9,10] Activated carbon is one the most versatile adsorbents due to its physicochemical properties (i.e., high specific surface area and porosity).[9] More specifically, adsorption of pharmaceutical compounds on activated carbon shows a high potential in terms of adsorption efficiency.[11−13] The most recent results obtained for ibuprofen removal using activated carbon are reported in Table 1. As revealed, several activated carbons were tested and exhibiting high adsorption capacities. Often, the modeling approaches are simplified, assuming the pseudo-homogeneous models. Developing reliable models is of paramount importance to describe the adsorption process in terms of design, control, and optimization. For this reason, there is a clear need to describe adsorption kinetic data using reliable models based on the description of the involved diffusion phenomena: (i) fluid−solid; (ii) intraparticle; and (iii) surface diffusion. Hence, a dynamic intraparticle model (ADIM) for fluid−solid adsorption kinetics was developed by our research group[10] and was already tested with success by other authors.[14−16] The significance of this model lies in describing both the thermodynamics and kinetics of fluid−solid adsorption data simultaneously. Furthermore, it can be considered general and easily adapted for any specific case.[17] Baltrėnaitė-Gedienė et al.[16] applied this model to simulate the pore volume and surface diffusion in the case of Zn(II), Cu(II), and Mn(II) on lignin biochar.

Received: December 12, 2022
Revised: May 22, 2023

Table 1. Ibuprofen Removal from Waters Using Activated Carbons as Sorbents

activated carbon	q_{max} [mg g^{-1}]	surface area [m^2 g^{-1}]	endo/exo[a]	thermodynamic model/s	kinetic model/s	highlights	refs
chemically surface-modified activated carbon cloths oxidized by a NaOCl solution or thermally treated under N_2	491.9	1910	endo	Langmuir Freundlich	pseudo-first-order pseudo-second-order Elovich	IBU uptake increases as the pH decreases no influence was detected for both treatments on the kind of micropores where the adsorption of ibuprofen occurred	19
commercial granular activated carbon	34.0	1000	exo	multicomponent Langmuir		the highest adsorption capacity toward IBU was at around pH = 2, confirming the pH effect increasing temperature significantly affected the adsorption rate of IBU	20
activated carbon derived from *Quercus brantii* (Oak) acorn	35.49	235	endo	Langmuir Freundlich the Dubinin–Radushkevich (D–R)	pseudo-first-order pseudo-second-order intraparticle diffusion	oak acorn agricultural waste can be effectively applied as an active adsorbent for the removal of IBU in the aqueous media	21
$NiFe_2O_4$/activated carbon magnetic composite	261.35	564.4	endo	Langmuir Freundlich SIPS	pseudo-first-order pseudo-second-order	the adsorption uptake was higher in acid conditions the magnetic properties of this material make it easy to separate from the liquid phase by a simple magnetic field	22
KOH functionalized activated carbon from date palm leaflets	255.0	823	endo	Langmuir Freundlich	pseudo-first-order pseudo-second-order	IBU showed higher adsorption on oxidized activated carbon but faster adsorption kinetics on hydrophobic activated carbon surface functionalized activated carbon showed a promising solution for pharmaceutical removal with good recyclability	23
activated carbon derived from *Lemna minor*	141.8	1164.5	endo	Langmuir Freundlich Temkin intraparticle diffusion	pseudo-first-order pseudo-second-order film diffusion	both film diffusion and intraparticle diffusion were found to be the major processes facilitating adsorption adsorption conditions were optimized adsorption uptake was higher at pH = 3	24
embedded chitosan–poly (vinyl alcohol) on activated carbon biocomposite	32.3	357	endo	Langmuir Freundlich Dubinin–Radushkevich (D–R) Temkin Halsey Jovanovic Harkins–Jura	pseudo-first-order pseudo-second-order Elovich Weber–Morris Bangham	activated carbon biocomposites have the potential to be the most efficient adsorbents for the adsorption of pharmaceutical pollutants from wastewater	25
activated carbon prepared from effluent treatment plant sludge of the beverage industry	105.9	642		Langmuir Freundlich SIPS	pseudo-first-order pseudo-second-order	remarkable adsorptive capacities were observed in different pharmaceutical compounds the material prepared in could be a promising adsorbent for pharmaceutical wastewater industries	26
activated carbon derived from *Nauclea diderrichii* biomass	70.9	33.2	endo	Langmuir Freundlich	pseudo-first-order pseudo-second-order	adsorption kinetics data confirmed that increasing the temperature significantly affects the IBU adsorption on activated carbon	27
yeast-based carbon and magnetic composite	107.0	68		Langmuir Freundlich SIPS Dubinin Radushkevich (D–R) Temkin	pseudo-first-order pseudo-second-order	a new perspective was presented on the reuse of an adsorbent without the need for regeneration processes before their complete saturation	28
agricultural waste-based activated carbons	300.0	330		Langmuir Freundlich	pseudo-first-order pseudo-second-order	activated carbons prepared from red mombin seeds showed the best adsorption capacity activated carbon surface showed higher affinity toward diclofenac in comparison with paracetamol or ibuprofen	29

https://doi.org/10.1021/acs.langmuir.2c03350
Langmuir XXXX, XXX, XXX−XXX

Table 1. continued

activated carbon	q_{max} [mg g^{-1}]	surface area [m^2 g^{-1}]	endo/exo[a]	thermodynamic model/s	kinetic model/s	highlights	refs
commercial vegetable activated carbon produced from babassu coconut husk	85−107	639.9−731.3		Freundlich	PVSDM model	three-dimensional mass-transfer model (PVSDM 3D) was applied	30
				Langmuir		textural ultrasound modifications caused an increase in the ibuprofen adsorption capacity	
				Redlich−Peterson			
commercial activated carbon DARCO 20−40 mesh	18.5	650	endo	Freundlich	ADIM model	kinetic data were successfully interpreted with the dynamic intraparticle model	present study

[a]Endo: endothermic; exo: exothermic.

For the mentioned reasons, in the present paper, an indepth kinetic and thermodynamic investigation was conducted using commercial activated carbons, namely, DARCO 20−40. The collected data were interpreted using the ADIM model to retrieve physicochemical parameters needed for a future design of a continuously operating adsorption column.[18]

EXPERIMENTAL SECTION

Materials. DARCO 20−40 mesh (specific surface area of 629 m^2/g, average pore diameter of 3.7 nm, total pore volume of 0.748 cm^3/g, volumes of micropores 0.264 cm^3/g, mesopores 0.190 cm^3/g, and macropores 0.294 cm^3/g[31]) commercial granular activated carbon was supplied by Sigma-Aldrich and used as a sorbent without any pretreatment. Ibuprofen (4-isobutyl-α-methylphenylacetic acid, purity 99%) was supplied by Alfa Aesar.

Batch Adsorption Experiments. The kinetic study was performed in a jacketed batch vessel. All of the experiments were performed loading 150 mL IBU solution at 10 mg L^{-1} and neutral pH with a fixed quantity of sorbent. The ratio between the adsorbate and the adsorbent in the kinetic experiments was chosen after a preliminary investigation, allowing to obtain measurable experimental kinetic data. The temperature of the solution was controlled using an external thermostat, while the stirring rate was adjusted via a mechanical stirring system. In general, ibuprofen solution was loaded and preheated at the desired temperature level at a fixed stirring rate. Once the system was stable, the sorbent was added to the vessel. Liquid samples (around 0.5 cm^3) were withdrawn periodically to measure the evolution of ibuprofen concentration with time. The sampling line was provided with a sintered stainless steel filter installed to avoid sorbent loss during sampling. The withdrawn quantity was sufficient for analytical purposes, just marginally affecting the sorbent concentration along the kinetic run. The samples were stored in closed vials. A spectrophotometer (Jasco V-550 UV/vis) was used to detect the residual IBU concentration in aqueous solutions. A typical spectrum was reported in the supplementary material (Figure S1). A calibration curve was recorded at λ = 222 nm, where the IBU absorption reached the maximum value, obtaining the calibration curve reported in eq S1, valid in a concentration range between 0 and 0.05 mol/m^3 (Figure S2).

To investigate the adsorption kinetics, along with eventual mass-transfer effects, several experiments were conducted varying the operating conditions within a wide range (see Table S1).

Adsorption Isotherms. Adsorption isotherm experiments were conducted at three different temperatures of 303, 313, and 323 K. Different amounts of activated carbon were added to a set of vials containing 10 mL solutions with an initial concentration of 10 mg L^{-1}, varying the sorbent/ibuprofen ratio. The vials were kept under stirring at a fixed temperature for 3 days, to be sure that the system would reach thermodynamic equilibrium. Three sets of solutions were prepared to investigate the effect of temperature on the adsorption performance. It is worth noting that the experiments were conducted in triplicate to ensure the reproducibility of the results, obtaining an error of less than 5%, calculated as the standard deviation.

Adsorption Modeling. The dynamic model ADIM was proposed and tested in both batch and continuous adsorption modes in our previous research,[10,18,32] and it was used for the interpretation of the collected data on adsorption kinetics considering all possible diffusion processes and adsorption equilibrium. This model is based on the following mechanism which consists of four successive steps: (i) diffusion of the solute from the bulk liquid phase (where the solute concentration in the bulk liquid phase, C_B, is assumed constant at a generic time t) to the solid surface; (ii) intraparticle diffusion; (iii) equilibrium of the solute concentration between the liquid and solid phase; and (iv) diffusion of the adsorbate species to the particle surface. The following assumptions were adopted:

1. isothermal system,
2. monomodal particle size,

https://doi.org/10.1021/acs.langmuir.2c03350
Langmuir XXXX, XXX, XXX−XXX

3. adsorption equilibrium in the pore with average porosity and tortuosity of the particle, and
4. particle mass balance is adaptable based on the shape factor.

Following these hypotheses, it is possible to derive for the batch system, the mass balance equations for the bulk liquid phase (eq 1) and for the solid phase (eq 2)[10] by considering both the film diffusion and intraparticle diffusion limitations. The bulk accumulation is equal to the film mass-transfer (eq 1), and the overall accumulation for both liquid and solid phases is the sum of the pore and surface intraparticle diffusion (eq 2)

$$\varepsilon' \frac{\partial C_B}{\partial t} = -k_m a_{sp}(C_B - C_L|_{R_p}) \tag{1}$$

where C_B is the liquid bulk concentration, t the simulation time, k_m the fluid−solid mass-transfer coefficient, a_{sp} the sorbent specific surface area per volume of particle, C_L the concentration in the liquid pores, and ε' the fluid bulk/solid phase volumetric ratio

$$\varepsilon \frac{\partial C_L}{\partial t} + (1-\varepsilon)\frac{\partial C_S}{\partial t} = \varepsilon \frac{D_P}{r_P^S}\frac{\partial}{\partial r_P}\left(r_P^S \frac{\partial C_L}{\partial r_P}\right) + (1-\varepsilon)\frac{1}{r_P^S}\frac{\partial}{\partial r_P}\left(r_P^S D_S C_S \frac{\partial C^*}{\partial r_P}\right) \tag{2}$$

where ε is the sorbent porosity, C_S the concentration on the solid surface, r_P the sorbent radius, D_P the pore diffusion coefficient, D_S the surface diffusion coefficient, S the shape factor, and C* defined as in eq 3

$$C^* = \ln\left(\frac{C_S}{K_F}\right)^n \tag{3}$$

where K_F and n are the Freundlich isotherm parameters.

The following physical and chemical parameters were considered. The pore diffusivity (D_P) presented in eq 4 was calculated from the molecular diffusivity, correcting it with the porosity ε and tortuosity τ of the solid. The corresponding molecular diffusivity (D_0) was estimated based on the Wilke−Chang equation (eq 5)

$$D_P = \frac{\varepsilon}{\tau} D_0 \tag{4}$$

$$D_0 = \frac{7.4 \times 10^{-12}(\phi M_B)^{0.5} T}{\mu_B V_A} \tag{5}$$

where φ is the association factor (set to 2.6 for associating molecules), M_B the molecular weight of the solvent, T the temperature, μ_B the viscosity of the solvent, and V_A the molar volume calculated at the standard boiling point calculated using Le Bas correlation, V_A = 268 cm^3/mol.

To solve the mentioned set of partial differential equations, it is necessary to set appropriate boundary conditions.

Equations 6 and 7 represent the symmetry condition at the center of the particle (r_P = 0) for both liquid and adsorbed phases, whereas eq 8 expresses the steady-state hypothesis at the solid surface (r_P = R_P)

$$\left.\frac{\partial C_L}{\partial r_P}\right|_{r_P=0} = 0 \tag{6}$$

$$\left.\frac{\partial C_S}{\partial r_P}\right|_{r_P=0} = 0 \tag{7}$$

$$\varepsilon D_P \left.\frac{\partial C_L}{\partial t}\right|_{r_P=R_P} + (1-\varepsilon) D_P C_S \frac{\partial C^*}{\partial r_P} = k_m(C_b - C_L|_{R_P}) \tag{8}$$

Furthermore, the Freundlich isotherm (eq 9) was considered to evaluate the solute concentration in the solid at equilibrium

$$C_S = K_F C_L^{1/n} \tag{9}$$

where K_F is the Freundlich constant related to the adsorption capacity, and $1/n$ is the adsorption intensity factor.

More theoretical information about the ADIM and the mathematical demonstration of the mass balance equations can be found in refs 1018

Numerical Methods. The adsorption process introduced in the previous section is from the mathematical viewpoint for a system of partial differential equations (PDEs), ordinary differential equations (ODE), and algebraic equations (AEs). The simultaneous numerical solution of these equations is very challenging, and it was performed by using gPROMS ModelBuilder v.4.0. This software provides algorithms based on the method of lines to solve the coupled system of PDEs and ODEs. In particular, the second-order centered finite difference method of approximation was used as the discretization method of the radial coordinate in 100 points. The model input parameters, namely, the sorbent properties, are listed in Table 2. The surface diffusivity D_S and the mass-transfer coefficient k_m were estimated by submitting the experimental data to nonlinear regression analysis by using the MXLKHD mathematical solver for the parameter estimation included in the software, considering the typical ranges reported in our previous work.[10,18]

Table 2. Input Parameters for ADIM

symbol	value	unit
R_P	0.35×10^{-3}	m
S	2	
a_{sp}	8.57×10^3	m^2 m^{-3}
ε	0.38	
τ	4.46	
ρ_{solid}	1950	kg m^{-3}

RESULTS AND DISCUSSION

Adsorption Isotherms. Experiments were conducted at different temperatures to investigate the adsorption capacity trend with the temperature of the activated carbon and to determine the corresponding adsorption isotherm. The collected results are reported in Figure 1.

As revealed, the adsorption of IBU on activated carbon increases by increasing the temperature. The adsorption isotherms trends follow the Freundlich model as reported in the literature for this system (see Table 1).[21] This isotherm

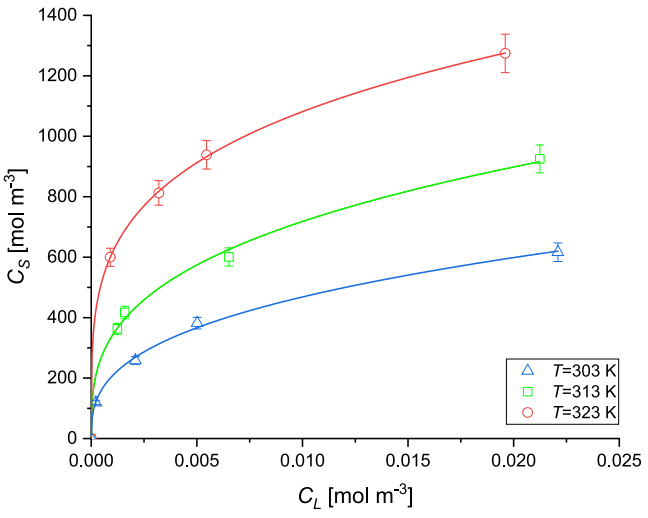

Figure 1. Adsorption isotherms at different temperatures. Symbols represent the experimental data and lines the calculated profiles.

https://doi.org/10.1021/acs.langmuir.2c03350
Langmuir XXXX, XXX, XXX−XXX

describes the adsorption on a heterogeneous surface due by sites characterized by different adsorption energies, with the possibility of interaction between the adsorbed molecules.[33] The estimated parameters at the three different temperatures are displayed in Table 3, together with 95% confidence

Table 3. Parameters Estimated for the Adsorption Isotherms

T [K]	K_F [(mol m^{-3})$^{1-1/n}$]	n [−]
303	2400 ± 100	2.8 ± 0.1
313	3000 ± 200	3.1 ± 0.1
323	3300 ± 40	4.1 ± 0.1

intervals. The values of the empirical constant n fall in the range of 1−10, indicating a strong interaction between IBU and the activated carbon.[34] Moreover, n increases with temperature, indicating a stronger interaction between the sorbent and adsorbate at higher temperatures, suggesting an endothermic adsorption mechanism.

This effect was already reported in the literature (see Table 1).[20,35,36] One explanation could be the ibuprofen change in the conformation with temperature, giving another conformer more strongly adsorbed. Certainly, the influence of mass transfer could be another possibility. These are surely just hypotheses and must be verified via dedicated experimentation and quantum chemistry computations.

Kinetic Investigation. Adsorption kinetics can be described by assuming a series of diffusion paths, where the molecules move from the bulk liquid phase to the inner part of the sorbent particles. The proposed model describes the adsorption kinetics with no rate-determining steps, including all of the possible paths from the film phase to intraparticle diffusion.[18]

The case of ibuprofen adsorption on activated carbons is well-suited as ibuprofen molecule dimensions (1.03 nm × 0.52 nm × 0.43 nm[37]) are compatible only with the mesopores and macropores. As DARCO 20−40 is characterized by a considerable fraction of micropores, intraparticle diffusion certainly limits the adsorption kinetics. To verify the mentioned assumption, Bangham's equation (eq 10) was used, in a first step, to verify if the intraparticle diffusion was the only rate-determining step of the adsorption process

$$\log\log\left(\frac{C_{B,0}}{C_{B,0}-q_t\rho_{bulk}}\right)=\log\left(\frac{k_b\rho_{bulk}}{2.303V}\right)+\alpha\log(t) \quad (10)$$

with q_t the adsorbed quantity calculated as $q_t = (C_{B,0} - C_B)/\rho_{bulk}$.

As an example, the plot of $\log\log[C_{B,0}/(C_{B,0} - q_t\rho_{bulk})]$ vs $\log t$ is reported in Figure 2 for the experiments performed at different T.

The goodness of fit of the Bangham model surely indicates the presence of intraparticle diffusion limitations. Therefore, R^2 values decrease when the temperature increases, indicating that the intraparticle diffusion becomes less important at higher temperatures. This conclusion is surely valid as diffusion adsorption increases at higher temperatures.

For the mentioned reasons, there is a clear necessity to use a sophisticated model that takes into consideration also the intraparticle diffusion. Thus, the ADIM model was used to give a deeper insight into fluid−solid, pore, and surface diffusion.

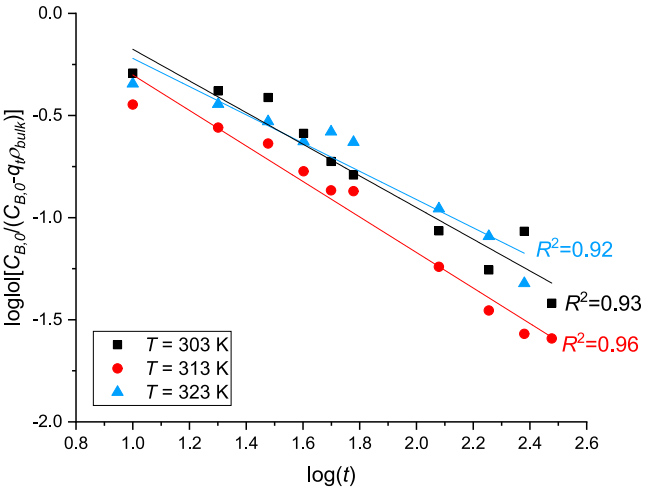

Figure 2. Bangham model for the adsorption of ibuprofen on activated carbon at different temperatures. Experimental conditions are ρ_{bulk} = 0.39 kg/m^3, $C_{B,0}$ = 0.05 mol/m^3, and v = 500 rpm.

The effect of stirring speed on the adsorption kinetics of IBU on activated carbon is depicted in Figure 3. The kinetic curves

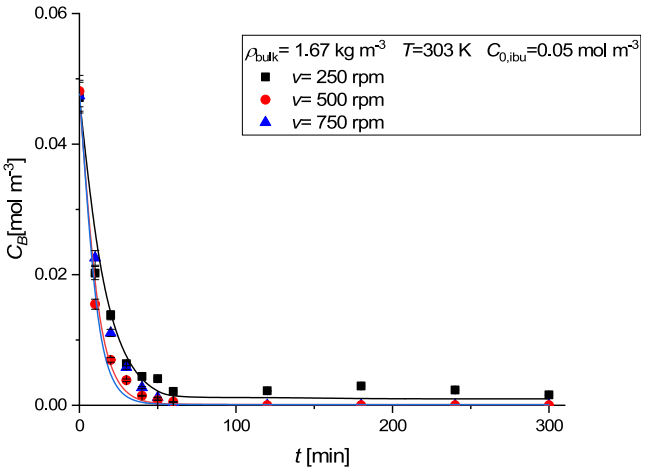

Figure 3. Adsorption kinetics at different stirring speeds; experimental conditions are ρ_{bulk} = 1.67 kg/m^3, $C_{B,0}$ = 0.05 mol/m^3, and T = 303 K. Symbols represent the experimental data and lines the calculated profiles.

show that the adsorption was rapid, reaching 80% of saturation during the first 40 min. Moreover, varying the stirring rate from 500 to 750 rpm does not lead to a significant change in the adsorption kinetics. This phenomenon is reflected in the trend of the k_m values in Table 4, indicating a first increase until reaching a plateau value, within the error.

Figures 4 and 5 show the effect of the initial concentration of IBU on adsorption at two different sorbent bulk densities of ρ_{bulk} = 0.39 kg m^{-3} and 0.82 kg m^{-3}, respectively. The experimental profiles show an increase in the initial slope when

Table 4. Mass-Transfer Coefficient at Various Stirring Rates

v [rpm]	k_m [m s^{-1}]
250	(1.3 ± 0.1) × 10^{-4}
500	(2.0 ± 0.8) × 10^{-4}
750	(3.0 ± 0.1) × 10^{-4}

https://doi.org/10.1021/acs.langmuir.2c03350
Langmuir XXXX, XXX, XXX−XXX

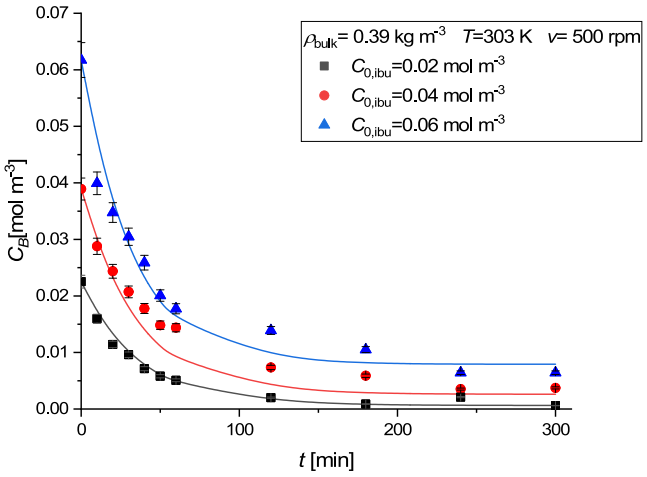

Figure 4. Effect of the initial concentration of IBU on the adsorption kinetics; experimental conditions: ρ_{bulk} = 0.39 kg/m^3, T = 303 K, and v = 500 rpm. Symbols represent the experimental data and lines the calculated profiles.

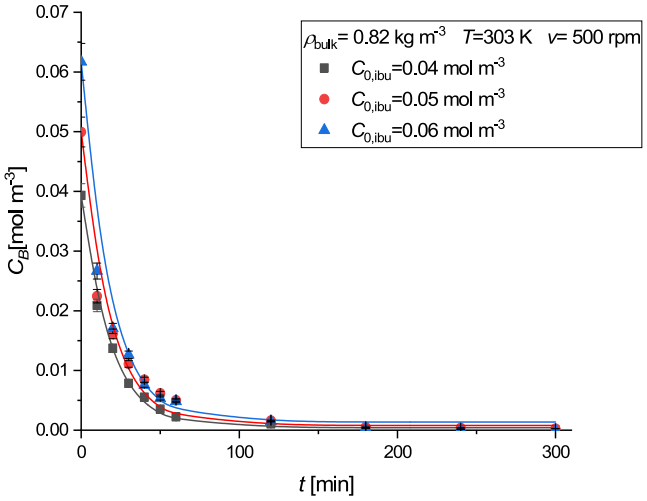

Figure 5. Effect of the initial concentration of IBU on the adsorption kinetics; experimental conditions: ρ_{bulk} = 0.82 kg/m^3, T = 303 K, and v = 500 rpm. Symbols represent the experimental data and lines the calculated profiles.

increasing the concentration of IBU (Figure 4). Moreover, the adsorption kinetics is strongly influenced by the amount of adsorbent used in the experiment (Figure 5): as the amount of sorbent loading increases, there is a corresponding increase in the adsorption kinetics.

The effect of temperature on the adsorption kinetics is presented in Figure 6. The experimental results indicate that the adsorption kinetics increases by increasing the temperature. This finding is in agreement with previous studies.[30,36,38] This could be attributed to the increase of diffusion of the molecules into the pores of the activated carbon.[21] Additionally, the overall positive surface charge leads to the donor−acceptor interactions between the aromatic ring of IBU as an electron acceptor and the surface carbonyl groups of the activated carbon as an electron donor. In addition, since k_m and D_S are temperature-dependent parameters, it was necessary to estimate their values for each temperature, as reported in Table 5. It is evident that the higher the temperature, the higher are both the liquid−solid mass-transfer coefficient and

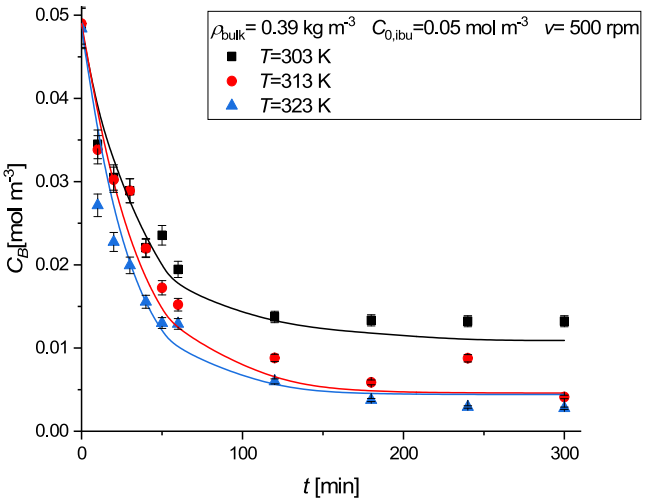

Figure 6. Effect of temperature on the adsorption kinetics; experimental conditions are ρ_{bulk} = 0.39 kg/m^3, $C_{B,0}$ = 0.05 mol/m^3, and v = 500 rpm. Symbols represent the experimental data and lines the calculated profiles.

Table 5. Estimated Parameters at Different Temperatures

T [K]	k_m[m s^{-1}]	D_S [m^2 s^{-1}]
303	(2.0 ± 0.5) × 10^{-4}	(0.50 ± 0.01) × 10^{-11}
313	(2.4 ± 0.2) × 10^{-4}	(0.9 ± 0.1) × 10^{-11}
323	(3.0 ± 0.4) × 10^{-4}	(2.0 ± 0.4) × 10^{-11}

the surface diffusivity, indicating a positive effect of temperature on both the external and internal diffusion steps.

The dependence of the surface diffusivity on temperature is shown in Figure 7A. It can be noticed that it follows an Arrhenius-like trend as demonstrated by Russo et al.[32] Thus, it is possible to use the mathematical expression as reported in eq 11

$$D_S = D_{S,0} \exp\left(-\frac{E_S}{RT}\right) \quad (11)$$

From the nonlinear data fit analysis, a surface activation energy E_S = 60 ± 7 kJ/mol was obtained.

In a similar way, by plotting the natural logarithm of k_m as a function of $1/T$, assuming an Arrhenius-like dependence, a linear trend is obtained (Figure 7B). From the slope of the fitting curve, it is possible to calculate the value of the activation energy E_A = 16 ± 1 kJ/mol required by the molecules to diffuse from the bulk liquid phase to the solid phase.

Figure 8 represents a comparison between the three different bulk densities, i.e., 0.39, 0.82, and 1.67 kg/m^3 at $C_{B,0}$ = 0.05 mol/m^3 while the temperature and stirring rate were kept constant. The results obtained at 303 K using a sorbent loading of 0.39 kg/m^3 lead to an adsorption capacity of 18.5 mg/g, that is in line with the results reported in the literature (see Table 1).

The adsorption kinetics is slightly influenced by the initial concentration of IBU. This can be attributed to more adsorptive active sites introduced when loading a bigger amount of activated carbon, and the corresponding initial slopes of the kinetic curves significantly increase, which is in agreement with the results reported in the literature.

https://doi.org/10.1021/acs.langmuir.2c03350
Langmuir XXXX, XXX, XXX−XXX

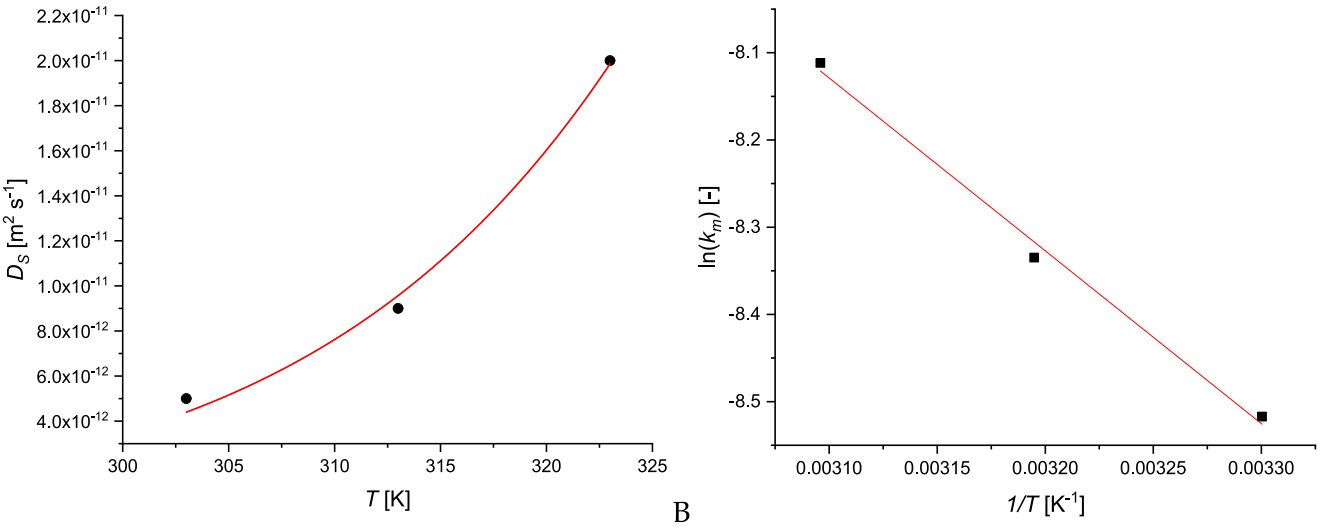

Figure 7. (A) Surface diffusion coefficient trend as a function of temperature. (B) Fluid−solid external mass-transfer coefficient trend as a function of temperature.

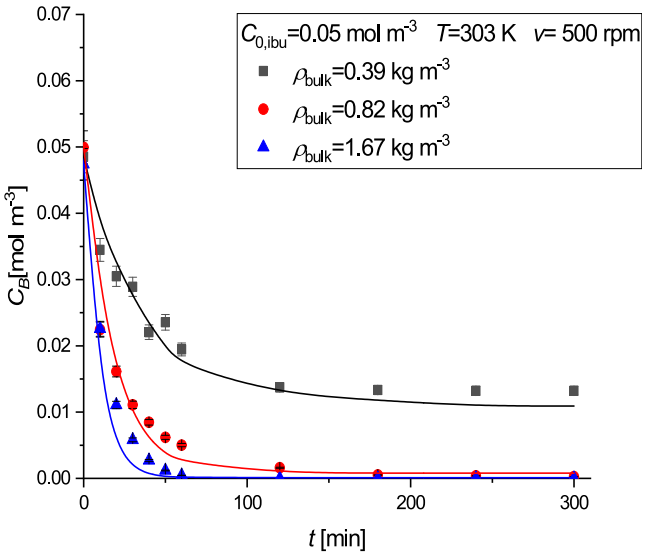

Figure 8. Effect of bulk density on the adsorption kinetics; experimental conditions are $C_{B,0}$ = 0.05 mol/m^3 and ν = 500 rpm. Symbols represent the experimental data and lines the calculated profiles.

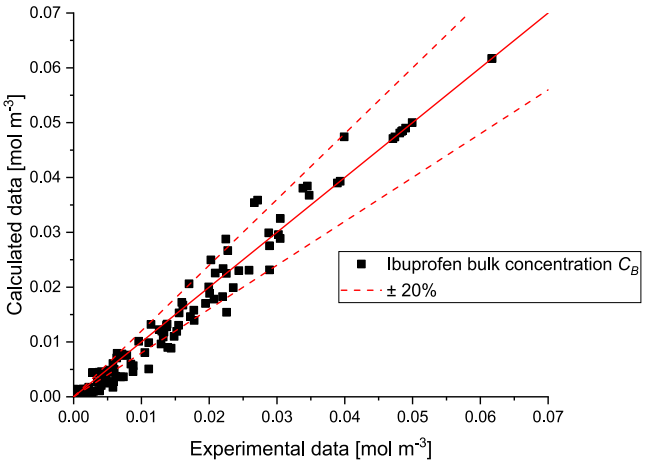

Figure 9. Parity plot of all of the kinetic data collected in the present article.

The parity plot for all of the kinetic data fitting is shown in Figure 9. Comparing the experimental results and model predictions, all of the points fall within a confidence interval of ±20%. In conclusion, the overall goodness of fit is corroborated by the coefficient of determination R^2 which equals 0.987.

The influence of textural properties on the adsorption kinetics was simulated by varying both the porosity and dimensions of the sorbent (Figure 10).

As revealed, the structural properties of sorbents can affect the adsorption performances. Figure 10A demonstrates that by increasing the sorbent porosity, a decrease of the adsorption capacity is expected, as the solid/fluid ratio is decreasing inside the sorbent particle. Figure 10B clearly indicates that bigger particles lead to a slower adsorption kinetics: de facto, the diffusion path is increasing when the radius of the sorbent particle is also increasing, leading to stronger concentration gradients inside the solid phase. These results unequivocally confirm flexibility of the model, able to predict different cases over a broad range of operation conditions.

CONCLUSIONS

In this work, the adsorption of ibuprofen, an emerging contaminant, on activated carbon was investigated. The best conditions for ibuprofen removal were identified. An extensive kinetic and equilibrium study was carried out with dedicated batch experiments to explore the effect of main operation conditions. The adsorption equilibrium data could be satisfactorily explained by the Freundlich model, indicating the strong bond between IBU and activated carbon and describing the heterogeneity of the surface sites with different adsorption energies. The ADIM model provided insights into the diffusion mechanism of IBU through the determination of k_m and D_S values, the parameters needed to design an adsorption column working in flow.

It must be pointed out that the results obtained in the present study are related to a model system, ibuprofen in water, adopted to test the ADIM model on ibuprofen adsorption. Working with a real matrix will potentially lead

https://doi.org/10.1021/acs.langmuir.2c03350
Langmuir XXXX, XXX, XXX−XXX

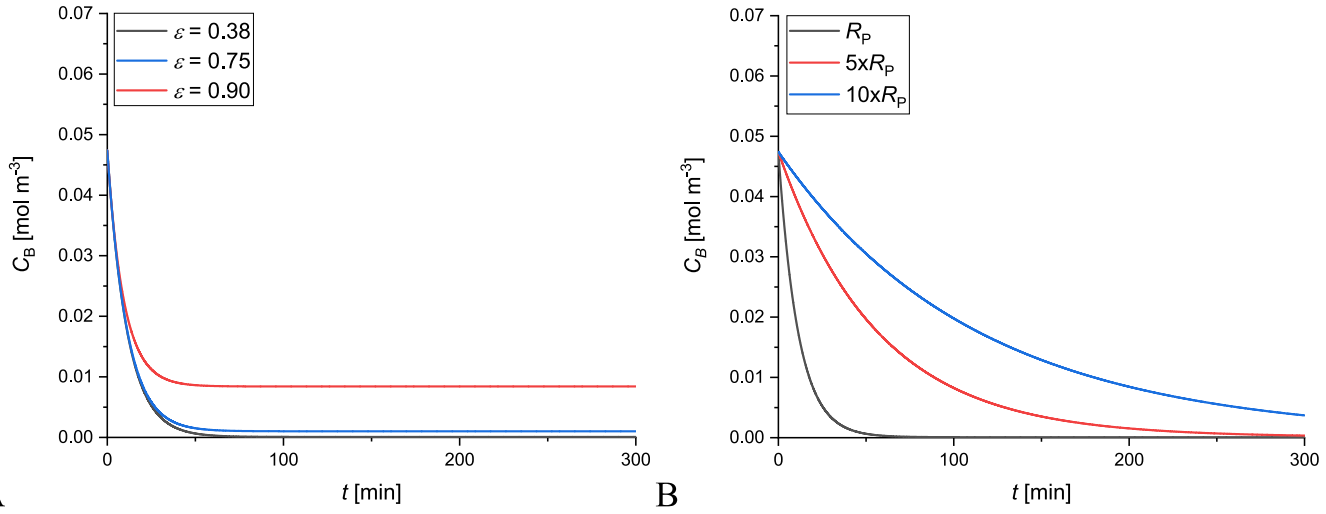

Figure 10. Simulations of the ibuprofen adsorption kinetics conducted at different (A) sorbent porosities and (B) sorbent dimensions. Simulations were conducted fixing T = 303 K and ρ_B = 1.67 kg/m^3.

to a more complex behavior, as the interference of other organic and inorganic compounds could lead to a decrease of the adsorption efficiency of the selected sorbent. As the composition of wastewaters strongly depends on their origin, it is not easy to simulate a priori a real matrix in laboratory, thus requiring testing different sorbents and adjusting adsorption parameters, and the latter is important when there is a natural influence of the adsorbed species.

■ ASSOCIATED CONTENT

Supporting Information

The Supporting Information is available free of charge at https://pubs.acs.org/doi/10.1021/acs.langmuir.2c03350.

UV−vis absorption spectrum of ibuprofen (Figure S1), related calibration curve (Figure S2), and list of the kinetic experiments (Tables S1) (PDF)

Activated carbon shows high adsorption capacity toward ibuprofen; both kinetic and thermodynamic information were obtained; Freundlich isotherm governs the adsorption equilibrium; kinetic data were successfully interpreted with the dynamic intraparticle model; and surface diffusivity trend with temperature was used to calculate the adsorption energy (PDF)

■ AUTHOR INFORMATION

Corresponding Author

Vincenzo Russo − *Department of Chemical Sciences, University of Naples Federico II, IT-80126 Naples, Italy; Laboratory of Industrial Chemistry and Reaction Engineering (TKR), Åbo Akademi, FI-20500 Turku/Åbo, Finland;* orcid.org/0000-0002-1867-739X; Email: v.russo@unina.it

Authors

Maryam Hmoudah − *Department of Chemical Sciences, University of Naples Federico II, IT-80126 Naples, Italy*

Michele Emanuele Fortunato − *Department of Chemical Sciences, University of Naples Federico II, IT-80126 Naples, Italy;* orcid.org/0000-0003-4414-6549

Rosanna Paparo − *Department of Chemical Sciences, University of Naples Federico II, IT-80126 Naples, Italy*

Marco Trifuoggi − *Department of Chemical Sciences, University of Naples Federico II, IT-80126 Naples, Italy*

Amjad El-Qanni − *Department of Chemical Engineering, An-Najah National University, P-400 Nablus, Palestine*

Riccardo Tesser − *Department of Chemical Sciences, University of Naples Federico II, IT-80126 Naples, Italy;* orcid.org/0000-0001-7002-7194

Dmitry Yu. Murzin − *Laboratory of Industrial Chemistry and Reaction Engineering (TKR), Åbo Akademi, FI-20500 Turku/Åbo, Finland;* orcid.org/0000-0003-0788-2643

Tapio Salmi − *Laboratory of Industrial Chemistry and Reaction Engineering (TKR), Åbo Akademi, FI-20500 Turku/Åbo, Finland;* orcid.org/0000-0002-9271-7425

Martino Di Serio − *Department of Chemical Sciences, University of Naples Federico II, IT-80126 Naples, Italy;* orcid.org/0000-0003-4489-7115

Complete contact information is available at: https://pubs.acs.org/10.1021/acs.langmuir.2c03350

Author Contributions

Writing—original draft: M.H. and M.E.F.; conceptualization: V.R., M.D.S., and T.S.; funding acquisition: M.D.S. and T.S.; investigation: R.P., M.H., and M.T.; formal analysis: M.E.F., R.T., and A.E.-Q.; supervision and project administration: V.R., M.D.S., and T.S.; data curation: M.E.F., D.Y.M., and R.T.; writing—review and editing: all of the authors equally.

Notes

The authors declare no competing financial interest.

Environmental Implication: The present study is focused on the removal of an emerging contaminant from waters, ibuprofen. In detail, an advanced numerical approach is proposed to describe the data collected using the batch adsorption apparatus. The work will be useful to design adsorption columns working in flow. Thus, it will be possible to install continuous devices for the abatement of ibuprofen from waters, allowing a better quality of streams.

The authors declare that the research was conducted in the absence of any commercial or financial relationships that could be construed as a potential conflict of interest.

https://doi.org/10.1021/acs.langmuir.2c03350
Langmuir XXXX, XXX, XXX−XXX

■ ACKNOWLEDGMENTS

The authors are grateful to Luigi Ebarone, Luigi Faro, and Vincenzo Liguori for the experimental support. The faculty for the future Program—Schlumberger Foundation—is acknowledged for providing a fellowship to Maryam Hmoudah.

■ LIST OF SYMBOLS

a_{sp}geometric specific area, $m^2 \cdot m^{-3}$
C_0adsorbate initial concentration, $mol \cdot m^{-3}$
$C_B$solute bulk concentration, $mol \cdot m^{-3}$
$C_L$solute concentration in the liquid of the pores, $mol \cdot m^{-3}$
$C_S$solute concentration in the solid, $mol \cdot m^{-3}$
$C_{S,*}$saturation solute solid concentration, $mol \cdot m^{-3}$
D_0molecular diffusivity, $m^2 \cdot s^{-1}$
$D_P$pore diffusivity based on the cross-sectional area, $m^2 \cdot s^{-1}$
$D_S$surface diffusivity, $m^2 \cdot s^{-1}$
k_bBangham's equation constant, $m^6\ kg^{-1}$
K_FFreundlich adsorption constant, $(mol \cdot m^{-3})^{1-1/n}$
$k_m$mass-transfer coefficient, $m \cdot s^{-1}$
$M_B$solvent molecular weight, $g\ mol^{-1}$
$n$adsorption intensity
$q_t$adsorbed amount at time t, $mol\ kg^{-1}$
$r_P$particle radial coordinate, m
$R_P$particle radius, m
Sshape factor
$t$time, s
Ttemperature, K
$V_A$molar volume of the solute at the standard boiling point, cm^3/mol
$V_P$particle volume, m^3
w_{ADS}adsorbent mass, g

Greek Symbols

αslope of Bangham's linear plot
εsolid particle porosity
ε'fluid bulk/solid phase volumetric ratio
$\mu_B$solvent viscosity, $kg \cdot m^{-1} \cdot s^{-1}$
ϕassociation factor
$\rho_B$solvent density, $kg \cdot m^{-3}$
ρ_{bulk}solid bulk density, $kg\ m^{-3}$
$\rho_S$solid density, $kg\ m^{-3}$
τtortuosity factor

■ REFERENCES

(1) Vollset, S. E.; Goren, E.; Yuan, C.-W.; Cao, J.; Smith, A. E.; Hsiao, T.; Bisignano, C.; Azhar, G. S.; Castro, E.; Chalek, J.; Dolgert, A. J.; Frank, T.; Fukutaki, K.; Hay, S. I.; Lozano, R.; Mokdad, A. H.; Nandakumar, V.; Pierce, M.; Pletcher, M.; Robalik, T.; Steuben, K. M.; Wunrow, H. Y.; Zlavog, B. S.; Murray, C. J. L. Fertility, Mortality, Migration, and Population Scenarios for 195 Countries and Territories from 2017 to 2100: A Forecasting Analysis for the Global Burden of Disease Study. *Lancet* **2020**, *396*, 1285−1306.

(2) Thalla, A. K.; Vannarath, A. S. Occurrence and Environmental Risks of Nonsteroidal Anti-Inflammatory Drugs in Urban Wastewater in the Southwest Monsoon Region of India. *Environ. Monit. Assess.* **2020**, *192*, No. 193.

(3) Martín, J.; Camacho-Muñoz, D.; Santos, J. L.; Aparicio, I.; Alonso, E. Occurrence of Pharmaceutical Compounds in Wastewater and Sludge from Wastewater Treatment Plants: Removal and Ecotoxicological Impact of Wastewater Discharges and Sludge Disposal. *J. Hazard. Mater.* **2012**, *239*−*240*, 40−47.

(4) Contardo-Jara, V.; Lorenz, C.; Pflugmacher, S.; Nützmann, G.; Kloas, W.; Wiegand, C. Exposure to Human Pharmaceuticals Carbamazepine, Ibuprofen and Bezafibrate Causes Molecular Effects in Dreissena Polymorpha. *Aquat. Toxicol.* **2011**, *105*, 428−437.

(5) Contreras, C. R.; López, D.; Leiva, A. M.; Domínguez, C.; Bayona, J. M.; Vidal, G. Removal of Organic Micropollutants in Wastewater Treated by Activated Sludge and Constructed Wetlands: A Comparative Study. *Water* **2019**, *11*, No. 2515.

(6) Russo, V.; Hmoudah, M.; Broccoli, F.; Iesce, M. R.; Jung, O.-S.; Di Serio, M. Applications of Metal Organic Frameworks in Wastewater Treatment: A Review on Adsorption and Photodegradation. *Front. Chem. Eng.* **2020**, *2*, No. 581487.

(7) Durán, A.; Monteagudo, J. M.; Martín, I. S. Operation Costs of the Solar Photo-Catalytic Degradation of Pharmaceuticals in Water: A Mini-Review. *Chemosphere* **2018**, *211*, 482−488.

(8) Couto, C. F.; Lange, L. C.; Amaral, M. C. S. Occurrence, Fate and Removal of Pharmaceutically Active Compounds (PhACs) in Water and Wastewater Treatment Plants—A Review. *J. Water Process Eng.* **2019**, *32*, No. 100927.

(9) Russo, V.; Trifuoggi, M.; Di Serio, M.; Tesser, R. Fluid-Solid Adsorption in Batch and Continuous Processing: A Review and Insights into Modeling. *Chem. Eng. Technol.* **2017**, *40*, 799−820.

(10) Russo, V.; Tesser, R.; Trifuoggi, M.; Giugni, M.; Di Serio, M. A Dynamic Intraparticle Model for Fluid−Solid Adsorption Kinetics. *Comput. Chem. Eng.* **2015**, *74*, 66−74.

(11) Bernal, V.; Giraldo, L.; Moreno-Piraján, J. C. Insight into Adsorbate−Adsorbent Interactions between Aromatic Pharmaceutical Compounds and Activated Carbon: Equilibrium Isotherms and Thermodynamic Analysis. *Adsorption* **2020**, *26*, 153−163.

(12) Removal of pharmaceutical compounds from aqueous solution by novel activated carbon synthesized from lovegrass (Poaceae), SpringerLink, 2023. https://link.springer.com/article/10.1007/s11356-020-08617-3. (accessed February 07, 2023)

(13) Viegas, R. M. C.; Mestre, A. S.; Mesquita, E.; Campinas, M.; Andrade, M. A.; Carvalho, A. P.; Rosa, M. J. Assessing the Applicability of a New Carob Waste-Derived Powdered Activated Carbon to Control Pharmaceutical Compounds in Wastewater Treatment. *Sci. Total Environ.* **2020**, *743*, No. 140791.

(14) Inglezakis, V. J.; Fyrillas, M. M.; Park, J. Variable Diffusivity Homogeneous Surface Diffusion Model and Analysis of Merits and Fallacies of Simplified Adsorption Kinetics Equations. *J. Hazard. Mater.* **2019**, *367*, 224−245.

(15) Kumar, P. S.; Korving, L.; Keesman, K. J.; van Loosdrecht, M. C. M.; Witkamp, G.-J. Effect of Pore Size Distribution and Particle Size of Porous Metal Oxides on Phosphate Adsorption Capacity and Kinetics. *Chem. Eng. J.* **2019**, *358*, 160−169.

(16) Baltrėnaitė-Gedienė, E.; Leonavičienė, T.; Baltrėnas, P. Comparison of CU(II), MN(II) and ZN(II) Adsorption on Biochar Using Diagnostic and Simulation Models. *Chemosphere* **2020**, *245*, No. 125562.

(17) Mahayekh-Salehi, A.; Moussavi, G. Removal of Acetaminophen from the Contaminated Water Using Adsorption onto Carbon Activated with NH 4 Cl. *Desalin. Water Treat.* **2016**, *57*, 12861−12873.

(18) Russo, V.; Masiello, D.; Trifuoggi, M.; Di Serio, M.; Tesser, R. Design of an Adsorption Column for Methylene Blue Abatement over Silica: From Batch to Continuous Modeling. *Chem. Eng. J.* **2016**, *302*, 287−295.

(19) Guedidi, H.; Reinert, L.; Soneda, Y.; Bellakhal, N.; Duclaux, L. Adsorption of Ibuprofen from Aqueous Solution on Chemically Surface-Modified Activated Carbon Cloths. *Arabian J. Chem.* **2017**, *10*, S3584−S3594.

(20) Iovino, P.; Canzano, S.; Capasso, S.; Erto, A.; Musmarra, D. A Modeling Analysis for the Assessment of Ibuprofen Adsorption Mechanism onto Activated Carbons. *Chem. Eng. J.* **2015**, *277*, 360−367.

(21) Nourmoradi, H.; Moghadam, K. F.; Jafari, A.; Kamarehie, B. Removal of Acetaminophen and Ibuprofen from Aqueous Solutions by Activated Carbon Derived from *Quercus brantii* (Oak) Acorn as a Low-Cost Biosorbent. *J. Environ. Chem. Eng.* **2018**, *6*, 6807−6815.

(22) Fröhlich, A. C.; Foletto, E. L.; Dotto, G. L. Preparation and Characterization of NiFe2O4/Activated Carbon Composite as Potential Magnetic Adsorbent for Removal of Ibuprofen and

https://doi.org/10.1021/acs.langmuir.2c03350
Langmuir XXXX, XXX, XXX−XXX

Ketoprofen Pharmaceuticals from Aqueous Solutions. *J. Cleaner Prod.* **2019**, *229*, 828−837.
(23) Ali, S. N. F.; El-Shafey, E. I.; Al-Busafi, S.; Al-Lawati, H. A. J. Adsorption of Chlorpheniramine and Ibuprofen on Surface Functionalized Activated Carbons from Deionized Water and Spiked Hospital Wastewater. *J. Environ. Chem. Eng.* **2019**, *7*, No. 102860.
(24) Balarak, D.; Taheri, Z.; Shim, M. J.; Lee, S.-M.; Jeon, C. Adsorption Kinetics and Thermodynamics and Equilibrium of Ibuprofen from Aqueous Solutions by Activated Carbon Prepared from *Lemna minor*. *Desalin. Water Treat.* **2021**, *215*, 183−193.
(25) Sahin, O. I.; Saygi-Yalcin, B.; Saloglu, D. Adsorption of Ibuprofen from Wastewater Using Activated Carbon and Graphene Oxide Embedded Chitosan-PVA: Equilibrium, Kinetics, and Thermodynamic and Optimization with Central Composite Design. *Desalin. Water Treat.* **2020**, *179*, 396−417.
(26) Streit, A. F. M.; Collazzo, G. C.; Druzian, S. P.; Verdi, R. S.; Foletto, E. L.; Oliveira, L. F. S.; Dotto, G. L. Adsorption of Ibuprofen, Ketoprofen, and Paracetamol onto Activated Carbon Prepared from Effluent Treatment Plant Sludge of the Beverage Industry. *Chemosphere* **2021**, *262*, No. 128322.
(27) Omorogie, M. O.; Babalola, J. O.; Ismaeel, M. O.; McGettrick, J. D.; Watson, T. M.; Dawson, D. M.; Carta, M.; Kuehnel, M. F. Activated Carbon from *Nauclea diderrichii* Agricultural Waste−a Promising Adsorbent for Ibuprofen, Methylene Blue and CO2. *Adv. Powder Technol.* **2021**, *32*, 866−874.
(28) Labuto, G.; Carvalho, A. P.; Mestre, A. S.; dos Santos, M. S.; Modesto, H. R.; Martins, T. D.; Lemos, S. G.; da Silva, H. D. T.; Carrilho, E. N. V. M.; Carvalho, W. A. Individual and Competitive Adsorption of Ibuprofen and Caffeine from Primary Sewage Effluent by Yeast-Based Activated Carbon and Magnetic Carbon Nanocomposite. *Sustainable Chem. Pharm.* **2022**, *28*, No. 100703.
(29) Matějová, L.; Bednárek, J.; Tokarský, J.; Koutník, I.; Sokolová, B.; Cruz, G. J. F. Adsorption of the Most Common Non-Steroidal Analgesics from Aquatic Environment on Agricultural Wastes-Based Activated Carbons; Experimental Adsorption Study Supported by Molecular Modeling. *Appl. Surf. Sci.* **2022**, *605*, No. 154607.
(30) Fröhlich, A. C.; Ocampo-Pérez, R.; Diaz-Blancas, V.; Salau, N. P. G.; Dotto, G. L. Three-Dimensional Mass Transfer Modeling of Ibuprofen Adsorption on Activated Carbon Prepared by Sonication. *Chem. Eng. J.* **2018**, *341*, 65−74.
(31) Ahn, C. K.; Kim, Y. M.; Woo, S. H.; Park, J. M. Selective Adsorption of Phenanthrene Dissolved in Surfactant Solution Using Activated Carbon. *Chemosphere* **2007**, *69*, 1681−1688.
(32) Russo, V.; Tesser, R.; Masiello, D.; Trifuoggi, M.; Di Serio, M. Further Verification of Adsorption Dynamic Intraparticle Model (ADIM) for Fluid−Solid Adsorption Kinetics in Batch Reactors. *Chem. Eng. J.* **2016**, *283*, 1197−1202.
(33) Mestre, A. S.; Pires, J.; Nogueira, J. M. F.; Parra, J. B.; Carvalho, A. P.; Ania, C. O. Waste-Derived Activated Carbons for Removal of Ibuprofen from Solution: Role of Surface Chemistry and Pore Structure. *Bioresour. Technol.* **2009**, *100*, 1720−1726.
(34) Anah, L.; Astrini, N. Isotherm Adsorption Studies of Ni(II) Ion Removal from Aqueous Solutions by Modified Carboxymethyl Cellulose Hydrogel. *IOP Conf. Ser.: Earth Environ. Sci.* **2018**, *160*, No. 012017.
(35) Dubey, S. P.; Dwivedi, A. D.; Sillanpää, M.; Gopal, K. Artemisia Vulgaris-Derived Mesoporous Honeycomb-Shaped Activated Carbon for Ibuprofen Adsorption. *Chem. Eng. J.* **2010**, *165*, 537−544.
(36) Guedidi, H.; Reinert, L.; Lévêque, J.-M.; Soneda, Y.; Bellakhal, N.; Duclaux, L. The Effects of the Surface Oxidation of Activated Carbon, the Solution PH and the Temperature on Adsorption of Ibuprofen. *Carbon* **2013**, *54*, 432−443.
(37) Mestre, A. S.; Pires, J.; Nogueira, J. M. F.; Carvalho, A. P. Activated Carbons for the Adsorption of Ibuprofen. *Carbon* **2007**, *45*, 1979−1988.
(38) Bahamon, D.; Carro, L.; Guri, S.; Vega, L. F. Computational Study of Ibuprofen Removal from Water by Adsorption in Realistic Activated Carbons. *J. Colloid Interface Sci.* **2017**, *498*, 323−334.

https://doi.org/10.1021/acs.langmuir.2c03350
Langmuir XXXX, XXX, XXX−XXX

Publication V

Journal of Environmental Chemical Engineering 10 (2022) 107866

Contents lists available at ScienceDirect

Journal of Environmental Chemical Engineering

journal homepage: www.elsevier.com/locate/jece

Photodegradation of ibuprofen using CeO_2 nanostructured materials: Reaction kinetics, modeling, and thermodynamics

Noemi Gallucci [a,b], Maryam Hmoudah [a,c], Eugenie Martinez [d], Amjad El-Qanni [c], Martino Di Serio [a], Luigi Paduano [a,b], Giuseppe Vitiello [b,e,*], Vincenzo Russo [a,f,*]

[a] University of Naples Federico II, Department of Chemical Sciences, IT-80126 Naples, Italy
[b] CSGI, Center for Colloid and Surface Science, IT-50019 Sesto Fiorentino, FI, Italy
[c] An-Najah National University, Department of Chemical Engineering, Nablus, Palestine
[d] University of Grenoble Alpes, CEA, LETI, F-38000 Grenoble, France
[e] University of Naples Federico II, Department of Chemical, Materials and Production Engineering, IT-80125 Naples, Italy
[f] Åbo Akademi, Laboratory of Industrial Chemistry and Reaction Engineering, FI-20500 Turku/Åbo, Finland

ARTICLE INFO

Editor: Dr. G. Palmisano

Keywords:
Ibuprofen
CeO_2 nanoparticles
Photodegradation
Kinetic modeling
Thermodynamics

ABSTRACT

Ibuprofen is one the most used non-steroidal anti-inflammatory drug, which is considered an emerging pollutant that may contaminate surface and underground water. Photodegradation using nanomaterials is one of the most sustainable and cheap technologies that can be used in water purification. In this study, the photodegradation efficiency of in-house prepared ceria (CeO_2) nanostructured materials towards ibuprofen was assessed under UV irradiation. CeO_2 nanoparticles (NPs) were prepared through wet-chemical synthesis and characterized by several techniques. The photodegradation activity of the synthesized CeO_2-NPs was compared to the commercial Aeroxide TiO_2-P25. Small crystalline CeO_2-NPs were obtained with about 15 nm particle size, band-gap of 3.1 eV with irregular morphology. The surface area of CeO_2-NPs was estimated to be 76 ± 5 m^2/g. Dynamic light scattering analysis revealed that these nanoparticles have a strong tendency to self-aggregate and to form clusters in aqueous suspension. The results showed a slightly better performance of Aeroxide TiO_2-P25 compared to CeO_2-NPs. On the other hand, five reusability tests confirmed the stability of CeO_2-NPs in the reaction conditions, without any significant effect on their photodegradation activity. The goodness of the kinetic modeling of the experimental data was proven through the estimated kinetic parameters, together with the statistical information. The temperature effect confirmed that the higher the temperature, the greater the dissociation rate. Thus, there is a direct relationship between temperature, reaction rate, and the activation energy for each reaction. Furthermore, the thermodynamic parameters, namely: changes in Gibbs free energy (ΔG°), enthalpy (ΔH°), and entropy (ΔS°) have been reported revealing the efficient photodegradation performance of CeO_2-NPs.

1. Introduction

Pharmaceutical compounds, such as ibuprofen, have recently received a lot of attention due to their detection in water (surface and wastewater) and sediments [1]. Ibuprofen is considered one of the emerging pollutants that may contaminate surface and underground water due to the improper practices and disposal of unused medicine [2]. The presence of this compound in water bodies is considered problematic as many living beings can be adversely impacted due to the uncontrolled accumulation of these materials in the lipid tissues [3]. Numerous published studies and reviews about the occurrence, toxicity, and impact of ibuprofen were undertaken over the last few decades [4–7]. On the one hand, this material is resistant to conventional treatment methods such as sedimentation, coagulation, filtration, and biological processes [3,8]. On the other hand, most existing advanced wastewater treatment options, such as distillation, membrane filtration, and electrochemical treatment, are prohibitively expensive and face many operational challenges [9–11]. Therefore, photodegradation using nanomaterials is considered one of the sustainable state technologies that can be used in water purification [12–15]. This technology has many advantages because of the economic, environmentally friendly,

Abbreviations: 1-OH, 1-OH ibuprofen; 1-OXO, 1-OXO ibuprofen; CALC, Calculated; CI 95%, Confidence intervals calculated at 95%; EXP, Experimental; IBU, Ibuprofen; M, Correlation matrix.

* Correspondene to: University of Naples Federico II, Italy.
E-mail addresses: giuseppe.vitiello@unina.it (G. Vitiello), v.russo@unina.it (V. Russo).

https://doi.org/10.1016/j.jece.2022.107866
Received 8 March 2022; Received in revised form 20 April 2022; Accepted 4 May 2022
Available online 6 May 2022

Nomenclature

Abs	Absorbance [AU]
c_i	Concentration of component i [mol/m^3]
Ea_j	Activation energy for reaction j [kJ/mol]
F_{obj}	Objective function [–]
h	Plank constant [m^2 kg/s]
K_B	Boltzmann's constant [m^2 kg/s^2 K]
$k_{ref,j}$	Kinetic constant calculated at a reference temperature [(m^3/mol)(m^3/kg^n)s^{-1}]
n	Linearization coefficient for catalyst bulk density [–]
N_{data}	Number of available experimental data [–]
Q_{air}	Air volumetric flowrate [m^3/s]
r_j	Reaction rate of step j [mol/(kg s)]
r_{obs}	Observed reaction rate [mol/(m^3 s)]
R	Ideal gas constant [kJ/(K mol)]
t	Time [s]
T	Temperature [K]
T_{ref}	Reference temperature, 303 K [K]

Greek symbols

ΔG°	Gibbs free energy change [J/mol]
ΔH°	Enthalpy change [J/mol]
ΔS°	Entropy change [J/(mol K)]
v	Stirring rate [rpm]
ρ_B	Catalyst bulk density [kg/m^3]
ρ_{H2O}	Water density [kg/m^3]
υ_{ij}	Stoichiometric coefficient of component i in reaction j [–]

simple, and easily operated designs needed to eliminate contaminants of emerging concern from water [16]. This in turn improve drinking water quality and the safe reuse of water, thus protecting the environment, improving human health, and achieving sustainability goals [17].

Recently, cerium oxide has gained increasing attention for the degradation of organic contaminants in water [18–22]. In particular, a great interest has aroused the nanoparticles of cerium oxide nanoparticles (CeO_2-NPs) because of their reactivity, reusability, cost-effectiveness, and environmental impact [23]. Based on the literature survey presented in Table 1, most of the published works on the application of CeO_2-NPs solely in photodegradation focused on dyes, mainly on methylene blue. Therefore, paying attention to the photodegradation of emerging pollutants such as ibuprofen using CeO_2-NPs is important in the field of water purification. It should be mentioned that the uniqueness of these nanoparticles lies in the simplicity of conversion between Ce^{3+} and Ce^{4+}, the presence of defects, and the increase of the surface-to-volume ratio to CeO_2 in bulk [24–26]. Furthermore, the market price of Ce is around 4.57–4.71 $/kg compared to 11.1–11.7 $/kg for Ti [27], which oxides are nowadays considered the most efficient photocatalysts [28–30]. Thus, the use of CeO_2 could lead to a lower price of the catalyst.

In addition, CeO_2 is an n-type semiconductor with a band-gap at 3.1 eV [31,32], this wide band-gap of CeO_2 requires the use of UV light to activate the mechanism. To shift the band gap from 3.1 to 2.452.90 eV and, consequently, use visible light for photocatalytic activity, it is necessary to increase the number of defects in CeO_2-NPs [33]. The photocatalytic activity of CeO_2 is closely related to particle size, textural properties, and surface structure [34]. Therefore, an important parameter is the ratio Ce^{3+}/Ce^{4+}, which varies with the size of NPs that influence the photocatalytic activity. As Ce^{3+} switches to Ce^{4+} states, it results in high oxygen mobility in the CeO_2 lattice and in turn leads to a strong catalytic potential that happens without any structural modification of the fluorite lattice [33,35]. The change in energy can cause a surface effect on catalyst [24]. Another important parameter that determines the photocatalytic activity is the presence of oxygen vacancies in the CeO_2 lattice, as the oxygen vacancies vary, consequently, the properties of NPs vary [19,21,33,36].

In this paper, the synthesized CeO_2-NPs have been tested under

Table 1
Some previous published works on the photocatalytic activity of CeO_2 nanoparticles in photodegradation.

Synthesis	Pollutant (s)	Radiation	Highlights	Ref.
Co-precipitation method	Naphthol Blue Black dye	Sunlight	• CeO_2 has a low activity for the degradation of naphthol blue black dye. Doping with Mn showed increased photocatalytic activity.	[22]
An electron beam accelerator was used to modify pristine CeO_2	4-nitrophenol and methylene blue	Visible light	• EB can effectively narrow the band gap of metal oxides for the enhanced visible light photocatalytic activities.	[33]
Solvothermal method	Phenol and its derivatives (2-chlorophenol, 2-bromophenol and 2-nitrophenol)	Sunlight	• The interaction of UV photons induced defects at the surface of CeO_2.	[21]
Precipitation method	Methyl orange and methylene blue	UV-light	• CeO_2 nanoparticles showed a moderate degradation rate compared to other metal oxide-based nanoparticles.	[20]
Green synthesis using leaf extract of *Azadirachta indica* plant	Rhodamine B dye	UV-light	• Excellent photocatalytic activity of green CeO_2 nanoparticles towards RhB dye.	[37]
Hydrothermal method	Isopropyl alcohol	Visible light	• Confeito-like CeO_2 exhibits excellent performance for the decomposition of isopropyl alcohol to acetone. • Ce^{3+} induced oxygen vacancies in the lattice of CeO_{2-x}, and this resulted in an improvement in the activity.	[19]
Wet chemical method	Congo red and methyl orange	Visible light	• CeO_2 nanocubes showed high reactivity and stability for the photodegradation of dyes	[38]
Sonochemical-assisted method	Methylene blue	UV-light	• After 75 min of radiation, 85% of methylene blue were degraded.	[18]
Hydrothermal method	Methylene blue	In the dark, sunlight, and UV irradiation	• The performance varied based on the surface areas, nanoparticles shape and the content of oxygen vacancies.	[39]
Solution combustion technique	Methylene blue	UV-light	• The photocatalytic performance was optimized in terms of solution pH, catalyst dose, initial methylene blue, and UV irradiation time.	[40]
Commercial CeO_2 nanoparticles	Tropaeolin O	UV-light	• The effects of particle size and pH were investigated. • The degradation of Tropaeolin O was confirmed by toxicity experiments in the presence of CeO_2 NPs and marine crustaceans as A. salina.	[41]

ultraviolet (UV) irradiation for the photodegradation of ibuprofen. The performance of these NPs was compared with Aeroxide TiO_2-P25. Special attention was paid to the effect of air flow rate, stirring rate, temperature, catalyst bulk density, and initial concentration of the ibuprofen solution on the photodegradation efficiency of CeO_2-NPs. Reusability, kinetics modeling, activation energy, and thermodynamics parameterswere also addressed in this study.

2. Materials and methods

2.1. Materials

Ibuprofen solutions were prepared using 4-isobutyl-α-methylphenylacetic acid at 99% (Alfa Aesar). Cerium (III) nitrate hexahydrate salt ($Ce(NO_3)_3{\cdot}6H_2O$, purity > 99.999%), ammonia solution 30 v/v%, and hydrogen peroxide were purchased from Sigma-Aldrich (Milan, Italy). Milli-Q bidistilled water, also filtered using 0.20 μm filters, was obtained from Merck Millipore (Darmstadt, Germany). Commercial Aeroxide TiO_2-P25 was supplied by Evonik Industries (Essen, Germany) for comparative purposes in this study. All materials were used without any further treatment.

2.2. Methods

2.2.1. Synthesis of CeO_2 nanoparticles

Typically, CeO_2-NPs were prepared through a wet-chemistry synthesis in solvothermal conditions, according to reference [42]. First, 30 mL of an aqueous solution (0.5 M) of $Ce(NO_3)_3{\cdot}6H_2O$ salt was prepared and left under magnetic stirring for 10 min to induce a complete salt dissolution. Subsequently, 117 μL of hydrogen peroxide was added to the Ce(III) salt solution which was stirred for 5 min to favor the oxidation of Ce^{3+} to Ce^{4+}. A specific volume (~ 6 mL) of a diluted ammonia solution (7 M) was then added to this mixture to a pH of 8.8 to start the precipitation reaction. Afterward, the mixture was continuously stirred at 80 °C for 1 h to complete the reaction. After an hour, a yellow precipitate constituted by $Ce(OH)_4$ was obtained and washed three times with bidistilled Milli-Q water by centrifugation at 9000 rpm for 10 min. The pH was adjusted to pH 10 by using the ammonia solution and 30 mL of washed precipitate were treated at 120 °C for 24 h within a mini-reactor. The final CeO_2-NPs were repeatedly washed with bidistilled Milli-Q water by centrifugation at 9000 rpm for 10 min.

2.2.2. Physicochemical characterization

2.2.2.1. X-Ray diffraction (XRD) analysis. XRD measurements were performed with a PANalytical diffractometer (Malvern, Worcestershire, United Kingdom) with a nickel filter and CuKα radiation, with a step size of 0.02° and a counting time of 80 s per step, to investigate the formation and properties of CeO_2 crystalline phases. The average crystal size (τ) was evaluated using the Scherrer formula:

$$\tau = \frac{K\lambda}{\beta cos\theta} \quad (1)$$

where τ is the mean size of the crystallite domains, K is a dimensionless shape factor, λ is the X-ray wavelength, β is the broadening at half the maximum intensity (FWHM), θ is the Bragg angle.

2.2.2.2. X-ray photoelectron spectroscopy (XPS). Surface properties of CeO_2-NPs were investigated by XPS analyses which were carried out using a spectrometer VersaProbe II with a monochromatic Al Kν X-ray source ($h\nu$ = 1486,6 eV), a spot of 200 μm, and a dual-beam system (Ar^+ et $\bar{e}$) for charge compensation. The pass energy was set at 23.5 eV, leading to an overall energy resolution of 0.6 eV. Photoelectrons were collected at a take-off angle of 45°, which means a sampling depth of approximately 5 nm. The relative atomic composition (% at.) is given with an uncertainty of ± 20% using tabulated relative sensitivity factors. Decomposition of the spectra was done using Voigt functions after Shirley's background subtraction with the Multipak software.

2.2.2.3. Transmission electron microscope (TEM). Morphological properties of CeO_2-NPs were investigated by TEM. The analyzed sample was prepared by placing 10 μL of nanoparticle suspension on one side of a 200 mesh carbon-coated copper grid that was allowed to dry in air. TEM images were obtained using a FEI TECNAI G2 200 kV microscope (ThermoFisher Scientific, Waltham, USA) equipped with a high-angle annular dark-field (HAADF) detector for high-resolution imaging.

2.2.2.4. Dynamic light scattering (DLS). DLS measurements were performed to measure the size of CeO_2-NPs in an aqueous environment with a home-made instrument composed of a Photocor compact goniometer (Moscow, Russia), SMD 6000 Laser Quantum 50 mW light source (Laser Quantum, Fremont, CA, USA) operating at 532.5 Å, a photomultiplier (PMT-120-OP/B) and a correlator (Flex02-01D) from Correlator.com (Shenzhen, China). The experiments were carried out on 1 mL of an aqueous suspension of CeO_2-NPs at the constant temperature (25.0 ± 0.1) °C, by using a thermostatic bath and at the scattering angle θ of 90°. The scattered intensity correlation function was analyzed using a regularization algorithm. The diffusion coefficient of each population of particles was calculated as the z-average of the diffusion coefficients of corresponding distributions. These DLS measurements have been carried out in triplicate with the aim to verify the reproducibility. Specifically, each measurement was constituted by 12 scans of 60 s to determine the mean hydrodynamic radius and its error.

2.2.2.5. Surface area and porosimeter analysis. Specific surface area (S_{BET}) and the pore volume (V_P) of CeO_2-NPs were evaluated by generating seven-point isotherms at 77 K for N_2 adsorption (Autosorb-1, Quantachrome) using a particular amount of the sample capable of providing a specific surface area equal to 5 m^2 in the sample cell. The mesopore volume (V_{BJH}), the mean pore radius (r_P), and the pore size distributions were estimated by the Barrett–Joyner–Halenda (BJH) method applied to the desorption branch of the isotherm [43].

2.2.2.6. Ultra-violet and visible light diffuse reflection (UV–vis DRS) spectroscopy. UV-Vis DRS measurements on powdered CeO_2-NPs were carried out using a UV-2600i UV–VIS spectrophotometer, 230 V (Shimadzu, Milan, Italy), equipped with an integrating sphere ISR-2600Plus operating in a wavelength range of 220–1400 nm. Barium sulfate was exploited as a reflectance standard. The measured intensity was expressed as the value of the Kubelka–Munk function F(R), while the band-gap value was evaluated by linearization of the plot of $(F(R)h\nu)^{1/2}$ against $h\nu$.

2.2.2.7. High-pressure liquid chromatography (HPLC). Ibuprofen concentration analyses were carried out using an Agilent 1100 High Pressure Liquid Chromatography (HPLC) system, with a 70% w/w methanol, 30% w/w water mobile phase. The column used was a Phenomenex Luna C18, with a 5 μm particle size, 100 Å pore size, 250 mm length, and 4.6 mm internal diameter. The detector used was a diode array detector (DAD), with a 1024-element photodiode array, deuterium and tungsten lamps with a 190–950 nm. The software used for apparatus control and data collection was Agilent Chemstation. This system acquires the absorbance of the eluates in mAU (Absorbance Units) as a function of elution time in the whole emission interval of the lamps and outputs a 3D chromatogram with X elution time, Y wavelength, and Z signal intensity.

2.2.3. Photodegradation experimental set-up

Photodegradation experiments were conducted in a 1.5 L jacketed glass vessel, equipped with a three-neck head. The reactor was

connected to an ultra-thermostat to regulate the temperature at the desired level. The liquid temperature was monitored with a dedicated thermocouple. Air was fed to the reactor system using a digital flow-meter regulator (supplied by Bronkhorst), connected to a sintered filter used as a gas sparger, to provide a good gas-liquid interface in the mass transfer of air to the liquid phase. A coaxial 4 W UV lamp was mounted at the center of the reactor (Toshiba FL4BLB), characterized by a wavelength of $\lambda = 365$ nm, with dimensions of 15 cm × 1.5 cm. The liquid was stirred by a magnetic impeller at the desired rate.

In the classical execution of the experiment, the ibuprofen solution was prepared with the desired concentration and then loaded into the reactor and stirred at the set value. The reactor was closed with the lid and connected to the thermostat, set at a pre-specified reaction temperature. The airflow was adjusted with a pressure reducer to 1 bar and the digital flow meter was set at a fixed flow. At this point, the catalyst was loaded into the reactor. The reactor was then shielded before the UV lamp to reduce any ray dispersion, avoiding any risk to the operator. A first sample was collected to measure the concentration of ibuprofen (time = 0 sample). The reaction was then started by switching on the lamp, withdrawing samples periodically to follow the reaction kinetics until a maximum time of 5 h. Each sample was then centrifuged at 3300 rpm for 30 min, and the resulting liquid sample was analyzed by UV–VIS spectroscopy (UV-Vis Jasco V-550). A classical spectrum was reported in the Supplementary material (Fig. S.1). A calibration curve was built at $\lambda = 222$ nm, where ibuprofen absorption reached the maximum value, obtaining the calibration curve reported in Eq. (2), valid in a concentration range between 0.0 and 0.05 mol/m^3 (Fig. S.2).

$$c_{IBU} = (0.113 \pm 0.001)Abs,\ R^2 = 0.99 \quad (2)$$

Where *Abs* represents the absorbance and c_{IBU} is the ibuprofen concentration expressed in mol/m^3.

To investigate the reaction kinetics, together with eventual mass transfer limitations, several experiments were conducted by varying the operational conditions in a wide range. The summary of the adopted reaction conditions is reported in Table S.1.

2.2.4. Modeling and parameter estimation

Matlab R2020b was used to perform all the modeling activities reported in the present work. Ordinary differential equations were solved using the *ode23s* routine, while parameter estimation activity was performed with the *particleswarm* algorithm. The objective function was calculated as follows [34]:

$$F_{obj} = \frac{1}{N_{data}} \sqrt{\sum_{i=1}^{N_{data}} \left(\frac{c_{i,EXP} - c_{i,CALC}}{c_{i,EXP}} \right)^2} \quad (3)$$

The confidence intervals were calculated using the *nlparci* algorithm.

3. Results and discussion

3.1. Physico-chemical features of synthesized CeO_2 nanoparticles

Characterization of CeO_2 NPs was carried out using XRD and XPS measurements. The XRD pattern of CeO_2-NPs, shown in Fig. 1, indicated the presence of the typical peaks of a face-centered cubic (FCC) structure (JCPDS no. 81-0792) [34,44,45]. The peaks obtained at the diffraction angles (2θ) of 29°, 33°, 47°, 56°, and 59° correspond to the Miller indices (hkl) indicating the crystalline planes (111), (200), (220), (311) and (222) respectively, as shown in Fig. 1, and confirming the formation of CeO_2 nanoparticles with a fluorite-type crystalline structure. The mean crystallite sizes estimated from Scherrer's formula were close to 18 ± 1 nm.

Then XPS analysis was performed to obtain information on the chemical composition of the surface of the CeO_2 nanoparticles. The survey spectrum is plotted in Fig. 2A, showing the main characteristic

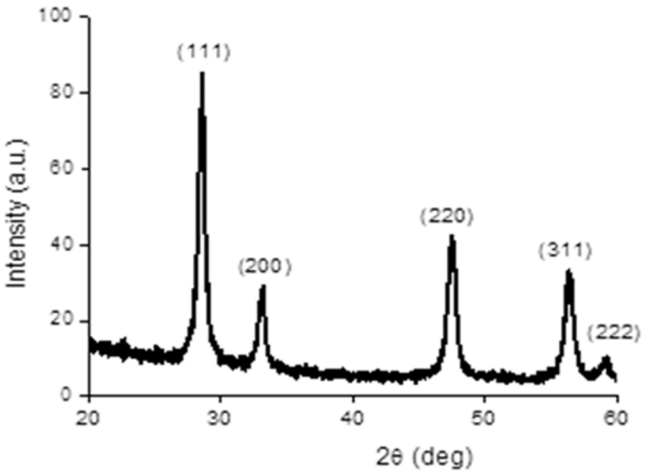

Fig. 1. XRD pattern of CeO_2 NPs.

peaks of CeO_2 (Ce 3*d*, Ce 4*d* and O 1*s*) as well as carbon contamination (C 1*s*). A zoom on the oxygen O1*s* core level is presented in the inset, highlighting two contributions related to O-Ce bonds from the CeO_2 NPs and O—C bonds from hydrocarbon surface contamination. The spectrum of the Ce3*d* core level is reported in Fig. 2B. This spectrum exhibits strong satellite features (cf^{1}L) to the main peaks (cf^0). For each component of the Ce $3d_{5/2}$ - Ce $3d_{3/2}$ doublet, 5 peaks were used to fit all these contributions, each of them being assigned to one of the Ce oxidation states (Ce^{3+} and Ce^{4+}) as indicated in Table S.2. The Ce^{3+}/Ce^{4+} ratio was estimated to be equal to 0.4, as deduced from the areas of these different components.

Morphological and textural features of CeO_2-NPs were analyzed by TEM (Fig. 3A). A representative TEM image shows the formation of small nanoparticles of about 15 nm in size and with irregular morphology. At the same time, it suggests a strong tendency of these nanoparticles to self-aggregate, forming clusters with a size comparable to that obtained by DLS analysis (Fig. 3B). As observed from the hydrodynamic radius distribution, the main population is centered at about 530 ± 70 nm confirming a fast and significant self-aggregation of bare CeO_2 nanoparticles when they were in an aqueous suspension. In addition, S_{BET} of CeO_2-NPs was measured by N_2 adsorption at 77 K and the estimated surface area was equal to 76 ± 5 m^2/g. The adsorption/desorption isotherm shows a type IV-hysteresis, which is typical of porous materials (see Fig. S.3). Size distribution of pores was estimated according to the BJH model based on the desorption branch of the isotherm, indicating that the total volume of the pores is equal to 0.22 cm^3/g, while the pore distribution (as derivative of the pore volume to the radius) shows the presence of a single population of pores with a diameter of 1.35 ± 0.15 nm.

Moreover, the optical properties of CeO_2-NPs at solid-state were also investigated by recording the DRS spectrum, displayed in Fig. 3C. The measured intensity was expressed as the value of the Kubelka-Munk function F(R) (see Fig. 3C) which indicates an absorption at $\lambda < 300$ nm. The optical band gap for the transition from the valence band (V_B) to the conduction band (C_B) was calculated by linearization of the graph of $(F(R)h\nu)^{1/2}$ against photon energy (as shown in Fig. 3D) and was equal to 3.1 eV, in agreement with the literature that reports a strikingly dependence on the preparation method [46].

3.2. Photodegradation experimental results

A first experiment was conducted in the absence of the catalyst, to verify eventual photodegradation due to the UV irradiation (Fig. S.4). As revealed, a maximum conversion was observed to be 5%, reaching a stable plateau value. This concludes that ibuprofen can be considered rather stable under UV light. A second blank experiment was conducted

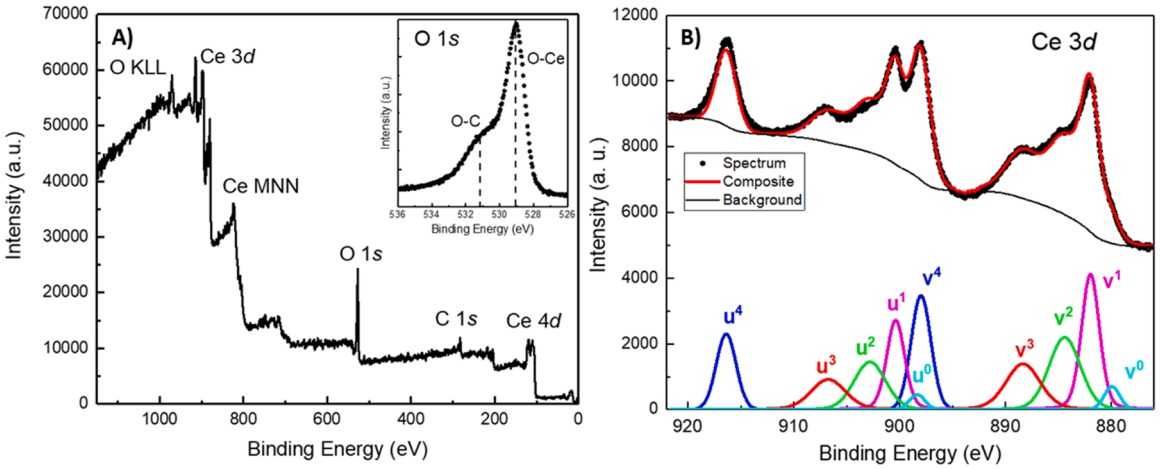

Fig. 2. **A**) XPS survey scan and O 1*s* spectrum **B**) Ce 3*d* XPS spectrum of the CeO_2 NPs.

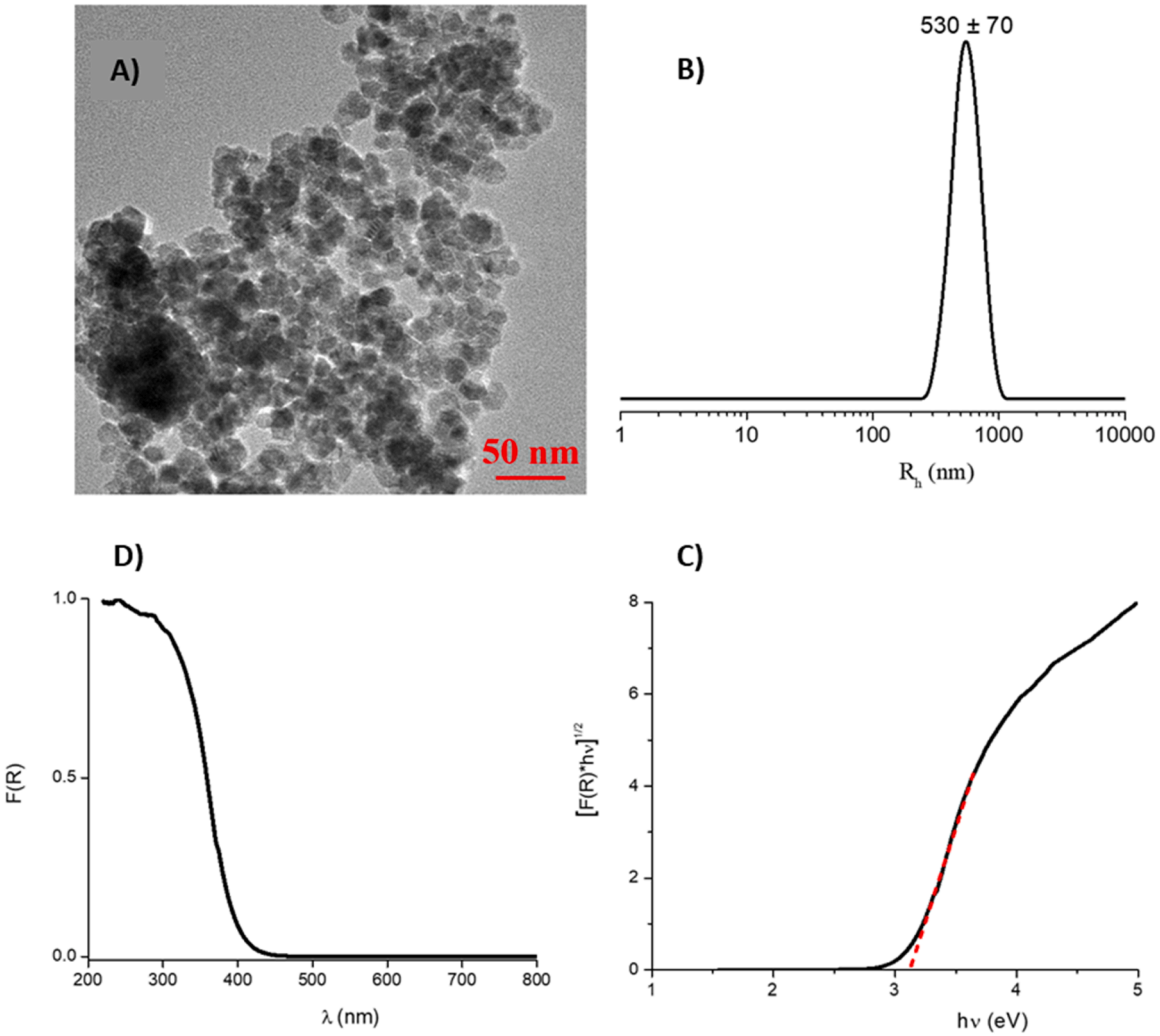

Fig. 3. **A**) TEM image, **B**) hydrodynamic radius distribution of CeO_2 NP in the aqueous medium, **C**) UV-DRS spectrum of powdered CeO_2.NPs, and **D**) estimation of the optical band gap using the modified Kubelka-Munk function.

by putting in contact the ibuprofen solution with CeO_2 nanoparticles, in the absence of UV irradiation. In this case, no ibuprofen adsorption was observed, probably due to the slightly big dimension of ibuprofen compared to the catalyst pores.

Furthermore, the synthesized material was compared with Aeroxide TiO_2-P25 which is considered nowadays a benchmark catalyst for photodegradation studies. Considering the fixed operation.

conditions, Aeroxide TiO_2-P25 shows slightly better performance

compared to CeO_2 (Fig. 4A). This promising result proves the novelty of these nanomaterials that can be attributed to their lower band-gap value (2.95 eV versus 3.30 eV of TiO_2-P25), thus, considered promising in an eventual industrial application. Before investigating the reaction kinetics, the catalyst was recovered from the experiment and reused for 5 times, to check the catalyst stability. The results are reported in Fig. 4B. In addition, TEM images for the reused CeO_2 NPs (Fig. S.5) showed no significant difference compared to Fig. 3A showing good stability as well as recyclability under the reaction conditions.

Different experiments were conducted to check the influence of both gas-liquid and liquid-solid mass transfer resistances. In particular, the airflow fed to the reactor was varied to verify whether the gas-liquid mass transfer could affect the overall rate of the reaction network (Fig. S.6). It can be concluded that by increasing the airflow, an increase in the reaction rate can be observed, reaching a stable plateau at $1.0 \cdot 10^{-6}$ m^3/s of airflow, confirming that gas-liquid mass transfer resistance can be neglected. Thus, all the other experiments were conducted imposing $1.0 \cdot 10^{-6}$ m^3/s airflow.

The impeller rate was varied in a range of 250–750 rpm to detect the optimal stirring rate to avoid fluid-solid mass transfer limitation (see Fig. S.7). It was found that beyond 500 rpm, a stable reaction rate was measured. Thus, the kinetics investigation was conducted imposing an optimal stirring rate of 750 rpm.

The influence of the reaction temperature was also investigated, as shown in Fig. 5. It is noted that by increasing the reaction temperature, an increase in the reaction conversion can be observed. When analyzing the samples, a second absorption peak was observed at $\lambda = 260$ nm, corresponding to 1-OXO ibuprofen, the most probable byproduct that can be formed [47]. This compound was verified by HPLC mass analysis. No further by-products were detected neither by HPLC mass nor by UV-Vis. It is likely that further photodegradation products will be formed at longer reaction times under harsh reaction conditions. The evolution of the by-product concentration with temperature follows a logical trend, showing an increase in the initial formation rate with temperature, passing then through a maximum as a result of its further photodegradation.

The influence of the catalyst loading on the reaction rate was investigated by conducting experiments using different bulk densities. Fig. 6 shows that by increasing the catalyst concentration, an increase in ibuprofen photodegradation was measured. Even the by-product shows a higher consumption after a higher rate of formation.

Finally, three different experiments were performed that varied the initial concentration of ibuprofen to verify the reaction order (Fig. 7). The results show that the higher the initial content of the contaminant, the faster the reaction rate, suggesting a first-order reaction. This aspect will be better described and discussed in the following experimental data kinetics modeling section. The same behavior was observed for 1-OXO ibuprofen, suggesting a higher formation rate when a more concentrated contaminant solution is used.

3.3. Kinetics modeling

To interpret the kinetics data, several assumptions must be made based on the experimental observations. First, as only ibuprofen and 1-OXO ibuprofen were detected, an in-series reaction mechanism was proposed, passing through the formation of 1-OH ibuprofen [48]. Thus, the following reaction mechanism was imposed:

$$\begin{aligned} IBU \; + \; O_2 &\xrightarrow{r_1} \; 1-OH \\ 1-OH \; + O_2 &\xrightarrow{r_2} \; 1-OXO \\ 1-\mathrm{OXO} \; + O_2 &\xrightarrow{r_3} \; other\ products \end{aligned} \tag{3}$$

Each elementary step was considered of a first-order for oxygen, taken at saturation. No adsorption was considered as the concentrations of both reactant and products are rather low. This assumption was confirmed by simple linearization, where $\ln(c_{IBu}/c_{IBu,0})$ was plotted vs. the experimental time, as demonstrated in Eq. (4).

$$\begin{aligned} \frac{dc_{IBU}}{dt} = -r\rho_B^n \rightarrow \frac{dc_{IBU}}{dt} = -kc_{IBU}\rho_B^n \rightarrow \int_{c_{IBU,0}}^{c_{IBU}} \frac{dc_{IBU}}{c_{IBU}} \\ = \int_0^t -k\rho_B^n dt \rightarrow \ln\left(\frac{c_{IBU}}{c_{IBU,0}}\right) = -k\rho_B^n t \end{aligned} \tag{4}$$

Data are aligned to a straight line, as revealed previously in Fig. 6C, demonstrating that the reaction kinetics follow a first-order rate law.

The oxygen concentration was considered to vary with temperature, imposing the following empirical equation fitted to the data published in the literature [42], to ensure the right oxygen concentration calculated at the temperature chosen for each experiment, Eq. (5).

$$c_{O_2} = \left(52.94\exp\left(-T/25.9\right) + 7.5{\cdot}10^{-4}\right)\rho_{H_2O} \tag{5}$$

The experimental data were interpreted with a pseudo-homogeneous single-phase model, since there were no fluid-solid or intraparticle diffusion limitations, from the results reported in the previous section. In particular, the Weisz-Prater criterion was calculated to ensure that intraparticle limitations were absent, but as particles were rather small (500 nm aggregates), this result suggests that no diffusion limitations affect the reaction kinetics. The general mass balance equation that was adopted is reported in Eq. (6).

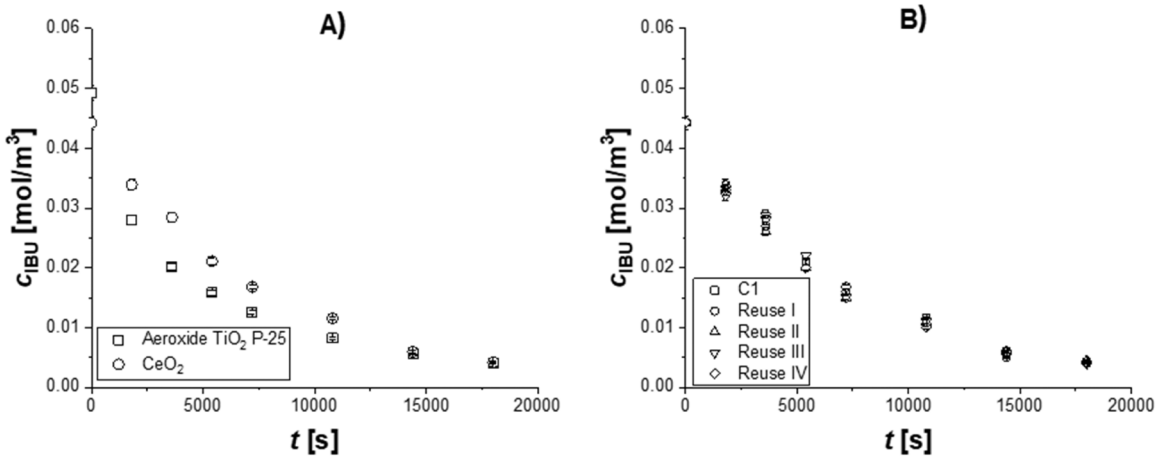

Fig. 4. (**A**) Comparison between TiO_2-P25 and CeO_2-NPs towards ibuprofen photodegradation. Adopted reaction conditions: $T = 303$ K, $c_{IBU,0} = 5 \cdot 10^{-2}$ mol/m^3, $\rho_B = 0.37$ kg/m^3, $\nu = 750$ rpm, UV irradiation. **B**) Results of reuse tests, in terms of ibuprofen concentration vs reaction time for different reuses. Experimental conditions: $T = 303$ K, $c_{IBU,0} = 5 \cdot 10^{-2}$ mol/m^3, $\rho_B = 0.37$ kg/m^3, $Q_{air} = 1.0 \cdot 10^{-6}$ m^3/s, and $\nu = 750$ rpm.

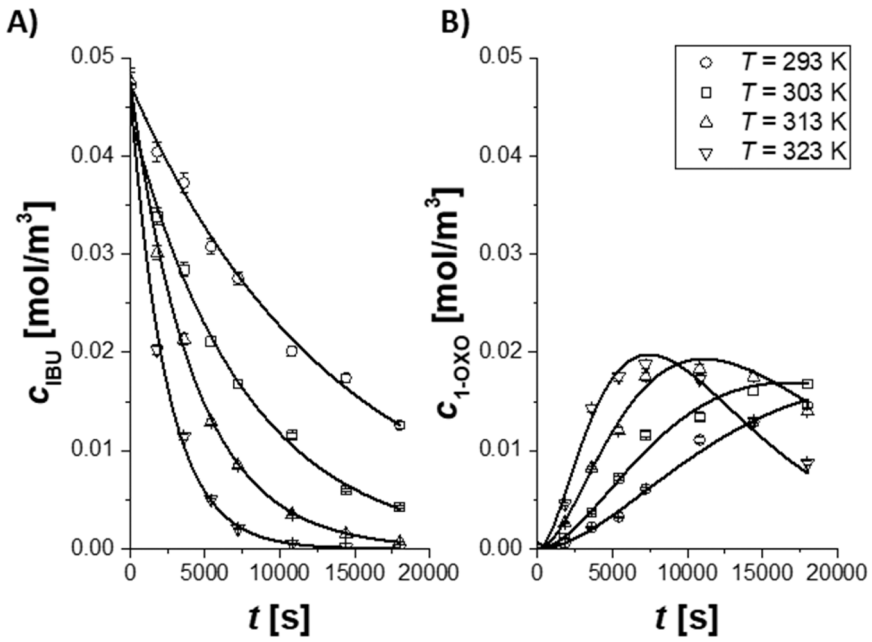

Fig. 5. Experimental results of the kinetic tests conducted at different temperatures, fixing $c_{IBU,0} = 5 \cdot 10^{-2}$ mol/m^3, $\rho_B = 0.37$ kg/m^3, $Q_{air} = 1.0 \cdot 10^{-6}$ m^3/s and $\nu = 750$ rpm. Trends of the concentration profiles vs the reaction time for **A**) ibuprofen and **B**) 1-OXO ibuprofen. Lines are the calculated profiles. The subplots refer to the same legend.

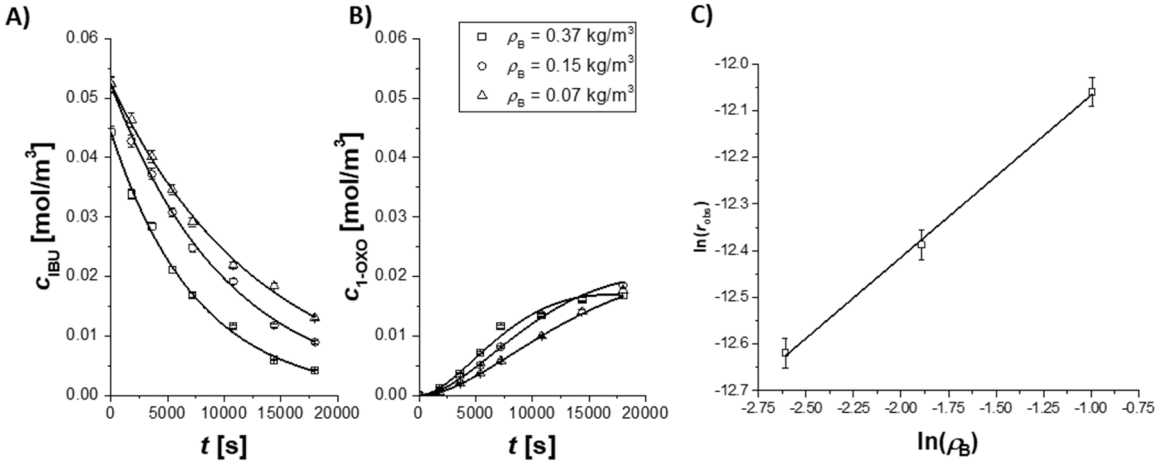

Fig. 6. Experimental results of the kinetic tests conducted at different catalyst loading, fixing $c_{IBU,0} = 5 \cdot 10^{-2}$ mol/m^3, $T = 303$ K, $Q_{air} = 1.0 \cdot 10^{-6}$ m^3/s and $\nu = 750$ rpm. Trends of the concentration profiles vs the reaction time for **A**) ibuprofen and **B**) 1-OXO ibuprofen. Lines are the calculated profiles. The subplots refer to the same legend. The panel **C**) represents catalyst bulk density linearization test.

$$\frac{dc_i}{dt} = \sum_{j=1}^{N_r} \upsilon_{ij} r_j \rho_B^n \tag{6}$$

The bulk density was elevated to a proportional coefficient n, to take into account the shielding effect of the catalyst loading on the UV-light penetration in the liquid phase [44]. This coefficient can be calculated directly from the experimental data, plotting the $\ln(r_{obs})$ vs $\ln(\rho_B)$, as in Eq. (7).

$$r_{obs} = r\rho_B^n \rightarrow \ln(r_{obs}) = \ln(r) + n\ln(\rho_B) \tag{7}$$

It is observed that the data are linear in Fig. 5C and the calculated coefficient is $n = 0.35 \pm 0.01$.

A parameter estimation analysis was performed simultaneously on C1, C6–C10 (Table S.1), to retrieve kinetic information, the kinetics constant was calculated at a reference temperature $T_{ref} = 303$ K, and activation energy for each reaction, adopting the modified Arrhenius equation reported in Eq. (8).

$$k_j = k_{ref,j} \exp\left(\frac{-Ea_j}{R}\left(\frac{1}{T} - \frac{1}{T_{ref}}\right)\right) \tag{8}$$

The summary of the obtained parameters, together with statistical information are reported in Table 2, while the obtained fits are presented earlier in Figs. 5–7.

The calculated activation energies presented in Table 2 are all within a range of kinetics regime. The three constants are of the same order of magnitude; thus, no rate-determining step can be assumed among the reactions involved. The calculated errors on all the kinetic parameters are below 12%. Only a slight correlation can be seen among the parameters. Hence, from Figs. 5–7 it is evident that the fit can be considered more than acceptable, confirming the goodness of the assumptions made.

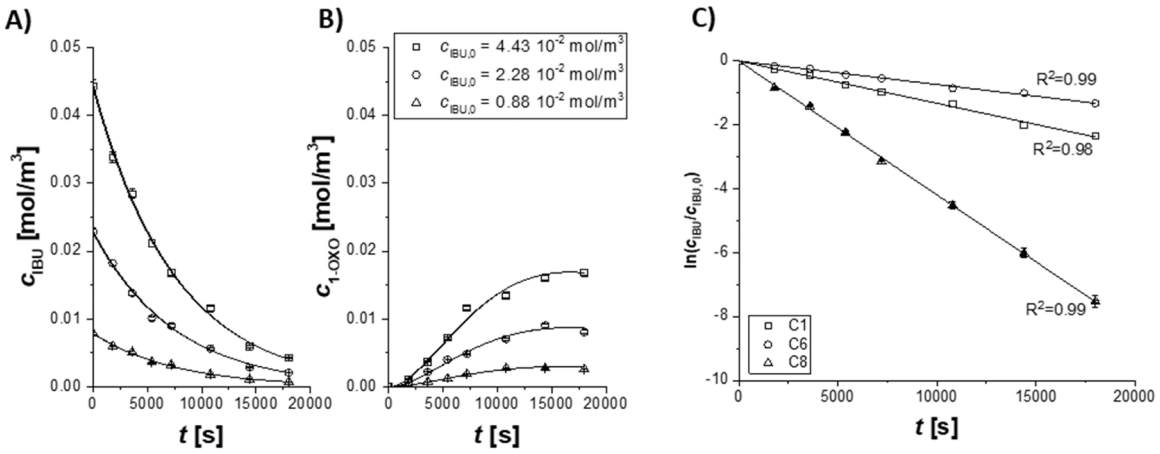

Fig. 7. Experimental results of the kinetic tests conducted at different initial concentrations of ibuprofen, fixing $T = 303$ K, $\rho_B = 0.37$ kg/m^3, $Q_{air} = 1.0 \cdot 10^{-6}$ m^3/s and $v = 750$ rpm. Trends of the concentration profiles vs the reaction time for **A**) ibuprofen and **B**) 1-OXO ibuprofen. Lines are the calculated profiles. The subplots refer to the same legend. Panel **C**) represents first-order linearization test.

Table 2
Summary of the estimated kinetic parameters, together with statistical information. $T_{ref} = 303$ K, CI 95% represents the confidence interval at 95%, *M* the correlation matrix.

Parameter	Value ± CI 95%	Units	%Error	M	$k_{ref,1}$	Ea_1	$k_{ref,2}$	Ea_2	$k_{ref,2}$	Ea_3
$k_{ref,1}$	$(1.59 \pm 0.05) \cdot 10^{-4}$	$(m^3/mol)(m^3/kg^n)s^{-1}$	1.3	$k_{ref,1}$	1.0					
Ea_1	55.8 ± 0.6	kJ/mol	1.0	Ea_1	-0.2	1.0				
$k_{ref,2}$	$(2.01 \pm 0.11) \cdot 10^{-4}$	$(m^3/mol)(m^3/kg^n)s^{-1}$	5.5	$k_{ref,2}$	-0.2	0.1	1.0			
Ea_2	29 ± 3	kJ/mol	11.8	Ea_2	0.1	-0.1	-0.6	1.0		
$k_{ref,3}$	$(1.08 \pm 0.07) \cdot 10^{-4}$	$(m^3/mol)(m^3/kg^n)s^{-1}$	6.1	$k_{ref,3}$	0.1	-0.1	0.7	-0.5	1.0	
Ea_3	31 ± 3	kJ/mol	10.6	Ea_3	-0.1	0.1	-0.6	0.5	-0.8	1.0

3.4. Thermodynamics analysis

The effect of different temperatures, i.e., 293, 303, 313, and 323 K on ibuprofen photodegradation using CeO_2-NPs was investigated. Table 3 summarizes the obtained rate constants and the corresponding values of the thermodynamic parameters namely; ΔG°, ΔH°, and ΔS°. It can be observed that increasing the reaction temperature, increases the rate constants and the corresponding photodegradation efficiency. This was previously confirmed in Fig. 5 and in the kinetics modeling section where the probability of collisions increases yielding into enhancing the photodegradation efficiency [49]. To estimate the thermodynamic parameters, Eqs. (9)–(11) were used.

$$\Delta H^\circ = E_a + RT \tag{9}$$

$$\ln(k/T) = \ln(K_B/h) + (\Delta S^\circ/R) - (\Delta H^\circ/RT) \tag{10}$$

$$\Delta G^\circ = \Delta H^\circ - T\Delta S^\circ \tag{11}$$

Where, ΔG° is the activation Gibbs free energy, ΔH° the change in enthalpy, ΔS° is the change in entropy, R is the ideal gas constant (8.314 J/mol K), K_B is Boltzmann constant (1.38×10^{-23} m^2 kg/s^2 K), h Plank constant (6.63×10^{-34} m^2 kg/s), k is the kinetics rate constant $(m^3/mol)s^{-1}$.

The relatively high positive values of ΔG° and ΔH° designate the endothermic non-spontaneous reaction forming a highly hydrated transition state complex with weak bonds for rapid degradation of the activated complex [49–51]. Moreover, the negative value of ΔS°, which is close to zero, suggests that the system exhibits a random behavior that supports a higher degree of degradation of ibuprofen into simple products [49].

4. Conclusions

This work investigates the ability of CeO_2 nanostructured materials, obtained by the wet-chemical approach, to exert a notable photodegradation of ibuprofen. The synthesis strategy led to the successful preparation of small crystalline CeO_2-NPs with a size of about 15 nm and a band gap of 3.1 eV against which the synthesized material showed comparable photocatalytic activity. XPS analysis was performed to gain a deeper understanding of the chemical composition of the surface of the CeO_2-NPs, where the ratio of Ce^{3+}/Ce^{4+} was estimated to be 0.4, as deduced from the areas of these different components. Based on the air flow rate and stirring speed study, both fluid-solid and intraparticle diffusion limitations can be neglected. The reusability of the CeO_2-NPs study indicated that they can be used repeatedly, without impacting their capacity, confirming their sustainability. It is worth mentioning, that CeO_2-NPs show similar activity to the commercial TiO_2-P25, hence the use of Ce can be more convenient when considering its market price

Table 3
Kinetic and thermodynamic parameters for the photodegradation of ibuprofen using CeO_2-NPs at $E_{a1} = 55.8 kJ/mol$.

T (K)	K $(m^3/mol)s^{-1}$	$\ln(k/T)$	$\Delta H^\circ/RT$	ΔH° $(kJ\,mol^{-1})$	ΔS° $(kJ\,mol^{-1}\,K^{-1})$	ΔG° $(kJ\,mol^{-1})$
293	2.7×10^{-5}	-16.18	23.91	58.2	− 0.14	100.0
303	5.9×10^{-5}	-15.45	23.15	58.3		101.5
313	1.2×10^{-4}	-14.78	22.44	58.4		103.0
323	2.3×10^{-4}	-14.15	21.78	58.5		104.5

that is lower than Ti. For the kinetics modeling, the experimental data were interpreted with a pseudo homogeneous single-phase model. The calculated activation energies were all within a range of the kinetic regime, with no rate-determining step among the involved reactions. The thermodynamic parameters of the photodegradation of ibuprofen have been reported. The relatively high positive values of ΔG° and ΔH° indicate the endothermic and nonspontaneous nature of the reaction forming a highly hydrated transition state complex with weak bonds for rapid degradation of the activated complex. While the positive value of ΔS° suggests that the system exhibits a random behavior with enhanced photodegradation performance of CeO_2 NPs towards ibuprofen. Overall, the findings promote the use of such a promising CeO_2 nanostructure for industrial level for ibuprofen-based pharmaceutical wastewater treatment.

CRediT authorship contribution statement

Vincenzo Russo and Giuseppe Vitiello wrote the original draft of the manuscript. The main conceptual ideas were drawn from the interactions between Vincenzo Russo and Giuseppe Vitiello, while the funds were obtained by the synergistic effect of the cooperation between Martino Di Serio and Luigi Paduano. The experimental work, data elaboration, and the formal analysis were carried out by Noemi Gallucci, Maryam Hmoudah, Amjad El-Qanni, and Eugenie Martinez. The final draft was revised by Giuseppe Vitiello and Vincenzo Russo.

Funding

The 12th executive program for scientific and technological cooperation between the Italian Republic and the Republic of Korea for the years 2019–2021 is acknowledged for financial support.

This project has received funding from the EU-H2020 Research and Innovation Program under Grant agreement no. 2018.1:677 (ID677), having benefitted from the access provided by CEA-LETI in Grenoble (France) within the framework of the NFFA-Europe Transnational Access Activity.

Declaration of Competing Interest

The authors declare that they have no known competing financial interests or personal relationships that could have appeared to influence the work reported in this paper.

Acknowledgments

The authors are grateful to Dr. Rocco Di Girolamo (Department of Chemical Science, University of Naples Federico II) for his support in TEM analysis and to Marica Chianese for her experimental support in conducting the kinetic experiments. The authors also thank CEA-LETI (Grenoble, France) for providing the access to XPS instrument.

Appendix A. Supporting information

Supplementary data associated with this article can be found in the online version at doi:10.1016/j.jece.2022.107866.

References

[1] B. Xu, F. Qi, D. Sun, Z. Chen, D. Robert, Cerium doped red mud catalytic ozonation for bezafibrate degradation in wastewater: efficiency, intermediates, and toxicity, Chemosphere 146 (2016) 22–31, https://doi.org/10.1016/j.chemosphere.2015.12.016.

[2] A. Kumar, G. Sharma, M. Naushad, A.a.H. Al-Muhtaseb, A. Kumar, I. Hira, T. Ahamad, A.A. Ghfar, F.J. Stadler, Visible photodegradation of ibuprofen and 2,4-D in simulated waste water using sustainable metal free-hybrids based on carbon nitride and biochar, J. Environ. Manag., vol. 231, 2019, pp. 1164–75. (https://doi.org/10.1016/j.jenvman.2018.11.015).

[3] S. Saeid, P. Tolvanen, N. Kumar, K. Eränen, J. Peltonen, M. Peurla, J.-P. Mikkola, A. Franz, T. Salmi, Advanced oxidation process for the removal of ibuprofen from aqueous solution: a non-catalytic and catalytic ozonation study in a semi-batch reactor, Appl. Catal. B: Environ. 230 (2018) 77–90, https://doi.org/10.1016/j.apcatb.2018.02.021.

[4] S.D. Richardson, S.Y. Kimura, Water analysis: emerging contaminants and current issues, Anal. Chem. 92 (1) (2020) 473–505, https://doi.org/10.1021/acs.analchem.9b05269.

[5] L.F.V. Francisco, B. do Amaral Crispim, J.C.V. Spósito, J.C.J. Solórzano, N. H. Maran, F. Kummrow, V.A. do Nascimento, C.C. Montagner, K.M.P. De Oliveira, A. Barufatti, Metals and emerging contaminants in groundwater and human health risk assessment, Environ. Sci. Pollut. Res. 26 (24) (2019) 24581–24594, https://doi.org/10.1007/s11356-019-05662-5.

[6] B.S. Rathi, P.S. Kumar, P.-L. Show, A review on effective removal of emerging contaminants from aquatic systems: current trends and scope for further research, J. Hazard. Mater. (2020), 124413, https://doi.org/10.1016/j.jhazmat.2020.124413.

[7] P.R. Rout, T.C. Zhang, P. Bhunia, R.Y. Surampalli, Treatment technologies for emerging contaminants in wastewater treatment plants: a review, Sci. Total Environ. 753 (2021), 141990, https://doi.org/10.1016/j.scitotenv.2020.141990.

[8] H. Chaker, S. Fourmentin, L. Chérif-Aouali, Efficient photocatalytic degradation of ibuprofen under visible light irradiation using silver and cerium Co-doped mesoporous TiO_2, ChemistrySelect 5 (38) (2020) 11787–11796, https://doi.org/10.1002/slct.202002730.

[9] G. Boczkaj, A. Fernandes, Wastewater treatment by means of advanced oxidation processes at basic pH conditions: a review, Chem. Eng. J. 320 (2017) 608–633, https://doi.org/10.1016/j.cej.2017.03.084.

[10] A. Gul, N.G. Khaligh, N.M. Julkapli, Surface modification of carbon-based nanoadsorbents for the advanced wastewater treatment, J. Mol. Struct. 1235 (2021), 130148, https://doi.org/10.1016/j.molstruc.2021.130148.

[11] A. El-Qanni, Development of Sustainable Nanosorbcats Based Technology for Hydrocarbons and Organic Pollutants Recovery from Industrial Wastewater, Chemical and Petroleum Engineering, University of Calgary, Calgary, AB, 2017.

[12] A. Ahmad, S.H. Mohd-Setapar, C.S. Chuong, A. Khatoon, W.A. Wani, R. Kumar, M. Rafatullah, Recent advances in new generation dye removal technologies: novel search for approaches to reprocess wastewater, RSC Adv. 5 (39) (2015) 30801–30818, https://doi.org/10.1039/C4RA16959J.

[13] I. Gehrke, A. Geiser, A. Somborn-Schulz, Innovations in nanotechnology for water treatment, Nanotechnol. Sci. Appl. 8 (2015) 1–17, https://doi.org/10.2147/NSA.S43773.

[14] A.S. Adeleye, J.R. Conway, K. Garner, Y. Huang, Y. Su, A.A. Keller, Engineered nanomaterials for water treatment and remediation: costs, benefits, and applicability, Chem. Eng. J. 286 (2016) 640–662, https://doi.org/10.1016/j.cej.2015.10.105.

[15] S. Dong, J. Feng, M. Fan, Y. Pi, L. Hu, X. Han, M. Liu, J. Sun, J. Sun, Recent developments in heterogeneous photocatalytic water treatment using visible light-responsive photocatalysts: a review, RSC Adv. 5 (19) (2015) 14610–14630, https://doi.org/10.1039/C4RA13734E.

[16] M.A. Sousa, C. Gonçalves, V.J.P. Vilar, R.A.R. Boaventura, M.F. Alpendurada, Suspended TiO_2-assisted photocatalytic degradation of emerging contaminants in a municipal WWTP effluent using a solar pilot plant with CPCs, Chem. Eng. J. 198–199 (2012) 301–309, https://doi.org/10.1016/j.cej.2012.05.060.

[17] C. Tortajada, Contributions of recycled wastewater to clean water and sanitation sustainable development goals, npj Clean Water 3 (1) (2020) 22, https://doi.org/10.1038/s41545-020-0069-3.

[18] M. Vatanparast, L. Saedi, Sonochemical-assisted synthesis and characterization of CeO_2 nanoparticles and its photocatalytic properties, J. Mater. Sci.: Mater. Electron. 29 (9) (2018) 7107–7113, https://doi.org/10.1007/s10854-018-8698-8.

[19] S. Yuán, B. Xu, Q. Zhang, S. Liu, J. Xie, M. Zhang, T. Ohno, Development of the visible-light response of CeO_{2-x} with a high Ce^{3+} content and its photocatalytic properties, ChemCatChem 10 (6) (2018) 1267–1271, https://doi.org/10.1002/cctc.201701767.

[20] L. Gnanasekaran, R. Hemamalini, R. Saravanan, K. Ravichandran, F. Gracia, S. Agarwal, V.K. Gupta, Synthesis and characterization of metal oxides (CeO_2, CuO, NiO, Mn_3O_4, SnO_2 and ZnO) nanoparticles as photo catalysts for degradation of textile dyes, J. Photochem. Photobiol. B: Biol. 173 (2017) 43–49, https://doi.org/10.1016/j.jphotobiol.2017.05.027.

[21] M. Aslam, M.T. Qamar, M.T. Soomro, I.M.I. Ismail, N. Salah, T. Almeelbi, M. A. Gondal, A. Hameed, The effect of sunlight induced surface defects on the photocatalytic activity of nanosized CeO_2 for the degradation of phenol and its derivatives, Appl. Catal. B: Environ. 180 (2016) 391–402, https://doi.org/10.1016/j.apcatb.2015.06.050.

[22] P. Borker, A.V. Salker, Solar assisted photocatalytic degradation of naphthol blue black dye using $Ce_{1-x}Mn_xO_2$, Mater. Chem. Phys. 103 (2) (2007) 366–370, https://doi.org/10.1016/j.matchemphys.2007.02.034.

[23] D. Majumder, I. Chakraborty, K. Mandal, S. Roy, Facet-dependent photodegradation of methylene blue using pristine CeO_2 nanostructures, ACS Omega 4 (2) (2019) 4243–4251, https://doi.org/10.1021/acsomega.8b03298.

[24] F. Naaz, U. Farooq, T. Ahmad, Ceria as an efficient nanocatalyst for organic transformations, nanocatalysts, IntechOpen (2019), https://doi.org/10.5772/intechopen.82688.

[25] J.A. Rodriguez, D.C. Grinter, Z. Liu, R.M. Palomino, S.D. Senanayake, Ceria-based model catalysts: fundamental studies on the importance of the metal–ceria interface in CO oxidation, the water–gas shift, CO_2 hydrogenation, and methane and alcohol reforming, Chem. Soc. Rev. 46 (7) (2017) 1824–1841, https://doi.org/10.1039/C6CS00863A.

[26] C. Maria Magdalane, K. Kaviyarasu, A. Raja, M.V. Arularasu, G.T. Mola, A.B. Isaev, N.A. Al-Dhabi, M.V. Arasu, B. Jeyaraj, J. Kennedy, M. Maaza, Photocatalytic decomposition effect of erbium doped cerium oxide nanostructures driven by visible light irradiation: investigation of cytotoxicity, antibacterial growth inhibition using catalyst, J. Photochem. Photobiol. B: Biol. 185 (2018) 275–282, https://doi.org/10.1016/j.jphotobiol.2018.06.011.
[27] S.M.M. (SMM), SMM Spot prices. ⟨https://www.metal.com/⟩, (Accessed 3rd June 2021).
[28] A.S. Weber, A.M. Grady, R.T. Koodali, Lanthanide modified semiconductor photocatalysts, Catal. Sci. Technol. 2 (4) (2012) 683–693, https://doi.org/10.1039/C2CY00552B.
[29] M.E. Kibar, Preparation of copper oxide-cerium oxide/nanotube-titanium dioxide photocatalyst for CO_2 conversion in solar light, React. Kinet. Mech. Catal. 134 (2) (2021) 937–950, https://doi.org/10.1007/s11144-021-02079-5.
[30] M. Ahamed, M.A.M. Khan, M.J. Akhtar, H.A. Alhadlaq, A. Alshamsan, Ag-doping regulates the cytotoxicity of TiO_2 nanoparticles via oxidative stress in human cancer cells, Sci. Rep. 7 (1) (2017) 17662, https://doi.org/10.1038/s41598-017-17559-9.
[31] Y.-C. Zhang, Z. Li, L. Zhang, L. Pan, X. Zhang, L. Wang, A. Fazal e, J.-J. Zou, Role of oxygen vacancies in photocatalytic water oxidation on ceria oxide: experiment and DFT studies, Appl. Catal. B: Environ. 224 (2018) 101–108, https://doi.org/10.1016/j.apcatb.2017.10.049.
[32] M. Ahamed, M.J. Akhtar, M.A.M. Khan, Z.M. Alaizeri, H.A. Alhadlaq, Evaluation of the cytotoxicity and oxidative stress response of CeO_2-RGO nanocomposites in human lung epithelial A549 cells, Nanomaterials 9 (12) (2019) 1709.
[33] M.M. Khan, S.A. Ansari, D. Pradhan, D.H. Han, J. Lee, M.H. Cho, Defect-induced band gap narrowed CeO_2 nanostructures for visible light activities, Ind. Eng. Chem. Res. 53 (23) (2014) 9754–9763, https://doi.org/10.1021/ie500986n.
[34] G. Jayakumar, A. Albert Irudayaraj, A. Dhayal Raj, Particle size effect on the properties of cerium oxide (CeO_2) nanoparticles synthesized by hydrothermal method, mechanics, Mater. Sci. Eng. J. 9 (1) (2017), https://doi.org/10.2412/mmse.3.4.481.
[35] B. Choudhury, A. Choudhury, Ce^{3+} and oxygen vacancy mediated tuning of structural and optical properties of CeO_2 nanoparticles, Mater. Chem. Phys. 131 (3) (2012) 666–671, https://doi.org/10.1016/j.matchemphys.2011.10.032.
[36] C. Yang, X. Yu, P.N. Pleßow, S. Heißler, P.G. Weidler, A. Nefedov, F. Studt, Y. Wang, C. Wöll, Rendering photoreactivity to ceria: the role of defects, Angew. Chem. Int. Ed. 56 (45) (2017) 14301–14305, https://doi.org/10.1002/anie.201707965.
[37] J.K. Sharma, P. Srivastava, S. Ameen, M.S. Akhtar, S.K. Sengupta, G. Singh, Phytoconstituents assisted green synthesis of cerium oxide nanoparticles for thermal decomposition and dye remediation, Mater. Res. Bull. 91 (2017) 98–107, https://doi.org/10.1016/j.materresbull.2017.03.034.
[38] P. Latha, K. Prakash, S. Karuthapandian, Effective photodegradation of CR & MO dyes by morphologically controlled cerium oxide nanocubes under visible light illumination, Optik 154 (2018) 242–250, https://doi.org/10.1016/j.ijleo.2017.10.054.
[39] S. Sehar, I. Naz, A. Rehman, W. Sun, S.S. Alhewairini, M.N. Zahid, A. Younis, Shape-controlled synthesis of cerium oxide nanoparticles for efficient dye photodegradation and antibacterial activities, Appl. Organomet. Chem. 35 (1) (2021), e6069, https://doi.org/10.1002/aoc.6069.
[40] S.J. Saadoon, M. Jarosova, P. Machek, M.M. Kadhim, M.H. Ali, A.D. Khalaji, Methylene blue photodegradation using as-synthesized CeO_2 nanoparticles, J. Chin. Chem. Soc. n/a (n/a) (2021), https://doi.org/10.1002/jccs.202100476.
[41] N.M. Lopés-Velasco, S.J. Bailón-Ruiz, Effect of the particle size and pH on the photocatalytic performance of cerium oxide (CeO_2) nanoparticles, MRS Adv. 6 (32) (2021) 769–773, https://doi.org/10.1557/s43580-021-00070-9.
[42] A.I.Y. Tok, F.Y.C. Boey, Z. Dong, X.L. Sun, Hydrothermal synthesis of CeO_2 nanoparticles, J. Mater. Process. Technol. 190 (1) (2007) 217–222, https://doi.org/10.1016/j.jmatprotec.2007.02.042.
[43] E.P. Barrett, L.G. Joyner, P.P. Halenda, The determination of pore volume and area distributions in porous substances. I. Computations from nitrogen isotherms, J. Am. Chem. Soc. 73 (1) (1951) 373–380, https://doi.org/10.1021/ja01145a126.
[44] D. Girija, H.S.B. Naik, C. Sudhamani, B.V. Kumar, Cerium oxide nanoparticles—a green, reusable, and highly efficient heterogeneous catalyst for the synthesis of polyhydroquinolines under solvent-free conditions, Arch. Appl. Sci. Res. 3 (3) (2011) 373–382.
[45] M. Okuda, Y. Suzumoto, I. Yamashita, Bioinspired synthesis of homogenous cerium oxide nanoparticles and two- or three-dimensional nanoparticle arrays using protein supramolecules, Cryst. Growth Des. 11 (6) (2011) 2540–2545, https://doi.org/10.1021/cg200299y.
[46] E. Kusmierek, A CeO_2 semiconductor as a photocatalytic and photoelectrocatalytic material for the remediation of pollutants in industrial wastewater: a review, Catalysts 10 (12) (2020), https://doi.org/10.3390/catal10121435.
[47] M. Kråkström, S. Saeid, P. Tolvanen, N. Kumar, T. Salmi, L. Kronberg, P. Eklund, Identification and quantification of transformation products formed during the ozonation of the non-steroidal anti-inflammatory pharmaceuticals ibuprofen and diclofenac, Ozone: Sci. Eng. (2021) 1–15, https://doi.org/10.1080/01919512.2021.1898928.
[48] S. Saeid, M. Kråkström, P. Tolvanen, N. Kumar, K. Eränen, M. Peurla, J.-P. Mikkola, L. Maël, L. Kronberg, P. Eklund, T. Salmi, Synthesis and characterization of metal modified catalysts for decomposition of ibuprofen from aqueous solutions, Catalysts 10 (7) (2020), https://doi.org/10.3390/catal10070786.
[49] K. Byrappa, A.K. Subramani, S. Ananda, K.M.L. Rai, R. Dinesh, M. Yoshimura, Photocatalytic degradation of rhodamine B dye using hydrothermally synthesized ZnO, Bull. Mater. Sci. 29 (5) (2006) 433–438, https://doi.org/10.1007/BF02914073.
[50] M. Rezaei, A. Nezamzadeh-Ejhieha, The ZnO-NiO nano-composite: a brief characterization, kinetic and thermodynamic study and study the Arrhenius model on the sulfasalazine photodegradation, Int. J. Hydrog. Energy 45 (46) (2020) 24749–24764, https://doi.org/10.1016/j.ijhydene.2020.06.258.
[51] A.S.M. Kuba, A.M.J.A.L. Shamari, Kinetics and thermodynamics study for photodegradation of brown HT dye by MnO and NiO as catalysis, Mater. Today: Proc. 49 (2022) 2741–2746, https://doi.org/10.1016/j.matpr.2021.09.256.

Publication VI

Photodegradation of ibuprofen using ZnO and TiO_2 nanoparticles: Comprehensive kinetic modeling, reaction mechanisms, and thermodynamics study

Maryam Hmoudah[1,2], Amjad El-Qanni[2], Carmela Chianese[1], Tapio Salmi[3], Martino Di Serio[1], Vincenzo Russo[1*]

[1] *University of Naples Federico II, Department of Chemical Sciences, IT-80126 Naples, Italy.*

[2] *An-Najah National University, Department of Chemical Engineering, Nablus, Palestine.*

[3] *Åbo Akademi, Laboratory of Industrial Chemistry and Reaction Engineering (TKR), FI-20500 Turku/Åbo.*

**corresponding author:* Vincenzo Russo (v.russo@unina.it) at University of Naples Federico II.*

Abstract

Photocatalytic activity, reaction kinetics, modeling, and thermodynamics of commercial TiO_2-P25 and ZnO nanoparticles (NPs) for ibuprofen (IBU) photodegradation were investigated. Photodegradation experiments were performed in a batch reactor under ultraviolet (UV) irradiation. The photocatalytic kinetic modeling was initiated by applying first and second order kinetic models and the corresponding reaction mechanisms were suggested. The photodegradation performances of TiO_2 and ZnO NPs were further studied and modeled under different operation conditions, by varying the reaction temperature, catalyst bulk density, and the initial concentration of the IBU solution. The chemical and physical-diffusive aspects and the goodness of the kinetic modeling was studied. The descriptive kinetic models for the experimental data were tested, through the estimated kinetic parameters, together with the statistical information, revealing that the reaction rate in the case of TiO_2 is of first order while the ZnO NPs follow second order kinetics with respect to IBU. The photodegradation mechanisms for both TiO_2 and ZnO NPs were determined to be Langmuir-Hinshelwood and Eley-Rideal, respectively. Thermodynamic parameters were assessed, particularly, Gibbs free energy ($\Delta G°$), enthalpy ($\Delta H°$) and entropy ($\Delta S°$) indicating the efficient photodegradation performance of these NPs.

Keywords: zinc oxide, titanium dioxide, nanoparticles, ibuprofen, photodegradation, kinetics, thermodynamics.

1. Introduction

Since the world population is increasing annually with an unsustainable rate, the rapid depletion of clean water sources on the planet increases [1]. Therefore, the need of wastewater treatment is more relevant than ever. Nowadays, more than 700 emerging contaminants (ECs) being either synthetically or naturally produced are chaotically disposed in water bodies [2, 3]. These ECs include personal-care products, organic wastewater compounds, and pharmaceutically active compounds which can be harmful to both ecological and human health. Ibuprofen, 2-(4-isobutylphenyl) propionic acid (IBU) is a well-known nonsteroidal anti-inflammatory drug that is widely detected in wastewaters [4-6]. Numerous studies and reviews pertaining to the occurrence, the toxicity, and the impact of this emerging contaminant has been undertaken over the last few decades due to the harmful bioactive nature of IBU [4, 7, 8]. Mezzelani et al. studied the occurrence of IBU and other pharmaceutical substances and concluded that the presence of such materials in aquatic bodies and the long-term exposure can cause many problematic consequences [9]. Thus, finding sustainable methods to purify contaminated water is one of the global priorities. Most of the existing advanced wastewater treatment options include physical separation of contaminants and biological oxidation, that are expensive and face many operational challenges [10, 11]. Furthermore, they are not efficient enough for the decontamination of toxic, nonbiodegradable organic compounds. Hence, heterogeneous photocatalysis using non-conventional solids can be one of the state sustainable and promising technologies for water purification [12]. These technologies have many advantages because they generate harmless by-products with easily operated equipment design to treat wastewater [13]. TiO_2 and ZnO nanoparticles are most widely used for different catalytic applications as they provide a high catalytic activity with high electron mobility and good chemical stability. [14-16]. Gnanaprakasam and coworkers [14] studied the

69 photocatalytic degradation of azodyes using in-house prepared TiO_2 and ZnO NPs under UV
70 irradiation. They proved that ZnO exhibits a better photocatalytic activity than TiO_2 towards acid
71 red 27 and coralene red F_3BS dyes. In the systematic review article of Zhao et al. [17] about the
72 advances in employing NPs for the photodegradation of emerging contaminants, the authors
73 confirmed that TiO_2 and ZnO nanoparticles have shown a great potential for removing emerging
74 contaminants. In the recent studies presented in Table 1, the photocatalytic degradation of IBU in
75 water using TiO_2 and ZnO, under artificial UV and solar irradiation was investigated. The authors
76 studied different parameters affecting the degradation rate and mineralization of IBU in batch and
77 continuous reactors. In this sense, performing studies on the reaction kinetics can be an important
78 pillar for prospective scale up systems of AOPs [18]. Moreover, studying the reaction rate
79 experimentally, the rate constant, and the activation energy which are independent of the scale,
80 will be insightful about the progress of the reaction, and thus the predicted reaction time.
81 Herein, the scope of this research is to investigate the photodegradation kinetic modeling,
82 photodegradation mechanisms, and thermodynamics of commercial TiO_2 and ZnO nanoparticles
83 towards IBU photodegradation. Different parameters were considered in the kinetic study. The
84 efficiency of TiO_2 and ZnO nanoparticles towards IBU photodegradation in terms of temperature,
85 catalyst bulk density and IBU solution initial concentration was studied. Kinetic modeling was
86 proposed considering descriptive kinetic models of the reaction, in addition to the chemical and
87 physical-diffusive aspects. Consequently, the parameter estimations characterizing the systems,
88 and the corresponding activation energies were determined. Finally, thermodynamics parameters
89 ($\Delta G°$, $\Delta H°$, and $\Delta S°$) were assessed.

90 **Table 1**. Some previous published works on the photocatalytic activity of commercial TiO_2 and ZnO NPs towards IBU
91 photodegradation.

NPs	Process parameters	Reactor type with light radiation	Highlights	Reference
ZnO	• $C_{IBU,0}$ =5-60 mg/L, • C_{ZnO} = 10 mg/L	Batch reactor with UV–Vis solarium lamp (60 W).	• Smaller particles are more active than larger ones due to increased specific surface area and adsorption. • Intermediates such as benzene and phenolic derivatives were identified during photocatalytic degradation of IBU.	[19]
ZnO	• $C_{IBU,0}$ =10 mg/L, • C_{ZnO}= 0.5 g/L,	Batch reactor with 18 UV lamps (λ: 365 nm) Visible metal halide lamps (λ: 400–800 nm)	• The performance of the bare TiO_2 and ZnO were compared to TiO_2/ZnO, RGO/TiO_2 binary composites. • The synthesized heterojunction RGO/TiO_2/ZnO catalyst exhibited superior photocatalytic performance towards IBU degradation under visible light irradiation.	[20]
TiO_2, ZnO	• $C_{IBU,0}$ =20 mg/L, • C_{ZnO}= 1 g/L,	Continuous reactor with UV lamp (40 W)	• The main conclusions drawn were that both nanoparticles showed better performance under UV irradiation and acidic conditions for TiO_2, whereas ZnO had higher degradation efficiency under neutral conditions.	[21]
TiO_2 P-25	• $C_{IBU,0}$ =20-200 mg/L, • C_{TiO_2} = 0.1 g/L	Tubular photoreactor, Compound parabolic concentrator (CPC) under solar light.	• The time needed for a sufficient TOC removal was between 0.5 and 1.5 day to reach biodegradable properties of the treated solution. • The photocatalytic treatment increases the biodegradability of IBU solutions and coupling with post biological treatment was recommended.	[22]
TiO_2 P-25	• $C_{IBU,0}$ =20-200 mg/L, • C_{TiO_2} = 1g/L	Batch reactor with Xenon arc lamp, 450 W	• Sonophotocatalysis showed a slight better performance of IBU degradation when compared with photocatalysis.	[23]

			• IBU photodegredation intermediate were identified through HPLC–MS.	
TiO_2 P-25	• $C_{IBU,0}$ =1 mg/L, • C_{TiO_2}= 0.5 g/L,	Continuous reactor with Hg vapor lamp125 W	• The by-products generated during the photodegradation of IBU using TiO_2/UV showed to be more toxic to *Daphnia similis* than the original compound.	[24]
Synthesized TiO_2	• $C_{IBU,0}$ =0.02 mg/L, • C_{TiO_2}= 0.5 g/L,	Batch reactor with Simulated solar light	• Photocatalytic degradation of IBU was achieved using different phase ratios of TiO_2 photocatalyst. • The best performance was with 61.8% Anatase and 38.2% Brookite. • The prepared photocatalyst at specific conditions is very stable after eight cycles without loss its photocatalytic performance.	[25]
Sensitized TiO_2 film coated glass	• $C_{IBU,0}$ =200 mg/L, • C_{TiO_2}= 0.5 g/L,	Batch reactor with UV-Vis light	• *Begonia* extracts were used as sensitizers for TiO_2-based photodegradation of IBU showing promising performance.	[26]
Commercial TiO_2	• $C_{IBU,0}$ = 10^{-4} M, • C_{TiO_2}= 0.1–0.5 g/L,	Batch reactor with mercury lamp, 125 W	• The optimum photodegradation conditions were 0.03 g of TiO_2 and pH=5.0, reaching 100% decontamination in 5 min. • The proposed mechanism of IBU degradation into 4-isobutylacetophenone occurred through decarboxylation reaction followed by oxidation.	[27]
TiO_2 P-25	• $C_{IBU,0}$ =5-20 mg/L, • C_{TiO_2}= 0.25–2 g/L,	Batch reactor with polychromatic UVA lamp	• The maximum photoactivity of TiO_2 towards IBU was accomplished when the catalyst concentration was 0.8 g/L. • The photocatalytic degradation followed a pseudo-first-order reaction following Langmuir-Hinshelwood model.	[28]

92

2. Materials and methods

2.1 Materials

IBU solutions were prepared using 4-isobutyl-α-methylphenylacetic acid at 99% (Alfa Aesar). ZnO was purchased by Sigma-Aldrich (Milan, Italy). TiO_2-P25 was supplied by Evonik Industries (Essen, Germany). Bi-distilled Milli-Q water, also filtered using 0.20 μm filters, was obtained through Merck Millipore (Darmstadt, Germany). The characteristics of both NPs are listed in Tables S.1 and S.2 for TiO_2 and ZnO, respectively.

2.2 Photodegredation experiments

Photodegradation experiments were carried out following the same protocol as in our previous work [29]. In brief, 1.5 L jacketed glass vessel with a three-neck head was used and connected to ultra-thermostat to regulate the temperature. Air was fed to the reactor system using a digital flow-meter regulator (supplied by Bronkhorst), connected to a sintered filter used as gas sparger, to provide a good gas-liquid interface in the mass transfer of air to the liquid phase. UV lamp of 4W was coaxially mounted in the reactor (Toshiba FL4BLB), with a wavelength of λ=365nm.

In a typical photodegradation experiment, an IBU solution was prepared with the desired concentration, and was loaded into the magnetically stirred reactor vessel. The reactor was closed with a lid and connected to a thermostat, set at a pre-specified reaction temperature. The air flow was adjusted with a pressure reducer to 1 bar and the digital flow meter was set at a fixed flow, after which the catalyst was loaded into the reactor. The reactor was then shielded before switching on the UV lamp to reduce any ray dispersion. The initial concentration of IBU was measured, then the reaction was started by switching on the lamp, and samples were withdrawn periodically to follow the reaction kinetics until a maximum time of 5 h. Each sample was then centrifuged at 3000 rpm for 30 minutes, and the resulting liquid sample was analyzed by UV-VIS spectroscopy

(UV-Vis Jasco V-550). A typical spectrum is reported in Supplementary material (Figure S.1). A calibration curve was prepared at λ=222 nm, where the absorption of IBU reached the maximum value, obtaining the calibration curve reported in Eq. 1, valid in a concentration range between 0-0.05 mol/m^3 (Figure S.2).

$$C_{IBU} = (9.223 \pm 0.002)A, R^2 = 0.99 \quad (1)$$

where A represents the absorbance and C_{IBU} is the IBU concentration expressed in mol/m^3.

To investigate the reaction kinetics, along with eventual mass transfer limitations, several experiments were conducted by varying the operation conditions within a wide range. The summary of the adopted reaction conditions is provided in Tables S.3 and S.4 for TiO_2 and ZnO NPs, respectively.

2.3 Modeling and parameter estimation

All the modeling efforts were performed using Matlab R2020b. The *ode23s* routine was used to solve the underlying ordinary differential equations, while the parameter estimation, i.e. minimization of the objective function with *particleswarm* algorithm. The confidence intervals of the parameters were calculated using *nlparci* algorithm. The objective function was estimated as follows [30]:

$$F_{obj} = \frac{1}{N_{data}} \sqrt{\sum_{i=1}^{N_{data}} \left(\frac{c_{i,EXP} - c_{i,CALC}}{c_{i,EXP}} \right)^2} \quad (2)$$

3. Results and discussion

3.1 Evaluation of the external mass transfer limitations and intraparticle diffusion

The stability of IBU under UV irradiation and in the absence of the catalyst was verified and confirmed in our previous work [29] giving a maximum conversion of 5% before plateauing (Figure S.3). The influence of the gas-liquid transfer resistance was checked by varying air flow

rate to the reactor since the gas-liquid mass transfer could affect the overall rate of the reaction. The air flow rate effect is presented in Figures S.4 and S.5 for TiO_2 and ZnO, respectively. The result validated that increasing the air flow rate led to an increase in the observed reaction rate, up to 0.94×10^{-6} m^3/s reaching a stable plateau in both cases of ZnO. For TiO_2 nanoparticles, increasing the air flow rate showed a very slight mass transfer resistance effect which was negligible. Therefore, the impact of the gas-liquid mass transfer resistance can be neglected and thus, all the other experiments were conducted imposing $0.94\cdot10^{-6}$ m^3/s airflow. The kinetic investigations were performed on an optimal stirring rate of 750 rpm, which was proven in our previous work [29], where it was found that beyond 500 rpm, the reaction rate is stabilized.

The intraparticle diffusion limitations were assessed through the Weisz-Prater criterion as elucidated in eq 3,

$$C_{WP} = \frac{-r'_A(obs)\rho_C R^2}{D_e C_{As} \rho_B} \quad (3)$$

Where r'_A (obs) is the reaction observed rate in $mol/(m^3\cdot s)$, ρ_C is the density of the catalyst in kg/m^3, R is the particle radius in m, D_e is the effective diffusivity in m^2/s, C_{As} is the concentration of species A on the catalyst in mol/m^3, ρ_B is the bulk density in kg/m^3.

Based on the external mass transfer results, it is possible to assume that the concentration of IBU on the outer surface of the catalyst is the same as that in the bulk solution. Therefore, the effective diffusivity, was assumed to be of 1/10 of the molecular diffusivity of a given species, in an infinitely diluted liquid systems [31]. Therefore, the Wilke-Chang equation given in eq S.1 and the Le Bas increments for the solute molar volume, eq S.2 were employed. The obtained values of C_{WP} were 6.0×10^{-5} for ZnO and 3.7×10^{-7} for TiO_2 NPs. Since the values of $C_{WP} \ll 1$ for the two NPs, the intraparticle diffusion limitations can be ignored for both systems [31].

3.2 Reaction order for TiO_2 and ZnO nanoparticles

The following first order reaction kinetics was applied for TiO_2 and ZnO NPs at different temperatures.

$$\frac{dC_{IBU}}{dt} = -r\rho_B^n \rightarrow \frac{dC_{IBU}}{dt} = -kC_{IBU}\rho_B^n \rightarrow \int_{C_{IBU,0}}^{C_{IBU}} \frac{dC_{IBU}}{C_{IBU}} = \int_0^t -k\rho_B^n dt \rightarrow \ln\left(\frac{C_{IBU}}{C_{IBU,0}}\right) = -k\rho_B^n t \quad (4)$$

R^2 values for the first-order linearization test are presented in Table S.5 for both NPs. The high R^2 for TiO_2 NPs suggest a first-order kinetics, as illustrated in Figure 1, demonstrating that the reaction kinetics follows a first-order rate law. This observation is in agreement with the findings of Méndez-Arriaga and coworkers [32] where they elucidated that the most probable degradation path of IBU mainly follows the first step of the degradation, due to a hydroxylation process, especially at high initial concentrations of IBU.

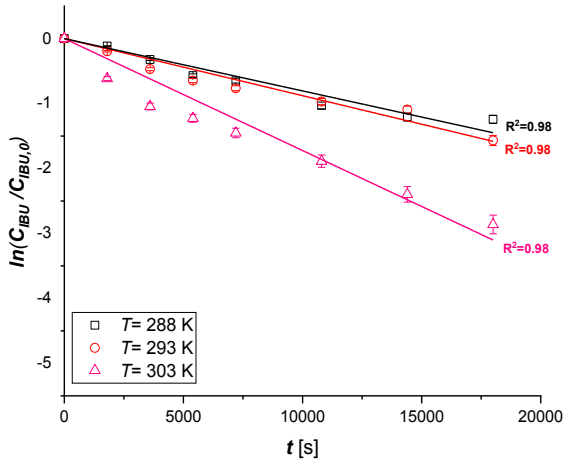

Figure 1. First order reaction kinetics plots at different temperatures using TiO_2, $C_{IBU,0} = 5 \cdot 10^{-2}$ mol/m^3, $\rho_B = 0.5$ kg/m^3, $Q_{air} = 0.94 \cdot 10^{-6}$ m^3/s and $v = 750$ rpm.

However, the fitting of ZnO nanoparticles was not good enough as given in Table S.5. Therefore, second order kinetics was considered as later step. The data were aligned to a straight line, as shown in Figure 2, elucidating that the reaction kinetics follows a second-order rate law,

$$\frac{dC_{IBU}}{dt} = -r\rho_B^n \rightarrow \frac{dC_{IBU}}{dt} = -kC_{IBU}^2\rho_B^n \rightarrow \int_{C_{IBU,0}}^{C_{IBU}} \frac{dC_{IBU}}{C_{IBU}^2} = \int_0^t -k\rho_B^n dt \rightarrow 1 - \left(\frac{C_{IBU,0}}{C_{IBU}}\right)$$

$$= -k\rho_B^n C_{IBU,0} t \quad (5)$$

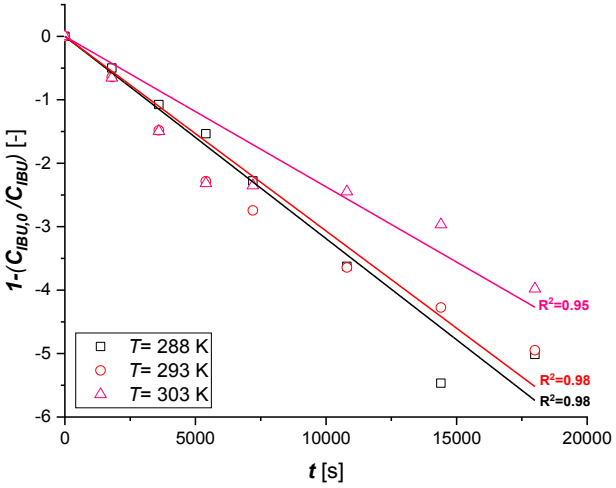

Figure 2. Second order kinetic plots at different temperatures using ZnO nanoparticles, $C_{IBU,0}$ = $5 \cdot 10^{-2}$ mol/m^3, ρ_B = 0.5 kg/m^3, Q_{air} = $0.94 \cdot 10^{-6}$ m^3/s and v = 750 rpm.

Based on the coordination compound theory, organic compounds, for example IBU, with their functional groups can bind, acting as Lewis bases, with metallic ions, e.g. zinc, that acts as a Lewis acid, forming ring structures called coordination compounds [33]. In particular, IBU contains a carboxylic group, which has a high affinity for zinc and participates with two molecules in the formation of the complex. This has also been studied by Kaur and coworkers [34].

The oxygen concentration in the liquid phase was estimated in each reaction step at different temperatures using the following empirical formula fitted to the data published in the literature [35], ensuring the correct oxygen concentration at each temperature,

$$C_{O_2} = (52.94\, exp(-T/25.9) + 7.5 \cdot 10^{-4})\rho_{H_2O} \quad (6)$$

The experimental data were interpreted with a pseudo-homogeneous single-phase model, as

neither fluid-solid nor intraparticle diffusion limitations appeared according to the results presented in section 3.1. The general mass balance equation is reported in equation 7,

$$\frac{dC_i}{dt} = \sum_{j=1}^{N_r} \upsilon_{ij} r_j \rho_B^n \quad (7)$$

where C_i is the concentration of component *i* in mol/m^3, υ_{ij} is the stoichiometric coefficient of component *i* in reaction *j*, r_j is the reaction rate of step *j* in mol/(kg.s), *n* linearization coefficient for catalyst bulk density, and ρ_B catalyst bulk density in kg/m^3.

In the evaluation of the reaction order, the catalyst bulk density was elevated to a proportional coefficient *n*, to take into consideration the shielding effect of the catalyst loading on the UV-light penetration in the liquid phase [36]. This coefficient was determined from the experimental data, plotting the $\ln(r_{obs})$ vs $\ln(\rho_B)$, as given in equation 8.

$$r_{obs} = r\rho_B^n \rightarrow ln(r_{obs}) = ln(r) + n\, ln(\rho_B) \quad (8)$$

Figures 3 and 4 show the plots of $\ln(r_{obs})$ vs $\ln(\rho_B)$, for both TiO_2 and ZnO NPs. The corresponding calculated coefficient of TiO_2 NPS was n=0.68 ± 0.09. In case of ZnO the calculated coefficient value was n=0.38 ± 0.09. The higher the value of the parameter *n* for TiO_2 NPs is attributed to the whiter color of these NPs which results in a bigger penetration shielding effect to light showing scattered behavior in comparison with ZnO NPs that tend to be grey.

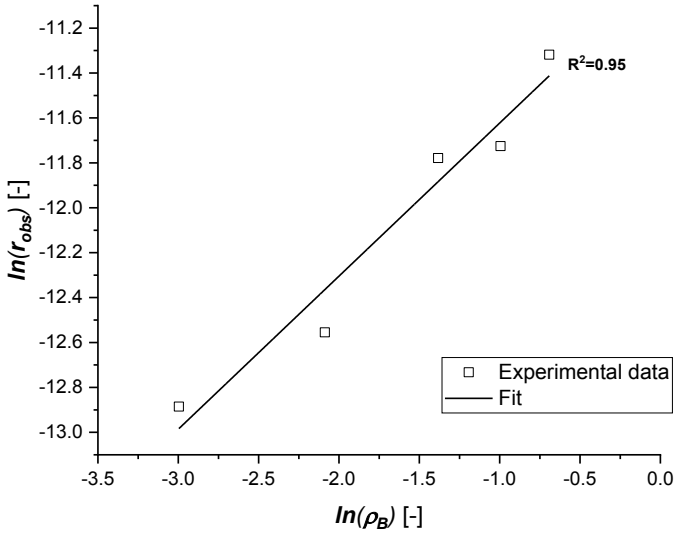

220
221 **Figure 3**. Logarithm of the reaction rate as a function of the logarithm of the bulk density for
222 TiO_2 nanoparticles T=303K, $C_{IBU,0}=5\cdot10^{-2}$ mol/m^3, $Q_{air}=0.94\cdot10^{-6}$ m^3/s, v = 750 rpm.

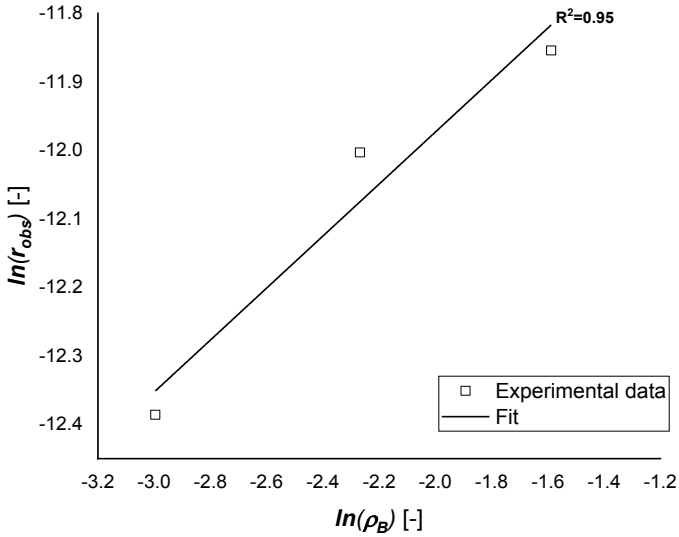

223
224 **Figure 4**. Logarithm of the reaction rate as a function of the logarithm of the bulk density for
225 ZnO nanoparticles T=303K, $C_{IBU,0}=5\cdot10^{-2}$ mol/m^3, $Q_{air}=0.94\cdot10^{-6}$ m^3/s, v = 750 rpm.

226 *3.3 Reaction mechanism*

227 In final stage of the kinetic modelling a Langmuir-Hinshelwood mechanism was proposed to
228 describe the experimental data and the subsequent parameter estimations were based on this model.
229 According to the model, both the reactants, IBU and oxygen, are adsorbed on the active sites of

the catalyst surface. The surface reaction between adsorbed oxygen and IBU is assumed to be the rate determining whereas the adsorption and desorption steps are rapid. Consequently, the reaction mechanism and the rate expression were described as follows,

$$\theta + \mathrm{IBU} \leftrightarrow \theta_{\mathrm{IBU}} \quad (a)$$

$$\mathrm{K_{IBU}} = \frac{\theta_{\mathrm{IBU}}}{\theta\,[\mathrm{IBU}]} \quad (b)$$

$$\theta + \mathrm{O_2} \leftrightarrow \theta_{\mathrm{O_2}} \quad (c)$$

$$\mathrm{K_{O_2}} = \frac{\theta_{\mathrm{O_2}}}{\theta\,[\mathrm{O_2}]} \quad (d)$$

$$\theta + \theta_{\mathrm{IBU}} + \theta_{\mathrm{O_2}} = 1 \quad (e)$$

$$\theta + \mathrm{K_{IBU}}\theta\,[\mathrm{IBU}] + \mathrm{K_{O_2}}\theta\,[\mathrm{O_2}] = 1 \quad (f)$$

$$\theta = \frac{1}{1 + \mathrm{K_{IBU}}[\mathrm{IBU}] + \mathrm{K_{O_2}}[\mathrm{O_2}]} \quad (g)$$

$$\mathrm{r} = \mathrm{k_c}\theta_{\mathrm{IBU}}\theta_{\mathrm{O_2}} = \mathrm{k_c}\,\mathrm{K_{IBU}}\theta\,[\mathrm{IBU}]\mathrm{K_{O_2}}\theta\,[\mathrm{O_2}] \quad (h)$$

$$\mathrm{r} = \frac{\mathrm{k_c}\,\mathrm{K_{IBU}}\mathrm{K_{O_2}}\,[\mathrm{IBU}][\mathrm{O_2}]}{(1 + \mathrm{K_{IBU}}[\mathrm{IBU}] + \mathrm{K_{O_2}}[\mathrm{O_2}])^2} \quad (i)$$

where θ is the fraction of the sites, k_c is the kinetic constant and K_{IBU} and K_{O2} are the adsorption constants of IBU and oxygen, respectively.

This model was applied for both TiO_2 and ZnO NPs. Parameter estimations for the kinetic constants and the adsorption constants were considered, using the modified Arrhenius equation and the Van't Hoff equation to describe the temperature dependences of the rate and equilibrium constants (eqs S.3 and S.4). The calculated values of the kinetic and adsorption constants are reported in Tables S6 and S7. The adsorption constant for O_2 in case of ZnO was very small around zero (Table S.7). This led to propose the Eley-Rideal mechanism for ZnO, where just one reactant, which is IBU, is adsorbed on the active sites of the catalyst surface, while the other one reacts from the bulk phase. Therefore, starting from the balance on the sites and through

mathematical manipulations, the following expression is obtained for the second order reaction rate of IBU on ZnO NPs.

$$\theta + 2\mathrm{IBU} \leftrightarrow \theta_{\mathrm{IBU}} \quad (j)$$

$$\mathrm{K'_{IBU}} = \frac{\theta_{\mathrm{IBU}}}{\theta\,[\mathrm{IBU}]^2} \quad (k)$$

$$\theta + \theta_{\mathrm{IBU}} = 1 \quad (l)$$

$$\theta + \mathrm{K'_{IBU}}\,\theta\,[\mathrm{IBU}]^2 = 1 \quad (m)$$

$$\theta = \frac{1}{1 + \mathrm{K'_{IBU}}\,[\mathrm{IBU}]^2} \quad (n)$$

$$\mathrm{r} = \mathrm{k'_c}\,\theta_{\mathrm{IBU}} = \mathrm{k'_c}\,\mathrm{K'_{IBU}}\,\theta\,[\mathrm{IBU}]^2 \quad (o)$$

$$\mathrm{k''_c} = \mathrm{k'_c}\,\mathrm{K'_{IBU}} \quad (p)$$

$$\mathrm{r} = \frac{\mathrm{k''_c}\,[\mathrm{IBU}]^2}{1 + \mathrm{K'_{IBU}}\,[\mathrm{IBU}]^2} \quad (q)$$

where k'c is the apparent kinetic constant as it has the equilibrium thermodynamic constant K.

3.4 Effect of temperature

Figure 5 shows the temperature effect on the IBU concentration for TiO_2 (Figure 5A) and ZnO NPs (Figure 5B), as a function of time, maintaining the other parameters constant. Remarkably, the degradation continuously increases with time, indicating the stability of the two photocatalysts. Specifically, the photodegradation trends of TiO_2 (Figure 5A) show that increasing the reaction temperature, increases the photodegradation efficiency up to 303 K. Beyond this temperature, no significant photodegradation can be observed. This could be attributed to the rapid recombination rate of photogenerated electron-hole pairs, which perturbs the photodegradation reaction at higher temperatures [37]. Whereas the photodegradation efficiency of ZnO NPs (Figure 5B), was markedly affected by increasing the temperature.

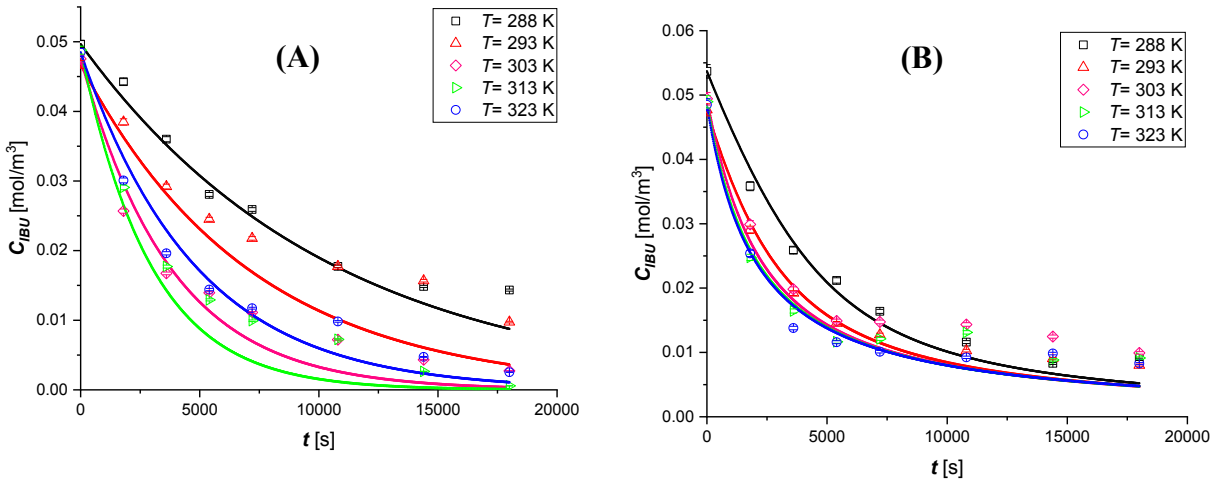

Figure 5. Experimental results of the kinetic tests conducted at different temperatures, fixing $C_{IBU,0} = 4 \cdot 10^{-2}$ mol/m^3, $\rho_B = 0.5$ kg/m^3, $Q_{air} = 0.94 \cdot 10^{-6}$ m^3/s and $v = 750$ rpm. Trends of the concentration profiles *vs* the reaction time for **A**) TiO_2 and **B**) ZnO.

3.5 Effect of catalyst bulk density

The effect of the catalyst bulk density was evaluated by changing the catalyst load while other system parameters were fixed. Figure 6 presents the trends detected using different catalyst loads of TiO_2 (Figure 6A) and ZnO (Figure 6B) NPs within the range of 0.05 and 0.5 kg/m^3. Generally, the concentration of IBU decreases upon increasing the catalyst load. The IBU concentration almost approached zero in case of TiO_2 NPs at ρB value of 0.5 kg/m^3. The possible explanation is that the increase in the number of active surface sites available for the photocatalytic reaction, enhances the generation of hydroxyl radicals due to the increase of the concentration of charge carriers [28]. This is in agreement with the findings of Jallouli and coworkers [38], where the IBU removal reached 100% showing no shielding effect at catalyst load up to 4 kg/m^3. On the other hand, increasing the catalyst load of ZnO NPs in the range of ρ_B 0.2 to 0.5 kg/m^3 did not give any significant effect on the performance, as the three kinetic curves are almost overlapped. Conversely, increasing the load beyond 0.37 kg/m^3, reduced the degradation efficiency of ZnO NPs. This can be explained by the screening effect that the catalyst exerts on the penetration of

294 UV light, thus retarding the chemical reaction [28, 38]. In other words, as the catalyst concentration
295 increases, the reaction rate increases and then the screening effect prevails. Moreover, possible
296 loss in the surface area of the NPs can be caused by the agglomeration at high loading, and thus
297 preventing the absorption of photons by the catalyst [28].

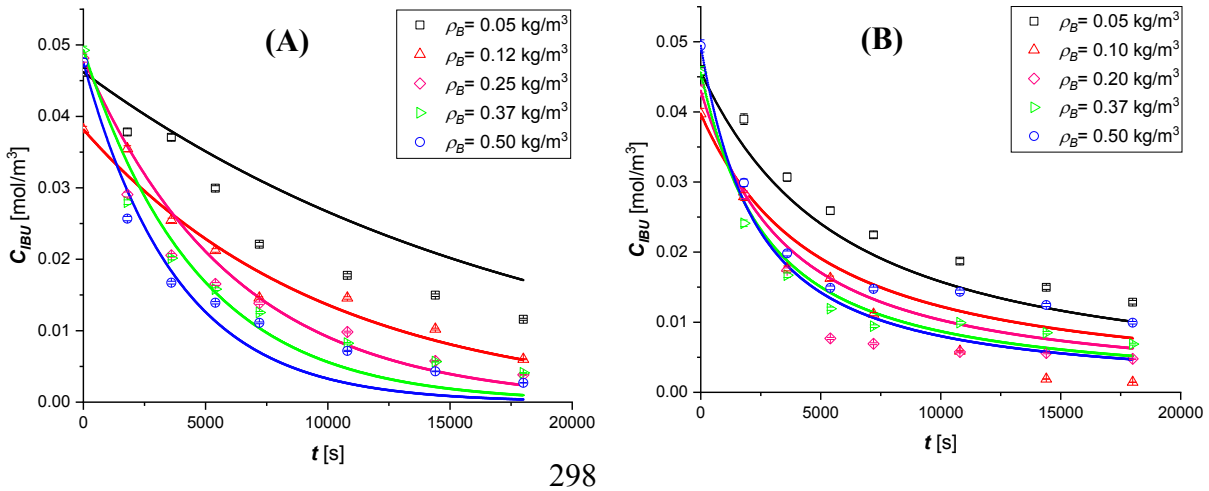

298

299 **Figure 6.** Experimental results of the kinetic tests conducted at different catalyst loading, fixing
300 $C_{IBU,0} = 4 \cdot 10^{-2}$ mol/m^3, $T = 303$K, $Q_{air} = 0.94 \cdot 10^{-6}$ m^3/s and $v = 750$ rpm. Trends of the concentration
301 profiles *vs* the reaction time for **A**) TiO_2 and **B**) ZnO.
302
303 *3.6 Effect of the initial concentration of IBU*

304 The initial concentration effect of IBU was studied to verify the reaction order as demonstrated in
305 Figure 7. As observed, the higher the concentration of IBU is in the solution, the lower
306 photodegradation efficiency. Similar findings have been reported by Choina and coworkers [19]
307 where the photodegradation of IBU on ZnO was higher at low concentrations (<5 ppm) in
308 comparison with concentrated solutions. Plausibly, fewer radicals were shared for each IBU
309 molecule and so the lower percentage of degradation is obtained, as attributed by Bennemla et al.
310 [28]. Nevertheless, the detected IBU concentrations in wastewater bodies are usually less that
311 1µg/L [38], which is sufficiently low. However, further studies are needed to evaluate the
312 efficiency of these systems with lower pollutant concentrations.

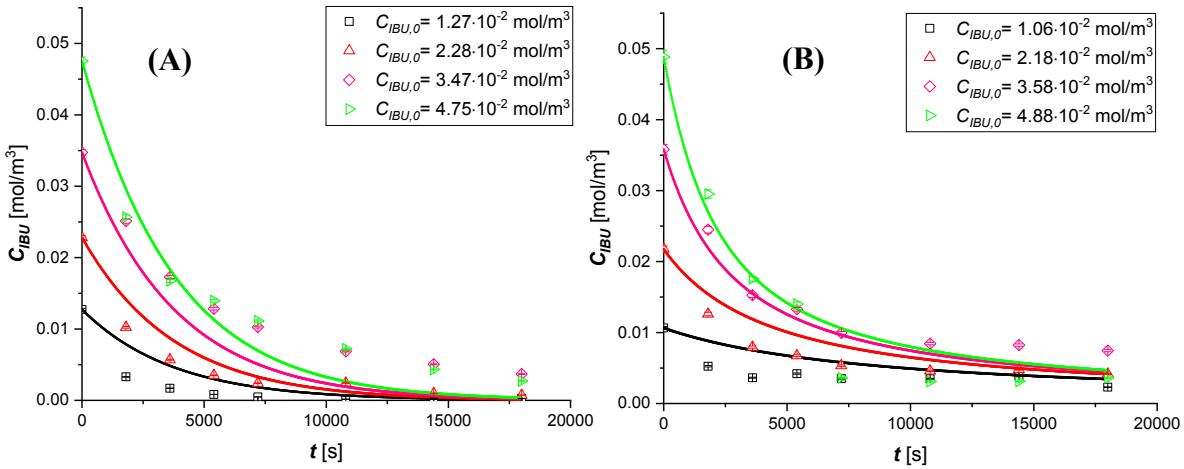

Figure 7. Experimental results of the kinetic tests conducted at different catalyst loading, fixing ρ_B = 0.5 kg/m^3, T = 303K, Q_{air} = 0.94·10^{-6} m^3/s and v = 750 rpm. Trends of the concentration profiles *vs* the reaction time for **A**) TiO_2 and **B**) ZnO.

3.7 Kinetic modeling and parameter estimation analysis

The following reactions were first hypothesized, in which the adsorption of IBU and oxygen on the free sites of the catalyst is considered, and the subsequent mechanism of radical activation leading to the formation of radicals and reaction products,

$$\mathrm{IBU} + \theta \leftrightarrow \theta_{\mathrm{IBU}} \qquad (r)$$

$$\mathrm{O_2} + \theta \leftrightarrow \theta_{\mathrm{O_2}} \qquad (s)$$

$$\theta_{\mathrm{O_2}} + \mathrm{e^-} \rightarrow 2\theta_{\mathrm{O\cdot}} \qquad (t)$$

$$\theta_{\mathrm{IBU}} + 2\theta_{\mathrm{O\cdot}} \rightarrow \mathrm{products} + 2\theta \qquad (u)$$

Considering all the reactions, the following mechanism is suggested [31] and the corresponding parameter estimation analysis was conducted simultaneously to retrieve kinetic information,

$$IBU + \frac{1}{2}O_2 \xrightarrow{r_1} 1-OH \qquad (v)$$

$$1-OH + \frac{1}{2}O_2 \xrightarrow{r_2} 1-OXO \qquad (w)$$

$$1-OXO + \frac{1}{2}O_2 \xrightarrow{r_3} other\ products \qquad (x)$$

The kinetic constant was calculated at a reference temperature T_{ref} = 303K, and activation energy for each reaction, adopting the modified Arrhenius equation 9,

$$k_j = k_{ref,j} \exp\left(\frac{-Ea_j}{R}\left(\frac{1}{T} - \frac{1}{T_{ref}}\right)\right) \quad (9)$$

The summary of the estimated parameters, along with statistical information are reported in Tables 3-6 for TiO_2 and ZnO NPs, respectively. The corresponding fittings were presented previously in Figures 5-7 confirming the goodness of the fit. The tree constants listed in Tables 3 and 4 show variation in order and magnitude confirming that the rate-determining step between adsorbed oxygen and IBU can be assumed among the involved reactions.

Table 3. Summary of the statistical information for TiO_2 NPs. T_{ref} = 303K, M the correlation matrix.

M	$k_{ref,1}$	$E_{a,1}$	$k_{ref,2}$	$E_{a,2}$	$k_{ref,3}$	$E_{a,3}$	$K_{ref,IBl}$	K_{ref,O_2}	ΔH_{IBU}	ΔH_{O_2}
$k_{ref,1}$	1.00									
$E_{a,1}$	0.41	1.00								
$k_{ref,2}$	0.48	0.14	1.00							
$E_{a,2}$	-0.04	-0.61	-0.36	1.00						
$k_{ref,3}$	0.99	0.41	0.48	-0.04	1.00					
$E_{a,3}$	0.41	0.99	0.14	-0.61	0.41	1.00				
$K_{ref,IBU}$	-0.97	-0.55	-0.50	0.01	-0.97	-0.55	1.00			
K_{ref,O_2}	0.45	-0.35	0.07	0.20	0.46	-0.35	-0.22	1.00		
ΔH_{IBU}	-0.70	-0.82	-0.18	0.51	-0.70	-0.82	0.70	-0.25	1.00	
ΔH_{O_2}	-0.44	0.36	-0.07	-0.20	-0.44	0.36	0.20	-0.99	0.23	1.00

Table 4. Summary of the statistical information for ZnO NPs. T_{ref} = 303K, *M* the correlation matrix.

M	$k''_{ref,1}$	$E'_{a,1}$	$k''_{ref,2}$	$E'_{a,2}$	$k''_{ref,3}$	$E'_{a,3}$	$K'_{ref,IBU}$
$k''_{ref,1}$	1.00						
$E'_{a,1}$	0.95	1.00					
$k''_{ref,2}$	0.43	0.43	1.00				

$\mathbf{E'_{a,2}}$	0.21	0.22	-0.38	1.00			
$\mathbf{k''_{ref,3}}$	0.99	0.94	0.43	0.21	1.00		
$\mathbf{E'_{a,3}}$	0.90	0.97	0.41	0.23	0.89	1.00	
$\mathbf{K'_{ref,IBU}}$	-0.99	-0.95	-0.44	-0.20	-0.99	-0.89	1.00
$\mathbf{\Delta H'_{IBU}}$	-0.91	-0.99	-0.42	-0.25	-0.90	-0.98	0.90

345

346 The calculated activation energies presented in Tables 5 and 6 fall within a range of kinetic regime

347 with calculated error less than 25%.

348

349 **Table 5.** Summary of the estimated kinetic parameters for TiO_2 NPs, T_{ref} = 303K.

Parameter	Value	Unit
$\boldsymbol{k_{ref,1}}$	$2.2 \cdot 10^{-3}$	[mol/ (kg·s)]
$\boldsymbol{E_{a,1}}$	$26.9 \cdot 10^{3}$	[J/mol]
$\boldsymbol{k_{ref,2}}$	2.0	[mol/ (kg·s)]
$\boldsymbol{E_{a,2}}$	$10.1 \cdot 10^{3}$	[J/mol]
$\boldsymbol{k_{ref,3}}$	$2.7 \cdot 10^{-3}$	[mol/ (kg·s)]
$\boldsymbol{E_{a,3}}$	$38.8 \cdot 10^{3}$	[J/mol]
$\boldsymbol{K_{ref,IBU}}$	3.3	[m^3/mol]
$\boldsymbol{K_{ref,O_2}}$	12.6	[m^3/mol]
$\boldsymbol{\Delta H_{IBU}}$	$-95.4 \cdot 10^{3}$	[J/mol]
$\boldsymbol{\Delta H_{O_2}}$	$-112.1 \cdot 10^{3}$	[J/mol]

350

351

352 **Table 6.** Summary of the estimated kinetic parameters for ZnO NPs, T_{ref} = 303K.

Parameter	Value	Unit
$\boldsymbol{k''_{ref,1}}$	$9.1 \cdot 10^{-5}$	[m^6/ (kg·s·mol)]
$\boldsymbol{E'_{a,1}}$	$102.8 \cdot 10^{3}$	[J/mol]
$\boldsymbol{k''_{ref,2}}$	0.02	[m^6/ (kg·s·mol)]
$\boldsymbol{E'_{a,2}}$	$18.1 \cdot 10^{3}$	[J/mol]
$\boldsymbol{k''_{ref,3}}$	$3.0 \cdot 10^{-4}$	[m^6/ (kg·s·mol)]
$\boldsymbol{E'_{a,3}}$	$80.9 \cdot 10^{3}$	[J/mol]
$\boldsymbol{K'_{ref,IBU}}$	131.5	[m^6/mol^2]

$K'_{ref,O2}$	0	[m^6/mol^2]
$\Delta H'_{IBU}$	$-94.6 \cdot 10^3$	[J/mol]
ΔH_{O_2}	0	[J/mol]

353
354
355 *3.8 Thermodynamic analysis*

356 Studying the thermodynamic aspects is pivotal to understand the energetic consideration of a
357 reaction. The temperature variation effect on IBU photodegradation using TiO_2 and ZnO NPs was
358 investigated, and the results are collected in Tables 7 and 8. To estimate the thermodynamic
359 parameters, equations 10 – 12 were used:

360 $$\Delta H° = E_a + RT \quad (10)$$

361 $$\ln(k/T) = \ln(K_B/h) + (\Delta S°/R) - (\Delta H°/RT) \quad (11)$$

362 $$\Delta G° = \Delta H° - T\Delta S° \quad (12)$$

363 where, $\Delta G°$ is the activation Gibbs free energy, $\Delta H°$ the change in enthalpy, $\Delta S°$ is the change in
364 entropy, R is the ideal gas constant (8.314 J/mol.K), K_B is Boltzmann constant (1.38×10^{-23}
365 $m^2.kg/s^2.K$), h Planck constant (6.63×10^{-34} $m^2.kg/s$), k is the kinetics rate constant $(m^3/mol)s^{-1}$.
366 The estimated values of $\Delta G°$, $\Delta H°$ and $\Delta S°$ for TiO_2 NPs (Table 7) show that the reaction is non-
367 spontaneous, endothermic with a minor random behavior. Moreover, the increasing $\Delta G°$ values,
368 for TiO_2 NPs, as the temperature increases reduces the spontaneity of the reaction producing,
369 highly hydrated transition state complex, which needs enough energy to be produced [39-41]
370 which was validated in the previous sections, where the performance of TiO_2 NPs was lesser at
371 higher temperatures (Figure 5A), exhibiting low values of the reaction rate constants. The obtained
372 small and negative $\Delta S°$ value suggests that weak bonds are present in the activated complex
373 leading to a rapid degradation of IBU into simple products [40].

Table 7. Kinetic and thermodynamic parameters for the photodegradation of IBU using TiO_2 NPs at $E_{a1} = 26.9kJ/mol$.

T (K)	k $(m^3/mol)s^{-1}$	$ln(k/T)$	$\Delta H°/RT$	$\Delta H°$ $(kJ.mol^{-1})$	$\Delta S°$ $(kJ.mol^{-1}K^{-1})$	$\Delta G°$ $(kJ.mol^{-1})$
288	6.3×10^{-4}	-13.0	12.3	29.3	-0.21	90.9
293	7.6×10^{-4}	-12.9	12.1	29.4		92.0
303	1.1×10^{-3}	-12.5	11.7	29.5		94.2
313	1.5×10^{-3}	-12.2	11.4	29.5		96.4
323	2.1×10^{-3}	-11.9	11.0	29.6		98.6

For ZnO NPs, the rate constants and the corresponding values of the thermodynamic parameters, $\Delta G°, \Delta H°$, and $\Delta S°$ for ZnO NPs show that increasing the reaction temperature, notably increases the rate constants (Table 8). The appreciably high positive activation enthalpy proves that the endothermic reaction nature is possibly due to electrostatic attraction between the ZnO NPs and IBU, leading to a uniform adsorption of IBU molecules onto ZnO particles to accomplish an efficient photodegradation. This was previously confirmed in Eley-Rideal mechanism for ZnO, where just one reactant, which is IBU, is adsorbed on the active sites of the catalyst surface. Also, this was previously confirmed in Figure 5B and in the kinetic modeling section (Table 3), where the probability of collisions increases, yielding into enhancing the photodegradation efficiency of ZnO NPs [40].

Table 8. Kinetic and thermodynamic parameters for the photodegradation of IBU using ZnO NPs at $E_{a1} = 102.8kJ/mol$.

T (K)	k $(m^3/mol)s^{-1}$	$ln(k/T)$	$\Delta H°$ $/RT$	$\Delta H°$ $(kJ.mol^{-1})$	$\Delta S°$ $(kJ.mol^{-1}K^{-1})$	$\Delta G°$ $(kJ.mol^{-1})$
288	0.6	-6.2	43.9	105.2	0.11	74.5
293	1.2	-5.5	43.2	105.3		74.0
303	4.7	-4.2	41.8	105.3		73.0
313	10.7	-2.9	40.5	105.4		72.0
323	50.8	-1.7	39.2	105.5		71.0

4. Conclusions

This study was devoted to the photodegradation kinetics of IBU, using two semiconductor catalysts, TiO_2 and ZnO NPs. Extensive kinetic experiments were carried out in a batch reactor by varying the operating conditions such as temperature, catalyst load, and initial concentration of IBU. The air flow rate and stirring speed parameters were useful to exclude limitations to the gas-liquid and liquid-solid mass transfer, while further modelling efforts carried out neglecting the intraparticle diffusion effect. After evaluating the apparent reaction order and proposing a kinetic law for each material, a kinetic model was proposed, both to describe the trends of the experimental data and to estimate the model parameters such as frequency factors, activation energies, pre-exponentials of adsorption constants and enthalpies. Finally, to further characterize the system, thermodynamic analysis was carried out. In general, both TiO_2 and ZnO NP materials demonstrated a good photodegradation capacity of IBU, showing different behaviors under varying operation conditions. The reaction system was found to be suitable for the IBU photodegradation and it will be used in the future to investigate different reaction conditions considering studies on other emerging pollutants. This work opened the prospective future applications of these NPs in continuous processes that could be coupled with post biological unit to convert IBU to less harmful products.

Notation

Abs	Absorbance [-]
C_i	Concentration of component i [mol/m^3]
C_{IBU}	Concentration of ibuprofen [mol/m^3]
Ea_j	Activation energy for reaction j [kJ/mol]
F_{obj}	Objective function [-]

412	h	Planck's constant [m^2.kg/s]
413	K_B	Boltzmann's constant [m^2.kg/s^2.K]
414	K_{IBU}	Adsorption constant of ibuprofen
415	K'_{IBU}	Apparent adsorption constant of ibuprofen
416	K_{O2}	Adsorption constant of oxygen
417	k_c	Kinetic constant
418	$k'c$	Apparent kinetic constant
419	k''_c	Apparent kinetic constant
420	$k_{ref,j}$	Kinetic constant calculated at a reference temperature [(m^3/mol)(m^3/kg^n)s^{-1}]
421	n	Exponent for catalyst bulk density [-]
422	N_{data}	Number of available experimental data [-]
423	Q_{air}	Volumetric flow rate of air [m^3/s]
424	r_j	Reaction rate of step j [mol/(kg.s)]
425	r_{obs}	Observed reaction rate [mol/(m^3.s)]
426	R	Ideal gas constant [kJ/(K.mol)]
427	R^2	Coefficient of determination
428	t	Time [s]
429	T	Temperature [K]
430	T_{ref}	Reference temperature, 303K [K]
431		
432	***Greek symbols***	
433	$\mathbf{\Delta H'_{IBU}}$	Enthalpy change [J/mol]
434	$\Delta H°$	Enthalpy change [J/mol]

435	$\Delta G°$	Gibbs free energy change [J/mol]
436	$\Delta H°$	Enthalpy change [J/mol]
437	$\Delta S°$	Entropy change [J/(mol K)]
438	v	Stirring rate [rpm]
439	ρ_B	Catalyst bulk density [kg/m^3]
440	ρ_{H_2O}	Water density [kg/m^3]
441	υ_{ij}	Stoichiometric coefficient of component *i* in reaction *j* [-]
442	θ	Fraction of site [-]

443

444 ***Abbreviations***

445	1-OH	1-OH ibuprofen
446	1-OXO	1-OXO ibuprofen
447	NPs	Nanoparticles
448	CALC	Calculated
449	EXP	Experimental
450	IBU	Ibuprofen
451	M	Correlation matrix

452 **Acknowledgments**

453 The fellowship provided by Faculty for the future Program-Schlumberger Foundation to Maryam

454 Hmoudah is deeply acknowledged and appreciated.

455 **Conflict of Interest**

456 The authors declare that the research was conducted in the absence of any commercial or financial

457 relationships that could be construed as a potential conflict of interest.

458

Author Contributions

Maryam Hmoudah and Carmela Chianese performed the investigation, validation, writing – original draft, data curation, and formal analysis. Vincenzo Russo was responsible for conceptualization, methodology, writing – review and editing, and supervision. Amjad El-Qanni and Vincenzo Russo performed thermodynamics analysis. Martino Di Serio and Tapio Salmi contributed to writing – review and editing, funding and supervision.

References

[1] A. Boretti, L. Rosa, Reassessing the projections of the World Water Development Report, npj Clean Water 2(1) (2019) 15. https://doi.org/10.1038/s41545-019-0039-9.

[2] L.B. Barber, 1.13 - Emerging Contaminants, in: S. Ahuja (Ed.), Comprehensive Water Quality and Purification, Elsevier, Waltham, 2014, pp. 245-266. https://doi.org/https://doi.org/10.1016/B978-0-12-382182-9.00015-3.

[3] V. Geissen, H. Mol, E. Klumpp, G. Umlauf, M. Nadal, M. van der Ploeg, S.E.A.T.M. van de Zee, C.J. Ritsema, Emerging pollutants in the environment: A challenge for water resource management, International Soil and Water Conservation Research 3(1) (2015) 57-65. https://doi.org/https://doi.org/10.1016/j.iswcr.2015.03.002.

[4] S. Chopra, D. Kumar, Ibuprofen as an emerging organic contaminant in environment, distribution and remediation, Heliyon 6(6) (2020) e04087. https://doi.org/https://doi.org/10.1016/j.heliyon.2020.e04087.

[5] P. Iovino, S. Chianese, S. Canzano, M. Prisciandaro, D. Musmarra, Ibuprofen photodegradation in aqueous solutions, Environmental Science and Pollution Research 23(22) (2016) 22993-23004. https://doi.org/10.1007/s11356-016-7339-0.

[6] E. Brillas, A critical review on ibuprofen removal from synthetic waters, natural waters, and real wastewaters by advanced oxidation processes, Chemosphere 286 (2022) 131849. https://doi.org/https://doi.org/10.1016/j.chemosphere.2021.131849.

[7] J. Żur, A. Piński, A. Marchlewicz, K. Hupert-Kocurek, D. Wojcieszyńska, U. Guzik, Organic micropollutants paracetamol and ibuprofen—toxicity, biodegradation, and genetic background of their utilization by bacteria, Environmental Science and Pollution Research 25(22) (2018) 21498-21524. https://doi.org/10.1007/s11356-018-2517-x.

[8] H.-R. Buser, T. Poiger, M.D. Müller, Occurrence and Environmental Behavior of the Chiral Pharmaceutical Drug Ibuprofen in Surface Waters and in Wastewater, Environmental Science & Technology 33(15) (1999) 2529-2535. https://doi.org/10.1021/es981014w.

[9] M. Mezzelani, S. Gorbi, F. Regoli, Pharmaceuticals in the aquatic environments: Evidence of emerged threat and future challenges for marine organisms, Marine Environmental Research 140 (2018) 41-60. https://doi.org/https://doi.org/10.1016/j.marenvres.2018.05.001.

[10] A. Nqombolo, A. Mpupa, R.M. Moutloali, P.N. Nomngongo, Wastewater treatment using membrane technology, Wastewater and water quality 29 (2018).

[11] R. Raj, A. Tripathi, S. Das, M.M. Ghangrekar, Removal of caffeine from wastewater using electrochemical advanced oxidation process: A mini review, Case Studies in Chemical and Environmental Engineering 4 (2021) 100129. https://doi.org/https://doi.org/10.1016/j.cscee.2021.100129.

[12] I. Ortiz, M.J. Rivero, M. Margallo, Chapter 6 - Advanced oxidative and catalytic processes, in: C.M. Galanakis, E. Agrafioti (Eds.), Sustainable Water and Wastewater Processing, Elsevier2019, pp. 161-201. https://doi.org/https://doi.org/10.1016/B978-0-12-816170-8.00006-5.

[13] O.C. Olatunde, A.T. Kuvarega, D.C. Onwudiwe, Photo enhanced degradation of contaminants of emerging concern in waste water, Emerging Contaminants 6 (2020) 283-302. https://doi.org/https://doi.org/10.1016/j.emcon.2020.07.006.

[14] A. Gnanaprakasam, V.M. Sivakumar, P.L. Sivayogavalli, M. Thirumarimurugan, Characterization of TiO2 and ZnO nanoparticles and their applications in photocatalytic degradation of azodyes, Ecotoxicology and Environmental Safety 121 (2015) 121-125. https://doi.org/https://doi.org/10.1016/j.ecoenv.2015.04.043.

[15] P.-J. Lu, S.-C. Huang, Y.-P. Chen, L.-C. Chiueh, D.Y.-C. Shih, Analysis of titanium dioxide and zinc oxide nanoparticles in cosmetics, Journal of Food and Drug Analysis 23(3) (2015) 587-594. https://doi.org/https://doi.org/10.1016/j.jfda.2015.02.009.

[16] A. Raja, P. Rajasekaran, K. Selvakumar, M. Arunpandian, S. Asath Bahadur, M. Swaminathan, Wool roving textured reduced graphene oxide-HoVO4-ZnO nanocomposite for photocatalytic and supercapacitor performance, Electrochimica Acta 328 (2019) 135062. https://doi.org/https://doi.org/10.1016/j.electacta.2019.135062.

[17] L. Zhao, J. Deng, P. Sun, J. Liu, Y. Ji, N. Nakada, Z. Qiao, H. Tanaka, Y. Yang, Nanomaterials for treating emerging contaminants in water by adsorption and photocatalysis: Systematic review and bibliometric analysis, Science of The Total Environment 627 (2018) 1253-1263. https://doi.org/https://doi.org/10.1016/j.scitotenv.2018.02.006.

[18] C. Sidney Santana, M.D. Nicodemos Ramos, C.C. Vieira Velloso, A. Aguiar, Kinetic Evaluation of Dye Decolorization by Fenton Processes in the Presence of 3-Hydroxyanthranilic Acid, International Journal of Environmental Research and Public Health 16(9) (2019). https://doi.org/10.3390/ijerph16091602.

[19] J. Choina, A. Bagabas, C. Fischer, G.U. Flechsig, H. Kosslick, A. Alshammari, A. Schulz, The influence of the textural properties of ZnO nanoparticles on adsorption and photocatalytic remediation of water from pharmaceuticals, Catalysis Today 241 (2015) 47-54. https://doi.org/https://doi.org/10.1016/j.cattod.2014.05.014.

[20] E. Bilgin Simsek, B. Kilic, M. Asgin, A. Akan, Graphene oxide based heterojunction TiO2–ZnO catalysts with outstanding photocatalytic performance for bisphenol-A, ibuprofen and flurbiprofen, Journal of Industrial and Engineering Chemistry 59 (2018) 115-126. https://doi.org/https://doi.org/10.1016/j.jiec.2017.10.014.

[21] M. Tanveer, G.T. Guyer, G. Abbas, Photocatalytic degradation of ibuprofen in water using TiO2 and ZnO under artificial UV and solar irradiation, Water Environment Research 91(9) (2019) 822-829. https://doi.org/https://doi.org/10.1002/wer.1104.

[22] F. Méndez-Arriaga, M.I. Maldonado, J. Gimenez, S. Esplugas, S. Malato, Abatement of ibuprofen by solar photocatalysis process: Enhancement and scale up, Catalysis Today 144(1) (2009) 112-116. https://doi.org/https://doi.org/10.1016/j.cattod.2009.01.028.

[23] J. Madhavan, F. Grieser, M. Ashokkumar, Combined advanced oxidation processes for the synergistic degradation of ibuprofen in aqueous environments, Journal of Hazardous Materials 178(1) (2010) 202-208. https://doi.org/https://doi.org/10.1016/j.jhazmat.2010.01.064.

[24] M.R.A.S. Farley S. Braz, Flávio S. Silva, Sandro J. Andrade, Ana L. Fonseca, Márcia M. Kondo, Photocatalytic Degradation of Ibuprofen Using TiO2 and Ecotoxicological Assessment of Degradation Intermediates against *Daphnia similis*, Journal of Environmental Protection Vol.05No.07 (2014) 7. https://doi.org/10.4236/jep.2014.57063.

[25] T.M. Khedr, S.M. El-Sheikh, A.A. Ismail, D.W. Bahnemann, Highly efficient solar light-assisted TiO2 nanocrystalline for photodegradation of ibuprofen drug, Optical Materials 88 (2019) 117-127. https://doi.org/https://doi.org/10.1016/j.optmat.2018.11.027.

[26] K. Patterson, K. Howlett, K. Patterson, B. Wang, L. Jiang, Photodegradation of ibuprofen and four other pharmaceutical pollutants on natural pigments sensitized TiO2 nanoparticles, Water Environment Research 92(8) (2020) 1152-1161. https://doi.org/https://doi.org/10.1002/wer.1310.

[27] M.O. Miranda, W.E. Cabral Cavalcanti, F.F. Barbosa, J. Antonio de Sousa, F. Ivan da Silva, S.B.C. Pergher, T.P. Braga, Photocatalytic degradation of ibuprofen using titanium oxide: insights into the mechanism and preferential attack of radicals, RSC Advances 11(44) (2021) 27720-27733. https://doi.org/10.1039/D1RA04340D.

[28] M. Bennemla, S. Bouafia-Chergui, A. Amrane, M. Chabani, The photocatalytic degradation kinetics of the anti-inflammatory drug ibuprofen in aqueous solution under UV/TiO2 system and neural networks modeling, International Journal of Chemical Reactor Engineering (2022). https://doi.org/doi:10.1515/ijcre-2021-0170.

[29] N. Gallucci, M. Hmoudah, E. Martinez, A. El-Qanni, M. Di Serio, L. Paduano, G. Vitiello, V. Russo, Photodegradation of ibuprofen using CeO2 nanostructured materials: Reaction kinetics, modeling, and thermodynamics, Journal of Environmental Chemical Engineering 10(3) (2022) 107866. https://doi.org/https://doi.org/10.1016/j.jece.2022.107866.

[30] G. Jayakumar, A. Albert Irudayaraj, A. Dhayal Raj, Particle Size Effect on the Properties of Cerium Oxide (CeO2) Nanoparticles Synthesized by Hydrothermal Method, Mechanics, Materials Science & Engineering Journal 9(1) (2017). https://doi.org/10.2412/mmse.3.4.481.

568 [31] K. Miyabe, R. Isogai, Estimation of molecular diffusivity in liquid phase systems by the
569 Wilke–Chang equation, Journal of Chromatography A 1218(38) (2011) 6639-6645.
570 https://doi.org/https://doi.org/10.1016/j.chroma.2011.07.018.
571 [32] F. Méndez-Arriaga, S. Esplugas, J. Giménez, Photocatalytic degradation of non-steroidal anti-
572 inflammatory drugs with TiO2 and simulated solar irradiation, Water Research 42(3) (2008) 585-
573 594. https://doi.org/https://doi.org/10.1016/j.watres.2007.08.002.
574 [33] A. Schiavenin, P. Roberto dos Santos, R. Frassini, F.R. Paula, C.T. Pich, M. Roech-Ely, S.
575 Moura, Zinc organocomplexes containing non-steroid anti-inflammatories and plane aromatic
576 diimines: New potential drugs, Polyhedron 209 (2021) 115449.
577 https://doi.org/https://doi.org/10.1016/j.poly.2021.115449.
578 [34] A. Kaur, A. Umar, S.K. Kansal, Heterogeneous photocatalytic studies of analgesic and non-
579 steroidal anti-inflammatory drugs, Applied Catalysis A: General 510 (2016) 134-155.
580 https://doi.org/https://doi.org/10.1016/j.apcata.2015.11.008.
581 [35] M. Geng, Z. Duan, Prediction of oxygen solubility in pure water and brines up to high
582 temperatures and pressures, Geochimica et Cosmochimica Acta 74(19) (2010) 5631-5640.
583 https://doi.org/https://doi.org/10.1016/j.gca.2010.06.034.
584 [36] D. Girija, H.S.B. Naik, C. Sudhamani, B.V. Kumar, Cerium Oxide Nanoparticles—A Green,
585 Reusable, and Highly Efficient Heterogeneous Catalyst for the Synthesis of Polyhydroquinolines
586 under Solvent-Free Conditions, Archives of Applied Science Research 3(3) (2011) 373-382.
587 [37] C.B. Ong, L.Y. Ng, A.W. Mohammad, A review of ZnO nanoparticles as solar photocatalysts:
588 Synthesis, mechanisms and applications, Renewable and Sustainable Energy Reviews 81 (2018)
589 536-551. https://doi.org/https://doi.org/10.1016/j.rser.2017.08.020.

590 [38] N. Jallouli, L.M. Pastrana-Martínez, A.R. Ribeiro, N.F.F. Moreira, J.L. Faria, O. Hentati,
591 A.M.T. Silva, M. Ksibi, Heterogeneous photocatalytic degradation of ibuprofen in ultrapure water,
592 municipal and pharmaceutical industry wastewaters using a TiO2/UV-LED system, Chemical
593 Engineering Journal 334 (2018) 976-984.
594 https://doi.org/https://doi.org/10.1016/j.cej.2017.10.045.
595 [39] M. Rezaei, A. Nezamzadeh-Ejhieha, The ZnO-NiO nano-composite: A brief characterization,
596 kinetic and thermodynamic study and study the Arrhenius model on the sulfasalazine
597 photodegradation, International Journal of Hydrogen Energy 45(46) (2020) 24749-24764.
598 https://doi.org/https://doi.org/10.1016/j.ijhydene.2020.06.258.
599 [40] K. Byrappa, A.K. Subramani, S. Ananda, K.M.L. Rai, R. Dinesh, M. Yoshimura,
600 Photocatalytic degradation of rhodamine B dye using hydrothermally synthesized ZnO, Bulletin
601 of Materials Science 29(5) (2006) 433-438. https://doi.org/10.1007/BF02914073.
602 [41] A.S.M. Kuba, A.M.J.A.L. Shamari, Kinetics and thermodynamics study for photodegradation
603 of Brown HT dye by MnO and NiO as catalysis, Materials Today: Proceedings 49 (2022) 2741-
604 2746. https://doi.org/https://doi.org/10.1016/j.matpr.2021.09.256.
605

Publication VII

Adsorption of methylene blue on metakaolin-based geopolymers: a kinetic and thermodynamic investigation

Maryam Hmoudah[1,2], Rosanna Paparo[1], Michela De Luca[1], Michele Emanuele Fortunato[1], Riccardo Tesser[1], Martino Di Serio[1], Claudio Ferone[3], Giuseppina Roviello[3], Oreste Tarallo[1,*], Vincenzo Russo[1,*]

[1] Università degli Studi di Napoli Federico II, Department of Chemical Sciences, Via Cintia, IT-80126 Naples, Italy

[2] An-Najah National University, Department of Chemical Engineering, P-400 Nablus, Palestine.

[3] Università degli Studi di Napoli Parthenope, Department of Engineering, Centro Direzionale Isola C4, 80143 Naples, Italy

**corresponding authors:* Vincenzo Russo (v.russo@unina.it) and Oreste Tarallo (oreste.tarallo@unina.it).

Abstract – Metakaolin-based geopolymers with different molar ratios of Si/Al were synthesized and utilized as an efficient adsorbent for the removal of methylene blue (MB) as a model cationic dye from aqueous solution. Multiple analytical tools were applied in the characterization of the synthesized geopolymers. The influence of the main operation conditions on the adsorption kinetics of MB onto the geopolymer was examined under various operating conditions. Results showed a significant maximum MB adsorption capacity at the temperature of 30 °C for all four types of geopolymers studied (designed as A, B, C, and D) up to 35.3, 23.6, 25.5, 19.0 mg g^{-1}, respectively. The corresponding order of Si/Al ratio was A<C<B<D. Adsorption kinetics was so fast and reached equilibrium in 10 min and the experimental results were described using the adsorption dynamic intraparticle model (ADIM). The equilibrium data for MB removal was in agreement with Langmuir isotherm.

Keywords: Geopolymers; metakaolin; adsorption; methylene blue; wastewater treatment.

1. Introduction

The global population continues to grow, and so does the demand for industrial products, leading to the expansion of many industrial sectors [1,2]. This rapid increase in production also leads to generate considerable amounts of wastewater that may harbor noxious chemicals and dyes [3,4]. Therefore, wastewater treatment is important because it helps to remove harmful contaminants and pollutants from wastewater before it is discharged back into the environment [5,6] since inadequately treated wastewater has the potential to elicit deleterious effects on both the environment and human health [7].

In this context, wastewater treatment plays a crucial role in reducing the industry's environmental footprint and ensuring sustainable production practices. Textile industries are a case in point, where large amounts of water are used in the production process [8]. The chaotic discharge of textile wastewater causes severe pollution since they are rich in toxic metals (like chromium, antimony, and cobalt) and dangerous organic substances such as dyes [8,9]. Concerning the latter, it has been estimated that more than 700 thousand tons per year are produced annually [10] and the 2% of them are discharged directly in aqueous effluents generating massive volumes of colored wastewater [11]. Dyes are classified according to the chemical constitution, application class, and end use [12] and many of them are toxic and even cancerogenic [13]. Furthermore, they can reduce the transmission of light altering the biological metabolism of the hydrosphere and they may cause micro toxicity to marine life due to their tendency to sequester metals [14–17]. Thus, treatment of wastewater containing dyes is challenging and it is still in the spotlight of the scientific community since these compounds are recalcitrant organic molecules that show high resistance to aerobic digestion and high stability to light, heat, and oxidizing agents [11,18–20]. Several methods of dye wastewater treatment have been tested and reviewed in the last 30 years including photocatalytic degradation [4,21], sonochemical degradation, electrochemical degradation, integrated chemical-biological degradation, precipitation processes, coagulation, flocculation, and use of cation exchange membrane [10,22–24].

To date, by considering the advantages and disadvantages of these removal techniques, adsorption represents an interesting and promising technology that can be applied on an industrial scale due to its affordability, simplicity of design, ease of operation and insensitivity to toxic substances [25] and it does not result in the formation of harmful substances [26].

Methylene blue (MB) is used extensively in industries such as cotton, wood, and silk dyeing. Although it is not typically considered acutely toxic, the widespread release of MB can lead to the development of diseases and other adverse health effects in exposed populations[27,28]. At the state of the art, several papers deal with the adsorption of MB with different types of adsorbents. Commercial activated carbon represents the most popular choice for the removal of MB [29]. However, the focus of the scientific community has moved to find cheaper alternatives. Therefore, unconventional adsorbents were tested like fly ash, pine leaves, mango seeds, and clays [30] showing in some cases good removal capacities. Table 1 lists the recent studies of MB removal over the last two years, using different unconventional adsorbents, and various parameters were studied to explore economic, environmentally benign, and efficient adsorbents.

In this work, four different geopolymers obtained from two different types of metakaolin are tested for the removal of MB. Geopolymers are synthetic aluminum silicate materials, typically amorphous, [31] presenting a structure similar to tectosilicates, and so consisting of a three-dimensional network of SiO_4^{4-} tetrahedral units covalently linked together [32]. Often the silicon atoms, the center of the tetrahedral units, are replaced by aluminum atoms as in clays [31,33]. They are obtained via a polycondensation reaction, the so-called geopolymerization, through mixing an aluminum-silicate source such as metakaolin, fly ash, blast furnace slag, or synthetic raw materials (alumina and silica) with a strongly alkaline activating solution [31,34]. During geopolymerization, a gel is formed which acts as a glue for the unreacted particles and any fillers can be added as reinforcement. The process takes place at low temperatures, between 25 and 60 °C, with minimal shrinkage and rapid consolidation, from 5 to 10 hours, similar to quick-setting cement [35,36]. The most significant advantage of using geopolymers lies mainly in their environmental and economic sustainability [33].

Other advantages are the short preparation time, the controllable process, the low cost due to the low synthesis temperature and the absence of mechanical processing to obtain a finished product, and the possibility of producing the material *in situ* [37].

Metakaolin is often used to obtain geopolymers [33,37]. One of the key advantages of metakaolin is its high pozzolanic reactivity, which allows it to react quickly with alkali activators and form a strong, hardened material [38]. Metakaolin also has a high silica content, which contributes to the strength and durability of the final product [33,39]. Furthermore, the use of metakaolin in geopolymer synthesis can reduce the amount of waste materials generated from industrial processes, as it can be derived from the waste products of kaolin mining [40].

This work focuses on having an in-depth kinetic and thermodynamic understanding of the adsorption of metakaolin-based geopolymers for the removal of MB and compare it to the performance of a commercial activated carbon. The collected data obtained from the kinetics study were analyzed using the dynamic intraparticle model (ADIM) for fluid–solid adsorption developed and investigated by our research group. The retrieved physico-chemical parameters will be useful in the future design of a continuously operating adsorption column that can remove organic contaminants from wastewater.

Table 1. Some previously published works on the adsorption of MB using various types of adsorbents.

Adsorbent	Process parameters	Maximum adsorption capacity [mg g^{-1}]	Kinetic model/s	Thermodynamic model/s*	Highlights	Ref
Carboxylate-functionalized Hydrochar (CFHC)	• c_0 =50 mg L^{-1} • $C_{adsorbent}$ =800 mg L^{-1} • pH 2-10	at 30 ˚C: 155.57	• PFO • PSO • WFID	• Langmuir isotherm • Freundlich isotherm	• The adsorption equilibrium time for MB was 150 min. • The adsorption mechanism of MB followed π-π interaction, electric attraction, and hydrogen bonding between MB and CFHC. • The optimal adsorption pH was > 4.	[26]
MFI zeolite (NZ) and ZSM-5 zeolite (CZ)	• c_0 =50 mg L^{-1} • $C_{adsorbent}$ =0.5 mg L^{-1} • pH 2-10	at 25 ˚C: • NZ 476.19 • CZ 105.82	• PFO • PSO • WFID	• Langmuir isotherm • Freundlich isotherm • Temkin isotherm	• The kinetics of adsorption was so fast and reached equilibrium in 10 min. • The adsorption mechanism is based on electrostatic adsorption and hydrogen bonding between zeolite and MB. • The optimal pH value for the adsorption of MB was 11.	[41]
Natural clay	• c_0 =20 mg L^{-1} • $C_{adsorbent}$ =0.3 mg L^{-1} • pH 1-11	at 25 ˚C: 113.63	• PFO • PSO	• Langmuir isotherm • Freundlich isotherm • Temkin isotherm • BET isotherm	• The adsorption equilibrium time for MB was 120 min. • It was observed that as the adsorbent dose, stirring speed and temperature were increased, MB removal increased while increasing the initial concentration of MB and the clay particle size, the removal decreased. • The optimal pH value for the adsorption of MB was 5.	[42]
Cellulose, clay and sodium alginate composites	• c_0 =10 mg L^{-1} • $C_{adsorbent}$ =0.05 mg L^{-1} • pH 7-11	at 30 ˚C: 113.63	• PFO • PSO	• Langmuir isotherm • Freundlich isotherm	• The adsorption equilibrium time for MB was 60 min. • Physical interaction forces are involved in the adsorption mechanism. • The quantum chemical calculations provided insights about the interaction mechanism to	[43]

					understand the electrophilicity, nucleophilicity and the expected reactive sites of the composite. • The optimal pH value for the adsorption of MB was 11.	
Natural clay Na-bentonite	• c_0 =100 mg L^{-1} • $C_{adsorbent}$ =0.8 mg L^{-1} • pH 3-12	at 30 ˚C: 24.99	• PFO • PSO	• Langmuir isotherm • Freundlich isotherm	• The adsorption equilibrium time for MB was 60 min. • At pH >7, the active sites turn to more negatively charged onto the surface of Na-bentonite, improving the adsorption by electrostatic attraction forces. • The optimal pH value for the adsorption of MB was 7-10.	[44]
Moroccan clays	• c_0 =100-900 mg L^{-1} • $C_{adsorbent}$ =500 mg L^{-1} • pH 3-12	at 60 ˚C: 456.62	• PFO • PSO	• Langmuir isotherm • Freundlich isotherm	• The adsorption equilibrium time for MB was 60 min. • The rate-limiting step can be chemical adsorption involving valence forces through the sharing or exchange of electrons between the adsorbent and the adsorbate. • The optimal pH value for the adsorption of MB was 10.	[45]
Metakaolin-based geopolymers	• c_0 =50 mg L^{-1} • $C_{adsorbent}$ =0.5 mg L^{-1} • pH 2-10	Maximum adsorption capacity of geopolymers at 30 ˚C: Type A: 35.3 [mg g^{-1}] Type B: 23.6 [mg g^{-1}] Type C: 25.5 [mg g^{-1}] Type D: 19.0 [mg g^{-1}]	• ADIM	• Langmuir isotherm • Freundlich isotherm	• The kinetics of adsorption was so fast and reached equilibrium in 5 min. • The adsorption capacity of the type A geopolymer towards MB was significantly higher than that of activated carbon for the same surface area, owing to the electrostatic interactions between the cationic dye and the geopolymer. • The optimal pH value for the adsorption of MB was 8.7.	This study

*Pseudo first-order (PFO), Pseudo second-order (PSO), Weber-Morris intraparticle diffusion (IPD), Adsorption dynamic intraparticle model (ADIM)

2. Materials and methods

2.1 Materials

Methylene blue (*MW*= 319.76 g/mol) powder with purity > 98%, was supplied by ICN Biomedicals (Inc Ohio, USA). Commercial granular activated carbon DARCO 20-40 mesh (specific surface area of 650 m^2/g, average pore diameter of 3.7 nm, total pore volume of 0.748 cm^3/g) was supplied by Sigma Aldrich (Milan, Italy). Bi-distilled Milli-Q water, also filtered using 0.20 μm filters, was obtained through Merck Millipore (Darmstadt, Germany). Metakaolin MetaMax® (by BASF) was provided by Neuvendis s.p.a. (Milan, Italy), and metakaolin Mefisto® was supplied by Neuchem S.r.l. (Milan, Italy). The sodium silicate solution was supplied by Prochin Italia S.r.l (Caserta, Italy). The chemical composition of metakaolin and sodium silicate solution is shown in Table S1. Sodium hydroxide with reagent grade was supplied by Sigma-Aldrich (Milan, Italy). All materials were used as received without further purification.

2.2 Methods

2.2.1 Synthesis and characterization of geopolymers

The preparation of the four types of metakaolin-based geopolymers was carried out as dense specimens. The amounts of the different components are listed in Table S.2, while Table S.3 shows the molar ratios of Si/Al, Si/Na, and Al/Na. In a typical synthesis, an activating alkaline solution was prepared by dissolving solid sodium hydroxide in a sodium silicate solution. This highly exothermic reaction was carried out in a water and ice bath by gradual addition of sodium hydroxide to the sodium silicate solution, stirring until completely dissolved. The resulting solution was left to cool for 24 hours at room temperature. The composition of the solution obtained can be expressed as Na_2O: 1.34 SiO_2:10.48 H_2O. Metakaolin was added to the activating solution in variable quantities and mixed mechanically at 500 rpm. Mixtures were then poured into molds. The obtained samples were sealed at 95% relative humidity and stored at room temperature (23 ± 2°C) for 24 h. Then, they were placed

in an oven at 60°C for the next 24h. The samples were left sealed at room temperature for further five days and finally opened and left for 21 days at room temperature. The pictures of the produced geopolymers are shown in Figure S.1.

Different tools were employed to characterize the synthesized metakaolin-based geopolymers. Wide angle X-ray diffraction profiles were recorded with an Empyrean automatic powder diffractometer (PANalytical), using Cukα radiation (λ=1.5418Å) filtered with Nickel. The profiles were recorded by continuous scanning of the 2θ diffraction angle, in the range 5-60°, at a speed of 0.02°/s (Δ2θ = 0.1° and Δt = 5s). The phase recognition was carried out by using the ICDD-PDF-4+ 2021 (International Centre for Diffraction Data®) database. The morphological properties of the geopolymers were investigated using Scanning Electron Microscopy (SEM) technique by FEI Nova NanoSEM 450 at an accelerating voltage of 5 kV with Everhart Thornley Detector (ETD) on fresh fracture surfaces, after metallization with Au-Pd. Jasco Ultra-violet and visible (V-550 UV/VIS Spectrophotometer) was used to detect the residual MB amounts in the aqueous solutions after the adsorption. MB shows a major absorption band at 665 nm [46]. The calibration curve equation is reported in Figure S.2 which is valid in a concentration range between 0.0-0.5 mol m^{-3}. N_2 physisorption analysis was conducted using BET Autosorb 1 (Quantachrome) to determine the surface area and the pore volume of the geopolymers.

2.2.2 Pre-treatment of geopolymers

Before being used in the adsorption tests, the synthesized geopolymers were ball milled using Retsch GmbH Mills-Type PM 100 CM. The collected powder was sieved in the range 17-112 μm to have a uniform particle size. The samples were washed two times, under stirring at 600 rpm, with 500 mL of water for 30 minutes. This step was repeated four times under the same stirring rate until the pH value no longer showed appreciable variations and settled around the value of 8. The pH values were measured by using a Methrohm 914 pH meter. These washing cycles were necessary to remove salts and other impurities. The collected samples were dried in the oven at 60 °C overnight.

144 **2.2.3 Sorbents screening experiments**

145 To investigate the pH effect on adsorption capacity, each geopolymer (0.100 g) was suspended in 10
146 mL of water, and the pH of each solution was adjusted to 2, 5, 7, 9, and 12 using HCl or NaOH
147 solutions (0.1 M). After adjusting the pH, the solid was separated, and all samples were dried at 100
148 °C overnight. Then, batch adsorption screening tests were conducted by adding 5 mg of each
149 geopolymer (treated at different pH levels) to vials containing 10 mL of a a 15 mg L^{-1} MB solution.
150 The vials were placed in a thermostatic bath at 30°C for 24 hours and stirred magnetically at 500 rpm.
151 The pH of the dye solution in contact with the adsorbent was measured and vials were sealed. After
152 the test, the samples were centrifuged at 3000 rpm for 60 minutes to separate the solid and the
153 concentration of MB in the supernatant aqueous solution was detected by means of a UV/VIS Jasco
154 V-550 spectrophotometer. The uptake of MB q_{ads} (mg g^{-1}) was calculated as in Eq. 1.

155 $$q_{ads} = \left(\frac{c_0 - c_e}{w_{ads}} \right) V \quad (1)$$

156 where V is the solution volume (mL), c_0 is the initial MB concentration (mg L^{-1}), c_e is the equilibrium
157 MB concentration (mg L^{-1}) and w_{ads} is the weight of the dry geopolymer (g). Once the ideal pH
158 conditions were determined, the performance of the different geopolymers was tested and compared
159 under the same experimental conditions. The aim was to identify the best-performing geopolymer in
160 terms of MB adsorption uptake.

161

162 **2.2.4 Thermodynamic and kinetic experiments**

163 The adsorption isotherm experiments of MB onto the chosen geopolymer were performed at three
164 different temperatures i.e., 30, 40, and 50 °C respectively, at the ideal pH conditions determined by
165 previous investigation. A fixed quantity of the adsorbent (5 mg) was suspended in 10 mL MB
166 solutions with different initial concentrations (5–30 mg L^{-1}). The vials were placed in a water bath at
167 constant temperature and the solution was kept under stirring at 500 rpm for 3 hours. The adsorption
168 kinetics of MB onto the geopolymer was examined under various operating conditions which are:

169 temperature, solid bulk density (i.e., the sorbent mass per liquid phase volume), initial MB
170 concentration, and agitation speed as listed in Table S.4. In a typical kinetics investigation, 250 mL
171 of MB solution was prepared with a concentration of 30 mg L^{-1} and was then loaded in a 500 cm^3
172 glass jacketed three-necked reactor equipped with an impeller ensuring the desired rotational speed
173 and connected to a thermostat to ensure temperature control. 125 mg of the geopolymer was added
174 to the solution and stirred at 450 rpm. The reactor was closed with the lid and connected to the
175 thermostat, set at a pre-specified reaction temperature. Samples were withdrawn with a syringe at
176 different time intervals (0, 2, 4, 6, 8, 10, 30 and 60 min) then stored in sealed vials for subsequent
177 centrifugation at 3000 rpm for 60 minutes and UV-VIS analysis.
178
179 **2.2.5 Modelling activity**
180 The development of a mathematical model is necessary for the interpretation of the kinetic data,
181 collected in the batch experiments, considering all the possible phenomena occurring on a molecular
182 scale. Specifically, the ADIM was used to describe the adsorption kinetics of MB onto the type A
183 geopolymer. This mathematical model was proposed by Russo et al. [47] who tested it on a wide
184 number of pollutant/adsorbent systems of different chemical natures demonstrating its general
185 applicability [48]. In particular, the ADIM successfully described the adsorption kinetics of
186 methylene blue over silica in both batch and continuous devices [49]. According to the model, the
187 adsorption of the pollutant occurs in a four-steps mechanism: first, the dye molecules diffuse from
188 the bulk liquid phase, where its concentration is assumed to be constant in a fixed time *t*, to the liquid
189 film surrounding the solid; the adsorbate reaches the solid surface through the film diffusion and then
190 it diffuses along the particle radius in the pore; a local equilibrium is established between the liquid
191 and solid phases inside the particle, and finally, the solute can diffuse on the adsorbent surface. The
192 system was considered isothermal; the adsorbent particles were assumed to be spherical (shape factor
193 s=2), with the same size and characterized by an average porosity and tortuosity factor; the
194 intraparticle equilibrium is described, in this case, by the Langmuir adsorption isotherm. Based on

the above-mentioned mechanism and the proposed hypotheses, by dividing the system into two main domains (i.e., the liquid bulk and the intraparticle regions), the mass balance (Eqs. 2 and 3) for the batch system are:

$$\varepsilon' \frac{\partial C_B}{\partial t} = -k_m a_{sp}(C_B - C_L|_{R_p}) \tag{2}$$

$$\varepsilon \frac{\partial C_L}{\partial t} + (1-\varepsilon)\frac{\partial C_S}{\partial t} = \varepsilon \frac{D_P}{r_P^S}\frac{\partial}{\partial r_P}\left(r_P^S \frac{\partial C_L}{\partial r_P}\right) + (1-\varepsilon)\frac{1}{r_P^S}\frac{\partial}{\partial r_P}\left(r_P^S \frac{D_S}{1-C_S/C_S^*}\frac{\partial C_S}{\partial r_P}\right) \tag{3}$$

Eq. 2 describes the mass balance of the bulk phase where the accumulation term equals the fluid-solid mass transfer, while in Eq. 3, the overall accumulation term (for the liquid and the solid phase concentration inside the particle) equals the sum of the pore and surface diffusion limitations which are dependent on the values of the effective diffusivity D_P and the surface diffusivity D_S, respectively. The D_P value can be easily calculated from the molecular diffusivity of the solute in the bulk liquid phase D_0 (estimated from the Wilke-Chang correlation [50]) multiplied by the ratio between the porosity of the solid ε and the tortuosity factor τ (Eq. 4).

$$D_P = \frac{\varepsilon}{\tau} D_0 \tag{4}$$

D_S value range in the order of magnitude of 10^{-12} and 10^{-18} m^2/s and it depends on the interactions between the adsorbate and the adsorbent, so it is not directly calculable. Thus, it is estimated by fitting the experimental data.

The boundary conditions to solve the system of partial differential equations are: (i) the symmetry condition at the center of the particle (r_p=0) for both liquid and solid phases (Eqs. 5 and 6); (ii) the surface steady-state hypothesis at r_p=R_p expressed by Eq. 7.

$$\left.\frac{\partial C_L}{\partial r_P}\right|_{r_P=0} = 0 \tag{5}$$

$$\left.\frac{\partial C_S}{\partial r_P}\right|_{r_P=0} = 0 \tag{6}$$

$$\varepsilon D_P \left.\frac{\partial C_L}{\partial t}\right|_{r_P=R_P} + (1-\varepsilon)\frac{D_S}{1-C_S|_{r_p=R_p}/C_S^*}\left.\frac{\partial C_s^*}{\partial r_P}\right|_{r_p=R_p} = k_m(C_b - C_L|_{r_p=R_p}) \quad (7)$$

Another important condition is the local equilibrium between the concentration of the solute in the liquid and solid phase inside the particle, which is assumed to occur instantaneously, and it is expressed by the Langmuir adsorption isotherm (Eq. 8). The latter is used to evaluate the solute concentration in the solid (C_S) at the equilibrium.

$$C_S(t,r_p) = C_s^* b \frac{C_L(t,r_p)}{1+bC_L(t,r_p)} \quad (8)$$

The simultaneous solution of partial differential equations (PDEs), ordinary differential equations (ODEs) and algebraic equations (AEs) is rather difficult to perform. The method of lines, in particular the second order centered finite difference method, was adopted for discretizing the coordinate in 100 points thus converting the problem into a system of ODEs to obtain bulk concentration profile vs time. The model equations were implemented in g gPROMS ModelBuilder v.4.0 to perform all the calculations and to estimate the values of the surface diffusivity D_S and the tortuosity factor τ by submitting the experimental data to non-linear regression analysis. A list of the input parameters for the model is reported in Table 2. It should be noted that the external mass transfer coefficient k_m was fixed to a large value since the system was not limited by the fluid-solid mass transfer as discussed later.

Table 2. Input parameters for the model.

Symbol	Value	Unit
R_P	27.6×10^{-6}	m
s	2	-
a_{sp}	1.09×10^{5}	m^{-1}
ε	0.26	-
ρ_{solid}	943	kg m^{-3}
k_m	10.0	m s^{-1}
D_0	6.06×10^{-10}	m^2 s^{-1}

3. Results and discussions

3.1 Characterization

Figure 1 presents the WAXD patterns of the four types of metakaolin-based geopolymers synthesized. It can be observed that the samples are mostly amorphous with some diffraction peaks due to the presence of unreacted kaolinite, quartz and anatase that were already present in the starting metakaolins (see Figure S.5) and to some trona (sodium hydrogen carbonate hydrate) formed during reaction.

SEM images shown in Figure 2 describe the morphology of the tested samples. In all cases (Figure 2A-D), the morphology is typical of a geopolymeric material. In particular, a rather homogeneous and continuous structure is observed, with some small fractures most likely due to the mechanical stress to which the sample was subjected to obtain a fresh fracture surface to be observed by SEM. The lamellar crystals of unreacted kaolinite (detectable also in the X-ray pattern reported in Figure 1) are still evident and can be identified thanks to their distinctive morphology. Finally, the high-magnification images (Figure 2A'-D') point out also the typical fine morphology of geopolymeric samples, i.e. characterized by the presence of a sort of nanometric spheres deriving from the gel phase that the geopolymer undergoes during the polycondensation process[33,39].

The results of the surface area, pore size, and pore volume for the tested adsorbents are listed in Table 3 where data relative to commercial activated carbon used as reference material are reported too. As apparent, the geopolymer based adsorbent is characterized by a surface area that is at least one order of magnitude lower than the commercial activated carbon. As far as pore dimensions, in the case of commercial activated carbon we found an average pore volume of around 0.75 cm^3/g while in the case of geopolymer samples, average volume ranged from 0.2 to 0.4 cm^3/g, thus being around ¼ to ½ in respect to that of activated carbon.

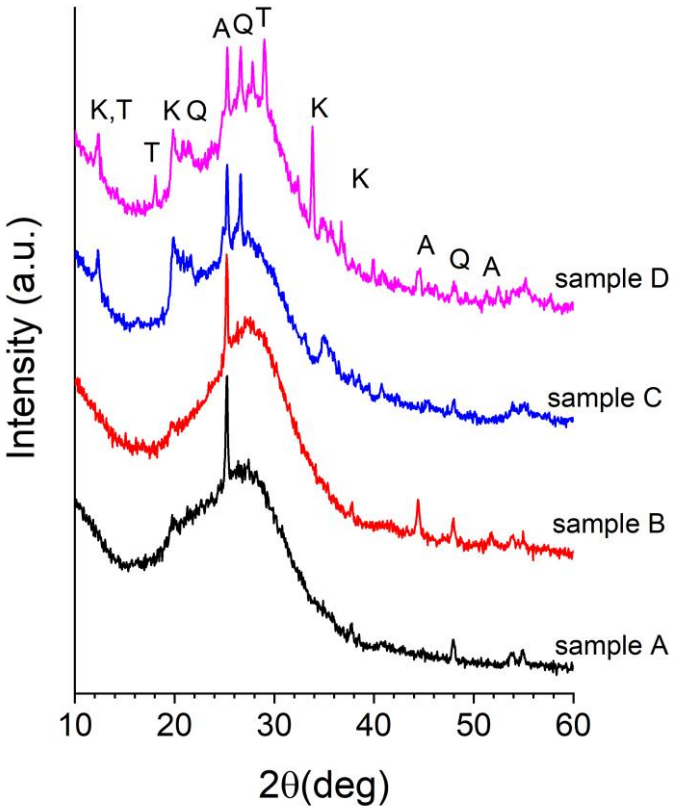

258

259 **Figure 1.** WAXD patterns of the geopolymers A, B, C, and D. Main diffraction peaks of the

260 crystalline phases have been indicated: A – anatase (01-070-7348); K – kaolinite (01-080-0886); Q-

261 quartz (01-083-0539), T- trona (00-001-1077).

262

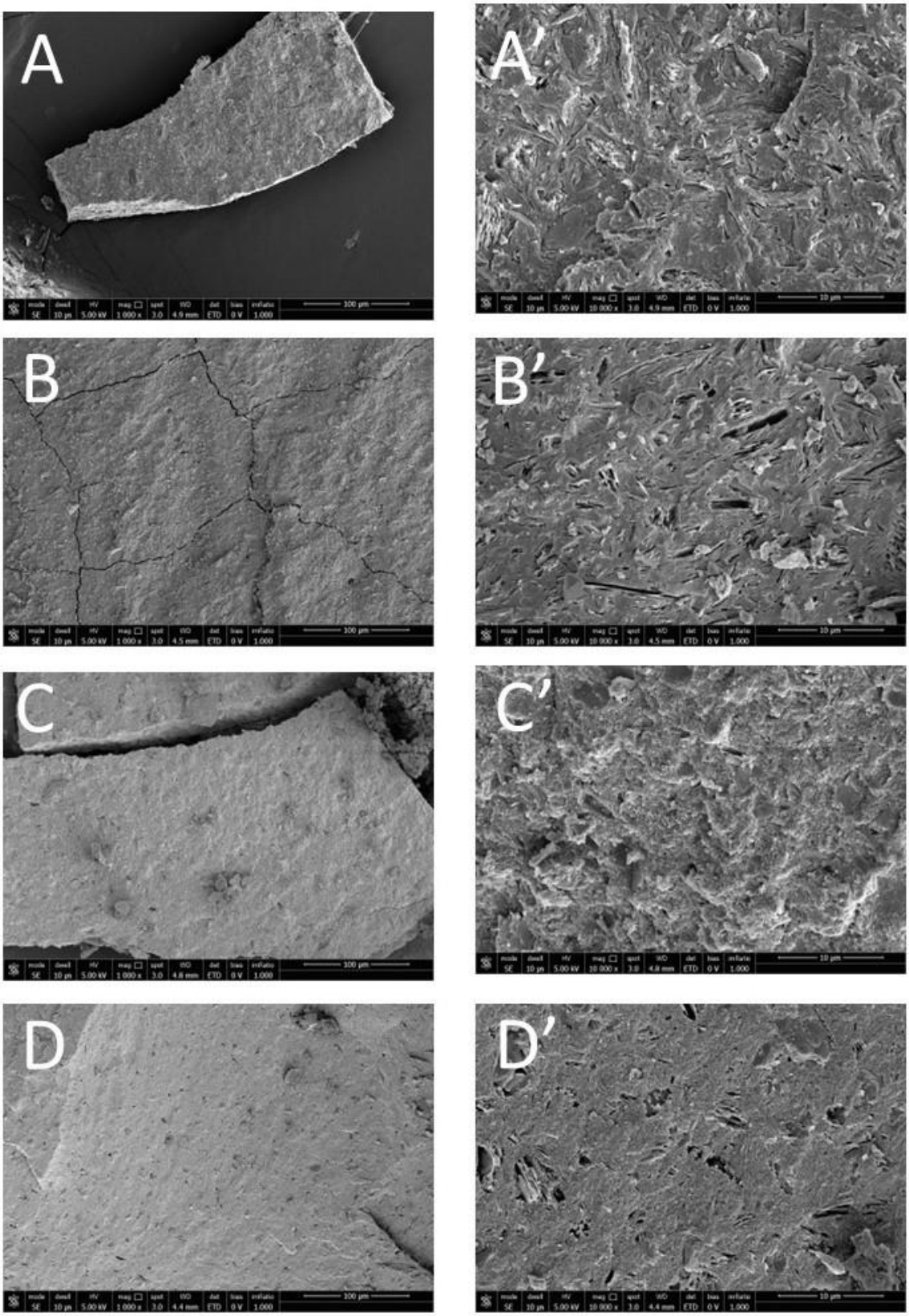

263

264 **Figure 2.** SEM images of fresh fracture surfaces of geopolymers A, B, C, and D at different

265 magnifications: A, B, C, D 1000x; A', B', C', D' 10000x.

266

Table 3. Textural properties of the adsorbents.

Geopolymer	Surface area [$m^2\ g^{-1}$]	Average pore volume [$cm^3\ g^{-1}$]	Si/Al [mol mol^{-1}]
Type A	51	0.371	1.51
Type B	44	0.186	1.74
Type C	43	0.256	1.64
Type D	34	0.237	1.89
Activated carbon	650	0.748	-

3.1 Screening tests

The adsorption tests conducted using geopolymers treated at different pH levels allowed the identification of the ideal pH conditions for maximum adsorption capacity. On the basis of the obtained results (see Figure S.3), further adsorption experiments were carried out at pH=7, which is a typical pH value found in real industrial wastewater containing methylene blue.

Each geopolymer was subjected to adsorption experiment to evaluate the adsorption performance of the four types of geopolymers, under identical experimental conditions (T= 30°C, C_0=8.02×10^{-2} mol m^{-3}; ρ_{bulk}= 0.50 kg m^{-3}, v=450 rpm, pH= 7). The uptake (q_{ads}) of MB for the four synthetic geopolymers is shown in Figure 3. Type A geopolymer was selected for the kinetic investigation since it displayed the highest uptake and affinity towards MB in comparison with types B, C, and D. This could be explained by taking into account the chemical structure of geopolymers (schematically reported in Figure S.4), consisting in a polyanionic network able to realize significant electrostatic interactions with the cationic MB. Thus, since Type A geopolymer is characterized not only by the highest surface area and pore volume between the studied samples (see Table 3), but also by the lower Si/Al ratio, it is likely to expect that it has the greatest adsorbing affinity towards positively charged pollutants, as MB.

Furthermore, the adsorption capacity of type A geopolymer was compared with commercial activated carbon under the same operational conditions. Type A geopolymer has a surface area of 51 $m^2\ g^{-1}$ while activated carbon has a surface area of 650 $m^2\ g^{-1}$, which is 10 times larger. For this reason, it is

289 considered more appropriate to normalize the q_{ads} results based on the surface area of the adsorbent
290 (Figure 4). It is evident that the adsorption capacity towards methylene blue of the type A geopolymer
291 is significantly higher than that of activated carbon for the same surface area. The obtained results
292 are proof of the great potential of this novel adsorbent in the removal of cationic dyes from
293 wastewater.

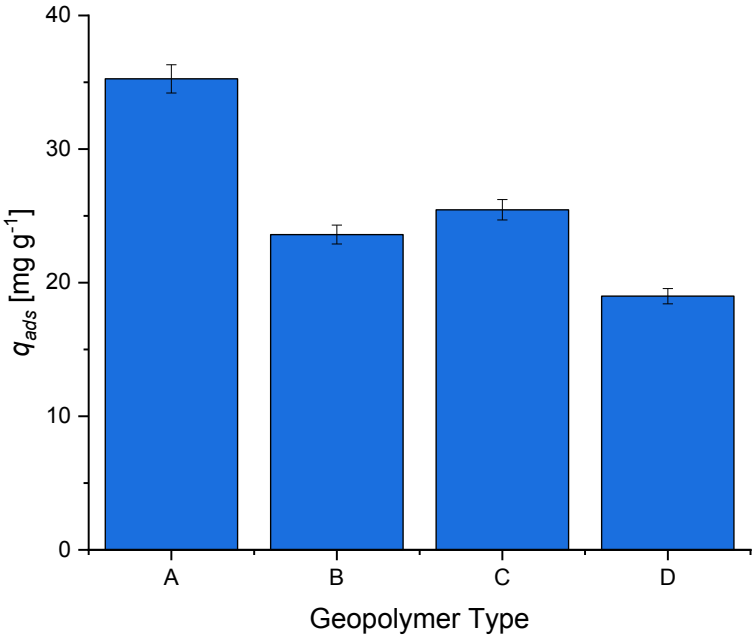

294

295 **Figure 3.** Adsorption uptake of MB by using different synthetic geopolymers.

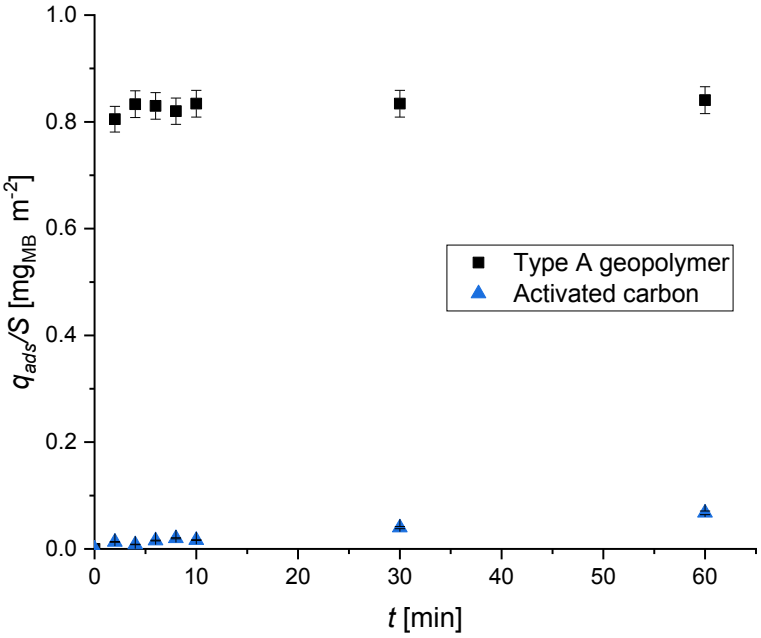

296

297 **Figure 4.** Adsorption uptake of MB normalized by the surface area of the adsorbent.

3.2 Adsorption isotherms

To investigate the adsorption capacity of the Type A geopolymer and to determine the corresponding adsorption isotherm, experiments were performed at three different temperatures i.e., 30, 40 and 50 °C. The experimental results of adsorption were fitted using both Langmuir and Freundlich adsorption isotherm models, to describe the trend of C_S vs C_B and to understand the equilibrium phenomena behind the adsorption process. The results, shown in Figure 5, clearly indicate that the experimental data were best fitted by the Langmuir isotherm. Moreover, the plateau values of concentration, collected from the kinetic experiments, match the Langmuir fitting line. According to the Langmuir model, the adsorption of the adsorbate is limited to a monolayer assuming a homogeneous adsorption process with no interaction between the adsorbed molecules. The mathematical expression of Langmuir isotherm is reported in Eq. 8. The estimated model parameters are shown in Table 4 along with the 95% confidence intervals.

Table 4. Estimated adsorption parameters of Langmuir model.

T [°C]	C_S^* [mol m^{-3}]	b [m^3 mol^{-1}]
30	120±10	1900±500
40	130±10	1800±400
50	134±3	1200±100

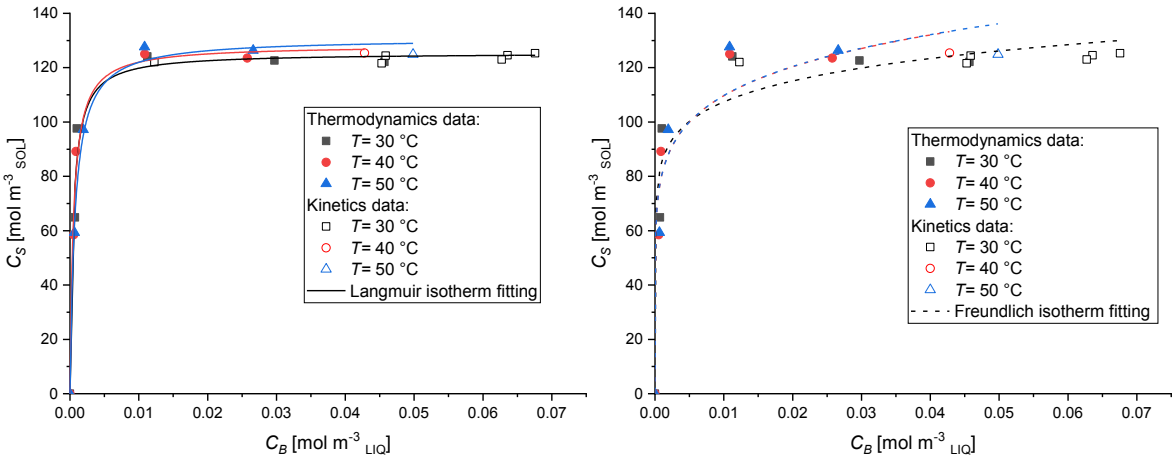

Figure 5. (a) Langmuir and (b) Freundlich isotherm plots for the adsorption of MB dye on Type A geopolymer at different temperatures.

Table 5 summarizes the calculated values of key thermodynamic parameters which are $\Delta G°$, $\Delta H°$, and $\Delta S°$ at different temperatures, i.e., 303, 313, and 323 K of the adsorption of MB onto Type A geopolymer. The thermodynamic parameters were estimated according to Eqs 9 – 10 [51,52].

$$\ln b = \frac{\Delta S^{\circ}}{R} - \frac{\Delta H^{\circ}}{RT} \quad (9)$$

$$\Delta G^{\circ} = -RT \ln K_C \quad (10)$$

where, b is the Langmuir adsorption parameter ($m^3\ mol^{-1}$), $\Delta G°$ (kJ mol^{-1}) is the activation Gibbs free energy, $\Delta H°$ (kJ mol^{-1}) is the change in enthalpy, $\Delta S°$ (kJ mol^{-1} K^{-1}) is the change in entropy, R is the ideal gas constant (8.314 J mol^{-1} K^{-1}), and T is the absolute temperature (K).

The obtained thermodynamic parameters are listed in Table 5. The negative values of $\Delta G°$ showed that the adsorption process is spontaneous and MB molecules have high affinity and uptake onto geopolymer Type A [53]. On the other hand, the negative value of $\Delta H°$ indicated that the adsorption process was relatively exothermic, this may be due to the destruction of binding sites between MB dye and the geopolymer. In this study, $\Delta H°$ is lower than 40 kJ/mol confirming that the adsorption is mainly physical in nature [42,53,54]. The positive value of $\Delta S°$ supports the randomness of the adsorbent surface after adsorption which is beneficial for spontaneous adsorption process [53].

Table 5. Kinetic and thermodynamic parameters for the adsorption of MB using on Type A geopolymer.

T [K]	$\Delta H°$ [kJ/mol]	$\Delta S°$ [kJ/(mol K)]	$\Delta G°$ [kJ/mol]	R^2
303			-19.02	
313	-18.54	0.25	-19.50	0.99
323			-19.04	

3.2 Adsorption kinetics

Evaluation of adsorption kinetics is important as it provides insights about the adsorption mechanism. In this section, the obtained results are reported in terms of the bulk liquid concentration of the MB normalized by the initial concentration in the solution (C_B/C_0) as a function of the time (t). The adsorption kinetics of methylene blue over Type A geopolymer was studied at different experimental conditions (listed in Table S4) by varying the stirring rate, the initial concentration of the dye, the adsorbent bulk density, and the temperature.

Figure 6 shows the concentration profiles at different stirring rates v. The curves are overlapped and a common uptake value of 50 % is obtained at different v, clearly indicating the absence of external mass transfer limitations to the kinetics of adsorption and the irrelevance of this effect. The latter justifies the choice of the authors to fix the fluid solid mass transfer coefficient k_m to a large value during the simulation activity.

The effect of the initial concentration of MB is shown in Figure 7. It can be noticed that the higher the initial concentration of MB, the lower the adsorption efficiency. This result can be considered in line with the assumption of a monolayer adsorption mechanism according to the Langmuir model.

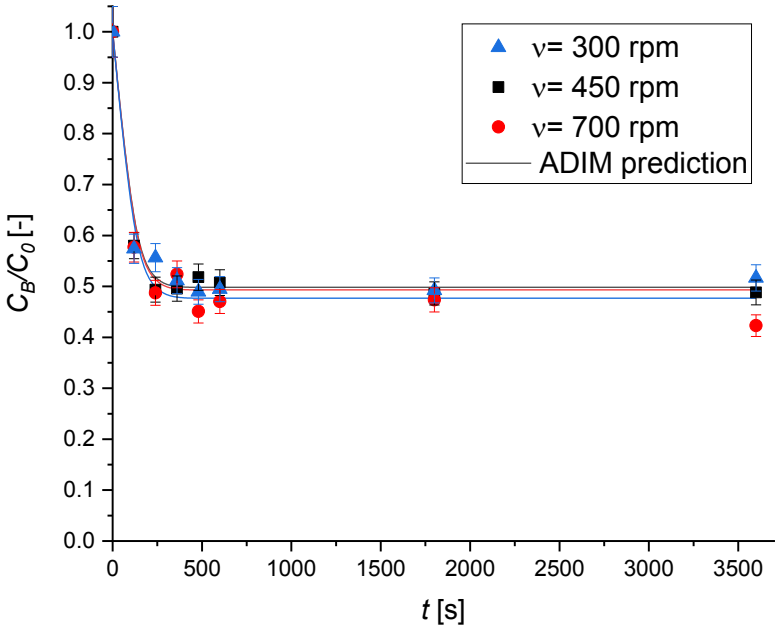

351

352 **Figure 6.** The effect of the stirring rate on the methylene blue adsorption kinetics over Type A

353 geopolymer. Experimental conditions are: T=30°C; C_0=8.02×10^{-2} mol m^{-3}; ρ_{bulk}= 0.50 kg m^{-3}.

354

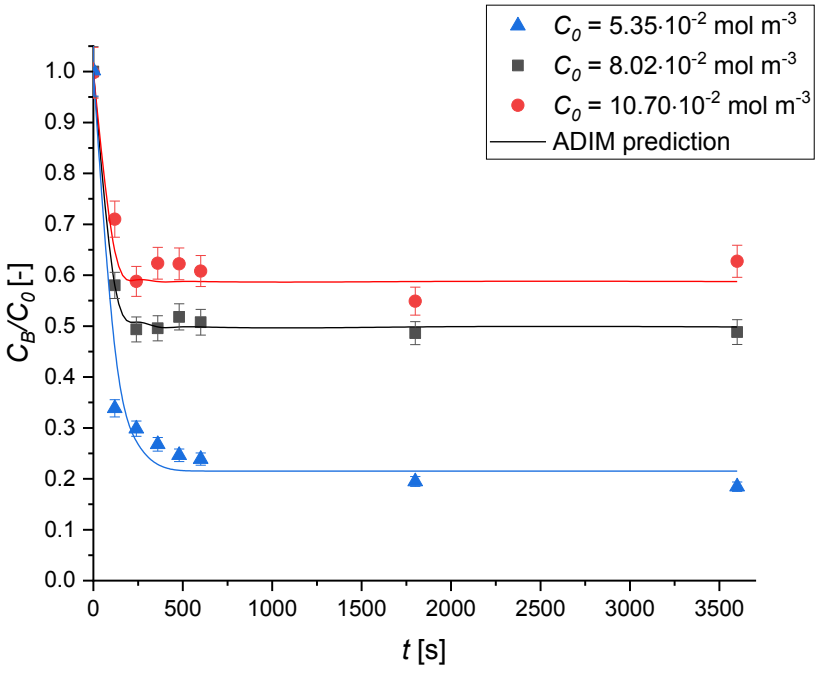

355

356 **Figure 7.** The effect of the initial concentration on the methylene blue adsorption kinetics over

357 Type A geopolymer. Experimental conditions are: T=30°C; v= 450 rpm; ρ_{bulk}= 0.50 kg m^{-3}.

The effect of the adsorbent bulk density on the adsorption kinetics was studied by varying the amount of the geopolymer added to the MB solution as shown in Figure 8.

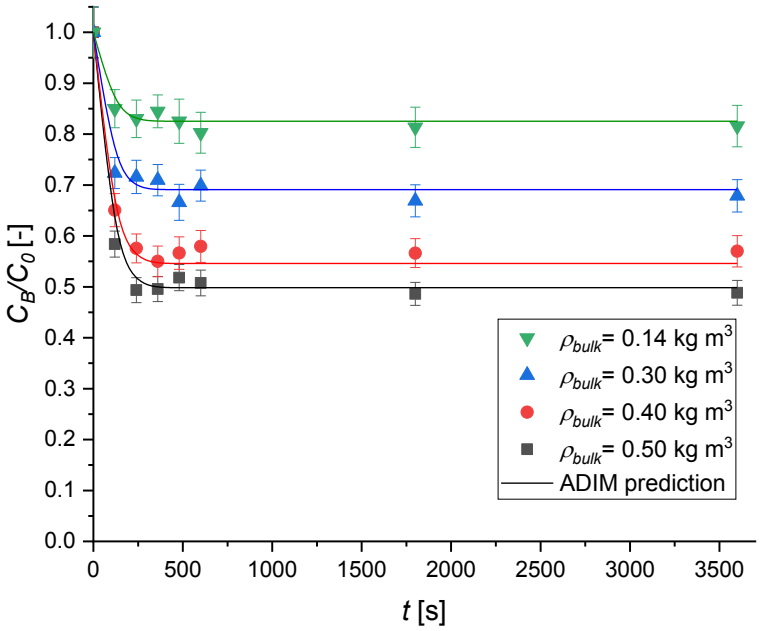

Figure 8. The effect of the adsorbent bulk density on the methylene blue adsorption kinetics over Type A geopolymer. Experimental conditions are: T=30°C; v= 450 rpm; C_0= 8.02×10^{-2} mol m^{-3}.

It is evident that using higher loading of solid increases the adsorption kinetics. In fact, the slope of the curves is higher, thus the adsorption is faster, by increasing the adsorbent bulk density. The uptake of the dye on the solid increases from 15 to 50 % by changing ρ_{bulk} from 0.14 to 0.50 kg m^{-3}.

In the end, kinetic experiments at different T were carried out to study the effect of temperature. The obtained results are presented in Figure 9 and they agree with what was observed in the adsorption isotherm study. It is seen that the temperature does not have a significant effect on the removal efficiency of MB and no appreciable improvement on the adsorption kinetics and solute uptake was noted.

The experimental data were analyzed by nonlinear regression, and it was possible to estimate the values of the tortuosity of the particles τ and that of the surface diffusivity D_S. The latter is a

temperature-dependent parameter so, it was necessary to determine its value at the different temperatures. The results of the parameter estimation are listed in Table 6.

The dependence of surface diffusivity from temperature can be expressed by an Arrhenius-like equation (Eq. 12)[47]. The estimated values of D_S are plotted against the temperature in Figure 10.

$$D_S = D_{S,0} \exp\left(-\frac{E_s}{RT}\right) \tag{12}$$

From the fitting of the values of D_S vs T, a surface activation energy E_S of 35±5 kJ/mol is obtained.

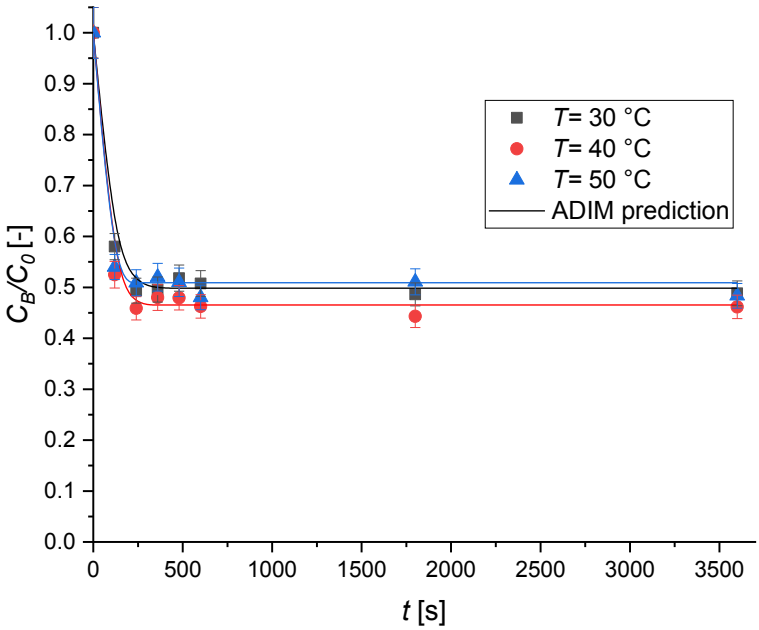

Figure 9. The effect of the temperature on the methylene blue adsorption kinetics over Type A geopolymer. Experimental conditions were set as: v= 450 rpm; C_0= 8.02×10^{-2} mol m^{-3}, ρ_{bulk}= 0.50 kg m^{-3}.

384 **Table 6.** Estimated parameters with statistical analysis.

PARAMETER	*T*=30° C	*T*=40° C	*T*=50° C
Ds×10^{13} [m^2 s^{-1}]	1.1±0.1	1.6±0.4	2.6±0.2
τ [-]		5±1	

385

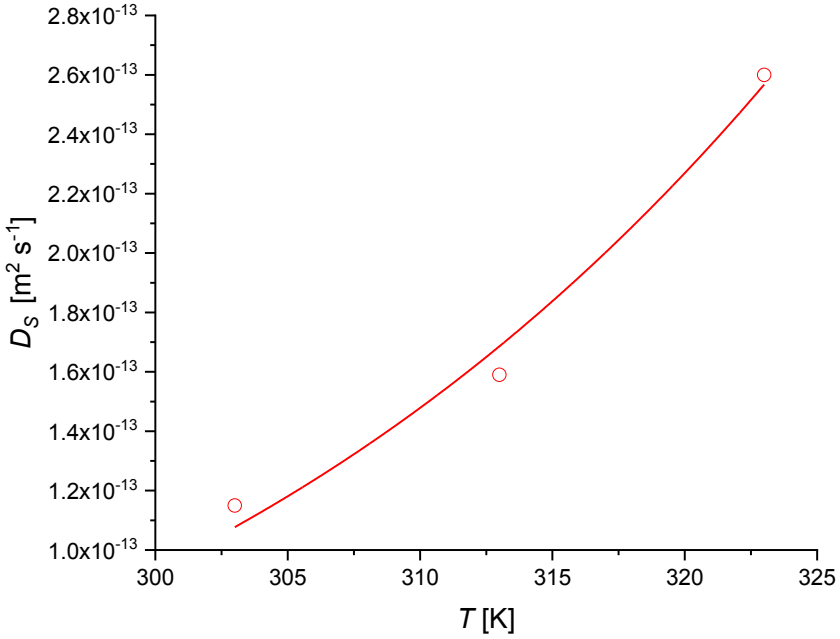

386

387 **Figure 10.** Surface diffusion coefficient trend as a function of temperature.

388

389 It must be underlined that a good fitting is obtained in every case, thus the ADIM was able to describe
390 the behavior of the system under the investigated conditions and to provide extended kinetics
391 information. This was further confirmed by the parity plot displayed in Figure 11. It shows the
392 agreement between the calculated and the experimental data in a confidence interval of ± 10%. In
393 addition, the overall correlation factor R^2 is equal to 0.99.

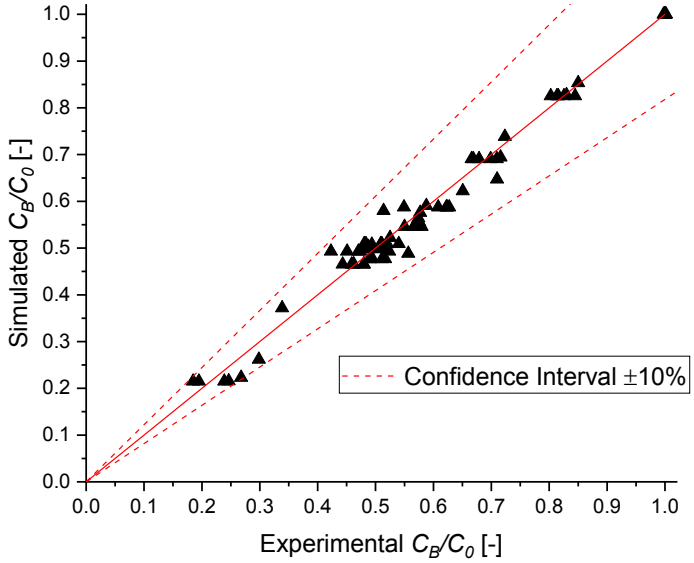

394

395 **Figure 11.** Parity plot of methylene blue normalized concentration.

396

4. Conclusions

In this work, metakaolin-based geopolymers were synthesized and applied for the removal of MB as a cationic model dye. Four different types of geopolymers were synthesized with different molar ratios of Si/Al. Multiple analytical tools were applied in the characterization of the synthesized geopolymers, confirming the formation of geopolymer particles with amorphous structure and morphology. Screening tests for the four types of geopolymers alluded that the geopolymer of type A has the highest adsorption capacity with the highest uptake and affinity towards MB. Moreover, the adsorption capacity of the type A geopolymer towards MB was significantly higher than that of activated carbon for the same surface area, owing to the electrostatic interactions between the cationic dye and the geopolymer, and the unique structural properties of these geopolymers. Subsequently, an extensive kinetic and equilibrium study was carried out in batch experiments to explore the effect of the main operation conditions such as temperature, solid bulk density, initial concentration of MB, and agitation speed on the adsorption kinetics of MB onto Type A geopolymer. Langmuir model showed the best fitting to the adsorption equilibrium indicating the strong bond between MB and Type A geopolymer and indicating that the adsorption process can be described as monolayer adsorption with homogeneous surface sites and adsorption energies. The ADIM model provided insights into the diffusion mechanism of MB through the determination of k_m and D_S values, parameters needed to design an adsorption column working in flow. Additionally, the thermodynamic analysis indicated that the adsorption of MB onto type A geopolymer was exothermic and spontaneous. Lastly, it is concluded from the results of this study that these geopolymers have good potential as adsorbent material for use in wastewater treatment applications.

List of symbols

a_{sp}	geometric specific area, $m^2 \cdot m^{-3}$
b	Langmuir adsorption parameter, $m^3 \cdot mol^{-1}$
c_0	adsorbate initial concentration, $mg \cdot L^{-1}$
C_0	adsorbate initial concentration, $mol \cdot m^{-3}$
$C_{adsorbent}$	adsorbent concentration, $mg \cdot L^{-1}$
C_B	solute bulk concentration, $mol \cdot m^{-3}$
c_e	adsorbate equilibrium concentration, $mg \cdot L^{-1}$
C_L	solute concentration in the liquid of the pores, $mol \cdot m^{-3}$
C_S	solute concentration in the solid, $mol \cdot m^{-3}$
C_S^*	saturation solute solid concentration, $mol \cdot m^{-3}$
D_0	molecular diffusivity, $m^2 \cdot s^{-1}$
D_P	pore diffusivity based on the cross-sectional area, $m^2 \cdot s^{-1}$
D_S	surface diffusivity, $m^2 \cdot s^{-1}$
k_m	mass transfer coefficient, $m \cdot s^{-1}$
MB	Methylene blue
MW	Molecular Weight, $mol\ g^{-1}$
q_{ads}	adsorbed amount at time t, $mol\ kg^{-1}$
r_P	particle radial coordinate, m
R_P	particle radius, m
s	shape factor, -
S	specific surface area, $m^2\ g^{-1}$
t	time, s
T	temperature, K
V_P	particle volume, m^3

443 w_{ADS} adsorbent mass, g

444

445 ***Greek symbols***

446 ε solid particle porosity, -

447 ε' liquid bulk-solid phase volumetric ratio, -

448 ρ_{bulk} solid bulk density, kg m^{-3}

449 ρ_{solid} solid density, kg m^{-3}

450 τ tortuosity factor, -

Author Contributions

The main conceptual ideas were drawn by Vincenzo Russo, Oreste Tarallo, and Martino Di Serio. The experimental work was conducted by Maryam Hmoudah, Michela De Luca, and Rosanna Paparo. The data elaboration was made by Michele Emanuele Fortunato, Oreste Tarallo and Vincenzo Russo. Michele Emanuele Fortunato, Vincenzo Russo, Oreste Tarallo and Maryam Hmoudah wrote the original draft of the manuscript. Vincenzo Russo, Oreste Tarallo, Claudio Ferone, Giuseppina Roviello, and Riccardo Tesser conducted the work conceptualization, data curation, and formal analysis. Maryam Hmoudah and Vincenzo Russo performed thermodynamics analysis. Martino Di Serio contributed to writing review, editing, funding, and supervision. The final draft was revised by all the authors.

Acknowledgments

The fellowship provided by Faculty for the Future Program—Schlumberger Foundation to Maryam Hmoudah is deeply acknowledged and appreciated.

Funding

No funds were used to conduct this study.

References

[1] A. Tebeje, Z. Worku, T.T.I. Nkambule, J. Fito, Adsorption of chemical oxygen demand from textile industrial wastewater through locally prepared bentonite adsorbent, International Journal of Environmental Science and Technology. 19 (2022) 1893–1906. https://doi.org/10.1007/S13762-021-03230-4/FIGURES/8.

[2] V. Russo, M. Hmoudah, F. Broccoli, M.R. Iesce, O.-S. Jung, M. Di Serio, Applications of Metal Organic Frameworks in Wastewater Treatment: A Review on Adsorption and Photodegradation, Frontiers in Chemical Engineering. 2 (2020) 581487. https://doi.org/10.3389/FCENG.2020.581487.

[3] S. Manikandan, R. Subbaiya, M. Saravanan, M. Ponraj, M. Selvam, A. Pugazhendhi, A critical review of advanced nanotechnology and hybrid membrane based water recycling, reuse, and wastewater treatment processes, Chemosphere. 289 (2022) 132867. https://doi.org/10.1016/J.CHEMOSPHERE.2021.132867.

[4] N. Gallucci, M. Hmoudah, E. Martinez, A. El-Qanni, M. Di Serio, L. Paduano, G. Vitiello, V. Russo, Photodegradation of ibuprofen using CeO2 nanostructured materials: Reaction kinetics, modeling, and thermodynamics, J Environ Chem Eng. 10 (2022) 107866. https://doi.org/10.1016/J.JECE.2022.107866.

[5] J.O. Eniola, R. Kumar, M.A. Barakat, J. Rashid, A review on conventional and advanced hybrid technologies for pharmaceutical wastewater treatment, J Clean Prod. 356 (2022) 131826. https://doi.org/10.1016/J.JCLEPRO.2022.131826.

[6] B.S. Rathi, P.S. Kumar, Application of adsorption process for effective removal of emerging contaminants from water and wastewater, Environmental Pollution. 280 (2021) 116995. https://doi.org/10.1016/J.ENVPOL.2021.116995.

[7] S. Garg, Z.Z. Chowdhury, A.N.M. Faisal, N.P. Rumjit, P. Thomas, Impact of Industrail Wastewater on Environment and Human Health, in: Advanced Industrial Wastewater

493 Treatment and Reclamation of Water , 2021: pp. 197–209.
494 https://link.springer.com/bookseries/7487.
495 [8] R. Pratap Singh, P. Kumar Singh, R. Gupta, R. Lakhan Singh, R.P. Singh, P.K. Singh, R.
496 Gupta, R.L. Singh, Treatment and Recycling of Wastewater from Textile Industry, (2019)
497 225–266. https://doi.org/10.1007/978-981-13-1468-1_8.
498 [9] K. Yang, Y. Liu, Y. Li, Z. Cao, C. Zhou, Z. Wang, X. Zhou, S.A. Baig, X. Xu, Applications
499 and characteristics of Fe-Mn binary oxides for Sb(V) removal in textile wastewater: Selective
500 adsorption and the fixed-bed column study, Chemosphere. 232 (2019) 254–263.
501 https://doi.org/10.1016/J.CHEMOSPHERE.2019.05.194.
502 [10] G. Crini, Non-conventional low-cost adsorbents for dye removal: A review, Bioresour
503 Technol. 97 (2006) 1061–1085. https://doi.org/10.1016/J.BIORTECH.2005.05.001.
504 [11] C.I. Pearce, J.R. Lloyd, J.T. Guthrie, The removal of colour from textile wastewater using
505 whole bacterial cells: A review, Dyes and Pigments. 58 (2003) 179–196.
506 https://doi.org/10.1016/S0143-7208(03)00064-0.
507 [12] Y.M. Slokar, A. Majcen Le Marechal, Methods of decoloration of textile wastewaters, Dyes
508 and Pigments. 37 (1998) 335–356. https://doi.org/10.1016/S0143-7208(97)00075-2.
509 [13] W. Delée, C. O'Neill, F.R. Hawkes, H.M. Pinheiro, Anaerobic treatment of textile effluents:
510 A review, Journal of Chemical Technology and Biotechnology. 73 (1998) 323–335.
511 https://doi.org/10.1002/(SICI)1097-4660(199812)73:4<323::AID-JCTB976>3.0.CO;2-S.
512 [14] S.M. Ghoreishi, R. Haghighi, Chemical catalytic reaction and biological oxidation for
513 treatment of non-biodegradable textile effluent, Chemical Engineering Journal. 95 (2003) 163–
514 169. https://doi.org/10.1016/S1385-8947(03)00100-1.
515 [15] M.F.R. Pereira, S.F. Soares, J.J.M. Órfão, J.L. Figueiredo, Adsorption of dyes on activated
516 carbons: influence of surface chemical groups, Carbon N Y. 41 (2003) 811–821.
517 https://doi.org/10.1016/S0008-6223(02)00406-2.

[16] P.C. Vandevivere, R. Bianchi2, W. Verstraete1, Review Treatment and Reuse of Wastewater from the Textile Wet-Processing Industry: Review of Emerging Technologies, J. Chem. T Echnol. Biotechnol. 72 (1998) 289–302. https://doi.org/10.1002/(SICI)1097-4660(199808)72:4.

[17] T. Robinson, G. McMullan, R. Marchant, P. Nigam, Remediation of dyes in textile effluent: a critical review on current treatment technologies with a proposed alternative, Bioresour Technol. 77 (2001) 247–255. https://doi.org/10.1016/S0960-8524(00)00080-8.

[18] G. McMullan, C. Meehan, A. Conneely, N. Kirby, T. Robinson, P. Nigam, I.M. Banat, R. Marchant, W.F. Smyth, Microbial decolourisation and degradation of textile dyes, Appl Microbiol Biotechnol. 56 (2001) 81–87. https://doi.org/10.1007/S002530000587.

[19] S. Ibrahim, W.Z. Shuy, H.M. Ang, S. Wang, Preparation of bioadsorbents for effective adsorption of a reactive dye in aqueous solution, Asia-Pacific Journal of Chemical Engineering. 5 (2010) 563–569. https://doi.org/10.1002/APJ.446.

[20] M. Hmoudah, A. El-Qanni, S. Abuhatab, N.N. Marei, A. El-Hamouz, B.J.A. Tarboush, I.H. Alsurakji, H.M. Baniowda, V. Russo, M. Di Serio, Competitive adsorption of Alizarin Red S and Bromocresol Green from aqueous solutions using brookite TiO2 nanoparticles: experimental and molecular dynamics simulation, Environmental Science and Pollution Research. 29 (2022) 77992–78008. https://doi.org/10.1007/s11356-022-21368-7.

[21] M. Toscanesi, V. Russo, A. Medici, A. Giarra, M. Hmoudah, M. Di Serio, M. Trifuoggi, Heterogeneous Photodegradation for the Abatement of Recalcitrant COD in Synthetic Tanning Wastewater, ChemEngineering. 6 (2022). https://doi.org/10.3390/chemengineering6020025.

[22] K.A. Adegoke, O.S. Bello, Dye sequestration using agricultural wastes as adsorbents, Water Resour Ind. 12 (2015) 8–24. https://doi.org/10.1016/j.wri.2015.09.002.

[23] J. Qiu, P. Fan, Y. Feng, F. Liu, C. Ling, A. Li, Comparison of the adsorption behaviors for methylene blue on two renewable gels with different physical state, Environmental Pollution. 254 (2019) 113117. https://doi.org/10.1016/J.ENVPOL.2019.113117.

544 [24] L.Y. Jun, R.R. Karri, N.M. Mubarak, L.S. Yon, C.H. Bing, M. Khalid, P. Jagadish, E.C.
545 Abdullah, Modelling of methylene blue adsorption using peroxidase immobilized
546 functionalized Buckypaper/polyvinyl alcohol membrane via ant colony optimization,
547 Environmental Pollution. 259 (2020) 113940.
548 https://doi.org/10.1016/J.ENVPOL.2020.113940.
549 [25] V.K. Garg, M. Amita, R. Kumar, R. Gupta, Basic dye (methylene blue) removal from
550 simulated wastewater by adsorption using Indian Rosewood sawdust: a timber industry waste,
551 Dyes and Pigments. 63 (2004) 243–250. https://doi.org/10.1016/J.DYEPIG.2004.03.005.
552 [26] B. Li, J. Guo, K. Lv, J. Fan, Adsorption of methylene blue and Cd(II) onto maleylated modified
553 hydrochar from water, Environmental Pollution. 254 (2019) 113014.
554 https://doi.org/10.1016/J.ENVPOL.2019.113014.
555 [27] S. Abuhatab, A. El-Qanni, N.N. Marei, M. Hmoudah, A. El-Hamouz, Sustainable competitive
556 adsorption of methylene blue and acid red 88 from synthetic wastewater using NiO and/or
557 MgO silicate based nanosorbcats: experimental and computational modeling studies, RSC
558 Adv. 9 (2019) 35483–35498. https://doi.org/10.1039/C9RA07001J.
559 [28] A. El-Qanni, N.N. Nassar, G. Vitale, A. Hassan, Maghemite nanosorbcats for methylene blue
560 adsorption and subsequent catalytic thermo-oxidative decomposition: Computational
561 modeling and thermodynamics studies, J Colloid Interface Sci. 461 (2016) 396–408.
562 https://doi.org/10.1016/J.JCIS.2015.09.041.
563 [29] M. Rafatullah, O. Sulaiman, R. Hashim, A. Ahmad, Adsorption of methylene blue on low-cost
564 adsorbents: A review, J Hazard Mater. 177 (2010) 70–80.
565 https://doi.org/10.1016/j.jhazmat.2009.12.047.
566 [30] M.T. Yagub, T.K. Sen, S. Afroze, H.M. Ang, Dye and its removal from aqueous solution by
567 adsorption: A review, Adv Colloid Interface Sci. 209 (2014) 172–184.
568 https://doi.org/10.1016/J.CIS.2014.04.002.

569 [31] C. Ferone, G. Roviello, F. Colangelo, R. Cioffi, O. Tarallo, Novel hybrid organic-geopolymer
570 materials, Appl Clay Sci. 73 (2013) 42–50. https://doi.org/10.1016/J.CLAY.2012.11.001.
571 [32] G. Roviello, L. Ricciotti, O. Tarallo, C. Ferone, F. Colangelo, V. Roviello, R. Cioffi,
572 Innovative Fly Ash Geopolymer-Epoxy Composites: Preparation, Microstructure and
573 Mechanical Properties, Materials 2016, Vol. 9, Page 461. 9 (2016) 461.
574 https://doi.org/10.3390/MA9060461.
575 [33] G. Roviello, C. Menna, O. Tarallo, L. Ricciotti, C. Ferone, F. Colangelo, D. Asprone, R. di
576 Maggio, E. Cappelletto, A. Prota, R. Cioffi, Preparation, structure and properties of hybrid
577 materials based on geopolymers and polysiloxanes, Mater Des. 87 (2015) 82–94.
578 https://doi.org/10.1016/J.MATDES.2015.08.006.
579 [34] G. Roviello, E. Chianese, C. Ferone, L. Ricciotti, V. Roviello, R. Cioff, O. Tarallo, Hybrid
580 Geopolymeric Foams for the Removal of Metallic Ions from Aqueous Waste Solutions,
581 Materials 2019, Vol. 12, Page 4091. 12 (2019) 4091. https://doi.org/10.3390/MA12244091.
582 [35] G. Roviello, C. Menna, O. Tarallo, L. Ricciotti, F. Messina, C. Ferone, D. Asprone, R. Cioffi,
583 Lightweight geopolymer-based hybrid materials, Compos B Eng. 128 (2017) 225–237.
584 https://doi.org/10.1016/J.COMPOSITESB.2017.07.020.
585 [36] F. Messina, C. Ferone, F. Colangelo, R. Cioffi, Low temperature alkaline activation of
586 weathered fly ash: Influence of mineral admixtures on early age performance, Constr Build
587 Mater. 86 (2015) 169–177. https://doi.org/10.1016/J.CONBUILDMAT.2015.02.069.
588 [37] J. Zhao, L. Tong, B. Li, T. Chen, C. Wang, G. Yang, Y. Zheng, Eco-friendly geopolymer
589 materials: A review of performance improvement, potential application and sustainability
590 assessment, J Clean Prod. 307 (2021). https://doi.org/10.1016/j.jclepro.2021.127085.
591 [38] A.L. Yadav, V. Sairam, K. Srinivasan, L. Muruganandam, Synthesis and characterization of
592 geopolymer from metakaolin and sugarcane bagasse ash, Constr Build Mater. 258 (2020).
593 https://doi.org/10.1016/j.conbuildmat.2020.119231.

[39] P. Duxson, S.W. Mallicoat, G.C. Lukey, W.M. Kriven, J.S.J. van Deventer, The effect of alkali and Si/Al ratio on the development of mechanical properties of metakaolin-based geopolymers, Colloids Surf A Physicochem Eng Asp. 292 (2007) 8–20. https://doi.org/10.1016/J.COLSURFA.2006.05.044.

[40] I. Perná, M. Šupová, T. Hanzlíček, A. Špaldoňová, The synthesis and characterization of geopolymers based on metakaolin and high LOI straw ash, Constr Build Mater. 228 (2019). https://doi.org/10.1016/j.conbuildmat.2019.116765.

[41] Y. Ji, F. Xu, W. Wei, H. Gao, K. Zhang, G. Zhang, Y. Xu, P. Zhang, Efficient and fast adsorption of methylene blue dye onto a nanosheet MFI zeolite, J Solid State Chem. 295 (2021) 121917. https://doi.org/10.1016/J.JSSC.2020.121917.

[42] Z. Bingül, Determination of affecting parameters on removal of methylene blue dyestuff from aqueous solutions using natural clay: Isotherm, kinetic, and thermodynamic studies, J Mol Struct. 1250 (2022). https://doi.org/10.1016/j.molstruc.2021.131729.

[43] A. Kausar, S.U. Rehman, F. Khalid, A. Bonilla-Petriciolet, D.I. Mendoza-Castillo, H.N. Bhatti, S.M. Ibrahim, M. Iqbal, Cellulose, clay and sodium alginate composites for the removal of methylene blue dye: Experimental and DFT studies, Int J Biol Macromol. 209 (2022) 576–585. https://doi.org/10.1016/j.ijbiomac.2022.04.044.

[44] M.R. Islam, M.G. Mostafa, Adsorption kinetics, isotherms and thermodynamic studies of methyl blue in textile dye effluent on natural clay adsorbent, Sustain Water Resour Manag. 8 (2022). https://doi.org/10.1007/s40899-022-00640-1.

[45] M. Loutfi, R. Mariouch, I. Mariouch, M. Belfaquir, M.S. ElYoubi, Adsorption of methylene blue dye from aqueous solutions onto natural clay: Equilibrium and kinetic studies, Mater Today Proc. 72 (2023) 3638–3643. https://doi.org/10.1016/j.matpr.2022.08.412.

[46] S. Selvam, I. Sarkar, Bile salt induced solubilization of methylene blue: Study on methylene blue fluorescence properties and molecular mechanics calculation, J Pharm Anal. 7 (2017) 71–75. https://doi.org/10.1016/J.JPHA.2016.07.006.

620 [47] V. Russo, R. Tesser, M. Trifuoggi, M. Giugni, M. Di Serio, A dynamic intraparticle model for
621 fluid-solid adsorption kinetics, Comput Chem Eng. 74 (2015) 66–74.
622 https://doi.org/10.1016/j.compchemeng.2015.01.001.
623 [48] V. Russo, R. Tesser, D. Masiello, M. Trifuoggi, M. Di Serio, Further verification of adsorption
624 dynamic intraparticle model (ADIM) for fluid-solid adsorption kinetics in batch reactors,
625 Chemical Engineering Journal. 283 (2016) 1197–1202.
626 https://doi.org/10.1016/j.cej.2015.08.066.
627 [49] V. Russo, D. Masiello, M. Trifuoggi, M. Di Serio, R. Tesser, Design of an adsorption column
628 for methylene blue abatement over silica: From batch to continuous modeling, Chemical
629 Engineering Journal. 302 (2016) 287–295. https://doi.org/10.1016/j.cej.2016.05.020.
630 [50] C.R. Wilke, P. Chang, Correlation of diffusion coefficients in dilute solutions, AIChE Journal.
631 1 (1955) 264–270. https://doi.org/10.1002/AIC.690010222.
632 [51] H. Chandarana, P. Senthil Kumar, M. Seenuvasan, M. Anil Kumar, Kinetics, equilibrium and
633 thermodynamic investigations of methylene blue dye removal using Casuarina equisetifolia
634 pines, Chemosphere. 285 (2021) 131480.
635 https://doi.org/10.1016/J.CHEMOSPHERE.2021.131480.
636 [52] Y. Bulut, H. Aydin, A kinetics and thermodynamics study of methylene blue adsorption on
637 wheat shells, Desalination. 194 (2006) 259–267.
638 https://doi.org/10.1016/J.DESAL.2005.10.032.
639 [53] H.N. Tran, Improper Estimation of Thermodynamic Parameters in Adsorption Studies with
640 Distribution Coefficient K D(q e/ C e) or Freundlich Constant (K F): Considerations from the
641 Derivation of Dimensionless Thermodynamic Equilibrium Constant and Suggestions,
642 Adsorption Science and Technology. 2022 (2022). https://doi.org/10.1155/2022/5553212.
643 [54] S.D.K. Seera, D. Kundu, P. Gami, P.K. Naik, T. Banerjee, Synthesis and characterization of
644 xylan-gelatin cross-linked reusable hydrogel for the adsorption of methylene blue, Carbohydr
645 Polym. 256 (2021). https://doi.org/10.1016/j.carbpol.2020.117520.